Lecture Notes in Mathematics 2212
CIME Foundation Subseries

Angiolo Farina · Lorenzo Fusi
Andro Mikelić · Giuseppe Saccomandi
Adélia Sequeira · Eleuterio F. Toro

Non-Newtonian Fluid Mechanics and Complex Flows

Levico Terme, Italy 2016

Angiolo Farina · Andro Mikelić
Fabio Rosso *Editors*

FONDAZIONE C.I.M.E.
Springer

Lecture Notes in Mathematics 2212

More information about this series at http://www.springer.com/series/304

Fondazione C.I.M.E., Firenze

C.I.M.E. stands for *Centro Internazionale Matematico Estivo*, that is, International Mathematical Summer Centre. Conceived in the early fifties, it was born in 1954 in Florence, Italy, and welcomed by the world mathematical community: it continues successfully, year for year, to this day.

Many mathematicians from all over the world have been involved in a way or another in C.I.M.E.'s activities over the years. The main purpose and mode of functioning of the Centre may be summarised as follows: every year, during the summer, sessions on different themes from pure and applied mathematics are offered by application to mathematicians from all countries. A Session is generally based on three or four main courses given by specialists of international renown, plus a certain number of seminars, and is held in an attractive rural location in Italy.

The aim of a C.I.M.E. session is to bring to the attention of younger researchers the origins, development, and perspectives of some very active branch of mathematical research. The topics of the courses are generally of international resonance. The full immersion atmosphere of the courses and the daily exchange among participants are thus an initiation to international collaboration in mathematical research.

C.I.M.E. Director (2002 – 2014)
Pietro Zecca
Dipartimento di Energetica "S. Stecco"
Università di Firenze
Via S. Marta, 3
50139 Florence
Italy
e-mail: zecca@unifi.it

C.I.M.E. Director (2015 –)
Elvira Mascolo
Dipartimento di Matematica "U. Dini"
Università di Firenze
viale G.B. Morgagni 67/A
50134 Florence
Italy
e-mail: mascolo@math.unifi.it

C.I.M.E. Secretary
Paolo Salani
Dipartimento di Matematica "U. Dini"
Università di Firenze
viale G.B. Morgagni 67/A
50134 Florence
Italy
e-mail: salani@math.unifi.it

CIME activity is carried out with the collaboration and financial support of INdAM (Istituto Nazionale di Alta Matematica)

For more information see CIME's homepage: **http://www.cime.unifi.it**

Angiolo Farina • Lorenzo Fusi • Andro Mikelić •
Giuseppe Saccomandi • Adélia Sequeira •
Eleuterio F. Toro

Non-Newtonian Fluid Mechanics and Complex Flows

Levico Terme, Italy 2016

Angiolo Farina • Andro Mikelić • Fabio Rosso
Editors

In collaboration with

CIRM
CENTRO INTERNAZIONALE
PER LA RICERCA MATEMATICA

Springer

FONDAZIONE CIME
ROBERTO CONTI
CENTRO INTERNAZIONALE MATEMATICO ESTIVO
INTERNATIONAL MATHEMATICAL SUMMER CENTER

Authors

Angiolo Farina
Dipartimento di Matematica e
Informatica “Ulisse Dini”
Università degli Studi di Firenze
Firenze, Italy

Lorenzo Fusi
Dipartimento di Matematica e
Informatica “Ulisse Dini”
Università degli Studi di Firenze
Firenze, Italy

Andro Mikelić
Département de Mathématiques
Institut Camille Jordan
Université Claude Bernard Lyon 1
Villeurbanne, France

Giuseppe Saccomandi
Dipartimento di Ingegneria
Università degli Studi di Perugia
Perugia, Italy

Adélia Sequeira
Department de Matemática
Instituto Superior Técnico
Lisboa, Portugal

Eleuterio F. Toro
Dipartimento di Matematica
University of Trento
Trento, Italy

Editors

Angiolo Farina
Dipartimento di Matematica e
Informatica “Ulisse Dini”
Università degli Studi di Firenze
Firenze, Italy

Andro Mikelić
Département de Mathématiques
Institut Camille Jordan
Université Claude Bernard Lyon 1
Villeurbanne, France

Fabio Rosso
Dipartimento di Matematica e
Informatica “Ulisse Dini”
Università degli Studi di Firenze
Firenze, Italy

ISSN 0075-8434 ISSN 1617-9692 (electronic)
Lecture Notes in Mathematics
C.I.M.E. Foundation Subseries
ISBN 978-3-319-74795-8 ISBN 978-3-319-74796-5 (eBook)
https://doi.org/10.1007/978-3-319-74796-5

Library of Congress Control Number: 2018938092

Mathematics Subject Classification (2010): 92-XX, 35-XX

Printed on acid-free paper

This Springer imprint is published by the registered company Springer International Publishing AG part of Springer Nature.
The registered company address is: Gewerbestrasse 11, 6330 Cham, Switzerland

Preface

CIME activity is carried out with the collaboration and financial support of INdAM (Istituto Nazionale di Alta Matematica), partially supported by the University of Firenze under the Fondi di Ateneo research grants.

The CIME-CIRM Course on "New Trends in Non-Newtonian Fluid Mechanics and Complex Flows" was held in Levico Terme (Italy) from August 29 to September 2, 2016. The course was codirected by Andro Mikelić (Université Claude Bernard Lyon 1, France), Fabio Rosso, and Angiolo Farina (Università di Firenze, Italy).

The course was attended by 32 participants, about half of them not coming from Italy.

All the lecturers tried to emphasize physical and mathematical methods that cross disciplinary boundaries, putting in evidence those aspects of flow problems relevant to biology and industrial processes.

The following topics were treated:

1. Hemorheology: Non-Newtonian Constitutive Models for Blood Flow Simulations (Adélia Sequeira, Instituto Superior Técnico, Lisboa, Portugal)
2. Old problems revisited from new perspectives in implicit theories of fluids (Giuseppe Saccomandi and Luigi Vergori, Università di Perugia, Italy).
3. Lectures on Hyperbolic Equations and their Numerical Approximation (Eleuterio F. Toro, Università di Trento, Italy).
4. An Introduction to the Homogenization Modeling of Non-Newtonian and Electrokinetic Flows in Porous Media (Andro Mikelić, Université Lyon 1, France).
5. Viscoplastic Fluids: Mathematical Modeling and Applications (Angiolo Farina and Lorenzo Fusi, Università di Firenze, Italy).

The focus was largely on non-Newtonian fluids and their applications on blood flow, with some digression to the numerical approximation of hyperbolic equations. Actually, the goal of the course was to present a series of challenging mathematical problems arising in non-Newtonian fluid dynamics. Essentially the lectures focused on (i) mathematical and physical modeling of a variety of problems that address current work and (ii) the numerical and analytical treatment of some of these problems.

Although the course presented a remarkable review of quite advanced problems in non-Newtonian flows and in the mathematics involved, one easily realizes that such a research area is extremely rich and calls for an impressively large variety of mathematical methods.

This volume collects lecture notes of the courses and therefore focuses only on a limited number of problems which, however, are typical in the field of non-Newtonian flows. Such volume can certainly be useful not only to applied mathematicians but also to physicists, biologists, and engineers, who can find in it an overview of the most advanced models and methods.

The first chapter is devoted to the lectures given by Adélia Sequeira. She presented a fascinating and quite difficult lecture about the rheology of the blood and some recent advances in this field (which is very active because of the numerous applications to the circulatory system diseases). The audience was very excited by her colorful slides and videos showing blood flow in very complex geometries such as those seen in aneurysms. She posed stimulating questions about the impact of the most significant non-Newtonian characteristics of blood on its flow behavior. We had exciting afternoon sessions discussing such problems.

Giuseppe Saccomandi gave a series of lectures on implicit constitutive models for the Cauchy stress tensor which provided an excellent complementary view of the subjects treated by Farina and Fusi. He investigated some classical problems in fluid mechanics (such as the onset of Rayleigh–Bénard convection, laminar flows, and flows over an inclined plane) by employing implicit constitutive relations for the stress tensor.

The chapter by Eleuterio F. Toro illustrates some recent techniques for the numerical solution of mathematical equations arising in all areas of physics especially in the mechanics of non-Newtonian fluids. Actually the issues of accurate solutions and efficiency are becoming increasingly important given the growing trend to use mathematical models (PDEs) and the physics they embody. Only very accurate solutions of the PDEs will achieve this and also reveal limitations of the mathematical models (the governing equations and their parameters).

Then we have a chapter by A. Mikelić on the flow of complex fluids (quasi-Newtonian and electrokinetic flows) through porous media (a problem common to many engineering applications). The modeling of filtration was developed exploiting a homogenization technique.

The last chapter, by A. Farina and L. Fusi, deals with the flow of Bingham fluids in geometry characterized by a small aspect ratio. The so-called lubrication paradox is analyzed and the way of circumventing this difficulty is explained.

We must abstain from commenting the scientific level of this volume, since we are among the contributors, but at least we wish to express our deep gratitude to the authors for their valuable work. Finally, we wish to thank CIRM and CIME

for having made this course possible. Particular thanks to the Director of CIME, Prof. Elvira Mascolo, to the Director of CIRM Prof. Marco Andreatta, and to the Secretary of CIRM, Mr. Augusto Micheletti who took care of so many details.

Firenze, Italy — Angiolo Farina
Villeurbanne, France — Andro Mikelić
Firenze, Italy — Fabio Rosso

The original version of the book was revised. The correction to the book is available at https://doi.org/10.1007/978-3-319-74796-5_6

Contents

Hemorheology: Non-Newtonian Constitutive Models for Blood Flow Simulations

Adélia Sequeira

Abstract Experimental studies over many years have shown that blood flow exhibits non-Newtonian characteristics such as shear-thinning, viscoelasticity, yield stress and thixotropy. The complex rheology of blood is influenced by numerous factors including plasma viscosity, hematocrit and in particular, the ability of erythrocytes to form aggregates when at rest or at low shear rates and to deform at high shear rates, storing and releasing energy. Hemodynamic analysis of blood flow in vascular beds and prosthetic devices requires the rheological behavior of blood to be characterized by phenomenological constitutive equations relating the stress to the rate of deformation and flow. The objective of this chapter is to present a short overview of some macroscopic constitutive models that can mathematically characterize the rheology of blood and describe their known phenomenological properties. Some test cases formulated in idealized and anatomically realistic vessels will be considered to investigate the impact of the most significant non-Newtonian characteristics of blood on its flow behavior, based on numerical simulations of different blood constitutive equation under given sets of physiological flow conditions.

1 Introduction

Rheology is the science of the flow and deformation behavior of solid or fluid materials, including liquids and gases. This field deals with the theoretical notions of kinematics and dynamics, conservation laws and constitutive equations, describing the cross links between force, deformation and flow. It is also considered to be the study of stress-strain relationship in materials. When rheology is applied to the

A. Sequeira (✉)
Department of Mathematics, Instituto Superior Técnico, ULisboa, Center for Computational and Stochastic Mathematics - CEMAT, Lisboa, Portugal
e-mail: adelia.sequeira@math.tecnico.ulisboa.pt

A. Farina et al. (eds.), *Non-Newtonian Fluid Mechanics and Complex Flows*,
Lecture Notes in Mathematics 2212, https://doi.org/10.1007/978-3-319-74796-5_1

analysis of the properties of blood flow and its formed cellular elements it is called *hemorheology*. It involves the investigation of the macroscopic bulk properties of blood, determined in rheometric experiments, and its microscopic properties *in vitro* and *in vivo* (e.g. [129]). It also includes interactions among blood cellular components and between these components and endothelial cells that line blood vessels (microhemorheology).

The unceasing progress in the field of hemorheology is derived from its clinical interest since many cardiovascular diseases have their primary cause in blood flow pathologies. On the other hand, hemorheological abnormalities can be considered as a result (or a sign) of insufficient circulatory function. Basically, pathologies with hematological origin like leukemia, hemolytic anemia, thalassemia or pathologies associated with the risk factors of thrombosis and atherosclerosis like myocardial infarction, hypertension, strokes or diabetes are mainly related to disturbances of local homeostasis. For instance, small size lesions that may occur spontaneously in blood vessels due to endothelial injuries are quite common in small vessels. They can result in internal bleeding, infections or irreversible malfunction in the microcirculation (for example in the brain) and can lead to death. Cardiovascular diseases, including microcirculatory or macrocirculatory disorders are major causes of morbidity and mortality in developed countries and constitute a significant part of total health costs.

Human blood accounts for about 8% of total body weight, averaging 5200 ml. The circulatory system forms a closed loop for the flow of blood that achieves important functions, carrying oxygen, nutrients and various substances from the lungs to the tissues of the body and carbon dioxide back to the lungs, removing waste products of cells metabolism. Blood also plays a key role as a immune protection against foreign bodies (see e.g. [121]). The circulatory system consists of two separate parts, the systemic circulation and the pulmonary circulation, connected by the heart, a complex organ that acts like a pump to maintain a constant flow and is affected by the rest of the circulatory system. Oxygenated blood from the lungs is pumped by the left heart through the pulmonary veins into the systemic arteries, which form a tree of progressively smaller vessels, beginning with the aorta, branching to the small arteries, then to the arterioles and finally to the capillaries, where the exchange of gases takes place. Leaving the capillaries, the blood enters the systemic veins, through which it flows in vessels of progressively increasing size toward the right heart. The systemic veins consist of venules, small veins and the vena cava. The right heart pumps blood into the pulmonary arteries, which form a tree that distributes blood to the lungs, where blood leaves carbon dioxide and is purified with oxygen (e.g. [120]). A representation of the human circulatory system is shown in Fig. 1.

There are significant quantitative differences in pressure and blood volume, between the pulmonary and systemic circuits, but the output of the right and left sides of the heart must be in equilibrium. Veins are low pressure vessels with a low flow and their vessel walls are thin, in contrast to arteries. Table 1 (see [38]) displays average dimensions collected from different sources (Gabe et al. [46], Mao et al. [79], Feher [40], Caro et al. [24], Fung [45], Guyton [55], Gregg [54]),

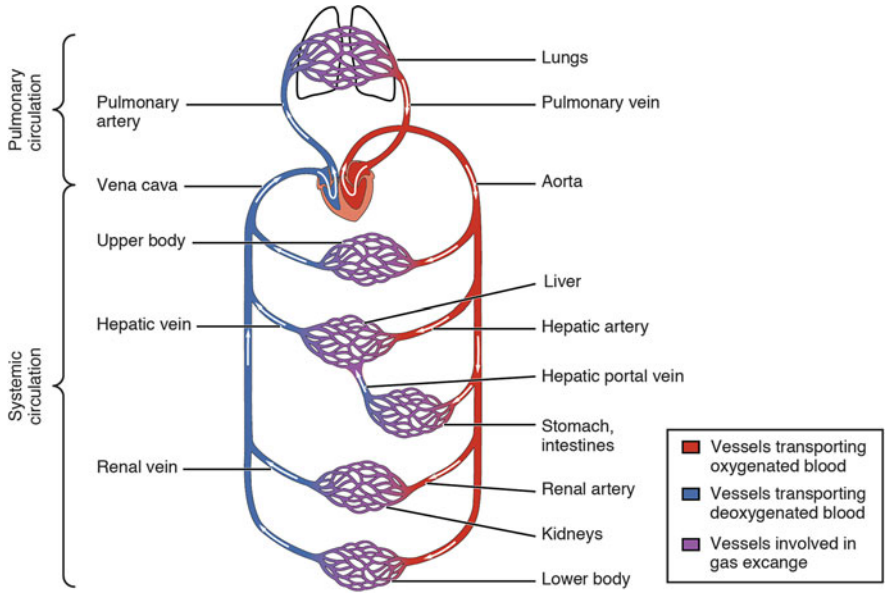

Fig. 1 Circulatory system diagram [Anatomy & Physiology, OpenStax College]

Table 1 Systemic circulation: average physiological parameters

Vessel	Nr.	Diam. (cm)	Cross-sectional area (cm^2)	Wall thickness (cm)	Mean pressure (kPa)	Mean velocity (cm/s)
Aorta	1	3	7	2×10^{-1}	12.5	12
Arteries	8×10^3	10^{-1}	8×10^{-3}	10^{-1}	12	45
Arterioles	10^7	5×10^{-3}	2×10^{-5}	2×10^{-3}	7	5
Capillaries	10^{10}	8×10^{-4}	5×10^{-7}	10^{-4}	3	0.1
Venules	4×10^7	10^{-2}	7.9×10^{-5}	2×10^{-4}	1.5	2
Veins	8×10^3	1.8×10^{-1}	10^{-1}	5×10^{-2}	1	10
Venae cavae	2	3	6	0.15	0.5	14

McDonald [82]). It is quite difficult to find complete and coherent parameters of this type when we compare all data provided by the different authors (see also e.g. [94, 122, 123]). In fact, all data concerning human blood are subjected to large variations, according to sex, body weight, and health conditions.

Despite the research and development efforts of many laboratories around the world, no blood substitute has yet been developed that can carry out the essential functions that whole blood performs in the circulatory system, and most specially for delivery and exchange in the microcirculation. Clearly there is a need for a better understanding of the special characteristics of blood and its flow properties. Therefore, together with laboratory trials, the mathematical and numerical study of

constitutive models that can capture the rheological response of blood over a range of flow conditions is ultimately recognised as an important tool for clinical diagnosis and therapeutic planning (see e.g. [33, 76]).

The aim of this chapter is to present an overview of the rheological properties of blood and its formed cellular elements, including the non-Newtonian characteristics of blood, and discuss some of the phenomenological macroscopic constitutive models that have been proposed in the literature to capture these properties. Moreover, in order to investigate the influence of the most significant non-Newtonian effects on blood flow behavior, some numerical test cases will be considered.

A review of blood rheology and of some of the most relevant constitutive models for blood can be found in e.g. [108, 109]. For a concise historical background about the development of hematology from the antiquity to the nineteenth century, see [38].

2 Blood Rheology

2.1 Blood Components

Blood is a concentrated heterogeneous suspension of several formed cellular elements, the *blood cells* or *hematocytes*, red blood cells (RBCs or *erythrocytes*), white blood cells (WBCs or *leukocytes*) and platelets (*thrombocytes*), in an aqueous polymeric and ionic solution (mainly Na^+, K^+, Ca^{2+} and CI^-), the *plasma*. Plasma represents ∼55% of the blood volume and is composed of ∼92% water and ∼3% particles, namely, electrolytes, organic molecules, numerous proteins (albumin, globulins and fibrinogen) and waste products. Plasma represents ∼55% of the blood volume and its central physiological function is to transport these dissolved substances, nutrients, wastes and the formed cellular elements throughout the circulatory system.

Normal erythrocytes are biconcave discs with a typical diameter of 6–8 μm and a maximal thickness of 1.9 μm [75]. In mammals these cells are non-nucleated and consist of a concentrated hemoglobin solution enveloped by a highly flexible membrane. The average volume of an erythrocyte is 90 μm^3 ([24]). Their number per cubic millimetre of blood is approximately 5 to 6 $\times$ 10^6 and they represent approximately 40 to 45% by volume of the normal human blood and more than 99% of all blood cells. The first percentage is called *hematocrit*. The primary function of erythrocytes is to transport oxygen and carbon dioxide carrying hemoglobin and a small portion of carbonic anhydrase, which catalyzes the reversible formation of carbonic acid from carbon dioxide and water.

Leukocytes are roughly spherical and much larger than erythrocytes, but they exist in a smaller number in blood: their diameter ranges between 6 and 17 μm and there are approximately 7 to 11 $\times$ 10^3 per cubic millimetre in a normal adult. Leukocytes are subdivided into main classes: granulocytes (65%) and agranulo-

cytes, comprising lymphocytes (30%), monocytes (5%) and natural killer cells. Granulocytes are further subdivided into neutrophils (95%), eosinophils (4%) and basophils (1%). The leukocytes maintain adhesion to the endothelium through rolling and play a vital role in fighting infection and thus are able to migrate out of the blood vessels and into the tissues. They have a slight influence on the rheology of blood, except in the capillaries or in disease states. For a better understanding of leukocytes biomechanical behavior, see e.g. [9, 34, 69, 72, 113]).

Thrombocytes are small discoid non-nucleated cell fragments, much smaller than erythrocytes and leukocytes, having a diameter 2–4 μm (and approximately 2–3 μm^3 in volume). Despite their smallness, thrombocytes (platelets) can perform an incredible number of actions, interacting with the environment by means of a rich array of receptors on their membrane and they are a vital component of the blood clotting mechanism. Blood coagulation is an extremely complex biological process in which blood forms clots (*thrombus*) to prevent bleeding (*hemostasis*); it is followed by their dissolution (fibrinolysis) and the subsequent repair of the injured tissue. The process involves large sequences of chemical reactions of complicated nature (*cascades*) and different interactions between the plasma, the vessel wall and activated thrombocytes (platelets), with a huge impact of the flowing blood on the resulting fibrin-platelets thrombus production and growth. There is a large number of books and review chapters on hemostasis (see e.g. [20, 38, 39, 66, 80, 135] and the references cited therein.

The total volume concentration of leukocytes and thrombocytes is only about 1%. All these cells are deformable but erythrocytes undergo a higher deformation, in particular when they pass through the capillaries. Deformations occur through a rearrangement of the cytoskeleton that supports cells shape avoiding rupture of the cell membranes.

Blood cells are continuously produced by the bone marrow over a human's life and they all reach ultimate maturity via a process called *hematocytopoiesis*. For example, erythrocytes have an average lifetime of 120 days and the body must produce about 3×10^9 new erythrocytes for each kilogram of body weight every day. Due to ageing and rupturing they must be constantly replaced (see e.g. [65]).

2.2 Non-Newtonian Properties of Blood

The non-Newtonian behavior of blood is largely due to three characteristics of RBCs: their ability to form aggregates when at rest or at low shear rates, their general distribution in the flowing plasma, namely the ability of these 3D microstructures to deform and store energy and their tendency to align in the flow direction, at high shear rates (e.g. [29, 111]). The high deformability of RBCs is due to the absence of a nucleus, to the elastic and viscous properties of its membrane and also to geometric factors such as the shape, volume and membrane surface area [27].

Rheometers are precision instruments applied to measure wide ranges of stress, strain, and strain rate of a material. The following kinds of rheometers are the

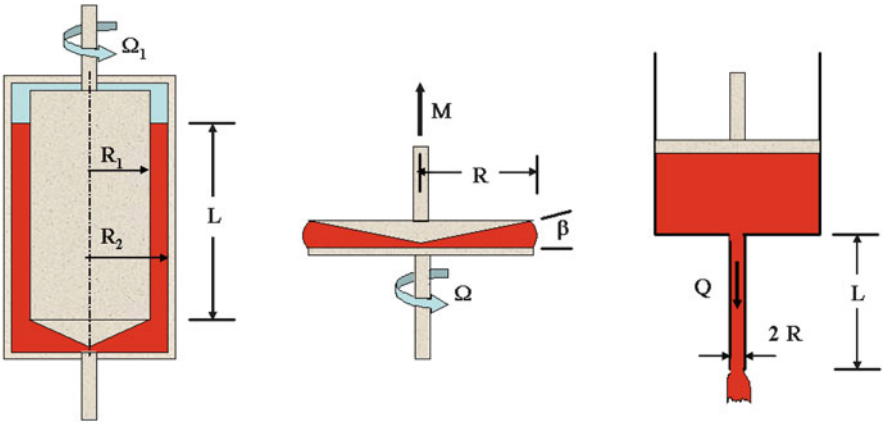

Fig. 2 Representation of the three mostly used rheometers in blood measurements (from [109])

mostly used to measure blood flow properties: the concentric cylindrical rheometer (Couette rheometer), the cone and plate rheometer and the capillary rheometer, Fig. 2. In the Couette rheometer, blood is placed in the annulus between two concentric cylinders and it's motion is driven by the rotation of one or both cylinders; In the cone and plate rheometer, blood is loaded between the cone and the plate and driven by the rotation of the cone; the capillary rheometer is of simple use and the test fluid is driven by gravity, compressed gas or a piston from a reservoir through a cylinder rigid tube. These rheometers can be used to obtain approximate measurements of viscometric and viscoelastic material functions (see e.g [109]).

As discussed below, it has been experimentally verified that the response of RBCs in shear flows undergoes three flow regimes: at low shear rates, in the presence of fibrinogen and large globulins (proteins found in plasma) erythrocytes form a complex three dimensional microstructure (*rouleaux*), while at high shear rates, this microstructure is lost and flow induced radial migration may lead to a non-homogeneous distribution of erythrocytes. A transition in microstructure is found between these two regimes.

To better analyze the experimental data on blood it is helpful to explore the literature on the rheology of particle suspensions. For rigid particles, a vast amount of published literature exists (see e.g. [35, 110]). However, the study of suspensions of multiple, interacting and highly deformable particles such as blood, has received less attention and presents a challenge for researchers in both theoretical and computational fluid dynamics.

2.2.1 Viscosity of Blood

Here we refer to the *apparent viscosity* of blood (or, more generally of a non-Newtonian fluid, independently of the specific rheological model), as the quantity

measured by a viscometer, for shear rates in the expected natural range. This is approximately an average measure of the fluid resistance to flow. The expression *relative viscosity* is also used for blood, denoting the ratio of the suspension viscosity (apparent viscosity) to the viscosity of the suspending fluid (plasma). Commonly used viscosity units are: *poise* (*P*), *centipoise* (*cP*), which is 0.01 P and pascal-second (*Pa s*), the SI unit of viscosity equivalent to Newton-second per square metre ($N\,s/m^2$). One poise is exactly 0.1 Pa s.

Usually blood has higher viscosity than plasma, and when the hematocrit rises, the viscosity of the suspension increases and the non-Newtonian behavior of blood becomes more relevant, in particular at very low shear rates. As mentioned above, for blood at rest or at very low shear rates the erythrocytes have the ability to form a primary aggregate structure of rod shaped stacks of individual cells (rouleaux), that align to each other and form a secondary structure consisting of branched three-dimensional (3D) aggregates [112]. The apparent viscosity (measured by a viscometer) increases slowly until a shear rate less than $1\,s^{-1}$, and then it increases significantly [24]. It has been experimentally observed that rouleaux will not form if the erythrocytes have been hardened or in the absence of fibrinogen and globulins [28]. In fact, suspensions of erythrocytes in plasma demonstrate a strong non-Newtonian behavior whereas when they are in suspension in physiological saline (with no fibrinogen or globulins) the behavior of the fluid is Newtonian [32, 85]. For standing blood subjected to a shear stress lower than a critical value, these 3D structures resist to flow until a certain force is applied and blood exhibits a yield stress behavior. This can happen only if the hematocrit is high enough. The existence of yield stress for blood will be discussed below (see Sect. 2.2.2).

At moderate to high shear rates, RBCs are dispersed in the plasma and the properties of the blood are influenced by their tendency to align and form layers in the flow, as well as by their deformation. The effect of RBC deformability on the viscosity of suspensions was clearly described in [28].

For shear rates above $400\,s^{-1}$, erythrocytes lose their biconcave shape, become fully elongated and are transformed into ellipsoids with major axes parallel to the flow direction. The tumbling of the erythrocytes is absent, there are almost no collisions, and their contours change according to the tank-trading motion of the cells membranes about their interior. The apparent viscosity decreases and this becomes more evident in smaller than in larger vessels. This happens with vessels of internal diameter less than 1 mm and it is even more pronounced in vessels with a diameter of 100–200 µ m. The geometric packing effects and radial migration of erythrocytes can act to lower the hematocrit adjacent to the vessel wall and contribute to decrease the blood viscosity. This is known as the *Fåhraeus–Lindqvist* effect, [41, 42]. *Plasma skimming* is another effect that results in diminishing the viscosity when blood flows into small lateral vessels compared with the parent vessel.

As a consequence of this behavior we can say that one of the most important non-Newtonian characteristics of blood is the shear-thinning viscosity. This happens in small size vessels or in regions of stable recirculation, like in the venous system and parts of the arterial vasculature where geometry has been altered and erythrocyte

aggregates become more stable, like downstream a stenosis or inside a saccular aneurysm. However, in most parts of the arterial system, blood flow is Newtonian in normal physiological conditions.

Numerous techniques have been developed to quantify erythrocytes aggregation in a flow field, with applications to *in vitro* flow models or to *in vitro* microvascular measurements.These include estimates of aggregate size from direct measurements, Fourier analysis of spatial variation in light intensity, analysis of transmitted and reflected light, and measurement of the light scattering properties of RBCs (see e.g. [15, 51, 93, 96]).

Experiments on blood at low shear rates are very difficult to perform and there remains a controversy over the blood flow behavior in the limit of shear rate tending to zero. Figure 3 displays the shear-thinning behavior of whole blood as experimentally observed by Chien et al. [28]. Each of these data points represents an equilibrium value obtained at a fixed shear rate.

In addition, it is important to point out that, like in many other liquids, the viscosity of whole blood is also strongly dependent on temperature and, when comparing blood viscosity data from different sources, the temperature at which data was obtained must be considered. The dependence of blood viscosity on temperature is similar to that of water for temperatures ranging from 10 °C to 40 °C and shear rates from 1 to 100 s^{-1} [84]. The variation of plasma temperature follows approximately that of water [25] and, consequently, blood viscosity is often related to plasma or water viscosity, at the same temperature.

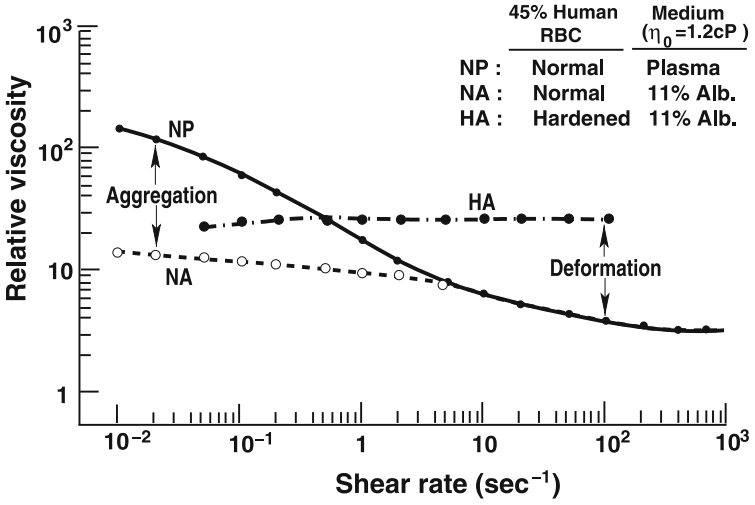

Fig. 3 Variation of the relative viscosity as a function of the shear rate for normal RBC in heparinised plasma (NP), normal RBC in albumin-Ringer solution (NA) and hardened RBCs in albumin-Ringer solution (HA) at a temperature of 37°C, hematocrit $Ht = 45\%$ using a Couette viscometer (reproduced from [28])

2.2.2 Yield Stress of Blood

Some bodies, like pastes, do not deform when the shear stress is below a critical value, while they start flowing like a fluid if the stress exceeds that threshold. The phenomenon is explained by the rupture of inner bonds. Systems with an yield stress are called Bingham fluids [14]. This critical stress level, called the yield value or yield, is typically treated as a constant material property of the fluid. An extensive description of methods for measuring yield stress is given in [89, 92].

Blood also demonstrates yield stress although there is a controversy about this issue. Reported values for the yield stress of blood have a great variation ranging from 0.002 to 0.40 dynes/cm^2, see e.g. [32]. This variation has been attributed to artifacts arising from interactions between the erythrocytes and surfaces of the rheometer as well as to the experimental methods used to measure the yield stress and the length of time over which the experiments are run [11]. Rather than treating the yield stress as a constant, it should be considered as a function of time and linked to thixotropy, as later proposed by other researchers [88]. Some studies have indicated that yield stress is correlated to the hematocrit level and to the concentration of fibrinogen in blood plasma. When the hematocrit level falls below a critical level, the yield stress characteristic of blood becomes negligible [83].

2.2.3 Viscoelasticity and Thixotropy of Blood

Viscoelastic fluids are viscous fluids which have the ability to store and release energy. The viscoelasticity of blood at normal hematocrits is primarily attributed to the reversible deformation of the RBCs 3D microstructures [30, 128]. Elastic energy is due to the properties of the RBC membrane which exhibits stress relaxation [36, 119] and the bridging mechanisms within the 3D structure. Moreover, the experimental results of Thurston [124] have shown that the relaxation time depends on the shear rate. Thurston was the first to measure the viscoelastic properties of blood and the dependence of blood viscoelasticity on factors such as temperature, hematocrit and RBC properties. He has contributed to most of the experimental work developed in this area (see [128] and the references cited therein).

The viscoelastic effects in blood circulation are magnified by its pulsatile nature and by the elastic properties of the blood vessels and the porous tissue through which blood is transported [23] and there is an interaction between the viscoelastic behavior of blood with that of the vessel wall and porous tissue.

In view of the available experimental evidence, it is reasonable to develop non-Newtonian fluid models for blood that are capable of shear-thinning and stress relaxation, with the relaxation time depending on the shear rate. To date, very little is known concerning the response of such fluids. In fact, viscoelastic properties are of relatively small magnitude and they have generally only been measured in the context of linear viscoelasticity. By shear rates of the order of $10\,s^{-1}$ the elastic nature of blood is negligible as evidenced by a merging of the oscillatory and steady flow viscosities. However, if viscoelastic constitutive equations are used

to model blood in the circulatory system in higher shear rates conditions, the finite viscoelastic behavior of blood should be considered. Viscoelastic constitutive models for blood will be discussed below (see Sect. 2.3.4).

Another important non-Newtonian property of blood closely related to shear-thinning, is the thixotropic behavior, essentially due to the finite time required for the formation and dissolution of the 3D aggregates of erythrocytes. Indeed, the build-up and breakdown of the 3D microstructures, their elongation and recovery, and the formation and breakdown of layers of the aligned erythrocytes evolve in a finite time, and these processes can play an important role in blood rheometry [11]. There is a large variety of published definitions for thixotropy, in the fields of industrial or biological applications. The following definition can be found in [12]: "When a reduction in magnitude of rheological properties of a system, such as elastic modulus, yield stress, and viscosity, for example, occurs reversibly and isothermally with a distinct time dependence on application of shear strain, the system is described as *thixotropic*". Fluids whose behavior is opposite to thixotropic fluid (i.e. thickening under stress) are called *rheopectic*.

Thixotropy is more pronounced at low shear rates with a long time scale. The effect in blood flow is less pronounced than other non-Newtonian effects [78] and this can explain the limited studies devoted to this property.

It should be emphasized that most of the reported non-Newtonian properties and rheological parameters of blood are obtained *in vitro*, as indicators of *in vivo* real measurements. Experimenting with blood out of the body can find many obstacles. The simple process of extracting blood may apply high stresses, altering the original rheological properties. Then partial coagulation, particularly in the absence of flow, can severely influence the values of viscosity, viscoelastic or yield stress parameters. Moreover, the consistency of these approximations depends on the information about experimental and individual conditions. Complementary studies of sensitivity analysis and uncertainty quantification should be performed, especially when those values are used for patient-specific modeling and simulations.

2.3 Constitutive Models for Blood

The mechanical properties of blood should be studied by considering a fluid containing a suspension of particles. A fluid is said to be Newtonian if it satisfies the Newton's law of viscosity (the shear stress is proportional to the rate of shear and the viscosity is the constant of proportionality). Blood plasma, which consists mostly of water, is a Newtonian fluid. However, the whole blood has complex mechanical properties which become particularly significant when the particles size is much larger, or at least comparable, with the lumen size. In this case, which happens at the microcirculation level (in the small arterioles and capillaries) blood cannot be modelled has a homogeneous fluid and it is essential to consider it as a suspension of blood cells (specially erythrocytes) in plasma. The presence of the blood cellular elements and their interactions leads to significant changes in the blood rheological

properties and reliable measurements need to be performed to derive appropriate microstructural models (see e.g. [101, 115, 134]).

Blood is a non-Newtonian fluid, but it can however be regarded as Newtonian depending on the size of the blood vessels and the flow behavior, as in arteries with diameters larger than 100 μ m where measurements of the apparent viscosity show that it ranges from 0.003 to 0.004 Pa s and the typical Reynolds number is about 0.5.

Here we assume that all macroscopic length and time scales are sufficiently large compared to length and time scales at the level of an individual erythrocyte so that the continuum hypothesis holds. Thus the models presented here are not appropriate in the capillary network. For an overview of hemorheology in the microcirculation we refer the reader to the review article of Popel and Johnson [101], as already referred.

2.3.1 Constant Viscosity Models

As a first step towards the macroscopic modeling of blood flow we consider the most general form of constitutive equations for incompressible viscous fluids, defining the Cauchy stress tensor $\mathbf{T}$ such that

$$\mathbf{T} = -p\mathbf{I} + \boldsymbol{\tau}, \tag{1}$$

where p (pressure) is the Lagrange multiplier arising from the incompressibility constraint, $\mathbf{I}$ is the identity matrix and $\boldsymbol{\tau}$ is the *extra-stress* (or deviatoric stress) tensor, representing the forces which the material develops in response to being deformed.

In large vessels normal blood has a *Newtonian* behavior, meaning that the extra-stress is proportional to the symmetric part of the velocity gradient,

$$\boldsymbol{\tau} = 2\mu\mathbf{D}(\mathbf{u}), \tag{2}$$

where μ is the (constant) dynamic viscosity of blood and the tensor $\mathbf{D}(\mathbf{u}) \equiv \mathbf{D} = (\nabla\mathbf{u} + \nabla\mathbf{u}^T)/2$ is the symmetric part of the velocity gradient (rate of deformation or strain rate) [118]. Taking into account the principles of conservation of linear momentum and conservation of mass (reduced to a divergence-free constraint) for isothermal incompressible flows, the substitution of $\boldsymbol{\tau}$ given by (2) in the Cauchy stress equation (1) leads to the system

$$\begin{cases} \rho\dfrac{\partial\mathbf{u}}{\partial t} + \rho(\mathbf{u}\cdot\nabla)\mathbf{u} = -\nabla p + \nabla\cdot 2\mu\mathbf{D}(\mathbf{u}), \\ \nabla\cdot\mathbf{u} = 0, \end{cases} \tag{3}$$

where $\mathbf{u}$ and p denote the blood velocity and pressure, with $t \geq 0$ and ρ is the blood density.

In this case, since μ is constant, from the continuity equation we obtain

$$\nabla \cdot [\mu(\nabla \mathbf{u} + \nabla \mathbf{u}^T)] = \mu(\Delta \mathbf{u} + \nabla \nabla . \mathbf{u}) = \mu \Delta \mathbf{u}$$

and system (3) is written in form

$$\begin{cases} \rho \dfrac{\partial \mathbf{u}}{\partial t} - \mu \Delta \mathbf{u} + \rho(\mathbf{u} \cdot \nabla)\mathbf{u} + \nabla p = 0, \\ \nabla \cdot \mathbf{u} = 0. \end{cases} \tag{4}$$

These are the well-known incompressible Navier-Stokes (NS) equations (proposed by **Navier** in 1822 and later by **Stokes** in 1845). Here $\rho(\mathbf{u} \cdot \nabla)\mathbf{u}$ is the nonlinear convective term and $\nabla \cdot [\mu(\nabla \mathbf{u} + \nabla \mathbf{u}^T)]$ is the diffusion term showing the role of viscosity in propagating momentum. In the larger arteries and veins there is a predominance of inertial effects over the viscous ones. System (4) must be closed with appropriate initial and boundary conditions.

The NS equations can also be rescaled and written in a non-dimensional form by introducing the following quantities:

$$x = \frac{\tilde{x}}{R}, \qquad t = \frac{U\tilde{t}}{R}, \qquad p = \frac{\tilde{p}R\mu}{U},$$

where the symbol $\tilde{}$ is attached to dimensional parameters (R represents a reference length—the radius of the vessel, U is a characteristic velocity—the mean blood flow velocity). We also introduce the important dimensionless quantity used in fluid mechanics, the *Reynolds number—Re* defined as $Re = \frac{\rho UR}{\mu}$, that means the ratio of momentum forces to viscous forces, and quantifies the relation between these two forces for given flow conditions. More precisely, the NS equations can be written in a simplified form as

$$\begin{cases} Re\left(\dfrac{\partial \mathbf{u}}{\partial t} + (\mathbf{u} \cdot \nabla)\mathbf{u}\right) - \Delta \mathbf{u} + \nabla p = 0, \\ \nabla \cdot \mathbf{u} = 0. \end{cases} \tag{5}$$

When $Re \ll 1$ (for instance blood flow in smaller arteries), we may neglect the convective term compared to the viscous contribution. Then blood could be modeled by the simpler Stokes equations (creeping flow or Stokes flow). However, as already mentioned, in the smaller arteries the non-Newtonian behavior of blood becomes relevant. On the other hand, when $Re \gg 1$ (*high Reynolds number flows*) the flow becomes unstable. In normal physiological conditions instabilities can occur in some vascular regions, in particular in the systolic phase at the exit of the aortic valve or in bifurcations, but normally there is no time for the flow to develop turbulence. In pathological conditions, like in case of severe anaemia (low blood viscosity) or due to the presence of a stenosis (stenotic artery), the transition from laminar to turbulent flow can occur [44]. Such conditions are nevertheless rare and consequently turbulent flow models are not used in cardiovascular modeling and simulations.

From the analytical and numerical view points the Navier-Stokes system with appropriate initial and boundary conditions has been the object of intensive research, but there are still important issues to be solved. In the mathematical theory, we emphasize the famous global in time uniqueness in 3D, related to the regularity of solution. (see e.g. [47, 48]).

Since the pioneering work of Perktold in the late 1980s and early 1990s [97, 98], much of the research in modeling blood flow in the human arterial system has focused on the numerical solution of the 3D Navier-Stokes system which provides hemodynamic factors like blood flow velocity and pressure fields, and wall shear stress (WSS) or the wall compliance (e.g. [99, 100]), difficult to extract using simpler models and experimental measurements.

2.3.2 Generalized Newtonian Models

As already discussed, this set of equations is commonly used to describe blood flow in healthy arteries. However, under certain experimental or physiological conditions, particularly at low shear rates, blood exhibits relevant non-Newtonian characteristics and more complex constitutive models need to be used. In this case, we require a more general constitutive equation relating the state of stress to the rate of deformation. It can be shown that the most general model of the form (1) with $\boldsymbol{\tau} = \boldsymbol{\tau}(\nabla \mathbf{u})$, satisfying invariance requirements, can be written as [10]

$$\boldsymbol{\tau} = \phi_1(\mathrm{II}_{\mathbf{D}}, \mathrm{III}_{\mathbf{D}})\mathbf{D}(\mathbf{u}) + \phi_2(\mathrm{II}_{\mathbf{D}}, \mathrm{III}_{\mathbf{D}})\mathbf{D}(\mathbf{u})^2 \tag{6}$$

where $\mathrm{II}_{\mathbf{D}}$ and $\mathrm{III}_{\mathbf{D}}$ are the second and third principal invariants of the rate of deformation tensor $\mathbf{D} = \mathbf{D}(\mathbf{u})$. These invariants are given by

$$\mathrm{II}_{\mathbf{D}} = 1/2\,((\mathrm{tr}\,\mathbf{D}(\mathbf{u}))^2 - \mathrm{tr}\,(\mathbf{D}(\mathbf{u}))^2), \qquad \mathrm{III}_{\mathbf{D}} = \det(\mathbf{D}(\mathbf{u})). \tag{7}$$

where $t\mathrm{tr}\,\mathbf{D} = \mathrm{I}_{\mathbf{D}} = 0$ for divergence free velocity fields, essential for incompressible fluids (isochoric motions). To simplify the notation, from now on $\mathbf{D}(\mathbf{u})$ will be replaced by $\mathbf{D}$,

Incompressible fluids of the form (6) are typically called *Reiner-Rivlin fluids*. We remark that the presence of ϕ_2 in (6) is necessary to match experimental results on "real" fluids and the dependence on the value of II_D is often neglected [10].

Therefore, attention is particularly given to a special class of Reiner-Rivlin fluids called *generalized Newtonian fluids*, for which

$$\boldsymbol{\tau} = 2\mu(\mathrm{II}_{\mathbf{D}}, \mathrm{III}_{\mathbf{D}})\mathbf{D}, \tag{8}$$

Since for "real" fluids $\mathrm{III}_{\mathbf{D}}$ is identically zero and $\mathrm{II}_{\mathbf{D}}$ is not a positive constant, it is useful to introduce a measure of the rate of deformation, the *shear rate* denoted by $\dot{\gamma}$ and defined by

$$\dot{\gamma} = \sqrt{2\,\mathrm{tr}\,(\mathbf{D}^2)} = \sqrt{-4\,\mathrm{II}_{\mathbf{D}}}. \tag{9}$$

and write the stress tensor for the generalized Newtonian model (8) in the form

$$\boldsymbol{\tau} = 2\mu(\dot{\gamma})\mathbf{D}, \tag{10}$$

where $\mu(\dot{\gamma})$ is a shear dependent viscosity function.

A simple example of a generalized Newtonian fluid is the *power-law* fluid, for which the viscosity function is given by

$$\mu(\dot{\gamma}) = K\,\dot{\gamma}^{n-1}, \tag{11}$$

the positive constants n and K being the power-law index and the consistency, respectively. This model includes, as a particular case, the constant viscosity fluid (Newtonian) when $n = 1$. For $n < 1$ it leads to a monotonic decreasing function of the shear rate (shear-thinning fluid) and for $n > 1$ the viscosity increases with shear rate (shear thickening fluid). The shear-thinning power-law model is often used for blood, due to the analytical solutions easily obtained for its governing equations, but there is a shortcoming since it predicts an unbounded viscosity at zero shear rate and zero viscosity when $\dot{\gamma} \to \infty$, which is unphysical.

One of the important extensions of the power-law model is due to Walburn and Schneck [133] who considered the dependence of the viscosity on the hematocrit (*Ht*) and total protein minus albumin (*TPMA*) in the constants n and K, based on nonlinear regression analysis, and found

$$K = C_1 exp(C_2 Ht), \qquad n = 1 - C_3 Ht. \tag{12}$$

According to Cho and Kensey [31] commonly used values in the literature for blood density ρ and for the asymptotic viscosities at zero and infinity shear rates μ_o and μ_∞, at 37 °C, are the following

$$\rho = 1056\,\text{kg/m}^3, \qquad \mu_o = 0.056\,\text{Pa s}, \qquad \mu_\infty = 0.00345\,\text{Pa s}, \tag{13}$$

where the values of

$$\mu_0 = \lim_{\dot{\gamma}\to 0} \mu(\dot{\gamma}), \quad \mu_\infty = \lim_{\dot{\gamma}\to \infty} \mu_(\dot{\gamma}).$$

were obtained from a set of data including both human and canine blood and for hematocrits ranging from 33–45%.

Note that the values in (13) are only significant for theoretical constitutive models. In practice, the lower limit in shear rate at which viscosity can be measured is limited by experimental trials. The high shear rate limit has no real physical meaning and it is taken as the highest shear value.

As discussed earlier in this chapter (Sect. 2.2) the material parameters of blood are quite sensitive to the state of blood constituents as well as temperature [84].

Table 2 Material constants for power-law model obtained by various researchers using fit of (11) to human blood data at different hematocrits

Ht (%)	n	k	Source
40.5	0.828	0.009267	Kim et al. [67], 37 °C
35	0.8254	0.0880	Walburn and Schneck [133], 37 °C
40	0.8004	0.1147	
45	0.7755	0.1482	
45	0.61	0.42	Liepsch and Moravec [73], 23 °C

For comparison, results predicted from the Walburn-Schneck model (12) are shown

The dependence on hematocrit is included in material parameters for the power-law model that were obtained for human blood, Table 2. The corresponding viscosity functions are shown in Fig. 2. The viscosity functions obtained from [67] for $Ht = 40, 5\%$ and [133] for $Ht = 40\%$, are quite close. In contrast, those in [73] and [133] for $Ht = 45\%$ are substantially different, possibly due to the difference in temperatures.

Other viscosity functions with bounded and non-zero limiting values of viscosity can be written in the general form

$$\mu(\dot{\gamma}) = \mu_\infty + (\mu_0 - \mu_\infty)F(\dot{\gamma})$$

or, in non-dimensional form as

$$\frac{\mu(\dot{\gamma}) - \mu_\infty}{\mu_0 - \mu_\infty}.$$

Here, $F(\dot{\gamma})$ is a shear dependent function, satisfying the following natural limit conditions

$$\lim_{\dot{\gamma}\to 0} F(\dot{\gamma}) = 1, \quad \lim_{\dot{\gamma}\to \infty} F(\dot{\gamma}) = 0.$$

Different choices of the function $F(\dot{\gamma})$ correspond to different models for blood flow, with material constants quite sensitive and depending on a number of factors including hematocrit, temperature, plasma viscosity, age of erythrocytes, exercise level, gender or disease state (Fig. 4).

Table 3 includes some of the most common generalized Newtonian models that have been considered in the literature for the shear dependent viscosity of whole blood. Values for the material constants given in this table were obtained by Cho and Kensey[31]. As mentioned above those set of values were obtained for human and canine blood (Ht ranging from 33%–45%), using a nonlinear least squares analysis.

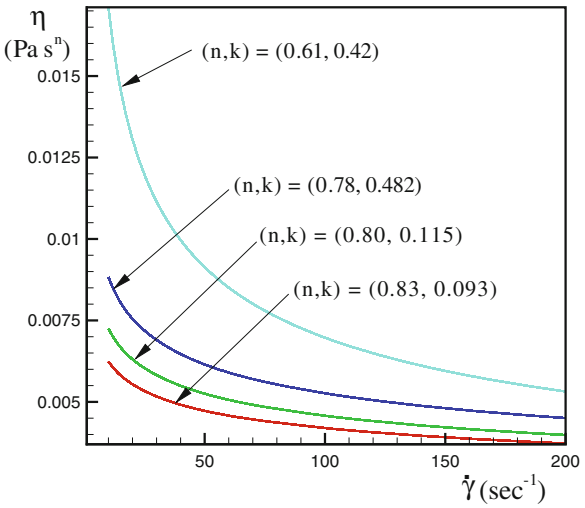

Fig. 4 Comparison of viscosity functions of $\dot{\gamma}$ for extensions of the power-law model (11) using material constants given by different authors (Table 2) obtained by curve fit to experiments

Table 3 Material constants for various generalized Newtonian models for blood with $\mu_0 = 0.056\,\text{Pa s}$, $\mu_\infty = 0.00345\,\text{Pa s}$

Model	$\frac{\mu(\dot{\gamma}) - \mu_\infty}{\mu_0 - \mu_\infty}$	Material constants for blood
Powell-Eyring	$\frac{\sinh^{-1}(\lambda\dot{\gamma})}{\lambda\dot{\gamma}}$	$\lambda = 5.383\,\text{s}$
Cross	$\frac{1}{1+(\lambda\dot{\gamma})^m}$	$\lambda = 1.007\,\text{s}$, $m = 1.028$
Modified cross	$\frac{1}{(1+(\lambda\dot{\gamma})^m)^a}$	$\lambda = 3.736\,\text{s}$, $m = 2.406$, $a = 0.254$
Carreau	$(1+(\lambda\dot{\gamma})^2)^{(n-1)/2}$	$\lambda = 3.313\,\text{s}$, $n = 0.3568$
Carreau-Yasuda	$(1+(\lambda\dot{\gamma})^a)^{(n-1)/a}$	$\lambda = 1.902\,\text{s}$, $n = 0.22$, $a = 1.25$

2.3.3 Yield Stress Models

Yield stress models can be useful to model blood flow in capillaries and some porous structures where flow at very low shear rates occurs. Yield stress materials require a finite shear stress $\boldsymbol{\tau}_Y$ (the yield stress) to start flowing. A relatively simple, and physically relevant yield criterion is given by

$$\sqrt{|\text{II}_{\boldsymbol{\tau}}|} = \boldsymbol{\tau}_Y, \tag{14}$$

where $\text{II}_{\boldsymbol{\tau}}$ is the second invariant of the extra stress tensor, $\boldsymbol{\tau}$ (defined in (7)). Therefore, for $\sqrt{|\text{II}_{\boldsymbol{\tau}}|} < \boldsymbol{\tau}_Y$, the fluid will not flow.

The most usual yield stress model for blood is the Casson model (e.g. [86, 114]) which, for simple shear flow, has the form

$$\begin{aligned} &\sqrt{|\mathrm{II}_{\boldsymbol{\tau}}|} < \boldsymbol{\tau}_Y \Longrightarrow \mathbf{D} = 0 \\ &\sqrt{|\mathrm{II}_{\boldsymbol{\tau}}|} \geq \boldsymbol{\tau}_Y \Longrightarrow \begin{cases} \mathbf{D} = \frac{1}{2\mu_N}\left(1 - \frac{\sqrt{\boldsymbol{\tau}_Y}}{\sqrt[4]{|\mathrm{II}_{\boldsymbol{\tau}}|}}\right)^2 \boldsymbol{\tau} \\ \boldsymbol{\tau} = 2\left(\sqrt{\mu_N} + \frac{\sqrt{\boldsymbol{\tau}_Y}}{\sqrt[4]{4|\mathrm{II}_{\mathbf{D}}|}}\right)^2 \mathbf{D}. \end{cases} \end{aligned} \tag{15}$$

The Newtonian constitutive equation is a special case of (15) for $\boldsymbol{\tau}_Y$ equal to zero, μ_N being the Newtonian viscosity. The Casson fluid behaves rigidly until the yield criterion (14) is verified, and after that it displays a shear-thinning behavior.

Other yield stress models used for blood are the Bingham model [102] given by

$$\begin{aligned} &\sqrt{|\mathrm{II}_{\boldsymbol{\tau}}|} < \boldsymbol{\tau}_Y \Longrightarrow \mathbf{D} = 0 \\ &\sqrt{|\mathrm{II}_{\boldsymbol{\tau}}|} \geq \boldsymbol{\tau}_Y \Longrightarrow \begin{cases} \mathbf{D} = \frac{1}{2\mu}\left(1 - \frac{\sqrt{\boldsymbol{\tau}_Y}}{\sqrt{|\mathrm{II}_{\boldsymbol{\tau}}|}}\right) \boldsymbol{\tau} \\ \boldsymbol{\tau} = 2\left(\mu + \frac{\boldsymbol{\tau}_Y}{2\sqrt{|\mathrm{II}_{\mathbf{D}}|}}\right) \mathbf{D}. \end{cases} \end{aligned} \tag{16}$$

where μ is the constant viscosity attained once the material flows, or the Herschel-Bulkley model (see e.g. [56]) which is similar to the Bingham model (16) which behaves as a power-law viscosity model once it begins to flow (μ in (16) is replaced by the power-law viscosity $\mu(\dot{\gamma}) = K\,\dot{\gamma}^{n-1}$, defined in (11)

$$\begin{aligned} &\sqrt{|\mathrm{II}_{\boldsymbol{\tau}}|} < \tau_Y \Longrightarrow \mathbf{D} = 0 \\ &\sqrt{|\mathrm{II}_{\boldsymbol{\tau}}|} \geq \boldsymbol{\tau}_Y \Longrightarrow \begin{cases} \mathbf{D} = \frac{1}{2K\,\dot{\gamma}^{n-1}}\left(1 - \frac{\sqrt{\boldsymbol{\tau}_Y}}{\sqrt{|\mathrm{II}_{\boldsymbol{\tau}}|}}\right) \boldsymbol{\tau} \\ \boldsymbol{\tau} = 2\left(K\,\dot{\gamma}^{n-1} + \frac{\boldsymbol{\tau}_Y}{2\sqrt{|\mathrm{II}_{\mathbf{D}}|}}\right) \mathbf{D}. \end{cases} \end{aligned} \tag{17}$$

Quemada [105] also developed a constitutive model suitable for blood, using an approach with the apparent viscosity μ given by

$$\mu(\dot{\gamma}) = \mu_F \left(1 - \frac{1}{2}\frac{k_0 + k_\infty\sqrt{\dot{\gamma}/\dot{\gamma}_c}}{1 + \sqrt{\dot{\gamma}/\dot{\gamma}_c}}\varphi\right)^{-2}, \tag{18}$$

where μ_F, φ and $\dot{\gamma}_c$ are the viscosity of the suspending fluid, the volume concentration of the dispersed phase and a critical shear rate, respectively. Table 4 provides material parameters for the Quemada and Casson models for blood used in [91].

Table 4 Material constants for Quemada (18) and Casson (15) models: $Ht = 45\%$ and temperature $T = 37\,^{\circ}\mathrm{C}$

Model	Material constants for blood
Quemada	$\mu_F = 1.2\,\mathrm{mPa\,s}$ $k_\infty = 2.07$ $k_0 = 4.33$
	$\dot{\gamma}_c = 1.88\,\mathrm{s}^{-1}$ $\varphi = 0.45$
Casson	$\mu_N = 3.1\,\mathrm{mPa\,s}$

As discussed above, the existence of a yield stress and its use as a material parameter is still nowadays a controversial issue, due to the sensitivity of yield stress measurements.

2.3.4 Viscoelastic Models

There is a large number of *in vitro* experiments confirming that blood can store and dissipate energy during the aggregation of the erythrocytes and the distortion of the formed 3D microstructures (e.g. [30, 77, 125, 131]. As previously mentioned in Sect. 2.2.3, Thurston [124] was among the earliest to recognise the viscoelastic nature of blood and that the viscoelastic behaviour is less prominent with increasing shear rate. In view of the available experimental evidence, it is reasonable to develop non-Newtonian fluid models for blood that are capable of shear-thinning and stress relaxation, with the relaxation time depending on the shear rate.

None of the models already presented in the previous sections re able to capture the viscoelastic response of blood. One of the simplest quasi-linear rate-type viscoelastic models accounting for the viscoelasticity of blood is the Maxwell model

$$\boldsymbol{\tau} + \lambda_1 \frac{\delta \boldsymbol{\tau}}{\delta t} = 2\mu \mathbf{D}, \tag{19}$$

where λ_1 is the relaxation time and the operator $\delta(.)/\delta t$ stands for the so-called *upper-convected derivative* defined by

$$\delta \boldsymbol{\tau}/\delta t = \overset{\nabla}{\boldsymbol{\tau}} =: \frac{D\boldsymbol{\tau}}{Dt} - \mathbf{L}\boldsymbol{\tau} - \boldsymbol{\tau}\mathbf{L}^T \tag{20}$$

with $\mathbf{L} = \nabla \mathbf{u} + \nabla \mathbf{u}^T =: 2\mathbf{D}$. This is a generalization of the material time derivative,

$$\frac{D\boldsymbol{\tau}}{Dt} = \frac{\partial \boldsymbol{\tau}}{\partial t} + \frac{\partial \boldsymbol{\tau}}{\partial \mathbf{x}} \frac{d\mathbf{x}}{dt}. \tag{21}$$

$\delta \boldsymbol{\tau}/\delta t$ is chosen to be objective under a superposed rigid body motion, meaning that it is frame indifferent or that the response of the material is not affected by its location and orientation. The resulting second-order tensor is symmetric [108].

A generalized Maxwell model that was applicable to one dimensional flow simulations was proposed by Thurston [127] who observed later that, beyond a critical shear rate, the nonlinear behavior is related to the microstructural changes that occur in blood. Thurston's work was suggested to be more applicable to venous or low shear unhealthy blood flow than to arterial flows. Recently, a generalized Maxwell model related to the microstructure of blood, inspired on the behaviour of transient networks in polymers, and exhibiting shear-thinning, viscoelasticity and thixotropy, has been derived by Owens [95].

A more general class of rate-type models, called Oldroyd type models, is defined by

$$\boldsymbol{\tau} + \lambda_1 \frac{\delta \boldsymbol{\tau}}{\delta t} = 2\mu(\mathbf{D} + \lambda_2 \frac{\delta \mathbf{D}}{\delta t}), \tag{22}$$

where λ_2 denotes the retardation time, λ_1 is the relaxation time and these material coefficients are such that $0 \leq \lambda_2 < \lambda_1$. The Oldroyd type fluids can be considered as Maxwell fluids with additional viscosity. This type of models (22) contain the previous (19) model and (2) as particular cases.

In order to better understand the theory of viscoelasticity it is useful to illustrate the typical behavior of viscoelastic materials by simple mechanical models, where a dashpot (piston moving inside a cylinder filled with liquid) represents a viscous (Newtonian) fluid and a spring stands for an elastic (Hookean) solid. These elements can be connected in series or in parallel and the analysis of the behavior of different viscoelastic materials can be done through their combinations representing various deformation-stress models [43, 81]. Figure 5 shows an elastic spring and a dashpot in series, representing the one-dimensional mechanical analogue to (19). Here, the speed of movement γ_V is an analogue of the rate of deformation, the coefficient of proportionality μ (for the viscous element) is an analogue of viscosity, γ_E can be treated as a relative deformation, G as the elastic modulus and the force $\boldsymbol{\tau}$ is an analogue of the extra stress $\boldsymbol{\tau}$ in (19). The ratio between the viscosity μ and elastic modulus G is hidden in the relaxation time parameter λ_1.

The combination of the Newtonian and the Maxwell models joined in parallel is shown in Fig. 6 which represents the mechanical analogue to the Oldroyd model (22).

Here the total viscosity μ is defined as $\mu = \mu_s + \mu_e$, where μ_s and μ_e are the solvent and the elastic (or polymeric) viscosity coefficients, respectively. Moreover,

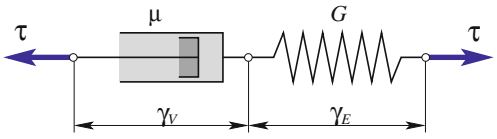

Fig. 5 Mechanical analogue of the Maxwell model

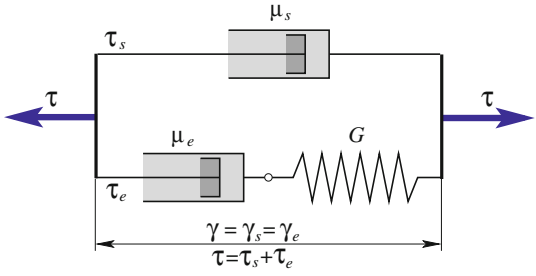

Fig. 6 Mechanical analogue of an Oldroyd-type model

parameters λ_1, λ_2 are defined by

$$\lambda_1 = \frac{\mu_e}{G}, \qquad \lambda_2 = \lambda_1 \frac{\mu_s}{\mu_s + \mu_e} \tag{23}$$

and, as stated above, they verify the inequality $0 \leq \lambda_2 < \lambda_1$ (assuming μ_e is not zero).

The total force $\boldsymbol{\tau}$ can be expressed as the sum of the Newtonian solvent contribution $\boldsymbol{\tau}_\mathbf{s}$ and its viscoelastic counterpart $\boldsymbol{\tau}_\mathbf{e}$. In a similar manner, the extra stress tensor $\boldsymbol{\tau}$ in Eq. (22) is decomposed into its Newtonian part $\boldsymbol{\tau}_s$ and its elastic part $\boldsymbol{\tau}_e$,

$$\boldsymbol{\tau} = \boldsymbol{\tau}_s + \boldsymbol{\tau}_e, \tag{24}$$

such that

$$\boldsymbol{\tau}_s = 2\mu_s \mathbf{D} \tag{25}$$

and $\boldsymbol{\tau}_e$ satisfies a constitutive equation of Maxwell type, namely

$$\boldsymbol{\tau}_e + \lambda_1 \frac{\delta \boldsymbol{\tau}_e}{\delta t} = 2\mu_e \mathbf{D}. \tag{26}$$

A one-parameter family of frame indifferent convected derivatives of a tensor $\boldsymbol{\tau}$ takes the general form

$$\left(\frac{\delta \boldsymbol{\tau}}{\delta t}\right)_a = \frac{D\boldsymbol{\tau}}{Dt} - \mathbf{W}\boldsymbol{\tau} + \boldsymbol{\tau}\mathbf{W} + a(\mathbf{D}\boldsymbol{\tau} + \boldsymbol{\tau}\mathbf{D}), \qquad a \in [-1, 1] \tag{27}$$

where $\mathbf{W}$ represents the anti-symmetric part of the velocity gradient. The particular value $a = -1$ corresponds to the upper-convected time derivative (20) (see e.g. [64]).

We now recall Eq. (26) for the elastic part of the extra stress tensor. It can be rewritten as

$$\frac{\delta \boldsymbol{\tau}_e}{\delta t} = \frac{2\mu_e}{\lambda_1}\mathbf{D} - \frac{1}{\lambda}\boldsymbol{\tau}_e \tag{28}$$

or, in terms of the classical material time derivative, as

$$\frac{D\boldsymbol{\tau}_e}{Dt} + \left(\frac{\delta \boldsymbol{\tau}_e}{\delta t} - \frac{D\boldsymbol{\tau}_e}{Dt}\right) = \frac{2\mu_e}{\lambda_1}\mathbf{D} - \frac{1}{\lambda_1}\boldsymbol{\tau}_e, \tag{29}$$

with the term in brackets representing a kind of "objective correction" of the material time derivative. Moving this term to the right-hand side and expanding

the remaining time derivative on the left, we get the following transport equation for $\boldsymbol{\tau}_e$

$$\frac{\partial \boldsymbol{\tau}_e}{\partial t} + (\mathbf{u} \cdot \nabla)\, \boldsymbol{\tau}_e = \frac{2\mu_e}{\lambda_1}\mathbf{D} - \frac{1}{\lambda_1}\boldsymbol{\tau}_e - \left(\frac{\delta \boldsymbol{\tau}_e}{\delta t} - \frac{D\boldsymbol{\tau}_e}{Dt}\right). \tag{30}$$

Using Eq. (27) with $a = -1$, corresponding to the upper-convected time derivative, transport equation (30) becomes

$$\frac{\partial \boldsymbol{\tau}_e}{\partial t} + (\mathbf{u} \cdot \nabla)\, \boldsymbol{\tau}_e = \frac{2\mu_e}{\lambda_1}\mathbf{D} - \frac{1}{\lambda_1}\boldsymbol{\tau}_e + (\mathbf{W}\boldsymbol{\tau}_e - \boldsymbol{\tau}_e\mathbf{W}) + (\mathbf{D}\boldsymbol{\tau}_e + \boldsymbol{\tau}_e\mathbf{D}). \tag{31}$$

This is the constitutive equation for the viscoelastic isothermal Oldroyd-B fluid.

The governing equations for the Oldroyd-B fluid are obtained by considering the basic principles of conservation of linear momentum and mass for isothermal incompressible flows, where the extra stress $\boldsymbol{\tau}$ is decomposed as in (24), the Newtonian part $\boldsymbol{\tau}_s$ being represented by (25) and the viscoelastic component $\boldsymbol{\tau}_e$ satisfying the constitutive equation (31).

Remark 1 An important non-dimensional parameter characterizing the viscoelastic effects in the flow is the *Weissenberg number* defined as $We = \frac{\lambda_1 U}{L}$, where U denotes a characteristic velocity and L is a characteristic length of the flow. In this case the Weissenberg number can be interpreted as the ratio between "memory" and advection time-scales. It relates the relaxation time to the time the fluid particle needs to pass the distance L while advected at speed U.

The Oldroyd-B model accounts for the viscoelasticity of blood but not for its shear-thinning behavior. However, replacing the constant viscosity μ in $\boldsymbol{\tau}_s$ by a shear dependent viscosity function $\mu(\dot{\gamma})$, i. e.

$$\boldsymbol{\tau}_s = 2\mu(\dot{\gamma})\mathbf{D}, \tag{32}$$

using, for instance one of the generalized Newtonian models listed in Table 3 with the corresponding parameters, we obtain a generalized Oldroyd-B (*GOB*) model that can be appropriate to describe blood flow behavior.

Other viscoelastic constitutive models of differential type, suitable to account for blood rheology have been proposed in the recent literature. The empirical five—constant generalized Oldroyd -B model studied in [132] belongs to this class. It is a shear-thinning Oldroyd-B model with the shear-dependent viscosity $\mu(\dot{\gamma})$ in (32) defined by

$$\mu(\dot{\gamma}) = \mu_\infty + (\mu_0 - \mu_\infty)\left[\frac{1 + \ln(1 + \Lambda\dot{\gamma})}{(1 + \Lambda\dot{\gamma})}\right]. \tag{33}$$

This viscosity function has been derived by fitting experimental data for steady capillary one-dimensional flows to determine the constants, $\mu_0 = 200\,\text{mPa s}$, $\mu_\infty = 6.5\,\text{mPa s}$ and $\Lambda = 11.14\,\text{s}$, and generalizing such curve fits to three dimensions.

The previous model captures the shear-thinning behavior of blood over a large range of shear rates but it has some limitations, since the relaxation times do not depend on the shear rate, which does not agree with experimental observations for blood. An appropriate model should consider blood as a viscoelastic fluid capable of instantaneous elastic response. The theory developed by Rajagopal and Srinivasa in [107] is particularly well suited to develop a model for blood. This framework needs the specification of how the body stores and dissipates energy, by introducing a precise Helmholtz potential associated with the body and a rate of dissipation function, respectively. However, not all viscoelastic fluids can be described within that earlier framework (see [107] for further details).

The model developed by Anand and Rajagopal [2], derived from the general thermodynamic framework stated in [107], includes relaxation times depending on the shear rate, gives good agreement with experimental data in steady Poiseuille and oscillatory flows and has proven to be successful in describing the response of blood. This model contains the Oldroyd-B model as a special sub-class and is particularly well suited to describe the instantaneous elastic response of blood, under physiological conditions. Numerical simulations in some idealized geometries to investigate the combined effects of flow inertia, viscosity and viscoelasticity, can be found in [19]. Anand et al. [1, 3] have also studied the problem of the formation and lysis of blood clots, as well as the problem of ATIII and protein C deficiency [4] within the context of the above model. See also numerical simulations in [117]. An improvement of this model can be found in [5].

The set of governing equations derived in [2], the so-called (*BModel*), are based on the principles of conservation of linear momentum and mass for an isothermal incompressible fluid, with the extra stress tensor decomposed as follows:

$$\mathbf{T} = -p\mathbf{I} + \eta\,\mathbf{B}_{\kappa_p(t)} + \mu_s\mathbf{D} \tag{34}$$

where η and μ_s are positive material parameters (μ_s is the Newtonian viscosity), $\mathbf{B}_{\kappa_p(t)}$ is the elastic stretch tensor and the subscript $\kappa_p(t)$ is used to emphasize that the stretch is expressed with respect to the natural (time dependent) configuration $\kappa_p(t)$.

The upper-convected time derivative of the elastic stretch tensor $\mathbf{B}_{\kappa_p(t)}$ can be written as

$$\delta\mathbf{B}_{\kappa_{p(t)}}/\delta t = \overset{\triangledown}{\mathbf{B}}_{\kappa_{p(t)}} =: -\frac{1}{\tau(\mathbf{B}_{\kappa_{p(t)}})}\left[\mathbf{B}_{\kappa_{p(t)}} - \lambda\mathbf{I}\right]. \tag{35}$$

Here $\tau = \tau(\mathbf{B}_{\kappa_{p(t)}})$ defined by

$$\frac{1}{\tau(\mathbf{B}_{\kappa_{p(t)}})} = 2K\left(\text{tr}(\mathbf{B}_{\kappa_{p(t)}}) - 3\lambda\right)^n. \tag{36}$$

(where K is a material parameter) has the dimension of time and plays a role similar to the relaxation time λ_1 in the classical Oldroyd-B (22) or Maxwell (19) models. The coefficient λ depends on the trace of the inverse of the tensor $\mathbf{B}_{\kappa_{p(t)}}$ according to

$$\lambda = \frac{3}{\mathrm{tr}\left(\mathbf{B}^{-1}_{\kappa_{p(t)}}\right)}. \tag{37}$$

Using the definition of the upper-convected time derivative (20), the left-hand side of (35) can be rewritten in a more conventional form in terms of the material time derivative:

$$\frac{D\mathbf{B}_{\kappa_{p(t)}}}{Dt} - \left[\mathbf{L}\mathbf{B}_{\kappa_{p(t)}} + \mathbf{B}_{\kappa_{p(t)}}\mathbf{L}^T\right] = -\frac{1}{\tau\left(\mathbf{B}_{\kappa_{p(t)}}\right)}\left[\mathbf{B}_{\kappa_{p(t)}} - \lambda\mathbf{I}\right] \tag{38}$$

Finally, expanding the material time derivative on the left-hand side we end up with

$$\frac{\partial\mathbf{B}_{\kappa_{p(t)}}}{\partial t} + (\mathbf{u}\cdot\nabla)\,\mathbf{B}_{\kappa_{p(t)}} = -\frac{1}{\tau}\left[\mathbf{B}_{\kappa_{p(t)}} - \lambda\mathbf{I}\right] + \left[\mathbf{L}\mathbf{B}_{\kappa_{p(t)}} + \mathbf{B}_{\kappa_{p(t)}}\mathbf{L}^T\right] \tag{39}$$

where the coefficients λ and τ are scalar functions of the tensor $\mathbf{B}_{\kappa_{p(t)}}$ and its invariants, according to (37) and (36), respectively.

It is interesting to remark that the constitutive equations (39) for the (*BModel*) and (31) for the classical Oldroyd-B (upper-convected Maxwell) model have a similar form.

Predictions of the coefficients for the proposed (*BModel*) in [2]

$$\mu_s = 0.01\,\mathrm{Pa\,s}; \quad \eta = 0.0227\,\mathrm{N/m^2}; \quad n = 0.7525; \quad K = 1.2056\,\mathrm{s^{-1}} \tag{40}$$

(with n positive to ensure the shear-thinning behavior) have been compared with the data for human blood [126].

More details related to the (*BModel*) and the notation used here can be found in [2, 107] and also in [16, 19] where its implementation has been performed and some numerical results have been obtained.

All models considered above can be solved for the variables velocity, pressure and shear stress, provided the viscosity function, flow parameters and appropriate boundary conditions are given.

With respect to boundary conditions for the Navier-Stokes and generalized Navier-Stokes equations, it is necessary to prescribe either the velocity or the surface traction force (Dirichlet or Neumann boundary conditions, respectively) at the inflow boundary. Usually, physiological data are not available and a fully developed Poiseuille velocity profile (or the Womersley solution, in the unsteady case) can be prescribed. This is an acceptable idealization of the inflow condition

in relatively long straight vessel segments. At the vessel wall, the no-slip condition, expressing that the velocity at the wall boundary is the wall velocity, is appropriate, if we consider rigid wall vessels. At the outflow boundary, a condition prescribing surface traction force can be applied.

The Oldroyd-B and generalized Oldroyd-B models are of mixed elliptic-hyperbolic type (or parabolic-hyperbolic, in the unsteady case). The extra stresses behave hyperbolic, which means that they are only determined by past time. For these models the boundary conditions are the same as for the Navier-Stokes and generalized Navier-Stokes equations, supplemented by the specification of all the stress components representing the fluid memory at the inlet boundary [64].

3 Numerical Simulations of Non-Newtonian Blood Flow Models

Several methods have been used in modeling and simulation of the Non-Newtonian effects in blood rheology, including analytical, stochastic and numerical methods (finite elements, finite differences, finite volumes, spectral collocation, particle methods). No single model can capture the complex blood characteristics and different models have been used to represent blood rheology. Since most of the Non-Newtonian characteristics derive from the behavior of RBCs in shear flows, in particular their concentration, distribution and mechanical properties, generalized Newtonian models, namely Carreau, Carreau-Yasuda and Cross (e.g. [8, 9, 16, 21, 22, 26, 49, 50, 52, 53, 61–63, 68, 74, 87, 106, 116]) are the most popular models found in literature. However, Casson (e.g. [57, 70, 83, 86, 87]) and shear-thinning viscoelastic models (e.g. [2–5, 18, 19, 58, 90, 132]) have also been largely used.

A comparative numerical study of three different test cases is presented to illustrate the influence of the shear-thinning and viscoelastic effects on the qualitative behavior of blood flow in rigid-walled medium sized idealized and realistic vessels, using some of the models described in the previous section.

Remark 2 Blood flow interacts mechanically with the vessel wall, resulting in pressure waves propagating in arteries, which deform under the action of blood pressure. In order to capture these phenomena, complex fluid-structure interaction (FSI) problems must be considered, coupling physiologically meaningful models for both the blood and the vessel wall. To simplify the presentation wall compliance is not considered in the test cases.

3.1 Numerical Simulations in Idealized Geometries

3.1.1 Stenosed Vessel

The first test case is a simple 2D non-symmetric (with respect to the bulk flow direction) channel with a local constriction, modeling a cosine-shape stenosed blood vessel, with 75% area reduction, represented in Fig. 7.

To account for the shear-thinning behavior of blood we choose the generalized Newtonian Carreau model defined in Sect. 2.3.2 (see Table 3)

$$\mu(\dot{\gamma}) = \mu_\infty + (\mu_0 - \mu_\infty)(1 + (\lambda\dot{\gamma})^2)^{(n-1)/2} \tag{41}$$

with material parameters

$$\mu_0 = 0.639\,\text{Pa s}; \quad \mu_\infty = 0.0045\,\text{Pa s}; \quad \lambda = 10.03\,\text{s}; \quad n = 0.35 \tag{42}$$

and, for the purpose of comparison, blood is also modeled as a Newtonian fluid with a constant viscosity $\mu = 0.0035\,\text{Pa s}$, corresponding an average experimental viscosity in the range $\dot{\gamma} \in [2, 1000]\,\text{s}^{-1}$. Blood density is $\rho = 1.06\,\text{g cm}^{-3}$, in both cases.

The experimental viscosity data used in this test case were obtained by M. Kameneva (Univ. Pittsburgh) for normal human blood at temperature $T = 23\,^\circ\text{C}$ and hematocrit $Ht = 40\%$ (see [108]. The main goal is to investigate the influence of inertia and shear-thinning effects on the qualitative behavior of blood flow in this idealized stenosed vessel.

For the numerical approximation of each one of the governing systems of PDEs, a backward Euler scheme is used for time discretization and, at each time step, a finite element space discretization of the velocity-pressure formulation (with P_2-P_1 elements) is implemented, using a splitting scheme with algebraic factorization (e.g. [103]). The computational domain is discretized into 2858 internal triangular elements and a boundary layer mesh consisting of 472 quadrilateral elements (Fig. 7). A fully developed Poiseuille parabolic velocity profile with flow rate $Q = 2.0\,\text{cm}^3/\text{s}$ is prescribed at the inlet and homogeneous Neumann conditions for the velocity components (zero normal stresses) are imposed at the outlet. The initial-boundary value problems are also endowed with an initial condition $\mathbf{u} = \mathbf{u}_0$, for $t = 0$, and with a no-slip boundary condition $\mathbf{u} = \mathbf{0}$ prescribed at the vessel wall.

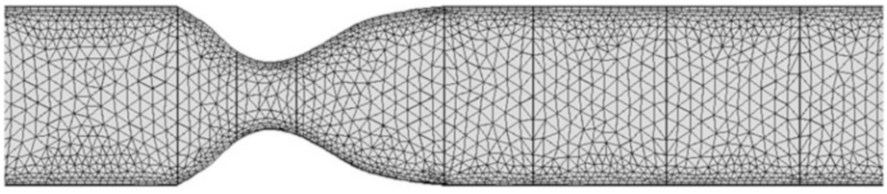

Fig. 7 Stenosed vessel: computational grid structure

Figures 8, 9 show a comparison between the velocity contours corresponding to the Newtonian (*NS*) and the Carreau models, with parameters introduced above, using the same color scale (units in m/s). As expected, in both figures we observe a similar behavior at the stenosis site, but the area reduction in the stenosed region leads to a significant local flow acceleration near the wall and the appearance of recirculation patterns corresponding to two regions of reversal flow, downstream the stenosis. In the two cases the flow structure is similar but the impact of the non-Newtonian effects in the flow separation behind the stenosis is non-negligible, with the velocity close to the wall developing a slower backflow in a larger region for the (*NS*) flow model than for the generalized Newtonian Carreau model. In the vessel's centreline the velocity profile is flatter for the Carreau flow, which corresponds to a reduction in the maximum velocity magnitude. As a result, the near wall flow is accelerated and thus the recirculation zones become shorter, compared to those for the (*NS*) flow.

This is a simple numerical study of the shear-thinning effects of the Carreau flow model compared to the inertial effects of the (*NS*) model. It could be completed by choosing different flow rates at the inflow boundary, other shear-thinning or viscoelastic shear-thinning models, as those derived in the previous Section, and the effect of the stenosis severity on the recirculation zone length downstream the stenosis. Moreover, hemodynamic flow indicators like the wall-shear stress (WSS) exerted on the wall, defined below (44), the time-averaged wall shear stress (TAWSS) or the oscillatory shear index (OSI) during a cardiac cycle, could also be investigated. This will be partially explored in the next test cases.

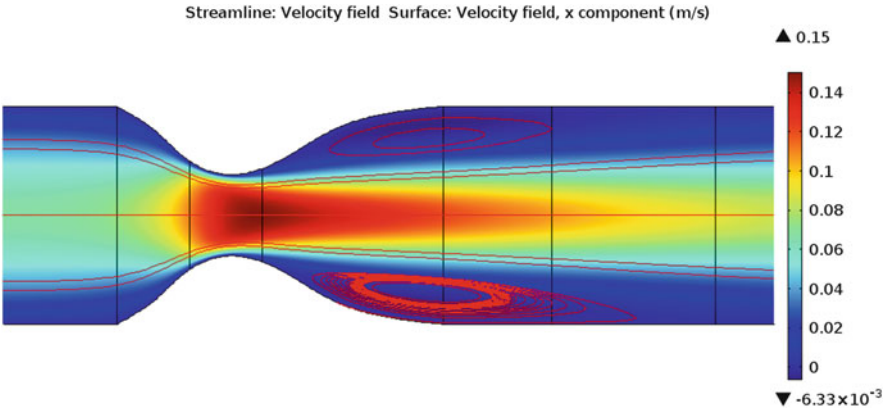

Fig. 8 Velocity magnitude contours and recirculation streamlines behind the stenosis for the Newtonian flow. A velocity legend is shown on the right

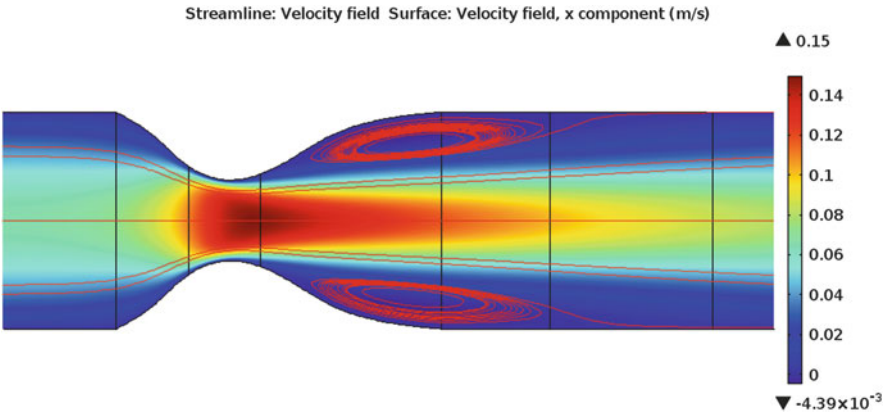

Fig. 9 Velocity magnitude contours and recirculation streamlines behind the stenosis for the generalized Newtonian flow. A velocity legend is shown on the right

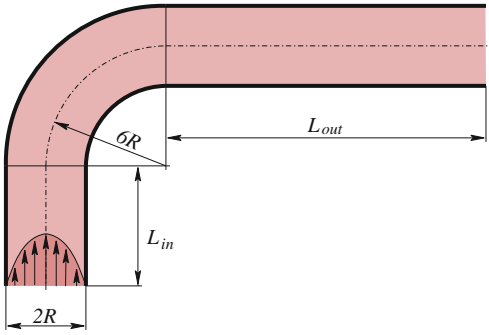

Fig. 10 Geometric representation of a curved vessel

3.1.2 Curved Vessel

Flows in curved vessels are significantly more complex than flows in straight vessels. For inertial Newtonian flows it is well known that a slight curvature of the vessel axis induces centrifugal forces on the fluid and, in addition to the primary initial flow, a secondary motion appears, sending fluid outward along the symmetry axis and returning along the upper and lower curved surfaces. This secondary motion is induced by a discrepancy between the cross-stream pressure gradient and the centrifugal forces developed at the curvature sites, and consists of a pair of symmetrical counter-rotating vortices that is superposed to the axial flow. This results in asymmetrical wall stresses with high shear and low pressure regions (see e.g. [6, 7, 13, 37]).

A 90° 3D curved vessel with circular cross-section (Fig. 10) has been chosen as a second test case, to study the shear-thinning and viscoelastic effects in the presence of high streamline curvature and non-negligible secondary flows (see [19]).

Numerical simulations have been performed to compare the predictions of the above described shear-thinning viscoelastic fluid model for blood flow (39), further denoted as (*BModel*), with those of the classical Newtonian (*NS*) model and a generalized Oldroyd-B (*GOB*) model. The material parameters used for the (*BModel*) are those listed in (40). The (*GOB*) model used here is obtained from the Oldroyd-B model (31) replacing the total (constant) viscosity by the shear dependent viscosity given by the modified Cross function defined in Sect. 2.3.2

$$\mu(\dot{\gamma}) = \mu_\infty + (\mu_0 - \mu_\infty)\frac{1}{(1 + (\lambda\dot{\gamma})^m)^a} \tag{43}$$

The asymptotic viscosities μ_0 and μ_∞ at low and high shear rates, have been adjusted to fit the *bModel*'s parameters, namely $\mu_0 = 0.0736\,\text{Pa s}$ and $\mu_\infty = 0.005\,\text{Pa s}$ and the parameters λ, m and a, estimated by curve fitting of experimental data, have been taken from [17] (see also [71]).

The numerical method used to solve the governing equations is based on a spatial finite-volume discretization on structured grids and an explicit Runge-Kutta time-stepping scheme, namely a robust modified Runge-Kutta four-stage method [60]. The computational mesh is structured and consists of hexahedral primary control volumes. To evaluate the viscous numerical fluxes also dual finite volumes with octahedral shape and centered around the primary cell faces are used.

The space discretization is based on a simple central finite-volume discretization on a structured wall-fitted mesh with hexahedral cells and non-uniform axial cell spacing. A multiblock grid topology was used to avoid high distortion of cells. The viscous fluxes are also discretized in a finite-volume style over a diamond-shaped cells adjoint to primary control volumes faces.

A pressure stabilization technique has been used in the present simulations (see e.g. [130]) to avoid numerical oscillations in the pressure, which are mainly due to the presence of strong gradients. Moreover, since the Reynolds number used in the simulations was quite low (of the order of 10^2), no additional stabilization was needed for the flow variables. This approach has been adopted in earlier papers. For further details see e.g. [16–19] and the references therein.

A parabolic velocity profile with flow rate $Q = 2.0\,\text{cm}^3/\text{s}$, prescribed at the inlet of the curved vessel has been considered for the simulations of the *bModel* and the *GOB* and *NS* models. This flow rate is sufficiently high to capture the secondary flows pattern (see Fig. 12). Homogeneous Neumann conditions for the velocity components were imposed at the outlet and no-slip conditions were prescribed at the vessel wall. Pressure was fixed at the outlet and extrapolated at the other boundaries. Moreover, in the case of the *bModel*, homogeneous Neumann boundary conditions were prescribed at all boundaries for the components of tensor $\mathbf{B}_{\kappa_p(t)}$. As an alternative, some simulations have been performed using a Dirichlet type boundary condition $\mathbf{B}_{\kappa_p(t)} = \mathbf{1}$ prescribed at the inlet, but no significant impact on the solution has been found.

One of the important features of the flow predicted by the *bModel* is related to the axial velocity profile. This can clearly be observed in Fig. 11 showing, for the three models *NS*, *GOB* and *bModel*, plots of the axial velocity profiles in three different

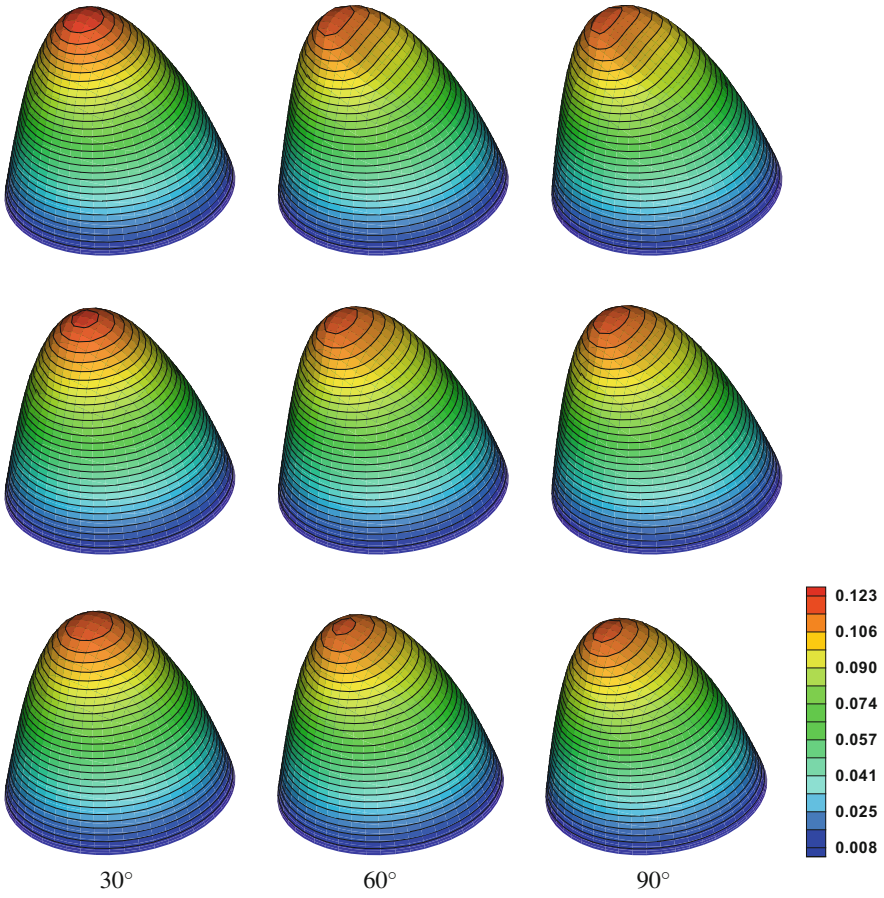

Fig. 11 Axial velocity profiles for *NS* flows (top row), *GOB* flows (middle row) and *bModel* flows (bottom row) in three different cross-sections at the bended part of the curved vessel (30°, 60°, 90°)

cross-sections of the curved vessel, placed at 30°, 60° and 90°. In the case of the *bModel* and *GOB* model flatter axial velocity profiles are obtained when compared to the *NS* model. As in the case of the flow in the stenosed vessel, this effect can be attributed to the shear-thinning behavior predicted by the first two models where the low shear rates around the centerline of the vessel lead to a local increase of the apparent viscosity. Based on these simulations, we can conclude that the shear-thinning effect is dominant when compared to the viscoelastic one. However, further numerical experiments could be performed to confirm this assumption.

Curvature effects are observed in the contours of the axial velocity, which are shifted away from the central axis as the curvature of the vessel increases from 30° to 90° (see Fig. 12 and, more clearly, Fig. 13). Secondary flow streamlines have a similar qualitative behavior for the three models *NS*, *GOB* and *bModel*, as shown in

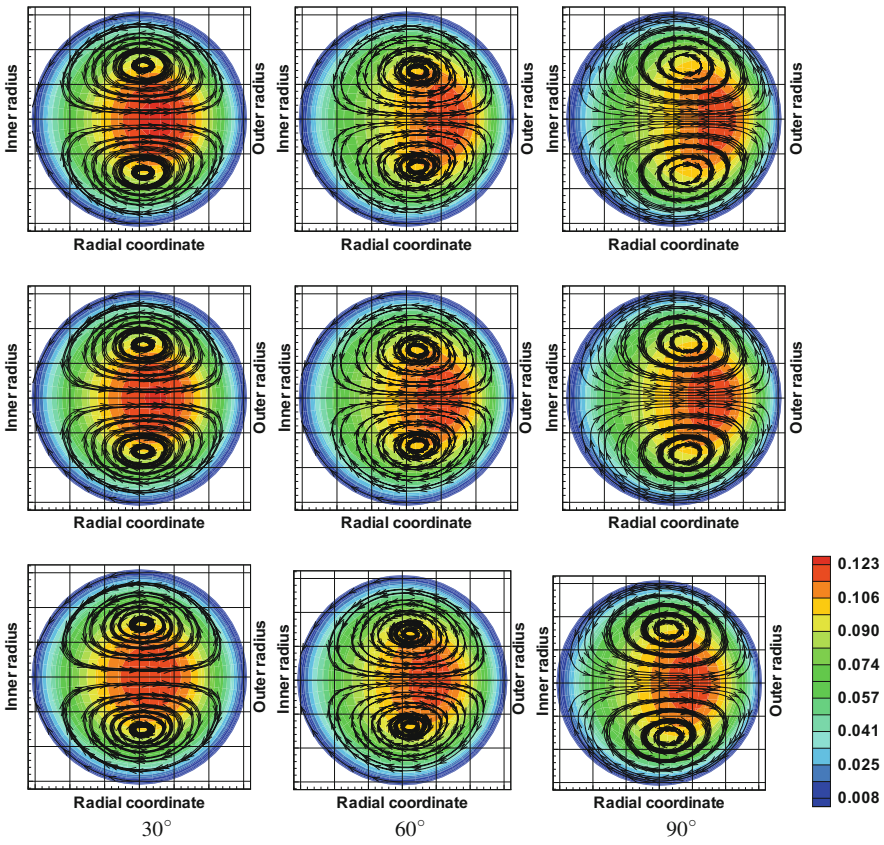

Fig. 12 Axial velocity magnitude contours and secondary flow streamlines for the *NS* (top row), *GOB* (middle row) and the *bModel* flows (bottom row) in three different cross-sections at the bended part of the curved vessel (30°, 60°, 90°)

Fig. 12. Further differences are visible while comparing the axial and radial velocity contours shown in Figs. 13 and 14. From Fig. 14 we realize that the magnitude of the secondary flow velocities is clearly lower for the models *GOB* and *bModel* than for the *NS* model, due to the shear-thinning behavior captured by the first two models for which lower shear rates lead to a higher apparent viscosity.

Figures 15 and 16 show the relative axial velocity differences (normalized by the characteristic velocity U) between the *bModel* and the classical *NS* model (Fig. 15, left and Fig. 16, top row) and between the two shear-thinning viscoelastic models *bModel* and *GOB* (Fig. 15, right and Fig. 16, bottom row). The color scale (in physical units m/s) is used to emphasize the set of flow regions varying from those where differences of solutions can be neglected (in black) to regions of the highest difference in the flow regime (in red or dark blue). The differences on the axial velocity between the *bModel* and the Newtonian model along the curved vessel

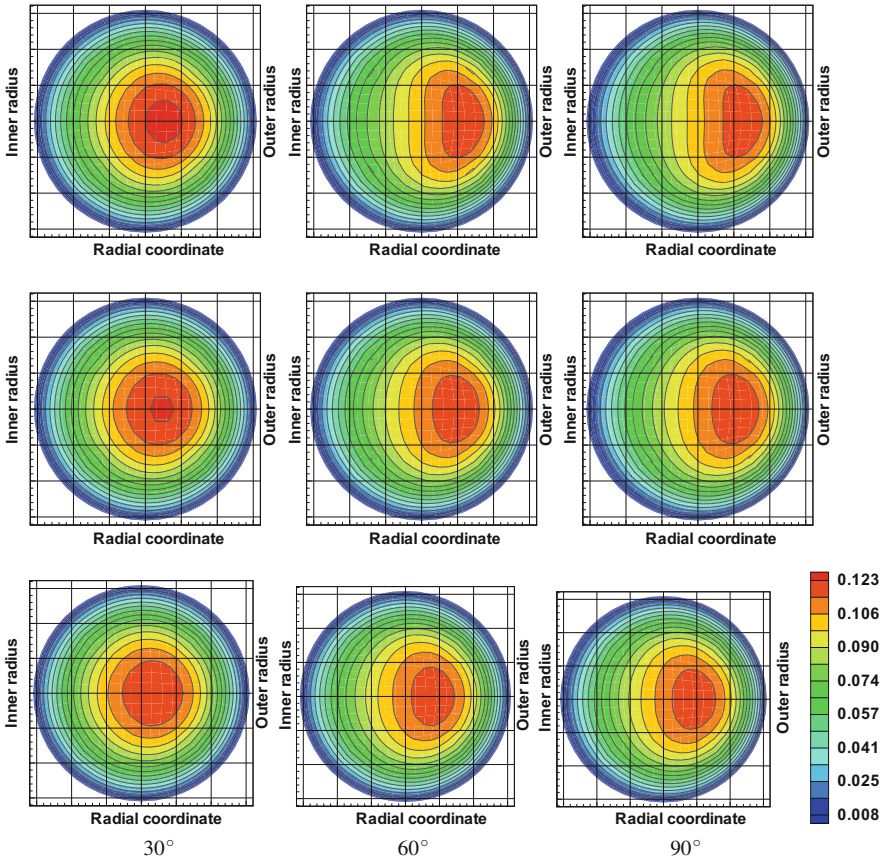

Fig. 13 Axial velocity magnitude contours for the *NS* (top row), *GOB* (middle row) and the *bModel* flows (bottom row) in three different cross-sections at the bended part of the curved vessel (30°, 60°, 90°)

(Fig. 15, left) show the expected slow-down of the core flow (caused by the shear-thinning behavior) in the straight inlet part of the vessel. This is compensated by a faster near-wall flow. As soon as the flow reaches the bended part of the curved vessel, the slow core of the flow is pushed towards the outer wall (see top row in Fig. 16 for a more detailed view), while close to the inner radius of the bend, the flow accelerates. A similar (although weaker) tendency of the flow behavior can also be seen for the difference between the *bModel* and *GOB* models (Fig. 15, right and Fig. 16, low row). This is mainly due to the fact that both models have a shear-thinning viscosity. In the *bModel* shear-thinning effects seem to be slightly more pronounced than in the *GOB* model.

To summarize, we conclude that results obtained with both *bModel* and *GOB* blood flow models are very similar, when compared to those obtained with the

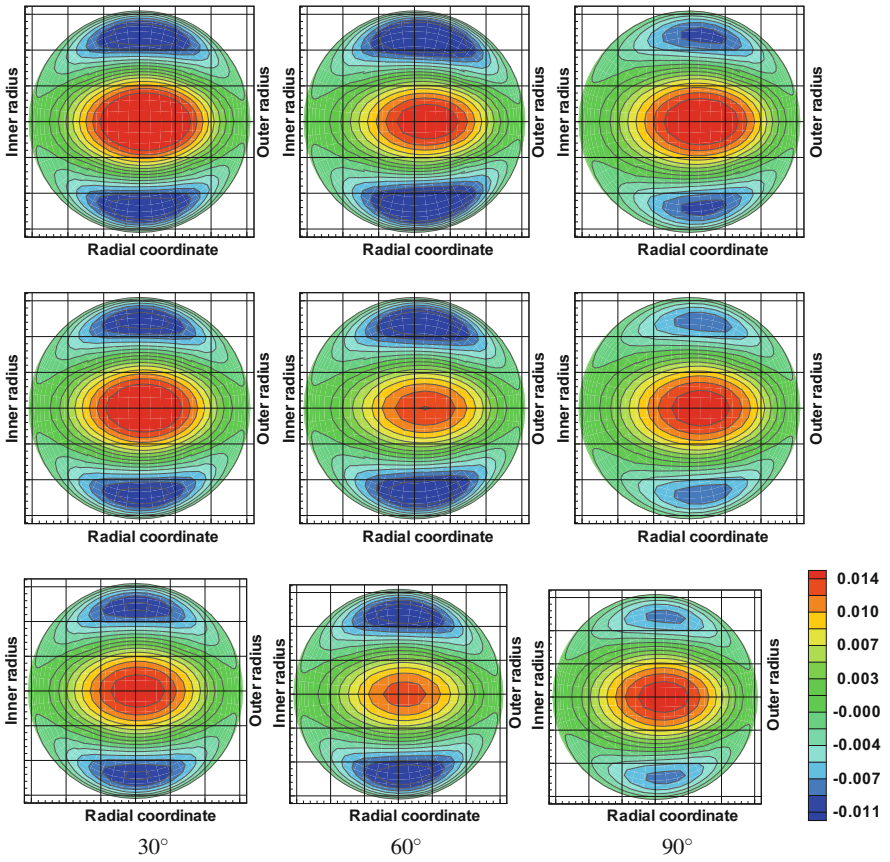

Fig. 14 Radial velocity magnitude contours for the *NS* (top row), *GOB* (middle row) and the *bModel* flows (bottom row) in three different cross-sections at the bended part of the curved vessel (30°, 60°, 90°)

NS model, showing in particular that the more complex *bModel* has been properly implemented and that the shear-thinning and viscoelastic rheological characteristics are dominant with respect to inertia. Future numerical simulations in curved vessels with different curvatures can provide a deeper insight into this investigation.

3.2 Numerical Simulations in a Realistic Geometry: Stenosed Carotid Bifurcation

Now we consider an anatomically 3D realistic model of a diseased human carotid bifurcation, smoothly reconstructed from an MRI medical image, as shown in

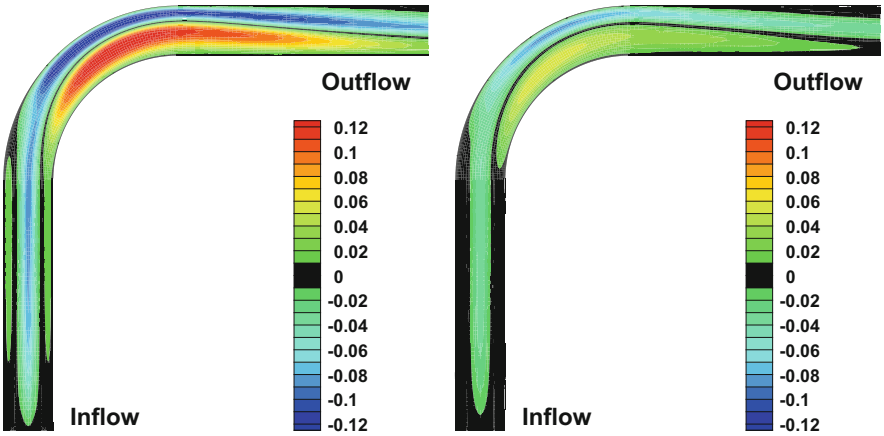

Fig. 15 Relative difference of the axial velocity along the curved vessel $(u_{bModel} - u_{NS})/U$ (left) and $(u_{bNOB} - u_{GOB})/U$ (right)

Fig. 17. The common carotid artery bifurcates into the internal and external carotid arteries that supply blood into the brain and the face, respectively. A stenosis of about 75% has been generated in the internal carotid artery (ICA), near the bifurcation region, where narrowing or constrictions of the arterial inner surface, caused by atherosclerosis usually occur and are responsible for about 10% of ischemic strokes. The accumulation of plaques on the arterial wall is a progressive disease accelerated by local irregular flow fields such as separation and flow-reversal zones, which already occur at milder degrees of stenosis. It is well established that once a mild stenosis is formed in the artery, altered blood flow and stress distribution in the arterial wall contribute to further progression of the disease.The present study can be regarded as a follow-up investigation of the influence of hemodynamic factors on atherosclerosis development, after the disease has been recognized.

The main goal is to investigate inertial and shear-thinning effects in unsteady simulations using the time-dependent incompressible Newtonian (*NS*) and the generalized Newtonian Carreau models defined in Sect. 2.3.2, see also (41). The shear-thinning viscosity parameters used in this study are the physiological values previously used for the Carreau model in the first test case (42), Sect. 3.1. For the Newtonian model we also impose a constant viscosity $\mu = 0.0035$ Pa s, and blood density is $\rho = 1.06\,\mathrm{g\,cm^{-3}}$, in both cases. A fully developed laminar velocity profile with flow rate $Q = 5.5\,\mathrm{cm^3/s}$ is imposed at the inlet of the central carotid artery (main branch before bifurcation). Since the inflow diameter is 0.62 cm, this mean physiologic flow rate $Q = 5.5\,\mathrm{cm^3/s}$ results in a Reynolds number $Re = 300$ in the Newtonian case. The diameters of the outflow sections of the internal and external carotid arteries are equal to 0.25 cm and 0.22 cm, respectively. The total length of the domain, from upstream to downstream is approximately 5.4 cm. No-slip boundary conditions are imposed at the vessel wall.

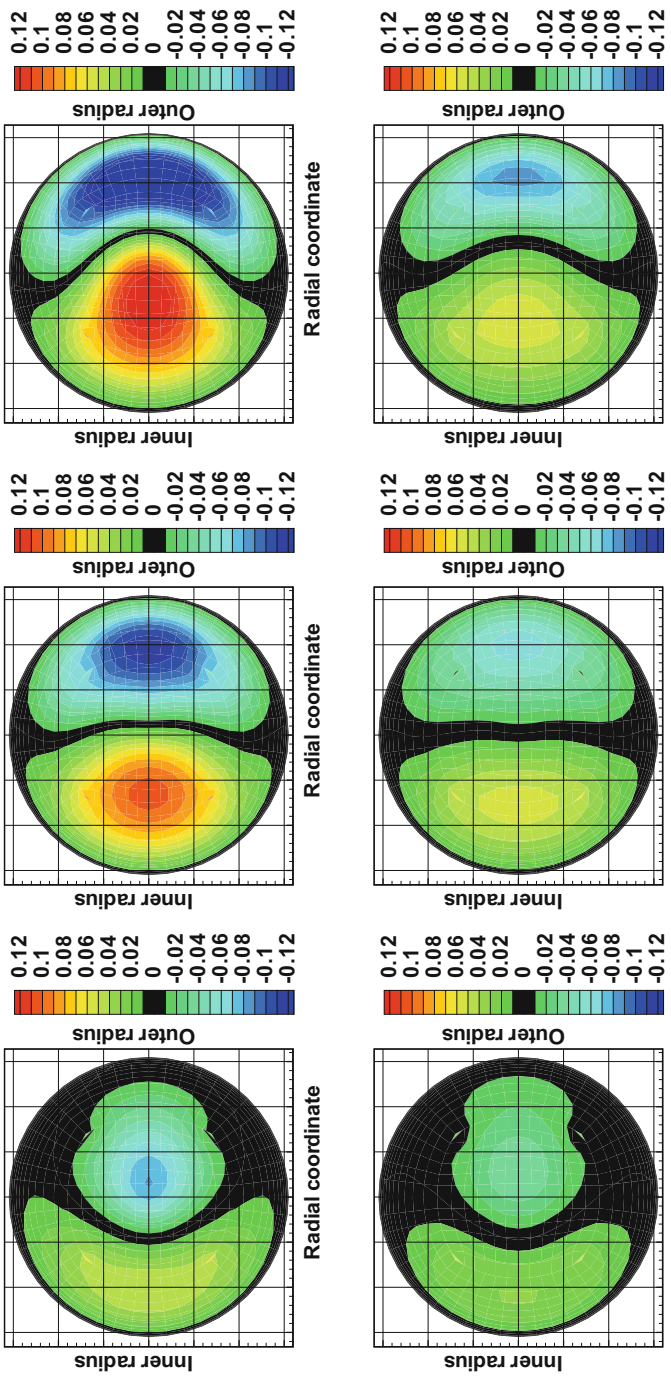

Fig. 16 Relative differences between the axial velocity magnitude contours $(u_{bModel} - u_{NS})/U$ (top row) and $(u_{bModel} - u_{GOB})/U$ (bottom row) in three different cross-sections at the bended part of the curved vessel (30°, 60°, 90°)

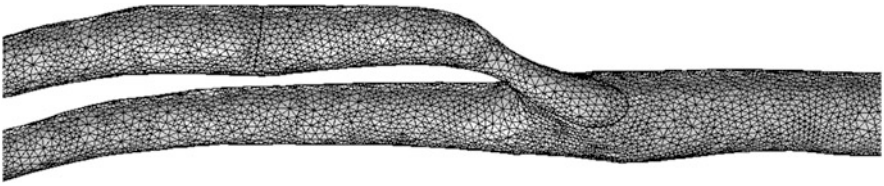

Fig. 17 Computational mesh used for the blood flow simulations in a stenosed carotid artery bifurcation

The conditions applied at the outlets are usually imposed in order to guarantee the well-posedness of the differential problems, for sufficiently smooth and small data. As in the previous test cases, we impose the "standard" homogeneous Neumann conditions at the outlets. However, these conditions are unphysical for the case of a human vessel, since they neglect completely the presence of the remaining part of the circulatory system, which is usually not implemented using a 3D model due to the limited capacity of current computers. Moreover, only averaged data (mean velocity and mean pressure values) are available at the artificial boundaries and alternative boundary conditions need to be used, reflecting the physics of the given problem. A possible strategy consists in coupling the 3D Navier-Stokes (or the generalized Navier-Stokes) equations with reduced 1D (distributed parameter) or 0D (lumped parameter) approximations of the full equations that, in a simplified way, can represent the remaining part of the circulatory system and act as absorbing boundary conditions. The coupling of these heterogeneous models, using appropriate transmission conditions and efficient techniques for their numerical computation, usually called *geometrical multiscale* approach, represents a decreased level of accuracy which is compensated by its lower computational cost. This issue has been addressed by several authors and is still nowadays a matter of active research (see e.g. [104] for a recent overview referring to the original works on the subject)

A finite element approach has been adopted for the numerical solution of the governing equations associated to both models. The patient-specific geometry is discretized with 327,896 tetrahedral elements. A backward Euler scheme is used for time discretization and, at each time step (0.5×10^{-3} s), a velocity-pressure splitting scheme with algebraic factorization is implemented to discretize in space (see, e.g. [103]). Lagrange low order $P_1 - P_1$ elements have been adopted and this requires stabilization techniques like the Streamline upwind/Petrov Galerkin method (SUPG-method) in order to avoid oscillations in the numerical solutions [59]. The SUPG-method yields a substantial increase in accuracy because stabilizing artificial diffusivity is added only in the direction of the streamlines and crosswind diffusion effects are avoided.

An important commonly adopted flow indicator is the wall shear stress (WSS). Knowing the velocity and pressure fields it is possible to obtain stresses, in particular WSS which represents the tangential component of the surface force at the vessel

wall, acting against the fluid flow.

$$WSS := -(\boldsymbol{\tau} \cdot \mathbf{n}) \cdot \mathbf{t}. \tag{44}$$

Here $\mathbf{n}$ is the local wall-normal unit vector (pointing towards the fluid domain) and $\mathbf{t}$ is the corresponding unit tangential vector.

WSS may cause alterations in the endothelium and has a great influence in many inflammatory diseases, including atherosclerosis, the development of aneurysms and clotting.

Hemodynamics in the stenosed carotid bifurcation was assessed in terms of the streamlines, magnitude of the velocity vector field and WSS distribution downstream the stenosis.

The difference between the solutions obtained using the *NS* model and generalized Newtonian Carreau model can be observed in Fig. 18 representing the

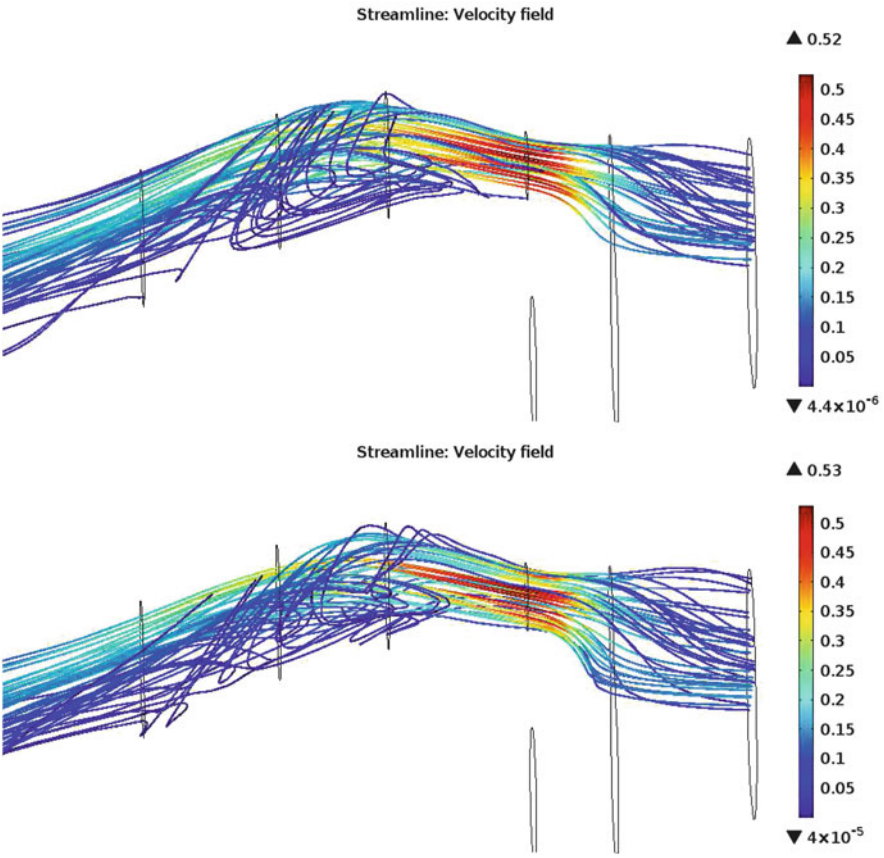

Fig. 18 Streamlines in the recirculation area downstream the stenosis in the ICA branch: for the *NS* flow (top); for the generalized Newtonian flow (bottom)

streamlines behind the stenosed region of ICA for both models. As expected, the flow behavior behind the stenosis site is quite similar, with the presence of reversal flow streamlines due to the local flow acceleration. However, the shear-thinning effects are quite visible, since the density of recirculating streamlines for the Newtonian flow is higher than for the non-Newtonian one, due to the local increase of the apparent viscosity at low shear rates, which become closer to μ_0. This also results in a larger recirculation region for the Newtonian flow, as seen in Fig. 19, when compared to Fig. 20, where the recirculation zones are marked in grey color.

Comparing the wall shear stress distribution, depicted in Figs. 21 and 22 we conclude that the higher WSS values are located in the stenosed region predicted by

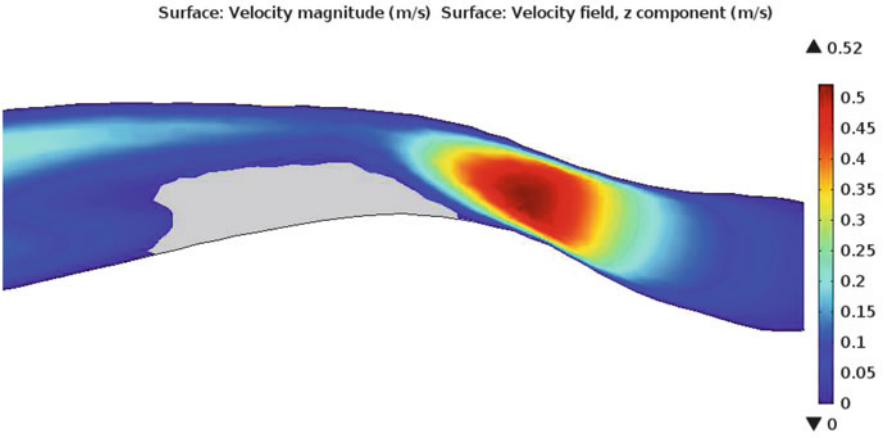

Fig. 19 Axial velocity magnitude contours and recirculation area downstream the stenosis in the ICA branch for the *NS* flow

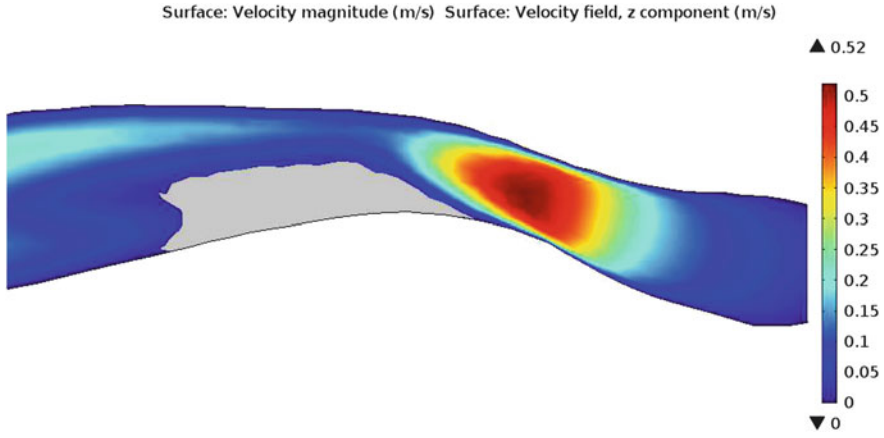

Fig. 20 Axial velocity magnitude contours and recirculation area downstream the stenosis in the ICA branch for the generalized Newtonian flow

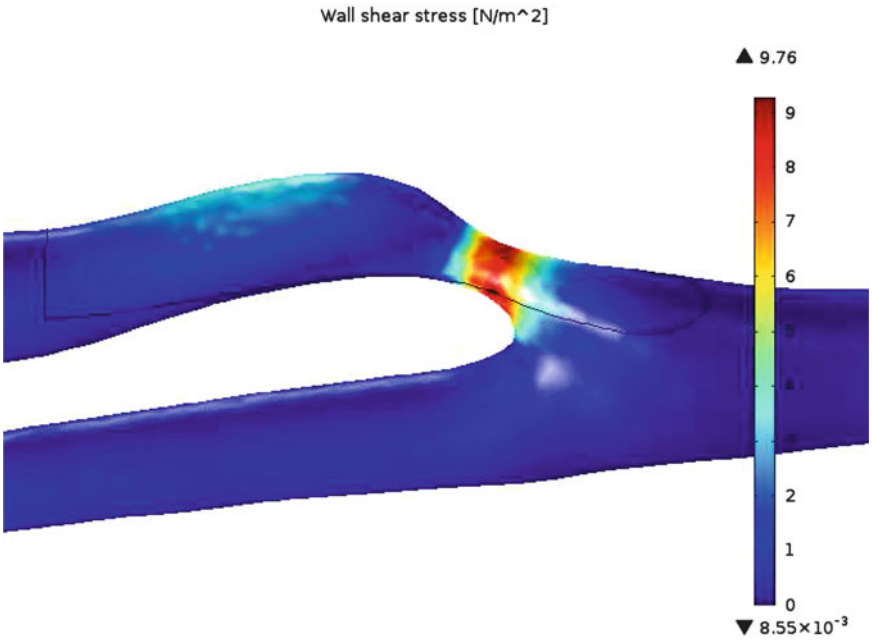

Fig. 21 Contours of the wall shear stress (WSS) distribution for the *NS* flow

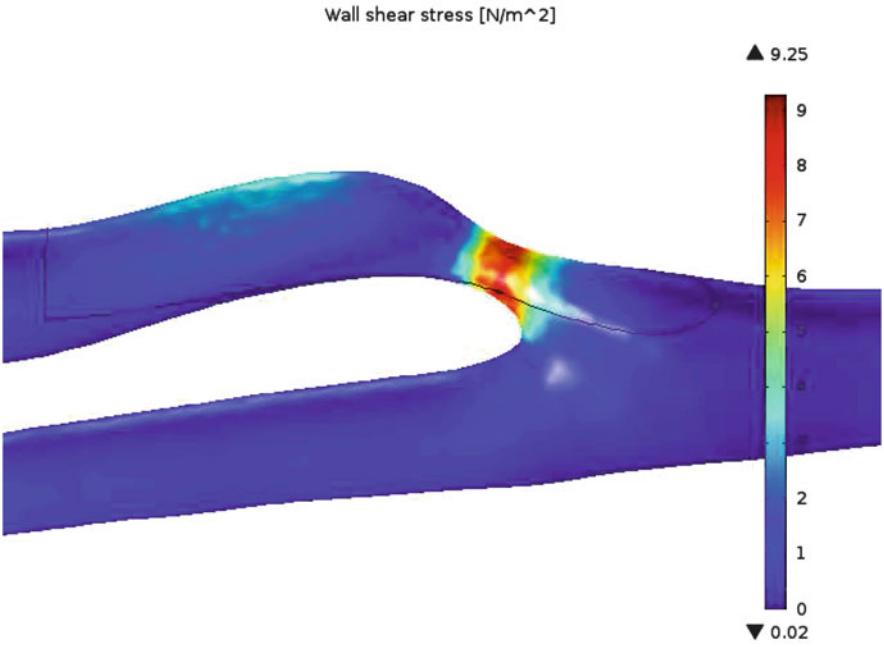

Fig. 22 Contours of the wall shear stress (WSS) distribution for the generalized Newtonian flow

the generalized Newtonian model. Also in the curved part of the stenosed branch, WSS seems to be slightly higher in the shear-thinning case. The reason for this is likely related to the non-uniform viscosity distribution along the vessel, leading to important discrepancies between Newtonian and generalized Newtonian model predictions. Therefore, it is of major importance to understand the influence of the viscosity distribution in complex flow situations.

Acknowledgements This research was partially supported by FCT—Fundação para a Ciência e a Tecnologia through the PHYSIOMATH project—"Mathematical and Computational Modeling of Human Physiology" (EXCL/MAT-NAN/0114/2012) and the Project UID/Multi/04621/2013 of the CEMAT—Center for Computational and Stochastic Mathematics, Instituto Superior Técnico, University of Lisbon.

References

1. Anand, M., Rajagopal, K., Rajagopal, K.R.: A model incorporating some of the mechanical and biochemical factors underlying clot formation and dissolution in flowing blood. Comput. Math. Methods Med. **5**(3–4), 183–218 (2003)
2. Anand, M., Rajagopal, K.R.: A shear-thinning viscoelastic fluid model for describing the flow of blood. Int. J. Cardiovasc. Med. Sci. **4**(2), 59–68 (2004)
3. Anand, M., Rajagopal, K., Rajagopal, K.R.: A model for the formation and lysis of blood clots. Pathophysiol. Haemost. Thromb. **34**, 109–120 (2005)
4. Anand, M., Rajagopal, K., Rajagopal, K.R.: A model for the formation, growth, and lysis of clots in quiescent plasma. A comparison between the effects of antithrombin III deficiency and protein C deficiency. J. Theor. Biol. **253**(4), 725–738 (2008)
5. Anand, M., Kwack, J., Masud, A.: A new Oldroyd-B model for blood in complex geometries. Int. J. Eng. Sci. **72**, 78–88 (2013)
6. Arada, N., Pires, M., Sequeira, A.: Numerical simulations of shear-thinning Oldroyd-B fluids in curved pipes. IASME Trans. **6**(2), 948–959 (2005)
7. Arada, N., Pires, M., Sequeira, A.: Viscosity effects on flows of generalized Newtonian fluids through curved pipes. Comput. Math. Appl. **53**, 625–646 (2007)
8. Artoli, A.M., Sequeira, A.: Mesoscopic simulations of unsteady shear-thinning flows. In: Computational Science - ICCS, pp. 78–85 (2006)
9. Artoli, A.M., Sequeira, A., Silva-Herdade, A.S., Saldanha, C.: Leokocytes rolling and recruitment by endothelial cells: hemorheological experiments and numerical simulations. J. Biomech. **40**, 3493–3502 (2007)
10. Astarita, G., Marrucci, G.: Principles of Non-Newtonian Fluid Mechanics. McGraw Hill, New York (1974)
11. Barnes, H.A.: Thixotropy - a review. J. Non-Newtonian Fluid Mech. **70**, 1–33 (1997)
12. Bauer, W.H., Collins, E.A.: Thixotropy and dilatancy. In: Eirich, F.R. (ed.) Rheology, Theory and Applications, vol. 4. Academic, New York (1967)
13. Berger, A.A., Talbot, L., Yao, L.-S.: Flow in curved pipes. Annu. Rev. Fluid Mech. **15**, 461–512 (1983)
14. Bingham, E.C.: An investigation of the laws of plastic flow. U.S. Bur. Stand. Bull. **13**, 309–353 (1916)
15. Bishop, J.J., Popel, A.S., Intaglietta, M., Johnson, P.C.: Relashionship between erythrocyte aggregate size and flow rate in skeletal muscle venules. Am. J. Physiol. **286**, H113–H120 (2004)

16. Bodnár, T., Sequeira, A.: Numerical simulation of the coagulation dynamics of blood. Comput. Math. Methods Med. **9**(2), 83–104 (2008)
17. Bodnár, T., Sequeira, A.: Numerical study of the significance of the non-Newtonian nature of blood in steady flow through a stenosed vessel. In: Rannacher, R., Sequeira, A. (eds.) Advances in Mathematical Fluid Mechanics, pp. 83–104. Springer, Berlin (2010)
18. Bodnár, T., Sequeira, A., Pirkl, L.: Numerical simulations of blood flow in a stenosed vessel under different flow rates using a generalized Oldroyd-B Model. Numerical Analysis and Applied Mathematics, vol. 2, pp. 645–648. American Institute of Physics, New York (2009)
19. Bodnár, T., Rajagopal, K.R., Sequeira, A.: Simulation of the three-dimensional flow of blood using a shear-thinning viscoelastic fluid model. Math. Model. Nat. Phenom. **6**(5), 1–24 (2011)
20. Bodnár, T., Fasano, A., Sequeira, A.: Mathematical Models for Blood Coagulation. In: Bodnár, T., Galdi, G.P., Nečasová, S. (eds.) Fluid-Structure Interaction and Biomedical Applications. Advances in Mathematical Fluid Mechanics, Chap. 7, pp. 483–569, Birkhäuser, Basel (2014)
21. Box, F.M.A., van der Geest, R.J., Rutten, M.C.M., Reiber, J.H.C.: The Influence of flow, vessel diameter, and Non-Newtonian blood viscosity on the wall shear stress in a carotid bifurcation model for unsteady flow. Investig. Radiol. **40**(5), 277–294 (2005)
22. Boyd, J., Buick, J.M., Green, S.: Comparison of Newtonian and Non-Newtonian oscillatory flows using the Lattice Boltzmann method. In: World Congress on Medical Physics and Biomedical Engineering, IFMBE Proceedings, vol. 14, pp. 3395–3399 (2007)
23. Čanić, S., Hartley, C.J., Rosenstrauch, D., Tambača, J., Guidoboni, G., Mikelić, A.: Blood flow in compliant arteries: an effective viscoelastic reduced model, numerics and experimental validation. Ann. Biomed. Eng. **34**(4), 575–592 (2006)
24. Caro, C.G., Pedley, T.J., Schroter, R.C., Seed, W.A., Parker, R.H.: The Mechanics of the Circulation, 2nd edn. Oxford University Press, Oxford (2012)
25. Charm, S.E., Kurland, G.S.: Blood Flow and Microcirculation. Wiley, New York (1974)
26. Chen, J., Lu, X.-Y., Wang, W.: Non-Newtonian effects of blood flow on hemodynamics in distal vascular graft anastomoses. J. Biomech. **39**, 1983–1995 (2006)
27. Chien, S.: Red cell deformability and its relevance to blood flow. Ann. Rev. Physiol. **49**, 177–192 (1987)
28. Chien, S., Usami, S., Dellenback, R.J., Gregersen, M.I.: Shear dependence of effective cell volume as a determinant of blood viscosity. Science **168**, 977–979 (1970)
29. Chien, S., Usami, S., Dellenback, R.J., Gregersen, M.I.: Shear-dependent deformation of erythrocytes in rheology of human blood. Am. J. Physiol. **219**, 136–142 (1970)
30. Chien, S., King, R.G., Skalak, R., Usami, S., Copley, A.L.: Viscoelastic properties of human blood and red cell suspensions. Biorheology **12**, 341–346 (1975)
31. Cho, Y.I., Kensey, K.R.: Effects of the Non-Newtonian viscosity of blood on flows in a diseased arterial vessel. Part I: steady flows. Biorheology **28**, 241–262 (1991)
32. Dintenfass, L.: Blood Microrheology - Viscosity Factors in Blood Flow, Ischaemia and Thrombosis. Butterworth, London (1971)
33. Dintenfass, L.: Blood Viscosity, Hyperviscosity and Hyperviscosaemia. MTP Press Ltd, Lancaster (1985)
34. Dong, C., Lei, X.X.: Biomechanics of cell rolling: shear flow, cell-surface adhesion and cell deformability. J. Biomech. **33**(1), 35–43 (2000)
35. Dupin, M.M., Halliday, I., Care, C.M., Alboul, L., Munn, L.L.: Modeling the flow of dense suspensions of deformable particles in three dimensions. Phys. Rev. E **75**, 066707 (2007)
36. Evans, E.A., Hochmuth, R.M.: Membrane viscoelasticity. Biophys. J. **16**(1), 1–11 (1976)
37. Fan, Y., Tanner, R.I., Phan-Thien, N.: Fully developed viscous and viscoelastic flows in curved pipes. J. Fluid Mech. **440**, 327–357 (2001)
38. Fasano, A., Sequeira, A.: Hemomath. The Mathematics of Blood. MS&A - Modeling, Simulation and Applications Series, vol. 18. Springer, Cham (2017). ISBN: 978-3-319-60512-8
39. Fasano, A., Santos, R., Sequeira, A.: Blood coagulation: a puzzle for biologists, a maze for mathematicians. In: Ambrosi, D., Quarteroni, A., Rozza, G. (eds.) Modelling Physiological Flows, Chap. 3, pp. 44–77. Springer Italia, Milano (2011). https://doi.org/10.1007/978-88-470-1935-53

40. Feher, J.J.: Quantitative Human Physiology: An Introduction. Elsevier, Academic, Amsterdam, New York (2012)
41. Fåhraeus, R.: The suspension stability of blood. Physiol. Rer. **9**, 241–274 (1929)
42. Fåhraeus, R., Lindqvist, T.: The viscosity of blood in narrow capillary tubes. Am. J. Physiol. **96**, 362–368 (1931)
43. Ferry, J.D.: Viscoelastic Properties of Polymers. Wiley, New York (1980)
44. Formaggia, L., Perktold, K., Quarteroni, A.: Basic mathematical models and motivations. In: Formaggia, L., Quarteroni, A., Veneziani, A. (eds.) Cardiovascular Mathematics. Modeling and Simulation of the Circulatory System, vol. 1, pp. 46–75. Springer, Berlin (2009)
45. Fung, Y.C.: Biomechanics: Circulation. Springer, New York (1997)
46. Gabe, I.T., Gault, J.H., Ross, J., Mason, D.T., Mills, C.J., Schillingford, J.P., Braunwald, E.: Measurement of instantaneous blood flow velocity and pressure in conscious man with a catheter-tip velocity probe. Circulation **40**, 603–614 (1969)
47. Galdi, G.P.: An Introduction to the Mathematical Theory of the Navier-Stokes Equations: Linearised Steady Problems. Springer Tracts in Natural Phylosophy, 2nd Corrected edn., vol. 38. Springer, Berlin (1998)
48. Galdi, G.P.: An Introduction to the Mathematical Theory of the Navier-Stokes Equations: Nonlinear Steady Problems. Springer Tracts in Natural Phylosophy, 2nd Corrected edn., vol. 39, Springer, Berlin (1998)
49. Gambaruto, A.M., Janela, J., Moura, A., Sequeira, A.: Sensitivity of hemodynamics in a patient specific cerebral aneurysm to vascular geometry and blood rheology. Math. Biosci. Eng. **8**(2), 409–423 (2011)
50. Gambaruto, A., Janela, J., Moura, A., Sequeira, A.: Shear-thinning effects of hemodynamics in patient-specific cerebral aneurysms. Math. Biosci. Eng. **10**(3), 649–665 (2013)
51. Gaspar-Rosas, A., Thurston, G.B.: Erythrocyte aggregate rheology by transmitted and reflected light. Biorheology **25**, 471–487 (1988)
52. Guerra, T., Tiago, J., Sequeira, A.: Optimal control in blood flow simulations. Int. J. Non Linear Mech. **64**, 57–69 (2014)
53. Gijsen, F.J.H., Allanic, E., van de Vosse, F.N., Janssen, J.D.: The influence of the non-Newtonian properties of blood on the flow in large arteries: unsteady flow in a 90° curved tube. J. Biomech. **32**(6), 601–608 (1999)
54. Gregg, D.: Dynamycs of blood and lymph flow. In: Best, C., Taylor, N. (eds.) The Physiological Basis of Medical Practice. 8th edn. Williams and Wilkins, New York (1966)
55. Guyton, A.: Textbook of Medical Physiology, 8th edn. W.B. Saunders, Philadelphia, PA (1991)
56. Herschel, W.H., Bulkley, R.: Measurement of consistency as applied to rubber-benzene solutions. Proc. ASTM, Part II **26**, 621–629 (1926)
57. Huang, C., Chai, Z., Shi, B.: Non-Newtonian effect on hemodynamic characteristics of blood flow in stented cerebral aneurysm. Commun. Comput. Phys. **13**(3), 916–928 (2013)
58. Hundertmark-Zavková, A., Lukáčová-Medvidová, M.: Numerical study of shear-dependent Non-Newtonian fluids in compliant vessels. Comput. Math. Appl. **60**(3), 572–590 (2010)
59. Hughes, T.J.R., Franca, L., Balestra, M.: A new finite element method for computational fluid dynamics: V. Circumventing the Babuska-Brezzi condition: a stable Petrov-Galerkin formulation of the Stokes problem accommodating equal order interpolations. Comput. Methods Appl. Mech. Eng. **59**, 85–99 (1986)
60. Jameson, A., Schmidt, W., Turkel, E.: Numerical solutions of the Euler equations by finite volume methods using Runge-Kutta time-stepping scheme. In: AIAA 14th Fluid and Plasma Dynamics Conference, Palo Alto (1981), AIAA paper 81 - 1259 (1981)
61. Janela, J., Moura, A., Sequeira, A.: A 3D non-Newtonian fluid-structure interaction model for blood flow in arteries. J. Comput. Appl. Math. **234**(9), 2783–2791 (2010)
62. Janela, J., Moura, A., Sequeira, A.: Absorbing boundary conditions for a 3D non-Newtonian fluid - structure interaction model for blood flow in arteries. Int. J. Eng. Sci. **48**(11), 1332–1349 (2010)
63. Janela, J., Sequeira, A., Pontrelli, G., Succi, S., Ubertini, S.: Unstructured Lattice Boltzmann method for hemodynamic flows with shear-dependent viscosity. Int. J. Mod. Phys. C **21**(06), 795–811 (2010)

64. Joseph, D.D.: Fluid Dynamics of Viscoelastic Liquids. Springer, Berlin (1990)
65. Keener, J., Sneyd, J.: Mathematical Physiology. II: Systems Physiology, 2nd edn. Springer, Berlin (2008)
66. Key, N., Makris, M., O'Shaughnessy, D., Lillicrap, D. (eds.): Practical Hemostasis and Thrombosis, 2nd edn. Wiley-Blackwell, Hoboken (2009)
67. Kim, S., Cho, Y.I., Jeon, A.H., Hogenauer, B., Kensey, K.R.: A new method for blood viscosity measurement. J. Non-Newtonian Fluid Mech. **94**, 47–56 (2000)
68. Kim, Y.H., VandeVord, P.J., Lee, J.S.: Multiphase non-Newtonian effects on pulsatile hemodynamics in a coronary artery. Int. J. Numer. Methods Fluids **58**(7), 803–825 (2008)
69. King, M.R., Hammer, D.A.: Multiparticle adhesive dynamics: hydrodynamic recruitment of rolling leukocytes. PNAS **98**(26), 14919–14924 (2001)
70. Lee, B-K., Xue, S., Nam, J., Lim, H., Shin, S.: Determination of the blood viscosity and yield stress with a pressure-scanning capillary hemorheometer using constitutive models. Korea-Aust. Rheol. J. **23**(1), 1–6 (2011)
71. Leuprecht, A., Perktold, K.: Computer simulation of non-Newtonian effects of blood flow in large arteries. Comp. Methods Biomech. Biomech. Eng. **4**, 149–163 (2001)
72. Lichtman, M.A.: Rheology of leukocytes, leukocyte suspensions, and blood in leukemia. Possible relationship to clinical manifestations. J. Clin. Invest. **52**(2), 350–358 (1971)
73. Liepsch, D., Moravec, S.: Pulsatile flow of non-Newtonian fluid in distensible models of human arteries. Biorheology **21**, 571–586 (1984)
74. Liu, B., Tang, D.: Non-Newtonian effects on the wall shear stress of the blood flow in stenotic right coronary arteries. Int. Conf. Comput. Exp. Eng. Sci. **17**(2), 55–60 (2011)
75. Lopez, L., Duck, I.M., Hunt, W.A.: On the shape of the erythrocyte. Biophys J. **8**(11), 1228–1235 (1968)
76. Lowe, G.D.O. (ed.): Clinical Blood Rheology, vols. I and II. CRC Press, Boca Raton, FL (1998)
77. Lucius, M., Stolz, J.F.: Importance of erythrocyte aggregation on the viscoelastic and thixotropic properties of blood. Clin. Hemorheol. **7**, 63–70 (1987)
78. Mandal, P.K.: An unsteady analysis of Non-Newtonian blood flow through tapered arteries with a stenosis. Int. J. Non Linear Mech. **40**(1), 151–164 (2005)
79. Mao, S.S., Ahmadi, N., Shah, B., Beckmann, D., Chen, A., Ngo, L., Flores, F.R., Gao, Y.I., Budoff, M.J.: Normal thoracic aorta diameter on cardiac computed tomography in healthy asymptomatic adult; Impact of age and gender. Acad. Radiol. **15**, 827–834 (2008)
80. Marder, V.J., Aird, W.C., Bennett, J.S., Schulman. S., White, G.C. II (eds.): Hemostasis and Thrombosis: Basic Principles and Clinical Practice, 6th edn. Lippincott Williams & Wilkins, Wolters Kluwer, Philadelphia (2013)
81. Maxwell, J.C.: On the dynamical theory of gases. Philos. Trans. R. Soc. Lond. A **157**, 26–78 (1866)
82. McDonald, D.A.: Blood Flow in Arteries, 2nd edn. The Camelot Press Ltd., Southampton, Great Britain (1974)
83. Merrill, E.W.: Rheology of blood. Physiol. Rev. **49**(4), 863–888 (1969)
84. Merrill, E.W., Gilliland, E.R., Cokelet, G.R., Shin, H., Britten, A., Wells, R.E.: Rheology of human blood, near and at zero flow. Effects of temperature and hematocrit level. Biophys. J. **3**, 199–213 (1963)
85. Merrill, E.W., Cokelet, G.R., Britten, A., Wells, R.E.: Non-Newtonian rheology of human blood. Effect of fibrinogen deduced by subtraction. Circ. Res. **13**, 48–55 (1963)
86. Merrill, E.W., Margetts, W.G., Cokelet, G.C., Gilliland, E.R.: The Casson equation and rheology of the blood near shear zero. In: Copley, A.L. (ed.) Proceedings Fourth International Congress on Rheology, Part 4, pp. 135–143. New York, Interscience (1965)
87. Molla, M.M., Paul, M.C.: LES of non-Newtonian physiological blood flow in a model of arterial stenosis. Med. Eng. Phys. **34**(8), 1079–1087 (2012)
88. Moller, P.C.F., Mewis, J., Bonn, D.: Yield stress and thixotropy: on the difficulty of measuring yield stress in practice. Soft Matter **2**, 274–288 (2006)

89. Morris, C.L., Rucknagel, D.L., Shukla, R., Gruppo, R.A., Smith, C.M., Blackshear Jr., P.: Evaluation of the yield stress of normal blood as a function of fibrinogen concentration and hematocrit. Microvasc. Res. **37**(3), 323–338 (1989)
90. Nandakumar, N., Sahu, K.C., Anand, M.: Pulsatile flow of a shear-thinning model for blood through a two-dimensional stenosed channel. Eur. J. Mech. B. Fluids **49**, 29–35 (2015)
91. Neofytou, P.: Comparison of blood rheological models for physiological flow simulation. Biorheology **41**(6), 693–714 (2004)
92. Nguyen, Q.D., Boger, D.V.: Measuring the flow properties of yield stress fluids. Annu. Rev. **24**, 47–88 (1992)
93. Osterloch, K., Gaehtgens, P., Pries, A.R.: Determination of microvascular flow patternformation in vivo. Am. J. Physiol. **278**, H1142–H1152 (2000)
94. Ottensen, J.T., Olufsen, M.S., Larsen, J.K.: Applied Mathematical Models in Human Physiology. SIAM Monographs on Mathematical Modeling and Computation SIAM, Philadelphia (2004)
95. Owens, R.G.: A new microstructure-based constitutive model for human blood. J. Non - Newtonian Fluid Mech. **14**, 57–70 (2006)
96. Pearson, M.J., Lipowsky, H.H.: Influence of erythrocyte aggregation on leukocyte margination and adhesion in postcapillary venules of rat mesentery. Am. J. Physiol. **279**, H1460–H1471 (2000)
97. Perktold, K., Hilbert, D.: Numerical solution of pulsatile flow in a carotid bifurcation. J. Biomed. Eng. **8**, 193–199 (1986)
98. Perktold, K., Peter, R.: Numerical 3D-simulation of pulsatile wall shear stress in an arterial T-bifurcation model. J. Biomed. Eng. **12**, 2–12 (1990)
99. Perktold, K., Resh, M., Peter, R.O.: Three-dimensional numerical analysis of pulsatile blood flow and wall shear stress in the carotid artery bifurcation. J. Biomech. **24**, 409–420 (1991)
100. Perktold, K., Rappitsch, G.: Computer simulation of local blood flow and vessel mechanics in a compliant carotid artery bifurcation model. J. Biomech. **28**, 845–856 (1995)
101. Popel, A.S., Johnson, P.C.: Microcirculation and hemorheology. Annu. Rev. Fluid Mech. **37**, 43–69 (2005)
102. Prager, W.: Introduction to Mechanics of Continua. Dover Phoenix Edition, New York (1961)
103. Quarteroni, A., Saleri, F., Veneziani, A.: Factorization methods for the numerical approximation of the Navier-Stokes equations. Comput. Methods Appl. Mech. Eng. **188**, 505–526 (2000)
104. Quarteroni, A., Veneziani, A., Vergara, C.: Geometric multiscale modeling of the cardiovascular system, between theory and practice. Comput. Methods Appl. Mech. Eng. **302**, 193–252 (2016)
105. Quemada, D.: Rheology of concentrated disperse systems III. General features of the proposed non-Newtonian model. Comparison with experimental data. Rheol. Acta **17**, 643–653 (1978)
106. Ramalho, S., Moura, A.B., Gambaruto, A.M., Sequeira, A.: Influence of blood rheology and outflow boundary conditions in numerical simulations of cerebral aneurysms. In: Mathematical Methods and Models in Biomedicine. Lecture Notes on Mathematical Modelling in the Life Sciences, pp. 149–175. Springer, New York (2013)
107. Rajagopal, K.R., Srinivasa, A.R.: A thermodynamic frame work for rate-type fluid models. J. Non-Newtonian Fluid Mech. **80**, 207–227 (2000)
108. Robertson, A.M., Sequeira, A., Kameneva, M.V.: Hemorheology. In: Galdi, G.P., Rannacher, R., Robertson, A.M., Turek, S. (eds.) Hemodynamical Flows: Modeling, Analysis and Simulation. (Oberwolfach Seminars), vol. 37, pp. 63–120. Birkhäuser Verlag, Basel (2008)
109. Robertson, A.M., Sequeira, A., Owens, R.G.: Hemorheology. In: Formaggia, L., Quarteroni, A., Veneziani, A. (eds.) Cardiovascular Mathematics. Modeling and Simulation of the Circulatory System, vol. 1. Springer, Berlin (2009), pp. 211–242
110. Roco, M.C. (ed.): Particulate Two-Phase Flow. Series in Chemical Engineering. Butterworth-Heinemann Publisher, London (1993)
111. Schmid-Schönbein, H., Wells, R.E.: Fluid drop-like transition of erythrocytes under shear. Science **165**, 288–291 (1969)

112. Schmid-Schönbein, H., Wells, R.E.: Rheological properties of human erythrocytes and their influence upon anomalous viscosity of blood. Physiol. Rev. **63**, 147–219 (1971)
113. Schmid-Schönbein, H., Barroso-Aranda, J., Chavez-Chavez, R.: Microvascular leukocyte kinetics in the flow state. In: Boccalon, H. (ed.) Vascular Medicine, pp. 349–352. Elsevier, Amsterdam (1993)
114. Scott-Blair, G.W.: An equation for the flow of blood, plasma and serum through glass capillaries. Nature **183**, 613–614 (1959)
115. Secomb, T.W.: Mechanics and computational simulation of blood flow in microvessels. Med. Eng. Phys. **33**, 800–804 (2010)
116. Sequeira, A., Artoli, A.M., Silva-Herdade, A.S., Saldanha, C.: Leukocytes dynamics in microcirculation under shear-thinning blood flow. Comput. Math. Appl. **58**(5), 1035–1044 (2009)
117. Sequeira, A., Bodnár, T.: Blood coagulation simulations using a viscoelastic flow model. Math. Model. Nat. Phenom. **9**(6), 34–45 (2014)
118. Serrin, J.: Mathematical principles of classical fluid mechanics. In: Flugge, S., Truesdell, C. (eds.) Handbuch der Physik, vol. VIII/I. Springer, Berlin (1959)
119. Skalak, R., Tozeren, A., Zarda, R., Chein, S.: Strain energy function of red blood cell membranes. Biophys. J. **13**(3), 245–264 (1973)
120. Silverthorn, D.U.: Human Physiology. An Integrated Approach, 7th edn. Prentice Hall, Upper Saddle River, NJ (2015)
121. Thiriet, M.: Biology and Mechanics of Blood Flows. Part I: Biology. CRM Series in Mathematical Physics. Springer, Berlin (2008)
122. Thiriet, M.: Biology and Mechanics of Blood Flows. Part II: Mechanics and Medical Aspects. CRM Series in Mathematical Physics. Springer, Berlin (2008)
123. Thiriet, M., Parker, K.H.: Physiology and pathology of the cardiovascular system: a physical perspective. In: Formaggia, L., Quarteroni, A., Veneziani, A. (eds.) Cardiovascular Mathematics. Modeling and Simulation of the Circulatory System, vol. 1, pp. 1–46 Springer, Berlin (2009)
124. Thurston, G.B.: Viscoelasticity of human blood. Biophys. J. **12**, 1205–1217 (1972)
125. Thurston, G.B.: Frequency and shear rate dependence of viscoelasticity of human blood. Biorheology **10**, 375–381 (1973)
126. Thurston, G.B.: Elastic effects in pulsatile blood flow. Microvasc. Res. **9**, 145–157 (1975)
127. Thurston, G.B.: Non-Newtonian viscosity of human blood: flow induced changes in microstructure. Biorheology **31**(2), 179–192 (1994)
128. Thurston, G.B.: Viscoelastic properties of blood and blood analogs. Adv. Hemodyn. Hemorheol. **1**, 1–30 (1996)
129. Toksvang, L.N., Berg, R.M.G.: Using a classic paper by Robin Fåhraeus and Torsten Lindqvist to teach basic hemorheology. Adv. Physiol. Educ. **37**(2), 129–133 (2013)
130. Vierendeels, J., Riemslagh, K., Dick, E.: A multi-grid semi-implicit line-method for viscous incompressible and low-Mach-number flows on high aspect ratio grids. J. Comput. Phys. **154**, 310–344 (1999)
131. Vlastos, G., Lerche, D., Koch, B.: The superposition of steady on oscillatory shear and its effect on the viscoelasticity of human blood and a blood-like model fluid. Biorheology **34**, 19–36 (1997)
132. Yeleswarapu, K.K., Kameneva, M.V., Rajagopal, K.R., Antaki, J.F.: The flow of blood in tubes: theory and experiment. Mech. Res. Commun. **25**(3), 257–262 (1998)
133. Walburn, F.J., Schneck, D.J.: A constitutive equation for whole human blood. Biorheology **13**, 201–210 (1976)
134. Zhang, J., Johnson, P.C., Popel, A.S.: Effects of erythrocyte deformability and aggregation on the cell free layer and apparent viscosity of microscopic blood flows. Microvasc. Res. **77**(3), 265–272 (2009)
135. Zwaal, R.F., Hemker, H.C.: Blood Coagulation. Elsevier Science Publishers, North Holland (1986)

Old Problems Revisited from New Perspectives in Implicit Theories of Fluids

Giuseppe Saccomandi and Luigi Vergori

Abstract Three of the most studied problems in fluid dynamics are revisited within implicit theories of fluids. Specifically, the onset of convection, the determination of laminar flows and the motion of a fluid down an inclined plane are studied under the assumption that the Cauchy stress tensor and the rate-of-strain tensor are related through implicit constitutive equations. Particular attention is paid to fluids whose viscosities are pressure-dependent.

1 Introduction

The *principium reddendae rationis* is one of the most powerful tool that have been used in philosophical argumentations [28]. It has been used as principle by many philosophers (Spinoza, Liebniz, Descartes, Hamilton, to cite a few of them) and is very useful also in Science. Anaximander of Miletus suggestively used the *principium reddendae rationis* to argue that Earth was a round cylinder statically floating at the center of Universe without any support. In Anaximander's reasoning, since Earth was equidistant from all other bodies there was no reason why it should move in any one direction.

The *principium reddendae rationis* has been applied more rigorously in classical continuum mechanics, and, here, we shall appeal to it to sustain the suitability of introducing implicit constitutive relations rather than explicit models. The main aim of these notes is indeed the introduction, in the framework of implicit theories of

G. Saccomandi (✉)
Dipartimento di Ingegneria, Università degli Studi di Perugia, Perugia, Italy

School of Mathematics, Statistics and Applied Mathematics, National University of Ireland Galway, Galway, Ireland
e-mail: giuseppe.saccomandi@unipg.it

L. Vergori
Dipartimento di Ingegneria, Università degli Studi di Perugia, Perugia, Italy
e-mail: luigi.vergori@unipg.it

A. Farina et al. (eds.), *Non-Newtonian Fluid Mechanics and Complex Flows*,
Lecture Notes in Mathematics 2212, https://doi.org/10.1007/978-3-319-74796-5_2

fluids, of the class of fluids whose viscosities depend on pressure and that, for such a peculiarity, are called *piezo-viscous fluids* [10].

It is well known that in any continuum theory the motion of a real body $\mathscr{B}$ is governed by the balance laws of mass, linear and angular momenta, and energy as well as by the second law of Thermodynamics. In particular, if the Cauchy axiom holds, namely the internal actions in $\mathscr{B}$ can be represented only by a vector field, in the absence of body couples the balance of angular momentum requires that the Cauchy stress tensor T is symmetric, i.e. $\mathsf{T} = \mathsf{T}^T$, and the equations of mass, linear momentum and energy read

$$\dot{\rho} + \rho \mathrm{div} \boldsymbol{v} = 0, \tag{1}$$

$$\rho \dot{\boldsymbol{v}} = \mathrm{div} \mathsf{T} + \rho \boldsymbol{b}, \tag{2}$$

$$\rho \dot{e} + \mathrm{div} \boldsymbol{q} = \mathsf{T} \cdot \mathsf{D} + \rho r, \tag{3}$$

respectively. In (1)–(3) ρ denotes the mass density, $\boldsymbol{v}$ the velocity field, $\boldsymbol{b}$ the specific body force, e the specific internal energy, r the specific radiant heating, $\boldsymbol{q}$ the heat flux vector, and D the rate-of-strain tensor, i.e. the symmetric part of the velocity gradient $\mathsf{L} = \nabla \boldsymbol{v}$. The superimposed dot denotes the material time derivative.[1] The second law of Thermodynamics is instead usually written as the Clausius-Duhem inequality

$$\rho \dot{\eta} \geq \rho \frac{r}{\theta} - \mathrm{div} \left(\frac{\boldsymbol{q}}{\theta} \right), \tag{4}$$

with η denoting the specific entropy and θ the temperature.

Regarding the specific body force $\boldsymbol{b}$ as known, Eqs. (1)–(3) provide seven scalar equations for 13 scalar fields—the mass density ρ, the velocity components v_i $(i = 1, 2, 3)$, and the stress tensor components T_{ij} $(i, j = 1, 2, 3)$. The system of PDEs (1)–(3) is then not closed. The disparity in the number of equations and unknowns is however not surprising as (1)–(3) are valid for all the non-polar materials (i.e. materials satisfying the Cauchy axiom), but do not differentiate the special material the body is made of. Therefore, to obtain a system the number of equations of which matches the number of unknowns, one has to introduce some constitutive equations characterizing the thermomechanical response of the material.

Constitutive equations are very often referred to as constitutive relations. According to the Cambridge dictionary, a *relation* is *a connection or similarity between two things*. This is exactly what modelers well educated in mechanics usually do. They connect thermodynamical quantities through an equation which is specific to a particular material or substance.

[1] For the sake of self-consistency, if Σ is a smooth scalar, vector or tensor field defined on the trajectory of the body $\mathscr{B}$, $\dot{\Sigma} = \Sigma_t + (\boldsymbol{v} \cdot \nabla)\Sigma$.

For example, in classical fluid mechanics the stress tensor is related to the rate-of-strain tensor D, the density of the fluid and the temperature through an equation of the form

$$\mathsf{H}(\mathsf{T}, \mathsf{D}, \rho, \theta) = \mathsf{O}. \tag{5}$$

Such a relationship is sufficient to close the subsystem (1)–(3) and thus there is no clear reason (no *reddendae rationis*) to consider *a priori* an *explicit* representation of the form

$$\mathsf{T} = \hat{\mathsf{T}}(\mathsf{D}, \rho, \theta), \tag{6}$$

such as the Navier-Stokes constitutive equation:

$$\mathsf{T} = -p_{|E}(\rho, \theta)\mathsf{I} + \lambda(\rho, \theta)\mathrm{tr}(\mathsf{D})\mathsf{I} + 2\mu(\rho, \theta)\mathsf{D}, \tag{7}$$

where $p_{|E}$ is the pressure at thermodynamic equilibrium, and λ and μ are the bulk and shear viscosity, respectively. The reason of considering a representation of the form (6) stands exclusively in its mathematical ease.

The search for models of mathematical ease is common when dealing with problem of the motion of real bodies. A simple example comes from particle mechanics. It is well known that the motion of a free particle X is governed by Newton's second law

$$m\boldsymbol{a} = \boldsymbol{F}, \tag{8}$$

where m is the mass of the particle, $\boldsymbol{a}$ is the acceleration vector, and $\boldsymbol{F}$ is the resultant force acting on X. In direct problems the resultant force $\boldsymbol{F}$ is usually known, and the motion is to be determined by solving (8) under prescribed initial conditions for the position $\boldsymbol{x}$ and the velocity $\boldsymbol{v}$ of X. To solve uniquely the resulting Cauchy problem, one assumes that any *experimental* model for the force $\boldsymbol{F}$ depends on the motion of the particle through a relation of the form $\boldsymbol{F} = \widehat{\boldsymbol{F}}(\boldsymbol{x}, \boldsymbol{v}, t)$, where $\widehat{\boldsymbol{F}}$ satisfies the smoothness assumptions of Cauchy's theorem for ordinary differential equations.

Behind the introduction of a constitutive relation of the form (6) there is then the expectation that, in the framework of a field theory like continuum mechanics, any initial and boundary value problem (IBVP) governing the motion of a real body admits a unique solution as the Cauchy problem governing the motion of a free particle in the framework of Newtonian's particle mechanics.

Jacques Hadamard [18] introduced the concept of well-posedness of IBVPs. An IBVP is well posed if it admits a unique solution which depends continuously on the data (that is on initial and boundary conditions). Well-posedness in the sense of Hadamard has always influenced strongly applied mathematicians and scholars involved in continuum mechanics research when modeling a real-world phenomenon. From a mathematical point of view it is clear that well-posedness is intriguing. From the point of view of continuum mechanics well-posedness is closely related to the concept of determinism. From this perspective, the principle

of determinism for the stress stated in Truesdell and Noll's celebrated handbook [52],

> The stress in a body is determined by the history of the motion of that body,

can be regarded as a sort of 'pathway' to well-posedness.

John Ball and Richard James [5] commenting on the concept of well-posedness in the sense of Hadamard wrote:

> Any reader of that paper will see the unmistakable influence of Truesdell. At the end of the day, perhaps it would have been realized that Hadamard's notions of well-posedness are far too restrictive in the nonlinear setting, that non-uniqueness and even non-existence comprise acceptable behavior, and that there are probably no fundamental restrictions on the strain-energy function at all besides those arising from material symmetry and frame-indifference.

This means not only that the principle of determinism is highly questionable from a physical point of view, but also that *mathematical feasibility* is not a good argument to support explicit constitutive equations where stress is given in terms of motion.

Nature does not care if the relationship at the basis of its phenomena are graphs or functions. It is our idealization of natural phenomena that sometimes realizes the fact that relationships in the form of functions are more convenient. Moreover, an explicit approach rules out *a priori* the possibility to describe interesting phenomena like, for instance, constitutive branching. There is then no advantage to sacrifice the *principium reddendae rationis* on the altar of mathematical well-posedness and there are no *a priori* physical reason to support explicit constitutive equations.

It is well known that in an experiment it is possible to control stress or deformation. For example, when pulling a bar of steel it is possible to control the engineering stress and to record the engineering strain (the test is said to be performed in a *soft* device), or to control the engineering strain and to record the engineering stress (test performed in a *hard* device). Therefore, in the first case why can we not postulate that the motion in a body is determined by the history of the stress of that body? The fact that constitutive relationships are described by graphs and not functions is also confirmed by several experimental works (see [37] and references therein).

The aim of these lectures is to investigate classical problems in fluid mechanics (such as the onset of Rayleigh-Bénard convection, laminar flows and flows over an inclined plane) by employing implicit constitutive relations for the stress tensor. We do not claim that the use of such implicit constitutive models represents a scientific revolution. In the light of the previous discussion, we only claim that implicit constitutive equations are useful tools for investigating real-world phenomena and there is no a clear and neat reason to throw away *a priori* this class of relations.

These notes are not meant to be a detailed review of the literature concerning piezo-viscous fluids. The choices of the topics treated and the literature presented are based mainly on our personal tastes and pedagogical aims. The level of these lecture notes is basic and tailored for undergraduate students with an elementary knowledge of continuum mechanics.

2 Implicit Constitutive Models for the Cauchy Stress Tensor

Consider the constitutive relation for the Cauchy stress tensor T of a linearly viscous fluid given by

$$\mathsf{T} = -p\mathsf{I} + 2\mu\left[\mathsf{D} - \frac{1}{3}\mathrm{tr}(\mathsf{D})\mathsf{I}\right], \tag{9}$$

where

$$p = -\frac{1}{3}\mathrm{tr}\mathsf{T} \tag{10}$$

is the pressure and the positive parameter μ is the viscosity.

A quick look reveals that (9)–(10) differs from the classical constitutive model for the Cauchy stress

$$\mathsf{T} = -p\mathsf{I} + 2\mu\mathsf{D}. \tag{11}$$

In fact, contrarily to (11), in (9) and (10) it is explicitly stated what it is meant by "pressure": the negative of the mean normal stress. On using the terminology widely adopted in the literature, by "pressure" we mean the "mechanical pressure". It is extremely important point out this from the beginning not only because we are going to examine some aspects of the flows in fluids with material parameters depending on pressure, but also because, as observed by Rajagopal [36], the term "pressure" has been used in a plethora of different contexts and, as an unavoidable consequence, it has been often misused in the literature. Referring the interested reader to [36] for a detailed discussion on the issues related with the usage of the word "pressure", we limit to observe that, as argued by Huilgol [20], if one wishes to include pressure in the rheological material functions (as we intend to), defining the pressure through (10) is the only unambiguous way of introducing such a physical quantity. In addition, this definition can be used to interpret experimental data systematically both for compressible and incompressible fluids (the motions of which, as is well known, are subjected to the kinematic constraint $\mathrm{div}\boldsymbol{v} = \mathrm{tr}(\mathsf{D}) = 0$) [20].

It is widely accepted that the viscosity of fluids depends on temperature. In particular, experimental observations have shown that viscosity decreases with increasing temperature. On the other hand, there is also a vast literature on the dependence of the viscosity on pressure. For the sake of brevity, below, we report only some of the most important studies on this topic.

The first scholar to realize that the viscosity of a fluid may depend on pressure was Stokes. In fact, in his celebrated paper [49] on the constitutive response of fluids, Stokes stated

> Let us now consider in what cases it is allowable to suppose μ to be independent of the pressure. It has been concluded by Du Buat from his experiments on the motion of water in

> pipes and canals, that the total retardation of the velocity due to friction is not increased by increasing the pressure... I shall therefore suppose that for water, and by analogy for other incompressible fluids, μ is independent of the pressure.

Stokes's comment clearly implies that only in special circumstances the viscosity of a fluid is independent of pressure. While for flows in canals and pipes under normal conditions inclusion of the dependence of the viscosity on pressure does not affect the results of the experiments, there are several other situations where one needs to take this dependence into account. Eight decades later, Bridgman [10] gave a measure of the effect of pressure on the viscosity of water as well as of other forty-two pure liquids. In addition, Bridgman observed that, while it is true that all the physical quantities do vary with pressure, the variation in the viscosity with pressure may be far more dramatic than the variation of the other quantities with pressure. To this aim, Bridgman reported:

> It may be said in general that the effects of pressure on viscosity are greater than on any other physical property hitherto measured,[2] and vary very widely with the nature of the liquid. The increase of viscosity produced by 12000 kg varies from two or three fold to millions of fold for the liquids investigated here, whereas such properties as the volume decrease under 12000 kg seldom vary by as much as a factor of two from substance to substance.

As early as 1893, based on experiments on marine glue, Barus [6] proposed an empirical relation between the viscosity μ and the pressure p of the form

$$\mu(p,\theta) = \mu_{\text{ref}} \exp[\beta(\theta)(p - p_{\text{ref}})], \tag{12}$$

where μ_{ref} is the viscosity at the reference pressure p_{ref}, and the piezo-viscous coefficient β is temperature dependent. Later, Andrade [2] proposed a model expressing the viscosity in terms of the pressure, the mass density and the temperature, namely

$$\mu(p,\rho,\theta) = A\rho^{1/2} \exp[(p + \rho r^2)s/\theta], \tag{13}$$

where r, s and A are constants. References to much of the literature concerning the pressure dependence of the viscosity of fluids prior 1931 can be found in the book of Bridgman [11]. More recently, Laun has modeled the viscosity of polymer melts through

$$\mu(p,\theta) = \mu_{\text{ref}} \exp[\beta(p - p_{\text{ref}}) - \delta(\theta - \theta_{\text{ref}})], \tag{14}$$

where μ_{ref} is the viscosity at the reference state $(p_{\text{ref}}, \theta_{\text{ref}})$, and β and δ are positive constants. There have been numerous other experiments by Bair and coworkers that shows that the dependence of the viscosity on pressure is exponential (see the experiments of Bair and Kottke [4]). Mention must be made of the work of

[2]The other physical properties measured by Bridgman are the isothermal compressibility, the thermal expansion coefficient, the specific heat and the thermal conductivity.

Martín-Alfonso and co-workers [26] wherein an intricate relationship among the temperature, viscosity and pressure is provided for bitumen. In this context, it ought to be pointed out that the pressure dependence of the properties of bitumen was recognized very early. For instance, Saal and Koens [46] not only allowed for viscosity to depend on pressure (and hence on the mean normal stress), they also allowed it to depend on the shear stresses.

In virtue of the experimental evidences reported above, it is then reasonable to assume that the viscosity of a fluid depends on pressure and temperature. Consequently, since we have defined the pressure as the negative mean normal stress, the constitutive model (9) with $\mu = \mu(p, \theta)$ prescribes the Cauchy stress tensor in terms of the strain-rate tensor and temperature through the implicit relation

$$\mathsf{T} - \frac{1}{3}\mathrm{tr}(\mathsf{T})\mathsf{I} - 2\mu\left(-\frac{1}{3}\mathrm{tr}(\mathsf{T}), \theta\right)\mathsf{D} = \mathsf{O}. \tag{15}$$

In the following sections, we shall mainly use the implicit model (15) or its variants. However, for the sake of generality, we now determine the most general implicit model for the Cauchy stress of an isotropic fluid. We start with an implicit relation of the form

$$\mathsf{G}(\mathsf{T}, \mathsf{D}, \theta) = \mathsf{O}. \tag{16}$$

Since the fluid is isotropic, G is an isotropic tensor function of the two second-order tensors T and D, i.e. G satisfies the property

$$\mathsf{G}(\mathsf{Q}\mathsf{T}\mathsf{Q}^T, \mathsf{Q}\mathsf{D}\mathsf{Q}^T, \theta) = \mathsf{Q}\mathsf{G}(\mathsf{T}, \mathsf{D}, \theta)\mathsf{Q}^T, \tag{17}$$

for all proper orthogonal tensors Q. Next, following Spencer [48], the most general implicit model for the Cauchy stress tensor of an isotropic fluid can be written as

$$\begin{aligned} &\alpha_0\mathsf{I} + \alpha_1\mathsf{T} + \alpha_2\mathsf{D} + \alpha_3\mathsf{T}^2 + \alpha_4\mathsf{D}^2 + \alpha_5(\mathsf{T}\mathsf{D} + \mathsf{D}\mathsf{T}) \\ &+\alpha_6(\mathsf{T}^2\mathsf{D} + \mathsf{D}\mathsf{T}^2) + \alpha_7(\mathsf{T}\mathsf{D}^2 + \mathsf{D}^2\mathsf{T}) + \alpha_8(\mathsf{T}^2\mathsf{D}^2 + \mathsf{D}^2\mathsf{T}^2) = \mathsf{O}, \end{aligned} \tag{18}$$

where the coefficients α_i, $i = 0, 1, \ldots, 8$, depend on θ and the integrity basis of the two tensors T and D. The integrity basis consists of the invariants of any combination of tensor products up to second order. For the current problem, these are given by

$$\begin{gathered} \mathrm{tr}(\mathsf{T}),\ \mathrm{tr}(\mathsf{D}),\ \mathrm{tr}(\mathsf{T}^2),\ \mathrm{tr}(\mathsf{D}^2),\ \mathrm{tr}(\mathsf{T}^3),\ \mathrm{tr}(\mathsf{D}^3), \\ \mathrm{tr}(\mathsf{T}\mathsf{D}),\ \mathrm{tr}(\mathsf{T}^2\mathsf{D}),\ \mathrm{tr}(\mathsf{T}\mathsf{D}^2),\ \mathrm{tr}(\mathsf{T}^2\mathsf{D}^2). \end{gathered} \tag{19}$$

This is a minimal set of invariants since the trace of the product of two second-order Cartesian tensors is equal to the trace of the tensor product with the factors written in reverse.

When we consider fluid models of the form (18)–(19), with

$$\alpha_0 = -\frac{1}{3}\mathrm{tr}(\mathsf{T}) + 2\mu\left(-\frac{1}{3}\mathrm{tr}(\mathsf{T}), \theta\right)\mathrm{tr}(\mathsf{D}),$$
$$\alpha_1 = 1, \quad \alpha_2 = -2\mu\left(-\frac{1}{3}\mathrm{tr}(\mathsf{T}), \theta\right), \tag{20}$$

and all the remaining α_i equal to zero, we recover the model (15) for a piezo-viscous fluid.

It might seem that the previous discussion on implicit constitutive models for the Cauchy stress tensor is valid only for compressible isotropic fluids. The reader might be led to such a conclusion by the usual practice in continuum mechanics to associate a Lagrange multiplier with the constraint of incompressibility, split the stress tensor into the sum of the constraint stress T_C and the extra stress T_E, and assume that the constraint stress is workless and independent of the state variables, and the extra stress is independent of T_C [52]. This conclusion is not right and the discussion above can be easily adapted to incompressible isotropic fluids. In fact, Rajagopal [35] showed that, when dealing with incompressible fluids, appropriate choices of the material parameters α_i in (18) guarantee the incompressibility without the introduction of a Lagrange multiplier and any split of the stress tensor. In these notes we shall not introduce special models for incompressible fluids because, as we shall show in the following section, incompressibility is an approximation that is valid under specific flow regimes. Therefore, when dealing with these flow regimes, there is no need at all to introduce *a priori* appropriate models which automatically meet the kinematic restriction of invariability of volume elements during motion.

3 Isochoric Motions of Fluids as Approximations Under Different Flow Regimes

All real bodies are compressible. In fact, if a sufficiently high pressure is employed, the body undergoes a reduction in volume. On the contrary, for most liquids in Nature, experience teaches that volume increases with increasing temperature. However, it is possible that some bodies do not undergo a significant change in volume over a sufficiently large ranges of pressures or temperatures and can hence be approximated as being incompressible in those ranges. When the ranges of pressures and temperatures are what is considered 'normal', in view of day to day applications, the body is considered to be incompressible. Of course, what is deemed to be a 'significant change in volume' is quite arbitrary and it boils down to whether neglecting the volume change and modeling the body as an incompressible body yet captures the essential features of the response of the body when subject to external stimuli. Most liquids can be approximated as incompressible liquids provided the pressures to which they are subject to are not very high and temperature changes

are small enough. On the other hand, if the ranges of pressures and temperatures to which the liquid is subject are large, then volume changes do take place and, moreover, all the properties that characterize a fluid must be considered pressure- and temperature-dependent.

Müller [29] defined a body to be incompressible if the density and the internal energy depend only on temperature and do not depend on pressure. Appealing to the material frame indifference and the entropy principle Müller [29] showed that a Navier-Stokes-Fourier fluid cannot undergo changes in volume due to temperature changes. Such a behavior is clearly contradicted by experiments which show that volume changes do take place with temperature. Motivated by the fact that experimental evidence clearly contradicts Müller's conclusion (often referred to as the *Müller paradox*), Gouin et al. [16] studied a class of Navier-Stokes-Fourier fluids for which the internal energy, shear and bulk viscosities, and thermal conductivity depend on pressure and temperature, while the density depends only on temperature. They referred to such materials as quasi-thermally compressible fluids and found a critical value of the pressure, denoted by p_{cr}, below which a quasi-thermally compressible fluid behaves like a perfectly compressible fluid in Müller's sense. Since the value of p_{cr} is large with respect to the normal pressure conditions (for instance, for water at 20 °C, $p_{cr} \simeq 2 \times 10^5$ atm), Gouin et al. [16] concluded that a quasi thermal-incompressible fluid is experimentally similar to a perfectly incompressible fluid, removing in a such a way the Müller paradox.

The analysis of Gouin et al. [16] is based on the assumption that the density depends only on the temperature. Clearly, for a homogeneous fluid this assumption is equivalent to assuming that the deformation gradient F depends only on the temperature, i.e.

$$\det \mathsf{F} = \varphi(\theta). \tag{21}$$

Recently, Rajagopal et al. [42] proved that assumption (21) leads to three physically unrealistic deductions:

- the specific heat at constant volume is zero,
- thermodynamic instability (the specific entropy fails to be a concave function of the pressure and specific volume),
- imaginary speed of sound.

To overcome these drawbacks Rajagopal et al. [42] modified the assumption (21) by postulating that

$$\det \mathsf{F} = \varphi(p, \theta), \tag{22}$$

and showed that, for several classes of flow regimes of interest in the applications, the velocity field of a fluid with pressure and temperature dependent material properties is, to a first approximation, solenoidal. Therefore, in comparison to the findings by Gouin et al. [16], instead of determining pressure ranges in which a real fluid behaves like an idealized incompressible fluid, Rajagopal et al. [42]

determined the flow regimes in which the motions of a fluid can be regarded, to a first approximation, as isochoric.

3.1 Equations Governing the Flows in a Piezo-Viscous Fluid

To rigorously derive the sets of approximated equations we shall employ in the following sections, we follow the same procedure as in [42]. We start by assuming that the fluid is slightly compressible due to variations in the pressure and temperature and thus assume that (22) holds.

We also assume that the motion of the fluid is sufficiently smooth so that the derivatives that are taken are meaningful. Then, differentiating the determinant of the deformation gradient with respect to time yields

$$\operatorname{div}\boldsymbol{v} = -k_T(p,\theta)\dot{p} + \alpha(p,\theta)\dot{\theta}, \tag{23}$$

where

$$k_T = -\frac{1}{\varphi}\frac{\partial\varphi}{\partial p}, \quad \alpha = \frac{1}{\varphi}\frac{\partial\varphi}{\partial\theta} \tag{24}$$

are the isothermal compressibility and the coefficient of thermal expansion, respectively. Clearly, k_T and α are related through the integrability condition

$$\frac{\partial k_T}{\partial\theta} = -\frac{\partial\alpha}{\partial p}. \tag{25}$$

From (1) and (23) we deduce that

$$\frac{\dot{\rho}}{\rho} = k_T\dot{p} - \alpha\dot{\theta}. \tag{26}$$

Hence

$$\mathrm{d}\rho = \rho(k_T\mathrm{d}p - \alpha\mathrm{d}\theta), \tag{27}$$

and, denoting $v = 1/\rho$ the specific volume,

$$\mathrm{d}v = -\frac{k_T}{\rho}\mathrm{d}p + \frac{\alpha}{\rho}\mathrm{d}\theta. \tag{28}$$

Next, we introduce the enthalpy

$$h = e + pv, \tag{29}$$

and the Gibbs free enthalpy

$$g = h - \theta\eta, \tag{30}$$

and combine these two thermodynamic potentials with the balance equations (1)–(3) and the Clausius-Duhem inequality (4) to get

$$\rho(\dot{g} + \eta\dot{\theta}) - \dot{p} - p\mathrm{div}\boldsymbol{v} - \mathsf{T}\cdot\mathsf{D} + \frac{\boldsymbol{q}}{\theta}\cdot\nabla\theta \leq 0. \tag{31}$$

In our analysis we shall regard the mechanical pressure and the temperature as independent variables on which the material parameters of the fluid depend, and, since we are interested in fluids of grade 1 (see Truesdell and Noll [52]), the requirement of material frame indifference and the representation theorems for isotropic functions lead us to consider the Cauchy stress tensor to be constitutively prescribed by the implicit relation (15), the response functions of the specific internal energy and entropy to be of the form

$$e = \hat{e}(p, \theta, \mathrm{tr}(\mathsf{D})), \quad \eta = \hat{\eta}(p, \theta, \mathrm{tr}(\mathsf{D})), \tag{32}$$

and the heat flux vector given by the Fourier law

$$\boldsymbol{q} = -k(p, \theta)\nabla\theta, \tag{33}$$

with k being the thermal conductivity. Finally, we introduce the specific heats at constant pressure and at constant volume through

$$c_p = \left(\frac{\partial h}{\partial\theta}\right)_p, \quad c_v = \left(\frac{\partial e}{\partial\theta}\right)_v, \tag{34}$$

respectively, and the specific heat ratio $\gamma = c_p/c_v$ [15].

Inserting (9), (23) and (33) into (31) yields the inequality

$$\begin{aligned}\left(\rho\frac{\partial g}{\partial p} - 1\right)\dot{p} + \rho\left(\frac{\partial g}{\partial\theta} + \eta\right)\dot{\theta} + \rho\frac{\partial g}{\partial\mathrm{tr}(\mathsf{D})}\overline{\mathrm{tr}(\mathsf{D})}^{\cdot} \\ -2\mu\left\{\|\mathsf{D}\|^2 - \frac{1}{3}[\mathrm{tr}(\mathsf{D})]^2\right\} - \frac{k}{\theta}\|\nabla\theta\|^2 \leq 0,\end{aligned} \tag{35}$$

that holds true for any thermodynamical processes, i.e. for any fields ρ, $\boldsymbol{v}$ and θ satisfying the balance equations (1)–(3). Therefore, by using standard arguments in continuum thermodynamics, we deduce that

$$\frac{\partial g}{\partial p} = \frac{1}{\rho}, \quad \frac{\partial g}{\partial\theta} = -\eta, \quad \frac{\partial g}{\partial\mathrm{tr}(\mathsf{D})} = 0, \tag{36}$$

and the constitutive functions for the viscosity of the fluid μ and the thermal conductivity k are non-negative.

From (36) we deduce that the differential of the Gibbs free enthalpy is

$$\mathrm{d}g = \frac{1}{\rho}\mathrm{d}p - \eta \mathrm{d}\theta \tag{37}$$

and the constitutive functions for the specific internal energy and entropy are, respectively, of the form $e = \hat{e}(p,\theta)$ and $\eta = \hat{\eta}(p,\theta)$ (namely, both the specific internal energy and the specific entropy do not depend on $\mathrm{tr}(\mathsf{D})$), with

$$\left(\frac{\partial \eta}{\partial p}\right)_{\theta} = -\frac{\alpha}{\rho}. \tag{38}$$

Next, combining (29) and (30) with (37) yields

$$\theta \mathrm{d}\eta = \mathrm{d}e + p\mathrm{d}v \tag{39}$$

which in turn leads to

$$\theta\left(\frac{\partial \hat{\eta}}{\partial \theta}\right)_{v} = \left(\frac{\partial \hat{e}}{\partial \theta}\right)_{v} = c_v, \tag{40}$$

and then by virtue of (27) and (28) we obtain

$$\theta\left(\frac{\partial \hat{\eta}}{\partial \theta}\right)_{p} = \left(\frac{\partial \hat{e}}{\partial \theta}\right)_{p} + \frac{\alpha}{\rho}p = \left(\frac{\partial h}{\partial \theta}\right)_{p} = c_p. \tag{41}$$

As far the specific internal energy is concerned, from $(36)_1$, (38) and (41) we have

$$\left(\frac{\partial \hat{e}}{\partial p}\right)_{\theta} = \frac{k_T p - \alpha\theta}{\rho}, \quad \left(\frac{\partial \hat{e}}{\partial \theta}\right)_{p} = c_p - \frac{\alpha}{\rho}p. \tag{42}$$

Finally, by using (9), (23) and (42) the equations of balance of linear momentum (2) and energy (3) can be expressed as

$$\rho\dot{\boldsymbol{v}} = -\nabla p + 2\mathrm{div}\left\{\mu\left[\mathsf{D} - \frac{1}{3}(\mathrm{div}\boldsymbol{v})\mathsf{I}\right]\right\} + \rho\boldsymbol{b} \tag{43}$$

and

$$-\alpha\theta\dot{p} + \rho c_p\dot{\theta} = \mathrm{div}(k\nabla\theta) + 2\mu\left[\|\mathsf{D}\|^2 - \frac{1}{3}(\mathrm{div}\boldsymbol{v})^2\right] + \rho r, \tag{44}$$

respectively. Equations (26), (23), (43) and (44) constitute a system of partial differential equations for determining the thermodynamic fields ρ, $\boldsymbol{v}$, p and θ.

3.2 Approximations

In order to introduce the most appropriate non-dimensionalization, it is necessary to record before some thermodynamic identities. Rajagopal et al. [42] observed that the specific heats ratio $\gamma > 1$, the isothermal compressibility is related to the speed of sound C in the fluid through

$$k_T = \frac{\gamma}{\rho C^2}, \tag{45}$$

and the square of the coefficient of thermal expansion can be written as

$$\alpha^2 = \frac{c_p(\gamma - 1)}{C^2\theta}. \tag{46}$$

Let $Oxyz$ be a Cartesian frame of reference with orthonormal basis $\{\boldsymbol{i}, \boldsymbol{j}, \boldsymbol{k}\}$. Let $\Omega_d = \mathbb{R}^2 \times [0, d]$ be a horizontal fluid layer of thickness d and assume that gravity is the only body force acting on the fluid, namely $\boldsymbol{b} = -g\boldsymbol{k}$, where g is the acceleration due to gravity.[3] We assume also that no heat is supplied, i.e., $r = 0$. To non-dimensionalize the equations governing the fluid motion, we choose a convenient reference state $(p_{\text{ref}}, \theta_{\text{ref}})$ and introduce the following scales

$$\begin{gathered} \boldsymbol{x}^* = \frac{\boldsymbol{x}}{d}, \quad \boldsymbol{v}^* = \frac{\boldsymbol{v}}{V}, \quad \rho^* = \frac{\rho}{\rho_{\text{ref}}}, \quad t^* = \frac{V}{d}t, \\ p^* = \frac{p - p_{\text{ref}}}{\rho_{\text{ref}} g d}, \quad \theta^* = \frac{\theta - \theta_{\text{ref}}}{\theta_M - \theta_m}, \quad \alpha^* = \frac{\alpha}{\alpha_{\text{ref}}}, \quad C^* = \frac{C}{C_{\text{ref}}}, \\ \mu^* = \frac{\mu}{\mu_{\text{ref}}}, \quad c_p^* = \frac{c_p}{c_{p_{\text{ref}}}}, \quad k_T^* = \frac{\rho_{\text{ref}} C_{\text{ref}}^2}{\gamma_{\text{ref}}} k_T. \end{gathered} \tag{47}$$

In (47) the subscript 'ref' indicates that the corresponding material parameters are evaluated at the reference state $(p_{\text{ref}}, \theta_{\text{ref}})$, V is the reference velocity, $\theta_M = \max_{\Omega} \theta$, $\theta_m = \min_{\Omega} \theta$ and the isothermal compressibility has been scaled by taking into account (45). Hereinafter, we choose θ_M as the reference temperature, *viz* $\theta_{\text{ref}} = \theta_M$.

Substituting (47) into (23), (26), (43) and (44) yields the dimensionless equations (omitting the asterisks for convenience)

$$\operatorname{div} \boldsymbol{v} = -\gamma_{\text{ref}} \frac{\text{Ma}^2}{\text{Fr}^2} \rho k_T \dot{p} + \alpha_{\text{ref}} (\theta_M - \theta_m) \alpha \dot{\theta}, \tag{48}$$

$$\dot{\rho} = \gamma_{\text{ref}} \frac{\text{Ma}^2}{\text{Fr}^2} \rho k_T \dot{p} - \alpha_{\text{ref}} (\theta_M - \theta_m) \rho \alpha \dot{\theta}, \tag{49}$$

[3] Assuming that Ω is a horizontal layer is convenient for deriving the set of approximations we shall adopt in this paper. However, the analysis we are going to perform can be adapted, by means of slight changes, to the case in which Ω is bounded in one direction provided that such a direction is non-horizontal.

$$\mathrm{Fr}^2\rho\dot{\boldsymbol{v}} = -\nabla p + 2\frac{\mathrm{Fr}^2}{\mathrm{Re}}\mathrm{div}\left\{\mu\left[\mathsf{D} - \frac{1}{3}(\mathrm{div}\boldsymbol{v})\mathsf{I}\right]\right\} - \rho\boldsymbol{k}, \tag{50}$$

$$-\alpha_{\mathrm{ref}}(\theta_M - \theta_m)\frac{\mathrm{ReBr}}{\mathrm{Fr}^2}\alpha\left(\theta + \frac{1}{\mathrm{Ca}}\right)\dot{p} + \mathrm{Pe}\rho c_p\dot{\theta} = \mathrm{div}(k\nabla\theta) + 2\mathrm{Br}\mu\left[\|\mathsf{D}\|^2 - \frac{1}{3}(\mathrm{div}\boldsymbol{v})^2\right], \tag{51}$$

where

$$\begin{gathered}\mathrm{Ma} = \frac{V}{C_{\mathrm{ref}}}, \quad \mathrm{Fr}^2 = \frac{V^2}{gd}, \quad \mathrm{Re} = \frac{\rho_{\mathrm{ref}}Vd}{\mu_{\mathrm{ref}}}, \\ \mathrm{Br} = \frac{\mu_{\mathrm{ref}}V^2}{k_{\mathrm{ref}}(\theta_M - \theta_m)}, \quad \mathrm{Pe} = \frac{\rho_{\mathrm{ref}}c_{p_{\mathrm{ref}}}Vd}{k_{\mathrm{ref}}}, \quad \mathrm{Ca} = \frac{\theta_M - \theta_m}{\theta_M}\end{gathered} \tag{52}$$

are the Mach, second Froude, Reynolds, Brinkman, Péclet and Carnot numbers, respectively.

We now assume that the material parameters α, k_T, c_p and k are analytic functions and limit our analysis to the departures of the pressure and temperature from the reference state $(p_{\mathrm{ref}}, \theta_M)$ for which we can write

$$\alpha(p,\theta) = \sum_{j_1,j_2=0}^{+\infty}\frac{1}{j_1!j_2!}\frac{\partial^{j_1+j_2}\alpha}{\partial p^{j_1}\partial\theta^{j_2}}(0,0)p^{j_1}\theta^{j_2}, \tag{53}$$

$$k_T(p,\theta) = \sum_{j_1,j_2=0}^{+\infty}\frac{1}{j_1!j_2!}\frac{\partial^{j_1+j_2}k_T}{\partial p^{j_1}\partial\theta^{j_2}}(0,0)p^{j_1}\theta^{j_2}, \tag{54}$$

$$c_p(p,\theta) = \sum_{j_1,j_2=0}^{+\infty}\frac{1}{j_1!j_2!}\frac{\partial^{j_1+j_2}c_p}{\partial p^{j_1}\partial\theta^{j_2}}(0,0)p^{j_1}\theta^{j_2}, \tag{55}$$

and

$$k(p,\theta) = \sum_{j_1,j_2=0}^{+\infty}\frac{1}{j_1!j_2!}\frac{\partial^{j_1+j_2}k}{\partial p^{j_1}\partial\theta^{j_2}}(0,0)p^{j_1}\theta^{j_2}. \tag{56}$$

From the integrability condition (25), the expansions (53) and (54) and the scales (47) we deduce that

$$\gamma_{\mathrm{ref}}\frac{\mathrm{Ma}^2}{\mathrm{Fr}^2}\frac{\partial^{j_1+j_2}k_T}{\partial p^{j_1-1}\partial\theta^{j_2+1}}(0,0) = -\alpha_{\mathrm{ref}}(\theta_M - \theta_m)\frac{\partial^{j_1+j_2}\alpha}{\partial p^{j_1}\partial\theta^{j_2}}(0,0), \tag{57}$$

for all $(j_1, j_2) \in \mathbb{N} \times \mathbb{N}_0$. In virtue of (57) we can integrate equation (49) to obtain

$$\rho = \exp\Bigg[- \alpha_{\mathrm{ref}}(\theta_M - \theta_m) \sum_{j_1, j_2 = 0}^{+\infty} \frac{1}{j_1!(j_2+1)!} \frac{\partial^{j_1+j_2}\alpha}{\partial p^{j_1} \partial \theta^{j_2}}(0,0) p^{j_1} \theta^{j_2+1} \tag{58}$$

$$+ \gamma_{\mathrm{ref}} \frac{\mathrm{Ma}^2}{\mathrm{Fr}^2} \sum_{j_1=0}^{+\infty} \frac{1}{(j_1+1)!} \frac{\partial^{j_1} k_T}{\partial p^{j_1}}(0,0) p^{j_1+1} \Bigg].$$

Evaluating the identity (46) at the reference state $(p_{\mathrm{ref}}, \theta_M)$ yields the following relation

$$\alpha_{\mathrm{ref}}^2 (\theta_M - \theta_m)^2 = \frac{\mathrm{Ma}^2}{\mathrm{E}} \mathrm{Ca}(\gamma_{\mathrm{ref}} - 1), \tag{59}$$

where

$$\mathrm{E} = \frac{V^2}{c_{p_{\mathrm{ref}}}(\theta_M - \theta_m)} \tag{60}$$

is the Eckert number. We henceforth consider thermodynamic processes for which

$$\alpha_{\mathrm{ref}}(\theta_M - \theta_m) \equiv \varepsilon \ll 1. \tag{61}$$

Therefore, as long as $\mathrm{E}/[\mathrm{Fr}^2 \mathrm{Ca}(\gamma_{\mathrm{ref}} - 1)]$ is of order $O(1)$ or smaller, from (59) we deduce that $\mathrm{Ma}^2/\mathrm{Fr}^2$ is of order $O(\varepsilon^2)$ or smaller.

We are now in position to carry out a perturbation analysis with respect to the small parameter ε. Let

$$\boldsymbol{v} = \sum_{n=0}^{+\infty} \varepsilon^2 \boldsymbol{v}_n, \quad p = \sum_{n=0}^{+\infty} \varepsilon^n p_n, \quad \theta = \sum_{n=0}^{+\infty} \varepsilon^n \theta_n \tag{62}$$

be the power series in ε of the thermodynamic fields $\boldsymbol{v}$, p and θ. As far as the power series expansion of the fluid density is concerned, it may be derived from (58) and $(62)_{2,3}$ by taking into account the fact that $\mathrm{Ma}^2/\mathrm{Fr}^2$ is of order $O(\varepsilon^2)$. However, the expression is quite complicated and of no interest to our analysis. In our analytical scheme it suffices to know that

$$\rho = 1 - \varepsilon \sum_{j_1, j_2 = 0}^{+\infty} \frac{1}{j_1!(j_2+1)!} \frac{\partial^{j_1+j_2}\alpha}{\partial p^{j_1} \partial \theta^{j_2}}(0,0) p_0^{j_1} \theta_0^{j_2+1} + o(\varepsilon) \tag{63}$$

$$= 1 - \varepsilon \int_0^{\theta_0} \alpha(p_0, \theta_0) \mathrm{d}\theta_0 + o(\varepsilon),$$

where $o(\varepsilon)$ accounts for terms of order $O(\varepsilon^2)$ and higher. Therefore, by inserting (62) and (63) into (48), (50) and (51) we deduce a system of equations from which different approximations can be derived:

$$\sum_{n=0}^{+\infty}\varepsilon^n \mathrm{div}\boldsymbol{v}_n = -\gamma_{\mathrm{ref}}\frac{\mathrm{Ma}^2}{\mathrm{Fr}^2}\sum_{n=0}^{+\infty}\varepsilon^n\left[k_T(p,\theta)\left(\frac{\partial p}{\partial t}+\boldsymbol{v}\cdot\nabla p\right)\right]_n + \sum_{n=0}^{+\infty}\varepsilon^{n+1}\left[\alpha(p,\theta)\left(\frac{\partial \theta}{\partial t}+\boldsymbol{v}\cdot\nabla\theta\right)\right]_n, \tag{64}$$

$$\begin{aligned}&\mathrm{Fr}^2\sum_{n=0}^{+\infty}\varepsilon^n\left\{\rho\left[\frac{\partial \boldsymbol{v}}{\partial t}+(\boldsymbol{v}\cdot\nabla)\boldsymbol{v}\right]\right\}_n\\ &\quad=-\sum_{n=0}^{+\infty}\varepsilon^n\nabla p_n+2\frac{\mathrm{Fr}^2}{\mathrm{Re}}\sum_{n=0}^{+\infty}\varepsilon^n\left\{\mathrm{div}\left[\mu(p,\theta)\left(\mathsf{D}-\frac{1}{3}(\mathrm{div}\boldsymbol{v})\mathrm{I}\right)\right]\right\}_n\\ &\quad\quad-\left[1-\varepsilon\int_0^{\theta_0}\alpha(p_0,\theta_0)\mathrm{d}\theta_0+o(\varepsilon)\right]\boldsymbol{k}\end{aligned} \tag{65}$$

and

$$\begin{aligned}&-\frac{\mathrm{ReBr}}{\mathrm{Fr}^2}\sum_{n=0}^{+\infty}\varepsilon^{n+1}\left[\alpha(p,\theta)\left(\theta+\frac{1}{\mathrm{Ca}}\right)\left(\frac{\partial p}{\partial t}+\boldsymbol{v}\cdot\nabla p\right)\right]_n\\ &+\mathrm{Pe}\sum_{n=0}^{+\infty}\varepsilon^n\left[\rho c_p(p,\theta)\left(\frac{\partial\theta}{\partial t}+\boldsymbol{v}\cdot\nabla\theta\right)\right]_n\\ &\quad=\sum_{n=0}^{+\infty}\varepsilon^n\{\mathrm{div}[k(p,\theta)\nabla\theta]\}_n+2\mathrm{Br}\sum_{n=0}^{+\infty}\varepsilon^n\left\{\mu(p,\theta)\left[\|\mathsf{D}\|^2-\frac{1}{3}(\mathrm{div}\boldsymbol{v})^2\right]\right\}_n.\end{aligned} \tag{66}$$

Since $\gamma_{\mathrm{ref}}\mathrm{Ma}^2/\mathrm{Fr}^2$ is of order $O(\varepsilon^2)$ or smaller, collecting terms of order $O(1)$ in (64) yields

$$\mathrm{div}\boldsymbol{v}_0 = 0, \tag{67}$$

whence the fluid motions can be regarded as isochoric to a first approximation.

According to the magnitude of the dimensionless numbers occurring in (64) and (65), we can derive different sets of approximate equations such as, just to mention a few of them, those which have been employed in the last few years to study the flows at low Reynolds and Froude numbers [42, 53], the effects of viscous dissipation in a piezo-viscous fluid [40], viscous stratified flows [17, 56]

turbulence in forced convection [55], and heat transfer in turbulent mixed convection [54]. Here, we instead derive the flow regimes for which (63)–(66) approximate to generalizations of the celebrated Oberbeck-Boussinesq approximation and the Navier-Stokes-Fourier equations for fluids with variable material properties.

3.2.1 Generalized Oberbeck-Boussinesq Approximation

If the second Froude number is of order $O(\varepsilon)$, the Reynolds number of order of unity, the Brinkman number of order $O(\varepsilon)$ or smaller and the Péclet number of order of unity or greater, then at the leading order equations (65) and (66) are

$$\nabla p_0 + \boldsymbol{k} = \boldsymbol{0} \tag{68}$$

and

$$\mathrm{Pe} c_p(p_0, \theta_0)\dot{\theta}_0 = \mathrm{div}[k(p_0, \theta_0)\nabla\theta_0]. \tag{69}$$

Obviously, Eq. (68) can be integrated and, taking the atmospheric pressure as the reference pressure, we deduce that p_0 coincides with the hydrostatic pressure $p_h = 1 - z$. We now notice that Eqs. (67) and (69) are not sufficient to determine all the thermodynamic fields at $O(1)$. Therefore, in order to attain the closure, we collect the terms of order $O(\varepsilon)$ in (65) and, in view of (67), get

$$\mathrm{Fr}^2\dot{\boldsymbol{v}}_0 = \varepsilon\nabla p_1 + 2\frac{\mathrm{Fr}^2}{\mathrm{Re}}\mathrm{div}[\mu(p_h, \theta_0)\mathsf{D}_0] + \varepsilon\left[\int_0^{\theta_0}\alpha(p_h, \theta_0)\mathrm{d}\theta_0\right]\boldsymbol{k}. \tag{70}$$

Now equations (67), (69) and (70) form a closed system, in which p_1 can be regarded as the hydrodynamic pressure. Finally, setting $P = \varepsilon p_1$, re-dimensionalizing (67), (69) and (70), and omitting the subscript '0' yield the generalized Oberbeck-Boussinesq approximation derived by Rajagopal et al. [39]

$$\begin{cases} \rho_{\mathrm{ref}}\dot{\boldsymbol{v}} = -\nabla P + 2\mathrm{div}[\mu(p_h, \theta)\mathsf{D}] + \rho_{\mathrm{ref}} g\left[\displaystyle\int_{\theta_{\mathrm{ref}}}^{\theta}\alpha(p_h, \theta)\mathrm{d}\theta\right]\boldsymbol{k}, \\ \mathrm{div}\boldsymbol{v} = 0, \\ \rho_{\mathrm{ref}} c_p(p_h, \theta)\dot{\theta} = \mathrm{div}[k(p_h, \theta)\nabla\theta], \end{cases} \tag{71}$$

where the dimensionalized hydrostatic pressure is given by the well-known Stevin's law $p_h = \rho_{\mathrm{ref}} g(d - z)$.

3.2.2 Generalized Navier-Stokes-Fourier Equations

Suppose that Fr^2, $\mathrm{Fr}^2/\mathrm{Re}$ and Pe are of order of unity or greater, and the Brinkman number is of order $O(\varepsilon)$ or smaller. Then collecting the terms of order $O(1)$ in Eqs. (65) and (66) and re-dimensionalizing lead to the Navier-Stokes-Fourier equations for a fluid with material properties depending on pressure and temperature:

$$\begin{cases} \rho_{\mathrm{ref}}\dot{\boldsymbol{v}} = -\nabla p + 2\mathrm{div}[\mu(p,\theta)\mathsf{D}] - \rho_{\mathrm{ref}} g\boldsymbol{k}, \\ \mathrm{div}\boldsymbol{v} = 0, \\ \rho_{\mathrm{ref}} c_p \dot{\theta} = \mathrm{div}[k(p,\theta)\nabla\theta]. \end{cases} \tag{72}$$

Obviously, in isothermal conditions (72) reduces to the Navier-Stokes equations for piezo-viscous fluids

$$\begin{cases} \rho_{\mathrm{ref}}\dot{\boldsymbol{v}} = -\nabla p + 2\mathrm{div}[\mu(p)\mathsf{D}] - \rho_{\mathrm{ref}} g\boldsymbol{k}, \\ \mathrm{div}\boldsymbol{v} = 0. \end{cases} \tag{73}$$

4 Rayleigh-Bénard Problem for Fluids with Pressure- and Temperature Dependent Viscosities

Problems involving thermal convection are amongst those that have been studied most assiduously in mechanics in virtue of their relevance to a plethora of problems in astrophysics and geophysics. Understanding thermal-convection is at the heart of explaining weather patterns, solar winds, flows in the interior of stars, thermal currents in oceans, as well as numerous important industrial applications. The prototypical theoretical model as well as experimental set up, within which one can systematically investigate the effect of thermal-convection, is the flow that occurs in a fluid layer due to a thermal gradient that is present across the layer. The earliest experiments of thermal-convection in a fluid layer, heated from below, were carried out by Bénard [7]. He found a pattern of polygonal cells, predominantly hexagonal, though a few rectangular, pentagonal and septagonal cellular structures were also present. Bénard also found that these cellular structures were also quite stable modes under certain circumstances. Lord Rayleigh [43] studied the stability of the flow in a fluid layer heated from below, when the upper layer was stress-free.

There have been numerous studies concerning the stability/instability of 'Rayleigh-Bénard flows'. Until a critical difference in temperature is reached, the main process for the transfer of heat is conduction and upon reaching the critical temperature gradient convective rolls set in. Depending on the nature of boundary conditions (flow between solid boundaries, flow when one boundary is free of stress, etc.) one finds various types of flows are possible. A detailed discussion of the literature pertinent to various aspects of Bénard convection can be found in [8, 12, 14, 23, 25, 30]. An elegant introduction to the problem can be found in the treatise by Chandrasekhar [13].

The governing equations for the study of Bénard convection are obtained by appealing to an approximation that was independently established by Oberbeck [31, 32] and Boussinesq [9]. Such an approximation was established for fluids with constant material parameters. Thus, since here we aim at studying the problem of the onset of convection in a fluid whose viscosity varies with pressure and temperature, we cannot appeal to the classical Oberbeck-Boussinesq approximation but we have to employ its generalization derived in Sect. 3.2.1. We shall next find a necessary and sufficient condition for the linear stability of the conduction solution and compare the critical thresholds for the onset of convection in fluids with pressure and temperature dependent viscosities with the classical results for fluids whose viscosity is constant.

4.1 Conduction Solution: Evolution Equations of Perturbations

Assume that the viscosity of the horizontal fluid layer Ω_d (see Sect. 3.2.1) is an analytic function of pressure and temperature, while the coefficient of thermal expansion, the specific heat at constant pressure and the thermal conductivity are constant. It is worth noting that this assumption is coherent with the experimental evidences by Bridgman [10] reported in Sect. 2 and permits to appreciate the effects of a variable viscosity on the critical threshold for the onset of convection. In this framework, the generalized Oberbeck-Boussinesq approximation (71) becomes

$$\begin{cases} \rho_{\text{ref}}\dot{\boldsymbol{v}} = -\nabla P + 2\text{div}[\mu(p_h,\theta)\mathsf{D}] + \rho_{\text{ref}} g\alpha(\theta-\theta_{\text{ref}})\boldsymbol{k}, \\ \text{div}\boldsymbol{v} = 0, \\ \rho_{\text{ref}} c_p \dot{\theta} = k\Delta\theta. \end{cases} \tag{74}$$

The appropriate boundary conditions for the temperature and hydrodynamic pressure to add to system (74) are

$$\begin{cases} \theta(x,y,0,t) = \theta_L, \quad \theta(x,y,d,t) = \theta_U, \\ P(x,y,d,t) = 0, \end{cases} \tag{75}$$

with $\theta_L > \theta_U$. Our aim is the study of stability of the steady static conduction solution m_0 to (74)–(75):

$$\begin{cases} \tilde{\boldsymbol{v}} = \boldsymbol{0}, \\ \tilde{\theta} = \theta_L - \dfrac{\theta_L - \theta_U}{d} z, \\ \tilde{P} = \rho_{\text{ref}} g\alpha(\theta_L - \theta_U) z \left(1 - \dfrac{z}{2d}\right). \end{cases} \tag{76}$$

In order to study the stability of the conduction solution m_0 we introduce the perturbations $\boldsymbol{u} = u\boldsymbol{i} + v\boldsymbol{j} + w\boldsymbol{k}$, ϑ and Π to $\tilde{\boldsymbol{v}}$, $\tilde{\theta}$ and $\tilde{P}$, respectively, i.e.

$$\boldsymbol{v} = \tilde{\boldsymbol{v}} + \boldsymbol{u}, \quad \theta = \tilde{\theta} + \vartheta, \quad P = \tilde{P} + \Pi. \tag{77}$$

Then, inserting (77) into (74) gives the evolution equations of perturbations

$$\begin{cases} \rho_{\text{ref}}(\boldsymbol{u}_t + \boldsymbol{u}\cdot\nabla\boldsymbol{u}) = -\nabla\Pi + \mu(p_h, \tilde{\theta}+\vartheta)\Delta\boldsymbol{u} \\ \qquad\qquad +[\nabla\boldsymbol{u} + (\nabla\boldsymbol{u})^T]\nabla\mu(p_h, \tilde{\theta}+\vartheta) + \rho_{\text{ref}} g\alpha\vartheta\boldsymbol{k}, \\ \operatorname{div}\boldsymbol{u} = 0, \\ \rho_{\text{ref}} c_p\left(\vartheta_t + \boldsymbol{u}\cdot\nabla\vartheta - \dfrac{\theta_L - \theta_U}{d}w\right) = k\Delta\vartheta, \end{cases} \tag{78}$$

that are valid for all $(x, y, z, t) \in \mathbb{R}^2 \times [0, d] \times [0, +\infty[$. To (78) we append the initial conditions

$$\boldsymbol{u}(\boldsymbol{x}, 0) = \boldsymbol{u}_0(\boldsymbol{x}), \quad \vartheta(\boldsymbol{x}, 0) = \vartheta_0(\boldsymbol{x}), \tag{79}$$

and the boundary conditions

$$\Pi(x, y, d, t) = 0, \quad \vartheta(x, y, 0, t) = \vartheta(x, y, d, t) = 0, \tag{80}$$

and

$$\boldsymbol{u}(x, y, 0, t) = \boldsymbol{u}(x, y, d, t) = \boldsymbol{0} \tag{81}$$

for rigid boundaries, or

$$u_z = v_z = 0 \text{ and } w = 0 \quad \text{on } z = 0, d \tag{82}$$

for stress-free bounding surfaces. We refer to [13] for the derivation of the boundary conditions (81) and (82). In (79) $\boldsymbol{u}_0$ and ϑ_0 are regular fields, with $\boldsymbol{u}_0$ being divergence-free.

4.2 Linear Stability Analysis

Since the viscosity is an analytic function of the temperature and pressure, for sufficiently small disturbances we can approximate the two terms containing μ in $(78)_1$ as:

$$\mu(p_h, \tilde{\theta}+\vartheta)\Delta\boldsymbol{u} = \left[\sum_{n=0}^{+\infty} \frac{1}{n!}\frac{\partial^n \mu}{\partial\theta^n}(p_h, \tilde{\theta})\vartheta^n\right]\Delta\boldsymbol{u} \approx \mu(p_h, \tilde{\theta})\Delta\boldsymbol{u} \equiv \hat{\mu}(z)\Delta\boldsymbol{u}, \tag{83}$$

and

$$[\nabla \boldsymbol{u} + (\nabla \boldsymbol{u})^T]\nabla\mu(p_h, \tilde{\theta} + \vartheta) = [\nabla \boldsymbol{u} + (\nabla \boldsymbol{u})^T]\left\{\sum_{n=0}^{+\infty} \frac{1}{n!}\nabla\left[\frac{\partial^n \mu}{\partial \theta^n}(p_h, \tilde{\theta})\vartheta^n\right]\right\}$$
$$\approx \hat{\mu}'(z)\left[(u_z + w_x)\boldsymbol{i} + (v_z + w_y)\boldsymbol{j} + 2w_z\boldsymbol{k}\right], \quad (84)$$

where, henceforth, a prime denotes the derivative of a function which depends only on one variable.

Thanks to (83) and (84) we can linearize the evolution equations of perturbations (78) to obtain

$$\begin{cases} \rho_{\text{ref}}\boldsymbol{u}_t = -\nabla\Pi + \hat{\mu}(z)\Delta\boldsymbol{u} \\ \qquad\qquad +\hat{\mu}'(z)\left[(u_z + w_x)\boldsymbol{i} + (v_z + w_y)\boldsymbol{j} + 2w_z\boldsymbol{k}\right] + \rho_{\text{ref}} g\alpha\vartheta\boldsymbol{k}, \\ \text{div}\boldsymbol{u} = 0, \\ \rho_{\text{ref}} c_p\left(\vartheta_t - \dfrac{\theta_L - \theta_U}{d}w\right) = k\Delta\vartheta. \end{cases} \quad (85)$$

It is now convenient to non-dimensionalize (85) and the boundary conditions (80)–(82) by introducing the following scales:

$$\boldsymbol{x}^* = \frac{\boldsymbol{x}}{d}, \quad t^* = \frac{\mu_{\text{ref}}}{\rho_{\text{ref}} d^2}t, \quad \boldsymbol{u}^* = \frac{\rho_{\text{ref}} d}{\mu_{\text{ref}}}\boldsymbol{u}, \quad \mu^* = \frac{\mu}{\mu_{\text{ref}}},$$
$$p_h^* = \frac{p_h}{\rho_{\text{ref}} g d} = 1 - z^*, \quad \bar{\theta}^* = \frac{\bar{\theta} - \theta_U}{\theta_L - \theta_U} = 1 - z^*, \quad (86)$$
$$\Pi^* = \frac{\rho_{\text{ref}} d^2}{\mu_{\text{ref}}^2}\Pi, \quad \vartheta^* = \frac{\vartheta}{\theta_L - \theta_U}.$$

Inserting the dimensionless quantities (86) into (85) and (80)–(82) yields the non-dimensional equations (omitting the asterisks)

$$\begin{cases} \boldsymbol{u}_t = -\nabla\Pi + \hat{\mu}(z)\Delta\boldsymbol{u} \\ \qquad\qquad +\hat{\mu}'(z)\left[(u_z + w_x)\boldsymbol{i} + (v_z + w_y)\boldsymbol{j} + 2w_z\boldsymbol{k}\right] + \dfrac{\mathcal{R}}{\text{Pr}}\vartheta\boldsymbol{k}, \\ \text{div}\boldsymbol{u} = 0, \\ \text{Pr}\,(\vartheta_t - w) = \Delta\vartheta, \end{cases} \quad (87)$$

where

$$\mathcal{R} = \frac{\rho_{\text{ref}}^2 g d^3 c_p \alpha(\theta_L - \theta_U)}{\mu_{\text{ref}} k} \quad \text{and} \quad \text{Pr} = \frac{c_p \mu_{\text{ref}}}{k} \quad (88)$$

are the Rayleigh and Prandtl numbers, respectively, and the dimensionless boundary conditions

$$\Pi(x, y, 1, t) = 0, \quad u = v = w = \vartheta = 0 \quad \text{on } z = 0, 1 \quad (89)$$

for rigid boundaries, and

$$\Pi(x, y, 1, t) = 0, \quad u_z = v_z = w = \vartheta = 0 \quad \text{on } z = 0, 1 \tag{90}$$

for bounding surfaces free of stress.

As common praxis in the linear stability analysis of isochoric flows, we take the third component of the curlcurl of (87) to eliminate the disturbance Π and obtain the following coupled system in w and ϑ:

$$\begin{cases} \dfrac{\partial}{\partial t}\Delta w = 2\hat{\mu}'(z)\dfrac{\partial}{\partial z}\Delta w + \hat{\mu}(z)\Delta\Delta w + \hat{\mu}''(z)\dfrac{\partial^2 w}{\partial z^2} \\ \qquad\qquad -\hat{\mu}''(z)\Delta_s w + \dfrac{\mathcal{R}}{\mathrm{Pr}}\Delta_s\vartheta, \\ \mathrm{Pr}(\theta_t - w) = \Delta\vartheta, \end{cases} \tag{91}$$

where $\Delta_s = \dfrac{\partial^2}{\partial x^2} + \dfrac{\partial^2}{\partial y^2}$ is the so-called horizontal Laplacian. Since the coefficients in equations (91) depend only on z, the equations admit solutions which depend on x, y and t exponentially. We therefore look for solutions of the form:

$$\begin{cases} w(x, y, z, t) = \dfrac{W(z)}{\mathrm{Pr}}\exp[i(a_x x + a_y y) + \sigma t], \\ \vartheta(x, y, z, t) = \dfrac{\Theta(z)}{\sqrt{\mathcal{R}}}\exp[i(a_x x + a_y y) + \sigma t], \end{cases} \tag{92}$$

in which it is understood that the real parts of these expressions must be taken into consideration to obtain physical quantities. The wave speed σ may be complex, say $\sigma = \sigma_r + i\sigma_i$. Thus, expressions (92) represent waves which travel in the x and y co-ordinate directions with phase speed σ_i/a, where $a = \sqrt{a_x^2 + a_y^2}$ is the two-dimensional wave number, and whose growth or decay in time is given by $\exp(\sigma_r t)$. A wave of the form (92) is then stable if $\sigma_r \leq 0$ (marginally stable if $\sigma_r = 0$), and unstable if $\sigma_r > 0$.

Setting $D = \mathrm{d}/\mathrm{d}z$ and inserting (92) into (91) gives the system of ordinary differential equations

$$\begin{cases} \sigma(D^2 - a^2)W = \hat{\mu}(z)(D^2 - a^2)^2 W + 2\hat{\mu}'(z)D(D^2 - a^2)W \\ \qquad\qquad +\hat{\mu}''(z)(D^2 + a^2)W - \sqrt{\mathcal{R}}a^2\Theta, \\ \sigma\mathrm{Pr}\Theta - \sqrt{\mathcal{R}}W = (D^2 - a^2)\Theta, \end{cases} \tag{93}$$

to which we add the boundary conditions

$$W = DW = \Theta = 0 \quad \text{at } z = 0, 1 \tag{94}$$

for rigid boundaries, or

$$W = D^2 W = \Theta = 0 \quad \text{at } z = 0, 1 \tag{95}$$

for stress-free boundaries.

Denoting by the superscript * the complex conjugate, multiplying $(93)_1$ by $W^\star$, $(93)_2$ by $a^2\Theta^\star$, summing and integrating over the interval [0, 1] taking into account the boundary conditions (94) or (95), we obtain

$$\sigma \int_0^1 [|DW|^2 + a^2(|W|^2 + \mathrm{Pr}|\Theta|^2)]\mathrm{d}z = a^2\sqrt{R}\int_0^1 (W\Theta^\star + W^\star\Theta)\mathrm{d}z \tag{96}$$
$$-\int_0^1 \hat{\mu}(z)[|(D^2 + a^2)W|^2 + 4a^2|DW|^2]\mathrm{d}z - a^2\int_0^1 (|D\Theta|^2 + a^2|\Theta|^2)\mathrm{d}z.$$

Considering the imaginary part of (96) yields that $\sigma_i = 0$, that is the wave speed of the perturbation is real. Therefore the linearized equations of Bénard convection (85) satisfy the strong form of principle of exchange of stabilities [50] also in the case of fluids with pressure- and temperature-dependent viscosity. In addition, rewriting (96) as

$$\sigma\mathcal{L}(W, \Theta; a^2) = \left[\sqrt{\mathcal{R}}\frac{\mathcal{I}(W, \Theta; a^2)}{\mathcal{D}(W, \Theta; a^2)} - 1\right]\mathcal{D}(W, \Theta; a^2), \tag{97}$$

with

$$\mathcal{L}(W, \Theta; a^2) = \int_0^1 [|DW|^2 + a^2(|W|^2 + \mathrm{Pr}|\Theta|^2)]\mathrm{d}z, \tag{98}$$

$$\mathcal{I}(W, \Theta; a^2) = a^2\int_0^1 (W\Theta^\star + W^\star\Theta)\mathrm{d}z \tag{99}$$

and

$$\mathcal{D}(W, \Theta; a^2) = \int_0^1 \hat{\mu}(z)[|(D^2 + a^2)W|^2 + 4a^2|DW|^2]\mathrm{d}z \tag{100}$$
$$+a^2\int_0^1 (|D\Theta|^2 + a^2|\Theta|^2)\mathrm{d}z,$$

we deduce that the modes (92) with two-dimensional wave number a are linearly stable if and only if

$$\mathcal{R} \le \mathcal{R}_L(a) \equiv \left[\max_{(W,\Theta)\in\mathscr{H}} \frac{\mathcal{I}(W, \Theta; a^2)}{\mathcal{D}(W, \Theta; a^2)}\right]^{-2}, \tag{101}$$

where $\mathscr{H}$ is the space of kinematically admissible disturbances:

$$\mathscr{H} = \left\{(W, \Theta) \in \mathrm{H}^2(0,1) \times \mathrm{H}^1(0,1) : W = DW = \Theta = 0 \text{ at } z = 0, 1\right\} \tag{102}$$

for rigid boundaries, or

$$\mathscr{H} = \left\{(W, \Theta) \in \mathrm{H}^2(0,1) \times \mathrm{H}^1(0,1) : W = D^2W = \Theta = 0 \text{ at } z = 0, 1\right\} \tag{103}$$

for stress-free bounding surfaces. The existence of the maximum of the functional $\mathcal{I}/\mathcal{D}$ in $\mathscr{H}$ can be proved by following similar arguments as in [45].

It is easy to check that the Euler-Lagrange equations associated with the variational problem (101) coincide with (93) with $\sigma = 0$ giving the marginally stable states. Following [13], (93) with $\sigma = 0$ can be simplified further to the following sixth-order ordinary differential equation

$$\hat{\mu}(z)(D^2-a^2)^3\Theta+2\hat{\mu}'(z)D(D^2-a^2)^2\Theta+\hat{\mu}''(z)(D^4-a^4)\Theta+\mathcal{R}a^2\Theta = 0 \tag{104}$$

to which we add the boundary conditions

$$\Theta = \mathrm{D}^2\Theta = D(D^2 - a^2)\Theta = 0 \quad \text{at } z = 0, 1 \tag{105}$$

for rigid boundaries, or

$$\Theta = D^2\Theta = D^4\Theta = 0 \quad \text{at } z = 0, 1 \tag{106}$$

for stress-free boundaries. The square of the maximum of the functional $\mathcal{I}/\mathcal{D}$ is then the reciprocal of the least eigenvalue of the characteristic-value problem (104) with boundary conditions (105) or (106) and thus the marginal stability curve has equation $\mathcal{R} = \mathcal{R}_L(a)$. Finally, we introduce the so-called critical Rayleigh number

$$\mathcal{R}_{cr} = \min_{a>0} \mathcal{R}_L(a), \tag{107}$$

and note that if $\mathcal{R} \leq \mathcal{R}_{cr}$ then all modes are stable, while if $\mathcal{R} > \mathcal{R}_{cr}$ there exists at least one unstable mode. Thus, we may conclude that the conduction solution m_0 is linearly stable if and only if

$$\mathcal{R} \leq \mathcal{R}_{cr}. \tag{108}$$

To appreciate the departures from the classical results for fluids with constant viscosities, in Table 1 we display the critical thresholds for the Rayleigh number for rigid and stress-free boundaries when the viscosity depends exponentially on pressure and temperature according to (14). In this case, the nondimensional

Table 1 Approximations of the critical Rayleigh and two-dimensional wave numbers against the dimensionless parameter Γ for (a) rigid and (b) stress-free boundaries

(a)

Γ	$\mathcal{R}_{cr}$	a_{cr}
0.5	2200.315	3.115
0.3	1986.687	3.116
0.2	1888.573	3.116
0.1	1795.744	3.116
0	1707.937	3.116
−0.1	1624.857	3.116
−0.2	1546.233	3.116
−0.3	1471.774	3.116
−0.5	1334.559	3.115

(b)

Γ	$\mathcal{R}_{cr}$	a_{cr}
0.5	850.079	2.216
0.3	765.847	2.219
0.2	727.500	2.221
0.1	691.451	2.221
0	657.548	2.221
−0.1	625.651	2.221
−0.2	595.627	2.221
−0.3	567.353	2.219
−0.5	515.599	2.216

viscosity function $\hat{\mu}$ reads

$$\hat{\mu} = \exp[\Gamma(1-z)] \quad \text{with} \quad \Gamma = \beta\rho_{\text{ref}} g d - \delta(\theta_L - \theta_U). \tag{109}$$

The critical thresholds $\mathcal{R}_{cr}$ have been found for different values of the dimensionless parameter Γ by solving the eigenvalue problems (104) and (105) or (106) with the aid of the MATLAB www.bvp4c solver. Observe that, both in the rigid and stress-free case the critical threshold $\mathcal{R}_{cr}$ increases with increasing Γ and equals the critical thresholds for fluids with constant viscosities when $\Gamma = 0$. This result is physically reasonable as the viscosity, and hence the resistance to motion from the rest state, increases as Γ increases. From the definition of Γ we can then assert that the pressure dependence of viscosity has a stabilizing effect on the onset of convection, in the sense that the critical threshold for the Rayleigh number is greater than the one that can be predicted starting from the assumption that viscosity is constant or dependent only on temperature.

The nonlinear stability of the conduction solution m_0 in a fluid whose viscosity is an analytic function of the pressure and temperature has been studied by Rajagopal et al. [38]. They proved that, under appropriate conditions on the initial disturbance of the temperature field ϑ_0, the conduction solution is nonlinearly stable with respect to the energy of the perturbations if inequality (108) holds. In this way, Rajagopal et al. proved that (108) is a necessary and sufficient condition for the local nonlinear stability of m_0.

5 Parallel Shear Flows of Piezo-Viscous Fluids

In the last two sections we shall consider isothermal flows in fluids with variable viscosities. In particular, in this section the viscosity will be assumed to depend only on pressure, while in the next section, to include shear-thickening/thinning effects, viscosity will be expressed in terms of pressure and shear.

The main goal of this section is the determination of some classes of steady unidirectional shear flows that are possible in a piezo-viscous fluid. We shall show that, under the assumption that gravity is the only body force acting on the fluid, Couette flows are possible for any constitutive model of the viscosity, whereas Poiseuille flows are possible only in fluids with constant viscosity. To the best of our knowledge, this result is novel as results on the existence of Poiseuille flows in piezo-viscous fluids are available only in the absence of body forces. Assuming that body forces are negligible compared to viscous forces and pressure gradients, Bair et al. [3] claimed to have proven that Poiseuille flows in piezo-viscous fluids are not possible, a secondary flow being necessary. This claim is not true in general. In fact, Hron et al. [19] showed that steady unidirectional flows are possible if the dependence of the viscosity on pressure is linear, and explicit exact continuous solutions can be established even if shear-thinning effects are included. On the other hand, for other forms of the viscosity, with polynomial and exponential dependence on the pressure, Hron et al. [19] reconfirmed the results of Bair et al. [3]. Two years later, Renardy [44] gave an elegant proof on the existence/nonexistence of Poiseuille flows in piezo-viscous fluids. He proved that, in the absence of body forces, Poiseuille flows are possible only if viscosity depends linearly on pressure. In what follows we shall consider also the case in which body forces are negligible and give an alternative proof of the result by Renardy [44].

5.1 Governing Equations

When gravity is the only force acting on the fluid, the equations governing the isothermal flows in the horizontal fluid layer Ω_d are the generalized Navier-Stokes equation (73).

We are here interested in two types of unidirectional flow: Couette flow, when one plate is fixed ($z = 0$) and the other one ($z = d$) moves with a prescribed velocity; and Poiseuille flow, when homogeneous Dirichlet boundary conditions at the plates $z = 0, d$ are considered. We then look for solutions to (73) of the form

$$\boldsymbol{v} = u(z)\boldsymbol{i}, \quad p = p(x, y, z), \tag{110}$$

which satisfy the following boundary conditions

$$u(0) = 0, \quad u(d) = V, \qquad \text{(Couette flow)}, \tag{111}$$

or

$$u(0) = u(d) = 0, \qquad \text{(Poiseuille flow)}. \tag{112}$$

Inserting the ansatz (110) into (73) and non-dimensionalizing the resulting system of pdes by means of the scales

$$\begin{aligned} \boldsymbol{x}^* = \frac{\boldsymbol{x}}{d}, \quad u^* = \frac{u}{U}, \quad p^* = \frac{p - p_{\text{ref}}}{\rho_{\text{ref}} g d}, \\ \mu^* = \frac{\mu}{\mu_{\text{ref}}}, \quad U = \frac{\rho_{\text{ref}} g d^2}{\mu_{\text{ref}}}, \quad \mu_{\text{ref}} = \mu(p_{\text{ref}}), \end{aligned} \tag{113}$$

yield (omitting the asterisks for simplicity of notation) the dimensionless equations

$$\begin{cases} p_x = \tau_z, \\ p_y = 0, \\ p_z = \tau_x - 1, \end{cases} \tag{114}$$

where

$$\tau = \mu(p) u_z \tag{115}$$

is the shear stress. To (114) we add the dimensionless boundary conditions

$$u(0) = 0, \quad u(1) = V^* \equiv \frac{V}{U}, \qquad \text{(Couette flow)}, \tag{116}$$

or

$$u(0) = u(1) = 0 \qquad \text{(Poiseuille flow)}. \tag{117}$$

From (114) we easily deduce that $p = p(x, z)$ and that both the shear stress and the pressure are solutions of the wave equation $\psi_{xx} - \psi_{zz} = 0$. This leads to the representations

$$\begin{cases} p = \Xi(x + z) + \Psi(x - z) - z, \\ \tau = \Xi(x + z) - \Psi(x - z). \end{cases} \tag{118}$$

5.2 *Couette Flows*

Let us first consider the Couette flows. Assuming that the pressure at the upper boundary is constant and equal to the reference pressure, namely $p(1) = 0$, from $(118)_1$ the functions Ξ and Ψ are such that $\Xi(x + 1) + \Psi(x - 1) = 1$ for all $x \in \mathbb{R}$, by which one deduces that Ξ and Ψ are of the form

$$\Xi(x + z) = a(x + z) + b, \quad \Psi(x - z) = -a(x - z) + 1 - 2a - b, \tag{119}$$

with a and b constants. Hence, inserting (119) into (118) we deduce that the pressure, and thus the shear stress, do not depend on x, whence $a = 0$ and

$$\begin{cases} p = 1 - z, \\ \tau = 2b - 1. \end{cases} \tag{120}$$

Finally, from (115), (116) and $(120)_2$ the velocity component u is found to be

$$u(z) = V^* \frac{\displaystyle\int_0^z \frac{\mathrm{d}z}{\mu(1-z)}}{\displaystyle\int_0^1 \frac{\mathrm{d}z}{\mu(1-z)}}. \tag{121}$$

Couette flows are then possible in a piezo-viscous fluid with a very general response function of the viscosity. As examples, if the (dimensionless) viscosity is given by a power law of the form

$$\mu(p) = 1 + \varpi p^n \quad (\varpi \geq 0,\ n > 0), \tag{122}$$

then

$$u(z) = 1 - \frac{\mathrm{LerchPhi}\left(-\varpi(1-z)^n, 1, \dfrac{1}{n}\right)}{\mathrm{LerchPhi}\left(-\varpi, 1, \dfrac{1}{n}\right)}(1-z), \tag{123}$$

where LerchPhi is the Lerch Phi function; while if viscosity depends exponentially on the pressure according to the Barus law

$$\mu(p) = \mathrm{e}^{\varpi p} \quad (\varpi \geq 0), \tag{124}$$

then

$$u(z) = \frac{\mathrm{e}^{\varpi z} - 1}{\mathrm{e}^{\varpi} - 1}. \tag{125}$$

Figure 1 displays the velocity profiles of the Couette flow for different models of the viscosity.

5.3 *Poiseuille Flows*

We now consider the Poiseuille flows and observe that, since the velocity field satisfies the boundary conditions (117), the assumption that either Ξ or Ψ is

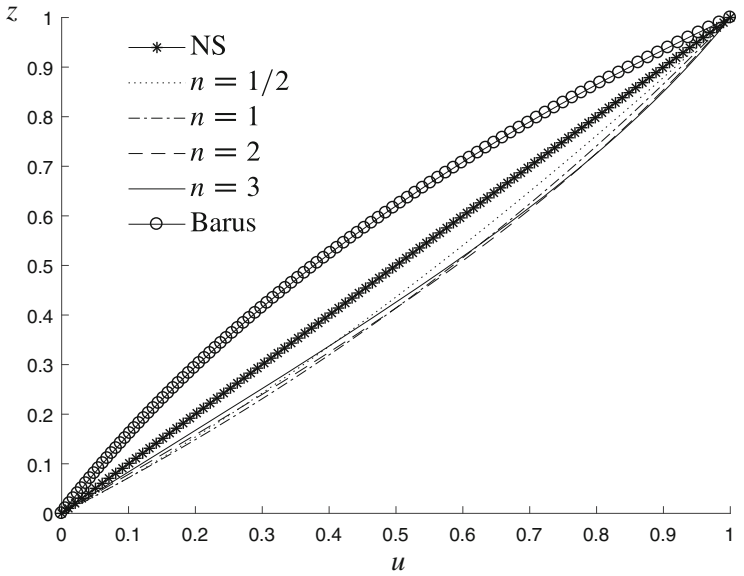

Fig. 1 Velocity profiles of the Couette flow when the dimensionless viscosity is constant (i.e. the classical Navier-Stokes (NS) model), or of the form (122) or (124). The dimensionless piezo-viscous coefficient ϖ is taken to be equal to unity

constant leads to the trivial flow $u \equiv 0$ (no motion). Thus, we have

$$\Xi'(x+z) \neq 0 \quad \text{and} \quad \Psi'(x-z) \neq 0. \tag{126}$$

Moreover, it can be easily proven that also the assumption $\mu'(p)u_z = \mu'(p)\tau/\mu(p) =$constant leads to the trivial motionless flow. Hence,

$$\nabla\left(\frac{\mu'(p)}{\mu(p)}\tau\right) \neq \mathbf{0}. \tag{127}$$

Next, from (115) we deduce that

$$0 = \frac{\partial u_z}{\partial x} = \frac{\partial}{\partial x}\left(\frac{\tau}{\mu(p)}\right) = \frac{\tau_x}{\mu(p)} - \frac{\mu'(p)}{\mu^2(p)}\tau p_x, \tag{128}$$

whence, on using $(114)_1$,

$$\mu(p)\tau_x - \mu'(p)\tau\tau_z = 0. \tag{129}$$

In the light of (126) and (127), on using the representations of p and τ (118), (129) can be rewritten as

$$\frac{\Xi'(x+z)}{\Psi'(x-z)} = \frac{\mu(p)+\mu'(p)[\Xi(x+z)-\Psi(x-z)]}{\mu(p)-\mu'(p)[\Xi(x+z)-\Psi(x-z)]}, \tag{130}$$

with p as in $(118)_1$. Therefore, because of the explicit dependence of the pressure on the vertical variable z (and not only through $\Xi(x+z)$ and $\Psi(x-z)$), (130) holds if and only if the viscosity of the fluid is constant. Consequently, when gravity is the only body force acting on the fluid, Poiseuille flows are possible only if the viscosity is constant, in which case

$$\begin{cases} p = A_0 x - z + \kappa, \\ u = \dfrac{A_0}{2} z(z-1), \end{cases} \tag{131}$$

where A_0 is the constant pressure gradient that induces the flow, and κ is an integration constant that, once A_0 is known, can be determined by measuring the pressure at a single point on the boundary.

Assume now that body forces are negligible compared to the viscous forces and pressure gradients. Then, following the same arguments as in the case in which the effects due gravity are taken into account we arrive at (130) with p given by

$$p = \Xi(x+z) + \Psi(x-z). \tag{132}$$

Since in the absence of body forces the pressure does not depend explicitly on z but only through $\Xi(x+z)$ and $\Psi(x-z)$, (130) with p as in (132) holds if and only if μ is a linear function of pressure. In other words, the dimensionless viscosity must be of the form

$$\mu(p) = 1 + \varpi p \quad (\varpi \geq 0). \tag{133}$$

For such a dependency on the pressure, a simple manipulation of (114) and (115) gives

$$\begin{cases} \dfrac{p_x}{1+\varpi p} = \dfrac{u_{zz}}{1-\varpi^2 u_z^2}, \\ \dfrac{p_z}{1+\varpi p} = \dfrac{\varpi u_z u_{zz}}{1-\varpi^2 u_z^2}. \end{cases} \tag{134}$$

Integrating $(134)_2$ yields

$$p = \frac{1}{\varpi}\left[\frac{\phi(x)}{\sqrt{1-\varpi^2 u_z^2}} - 1\right], \tag{135}$$

where $\phi(x)$ is an arbitrary function to be determined with the aid of $(134)_1$. Indeed, inserting (135) into $(134)_1$ we obtain

$$\frac{1}{\varpi}\frac{\phi'(x)}{\phi(x)} = \frac{u_{zz}}{1-\varpi^2 u_z^2}, \tag{136}$$

which holds if and only if

$$\frac{1}{\varpi}\frac{\phi'(x)}{\phi(x)} = A_0 \quad \text{and} \quad \frac{u_{zz}}{1-\varpi^2 u_z^2} = A_0, \tag{137}$$

with A_0 being constant. Next, integrating (137) and taking into account the boundary conditions (117), we derive the Poiseuille flow

$$\begin{cases} p = \dfrac{1}{\varpi}\left\{\kappa \exp(\varpi A_0 x)\cosh\left[\varpi A_0\left(z-\dfrac{1}{2}\right)\right]-1\right\}, \\ u = \dfrac{1}{\varpi^2 A_0}\ln\dfrac{\cosh\left[\varpi A_0\left(z-\dfrac{1}{2}\right)\right]}{\cosh\dfrac{\varpi A_0}{2}}, \end{cases} \tag{138}$$

where κ is an integration constant that, as indicated before, can be determined once A_0 is known. Finally, from $(138)_2$ it follows that the maximum speed in a Poiseuille flow decreases with increasing ϖ, and, in the limit as $\varpi \to 0$, the velocity profile tends to the one which has been determined for a fluid with constant viscosity (see Fig. 2).

6 Flow of Fluids with Pressure and Shear Dependent Viscosity Down an Inclined Plane

In this final section, we carry out an analysis of the flow of a fluid with a pressure and shear dependent viscosity down an inclined plane within the context of the lubrication approximation. It is legitimate to ask where the pressure dependence of viscosity could become important within the context of the lubrication approximation. Thin film flows are ubiquitous in engineering, geophysics, biology and elsewhere, and low aspect ratios are often the basis for simplified fluid dynamical models. An important relevant application in geophysics is the flow of glaciers and ice sheets as well as rock glaciers. For instance, while the ice sheet covering Antarctica is several kilometers thick, it however has a horizontal extent of several thousand kilometres, yielding a length scale ratio epsilon of order 10^{-3} [47]. These glaciers clearly exhibit non-Newtonian characteristics in that their viscosities depend on the shear rate so that their flows are modelled using a shallow-ice approximation and Glen's flow law [33]: in other words, as gravity currents with

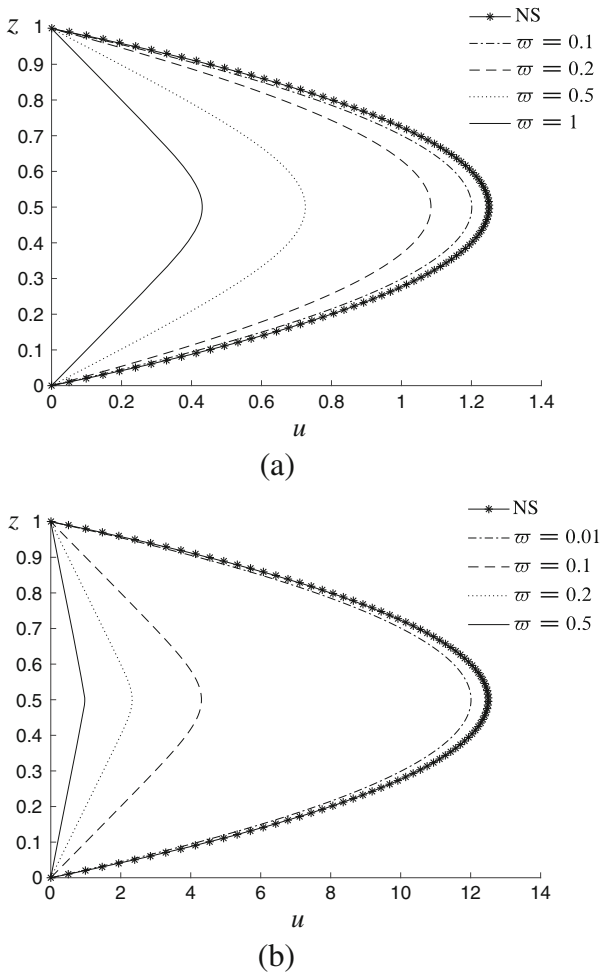

Fig. 2 Poiseuille flow. Velocity profiles for different values of the piezo-viscous coefficient ϖ and (**a**) $A_0 = -10$ and (**b**) $A_0 = -100$

non-Newtonian (power law) rheology. On the other hand, there are several papers that investigate the possibility of normal stress effects in the creep of polycrystalline ice (see, for instance, [27] and [24]). In particular, Jones and Chew [22] have shown that hydrostatic pressure decreases the creep of polycristalline ice slightly and, then, above 15 MPa, a minimum creep rate is reached followed by an increase in rate with increasing hydrostatic pressure. Therefore, in view of the depths of glaciers we would expect that the pressure would also influence the viscosity. As the viscosity depends on both the shear rate as well as the pressure, it is possible that these two effects could either compete against each other thereby mitigating their effects, or join forces to enhance the qualitative and quantitative differences. As the fluid can shear-thin or shear-thicken, both possibilities may come to pass.

6.1 Basic Equations

We consider a fluid moving on an inclined plane, whose angle of inclination is ι. Let now $Oxyz$ be a Cartesian frame of reference with fundamental unit vectors $\boldsymbol{i}, \boldsymbol{j}$ and $\boldsymbol{k}$, where the coordinate z is perpendicular to the plane, the x and y coordinates lie in the plane, y is horizontal and x increasing downward. We denote the components of the velocity $\boldsymbol{v}$ of the fluid in the directions x, y and z as u, v and w, respectively. The generalized Navier-Stokes equations read then

$$\begin{cases} \dfrac{\partial u}{\partial x} + \dfrac{\partial v}{\partial y} + \dfrac{\partial w}{\partial z} = 0, \\ \rho\left(\dfrac{\partial u}{\partial t} + u\dfrac{\partial u}{\partial x} + v\dfrac{\partial u}{\partial y} + w\dfrac{\partial u}{\partial z}\right) = -\dfrac{\partial p}{\partial x} + \dfrac{\partial S_{xx}}{\partial x} + \dfrac{\partial S_{xy}}{\partial y} + \dfrac{\partial S_{xz}}{\partial z} + \rho g \sin\iota, \\ \rho\left(\dfrac{\partial v}{\partial t} + u\dfrac{\partial v}{\partial x} + v\dfrac{\partial v}{\partial y} + w\dfrac{\partial v}{\partial z}\right) = -\dfrac{\partial p}{\partial y} + \dfrac{\partial S_{yx}}{\partial x} + \dfrac{\partial S_{yy}}{\partial y} + \dfrac{\partial S_{yz}}{\partial z}, \\ \rho\left(\dfrac{\partial w}{\partial t} + u\dfrac{\partial w}{\partial x} + v\dfrac{\partial w}{\partial y} + w\dfrac{\partial w}{\partial z}\right) = -\dfrac{\partial p}{\partial z} + \dfrac{\partial S_{zx}}{\partial x} + \dfrac{\partial S_{zy}}{\partial y} + \dfrac{\partial S_{zz}}{\partial z} - \rho g \cos\iota, \end{cases} \tag{139}$$

where the Cauchy stress is now given by the implicit relation

$$\mathsf{T} - \frac{1}{3}\mathrm{tr}(\mathsf{T}) - \mu\left(-\frac{1}{3}\mathrm{tr}(\mathsf{T}), \mathrm{tr}(\mathsf{D}^2)\right)\mathsf{D} = \mathsf{O}, \tag{140}$$

or, equivalently, since $\|\mathsf{D}\| = [\mathrm{tr}(\mathsf{D}^2)]^{1/2}$,

$$\mathsf{T} = -p\mathsf{I} + 2\mu(p, \|\mathsf{D}\|)\mathsf{D} \equiv -p\mathsf{I} + \mathsf{S}. \tag{141}$$

The viscosity is taken of the form

$$\mu(p, \|\mathsf{D}\|) = \varsigma(p - p_{\mathrm{ref}})\|\mathsf{D}\|^{(1-\chi)/\chi}, \tag{142}$$

with $\chi > 0$, p_{ref} the reference pressure and, as is reasonable to expect since the fluid viscosity increases as the pressure increases, ς is a positive function whose value increases with increasing pressure. Model (141), with a viscosity of the type (142), allows for a fluid that is capable of shear thinning, when $\chi > 1$, or shear thickening, when $\chi \in (0, 1)$. Here, for the sake of definiteness, we shall consider the following forms for ς:

$$\text{(exponential model)} \qquad \varsigma(p) = \varsigma_{\mathrm{ref}} e^{\beta(p - p_{\mathrm{ref}})}, \tag{143}$$

$$\text{(power law model)} \qquad \varsigma(p) = \varsigma_{\mathrm{ref}} + \beta(p - p_{\mathrm{ref}})^n, \tag{144}$$

where $\varsigma_{\text{ref}} > 0$, $\beta \geq 0$ and $n \geq 0$ are constants. In general, the material parameters that appear in (143) and (144) can be obtained by corroboration with experimental data. Here, in order to illustrate the effects due to the pressure dependence of viscosity, we merely carry out a parametric study.

We prescribe the following boundary conditions for the velocity and pressure fields

$$\begin{cases} u = v = w = 0 \text{ on } z = 0, \\ \mathsf{T}\boldsymbol{n} = -p_{\text{ref}}\boldsymbol{n} \quad \text{on } z = h(x, y, t), \end{cases} \tag{145}$$

where

$$\boldsymbol{n} = \frac{1}{\sqrt{1 + \left(\dfrac{\partial h}{\partial x}\right)^2 + \left(\dfrac{\partial h}{\partial y}\right)^2}} \left(-\frac{\partial h}{\partial x}\boldsymbol{i} - \frac{\partial h}{\partial y}\boldsymbol{j} + \boldsymbol{k} \right) \tag{146}$$

is the unit normal to the free surface of the current $z = h(x, y, t)$.

Let H and L denote the characteristic thickness and characteristic length along the plane of the current free surface $z = h(x, y, t)$, respectively. The main assumption in lubrication approximation is that the lengthscale ratio H/L is small [51]. Here, as we are interested in fluids whose viscosity depends on the pressure, we assume that the ratio H/L is small though H is large enough to have a significant dependence of the viscosity on the pressure.

As a consequence of the smallness of the lengthscale ratio H/L, the component of the velocity parallel to the plane is much larger than the normal component, so that

$$\sqrt{u^2 + v^2} \gg |w|. \tag{147}$$

We call U, V and W the characteristic velocities along x, y and z directions, respectively. Hence, $U_{\parallel} = \sqrt{U^2 + V^2}$ and W are the characteristic velocities parallel and perpendicular to the inclined plane, respectively. From Eqs. $(139)_1$ and (147) we find that $W = HU_{\parallel}/L$.

There are many ways of transforming the governing equation (139) and boundary conditions (145) into dimensionless expressions. Here we introduce a scaling which is similar to that introduced in [1]:

$$\begin{cases} \boldsymbol{x}^* = \dfrac{1}{L}(x\boldsymbol{i} + y\boldsymbol{j}) + \dfrac{z}{H}\boldsymbol{k}, \quad \boldsymbol{v}^* = \dfrac{1}{U_{\parallel}}(u\boldsymbol{i} + v\boldsymbol{j}) + \dfrac{w}{W}\boldsymbol{k}, \quad h^* = \dfrac{h}{H}, \\ W = \dfrac{H}{L}U_{\parallel}, \quad t^* = \dfrac{U_{\parallel}}{L}t, \quad p^* = \dfrac{p - p_{\text{ref}}}{\rho g \cos\iota H}, \quad \varsigma^* = \dfrac{\varsigma}{\varsigma_{\text{ref}}}. \end{cases} \tag{148}$$

Substituting the dimensionless quantities (148) into equations (139), (141) and (146) and into the boundary conditions (145) leads to (omitting all asterisks)

$$\begin{cases} \dfrac{\partial u}{\partial x}+\dfrac{\partial v}{\partial y}+\dfrac{\partial w}{\partial z}=0, \\ \epsilon\mathrm{Re}\left(\dfrac{\partial u}{\partial t}+u\dfrac{\partial u}{\partial x}+v\dfrac{\partial u}{\partial y}+w\dfrac{\partial u}{\partial z}\right)=\epsilon\dfrac{\mathrm{Re}}{\mathrm{Fr}^2}\left(\dfrac{\tan\iota}{\epsilon}-\dfrac{\partial p}{\partial x}\right) \\ \qquad\qquad +\epsilon\dfrac{\partial S_{xx}}{\partial x}+\epsilon\dfrac{\partial S_{xy}}{\partial y}+\dfrac{\partial S_{xz}}{\partial z}, \\ \epsilon\mathrm{Re}\left(\dfrac{\partial v}{\partial t}+u\dfrac{\partial v}{\partial x}+v\dfrac{\partial v}{\partial y}+w\dfrac{\partial v}{\partial z}\right)=-\epsilon\dfrac{\mathrm{Re}}{\mathrm{Fr}^2}\dfrac{\partial p}{\partial y} \\ \qquad\qquad +\epsilon\dfrac{\partial S_{yx}}{\partial x}+\epsilon\dfrac{\partial S_{yy}}{\partial y}+\dfrac{\partial S_{yz}}{\partial z}, \\ \epsilon^2\mathrm{Re}\left(\dfrac{\partial w}{\partial t}+u\dfrac{\partial w}{\partial x}+v\dfrac{\partial w}{\partial y}+w\dfrac{\partial w}{\partial z}\right)=-\dfrac{\mathrm{Re}}{\mathrm{Fr}^2}\left(1+\dfrac{\partial p}{\partial z}\right) \\ \qquad\qquad +\epsilon\dfrac{\partial S_{zx}}{\partial x}+\epsilon\dfrac{\partial S_{zy}}{\partial y}+\dfrac{\partial S_{zz}}{\partial z}, \end{cases} \tag{149}$$

$$\begin{cases} u=v=w=0 & \text{on } z=0, \\ (-p\mathsf{I}+\mathsf{S})\left(-\epsilon\dfrac{\partial h}{\partial x}\boldsymbol{i}-\epsilon\dfrac{\partial h}{\partial y}\boldsymbol{j}+\boldsymbol{k}\right)=\boldsymbol{0} & \text{on } z=h(x,y,t), \end{cases} \tag{150}$$

where $\epsilon = H/L \ll 1$, and

$$\begin{aligned} \mathsf{S}=\varsigma(p)\Bigg[&\epsilon^2\left(\frac{\partial u}{\partial x}\right)^2+\epsilon^2\left(\frac{\partial v}{\partial y}\right)^2+\epsilon^2\left(\frac{\partial w}{\partial z}\right)^2+\frac{\epsilon^2}{2}\left(\frac{\partial u}{\partial y}+\frac{\partial v}{\partial x}\right)^2+\frac{1}{2}\left(\frac{\partial u}{\partial z}+\epsilon^2\frac{\partial w}{\partial x}\right)^2 \\ &+\frac{1}{2}\left(\frac{\partial v}{\partial z}+\epsilon^2\frac{\partial w}{\partial y}\right)^2\Bigg]^{\frac{1-\chi}{2\chi}}\times\Bigg[2\epsilon\left(\frac{\partial u}{\partial x}\boldsymbol{i}\otimes\boldsymbol{i}+\frac{\partial v}{\partial y}\boldsymbol{j}\otimes\boldsymbol{j}+\frac{\partial w}{\partial z}\boldsymbol{k}\otimes\boldsymbol{k}\right) \\ &+\epsilon\left(\frac{\partial u}{\partial y}+\frac{\partial v}{\partial x}\right)(\boldsymbol{i}\otimes\boldsymbol{j}+\boldsymbol{j}\otimes\boldsymbol{i})+\left(\frac{\partial u}{\partial z}+\epsilon^2\frac{\partial w}{\partial x}\right)(\boldsymbol{i}\otimes\boldsymbol{k}+\boldsymbol{k}\otimes\boldsymbol{i}) \\ &+\left(\frac{\partial v}{\partial z}+\epsilon^2\frac{\partial w}{\partial y}\right)(\boldsymbol{j}\otimes\boldsymbol{k}+\boldsymbol{k}\otimes\boldsymbol{j})\Bigg]. \end{aligned} \tag{151}$$

In this framework the dimensionless version of ς is an increasing function such that $\varsigma(0)=1$. In particular, (143) and (144) become, respectively,

$$\varsigma(p)=\mathrm{e}^{\omega p} \quad \text{with} \quad \omega=\beta\rho g\cos\iota H, \tag{152}$$

and

$$\varsigma(p)=1+\omega p^n \quad \text{with} \quad \omega=\beta(\rho g\cos\iota H)^n. \tag{153}$$

The dimensionless quantities

$$\mathrm{Re} = \frac{\rho U_{\parallel}^{(2\chi-1)/\chi} H^{1/\chi}}{\varsigma_{\mathrm{ref}}} \quad \text{and} \quad \mathrm{Fr} = \frac{U_{\parallel}}{\sqrt{g \cos \iota H}} \tag{154}$$

are, respectively, the Reynolds and Froude numbers for a fluid film moving over an inclined plane.

Depending on the values considered for the characteristic scales, different types of flow regime occur. Here we shall focus on the following two types of flow regimes:

1. The *nearly steady uniform regime*, where the viscous contribution is comparable to the gravitational effect. In this case, we have

$$U_{\parallel} = \left[\frac{\rho g \sin \iota H^{(\chi+1)/\chi}}{\varsigma_{\mathrm{ref}}} \right]^{\chi} \tag{155}$$

and $\mathrm{Fr}^2 = O(\mathrm{Re})$. Inertial terms and pressure gradient terms must be negligible, which means $\epsilon \mathrm{Re} \ll 1$. Therefore, from (149) and (151) the approximate equations are found to be given by

$$\begin{cases} \dfrac{\partial u}{\partial x} + \dfrac{\partial v}{\partial y} + \dfrac{\partial w}{\partial z} = 0, \\ \dfrac{\partial}{\partial z} \left\{ \varsigma(p) \left[\left(\dfrac{\partial u}{\partial z} \right)^2 + \left(\dfrac{\partial v}{\partial z} \right)^2 \right]^{(1-\chi)/(2\chi)} \dfrac{\partial u}{\partial z} \right\} \\ \qquad\qquad + 2^{(1-\chi)/(2\chi)} = 0, \\ \dfrac{\partial}{\partial z} \left\{ \varsigma(p) \left[\left(\dfrac{\partial u}{\partial z} \right)^2 + \left(\dfrac{\partial v}{\partial z} \right)^2 \right]^{(1-\chi)/(2\chi)} \dfrac{\partial v}{\partial z} \right\} = 0, \\ \dfrac{\partial p}{\partial z} + 1 = 0. \end{cases} \tag{156}$$

2. The *viscous regime*, where the effect of the pressure gradient is balanced by stresses induced due to the viscosity within the bulk. In this case, we have

$$U_{\parallel} = \left[\frac{\rho g \cos \iota H^{(2\chi+1)/\chi}}{\varsigma_{\mathrm{ref}} L} \right]^{\chi} \tag{157}$$

and consequently $\mathrm{Fr}^2 = \epsilon \mathrm{Re}$. Inertial terms must be small compared to the effect of the pressure gradient and the slope must be gentle ($\tan \iota = O(\epsilon)$). This imposes the constraint $\epsilon \mathrm{Re} \ll 1$. In such a way, from (149) and (151) we deduce

the approximate equations

$$\begin{cases} \dfrac{\partial u}{\partial x}+\dfrac{\partial v}{\partial y}+\dfrac{\partial w}{\partial z}=0, \\ \dfrac{\partial}{\partial z}\left\{\varsigma(p)\left[\left(\dfrac{\partial u}{\partial z}\right)^2+\left(\dfrac{\partial v}{\partial z}\right)^2\right]^{(1-\chi)/(2\chi)}\dfrac{\partial u}{\partial z}\right\} \\ \qquad\qquad +2^{(1-\chi)/(2\chi)}\left(\dfrac{\tan\iota}{\epsilon}-\dfrac{\partial p}{\partial x}\right)=0, \\ \dfrac{\partial}{\partial z}\left\{\varsigma(p)\left[\left(\dfrac{\partial u}{\partial z}\right)^2+\left(\dfrac{\partial v}{\partial z}\right)^2\right]^{(1-\chi)/(2\chi)}\dfrac{\partial v}{\partial z}\right\} \\ \qquad\qquad -2^{(1-\chi)/(2\chi)}\dfrac{\partial p}{\partial y}=0, \\ \dfrac{\partial p}{\partial z}+1=0. \end{cases} \tag{158}$$

Moreover, from (150) and (151), by virtue of the smallness of ϵ, the boundary conditions (145) approximate to

$$\begin{cases} u=v=w=0 \text{ on } z=0, \\ p=0 \qquad\quad \text{on } z=h(x,y,t), \\ \dfrac{\partial u}{\partial z}=\dfrac{\partial v}{\partial z}=0 \quad \text{on } z=h(x,y,t). \end{cases} \tag{159}$$

Finally, we derive the evolution equation for the free surface $z=h(x,y,t)$. We first integrate the constraint of incompressibility over the flow depth to obtain, by means of boundary condition $(159)_1$,

$$\int_0^h\left(\frac{\partial u}{\partial x}+\frac{\partial v}{\partial y}+\frac{\partial w}{\partial z}\right)\mathrm{d}z=\frac{\partial}{\partial x}\int_0^h u\mathrm{d}z+\frac{\partial}{\partial y}\int_0^h v\mathrm{d}z-u_{|z=h}\frac{\partial h}{\partial x}-v_{|z=h}\frac{\partial h}{\partial y}-w_{|z=h}. \tag{160}$$

But, obviously,

$$w_{|z=h}=\frac{\mathrm{d}h}{\mathrm{d}t}=\frac{\partial h}{\partial t}+u_{|z=h}\frac{\partial h}{\partial x}+v_{|z=h}\frac{\partial h}{\partial y}. \tag{161}$$

Therefore, combining (160) and (161) gives the required equation for h:

$$h_t+\frac{\partial(h\bar{u})}{\partial x}+\frac{\partial(h\bar{v})}{\partial y}=0, \tag{162}$$

where we have introduced the depth-averaged variables defined as

$$\bar{\varphi}(x, y, t) = \frac{1}{h(x, y, t)} \int_0^{h(x,y,t)} \varphi(x, y, z, t) \mathrm{d}z. \tag{163}$$

6.2 Nearly Steady Uniform Regime

It is easy to verify that system (156) with boundary conditions (159) admits the solution

$$\begin{cases} u = 2^{(1-\chi)/2} \displaystyle\int_0^z \left[\frac{h-\zeta}{\varsigma(h-\zeta)}\right]^\chi \mathrm{d}\zeta, \\ v = 0, \\ w = -2^{(1-\chi)/2} \dfrac{\partial}{\partial x} \displaystyle\int_0^z \left\{ \int_0^{\zeta_1} \left[\frac{h-\zeta}{\varsigma(h-\zeta)}\right]^\chi \mathrm{d}\zeta_2 \right\} \mathrm{d}\zeta_1, \\ p = h - z. \end{cases} \tag{164}$$

Therefore

$$h\bar{u} = 2^{(1-\chi)/2} \int_0^h \xi \left[\frac{\xi}{\varsigma(\xi)}\right]^\chi \mathrm{d}\xi \equiv F(h) \tag{165}$$

and (162) becomes

$$\frac{\partial h}{\partial t} + F'(h) \frac{\partial h}{\partial x} = 0. \tag{166}$$

Equation (166) is a quasilinear first order partial differential equation whose general solution can be found by the method of characteristics. If $f(\xi)$ is an initial profile, then the corresponding solution is given by

$$h = f(x - F'(h)t). \tag{167}$$

The wave (167) breaks, i.e. its profile becomes multivalued, at time $t_B = -\left[F''(f(\xi_B)) \dfrac{\mathrm{d}f}{\mathrm{d}\xi}(\xi_B)\right]^{-1}$ at the point $x_B = \xi_B + F'(f(\xi_B))t_B$, provided that ξ_B satisfies the following two conditions

$$\begin{cases} F''(f(\xi_B)) \dfrac{\mathrm{d}f}{\mathrm{d}\xi}(\xi_B) < 0 \\ \left| F''(f(\xi_B)) \dfrac{\mathrm{d}f}{\mathrm{d}\xi}(\xi_B) \right| = \max \left| \dfrac{\mathrm{d}F'(f(\xi))}{\mathrm{d}\xi} \right|. \end{cases} \tag{168}$$

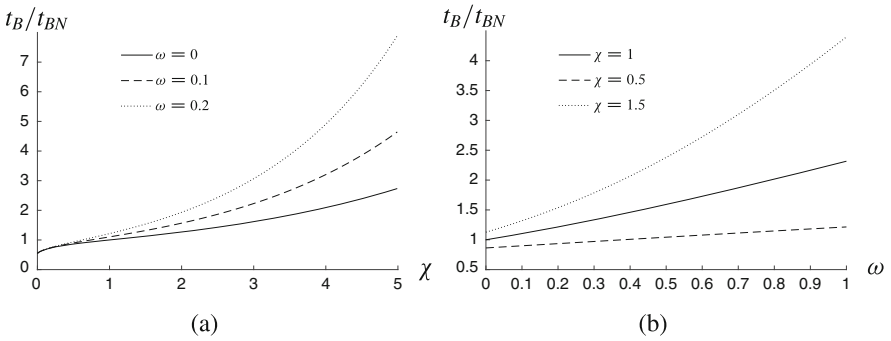

Fig. 3 Ratio t_B/t_{BN} as a function of (**a**) χ and (**b**) the piezo-viscous coefficient ω. The pressure-dependent parameter ς is assumed to be of the form (143) and the initial profile considered is $h(x, 0) = 1 - x^2$

Since ς is a positive increasing function, from (168) we deduce that the pressure dependence of the viscosity has the effect of delaying the time at which the wave could break. To quantify this delaying effect we consider ς of the form (152) and assume that $h(x, 0) = f(x) = 1 - x^2$. If the fluid is Newtonian with a constant viscosity μ_0 (i.e., $\chi = 1$ and $\varsigma(p - p_{\text{ref}}) = \mu_{\text{ref}}$ in (142)), it is easy to show that the wave breaks at time $t_{BN} = 3\sqrt{3}/8$. In order to make the differences between the non-Newtonian case that is being considered and the classical Newtonian case more evident, we have plotted the ratio between the breaking time t_B in the non-Newtonian case and t_{BN} as a function of χ (Fig. 3a) and as a function of the non-dimensional piezo-viscous coefficient ω (Fig. 3b). Furthermore, the solutions to the wave equation (166) with $\chi = 0.5$ (Fig. 4a) and $\chi = 1.5$ (Fig. 4b) are plotted at different times together with the profiles of the free surface $z = h(x, t)$ in the classical Newtonian case. We find that the solutions are qualitatively similar, though quantitatively different.

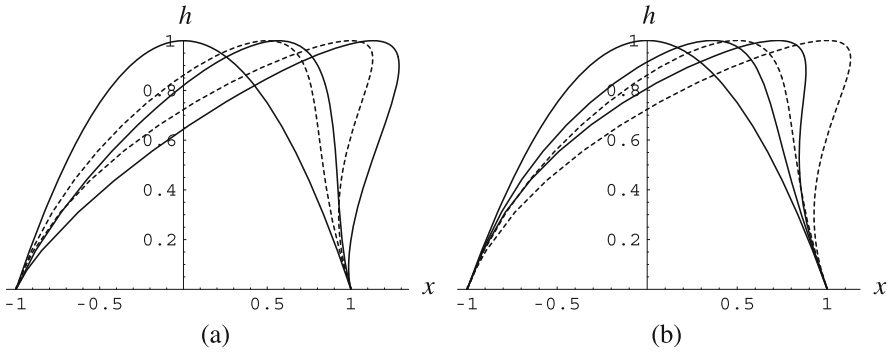

Fig. 4 Solutions of (166) with an initial profile $f(x) = 1 - x^2$ at $t = 0$, $t = 0.5$, $t = 1$. The dashed line represents the solution in the classical Newtonian case, whereas the solid line represents the solution in the case in which the dimensionless parameter ς depends on the pressure according to the law $\varsigma(p) = \mathrm{e}^{0.1p}$ and (**a**) $\chi = 0.5$ and (**b**) $\chi = 1.5$

Finally, in order to look for self-similar solutions of (166), we need to know whether F' is invertible. The invertibility of F' is linked with the equation

$$\chi h\varsigma'(h) - (\chi + 1)\varsigma(h) = 0. \tag{169}$$

Indeed, if (169) admits positive roots, the least of which we denote by $\hat{h}$, then F' is invertible in $[0, \hat{h}[$. On the contrary, if (169) does not admit positive roots, then F' is invertible in $[0, +\infty[$. In any case F' is continuous and increasing. It is interesting to show that some time after the initiation of the current, no matter what the initial shape, the solution tends to the unique self-similar solution of Eq. (166), i.e.

$$h(x, t) \to F'^{-1}\left(\frac{x}{t}\right) \quad \text{as} \quad t \to +\infty. \tag{170}$$

In order to prove (170), from (166) we deduce that h is constant along the characteristics given by

$$\frac{\mathrm{d}x}{\mathrm{d}t} = F'(h). \tag{171}$$

Thus, if initially $h(x, 0) = f(x)$, the characteristics are straight lines

$$x = x_0 + F'[f(x_0)]t, \tag{172}$$

with x_0 being the initial value of the characteristic. The solution of (166) is then

$$h(x, t) = F'^{-1}\left(\frac{x - x_0}{t}\right) \to F'^{-1}\left(\frac{x}{t}\right) \quad \text{as} \quad t \to +\infty. \tag{173}$$

If the viscosity does not depend on the pressure, Eq. (170) reduces to the self-similar solution found by Perazzo and Gratton [34] that in turn is the non-Newtonian counterpart of the self-similar solution derived by Huppert [21] for Newtonian fluids.

6.3 Viscous Regime

A lengthy but straightforward algebraic manipulation allows us to obtain the solution to the boundary-value problem (158)–(159):

$$\begin{cases} u = 2^{(1-\chi)/2}\left(\dfrac{\tan\iota}{\epsilon} - \dfrac{\partial h}{\partial x}\right)\left[\left(\dfrac{\partial h}{\partial x} - \dfrac{\tan\iota}{\epsilon}\right)^2 + \left(\dfrac{\partial h}{\partial y}\right)^2\right]^{(\chi-1)/2} \displaystyle\int_0^z \left[\frac{h-\zeta}{\varsigma\,(h-\zeta)}\right]^{\chi} \mathrm{d}\zeta, \\ v = -2^{(1-\chi)/2}\dfrac{\partial h}{\partial y}\left[\left(\dfrac{\partial h}{\partial x} - \dfrac{\tan\iota}{\epsilon}\right)^2 + \left(\dfrac{\partial h}{\partial y}\right)^2\right]^{(\chi-1)/2} \displaystyle\int_0^z \left[\frac{h-\zeta}{\varsigma\,(h-\zeta)}\right]^{\chi} \mathrm{d}\zeta, \\ w = -2^{(1-\chi)/2}\nabla_s \cdot \left\{\left|\dfrac{\tan\iota}{\epsilon}\boldsymbol{i} - \nabla_s h\right|^{\chi-1}\left(\dfrac{\tan\iota}{\epsilon}\boldsymbol{i} - \nabla_s h\right)\displaystyle\int_0^z \left[\int_0^{\zeta_1}\left(\frac{h-\zeta_2}{\varsigma(h-\zeta_2)}\right)^{\chi}\mathrm{d}\zeta_2\right]\mathrm{d}\zeta_1\right\}, \\ p = h - z, \end{cases} \tag{174}$$

where ∇_s is the two-dimensional gradient:

$$\nabla_s \varphi = \frac{\partial \varphi}{\partial x}\boldsymbol{i} + \frac{\partial \varphi}{\partial y}\boldsymbol{j}. \tag{175}$$

Then

$$h\bar{u} = F(h)\left(\frac{\tan\iota}{\epsilon} - \frac{\partial h}{\partial x}\right)\left[\left(\frac{\partial h}{\partial x} - \frac{\tan\iota}{\epsilon}\right)^2 + \left(\frac{\partial h}{\partial y}\right)^2\right]^{(\chi-1)/2}, \tag{176}$$

$$h\bar{v} = -F(h)\frac{\partial h}{\partial y}\left[\left(\frac{\partial h}{\partial x} - \frac{\tan\iota}{\epsilon}\right)^2 + \left(\frac{\partial h}{\partial y}\right)^2\right]^{(\chi-1)/2}, \tag{177}$$

so that (162) becomes

$$\frac{\partial h}{\partial t} + \nabla_s \cdot \left\{F(h)\left|\frac{\tan\iota}{\epsilon}\boldsymbol{i} - \nabla_s h\right|^{\chi-1}\left(\frac{\tan\iota}{\epsilon}\boldsymbol{i} - \nabla_s h\right)\right\} = 0. \tag{178}$$

Now let us make the further assumption that the flow depends only on the x coordinate. Then $\dfrac{\partial h}{\partial y} = 0$ (so that $v = 0$) and (178) reduces to

$$\frac{\partial h}{\partial t} + \frac{\partial}{\partial x}\left\{F(h)\left|\frac{\tan\iota}{\epsilon} - \frac{\partial h}{\partial x}\right|^{\chi-1}\left(\frac{\tan\iota}{\epsilon} - \frac{\partial h}{\partial x}\right)\right\} = 0. \tag{179}$$

To find traveling wave solutions we assume that h depends on the single variable $s \equiv x - ct$, where c is a constant which represents the wave speed. Since in what follows we shall assume that the inclined plane is infinite and limit our analysis to waves propagating downwards, we take $c > 0$. We refer the interested reader to [41] for a more detailed study of downslope and upslope traveling wave solutions. Inserting the ansatz $h = h(s)$ into (179) and integrating once, one obtains

$$\left|\frac{\tan\iota}{\epsilon} - \frac{\mathrm{d}h}{\mathrm{d}s}\right|^{\chi-1}\left(\frac{\tan\iota}{\epsilon} - \frac{\mathrm{d}h}{\mathrm{d}s}\right) = \frac{c_1 + ch}{F(h)}, \tag{180}$$

c_1 being an integration constant. Let $c_1 = 0$ in (180). Then, (180) may be written as

$$\frac{\mathrm{d}h}{\mathrm{d}s} = \frac{\tan\iota}{\epsilon} - \left[\frac{ch}{F(h)}\right]^{1/\chi}. \tag{181}$$

In order to discuss the integrability of Eq. (181) with $c > 0$, we have to find the positive roots of the following equation

$$\left(\frac{\tan\iota}{\epsilon}\right)^{\chi} F(h) - ch = 0. \tag{182}$$

The roots of (182) may be found numerically. Nevertheless, we can deduce the number of positive roots of (182) by studying the function $\mathscr{F}(h) \equiv (\tan\iota/\epsilon)^{\chi} F(h)/h$. $\mathscr{F}$ is a continuous differentiable function that tends to zero as $h \to 0$, whose derivative may be written as

$$\begin{aligned}\mathscr{F}'(h) &= \left(\frac{\tan\iota}{\epsilon}\right)^{\chi} \frac{1}{h^2}\int_0^h \xi F''(\xi)\mathrm{d}\xi \\ &= 2^{(1-\chi)/2}\left(\frac{\tan\iota}{\epsilon}\right)^{\chi} \frac{1}{h^2}\int_0^h \left(\frac{\xi}{\varsigma(\xi)}\right)^{\chi+1} \left[(\chi+1)\varsigma(\xi) - \chi\xi\varsigma'(\xi)\right]\mathrm{d}\xi.\end{aligned} \tag{183}$$

From (183) it follows that $\mathscr{F}'$ is positive in a neighbourhood of $h = 0$, but it might change sign away from zero if (169) admits positive roots. Here, for the sake of simplicity, we shall limit our analysis to the constitutive functions for which (169) admits at most one positive root. It is easy to recognize that models (152) and (153) meet this requirement.

We are now able to say how many positive roots (182) admits. In fact:

1. if $[\varsigma(h)/h]^{\chi}$ has linear growth as $h \to +\infty$, then $\mathscr{F}$ is increasing and tends to $l > 0$ as $h \to +\infty$ so that (182) with $c \in]0, l[$ admits only one positive root, whereas it does not admit a positive root for $c \geq l$;
2. if $[\varsigma(h)/h]^{\chi}$ has sublinear growth as $h \to +\infty$, then $\mathscr{F}$ is increasing and tends to $+\infty$ as $h \to +\infty$ so that, for any $c > 0$, (182) admits a unique positive root;
3. if $[\varsigma(h)/h]^{\chi}$ has superlinear growth as $h \to +\infty$, then $\mathscr{F}$ attains its absolute maximum at $h = h_* > 0$ and tends to zero as $h \to +\infty$ so that (182) admits two positive roots if $c \in]0, \mathscr{F}(h_*)[$, only one positive root if $c = \mathscr{F}(h_*)$, and no positive root for $c > \mathscr{F}(h_*)$.

According to the number of positive roots of (182), one, two or three families of solutions to (180) may arise.

If (182) does not admit a positive root, then Eq. (180) may be numerically integrated over the range $(0, \bar{h})$ for all $\bar{h} > 0$. In this case the general solution is a decreasing function defined over the interval $(-\infty, c_2)$, c_2 being an integration constant and tends to $+\infty$ as $s \to -\infty$. Therefore, we do not consider these solutions as they do not satisfy the lubrication approximation.

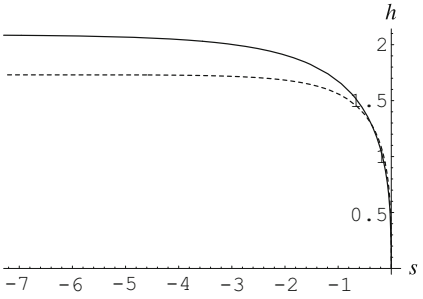

Fig. 5 Profiles of downslope traveling waves behind a front. The solid line represents the traveling wave solution when $\chi = 1.5$ and $\varsigma(p) = 1 + 0.2p$, whereas the dashed line represents the traveling wave solution in the classical Newtonian case. We have considered $(\tan \iota)/\epsilon = 1$ and $c = 1$

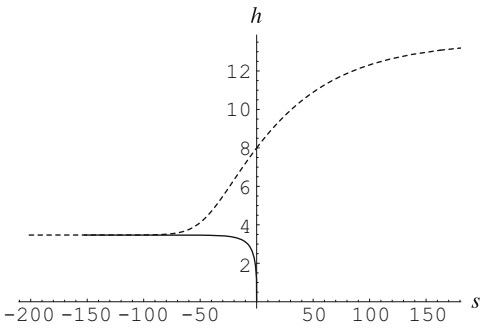

Fig. 6 Profiles of downslope traveling waves solutions for $\chi = 1.1$, $\varsigma(p) = 1 + 0.05p^3$, $\tan \iota/\epsilon = 0.5$ and $c = 1$. In the case we are considering two families of downslope traveling wave solutions that satisfy the lubrication approximation arise (see the text): downslope traveling waves behind a front (solid line) and compressive shock waves (dashed line)

If (182) admits only one positive root h_m, then two families of solutions to (180) arise. The first is formed by bounded decreasing functions defined over the range $(-\infty, c_2)$ satisfying the inequality $0 \leq h \leq h_m$. For these solutions we have $h \to h_m$ as $s \to -\infty$. Then they represent traveling waves behind a front running downslope that, far behind the front ($s \to -\infty$), tend to the steady downslope flow $h = h_m$ (see Fig. 5). The other family is formed by increasing functions bounded from below for which $h \geq h_m$. These solutions represents downslope traveling waves with no front for which $h \to h_m$ as $s \to -\infty$ and $h \to +\infty$ as $s \to +\infty$. Therefore, they do not satisfy the lubrication approximation.

If (182) admits two positive roots, $h_m < h_M$, then, as well as the downslope traveling waves behind a front, two other families of solutions to (180) arise, representing downslope traveling waves with no front (Fig. 6). The former is constituted by bounded increasing functions satisfying the inequality $h_m \leq h \leq h_M$ and for which we have $h \to h_m$ as $s \to -\infty$ and $h \to h_M$ as $s \to +\infty$. The

latter is formed by decreasing functions that are bounded from below as they satisfy the inequality $h \geq h_M$ and for which we have $h \to +\infty$ as $s \to -\infty$ and $h \to h_M$ as $s \to +\infty$. We disregard the traveling wave solutions belonging to this family as the length-scale ratio fails to be small as $s \to -\infty$. On the contrary, the former class of downslope travelling waves with no front satisfies the lubrication approximation. Furthermore, as shown by Rajagopal et al. [41], the waves belonging to this family are compressive shock waves which can also be viewed as heteroclinic orbits connecting the two equilibria $h = h_m$ and $h = h_M$ of (181) (see Fig. 6).

We finally observe that

$$F(h) \simeq 2^{(\chi-1)/2} \frac{h^{\chi+2}}{\chi+2} \quad \text{as} \quad h \to 0. \tag{184}$$

Therefore near the wave front, where the effects of pressure can be neglected, the solution to Eq. (180) is approximated by that found by Perazzo and Gratton [34], namely

$$\begin{aligned} &\frac{\tan\iota}{\epsilon}(s - c_2) \\ &= h\left\{1 - {}_2F_1\left[\frac{\chi}{\chi+1}, 1, \frac{2\chi+1}{\chi+1}, \frac{\tan\iota}{\epsilon}\left(\frac{c(\chi+2)}{2^{(1-\chi)/2}}\right)^{-1/\chi} h^{1+1/\chi}\right]\right\}, \end{aligned} \tag{185}$$

with ${}_2F_1(a, b, c, d)$ being the hypergeometric function. From (185) we deduce that h' tends to infinity as $s \to c_2$. Hence, near the wave front, the component of the fluid velocity normal to the incline is not small with respect to the parallel component and thus the solution does not satisfy the lubrication approximation.

References

1. Ancey, C.: Plasticity and geophysical flows: a review. J. Non-Newtonian Fluid Mech. **142**, 4–35 (2007)
2. Andrade, E.N., Da, C.: The viscosity of liquids. Nature **125**, 309–310 (1930)
3. Bair S., Khonsari M., Winer W.O.: High pressure rheology of lubricants and limitations of the Reynolds equation. Tribol. Int. **31**, 573–586 (1998)
4. Bair S., Kottke P.: Pressure-viscosity relationship for elastohydrodynamics. Tribol. Trans. **46**, 289–295 (2003)
5. Ball, J.M., James, R.D.: The scientific life and influence of Clifford Ambrose Truesdell III. Arch. Ration. Mech. Anal. **161**, 1–26 (2002)
6. Barus C.: Isotherms, isopiestics and isometrics relative to viscosity. Am. J. Sci. **45**, 87–96 (1893)
7. Bénard H.: Les tourbillons cellulaires dans une nappe liquide, Revue Gén. Sci. pures et Appl. **11**, 1261–1271 and 1309–1328 (1900)

8. Bodenschatz, E., Pesch, W., Ahlers G.: Recent developements in Rayleigh-Bénard convection. Annu. Rev. Fluid Mech. **32**, 708–778 (2000)
9. Boussinesq, J.: Théorie Analytique de la Chaleur. Gauthier-Villars, Paris (1903)
10. Bridgman, P.W.: The effect of pressure on the viscosity of forty-three pure liquids. Proc. Am. Acad. Arts Sci. **61**, 57–99 (1926)
11. Bridgman, P.W.: The physics of high pressure. G. Bell and Sons, London (1931)
12. Busse, F.: Non-linear properties of thermal convection. Rep. Prog. Phys. **41**, 1929–1967 (1978)
13. Chandrasekhar, S.: Hydrodynamic and Hydromagnetic Stability. Clarendon Press, Oxford (1961)
14. Cross, M.C., Hahenberg, P.C.: Pattern formation outside of equilibrium. Rev. Mod. Phys. **65**, 851–1112 (1993)
15. Fermi, E.: Thermodynamics. Dover Publications, New York (1956).
16. Gouin, H., Muracchini, A., Ruggeri, T.: On the Müller paradox for thermal-incompressible media. Contin. Mech. Thermodyn. **24**, 505–513 (2012)
17. Govindarajan, R., Chandra Sahu, K.: Instabilities in viscosity-stratified flow. Annu. Rev. Fluid Mech. **46**, 331–353 (2014)
18. Hadamard, J.: Sur les problèmes aux dérivées partielles et leur signification physique. Princeton Univ. Bull. **13**, 49–52 (1902)
19. Hron, J., Malek, J., Rajagopal, K.R.: Simple flows of fluids with pressure-dependent viscosities. Proc. R. Soc. Lond. Ser. A **257**, 1603–1622 (2001)
20. Huilgol, R.R.: On the definition of pressure in rheology. Rheol. Bull. **78**(2), 12, 14–15 and 29 (2009)
21. Huppert, H.E.: Flow and instability of a viscous current down a slope. Nature **300**, 427–429 (1982)
22. Jones, S.J., Chew H.A.M.: Creep of Ice as a Function of Hydrostatic pressure. J. Phys. Chem. **87**, 4064–4066 (1983)
23. Koschmieder, E.L.: Bénard Cells and Taylor Vortices. Cambridge University Press, Cambridge (1993)
24. Man, C.S., Sun, Q.X.: On the significance of normal stresses effects in the flow of glaciers. J. Glaciol. **33**, 268–273 (1987)
25. Manneville, P.: Rayleigh-Bénard convection: thirty years of experimental, theoretical and modelling work. In: Mutabazi, I., Wesfried, J.E., Gunyon (eds.) Dynamics of Spatio-Temporal Cellular Structures. Springer Tracts in Modern Physics, vol. 207. Springer, Berlin (2006)
26. Martín-Alfonso, M.J., Martínez-Boza, F.J., Navarro, F.J., Fernández, M., Gallegos, C.: Pressure-temperature-viscosity relationship for heavy petroleum fractions. Fuel **86**, 227–233 (2007)
27. McTigue, D.F., Passman, S.L., Jones, S.J.: Normal stress effect in the creep of ice. J. Glaciol. **31**, 120–126 (1985)
28. Melamed, Y., Lin, M.: Principle of Sufficient Reason. The Stanford Encyclopedia of Philosophy (Spring 2017 edn.) Zalta, E.N. (ed.) https://plato.stanford.edu/archives/spr2017/entries/sufficient-reason
29. Müller, I.: Thermodynamics. Pitman, London (1985)
30. Newell, A.C., Passot, T., Lega, J.: Order parameter equations for patterns. Annu. Rev. Fluid Mech. **25**, 399–453 (1993)
31. Oberbeck, A.: Über die Wärmleitung der Flüssigkeiten bei Berücksichtigung der Strömungen infolge von Temperaturdifferenzen. Ann. Phys. Chem. **7**, 271–292 (1879)
32. Oberbeck, A.: Über die Bewegungsercheinungen der Atmosphäre. Sitz. Ber. K. Preuss. Akad. Miss. 383–395 and 1120–1138 (1888)
33. Paterson, W.S.B.: The Physics of Glaciers, 3rd edn. Pergamon, Trowbridge (1994)
34. Perazzo, C.A., Gratton, J.: Thin film of non-Newtonian fluid on an incline. Phys. Rev. E **67**, 016307 (2003)
35. Rajagopal, K.R.: On implicit constitutive theories. J. Fluid Mech. **550**, 243–249 (2006)
36. Rajagopal, K.R.: Remarks on the notion of pressure. Int. J. Non Linear Mech. **71**, 165–172 (2015)

37. Rajagopal, K.R., Saccomandi, G.: A Novel approach to the description of constitutive relations. Front. Mater. **3**, id.36 (2016)
38. Rajagopal, K.R., Saccomandi, G., Vergori, L.: Stability analysis of the Rayleigh-Bénard convection for a fluid with temperature and pressure dependent viscosity. Z. Angew. Math. Phys. **60**, 739–755 (2009)
39. Rajagopal, K.R., Saccomandi, G., Vergori, L.: On the Oberbeck-Boussinesq approximation in fluids with pressure-dependent viscosities. Nonlinear Anal. Real World Appl. **10**, 1139–1150 (2009)
40. Rajagopal, K.R., Saccomandi, G., Vergori, L.: Couette flow with frictional heating in a fluid with temperature and pressure dependent viscosity. Int. J. Heat Mass Transf. **54**, 783–789 (2011)
41. Rajagopal, K.R., Saccomandi, G., Vergori, L.: Flow of fluids with pressure- and shear-dependent viscosity down an inclined plane. J. Fluid Mech. **706**, 173–189 (2012)
42. Rajagopal, K.R., Saccomandi, G., Vergori, L.: On the approximation of isochoric motions of fluids under different flow conditions. Proc. R. Soc. Lond. Ser. A **471**(2180), 20150159 (2015)
43. Rayleigh, L.: On convective currents in a horizontal layer of fluid when the higher temperature is on the under side. Philos. Mag. **32**, 529–546 (1916)
44. Renardy, M.: Parallel shear flows of fluids with a pressure-dependent viscosity. J. Non-Newtonian Fluid Mech. **114**, 229–236 (2003)
45. Rionero, S.: Metodi variazionali per la stabilitàăasintotica in media in magnetoidrodinamica. Ann. Mate. Pura Appl. **78**, 339–364 (1968)
46. Saal, R.N.J., Koens G.: Investigations into plastic properties of asphaltic bitumen. Physics **7**, 408–412 (1933)
47. Schoof, C., R.C.A. Hindmarsh, R.C.A.: Thin-film flows with wall slip: an asymptotic analysis of higher order glacier flow models. Q. J. Mech. Appl. Math. **63**, 73–114 (2010)
48. Spencer, A.J.M.: Theory of invariants. Continuum Physics Eringen, A.C. vol. 1, pt. 3. Academic, New York and London (1971)
49. Stokes, G.G.: On the theories of the internal friction of fluids in motion, and motion of elastic solids. Trans. Camb. Philos. Soc. **8**, 287–305 (1845)
50. Straughan, B.: The Energy Method, Stability and Nonlinear Convection. Series in Applied Mathematical Science, vol. 91. Springer, New York (1992)
51. Szeri, A.Z.: Fluid Film Lubrication: Theory and Design. Cambridge University Press, Cambridge (1998)
52. Truesdell, C., Noll, W.: The Non-Linear Field Theories of Mechanics. Springer, Berlin (2004)
53. Vergori, L.: Flows at small Reynolds and Froude numbers. Int. J. Eng. Sci. **48**, 1659–1670 (2010)
54. Zonta, F., Soldati, A.: Effect of temperature dependent fluid properties on heat transfer in turbulent mixed convection. J. Heat Transfer-Trans. ASME **136**, 022501 (2014)
55. Zonta, F., Marchioli, C., Soldati, A.: Modulation of turbulence in forced convection by temperature-dependent viscosity. J. Fluid Mech. **697**, 150–174 (2012)
56. Zonta, F., Onorato, M., Soldati, A.: Turbulence and internal waves in stably-stratified channel flow with temperature-dependent fluid properties. J. Fluid Mech. **697**, 175–203 (2012)

Lectures on Hyperbolic Equations and Their Numerical Approximation

Eleuterio F. Toro

Abstract These introductory lecture notes on numerical methods for hyperbolic equations are suitable for advanced undergraduate and postgraduate students in mathematics and engineering disciplines. More advanced approaches exist and will be indicated as appropriate. The material is divided into four sections. Section 1 presents an overview of hyperbolic equations and also some basic concepts on numerical discretization techniques. Section 2 deals with a specific example, the system of non-linear shallow water equations; the equations are analysed and the Riemann problem is solved exactly in complete detail. In Sect. 3 we first present the Godunov method as applied to a generic hyperbolic system and then specialised to the shallow water system in one space dimension; approximate solution methods for the Riemann problem are also given. Finally, Sect. 4 gives a brief overview of the ADER approach to construct high-order numerical methods for hyperbolic equations, based on the first order Godunov method. Much of the material of these lectures has been taken from the author's text books (Toro, Riemann solvers and numerical methods for fluid dynamics. A practical introduction, 3rd edn. Springer, Berlin (2009) and Toro, Shock-capturing methods for free-surface shallow flows. Wiley, Chichester (2001)), where further reading material can be found. I also recommend the textbook by Godlewski and Raviart (Numerical approximation of hyperbolic systems of conservation laws. Springer, New York (1996)) and that by LeVeque (Finite volume methods for hyperbolic problems. Cambridge University Press, Cambridge (2002)).

E. F. Toro (✉)
University of Trento, Trento, Italy
e-mail: eleuterio.toro@unitn.it

A. Farina et al. (eds.), *Non-Newtonian Fluid Mechanics and Complex Flows*,
Lecture Notes in Mathematics 2212, https://doi.org/10.1007/978-3-319-74796-5_3

1 Hyperbolic Equations

Many problems in science and engineering (e.g. wave propagation and transport phenomena) are governed by advection-diffusion-reaction partial differential equations (PDEs). In the scalar case (a single equation) we may write

$$\partial_t q(x,t) + \partial_x f(q(x,t)) = s(x,t,q(x,t)) + \partial_x(\alpha(x,t,q(x,t))\partial_x q(x,t)) \ , \tag{1}$$

where $q(x,t)$ is the *unknown*, called the *dependent variable*; $q(x,t)$ is a function of two *independent variables* x and t; $f(q)$ is a prescribed function of q called the *flux*, or *physical flux*; $s(x,t,q)$ is also a prescribed function, called the *source term*. The last term is called the diffusion term; $\alpha(x,t,q(x,t))$ is the *diffusion coefficient*. Equation (1) is parabolic due to the presence of the viscous term, a second-order term. In the rest of these lectures we shall be concerned exclusively with hyperbolic equations.

1.1 The Linear Advection Equation and Basic Concepts

A particular example of (1) is obtained by choosing

$$f(q) = \lambda q \ , \quad s(q) = 0 \ , \quad \alpha = 0 \ , \tag{2}$$

with λ a constant wave propagation speed, which leads to the *linear advection equation* (LAE)

$$\partial_t q + \lambda \partial_x q = 0 \ , \quad -\infty < x < \infty \ , \quad t > 0 \ . \tag{3}$$

Initial Value Problem (IVP) for the Linear Advection Equation We study the simplest case of (1), the linear advection equation, in which the spatial domain is infinite and an initial condition at the initial time $t = 0$ is prescribed, namely

$$\left.\begin{array}{ll} \text{PDE:} & \partial_t q + \lambda \partial_x q = 0 \ , \quad -\infty < x < \infty \ , \quad t > 0 \ , \\ \text{IC:} & q(x,0) = h(x) \ , \quad -\infty < x < \infty \ , \end{array}\right\} \tag{4}$$

where $h(x)$ is a prescribed function of distance x. Equation (4) defines a pure *initial-value problem* or *Cauchy problem*.

Characteristic Curves and the Solution *Characteristic curves*, or *characteristics*, are functions $x(t)$ in the x-t half-plane of independent variables satisfying the IVP

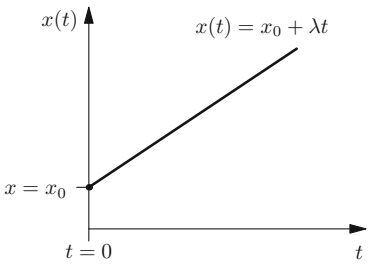

Fig. 1 Characteristic $x(t)$ in the t-x plane given by (6); x_0: foot of characteristic; positive characteristic speed λ

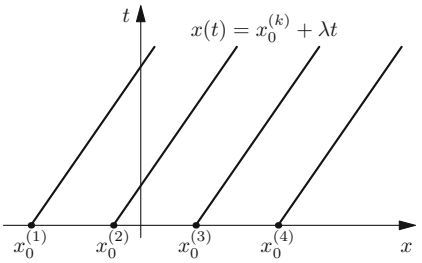

Fig. 2 Family of characteristic curves $x(t)$ in the x-t plane, for the case of positive characteristic speed λ. Compare with Fig. 1

for an ordinary differential equation (ODE), namely

$$\left.\begin{array}{ll} \text{ODE:} & \dfrac{dx}{dt} = \lambda \ , \quad t > 0 \ , \\ \text{IC:} & x(0) = x_0 \ , \end{array}\right\} \tag{5}$$

whose solution is immediate and reads

$$x = x_0 + \lambda t \ . \tag{6}$$

Figure 1 illustrates solution (6). In practice it is more common to represent characteristics in the x-t plane. The inclination of the characteristics depends on the characteristic speed λ, in fact on $1/\lambda$. In the linear case with constant coefficients, characteristics are all parallel to each other, as seen in Fig. 2.

Consider now the time-rate of change (or total derivative) of $q(x(t), t)$ along a characteristic curve $x = x(t)$

$$\frac{dq}{dt} = \frac{\partial q}{\partial t}\frac{dt}{dt} + \frac{\partial q}{\partial x}\frac{dx}{dt} \ . \tag{7}$$

But the curve $x(t)$ satisfies the ODE in (5). Then (7) becomes

$$\frac{dq}{dt} = \partial_t q + \lambda \partial_x q = 0 \ . \tag{8}$$

That is, $q(x,t)$ is constant along $x = x_0 + \lambda t$. Consequently, the PDE in (4) becomes an ODE, namely

$$\frac{dq}{dt} = 0 \ \text{ along the characteristic } x = x_0 + \lambda t \ .$$

This ODE states that $q(x,t)$ is constant along the characteristic. From the above observations, the value of $q(x,t)$ at a point (x,t) on the characteristic curve passing through (x,t) is equal to the value of q at the point x_0 called *the foot of the characteristic*. That is

$$q(x,t) = q(x_0,0) = h(x_0) \ . \tag{9}$$

But from (6)

$$x_0 = x - \lambda t$$

and therefore the solution of IVP (4) is

$$q(x,t) = h(x - \lambda t) \ , \tag{10}$$

which is the initial condition h in (4) evaluated at the position $x - \lambda t$. Figure 3 shows the three possible cases that can occur due to the value of the characteristic speed.

IVP Example Here we study in detail the following IVP

$$\begin{array}{l} \text{PDE: } \partial_t q + \lambda \partial_x q = 0 \ , \quad -\infty < x < \infty \ , \quad t > 0 \ , \\ \text{IC: } \quad q(x,0) = h(x) = \left\{ \begin{array}{ccc} 0 & \text{if} & x < -1 \ , \\ 1 - x^2 & \text{if} & -1 \le x \le 1 \ , \\ 0 & \text{if} & x > 1 \ . \end{array} \right. \end{array} \tag{11}$$

Solution According to formula (10) the solution of (11) is

$$q(x,t) = h(x - \lambda t) = \left\{ \begin{array}{ccc} 0 & \text{if} & x < -1 + \lambda t \ , \\ 1 - (x - \lambda t)^2 & \text{if} & -1 + \lambda t \le x \le 1 + \lambda t \ , \\ 0 & \text{if} & x > 1 + \lambda t \ . \end{array} \right. \tag{12}$$

Note that for a given speed λ and a chosen time t, the solution is simply a function of x, called a profile. See Fig. 4.

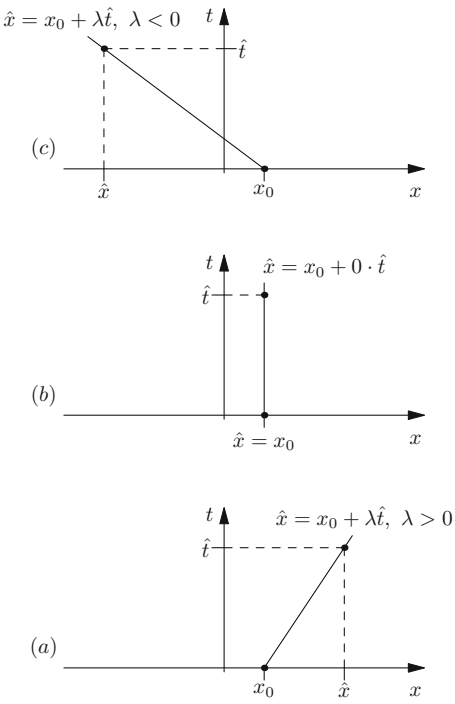

Fig. 3 The solution at point $(\hat{x}, \hat{t})$ is found by tracing the characteristic from $(\hat{x}, \hat{t})$ back to its foot x_0. There are three possibilities: (**a**) $\lambda > 0$, (**b**) $\lambda = 0$, (**c**) $\lambda < 0$

The Riemann Problem Riemann problem for the linear advection equation is the special IVP

$$\left.\begin{array}{l} \text{PDE: } \partial_t q + \lambda \partial_x q = 0\ , \quad -\infty < x < \infty\ , \quad t > 0\ , \\ \text{IC:} \quad q(x,0) = h(x) = \left\{ \begin{array}{l} q_L \text{ (constant) if } x < 0\ , \\ q_R \text{ (constant) if } x > 0\ , \end{array} \right. \end{array} \right\} \tag{13}$$

where q_L (left of 0) and q_R (right of 0) are constants.

Solution of the Riemann Problem From (10) it is obvious that the solution is

$$q(x,t) = h(x - \lambda t) = \left\{ \begin{array}{l} q_L \text{ if } x - \lambda t < 0 \leftrightarrow \frac{x}{t} < \lambda\ , \\ q_R \text{ if } x - \lambda t > 0 \leftrightarrow \frac{x}{t} > \lambda\ . \end{array} \right. \tag{14}$$

See Fig. 5.

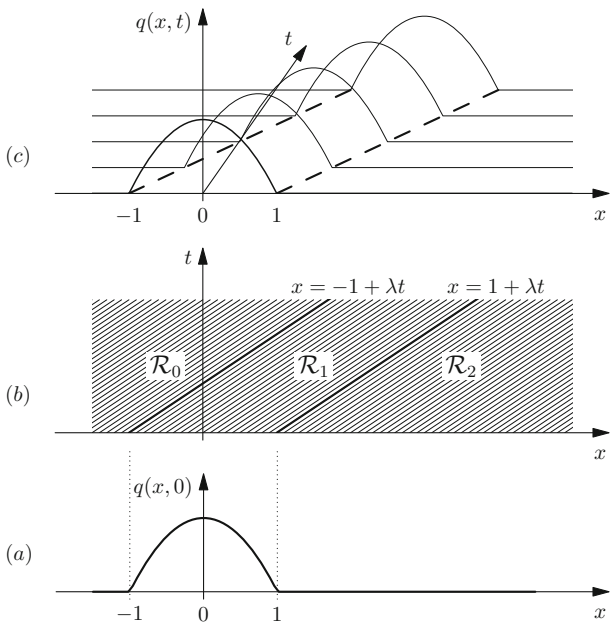

Fig. 4 Solution (12) of initial value problem (11). Frame (**a**) displays the initial condition $q(x, 0)$; frame (**b**) displays picture of characteristics in x-t space and frame (**c**) shows solution profiles $q(x, t_k)$ at different times t_k

1.2 Linear Systems

We now consider a general one-dimensional, time-dependent system of m linear hyperbolic equations with source terms, namely

$$\partial_t \mathbf{Q}(x,t) + \mathbf{A}\partial_x \mathbf{Q}(x,t) = \mathbf{S}(\mathbf{Q}(x,t)) \ . \tag{15}$$

Here $\mathbf{Q}$: unknowns, $\mathbf{A}$: matrix of coefficients (constant) and $\mathbf{S}(\mathbf{Q})$: source terms. These are given as follows

$$\mathbf{Q} = \begin{bmatrix} q_1 \\ \dots \\ q_i \\ \dots \\ q_m \end{bmatrix} \ , \quad \mathbf{A} = \begin{bmatrix} a_{11} & \dots & a_{1i} & \dots & a_{1m} \\ \dots & \dots & \dots & \dots & \dots \\ a_{i1} & \dots & a_{ii} & \dots & a_{im} \\ \dots & \dots & \dots & \dots & \dots \\ a_{m1} & \dots & a_{mi} & \dots & a_{mm} \end{bmatrix} \ , \quad \mathbf{S}(\mathbf{Q}) = \begin{bmatrix} s_1 \\ \dots \\ s_i \\ \dots \\ s_m \end{bmatrix} \ . \tag{16}$$

Note that the linear advection equation (3) is a special case of (15).

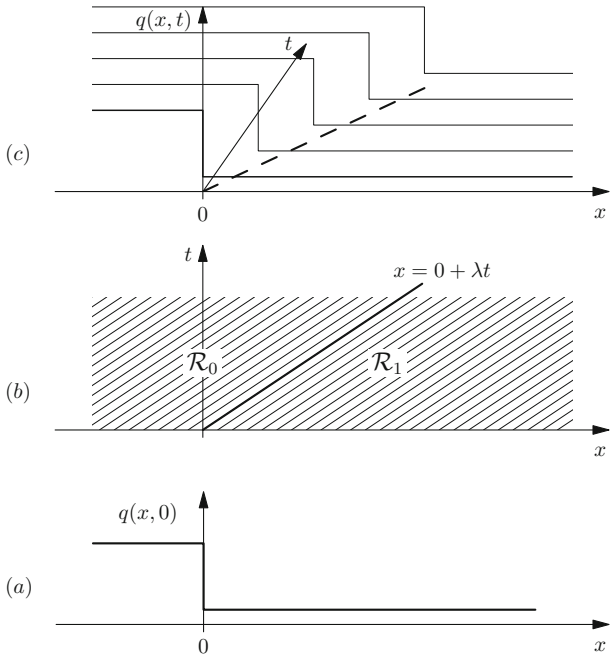

Fig. 5 Solution of Riemann problem (13). Frame (**a**) displays piece-wise constant initial condition $q(x, 0)$. Frame (**b**) displays picture of characteristics in x-t space. Frame (**c**) shows solution profiles $q(x, t_k)$ at different times t_k

Eigenvalues and Eigenvectors The **eigenvalues** of system (15) are the roots of the *characteristic polynomial*

$$P(\hat{\lambda}) \equiv Det(\mathbf{A} - \hat{\lambda}\mathbf{I}) = 0 \,. \tag{17}$$

Here $\mathbf{I}$: $m \times m$ unit matrix; $\hat{\lambda}$: a parameter; λ_i: eigenvalues, that is roots of (17), which if real numbers, are conventionally written in increasing order

$$\lambda_1 \leq \lambda_2 \leq \ldots \leq \lambda_i \leq \ldots \leq \lambda_{m-1} \leq \lambda_m \,. \tag{18}$$

A right eigenvector $\mathbf{R}_i$ of $\mathbf{A}$ corresponding to λ_i is column vector

$$\mathbf{R}_i = [r_{1i}\,, r_{2i}\,, \ldots\,, r_{ii}\,, \ldots\,, r_{mi}]^T\,, \tag{19}$$

such that

$$\mathbf{A}\mathbf{R}_i = \lambda_i \mathbf{R}_i \,. \tag{20}$$

The full set of m right eigenvectors corresponding to the eigenvalues (18) are

$$\mathbf{R}_1 \, , \mathbf{R}_2 \, , \ldots \, , \mathbf{R}_i \, , \ldots \, , \mathbf{R}_{m-1} \, , \mathbf{R}_m \, . \tag{21}$$

A left eigenvector $\mathbf{L}_i$ of $\mathbf{A}$ corresponding to λ_i is the row vector

$$\mathbf{L}_i = [l_{i1} \, , l_{i2} \, , \ldots \, , l_{ii} \, , \ldots \, , l_{im}] \, , \tag{22}$$

such that

$$\mathbf{L}_i \mathbf{A} = \lambda_i \mathbf{L}_i \, . \tag{23}$$

The m eigenvalues (18) generate corresponding m left eigenvectors

$$\mathbf{L}_1 \, , \mathbf{L}_2 \, , \ldots \, , \mathbf{L}_i \, , \ldots \, , \mathbf{L}_{m-1} \, , \mathbf{L}_m \, . \tag{24}$$

Hyperbolic System A system (15) is said to be hyperbolic if $\mathbf{A}$ has m real eigenvalues and a corresponding complete set of m linearly independent eigenvectors.

Note that for hyperbolicity, the eigenvalues are not required to be all distinct. What is important is that there is a *complete set of linearly independent eigenvectors, corresponding to the real eigenvalues*.

Strictly Hyperbolic System A hyperbolic system is said to be *strictly hyperbolic* if all eigenvalues of the system are distinct.

Weakly Hyperbolic System A system may have real but not distinct eigenvalues and still be hyperbolic if a *complete set* of linearly independent eigenvectors exists. However if all eigenvalues are real but no complete set of linearly independent eigenvectors exists then the system is called *weakly hyperbolic*, not to be mistaken with *non-strictly hyperbolic*.

Orthonormality of Eigenvectors The eigenvectors $\mathbf{L}_i$ and $\mathbf{R}_j$ are *orthonormal* if

$$\mathbf{L}_i \bullet \mathbf{R}_j = \begin{cases} 1 & \text{if } \; i = j \, , \\ 0 & \text{if } \; i \neq j \, . \end{cases} \tag{25}$$

Diagonalization and Characteristic Variables Consider $\mathbf{R} = [\mathbf{R}_1 \, , \ldots \, , \mathbf{R}_i \, , \ldots \, , \mathbf{R}_m]$: matrix whose columns are the right eigenvectors; Λ: diagonal matrix formed by eigenvalues. In full

$$\mathbf{R} = \begin{bmatrix} r_{11} & \ldots & r_{1i} & \ldots & r_{1m} \\ \ldots & \ldots & \ldots & \ldots & \ldots \\ r_{i1} & \ldots & r_{ii} & \ldots & r_{im} \\ \ldots & \ldots & \ldots & \ldots & \ldots \\ r_{m1} & \ldots & r_{mi} & \ldots & r_{mm} \end{bmatrix} \, , \quad \Lambda = \begin{bmatrix} \lambda_1 & \ldots & 0 & \ldots & 0 \\ \ldots & \ldots & \ldots & \ldots & \ldots \\ 0 & \ldots & \lambda_i & \ldots & 0 \\ \ldots & \ldots & \ldots & \ldots & \ldots \\ 0 & \ldots & 0 & \ldots & \lambda_m \end{bmatrix} \, . \tag{26}$$

Proposition *If* $\mathbf{A}$ *is the coefficient matrix of a hyperbolic system (15) then*

$$\mathbf{A} = \mathbf{R}\Lambda\mathbf{R}^{-1} \text{ or } \Lambda = \mathbf{R}^{-1}\mathbf{A}\mathbf{R} \,. \tag{27}$$

In this case $\mathbf{A}$ is said to be *diagonalisable* and consequently system (15) is said to be *diagonalisable*. The proof is left as an exercise.

Characteristic Variables The existence of $\mathbf{R}^{-1}$ makes it possible to define the *characteristic variables* $\mathbf{C} = [c_1, c_2, \ldots, c_m]^T$ via

$$\mathbf{C} = \mathbf{R}^{-1}\mathbf{Q} \quad \leftrightarrow \quad \mathbf{Q} = \mathbf{R}\mathbf{C} \,. \tag{28}$$

Calculating the partial derivatives, recalling that the coefficient matrix is constant, we have

$$\partial_t\mathbf{Q} = \mathbf{R}\partial_t\mathbf{C} \,, \quad \partial_x\mathbf{Q} = \mathbf{R}\partial_x\mathbf{C}$$

and direct substitution of the these expressions into Eq. (15) gives

$$\mathbf{R}\partial_t\mathbf{C} + \mathbf{A}\mathbf{R}\partial_x\mathbf{C} = \mathbf{S} \,.$$

Multiplication of this equation from the left by $\mathbf{R}^{-1}$ and use of (27) gives

$$\partial_t\mathbf{C} + \Lambda\partial_x\mathbf{C} = \hat{\mathbf{S}} \,, \quad \hat{\mathbf{S}} = \mathbf{R}^{-1}\mathbf{S} \,. \tag{29}$$

This is called the *canonical form* or *characteristic form* of system (15). Assuming $\hat{\mathbf{S}} = \mathbf{0}$ and writing the equations in full, we have

$$\partial_t \begin{bmatrix} c_1 \\ \ldots \\ c_i \\ \ldots \\ c_m \end{bmatrix} + \begin{bmatrix} \lambda_1 & \ldots & 0 & \ldots & 0 \\ \ldots & \ldots & \ldots & \ldots & \ldots \\ 0 & \ldots & \lambda_i & \ldots & 0 \\ \ldots & \ldots & \ldots & \ldots & \ldots \\ 0 & \ldots & 0 & \ldots & \lambda_m \end{bmatrix} \partial_x \begin{bmatrix} c_1 \\ \ldots \\ c_i \\ \ldots \\ c_m \end{bmatrix} = \begin{bmatrix} 0 \\ \ldots \\ 0 \\ \ldots \\ 0 \end{bmatrix} \,. \tag{30}$$

Clearly, each equation i-th of this system is of the form

$$\partial_t c_i + \lambda_i\partial_x c_i = 0 \,, \quad i = 1, \ldots, m \tag{31}$$

and involves the *single unknown* $c_i(x, t)$, which is decoupled from the remaining variables. Moreover, this equations is identical to the linear advection equation (3), with characteristic speed λ_i.

We have m decoupled equations, each one defining a characteristic curve. Thus, at any chosen point $(\hat{x}, \hat{t})$ in the x-t half-plane there are m characteristic curves $x_i(t)$

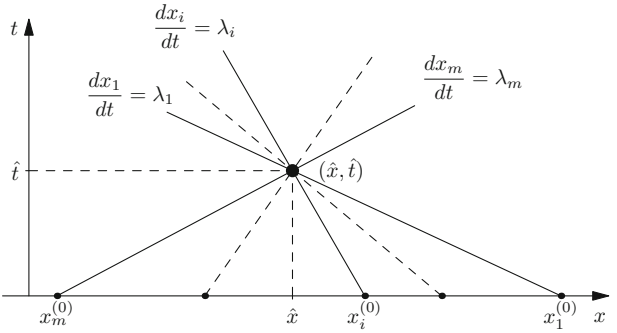

Fig. 6 The solution at a point $(\hat{x}, \hat{t})$ depends on the initial condition at the foot $x_i^{(0)}$ of each characteristic $x_i(t) = x_i^{(0)} + \lambda_i t$

passing through $(\hat{x}, \hat{t})$ and satisfying the m ODEs

$$\frac{dx_i}{dt} = \lambda_i \ , \quad \text{for } i = 1, \ldots, m \ , \tag{32}$$

as depicted in Fig. 6.

Remarks

- Each characteristic curve $x_i(t) = x_i^{(0)} + \lambda_i t$ intersects the x-axis at the point $x_i^{(0)}$, which is the *foot of the characteristic* passing through the point $(\hat{x}, \hat{t})$. The point $x_i^{(0)}$ is given as

$$x_i^{(0)} = \hat{x} - \lambda_i \hat{t} \ , \ \text{for } i = 1, 2, \ldots, m \ . \tag{33}$$

  See Fig. 6.
- Each Eq. (31) is just a linear advection equation whose solution at $(\hat{x}, \hat{t})$ is given by

$$c_i(\hat{x}, \hat{t}) = c_i^{(0)}(x_i^{(0)}) = c_i^{(0)}(\hat{x} - \lambda_i \hat{t}) \ , \ \text{for } i = 1, 2, \ldots, m \ , \tag{34}$$

  where $c_i^{(0)}(x)$ is the initial condition, at the initial time. The initial conditions for the characteristic variables are obtained from the transformation (28) applied to the initial condition $\mathbf{Q}(x, 0)$.
- Given the assumed order (18) of the distinct eigenvalues the following inequalities are satisfied.

$$x_m^{(0)} < x_{m-1}^{(0)} < \ldots < x_2^{(0)} < x_1^{(0)} \ . \tag{35}$$

Domain of Dependence The interval $[x_m^{(0)}, x_1^{(0)}]$ is called the domain of dependence of the point $(\hat{x}, \hat{t})$. See Fig. 6. The solution at $(\hat{x}, \hat{t})$ depends exclusively on initial data at points in the interval $[x_m^{(0)}, x_1^{(0)}]$. This is a distinguishing feature of hyperbolic equations. The initial data outside the domain of dependence can be changed in any manner we wish but this will not affect the solution at the point $(\hat{x}, \hat{t})$.

Proposition: The General Initial-Value Problem The solution of the general IVP for the linear homogeneous hyperbolic system

$$\left.\begin{array}{ll} \text{PDEs: } \partial_t \mathbf{Q} + \mathbf{A}\partial_x \mathbf{Q} = \mathbf{0}\ , -\infty < x < \infty\ ,\ t > 0\ , \\ \text{IC:} \quad \mathbf{Q}(x,0) = \mathbf{Q}^{(0)}(x) \end{array}\right\} \tag{36}$$

is given by

$$\mathbf{Q}(x,t) = \sum_{i=1}^{m} c_i(x,t)\mathbf{R}_i\ . \tag{37}$$

The coefficient $c_i(x,t)$ of the right eigenvector $\mathbf{R}_i$ is a characteristic variable. The proof is left as an exercise.

Remarks

1. The function $c_i(x,t)$ is the coefficient of $\mathbf{R}_i$ in an *eigenvector expansion* of the solution vector $\mathbf{Q}(x,t)$.
2. Given a point (x,t) in the x-t plane, the solution $\mathbf{Q}(x,t)$ depends only on the initial data at the m points $x_0^{(i)} = x - \lambda_i t$. See Fig. 6.
3. These points are the intersections of the characteristics of speed λ_i with the x-axis.
4. Solution (37) represents superposition of m waves of unchanged shape $c_i^{(0)}(x)\mathbf{R}_i$ propagated with speed λ_i.

Proposition: The Riemann Problem Solution The solution of Riemann problem

$$\left.\begin{array}{ll} \text{PDEs: } \partial_t \mathbf{Q} + \mathbf{A}\partial_x \mathbf{Q} = \mathbf{0}\ ,\ -\infty < x < \infty\ ,\ t > 0\ , \\ \text{IC:} \quad \mathbf{Q}(x,0) = \mathbf{Q}^{(0)}(x) = \begin{cases} \mathbf{Q}_\mathrm{L} \text{ if } x < 0\ , \\ \mathbf{Q}_\mathrm{R} \text{ if } x > 0\ , \end{cases} \end{array}\right\} \tag{38}$$

with $\mathbf{Q}_\mathrm{L}$ and $\mathbf{Q}_\mathrm{R}$ two constant vectors, is given by

$$\mathbf{Q}(x,t) = \sum_{i=1}^{I} c_{iR}\mathbf{R}_i + \sum_{i=I+1}^{m} c_{iL}\mathbf{R}_i\ , \tag{39}$$

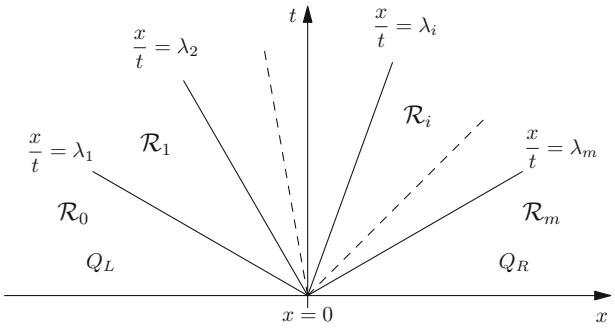

Fig. 7 Structure of the solution of the Riemann problem. There are m waves that divide the half x-t plane into $m + 1$ regions (wedges) $\mathscr{R}_i$, with $i = 0, 1, \ldots, m$

where

$$\sum_{i=1}^{m} c_{iL}\mathbf{R}_i = \mathbf{Q}_{\mathrm{L}} \ , \quad \sum_{i=1}^{m} c_{iR}\mathbf{R}_i = \mathbf{Q}_{\mathrm{R}} \tag{40}$$

and $I = I(x, t)$ is the maximum value of i for which $x - \lambda_i t > 0$. The proof is left as an exercise.

Remarks on the Solution of the Riemann Problem

1. The initial data consists of two constant vectors $\mathbf{Q}_{\mathrm{L}}$ and $\mathbf{Q}_{\mathrm{R}}$, separated by a discontinuity at $x = 0$.
2. This is a special case of IVP (36).
3. The structure of the solution of the Riemann problem (38) is depicted in Fig. 7, in the x-t plane.
4. The solution consists of a fan of m waves emanating from the origin, one wave for each eigenvalue λ_i. The speed of the wave i is the eigenvalue λ_i.
5. These m waves divide the x-t half plane into $m + 1$ constant regions

$$\mathscr{R}_i = \left\{ (x, t) / -\infty < x < \infty;\ t \geq 0;\ \lambda_i < \frac{x}{t} < \lambda_{i+1} \right\} \ , \tag{41}$$

for $i = 1, \ldots, m - 1$; $\mathscr{R}_0$ corresponds to the initial data $\mathbf{Q}_{\mathrm{L}}$ and $\mathscr{R}_m$ corresponds to the initial data $\mathbf{Q}_{\mathrm{R}}$. See Fig. 7.

Solving the Riemann problem means finding constant values for $\mathbf{Q}$ in regions $\mathscr{R}_i$ for $= 1, \ldots, m - 1$.

Corollary *The solution of the Riemann problem may be expressed as*

$$\mathbf{Q}(x, t) = \mathbf{Q}_{\mathrm{L}} + \sum_{i=1}^{I} \delta_i \mathbf{R}_i = \mathbf{Q}_{\mathrm{R}} - \sum_{i=I+1}^{m} \delta_i \mathbf{R}_i \ , \tag{42}$$

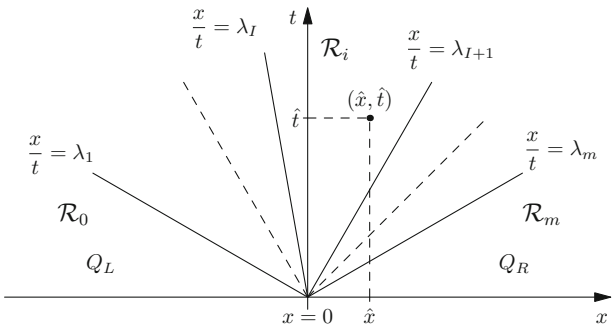

Fig. 8 The solution of the Riemann problem at a point $(\hat{x}, \hat{t})$ depends on the associated index $I = I(\hat{x}, \hat{t})$

where the coefficients $\Delta C = [\delta_1, \ldots, \delta_i, \ldots, \delta_m]^T$ *are the solution to the linear algebraic system*

$$\sum_{i=1}^{m} \delta_i \mathbf{R}_i = \Delta \mathbf{Q} \equiv \mathbf{Q}_R - \mathbf{Q}_L \, . \tag{43}$$

This form is more convenient. We only need to solve one linear system. The proof is left as an exercise. Figure 8 illustrates the solution at a point $(\hat{x}, \hat{t})$.

1.3 Non-linear Scalar Equations: Definitions and Examples

Consider the first-order PDE for the unknown function $q(x, t)$

$$\partial_t q + \partial_x f(q) = 0 \, . \tag{44}$$

This equation is called a **conservation law**, in which q is the **conserved variable**; $f(q)$ is the **flux function** or **physical flux**, a prescribed function of q. The equation is said to be written in *differential, conservative form*. One may express (44) in *quasi-linear form* as

$$\partial_t q + \lambda(q) \partial_x q = 0 \, , \qquad \lambda(q) = \frac{d}{dq} f(q) \equiv f'(q) \, . \tag{45}$$

Here $\lambda(q)$ is called **characteristic speed**.

Equations of the type (44) may be characterised by the behaviour of the flux $f(q)$ and its derivative, namely the characteristic speed $\lambda(q) = f'(q)$. There are three cases:

1. **Convex flux:** $\lambda(q)$ is a monotone *increasing* function of q, that is

$$\frac{d}{dq}\lambda(q) = \lambda'(q) = f''(q) > 0 , \quad \forall q . \tag{46}$$

2. **Concave flux:** $\lambda(q)$ is a monotone *decreasing* function of q, that is

$$\frac{d}{dq}\lambda(q) = \lambda'(q) = f''(q) < 0 , \quad \forall q . \tag{47}$$

3. **Non-convex, non-concave flux:** $\lambda(q)$ vanishes for some q, that is

$$\frac{d}{dq}\lambda(q) = \lambda'(q) = f''(q) = 0 , \quad \text{for some } q . \tag{48}$$

Example: The Inviscid Burgers' Equation

$$\left.\begin{aligned} &\partial_t q + \partial_x f(q) = 0 , \\ &f(q) = \frac{1}{2}q^2 , \\ &\lambda(q) = f'(q) = q , \quad \lambda'(q) = f''(q) = 1 > 0 , \quad \forall q . \end{aligned}\right\} \tag{49}$$

The flux is convex; the monotone increasing behaviour of $\lambda(q)$ means that larger values of q propagate faster than smaller values of q. This leads to wave distortion and shock formation. We note that the true Burgers equation is viscous, namely

$$\partial_t q + \partial_x f(q) = \alpha \partial_x^{(2)} q , \quad f(q) = \frac{1}{2}q^2 ,$$

where α is a viscosity (or diffusion) coefficient.

Example: A Traffic Flow Equation

$$\left.\begin{aligned} &\partial_t q + \partial_x f(q) = 0 , \\ &f(q) = u_{max}(1 - q/q_{max})q , \\ &\lambda(q) = f'(q) = u_{max}(1 - 2q/q_{max}) , \\ &\lambda'(q) = f''(q) = -2u_{max}/q_{max} < 0 , \quad \forall q . \end{aligned}\right\} \tag{50}$$

Here $u_{max} \geq 0$ and $q_{max} > 0$ are two constants, with $0 < q \leq q_{max}$. The flux is concave, larger values of q will propagate more slowly than smaller values of q, the opposite behaviour to that of Burgers' equation.

Solution Along Characteristics Consider the initial-value problem (or Cauchy problem)

$$\left.\begin{array}{ll} \text{PDE:} & \partial_t q + \partial_x f(q) = 0 \ , \\ \text{IC:} & q(x,0) = h(x) \ . \end{array}\right\} \tag{51}$$

As for LAE, solutions along characteristic curves $x = x(t)$, with

$$x = x_0 + \lambda(h(x_0))t \tag{52}$$

can be defined as

$$q(x,t) = h(x_0) = h(x - \lambda(h(x_0))t) \ . \tag{53}$$

Figure 9 depicts the situation.

Crossing Characteristics For non-linear equations, characteristics are no longer parallel, as in the linear case. Therefore, characteristic curves may cross, as illustrated in Fig. 10.

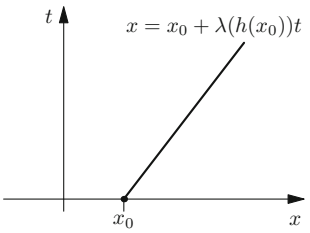

Fig. 9 Characteristic curve $x(t) = x_0 + \lambda(h(x_0))\ t$ emanating from x_0: foot of the characteristic

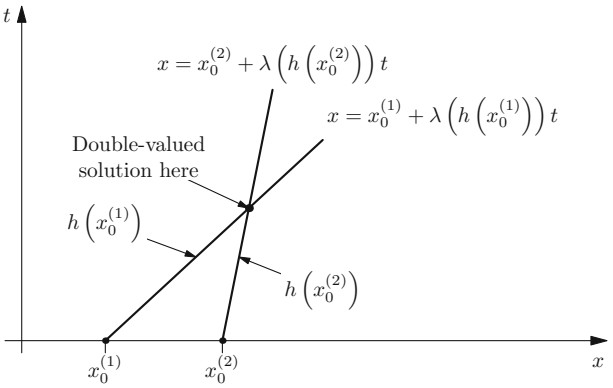

Fig. 10 Characteristics from $x_0^{(1)}$ and $x_0^{(2)}$ carry different initial values $h(x_0^{(1)})$ and $h(x_0^{(2)})$, leading to multi-valued solutions

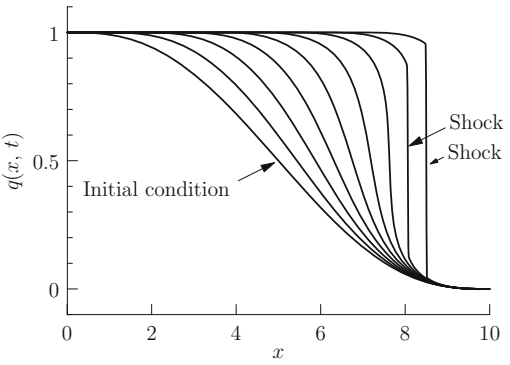

Fig. 11 Shock wave formation from smooth initial condition at time $t = 0$. Burgers' equation solved numerically with the first-order Godunov method on a very fine mesh

Shock Formation: A Numerical Example For non-linear equations, even if the initial data is continuous, discontinuities may develop in time. This is illustrated in Fig. 11 below, where a sequence of profiles corresponding to an increasing sequence of time values is shown, starting from $t = 0$, the initial condition.

The phenomenon of shock formation in non-linear equations calls for the extension of the definition of solution. To this end the equations are reformulated in terms of integral relations that no longer require continuity of the solution.

Integral Forms of the Equation Consider the general case written in differential conservative form

$$\partial_t q(x,t) + \partial_x f(q(x,t)) = s(q(x,t)) \; . \tag{54}$$

This equation includes a source term and is thus called a **balance law**. If $s(q(x,t)) = 0$ then the equation is a conservation law.

Here we study **integral forms**, to accommodate discontinuous solutions. We shall also derive a condition to be satisfied at discontinuities. To this end we consider a **control volume** V in the x-t plane, depicted in Fig. 12, defined as

$$V = [x_L, x_R] \times [t_1, t_2] \; . \tag{55}$$

We integrate Eq. (54) in space and time in the control volume V

$$\int_{x_L}^{x_R} \int_{t_1}^{t_2} [\partial_t q(x,t) + \partial_x f(q(x,t))] \, dxdt = \int_{x_L}^{x_R} \int_{t_1}^{t_2} s(q(x,t)) \, dxdt \; . \tag{56}$$

On rearranging the space and time integrals we obtain

$$\left.\begin{aligned} \int_{x_L}^{x_R} \left[\int_{t_1}^{t_2} \partial_t q(x,t) dt \right] dx = & - \int_{t_1}^{t_2} \left[\int_{x_L}^{x_R} \partial_x f(q(x,t)) dx \right] dt \\ & + \int_{x_L}^{x_R} \int_{t_1}^{t_2} s(q(x,t)) dxdt \; . \end{aligned} \right\} \tag{57}$$

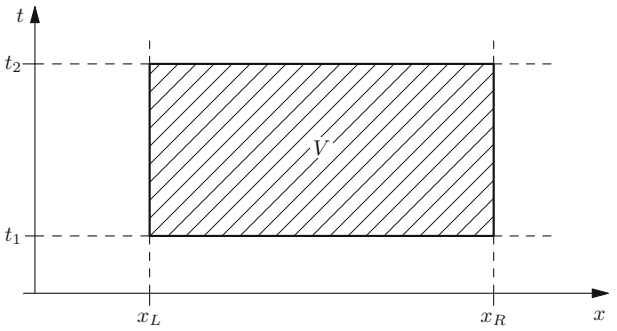

Fig. 12 Control volume $V = [x_L, x_R] \times [t_1, t_2]$ in x-t space. Equations will be integrated exactly on this volume to derive integral forms of the conservation laws

Exact space-time integration gives the **integral form** of the balance law (54), namely

$$\left.\begin{aligned}\int_{x_L}^{x_R} q(x,t_2)dx = \int_{x_L}^{x_R} q(x,t_1)dx - \left[\int_{t_1}^{t_2} f(q(x_R,t))dt - \int_{t_1}^{t_2} f(q(x_L,t))dt\right] \\ + \int_{x_L}^{x_R}\int_{t_1}^{t_2} s(q(x,t))dxdt\ .\end{aligned}\right\} \tag{58}$$

In the absence of the source term, the integral form states that *the amount of* $q(x,t)$ *in the interval* $[x_L, x_R]$ *at time* $t = t_2$ *is equal to the amount of* $q(x,t)$ *in the interval* $[x_L, x_R]$ *at time* $t = t_1$ *plus a difference of time integrals of the fluxes at the extreme points*. In the presence of a source term this statement is modified appropriately.

It is also convenient to obtain an averaged version of (58), namely

$$\left.\begin{aligned}\frac{1}{\Delta x}\int_{x_L}^{x_R} q(x,t_2)dx = \frac{1}{\Delta x}\int_{x_L}^{x_R} q(x,t_1)dx \\ -\frac{\Delta t}{\Delta x}\left[\frac{1}{\Delta t}\int_{t_1}^{t_2} f(q(x_R,t))dt - \frac{1}{\Delta t}\int_{t_1}^{t_2} f(q(x_L,t))dt\right] \\ +\frac{\Delta t}{\Delta x \Delta t}\int_{x_L}^{x_R}\int_{t_1}^{t_2} s(q(x,t))dxdt\ .\end{aligned}\right\} \tag{59}$$

The Finite Volume Formula The integral expression (59) can be written as

$$q^{new} = q^{old} - \frac{\Delta t}{\Delta x}\left[f_{right} - f_{left}\right] + \Delta t\ s_{vol}\ , \tag{60}$$

which is exact, with the following definitions

$$\left.\begin{aligned} q^{new} &= \frac{1}{\Delta x}\int_{x_L}^{x_R} q(x,t_2)dx\ , \\ q^{old} &= \frac{1}{\Delta x}\int_{x_L}^{x_R} q(x,t_1)dx\ , \\ f_{right} &= \frac{1}{\Delta t}\int_{t_1}^{t_2} f(q(x_R,t))dt\ , \\ f_{left} &= \frac{1}{\Delta t}\int_{t_1}^{t_2} f(q(x_L,t))dt\ , \\ s_{vol} &= \frac{1}{\Delta x \Delta t}\int_{x_L}^{x_R}\int_{t_1}^{t_2} s(q(x,t))dxdt\ . \end{aligned}\right\} \tag{61}$$

Numerical methods called finite volume methods, use the *finite volume formula* (60) to compute approximate solutions in which q^{old} is a known average of the solution at the previous time level and the remaining terms on the right hand side of (60) are found by appropriate approximations of the integrals in (61). The computational parameters Δt and Δx must be prescribed to complete the scheme to compute q^{new}.

Generalised Solutions and Rankine-Hugoniot Conditions A generalised (or weak) solution of the conservation law (54) is a function $q(x,t)$ that satisfies the integral form (58). Weak solutions admit discontinuities (shocks), which satisfy the *Rankine-Hugoniot jump condition.*

Proposition: Rankine-Hugoniot Condition A discontinuity of a weak solution of the conservation law (54), no source term, satisfies the Rankine-Hugoniot jump condition across it, namely

$$f(q(s_R,t)) - f(q(s_L,t)) = [q(s_R,t) - q(s_R,t)]\, s\ , \tag{62}$$

where $q(s_L,t)$ and $q(s_R,t)$ are limiting values from left and right of the discontinuity; $f(q(s_R,t))$ and $f(q(s_L,t))$ are the corresponding flux values and s is the speed of the discontinuity. For the proof see [1].

Summarising in order to admit discontinuous solutions one needs to formulate the equations in integral form and enforce the Rankine-Hugoniot condition across discontinuities, while in smooth parts of the solution one may formulate equations in differential form.

Example: Burgers's Equation Assume a shock wave of speed s with states q_L and q_R. The Rankine-Hugoniot condition gives

$$f(q_R) - f(q_L) = \frac{1}{2}q_R^2 - \frac{1}{2}q_L^2 = s(q_R - q_L)\ ,$$

from which the shock speed is given by

$$s = \frac{1}{2}(q_L + q_R) \ . \tag{63}$$

This is a very special case. The shock speed is a simple arithmetic average of the characteristic speeds either side of the shock.

A Non-uniqueness Example The enlarged set of solutions of the integral formulation includes smooth (classical) and discontinuous solutions. However, now the set is too large, it contains spurious, non-physical solutions. Hence this requires an admissibility criterion to discard *unphysical shocks*. To illustrate the question of non-uniqueness we consider the following example:

$$\left.\begin{array}{l} \text{PDE}: \partial_t q + \partial_x f(q) = 0 \ , \ f(q) = \frac{1}{2}q^2 \ , \\ \text{IC}: \quad q(x,0) = h(x) = \left\{ \begin{array}{l} q_L = 0 \text{ if } x < 0 \ , \\ q_R = 1 \text{ if } x > 0 \ . \end{array} \right. \end{array} \right\} \tag{64}$$

Solution 1: Rarefaction Wave One solution of the problem is the rarefaction wave (smooth)

$$q(x,t) = \left\{ \begin{array}{ll} q_{\text{L}} = 0 & \text{if} \quad x/t < 0 \ , \\ x/t & \text{if} \ \ 0 \le x/t \le 1 \ , \\ q_R = 1 & \text{if} \quad x/t > 1 \ . \end{array} \right. \tag{65}$$

Figure 13 illustrates solution and the corresponding picture of characteristics.

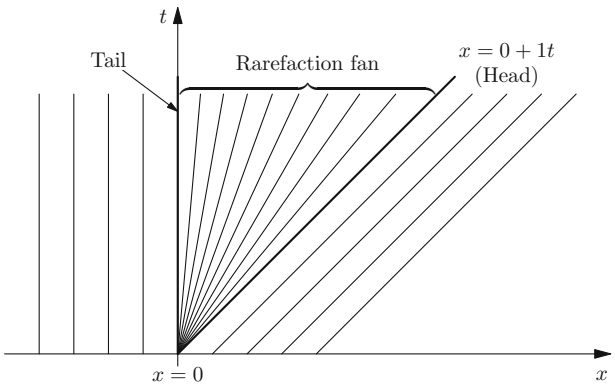

Fig. 13 Illustration of the rarefaction solution (65) to initial-value problem (64)

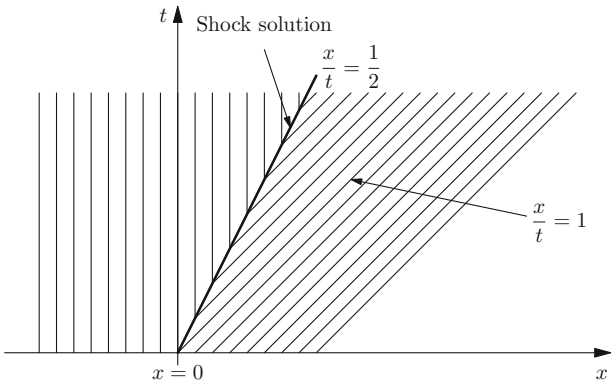

Fig. 14 Illustration of the shock solution (66) to problem (64). Characteristics diverge from the shock path

Solution 2: Shock Wave Another, discontinuous, solution (shock) is given as

$$q(x,t) = \begin{cases} 0 & \text{if } x/t < s = 1/2 \,, \\ 1 & \text{if } x/t > s = 1/2 \,. \end{cases} \tag{66}$$

Figure 14 shows the shock solution to problem (64). Note that characteristics diverge from the shock and the solution is therefore non-admissible. So the initial value problem (64) has at least two solutions.

Admissible Shocks: The Lax Entropy Condition The proposed solution (66) is not accepted as a *physical* solution. *Rarefaction shocks* are excluded. Admissible discontinuities are those arising from *compression*. This *compressibility* condition is ensured by the *Lax entropy condition:*

$$\lambda(q_L) > s > \lambda(q_R) \,. \tag{67}$$

s: shock speed, $\lambda(q_L)$ and $\lambda(q_R)$ are characteristic speeds. Note that characteristics *run into the shock*, which is *compressed* by the characteristics, see Fig. 15.

The Riemann Problem for Burgers's Equation The problem is defined as

$$\left.\begin{aligned} &\text{PDE}: \partial_t q + \partial_x f(q) = 0 \,, \quad f(q) = \tfrac{1}{2}q^2 \,, \\ &\text{IC}: \quad q(x,0) = \begin{cases} q_L & \text{if } x < 0 \,, \\ q_R & \text{if } x > 0 \,. \end{cases} \end{aligned}\right\} \tag{68}$$

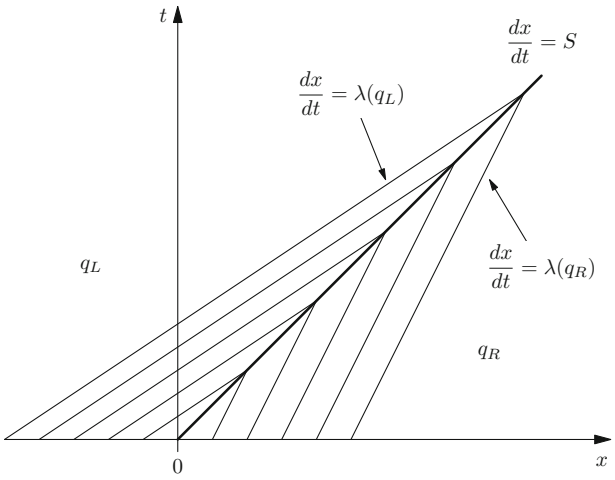

Fig. 15 Picture of characteristics for an entropy-satisfying shock. Characteristic curves run into the shock path

The solution is given by the following two cases, shock if $q_L > q_R$ and rarefaction otherwise:

$$\left.\begin{aligned} q(x,t) &= \left\{\begin{array}{ll} q_L & \text{if } x - st < 0 \\ q_R & \text{if } x - st > 0 \end{array}\right\} \text{ if } q_L > q_R \,, \\ s &= \tfrac{1}{2}(q_L + q_R) \\ q(x,t) &= \left\{\begin{array}{ll} q_L & \text{if } \dfrac{x}{t} \le q_L \\ \dfrac{x}{t} & \text{if } q_L < \dfrac{x}{t} < q_R \\ q_R & \text{if } \dfrac{x}{t} \ge q_R \end{array}\right\} \text{ if } q_L \le q_R \,. \end{aligned}\right\} \tag{69}$$

Figure 16 illustrates the solution structure for the two cases. The bottom frame shows the shock case while the top frame shows the rarefaction case.

First-Order Non-linear Systems To end this introductory section we state that the general setting is that of non-linear systems of m hyperbolic balance laws in three space dimensions, which written in differential conservative form read

$$\partial_t \mathbf{Q} + \partial_x \mathbf{F}(\mathbf{Q}) + \partial_y \mathbf{G}(\mathbf{Q}) + \partial_z \mathbf{H}(\mathbf{Q}) = \mathbf{S}(\mathbf{Q}) \,, \tag{70}$$

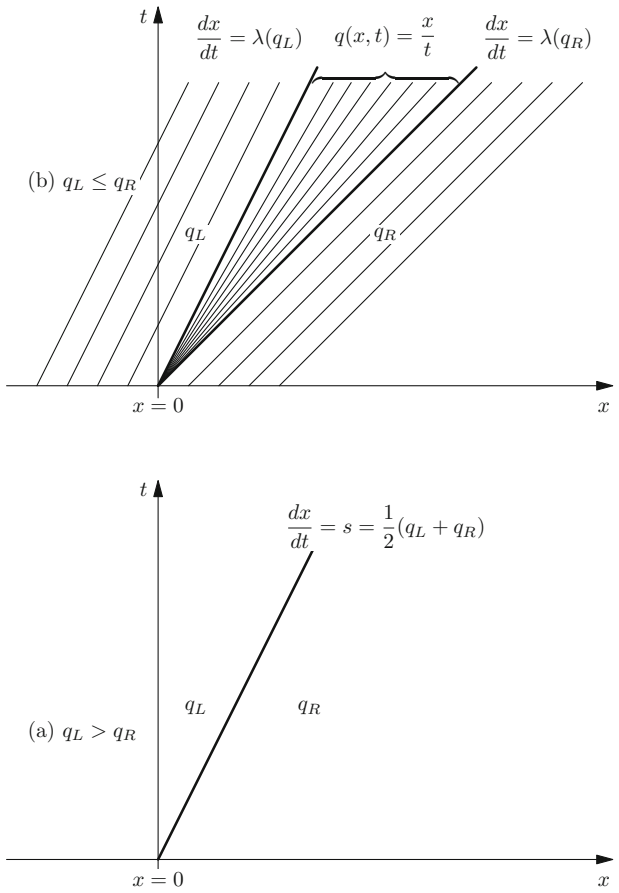

Fig. 16 Solution of the Riemann problem for the Burgers equation. Frame (**a**): shock wave if $q_L > q_R$. Frame (**b**): rarefaction wave if $q_L \leq q_R$

where

$$\mathbf{Q} = \begin{bmatrix} q_1 \\ q_2 \\ \cdots \\ q_m \end{bmatrix} \; ; \; \mathbf{F} = \begin{bmatrix} f_1 \\ f_2 \\ \cdots \\ f_m \end{bmatrix} \; ; \; \mathbf{G} = \begin{bmatrix} g_1 \\ g_2 \\ \cdots \\ g_m \end{bmatrix} \; ; \; \mathbf{H} = \begin{bmatrix} h_1 \\ h_2 \\ \cdots \\ h_m \end{bmatrix} \; ; \; \mathbf{S} = \begin{bmatrix} s_1 \\ s_2 \\ \cdots \\ s_m \end{bmatrix} . \tag{71}$$

Here the independent variables are: x, y, z and t. $\mathbf{Q}(x, y, z, t)$ is the vector of dependent variables, called *conserved variables*; $\mathbf{F}(\mathbf{Q})$ is the flux vector in the x-direction; $\mathbf{G}(\mathbf{Q})$ is the flux vector in the y-direction and $\mathbf{H}(\mathbf{Q})$ is the flux vector in

the z-direction; $\mathbf{S}(\mathbf{Q})$ is the vector of source terms. Fluxes and sources are prescribed functions of $\mathbf{Q}(x, y, z, t)$.

In this chapter we deal exclusively with the one-dimensional case (1D). For the more general case see for example [1–3] and [4].

1.4 Numerical Approximation of Hyperbolic Equations

Here we introduce some basic concepts on numerical discretization methods for hyperbolic equations, all based on the simplest equation. To this end we first consider the initial-boundary value problem (IBVP) for the linear advection equation

$$\left.\begin{array}{ll} \text{PDE:} & \partial_t q + \lambda \partial_x q = 0 \ , \quad x \in [a, b] \ , \ t > 0 \ , \\ \text{IC:} & q(x, 0) = h(x) \ , \quad x \in [a, b] \ , \ t = 0 \ , \\ \text{BCs:} & q(a, t) = b_L(t) \ ; \quad q(b, t) = b_R(t) \ , \ t \geq 0 \ . \end{array}\right\} \tag{72}$$

Here $[a, b]$ defines the spatial domain; $h(x)$ is the initial condition (IC) at the initial time $t = 0$, a prescribed function of x; $b_L(t)$ and $b_R(t)$ are prescribed functions of time and define boundary conditions (BCs) at $x = a$ (left) and at $x = b$ (right).

Finite Difference Discretisation One approach to solve problem (72) is by the method of finite differences, which requires the following steps:

1. *Partition of the spatial domain* $[a, b]$ into $M + 2$ equidistant points

$$x_i = a + i\Delta x \ , \quad i = 0, \ldots, M + 1 \ , \quad \Delta x = \frac{b - a}{M + 1} \ , \tag{73}$$

   where M is a chosen positive integer. See Fig. 17. There are M *interior points*: $x_1, x_2, \ldots, x_M$; and two *boundary points*: $x_0 = a$ and $x_{M+1} = b$.
2. *Partition of the temporal domain* $[0, T_{out}]$ into a set of time points, or time levels,

$$t_n = n\Delta t \ , \quad n = 0 \ , \ldots, N_{out} \ , \ldots \ . \tag{74}$$

   See Fig. 17. Here $t_0 = 0$: initial time; $T_{out} = \Delta t N_{out}$; Δt: timestep. We assume a fixed relationship between Δt and Δx of the form

$$\Delta x = \Delta t \times K \ , \quad K > 0 : \text{constant} \ . \tag{75}$$

The spatial mesh parameter Δx is chosen through the choice of M, that is, the number of interior points. There are no particular constraints in choosing M. The choice of the time step Δt is constrained by accuracy or stability considerations [4].

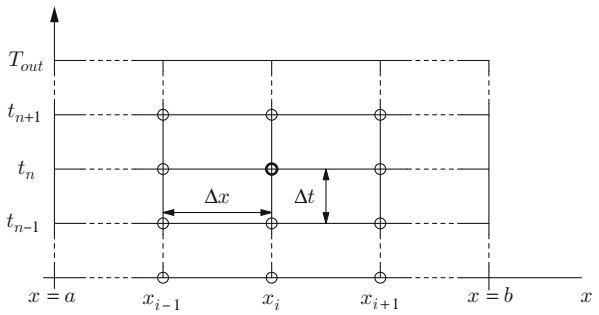

Fig. 17 Finite difference mesh defining a discrete set of points (x_i, t_n) resulting from partitions of the spatial x and temporal t domains

Discrete Values The continuous domain $[a, b] \times [0, \infty)$ has been replaced by a mesh made up of a finite number of points (x_i, t_n). We now need to replace the continuous distribution of the function $q(x, t)$ by a finite number of discrete values $q(x_i, t_n)$ associated with these points. Then in order to solve the differential equation in this discrete setting we also need to represent in discrete form the partial derivatives $\partial_t q(x, t)$ and $\partial_x q(x, t)$ in (72). Here we do so by finite difference approximations. In this manner the partial differential equation is represented by a *difference equation*, an expression that relates approximate discrete values of the solution at neighbouring points. The *differential operator* is replaced by a *numerical operator*, as we shall see.

Consider the generic point (x_i, t_n) of the mesh, as shown in Fig. 17. We seek an approximation to $q(x_i, t_n)$ and this will be denoted by q_i^n, that is

$$q_i^n \approx q(x_i, t_n) \ . \tag{76}$$

The temporal partial derivative $\partial_t q(x, t)$ can be approximated in a variety of ways, such as

$$\partial_t q(x_i, t_n) = \begin{cases} \dfrac{q(x_i, t_{n+1}) - q(x_i, t_n)}{\Delta t} + \mathcal{O}(\Delta t) \ , & \text{Forward} \ , \\ \dfrac{q(x_i, t_n) - q(x_i, t_{n-1})}{\Delta t} + \mathcal{O}(\Delta t) \ , & \text{Backward} \ , \\ \dfrac{q(x_i, t_{n+1}) - q(x_i, t_{n-1})}{2\Delta t} + \mathcal{O}(\Delta t^2) \ , & \text{Centred} \ . \end{cases} \tag{77}$$

Analogously, for the spatial partial derivative $\partial_x q(x, t)$ in (72) at the point (x_i, t_n) we write

$$\partial_x q(x_i, t_n) = \begin{cases} \dfrac{q(x_{i+1}, t_n) - q(x_i, t_n)}{\Delta x} + \mathcal{O}(\Delta x) \ , & \text{Forward} \ , \\ \dfrac{q(x_i, t_n) - q(x_{i-1}, t_n)}{\Delta x} + \mathcal{O}(\Delta x) \ , & \text{Backward} \ , \\ \dfrac{q(x_{i+1}, t_n) - q(x_{i-1}, t_n)}{2\Delta x} + \mathcal{O}(\Delta x^2) \ , & \text{Centred} \ . \end{cases} \tag{78}$$

Now, various combinations of these finite difference approximations will lead to various well-known methods.

The Method of Godunov: Finite Difference Version This method uses the following approximations to partial derivatives

$$\left.\begin{aligned} \partial_t q(x_i, t_n) &= \frac{q(x_i, t_{n+1}) - q(x_i, t_n)}{\Delta t} + \mathscr{O}(\Delta t) \ , \\ \partial_x q(x_i, t_n) &= \begin{cases} \dfrac{q(x_i, t_n) - q(x_{i-1}, t_n)}{\Delta x} + \mathscr{O}(\Delta x) \text{ if } \lambda > 0 \ , \\ \dfrac{q(x_{i+1}, t_n) - q(x_i, t_n)}{\Delta x} + \mathscr{O}(\Delta x) \text{ if } \lambda < 0 \ . \end{cases} \end{aligned}\right\} \tag{79}$$

Remarks

1. The time derivative is approximated by a *forward-in-time* formula.
2. The space derivative is approximated by a one-sided, **upwind**, space derivative discretisation, according to the sign of the wave propagation speed.
3. For linear equations the method was first proposed Courant, Isaacson and Rees (1952).
4. Godunov [5] extended the upwind method in **conservation form** to solve non-linear systems of hyperbolic equations, see Sect. 3.

The differential operator in (72) is

$$L_e(q) \equiv \partial_t q(x, t) + \lambda \partial_x q(x, t) = 0 \ , \tag{80}$$

which when applied to the point (x_i, t_n) of the mesh, for $\lambda > 0$, becomes

$$\left.\begin{aligned} L_e(q(x_i, t_n)) &= \partial_t q(x_i, t_n) + \lambda \partial_x q(x_i, t_n) \\ &= \frac{q(x_i, t_{n+1}) - q(x_i, t_n)}{\Delta t} + \mathscr{O}(\Delta t) \\ &\quad + \lambda [\frac{q(x_i, t_n) - q(x_{i-1}, t_n)}{\Delta x}] + \mathscr{O}(\Delta x) \\ &= 0 \ . \end{aligned}\right\} \tag{81}$$

Suppressing $\mathscr{O}(\Delta t) + \mathscr{O}(\Delta x)$ and replacing $q(x_i, t_n)$ by q_i^n gives

$$\frac{q_i^{n+1} - q_i^n}{\Delta t} + \lambda \left(\frac{q_i^n - q_{i-1}^n}{\Delta x} \right) = 0 \ .$$

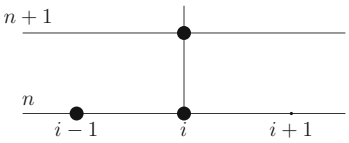

Fig. 18 Stencil for Godunov's method for positive characteristic speed λ. Note the one-sided (upwind) character of the stencil

Solving for q_i^{n+1} we obtain the numerical scheme

$$q_i^{n+1} = q_i^n - \frac{\lambda \Delta t}{\Delta x}\left(q_i^n - q_{i-1}^n\right) \ . \tag{82}$$

The **Courant-Friedrichs-Lewy number**, or the CFL number, or simply **Courant number** is defined as

$$c = \frac{\lambda \Delta t}{\Delta x} = \frac{\lambda}{\Delta x/\Delta t} \ . \tag{83}$$

This is a dimensionless quantity, it is the ratio of the speed λ in the PDE in (72) and the *mesh speed* $\Delta x/\Delta t$. Then the Godunov upwind scheme becomes

$$q_i^{n+1} = q_i^n - c\left(q_i^n - q_{i-1}^n\right) \ . \tag{84}$$

Figure 18 displays the stencil of scheme (84), which is the set of points of the mesh that contribute to the scheme

The FTCS method (Forward-in-Time Centred-in-Space) results from the following approximations to the partial derivatives

$$\left.\begin{aligned} \partial_t q(x_i, t_n) &= \frac{q(x_i, t_{n+1}) - q(x_i, t_n)}{\Delta t} + \mathscr{O}(\Delta t) \ , \\ \partial_x q(x_i, t_n) &= \frac{q(x_{i+1}, t_n) - q(x_{i-1}, t_n)}{2\Delta x} + \mathscr{O}(\Delta x^2) \ . \end{aligned}\right\} \tag{85}$$

Substituting of these into the PDE, suppressing error terms and replacing exact values by approximate values, yields

$$\frac{q_i^{n+1} - q_{i-1}^n}{\Delta t} + \lambda\left(\frac{q_{i+1}^n - q_{i-1}^n}{2\Delta x}\right) = 0 \ . \tag{86}$$

Solving for q_i^{n+1} we obtain the FTCS numerical scheme

$$q_i^{n+1} = q_i^n - \frac{1}{2}c(q_{i+1}^n - q_{i-1}^n) \ . \tag{87}$$

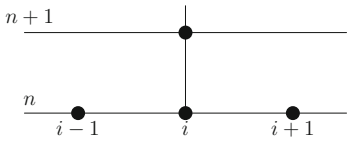

Fig. 19 Stencil for the FTCS method. Note the symmetric character of the stencil

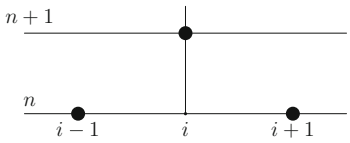

Fig. 20 Stencil for the Lax-Friedrichs method. Note the symmetry of the stencil and the missing point (x_i, t_n)

Figure 19 shows the stencil. Unfortunately, FTCS is useless; it is *unconditionally unstable*. FTCS uses the same approximation to the time derivative as the Godunov method, but the spatial derivative is approximated via a centred, second-order accurate, discretization. Naively, one would have expected a better method than Godunov's method. There are two ways to rescue FTCS. One modification results in the explicit Lax-Friedrichs scheme. The other way is to resort to an implicit version.

The Lax-Friedrichs method results from replacing q_i^n in the approximation to the time derivative of FTCS by a mean value, that is

$$q_i^n \longrightarrow \frac{1}{2}(q_{i-1}^n + q_{i+1}^n) \, .$$

Then

$$\frac{q_i^{n+1} - \frac{1}{2}(q_{i-1}^n + q_{i+1}^n)}{\Delta t} + \lambda \left(\frac{q_{i+1}^n - q_{i-1}^n}{2\Delta x} \right) = 0 \, , \tag{88}$$

yielding the Lax-Friedrichs scheme

$$q_i^{n+1} = \frac{1}{2}(1+c) q_{i-1}^n + \frac{1}{2}(1-c) q_{i+1}^n \, , \tag{89}$$

whose stencil is shown in Fig. 20.

The Lax-Wendroff Method The construction of this method follows a different approach, via the following steps:

1. The solution at (x_i, t_{n+1}) is expressed as a Taylor series in time

$$q(x_i, t_{n+1}) = q(x_i, t_n) + \Delta t \partial_t q(x_i, t_n) + \frac{1}{2} \Delta t^2 \partial_t^{(2)} q(x_i, t_n) + \mathscr{O}(\Delta t^3) \, . \tag{90}$$

2. By means of the Cauchy-Kowalewskaya method (or Lax-Wendroff procedure, as is sometimes called) one uses the PDE in (72) to replace time derivatives by

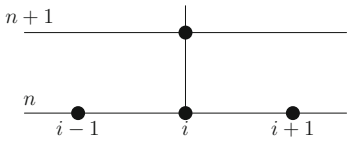

Fig. 21 Stencil for the Lax-Wendroff method. Note the symmetry of the stencil

space derivatives

$$\partial_t q(x,t) = -\lambda \partial_x q(x,t) \ , \quad \partial_t^{(2)} q(x,t) = \lambda^2 \partial_x^{(2)} q(x,t) \ . \tag{91}$$

In fact, for any order k, one can prove

$$\partial_t^{(k)} q(x,t) = (-\lambda)^k \partial_x^{(k)} q(x,t) \ . \tag{92}$$

3. By substituting (91) into (90) one obtains

$$q(x_i, t_{n+1}) = q(x_i, t_n) - \Delta t \lambda \partial_x q(x_i, t_n) + \frac{1}{2} \Delta t^2 \lambda^2 \partial_x^{(2)} q(x_i, t_n) + \mathscr{O}(\Delta t^3) \tag{93}$$

4. The spatial derivatives are approximated by centred finite differences

$$\left.\begin{aligned} \partial_x q(x_i, t_n) &= \frac{q(x_{i+1}, t_n) - q(x_{i-1}, t_n)}{2\Delta x} + \mathscr{O}(\Delta x^2) \ , \\ \partial_x^{(2)} q(x_i, t_n) &= \frac{q(x_{i+1}, t_n) - 2q(x_i, t_n) + q(x_{i-1}, t_n)}{\Delta x^2} + \mathscr{O}(\Delta x^2) \ . \end{aligned}\right\} \tag{94}$$

5. Finally, by substituting (94) into (93), neglecting truncation errors and replacing exact values $q(x_i, t_n)$ by q_i^n one obtains the Lax-Wendroff scheme

$$q_i^{n+1} = \frac{1}{2} c(1+c) q_{i-1}^n + (1 - c^2) q_i^n - \frac{1}{2} c(1-c) q_{i+1}^n \ , \tag{95}$$

whose stencil is shown in Fig. 21.

General Form of a Scheme and Examples All explicit schemes studied so far can be written in the general form

$$q_i^{n+1} = H(q_{i-l}^n, \ldots, q_i^n, \ldots, q_{i+r}^n) \ , \tag{96}$$

with l, r two non-negative integers and $H(\ldots)$ a real-valued function of $l + r + 1$ arguments and

$$q_i^n \approx q(x_i, t_n) \ , \quad q_i^n \to 0 \text{ as } |i| \to \infty \tag{97}$$

is a point-wise value that approximates the true solution $q(x, t)$ at the mesh point (x_i, t_n), with $x_i = i\Delta x$, $t_n = n\Delta t$.

Example: The Godunov Finite Difference Method When the Godunov scheme is written as in (96), we have

$$\left.\begin{array}{l} \text{For } \lambda > 0 \; H = cq_{i-1}^n + (1-c)q_i^n \; , \\ \text{For } \lambda < 0 \; H = (1+c)q_i^n - cq_{i+1}^n \; . \end{array}\right\} \tag{98}$$

Linear Schemes Linear schemes are a special class of schemes (96) for the linear advection equation in (72), of the form

$$q_i^{n+1} = \sum_{k=-l}^{k=r} b_k q_{i+k}^n \; , \tag{99}$$

in which the coefficients b_k are constant, that is, they do not depend on the solution.

Consider now two examples.

1. For the Godunov finite difference method we have two cases: For $\lambda > 0$ $l = 1$, $r = 0$, $b_{-1} = c$ and $b_0 = 1 - c$. For $\lambda < 0$ we have $l = 0$, $r = 1$, $b_0 = 1 + c$, $b_1 = -c$.
2. For the Lax-Wendroff method we have $l = 1$, $r = 1$, $b_{-1} = \frac{1}{2}(1 + c)c$, $b_0 = 1 - c^2$, $b_1 = -\frac{1}{2}(1 - c)c$.

Monotone Schemes A numerical scheme of the form (96) is called monotone if H satisfies

$$\frac{\partial}{\partial q_k^n} H(q_{i-l}^n, q_{i-l+1}^n, \ldots, q_i^n, \ldots, q_{i+r}^n) \geq 0 \; , \quad i - l \leq k \leq i + r \; . \tag{100}$$

Remark a linear scheme is monotone if and only if all its coefficients are non-negative. This follows from the definitions of linear schemes and monotonicity.

A Shortcut to Accuracy Through the Accuracy Lemma A linear scheme of the form (99) is p-th order accurate in space and time ($p \geq 0$) in the sense of local truncation error, if and only if

$$\sum_{k=-l}^{r} k^\eta b_k = (-c)^\eta \; , \quad \eta = 0, 1, \ldots, p \; , \quad c : \text{Courant Number.} \tag{101}$$

For notational convenience we introduce $0^0 = 1$.

Proof For the proof and extensions to two and three dimensions see [1].

Example: The Godunov Upwind Finite Difference Method For $\lambda > 0$ the scheme is

$$q_i^{n+1} = H(q_{i-l}^n, q_i^n) = cq_{i-l}^n + (1-c)q_i^n \ . \tag{102}$$

$l = 1, r = 0, b_{-1} = c, b_0 = 1 - c$. Then we need to verify identity (101) for all possible non-negative integer values of η.

$$\eta = 0 \ : \qquad (-1)^0 \times c + 0^0 \times (1-c) = c + 1 - c = 1 = (-c)^0 \ .$$

This merely says that the sum of the coefficients of the scheme is unity.

$$\eta = 1 \ : \qquad (-1)^1 \times c + 0^1 \times (1-c) = -c = (-c)^1 \ .$$

The Godunov scheme is first-order accurate. But just for fun we try:

$$\eta = 2 \ : \qquad (-1)^2 \times c + 0^2 \times (1-c) = c \neq (-c)^2 \ .$$

Thus the Godunov scheme is **not** second-order accurate, except for the trivial cases $c = 0$ and $c = 1$.

Godunov's Theorem [5] There are no monotone, linear schemes (99) for the linear advection equation with constant λ, of accuracy two or higher.

Proof It is sufficient to prove that there is no second order, linear, monotone method for LAE. Proceed by contradiction and assume there is a second order, linear, monotone method for LAE. From the accuracy lemma we must have:

$$s_\eta = \sum_{k=-l}^{r} k^\eta b_k = \left\{ \begin{array}{l} s_0 = 1 \ , \eta = 0 \ , \\ s_1 = -c \ , \eta = 1 \ , \\ s_2 = c^2 \ , \eta = 2 \ . \end{array} \right. \tag{103}$$

But, in particular, from (103) plus some algebraic manipulations one obtains

$$\left. \begin{array}{rl} s_2 &= \displaystyle\sum_{k=-l}^{r} k^2 b_k \\ &= \displaystyle\sum_{k=-l}^{r} (k+c)^2 b_k - 2c \sum_{k=-l}^{r} k b_k - c^2 \sum_{k=-l}^{r} b_k \\ &= \left[\displaystyle\sum_{k=-l}^{r} (k+c)^2 b_k \right] - 2cs_1 - c^2 s_0 \ . \end{array} \right\} \tag{104}$$

Use of (103) into (104) gives

$$c^2 = \left[\sum_{k=-l}^{r} (k+c)^2 b_k \right] + c^2 \ . \tag{105}$$

This implies a contradiction; for a monotone scheme all coefficients b_k are non-negative but not simultaneously zero. Thus Godunov's theorem is true □.

Consequences of Godunov's Theorem From the theorem we have that linear monotone schemes are at most first-order accurate. But first-order methods are too inaccurate to be of practical use and therefore one must search for other classes of schemes. This is down to finding ways of circumventing Godunov's theorem.The key to this lies on the assumption of linear schemes. Thus a necessary condition for a numerical scheme to be oscillation-free (without new extrema) and of high-order of accuracy (for smooth solutions) is to be non-linear. In simple terms: *Schemes must be non-linear, even when applied to linear equations.*

Recall that schemes can be expressed in **the general form** (96). In what follows we introduce other forms.

The conservative form is a particular class of schemes for hyperbolic equations and can be written in the form

$$q_i^{n+1} = q_i^n - \frac{\Delta t}{\Delta x} \left(f_{i+\frac{1}{2}} - f_{i-\frac{1}{2}} \right) \ , \tag{106}$$

where $f_{i+\frac{1}{2}}$ is the *numerical flux*. See definition (60).

The Viscous Form of a Scheme This requires a function $d_{i+\frac{1}{2}}$ of $2k$ variables

$$d_{i+\frac{1}{2}} = d_{i+\frac{1}{2}}(q_{i-k+1}^n, q_{i-k+1}^n, \ldots, q_i^n, \ldots, q_{i+k}^n) \ , \tag{107}$$

such that a three-point scheme can be written as

$$q_i^{n+1} = q_i^n - \frac{1}{2}\frac{\Delta t}{\Delta x}[f(q_{i+1}^n) - f(q_{i-1}^n)] + \frac{1}{2}(d_{i+\frac{1}{2}} \Delta q_{i+\frac{1}{2}} - d_{i-\frac{1}{2}} \Delta q_{i-\frac{1}{2}}) \ . \tag{108}$$

The function $d_{i+\frac{1}{2}}$ is called the *coefficient of numerical viscosity*.

Viscous Form of a Three-Point Linear Scheme We study the viscous form a three-point linear scheme of the form

$$q_i^{n+1} = b_{-1} q_{i-1}^n + b_0 q_i^n + b_1 q_{i+1}^n \ . \tag{109}$$

The coefficients b_{-1}, b_0 and b_1 are constant. Assume the scheme to be at least first-order. Then from the accuracy lemma, see (101), we have

$$b_{-1} + b_0 + b_1 = 1 \ , \quad b_{-1} - b_1 = c \ . \tag{110}$$

System (110) gives a one-parameter family of solutions. From the first equation we introduce $d = b_{-1} + b_1 = 1 - b_0$ and thus

$$b_{-1} = \frac{1}{2}(d + c) \ , \quad b_0 = 1 - d \ , \quad b_1 = \frac{1}{2}(d - c) \ . \tag{111}$$

Now in terms of d scheme (109) becomes

$$q_i^{n+1} = q_i^n - \frac{1}{2}c(q_{i+1}^n - q_{i-1}^n) + \frac{1}{2}d(q_{i+1}^n - 2q_i^n + q_{i-1}^n) \ . \tag{112}$$

This is the *viscous form* of scheme (109) and d is the *coefficient of numerical viscosity* of the scheme.

Remarks on the Viscous Form

1. Particular values of d give particular schemes, as we shall see.
2. The stability condition becomes

$$c^2 \leq d \leq 1 \ . \tag{113}$$

3. The monotonicity condition is

$$c \leq d \leq 1 \ . \tag{114}$$

4. A truncation error analysis gives *coefficient of numerical viscosity*

$$\alpha_{visc} = \frac{1}{2}\Delta x \lambda \left(\frac{d - c^2}{c} \right) \ . \tag{115}$$

Thus effectively the coefficient d measures the truncation error of the scheme.

Proposition *The Godunov upwind scheme for the linear advection equation is the monotone scheme with the smallest truncation error. The proof is left as an exercise.*

Well-known schemes are obtained by an appropriate choice d. The following four choices for d give four well-known numerical schemes:

$$d = \begin{cases} 1 & \rightarrow \text{ Lax-Friedrichs} \ , \\ \frac{1}{2}(1 + c^2) & \rightarrow \text{ FORCE} \ , \\ |c| & \rightarrow \text{ Godunov upwind} \ , \\ c^2 & \rightarrow \text{ Lax-Wendroff} \ . \end{cases} \tag{116}$$

Figure 22 shows the coefficient of numerical viscosity for all four schemes above. The region of monotone methods is contained in the dark triangular region. Schemes outside this region are not monotone. Of the monotone methods the least accurate

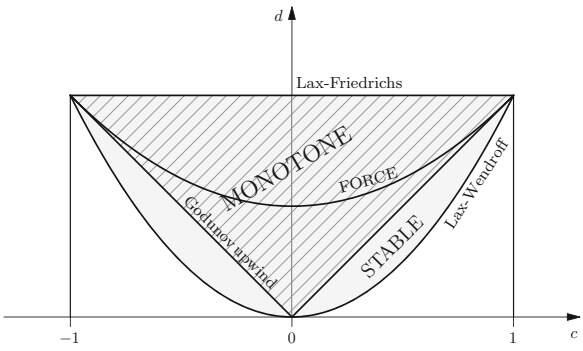

Fig. 22 Coefficient of numerical viscosity d for four schemes as functions of the Courant number c. Monote schemes lie inside the triangular region defined by the Godunov method (bottom) and the Lax-Friedrichs scheme (top)

method is the Lax-Friedrichs method and the most accurate method is the Godunov method. The FORCE method [6] is seen to lie in between these two methods. The Law-Wendroff method is the most accurate scheme of them all but it is not monotone. Stable schemes lie above the Lax-Wendroff method.

Sample Numerical Results Figures 23 and 24 show numerical results for the linear advection equation (symbols) compared to the exact solution (line) for the Lax-Friedrichs, Godunov and the Lax-Wendroff methods. Figure 23 shows the case of a smooth solution, while Fig. 24 shows the case of a discontinuous solution. For the smooth case of Fig. 23 we see that the Lax-Friedrichs method is the least accurate, just look at the peak value (unity); this is followed by the Godunov method, with Lax-Wendroff displaying the most accurate result. However, even for this smooth test problem, the Lax-Wendroff method shows *spurious oscillations* (overshoots and undershoots), mainly behind the wave. In fact the numerical solution has some negative values, which would be unphysical if $q(x, t)$ represented a concentration variable, for example.

Figure 24 shows results for the discontinuous case. Again the least accurate method is the Lax-Friedrichs method; note also the pairing of numerical values, which is a typical feature of this method. The Godunov method is a little bit more accurate but still far from representing well the square wave with its two discontinuities. The Lax-Wendroff method shows less spreading of the discontinuities (numerical diffusion) and its peak value is closer to the exact value; however the spurious oscillations, with negative values, make this method unsuitable for computing discontinuous solutions.

Note that the Lax-Friedrichs and Godunov methods do not show over and undershoots; this is due to the fact that these schemes are monotone. This property will prove useful when computing solutions to general hyperbolic systems. However, monotone methods are at most first-order accurate and thus they need to be extended to higher order of accuracy, by circumventing the Godunov theorem via the construction of non-linear methods. This subject will be addressed in Sect. 4.

Further Reading For further reading we recommend the following books [1–4].

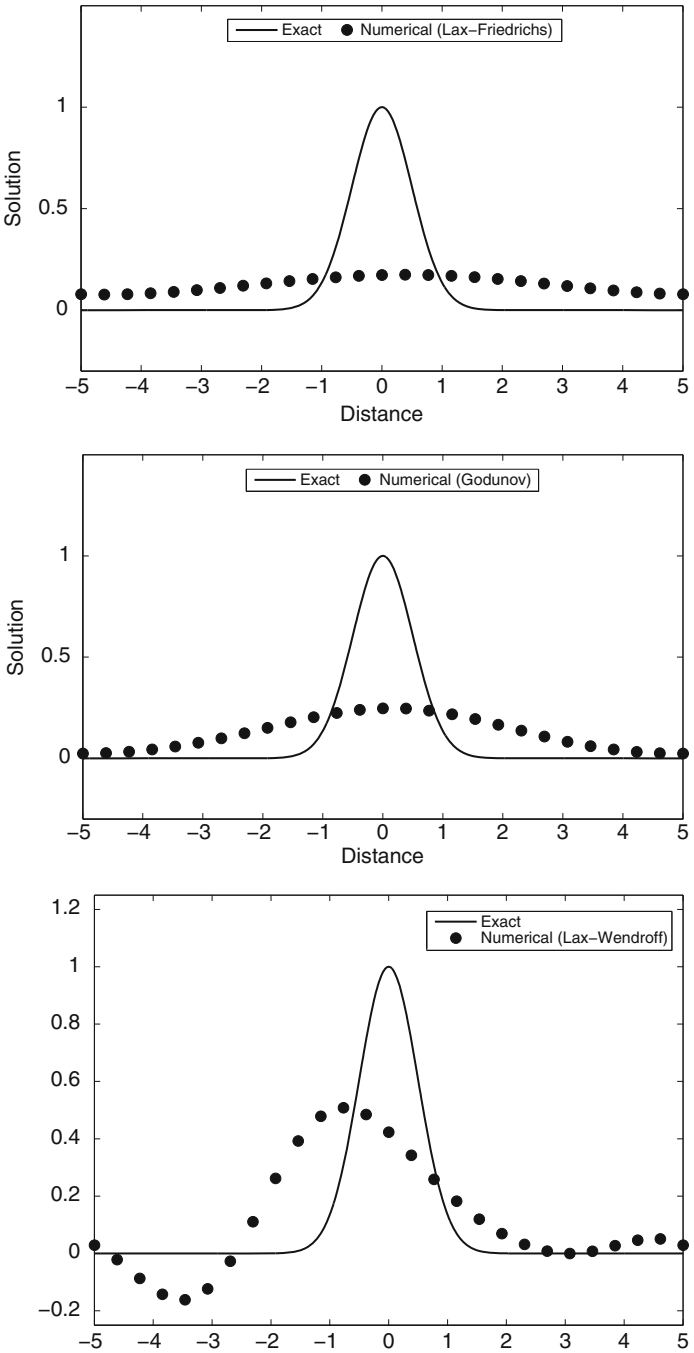

Fig. 23 Test 1 for smooth solution. Results at time $t = 100$ from the Lax-Friedrichs, Godunov and Lax-Wendroff methods. Mesh used M = 25 and Courant number CFL = 0.9

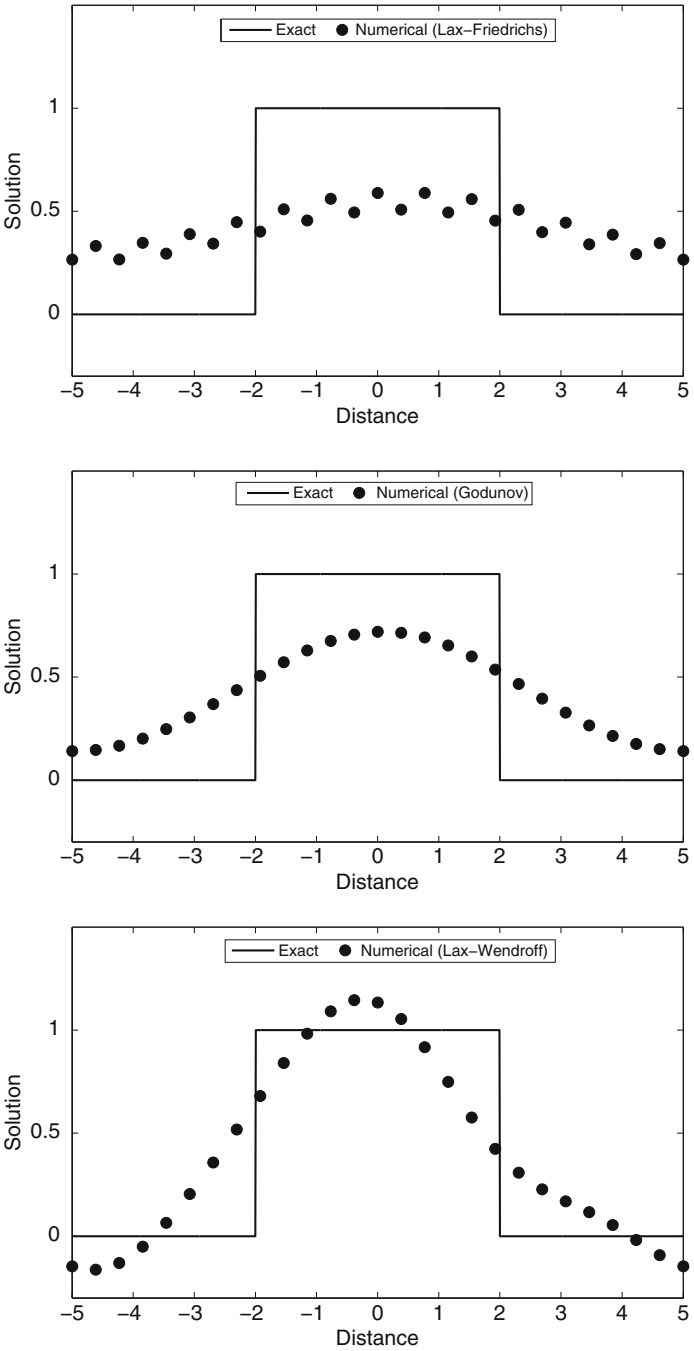

Fig. 24 Test 2 for discontinuous solution. Results at time $t = 100$ from the Lax-Friedrichs, Godunov and Lax-Wendroff methods. Mesh used M = 25 and Courant number CFL = 0.9

2 The Shallow Water Equations and the Riemann Problem

In this section we study a particular non-linear hyperbolic system of practical interest, namely the shallow water equations. We first establish the governing equations and some of their properties and then solve exactly the corresponding Riemann problem. For further reading see [2].

2.1 Equations, Properties and Wave Relations

The equation for conservation of mass reads

$$\partial_t h + \partial_x (hu) = 0 \,, \tag{117}$$

where $h(x,t)$ is water depth and $u(x,t)$ is the particle velocity. The equation for conservation of momentum reads

$$\partial_t (hu) + \partial_x (hu^2 + \frac{1}{2} g h^2) = 0 \,, \tag{118}$$

where g is the acceleration due to gravity. Recall that the *celerity* is defined as

$$a = \sqrt{gh} \,, \tag{119}$$

which is analogous to the *speed of sound* in a gas. In certain applications it is of interest to consider an additional PDE

$$\partial_t \psi + u \partial_x \psi = 0 \,. \tag{120}$$

$\psi(x,t)$ is transported with $u(x,t)$ and is often called a *passive scalar*. If we assume that solutions are smooth, then from (117) and (120) we obtain the conservation equation

$$\partial_t (h\psi) + \partial_x (h\psi u) = 0 \,. \tag{121}$$

Now the three equations of interest are (117), (118) and (121). These can be written in conservation form as

$$\partial_t \mathbf{Q} + \partial_x \mathbf{F}(\mathbf{Q}) = \mathbf{0} \,, \tag{122}$$

with

$$\mathbf{Q} = \begin{bmatrix} q_1 \\ q_2 \\ q_3 \end{bmatrix} = \begin{bmatrix} h \\ hu \\ h\psi \end{bmatrix} \,, \quad \mathbf{F}(\mathbf{Q}) = \begin{bmatrix} f_1 \\ f_2 \\ f_3 \end{bmatrix} = \begin{bmatrix} hu \\ hu^2 + \frac{1}{2} g h^2 \\ h\psi u \end{bmatrix} \,. \tag{123}$$

Here $\mathbf{Q}$ is called the vector of conserved variables and $\mathbf{F}(\mathbf{Q})$ if the physical flux vector.

Quasi-linear Form and Eigenvalues Equation (122) can be written in quasi-linear form as follows

$$\partial_t \mathbf{Q} + \mathbf{A}(\mathbf{Q})\partial_x \mathbf{Q} = \mathbf{0}\,, \tag{124}$$

where $\mathbf{A}(\mathbf{Q})$ is the Jacobian matrix given as

$$\mathbf{A}(\mathbf{Q}) = \begin{bmatrix} \dfrac{\partial f_1}{\partial q_1} & \dfrac{\partial f_1}{\partial q_2} & \dfrac{\partial f_1}{\partial q_3} \\ \dfrac{\partial f_2}{\partial q_1} & \dfrac{\partial f_2}{\partial q_2} & \dfrac{\partial f_2}{\partial q_3} \\ \dfrac{\partial f_3}{\partial q_1} & \dfrac{\partial f_3}{\partial q_2} & \dfrac{\partial f_3}{\partial q_3} \end{bmatrix}\,. \tag{125}$$

From (123) we have

$$\mathbf{F}(\mathbf{Q}) = \begin{bmatrix} f_1(q_1, q_2, q_3) \\ f_2(q_1, q_2, q_3) \\ f_3(q_1, q_2, q_3) \end{bmatrix} = \begin{bmatrix} hu \\ hu^2 + \frac{1}{2}gh^2 \\ h\psi u \end{bmatrix} = \begin{bmatrix} q_2 \\ \dfrac{q_2^2}{q_1} + \dfrac{1}{2}gq_1^2 \\ \dfrac{q_2 q_3}{q_1} \end{bmatrix}\,. \tag{126}$$

Note that each component f_k of the flux vector has been expressed in terms of the components q_j of the vector of conserved variables. This is necessary before proceeding to calculate the partial derivatives. Calculating now the partial derivatives in (125) and then using the physical variables u, a and ψ we may write the Jacobian matrix as

$$\mathbf{A}(\mathbf{Q}) = \begin{bmatrix} 0 & 1 & 0 \\ a^2 - u^2 & 2u & 0 \\ -u\psi & \psi & u \end{bmatrix}\,. \tag{127}$$

The eigenvalues are the roots of the *characteristic polynomial*

$$P(\hat{\lambda}) = Det(\mathbf{A} - \hat{\lambda}\mathbf{I}) = 0\,, \tag{128}$$

where $\mathbf{I}$ is the identity matrix and $\hat{\lambda}$ is a parameter. It is easily verified that

$$P(\hat{\lambda}) = (u - \hat{\lambda})[\hat{\lambda}(2u - \hat{\lambda}) + a^2 - u^2] = 0\,, \tag{129}$$

a cubic equation, for which three real solutions exist, and therefore the system has three real eigenvalues, namely

$$\lambda_1 = u - a \ , \quad \lambda_2 = u \ , \quad \lambda_3 = u + a \ . \tag{130}$$

Note that all three roots are distinct if $a \neq 0$.

Right Eigenvectors A right eigenvector $\mathbf{R}$ corresponding to $\hat{\lambda}$ satisfies

$$\mathbf{AR} = \hat{\lambda}\mathbf{R} \ . \tag{131}$$

For a generic $\mathbf{R} = [r_1, r_2, r_3]^T$ we have

$$\left.\begin{array}{rl} r_2 & = \hat{\lambda} r_1 \ , \\ (a^2 - u^2) r_1 + 2 u r_2 & = \hat{\lambda} r_2 \ , \\ -u\psi r_1 + \psi r_2 + u r_3 & = \hat{\lambda} r_3 \ . \end{array}\right\} \tag{132}$$

To find $\mathbf{R}_i$ corresponding to λ_i we substitute λ_i into (132) and solve the resulting system for r_1, r_2 and r_3 in terms of free parameters α_i. The result is

$$\mathbf{R}_1 = \alpha_1 \begin{bmatrix} 1 \\ u - a \\ \psi \end{bmatrix} \ , \quad \mathbf{R}_2 = \alpha_2 \begin{bmatrix} 0 \\ 0 \\ 1 \end{bmatrix} \ , \quad \mathbf{R}_3 = \alpha_3 \begin{bmatrix} 1 \\ u + a \\ \psi \end{bmatrix} \ , \tag{133}$$

where α_1, α_2 and α_3 are arbitrary *scaling factors* which can be chosen as desired.

Left Eigenvectors To compute a *left eigenvector* $\mathbf{L} = [l_1, l_2, l_3]$ corresponding to an eigenvalue $\hat{\lambda}$, we solve the system of algebraic equations

$$\mathbf{LA} = \hat{\lambda}\mathbf{L} \ . \tag{134}$$

The *left eigenvectors* of $\mathbf{A}$ are given by

$$\left.\begin{array}{l} \mathbf{L}_1 = \beta_1 \left[-(u + a) \ , \ 1 \ , \ 0 \right] \ , \\ \mathbf{L}_2 = \beta_2 \left[-\psi \ , \ 0 \ , \ 1 \right] \ , \\ \mathbf{L}_3 = \beta_3 \left[-(u - a) \ , \ 1 \ , \ 0 \right] \ , \end{array}\right\} \tag{135}$$

where the coefficients β_1, β_2, β_3 are arbitrary *scaling factors*.

Bi-orthonormality of Left and Right Eigenvectors The reader can easily verify that the right and left eigenvectors (133), (135) of the Jacobian matrix $\mathbf{A}$ are

bi-orthonormal, that is they satisfy the relations

$$\mathbf{L}_i \cdot \mathbf{R}_j = \begin{cases} 1 \text{ if } i = j \,, \\ \\ 0 \text{ if } i \neq j \,, \end{cases} \tag{136}$$

if the scaling factors are chosen thus

$$\beta_1 = \frac{1}{2a\alpha_1} \,, \quad \beta_2 = \frac{1}{\alpha_2} \,, \quad \beta_3 = -\frac{1}{2a\alpha_3} \,. \tag{137}$$

Nature of Characteristic Fields First recall that a λ_i-characteristic field is said to be *linearly degenerate* if

$$\nabla\lambda_i(\mathbf{Q}) \cdot \mathbf{R}_i(\mathbf{Q}) = 0 \,, \quad \forall \mathbf{Q} \in \Re^m \tag{138}$$

$$\nabla\lambda_i(\mathbf{Q}) = \left[\frac{\partial}{\partial q_1}\lambda_i \,, \; \frac{\partial}{\partial q_2}\lambda_i \,, \; \ldots \,, \; \frac{\partial}{\partial q_m}\lambda_i \right]^{\mathrm{T}} \,. \tag{139}$$

Now we show that *the λ_2-characteristic field is linearly degenerate*.

$$\lambda_2(\mathbf{Q}) = u = \frac{hu}{h} = \frac{q_2}{q_1}$$

$$\nabla\lambda_2(\mathbf{Q}) = \left[\frac{\partial}{\partial q_1}\lambda_2 \,, \; \frac{\partial}{\partial q_2}\lambda_2 \,, \; \frac{\partial}{\partial q_3}\lambda_2 \right]^{\mathrm{T}} = \left[-\frac{u}{h} \,, \; \frac{1}{h} \,, \; 0 \right]^{\mathrm{T}} \,.$$

Then

$$\nabla\lambda_2(\mathbf{Q}) \cdot \mathbf{R}_2(\mathbf{Q}) = 0 \tag{140}$$

for $\mathbf{Q} \in \Re^3$ and thus the λ_2-characteristic field is *linearly degenerate*.

The λ_1- and λ_3-characteristic fields are genuinely nonlinear. First recall that a λ_i-characteristic field is said to be *genuinely non-linear* if

$$\nabla\lambda_i(\mathbf{Q}) \cdot \mathbf{R}_i(\mathbf{Q}) \neq 0 \,, \quad \forall \mathbf{Q} \in \Re^m \,. \tag{141}$$

Simple calculations give

$$\nabla\lambda_1(\mathbf{Q}) \cdot \mathbf{R}_1(\mathbf{Q}) = -\tfrac{3}{2a} \neq 0 \;\text{ and }\; \nabla\lambda_3(\mathbf{Q}) \cdot \mathbf{R}_3(\mathbf{Q}) = \tfrac{3}{2a} \neq 0 \,. \tag{142}$$

Therefore the $\lambda_1(\mathbf{Q})$ and $\lambda_3(\mathbf{Q})$ characteristic fields are *genuinely non-linear*, if $a \neq 0$.

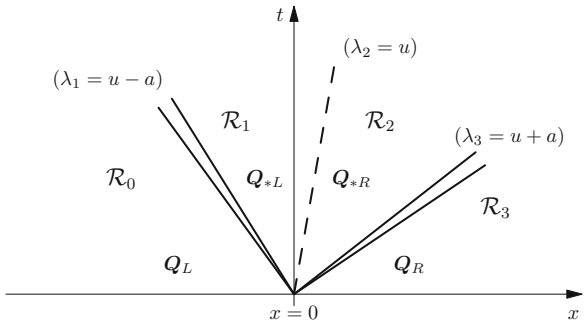

Fig. 25 Structure of the solution of the Riemann problem for the augmented 1D shallow water equations

2.2 The Riemann Problem

The Riemann problem for the shallow water equation (122) is the initial value problem

$$\left.\begin{array}{l} \text{PDEs: } \partial_t \mathbf{Q} + \partial_x \mathbf{F}(\mathbf{Q}) = \mathbf{0}\,, \quad -\infty < x < \infty\,,\ t > 0\,, \\ \text{ICs: } \quad \mathbf{Q}(x,0) = \begin{cases} \mathbf{Q}_L & \text{if } x < 0\,, \\ \mathbf{Q}_R & \text{if } x > 0\,. \end{cases} \end{array}\right\} \tag{143}$$

The vector of conservative variables $\mathbf{Q}$ and the vector of fluxes $\mathbf{F}(\mathbf{Q})$ are given in (123). $\mathbf{Q}_L$ and $\mathbf{Q}_R$ are two constant vectors that define the initial conditions of the problem.

Structure of the Solution of the Riemann Problem
The structure of the solution in the $x-t$ plane is shown in Fig. 25. Note that there are three wave families separating four constant regions. The outer waves are non-linear and are associated with shocks or rarefactions. The middle wave is linear (called contact discontinuity). The solution in regions $\mathscr{R}_0$ and $\mathscr{R}_3$ is known, corresponding to the initial data on the left and right respectively. The solution in regions $\mathscr{R}_1$ and $\mathscr{R}_2$ (Star Region) is unknown. The full problem of solving the Riemann problem is divided into two subproblems: Problem 1: *The Star Problem* and Problem 2: *The Complete Solution*. We start with the *The Star Problem* for which we first establish some conventional wave relations.

2.2.1 Wave Relations

Rarefactions and Generalized Riemann Invariants Generalized Riemann Invariants (GRIs) are relations that apply **across** the wave structure of simple waves in $x - t$ space. For a system of m equations consider the $\lambda_j(\mathbf{Q})$-characteristic

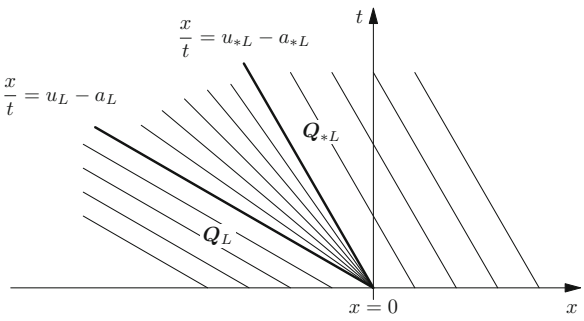

Fig. 26 Left rarefaction wave connecting states $\mathbf{Q}_L$ and $\mathbf{Q}_{*L}$. The characteristic line $x/t = u_L - a_L$ defines the **head** and the characteristic line $x/t = u_{*L} - a_{*L}$ defines the **tail**

field and the corresponding right eigenvector

$$\mathbf{R}_j = \left[r_{1j}, r_{2j}, \cdots, r_{mj}\right]^{\mathrm{T}} \ . \tag{144}$$

The GRIs apply *across* the wave structure and lead to $m - 1$ ODEs in phase space:

$$\frac{dq_1}{r_{1j}} = \frac{dq_2}{r_{2j}} = \frac{dq_3}{r_{3j}} = \cdots = \frac{dq_m}{r_{mj}} \ . \tag{145}$$

Equation (145) relate ratios of dq_i to r_{ij} and we emphasize that the ratios are to be interpreted as meaning proportionality, that is

$$dq_i \propto r_{ij} \ . \tag{146}$$

If $r_{ij} = 0$ then $dq_i = 0$ and therefore q_i does not change across the respective wave. We now apply these wave relations to study a particular class of waves.

Left Rarefaction Wave Assume a left rarefaction wave connecting $\mathbf{Q}_L$ (left) and $\mathbf{Q}_{*L}$ (right). See Fig. 26. The rarefaction wave occupies a wedge $\mathscr{R}_L$ defined as

$$\mathscr{R}_L = \left\{(x,t)/ \quad u_L - a_L \le \frac{x}{t} \le u_{*L} - a_{*L}\right\} \ , \tag{147}$$

where the characteristic line $x/t = u_L - a_L$ defines the **head** and the characteristic line $x/t = u_{*L} - a_{*L}$ defines the **tail**. $\lambda_1(\mathbf{Q})$ increases monotonically across the wave from head to tail. Application of GRIs across the λ_1-wave with $\mathbf{Q} = [h, hu, h\psi]^T$ and $\mathbf{R}_1 = [1, u - a, \psi]^T$ gives

$$\frac{dh}{1} = \frac{d(hu)}{u - a} = \frac{d(h\psi)}{\psi} \ . \tag{148}$$

From the first and third ratios $d\psi = 0$ and so across the λ_1 wave

$$\psi : \text{constant} \ . \tag{149}$$

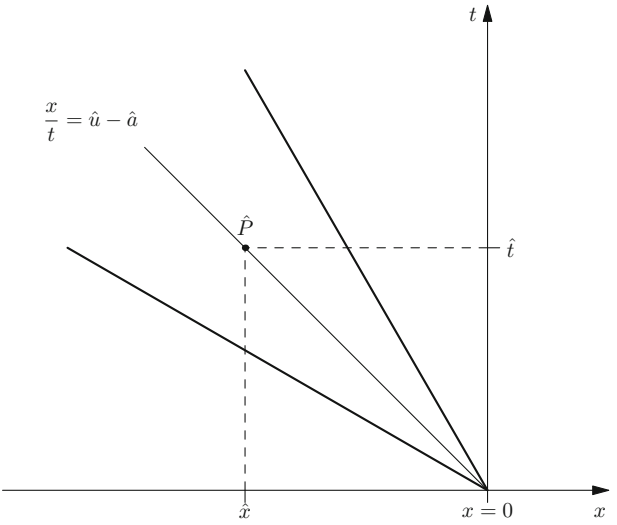

Fig. 27 Point $\hat{P} = (\hat{x}, \hat{t})$ inside left rarefaction wave. We seek the solution for the celerity a and the particle velocity u at the point $\hat{P}$ in terms of its prescribed coordinates $\hat{x}, \hat{t}$

Analogously, from first and second ratios, along with integration in phase space we obtain

$$u + 2a = \text{constant} \, . \tag{150}$$

From here we establish

$$u_{*L} + 2a_{*L} = u_L + 2a_L \, , \tag{151}$$

which we also express as

$$u_{*L} = u_L - f_L \, ; \quad f_L = 2(a_{*L} - a_L) \, . \tag{152}$$

Solution Inside a Rarefaction Consider a left rarefaction wave and a point inside the wave. See Fig. 27. The point inside the rarefaction wave is $\hat{P} = (\hat{x}, \hat{t}) \in \mathscr{R}_L$. Consider now a characteristic line through $\hat{P} = (\hat{x}, \hat{t})$ and the origin $(0, 0)$, of slope (known)

$$\frac{\hat{x}}{\hat{t}} = \hat{u} - \hat{a} \, . \tag{153}$$

The unknowns of the problem are $\hat{u} = u(\hat{x}, \hat{t})$ and $\hat{a} = a(\hat{x}, \hat{t})$, noting that h follows from a. Application of the left Riemann invariant (150) to connect the point $\hat{P}$ to the

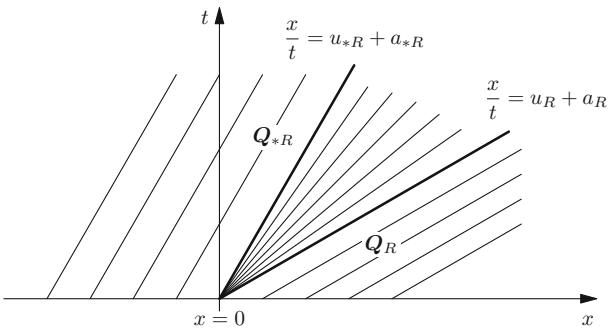

Fig. 28 Right rarefaction wave connecting states $\mathbf{Q}_{*R}$ and $\mathbf{Q}_R$. The characteristic line $x/t = u_R + a_R$ defines the head while $x/t = u_{*R} + a_{*R}$ defines the tail

left initial condition gives

$$\hat{u} + 2\hat{a} = u_L + 2a_L \, . \tag{154}$$

Equations (153) and (154) are two equations for the two unknowns $\hat{a}$ and $\hat{u}$, whose solution is

$$\hat{a}_L = a(\hat{x}, \hat{t}) = \frac{1}{3}(u_L + 2a_L - \frac{\hat{x}}{\hat{t}}) \, , \quad \hat{u}_L = u(\hat{x}, \hat{t}) = \frac{1}{3}(u_L + 2a_L + \frac{2\hat{x}}{\hat{t}}) \, . \tag{155}$$

Right Rarefaction Wave Assume a right rarefaction wave, as depicted in Fig. 28, connecting the constant states $\mathbf{Q}_{*R}$ (left) and $\mathbf{Q}_R$ (right). The wave occupies a wedge $\mathscr{R}_R$

$$\mathscr{R}_R = \left\{ (x,t) / \quad u_{*R} + a_{*R} \leq \frac{x}{t} \leq u_R + a_R \right\} \, . \tag{156}$$

$\lambda_3(\mathbf{Q})$ is monotone. The right generalized Riemann invariant gives

$$u - 2a = \text{constant} \, , \quad \psi \, : \text{constant} \, . \tag{157}$$

From here we obtain

$$u_{*R} - 2a_{*R} = u_R - 2a_R \, , \tag{158}$$

which we also express as

$$u_{*R} = u_R + f_R \, ; \quad f_R = 2(a_{*R} - a_R) \, . \tag{159}$$

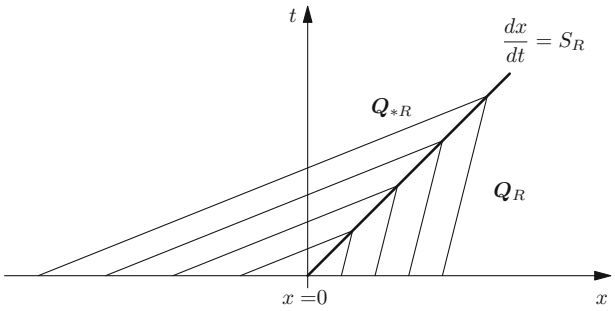

Fig. 29 Right-facing shock wave of speed S_R connecting constant states $\mathbf{Q}_R$ (ahead) and $\mathbf{Q}_{*R}$ (behind)

The solution at $\hat{P} = (\hat{x}, \hat{t}) \in \mathscr{R}_R$ inside the right rarefaction wave can easily be found to be

$$\hat{a}_R = \frac{1}{3}(-u_R + 2a_R + \frac{\hat{x}}{\hat{t}}) \ , \ \hat{u}_R = \frac{1}{3}(u_R - 2a_R + \frac{2\hat{x}}{\hat{t}}) \ . \tag{160}$$

Right-Facing Shock Wave Consider an isolated right-facing shock wave of speed S_R associated with the λ_3-characteristic field, as depicted in Fig. 29. For system (122), across the shock, the **Rankine-Hugoniot Conditions** apply and thus we have

$$S_R(\mathbf{Q}_R - \mathbf{Q}_{*R}) = \mathbf{F}(\mathbf{Q}_R) - \mathbf{F}(\mathbf{Q}_{*R}) \ . \tag{161}$$

In addition, the shock must also satisfy the Lax entropy condition

$$\lambda_3(\mathbf{Q}_{*R}) > S_R > \lambda_3(\mathbf{Q}_R) \ . \tag{162}$$

Characteristics run into the shock path, as illustrated in Fig. 29. Now we apply the transformation

$$\hat{u}_{*R} = u_{*R} - S_R \ , \quad \hat{u}_R = u_R - S_R \ , \tag{163}$$

which is illustrated in Fig. 30. In the new frame the shock propagation speed is 0 and the vectors of conserved variables and fluxes ahead of the shock are

$$\hat{\mathbf{Q}}_R = \begin{bmatrix} h_R \\ h_R\hat{u}_R \\ h_R\psi_R \end{bmatrix} \ , \quad \hat{\mathbf{F}}_R = \begin{bmatrix} h_R\hat{u}_R \\ h_R\hat{u}_R^2 + \frac{1}{2}gh_R^2 \\ h_R\hat{u}_R\psi_R \end{bmatrix} \ , \tag{164}$$

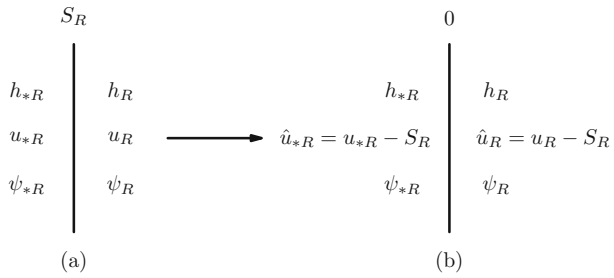

Fig. 30 Right shock wave in two frames of reference. Frame (**a**) is the original frame of reference and frame (**b**) is the moving frame of references in which the shock is stationary

while those behind the shock are

$$\hat{\mathbf{Q}}_{*R} = \begin{bmatrix} h_{*R} \\ h_{*R}\hat{u}_{*R} \\ h_{*R}\psi_{*R} \end{bmatrix} , \quad \hat{\mathbf{F}}_{*R} = \begin{bmatrix} h_{*R}\hat{u}_{*R} \\ h_{*R}\hat{u}_{*R}^2 + \frac{1}{2}gh_{*R}^2 \\ h_{*R}\hat{u}_{*R}\psi_{*R} \end{bmatrix} . \tag{165}$$

The Rankine-Hugoniot conditions in the moving frame are

$$\mathbf{F}(\hat{\mathbf{Q}}_{*R}) - \mathbf{F}(\hat{\mathbf{Q}}_R) = \mathbf{0} \times (\hat{\mathbf{Q}}_{*R} - \hat{\mathbf{Q}}_R) , \tag{166}$$

which give

$$\mathbf{F}(\hat{\mathbf{Q}}_{*R}) = \mathbf{F}(\hat{\mathbf{Q}}_R) .$$

The above flux equality written in full gives

$$\left.\begin{array}{rcl} h_{*R}\hat{u}_{*R} & = & h_R\hat{u}_R , \\ h_{*R}\hat{u}_{*R}^2 + \frac{1}{2}gh_{*R}^2 & = & h_R\hat{u}_R^2 + \frac{1}{2}gh_R^2 , \\ h_{*R}\hat{u}_{*R}\psi_{*R} & = & h_R\hat{u}_R\psi_R . \end{array}\right\} \tag{167}$$

The first equation in (167) says that the mass flux is constant across the shock, that is

$$-M_R \equiv h_{*R}\hat{u}_{*R} = h_R\hat{u}_R . \tag{168}$$

Using this into the third of Eq. (167) gives

$$\psi_{*R} = \psi_R . \tag{169}$$

That is, ψ is constant across the shock wave. Thus we only need to work with the first two equations in (167); the second one gives

$$(h_{*R}\hat{u}_{*R})\hat{u}_{*R} - (h_R\hat{u}_R)\hat{u}_R = \frac{1}{2}g(h_R^2 - h_{*R}^2) . \tag{170}$$

Use of (168) into (170) gives

$$M_R = \frac{\frac{1}{2}g(h_R^2 - h_{*R}^2)}{\hat{u}_R - \hat{u}_{*R}} \ . \tag{171}$$

But from (168) we write

$$\hat{u}_{*R} = -\frac{M_R}{h_{*R}} \ , \quad \hat{u}_R = -\frac{M_R}{h_R} \ . \tag{172}$$

Use of (172) into (171) followed by some manipulations yields

$$M_R = \sqrt{\frac{1}{2}gh_Rh_{*R}(h_R + h_{*R})} \ . \tag{173}$$

From (163)

$$u_{*R} = u_R + (\hat{u}_{*R} - \hat{u}_R) \ . \tag{174}$$

Inserting (172) into (174) followed by some algebraic manipulations gives

$$u_{*R} = u_R + f_R \ ; \quad f_R = (h_{*R} - h_R)\sqrt{\frac{1}{2}g\frac{(h_{*R} + h_R)}{h_Rh_{*R}}} \ . \tag{175}$$

From (163) we have

$$S_R = u_R - \hat{u}_R \ . \tag{176}$$

Use of (172) into (176) followed by manipulations gives

$$S_R = u_R + q_Ra_R \ , \quad q_R = \sqrt{\frac{1}{2}\frac{(h_R + h_{*R})h_{*R}}{h_R^2}} \ . \tag{177}$$

This expression relates the shock speed to the unknown depth h_{*R} behind the shock. Note that for the limiting case $h_{*R}/h_R = 1$ the shock speed coincides with the characteristic speed, that is $S_R = u + a$, as expected.

Left-Facing Shock Wave For a left-facing shock of speed S_L associated with the eigenvalue $\lambda_1 = u - a$ the analysis is similar to that of a right shock. See Fig. 31. First we define the transformation

$$\hat{u}_{*L} = u_{*L} - S_L \ ; \quad \hat{u}_L = u_L - S_L \ . \tag{178}$$

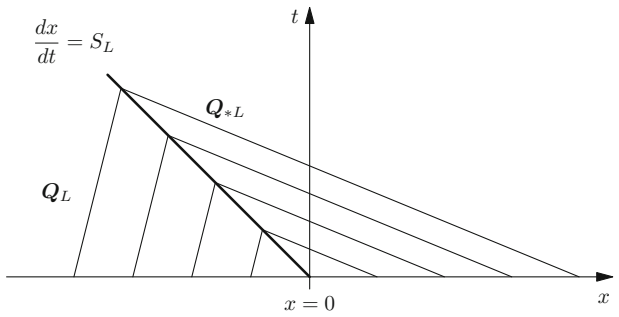

Fig. 31 Left-facing shock wave of speed S_L connecting states $\mathbf{Q}_L$ (ahead) and $\mathbf{Q}_{*L}$ (behind)

Then the Rankine-Hugoniot conditions give

$$\left.\begin{array}{rcl} h_{*L}\hat{u}_{*L} & = & h_L\hat{u}_L\,, \\ h_{*L}\hat{u}_{*L}^2 + \frac{1}{2}gh_{*L}^2 & = & h_L\hat{u}_L^2 + \frac{1}{2}gh_L^2\,, \\ h_{*L}\hat{u}_{*L}\psi_{*L} & = & h_L\hat{u}_L\psi_L\,. \end{array}\right\} \tag{179}$$

The first of Eq. (179) says that the mass flux

$$M_L \equiv h_{*L}\hat{u}_{*L} = h_L\hat{u}_L \tag{180}$$

is constant across the shock wave. Using this condition into the third of Eq. (179) gives

$$\psi_{*L} = \psi_L\,. \tag{181}$$

In other words the passive scalar ψ is constant across the right shock. Analogous manipulations to those for a right-facing shock yield

$$M_L = \sqrt{\frac{1}{2}gh_Lh_{*L}(h_L + h_{*L})} \tag{182}$$

and

$$u_{*L} = u_L - f_L\,; \quad f_L = (h_{*L} - h_L)\sqrt{\frac{1}{2}g\frac{(h_{*L} + h_L)}{h_Lh_{*L}}}\,. \tag{183}$$

This relates u_{*L} to h_{*L} via the function f_L. Also, from (178)

$$S_L = u_L - \hat{u}_L\,. \tag{184}$$

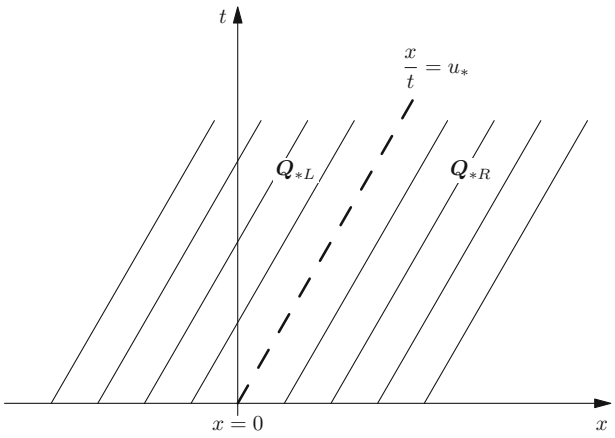

Fig. 32 Contact wave associated with the linearly degenerate field λ_2, connecting states $\mathbf{Q}_{*L}$ and $\mathbf{Q}_{*R}$. Characteristics either side of the wave are parallel to the wave, just as in the linear advection equation

Use of (180) into (184) followed by manipulations gives

$$S_L = u_L - q_L a_L \; ; \quad q_L = \sqrt{\frac{1}{2}\frac{(h_L + h_{*L})h_{*L}}{h_L^2}} \; . \tag{185}$$

This expression relates S_L to h_{*L}. Again, in the limiting case $h_{*L}/h_L = 1$ we have $S_L = u - a$.

Contact Discontinuity Wave An isolated contact discontinuity connecting the (constant) states $\mathbf{Q}_{*L}$ and $\mathbf{Q}_{*R}$ associated with the λ_2-characteristic field is depicted in Fig. 32. The wave is a single discontinuity travelling with speed u_* and characteristics either side of the discontinuity run parallel to it, namely

$$\lambda_2(\mathbf{Q}_{*L}) = u_* = \lambda_2(\mathbf{Q}_{*R}) \; . \tag{186}$$

An eigenvector analysis provides the sought jump conditions across the contact discontinuity. The right eigenvector corresponding to λ_2 is $\mathbf{R}_2 = [0, 0, 1]^T$, from which we have

$$\left.\begin{array}{l} u_{*L} = u_{*R} = u_* \; , \\ h_{*L} = h_{*R} = h_* \; , \\ \psi_{*L} \neq \psi_{*R} \; . \end{array}\right\} \tag{187}$$

Exercise Show that the above solution for the contact discontinuity wave satisfies the Rankine-Hugoniot conditions across the wave.

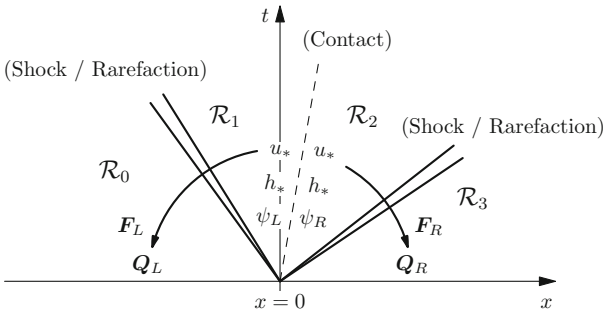

Fig. 33 Structure of the solution of the Riemann problem for the augmented shallow water equations

2.2.2 Solution of Problem 1: The Star Problem

Figure 33 depicts the structure of the solution of the Riemann problem in the $x - t$ plane. The left and right waves can be shocks or rarefactions. The velocity and depth are constant in the *Star Region*; ψ is also constant in $\mathscr{R}_1 \cup \mathscr{R}_0$ and in $\mathscr{R}_2 \cup \mathscr{R}_3$ but with a discontinuous jump across the contact wave. To find the velocity u_* and the depth h_* we first assemble together all the wave relations derived for each elementary wave in isolation. Note that the velocity u_* is connected to $\mathbf{Q}_L$ via a function f_L and that the velocity u_* is connected to $\mathbf{Q}_R$ via a function f_R; the functions f_L and f_R depend on the unknown depth h_*, the *wave type* (shock or rarefaction) and, parametrically, on the initial conditions $\mathbf{Q}_L$ and $\mathbf{Q}_R$, that is

$$f_L = f_L(h_*, w_L; \mathbf{Q}_L) \; ; \quad f_R = f_R(h_*, w_R; \mathbf{Q}_R) \; . \tag{188}$$

Here w_L and w_R denote logical variables that identify the wave type; w_K denotes either a shock or a rarefaction, for $K = L$ and $K = R$. The complete solution procedure for the *Star Problem* is then summarised in the following proposition.

Proposition *The solution h_* for the Riemann problem (143) is the root of*

$$f(h) \equiv f_L(h, w_L; h_L) + f_R(h, w_R; h_R) + \Delta u = 0 \; , \quad \Delta u \equiv u_R - u_L \; , \tag{189}$$

$$f_L(h, w_L; h_L) = \begin{cases} 2(\sqrt{gh} - \sqrt{gh_L}) & \text{if } \; h \le h_L \; (w_L\text{: rarefaction}) \; , \\ (h - h_L)\sqrt{\dfrac{1}{2} g \dfrac{(h + h_L)}{h h_L}} & \text{if } \; h > h_L \; (w_L\text{: shock}) \; , \end{cases} \tag{190}$$

$$f_R(h, w_R; h_R) = \begin{cases} 2(\sqrt{gh} - \sqrt{gh_R}) & \text{if } h \le h_R \ (w_R\text{: rarefaction}) , \\ (h - h_R)\sqrt{\dfrac{1}{2} g \dfrac{(h + h_R)}{h h_R}} & \text{if } h > h_R \ (w_R\text{: shock}) , \end{cases} \tag{191}$$

Once the depth h_* has been found the solution for the velocity u_* follows as

$$u_* = \tfrac{1}{2}(u_L + u_R) + \tfrac{1}{2}[f_R(h_*, w_R; h_R) - f_L(h_*, w_L; h_L)] . \tag{192}$$

Sketch of the Proof First note that the particle velocity u_* and depth h_* are constant across the contact discontinuity according to (187). In fact u_* and h_* are constant in the entire *Star region*. Then, the function f_L is used to relate u_* to the left initial condition $\mathbf{Q}_L$ across the left wave. In case the left wave is a shock we have the relation (183) and if it is a rarefaction we use (152). Analogously, the function f_R is used to relate u_* to the right initial condition $\mathbf{Q}_R$ across the right wave. If the right wave is a shock we have the relation (175) and if it is a rarefaction we use (159). As $u_* = u_{*L} = u_{*R}$, see (187), we can eliminate u_* resulting in Eq. (189). Then the particle velocity could be written in terms of the function f_L, for both the shock and rarefaction cases. See (183) and (152). So we could compute u_* directly from f_L once h_* is known. Alternatively, we could compute u_* directly from f_R using (175) or (159). Solution (192) results from a mean of the two possible solutions. This concludes the proof.

Iterative Solution for h_* We need to solve the algebraic non-linear equation (189) for the unknown h_* in the *Star Region*. To my knowledge, there is no general close-form solution available to this equation and therefore we must solve it *numerically* through an iteration procedure. To perform this task there are several methods available, one choice being the Newton-Raphson method

$$h^{(k+1)} = h^{(k)} - \frac{f(h^{(k)})}{f'(h^{(k)})} , \tag{193}$$

for $k = 0, 1, \ldots, K$. Here $f'(h)$ denotes the derivative of f with respect to h. The iteration (193) is stopped whenever the change in h is smaller than a prescribed small positive tolerance *TOL*, that is when

$$\Delta h \equiv \frac{|h^{(k+1)} - h^{(l)}|}{(h^{(k+1)} + h^{(l)})/2} < TOL . \tag{194}$$

Usually one takes $TOL = 10^{-6}$. Having formulated and solved numerically the Eq. (189) for h_*, the solution for u_* follows directly from (192).

The Two-Rarefaction Case and Guess Value The iterative procedure (193) requires a guess value $h^{(0)}$ to start the iteration. To this end we use a two-rarefaction

type approximation, as we now describe. Assume a-priori that the two non-linear waves associated with the eigenvalues λ_1 and λ_3 are both rarefaction waves. See Fig. 33. Then the functions f_L and f_R in (190), (191) respectively are those corresponding to rarefaction waves. Then (189) becomes

$$f(h) \equiv 2(a - a_L) + 2(a - a_R) + u_R - u_L = 0 \,, \tag{195}$$

which has exact solution, called the **Two-Rarefaction Solution**. For the celerity a one has

$$a_{TR} = \frac{1}{2}(a_L + a_R) - \frac{1}{4}(u_R - u_L) \,. \tag{196}$$

From the definition of celerity we obtain

$$h^{(0)} = \frac{a_{TR}^2}{g} \,, \tag{197}$$

which is used as a starting value in the iteration procedure (193).

2.2.3 Solution of Problem 2: The Complete Solution

Now we put together all the components of the solution so as to be able to compute the solution $\mathbf{Q}(x, t)$ for any given point (x, t) in the x-t half plane, $-\infty < x < \infty$ and $t \geq 0$. See Fig. 34. We call this task the solution sampling procedure in which we assume that the depth h_* and velocity u_* in the *Star Region* are already known. The solution $\mathbf{Q}(x, t)$ is sought at a specified time $\hat{t}$ for any x in a finite interval $[x_l, x_r]$ containing the full wave system, as depicted in Fig. 34. Then $\mathbf{Q}(x, \hat{t})$ is a function of x alone and gives a profile at time $\hat{t}$. To sample the solution we make use of the

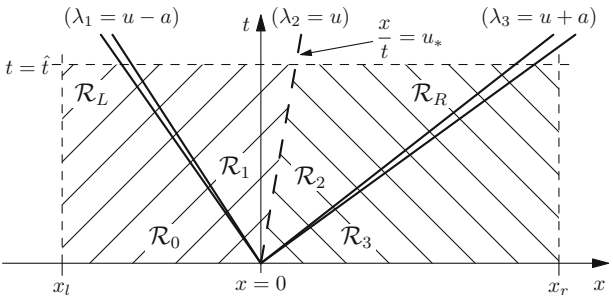

Fig. 34 Sampling the solution through the complete wave structure, at a chosen time $\hat{t}$

contact discontinuity to divide the full domain into the two subregions

$$\mathscr{R}_L = \left\{(x,t)/ \quad \frac{x}{t} \le u_*\right\} , \quad \mathscr{R}_R = \left\{(x,t)/ \quad u_* < \frac{x}{t}\right\} . \tag{198}$$

To perform the sampling we represent the solution in terms of the vector of physical variables $\mathbf{W} = [h, u, \psi]^T$ and make use of the similarity variable

$$\xi = x/\hat{t} \tag{199}$$

to locate the sampling point and assign the corresponding solution $\mathbf{W}(\xi)$. Note that ξ has dimensions of *velocity*. There are two cases.

- **Sampling point lies to the left of the contact.** The solution $\mathbf{W}(\xi)$ for $(x, \hat{t}) \in \mathscr{R}_L$ depends on the wave type. There are two possibilities:
  Left shock. If the left wave is a shock of speed S_L, then $\mathscr{R}_L$ is again subdivided into two subregions and the solution is

$$\mathbf{W}(\xi) \equiv \begin{cases} \mathbf{W}_{*L} = [h_*, u_*, \psi_L]^T & \text{if } S_L \le \xi \le u_* , \\ \mathbf{W}_L = [h_L, u_L, \psi_L]^T & \text{if } \quad \xi < S_L , \end{cases} \tag{200}$$

  where the shock speed S_L is given by (185).

  Left Rarefaction If the left wave is a rarefaction then $\mathscr{R}_L$ is subdivided into three subregions and the solution is

$$\mathbf{W}(\xi) = \begin{cases} \mathbf{W}_L = [h_L, u_L, \psi_L]^T & \text{if } \quad \xi \le u_L - a_L , \\ \mathbf{W}_{Lfan} = \left[\hat{h}_L, \hat{u}_L, \psi_L\right]^T & \text{if } u_L - a_L \le \xi \le u_* - a_* , \\ \mathbf{W}_{*L} = [h_*, u_*, \psi_L]^T & \text{if } \quad u_* - a_* \le \xi \le u_* , \end{cases} \tag{201}$$

  where $\hat{h}_L$ and $\hat{u}_L$ inside the left rarefaction are obtained from (155).

- **Sampling point lies to the right of the contact.** The solution $\mathbf{W}(\xi)$ for $(x, \hat{t}) \in \mathscr{R}_R$ depends on the type of the left wave present. Again there are two possibilities.
  Right shock. If the right wave is a shock of speed S_R, then $\mathscr{R}_R$ is again subdivided into two subregions and the solution is

$$\mathbf{W}(\xi) \equiv \begin{cases} \mathbf{W}_{*R} = [h_*, u_*, \psi_R]^T & \text{if } u_* \le \xi \le S_R , \\ \mathbf{W}_R = [h_R, u_R, \psi_R]^T & \text{if } \quad \xi > S_R , \end{cases} \tag{202}$$

  where the shock speed S_R is given by (177).

Table 1 Initial conditions for two Riemann problems for the shallow water equations

Test	x_0	T_{out}	h_L	u_L	h_R	u_R
1	10.0	7.0	1.0	2.5	0.1	0.0
2	25.0	2.5	1.0	10.0	1.0	-10.0

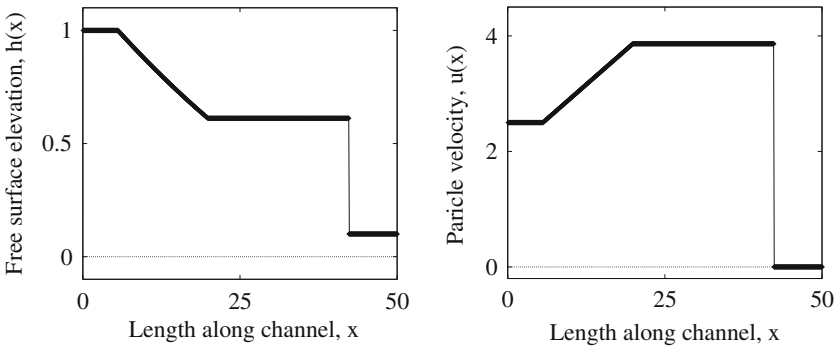

Fig. 35 Test 1. Solution profiles for h and u at the output time $T_{out} = 7.0s$. The solution consists of a left rarefaction and a right shock

Right Rarefaction If the right wave is a rarefaction then $\mathscr{R}_R$ is subdivided into three subregions and the solution is

$$\mathbf{W}(\xi) = \begin{cases} \mathbf{W}_R &= [h_R, u_R, \psi_R]^T \quad \text{if} \quad \xi > u_R + a_R \,, \\ \mathbf{W}_{Rfan} &= \left[\hat{h}_R, \hat{u}_R, \psi_R\right]^T \quad \text{if} \; u_{*R} + a_* \le \xi \le u_R + a_R \,, \\ \mathbf{W}_{*R} &= [h_*, u_*, \psi_R]^T \quad \text{if} \quad u_* \le \xi \le u_{*R} + a_* \,, \end{cases} \tag{203}$$

where $\hat{h}_R$ and $\hat{u}_R$ inside the right rarefaction are derived from (160).

Test Problems Here we solve two specific Riemann problems for the shallow water equations in a finite channel of length 50 m. Table 1 gives the initial conditions and computational details. Column 2 gives the position of the initial discontinuity and column 3 gives the output time. The remaining columns give the initial conditions for depth h and velocity u. Note that in these examples we have not considered the equation for a passive scalar. Figures 35 and 36 show profiles for tests 1 and 2 respectively.

2.3 Concluding Remarks

In this section we have introduced the 1D shallow water equations augmented by a passive scalar, and studied its salient mathematical properties. We have solved *exactly* the corresponding Riemann problem, whose solution can be used to construct Godunov-type finite volume numerical methods and discontinuous Galerkin

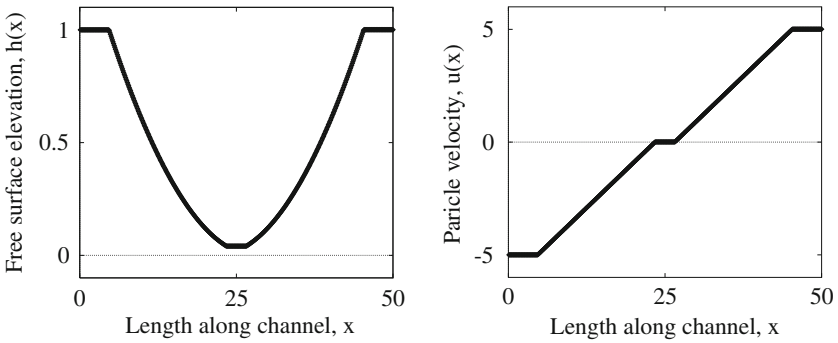

Fig. 36 Test 2. Solution profiles for h and u at the output time $T_{out} = 2.5s$. The solution consists of two rarefaction waves

finite element methods. Moreover, this exact solution can be used to construct approximate solutions (approximate Riemann solvers) to be used in numerical methods. Note also that the exact solution can be used to assess the correctness and accuracy of numerical computations intended for solving the shallow water equations.

Further reading material is found in [2] and [1] and in references therein.

3 Godunov's Method for the Shallow Water Equations

We study the Godunov method [5] as applied to a general non-linear hyperbolic system, and in particular as applied to the 1D shallow water equations. We consider two approaches for computing the Godunov flux: the first requires the calculation of *the Godunov state*, that is the state along the t-axis in the solution of the Riemann problem, see Sect. 2. Then, the numerical flux is simply the *physical flux* function evaluated at this Godunov state. In the second approach one calculates a numerical flux directly.

General Initial-Boundary Value Problem (IBVP) First we apply the Godunov's method to a generic nonlinear hyperbolic system. Consider the IBVP for any non-linear hyperbolic system

$$\left.\begin{array}{ll} \text{PDEs:} & \partial_t \mathbf{Q} + \partial_x \mathbf{F}(\mathbf{Q}) = \mathbf{0} \ , \quad x \in [a,b] \ , \quad t > 0 \ , \\ \text{ICs:} & \mathbf{Q}(x,0) = \mathbf{Q}^{(0)}(x) \ , \quad x \in [a,b] \ , \\ \text{BCs:} & \mathbf{Q}(a,t) = \mathbf{B}_L(t) \ , \quad \mathbf{Q}(b,t) = \mathbf{B}_R(t) \ , \quad t \geq 0 \ . \end{array}\right\} \tag{204}$$

$\mathbf{Q}(x,t)$ is the vector of conserved variables; $\mathbf{F}(\mathbf{Q})$ is the flux function, or *physical flux*; $\mathbf{Q}^{(0)}(x)$ is the initial condition; $\mathbf{B}_L(t)$ and $\mathbf{B}_R(t)$ are the boundary conditions on the left and right boundaries respectively, two prescribed functions of time.

3.1 The Finite Volume Method

Unlike the finite difference method introduced in Sect. 1, the finite volume discretisation of the domain considers a partition of the entire $x-t$ domain into space-time *finite volumes*, as in Fig. 12 of Sect. 1. In the numerical context these finite volumes are denoted as $V_i = [x_{i-\frac{1}{2}}, x_{i+\frac{1}{2}}] \times [t_n, t_{n+1}]$. Figure 37c shows three consecutive finite volumes. Here $\Delta t = t_{n+1} - t_n$ denotes the time step and $\Delta = x_{i+\frac{1}{2}} - x_{i-\frac{1}{2}}$ denotes the cell spatial size, or mesh size; $x_{i+\frac{1}{2}}$ denotes the volume interface. With this notation, the exact integration of the equations in the generic finite volume V_i gives the finite volume formula

$$\mathbf{Q}_i^{n+1} = \mathbf{Q}_i^n - \frac{\Delta t}{\Delta x}\left(\mathbf{F}_{i+\frac{1}{2}} - \mathbf{F}_{i-\frac{1}{2}}\right) , \tag{205}$$

with

$$\mathbf{Q}_i^n \approx \frac{1}{\Delta x}\int_{x_{i-\frac{1}{2}}}^{x_{i+\frac{1}{2}}} \mathbf{Q}(x, t_n)dx \tag{206}$$

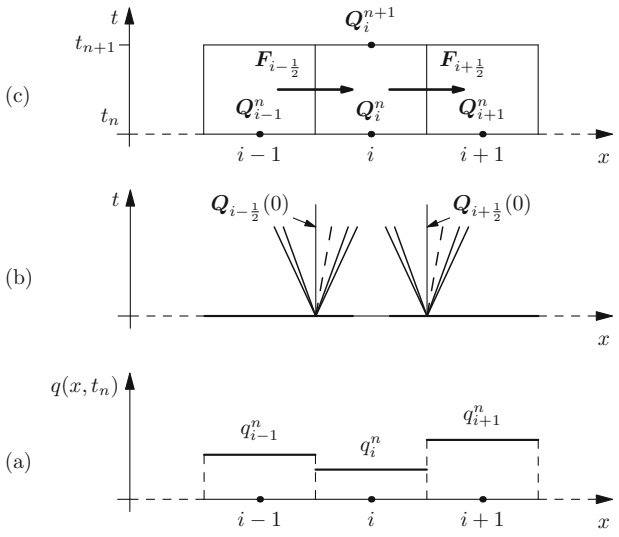

Fig. 37 Godunov's method for a hyperbolic system: (**a**) integral averages for one component q of the vector $\mathbf{Q}$ in each interval $[x_{i-\frac{1}{2}}, x_{i+\frac{1}{2}}]$ at time t_n give piece-wise constant data; (**b**) structure of solutions of Riemann problems at intercell boundaries determined by piece wise constant data; (**c**) finite volume formula to update averages using numerical fluxes

and

$$\mathbf{F}_{i+\frac{1}{2}} \approx \frac{1}{\Delta t}\int_{t_n}^{t_{n+1}} \mathbf{F}(\mathbf{Q}(x_{i+\frac{1}{2}}, t))dt \ . \tag{207}$$

See Eqs. (60) and (61) in Sect. 1. Formula (205) serves to update approximations to spatial integral averages (206) using numerical fluxes that are approximations to time integral averages (207) at the cell interface $x_{i+\frac{1}{2}}$. See Fig. 37.

3.1.1 The Godunov Flux

To define the finite volume scheme (205) we prescribe suitable approximations to the integral (207) to obtain the *numerical flux* $\mathbf{F}_{i+\frac{1}{2}}$. The Godunov upwind numerical flux $\mathbf{F}_{i+\frac{1}{2}}$ is computed from (207), making use of the solution $\mathbf{Q}_{i+\frac{1}{2}}(x/t)$ of the *local* Riemann problem

$$\left.\begin{array}{l} \text{PDEs: } \partial_t \mathbf{Q} + \partial_x \mathbf{F}(\mathbf{Q}) = \mathbf{0} \ , \\ \\ \text{ICs:} \quad \mathbf{Q}(x,0) = \left\{ \begin{array}{ll} \mathbf{Q}_L \equiv \mathbf{Q}_i^n & \text{if } \ x < 0 \ , \\ \\ \mathbf{Q}_R \equiv \mathbf{Q}_{i+1}^n & \text{if } \ x > 0 \ . \end{array} \right. \end{array} \right\} \tag{208}$$

The Godunov flux is computed from (207) and becomes

$$\mathbf{F}_{i+\frac{1}{2}} = \mathbf{F}(\mathbf{Q}_{i+\frac{1}{2}}(0)) \ . \tag{209}$$

$\mathbf{Q}_{i+\frac{1}{2}}(0)$ is called the *Godunov state* and results from $\mathbf{Q}_{i+\frac{1}{2}}(x/t)$ evaluated at the interface $x/t = 0$. Note that for convenience, at each interface $x_{i+\frac{1}{2}}$ and time level t_n we use *local coordinates* through a change from global to local coordinates as follows:

$$\left.\begin{array}{ll} \bar{x} = x - x_{i+\frac{1}{2}} & , \bar{t} = t - t^n \ , \\ x \in [x_i, x_{i+1}] & , \ t \in [t^n, t^{n+1}] \ , \\ \bar{x} \in [-\frac{\Delta x}{2}, \frac{\Delta x}{2}] & , \bar{t} \in [0, \Delta t] \ . \end{array} \right\} \tag{210}$$

We then use (x, t) to mean the local coordinates $(\bar{x}, \bar{t})$. See Fig. 38. In what follows we specialise Godunov's method to the shallow water equations.

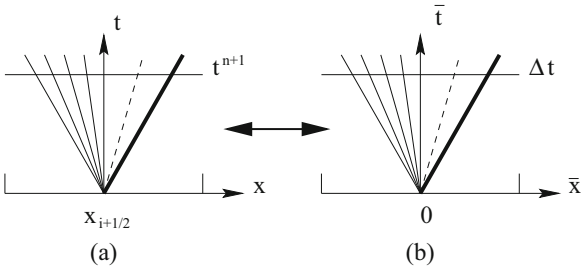

Fig. 38 Correspondence between the global (**a**) and local (**b**) frames of reference for the solution of the Riemann problem

3.1.2 Godunov Flux with the Exact Riemann Solver

One first solves the **Star problem**; the solution for h_* and u_* in the *Star Region* is found. To this end one solves the non-linear equation (using Newton-Raphson method, for example)

$$f(h) \equiv f_L(h) + f_R(h) + \Delta u = 0 \,, \quad \Delta u \equiv u_R - u_L \,. \tag{211}$$

All details on the Riemann problem are given in Sect. 2. Once the water depth $h = h_*$ has been found the velocity u_* is calculated as

$$u_* = \tfrac{1}{2}(u_L + u_R) + \tfrac{1}{2}[f_R(h_*) - f_L(h_*)] \,. \tag{212}$$

Note that not always the *Godunov state* needed for flux evaluation corresponds to the **Star State**, for which it is necessary to go through a *sampling procedure* to find the Godunov state $\mathbf{Q}_{i+\frac{1}{2}}(0)$ for flux evaluation, see Sect. 2.
If a **passive scalar** is present in the equations, then one simply chooses

$$\psi(x,t) = \begin{cases} \psi_L \;\; \text{if} \;\; \dfrac{x}{t} < u_* \,, \\ \\ \psi_R \;\; \text{if} \;\; \dfrac{x}{t} > u_* \,. \end{cases} \tag{213}$$

This completes the description of Godunov's flux as applied to the augmented 1D shallow water equations, using the exact Riemann solver.

In practice one resorts to approximate solution methods to find a Godunov-type flux. We next describe several approaches but before doing so we address some issues that emerge when having to choose an approximate Riemann solver. We first recall that the Godunov method is the most accurate monotone numerical method, as shown for the scalar linear case in Sect. 1. For systems, first recall that the concept of monotone method does not exist, it is only a scalar concept. Then, on the accuracy question, one knows that this depends crucially on the particular *Riemann solver* used. The exact solver is the best but at the cost of (i) complexity and (ii) computational expense. Computational expense however has to be seen in light of

efficiency, that is, in relation to the error. The computational expense of the exact Riemann solver is not excessive for systems such as for blood flow, shallow water and ideal gas dynamics. Still, approximate Riemann solvers can and are used for these systems but great care is required in choosing the appropriate approximation. The following remarks are in order:

1. Good approximate Riemann solvers are required to be:
   - **Complete:** their **wave model** contains all characteristic fields of the exact Riemann problem.
   - **Non-linear.** Linearised Riemann solvers have various defects and are thus to be avoided whenever possible.
2. The simplest Riemann solver is the Rusanov solver, as we shall see its wave model contains just one wave.
3. At the bottom of the hierarchy of numerical fluxes are **centred methods**, such as the Lax-Friedrichs and FORCE fluxes.
4. Centred, or symmetric, methods may be the simplest but not the most efficient, as we shall see later.

3.2 A Simple Linearised Riemann Solver

As an academic example here, we study a linearised Riemann solver, even if in practice, such solvers are to be avoided. We look for approximations to h_* and u_* in the *Star Region*. First we re-write the governing equations in terms of primitive, or physical, variables h, u and ψ.

$$\partial_t \mathbf{P} + \mathbf{M}(\mathbf{P})\partial_x \mathbf{P} = \mathbf{0} \,, \tag{214}$$

with

$$\mathbf{P} = \begin{bmatrix} h \\ u \\ \psi \end{bmatrix} \,, \quad \mathbf{M}(\mathbf{P}) = \begin{bmatrix} u & h & 0 \\ g & u & 0 \\ 0 & 0 & u \end{bmatrix} \,. \tag{215}$$

Denote the initial conditions for the Riemann problem as

$$\mathbf{P}_L = \begin{bmatrix} h_L \\ u_L \\ \psi_L \end{bmatrix} \,, \quad \mathbf{P}_R = \begin{bmatrix} h_R \\ u_R \\ \psi_R \end{bmatrix} \,. \tag{216}$$

Now assume $\mathbf{P}_L$ is close to $\mathbf{P}_R$ and linearise system (214) about

$$\tilde{h} = \frac{1}{2}(h_L + h_R) \,, \quad \tilde{u} = \frac{1}{2}(u_L + u_R) \tag{217}$$

so that the nonlinear system (214) becomes the linear system

$$\partial_t \mathbf{P} + \hat{\mathbf{M}} \partial_x \mathbf{P} = \mathbf{0} \ , \tag{218}$$

with constant coefficient matrix

$$\hat{\mathbf{M}} = \begin{bmatrix} \hat{u} & \hat{h} & 0 \\ g & \hat{u} & 0 \\ 0 & 0 & \hat{u} \end{bmatrix} \ . \tag{219}$$

The linear Riemann problem for (218) with initial conditions (216) is solved *exactly* by using standard methods for hyperbolic linear systems, see Sect. 1, to obtain

$$\left.\begin{aligned} h_* &= \frac{1}{2}(h_L + h_R) - \frac{1}{2}(u_R - u_L)/\bar{C} \ , \\ u_* &= \frac{1}{2}(u_L + u_R) - \frac{1}{2}(h_R - h_L)\bar{C} \ , \\ \bar{C} &= \sqrt{\frac{2g}{h_L + h_R}} \ . \end{aligned}\right\} \tag{220}$$

Remarks About the Linearised Solution

1. The solution for $\psi(x, y)$ is as given by (213), though u_* is an approximation.
2. A sampling procedure to find $\mathbf{Q}_{i+\frac{1}{2}}(0)$ for evaluating the numerical flux is required.
3. This Riemann solver is very simple but not robust enough.
4. It fails for strong rarefactions, near the vacuum state.
5. It fails for trans-critical (or sonic) flow, leading to entropy violating shocks (or rarefaction shocks).
6. This Riemann solver is **complete** but **linear**.
7. In general, linearised Riemann solvers are not recommended for practical use.

3.3 A Two-Rarefaction Riemann Solver

Starting from the exact Riemann solver, by directly assuming that both non-linear waves are rarefactions, constancy of Riemann invariants leads to

$$u_* + 2c_* = u_L + 2c_L \ , \quad u_* - 2c_* = u_R - 2c_R \ . \tag{221}$$

There follows that

$$\left.\begin{aligned} u_* &= \tfrac{1}{2}(u_L + u_R) - (c_R - c_L) \ , \\ c_* &= \tfrac{1}{2}(c_L + c_R) - \tfrac{1}{4}(u_R - u_L) \ , \\ h_* &= \tfrac{1}{g}(c_*)^2 \ . \end{aligned}\right\} \tag{222}$$

The solution for $\psi(x, y)$ is as given by (213), though u_* is an approximation. The sampling procedure to find $\mathbf{Q}_{i+\frac{1}{2}}(0)$ for evaluating the numerical flux is required; this is the same as for the exact Riemann solver. This Riemann solver is very simple, **complete** and **non-linear**; in practice it is also shown to be very robust.

3.4 The Harten-Lax-van Leer (HLL) Riemann Solver

We want to solve the Riemann problem (208) approximately with the aim of finding directly a numerical flux of the form

$$\mathbf{F}_0 = \frac{1}{T}\int_0^T \mathbf{F}(\mathbf{Q}(0, t))dt \tag{223}$$

for an arbitrary time $T > 0$ and where $\mathbf{Q}(0, t)$ is an approximate solution of the Riemann problem along the t-axis (the Godunov state); see Fig. 39. Here we construct a numerical flux following the HLL approach proposed by Harten, Lax and van Leer [7]. We first establish some useful relations obtained by applying the integral form of the conservation laws on appropriately chosen control volumes.

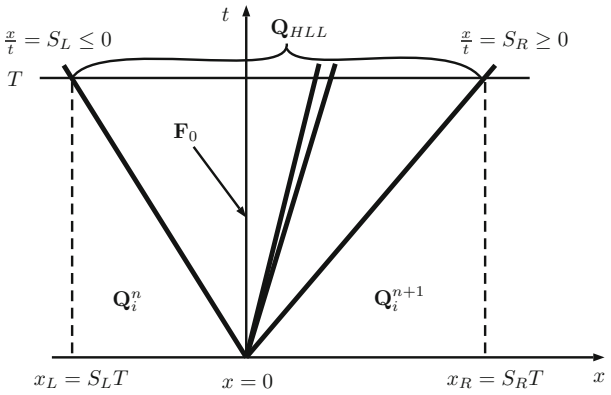

Fig. 39 Wave pattern used for the derivation of the HLL flux for a subcritical, or subsonic, wave pattern, $S_L \leq 0$ and $S_R \geq 0$

Consider the control volume $[x_L, 0] \times [0, T]$ in the space-time configuration of Fig. 39. Assume the fastest signals perturbing the constant initial states $\mathbf{Q}_L \equiv \mathbf{Q}_i^n$ and $\mathbf{Q}_R \equiv \mathbf{Q}_{i+1}^n$ emerging from the Riemann problem solution are S_L (for left travelling signals) and S_R (for right travelling signals). Assume the wave configuration is subsonic, that is $S_L \leq 0$ and $S_R \geq 0$. Then, for an arbitrary time $T > 0$ we define the distances

$$x_L = TS_L \ , \quad x_R = TS_R \ . \tag{224}$$

Applying the integral form of the conservation laws (204) in the control volume $[x_L, 0] \times [0, T]$ we obtain

$$\int_{x_L}^{0} \mathbf{Q}(x, T)dx = \int_{x_L}^{0} \mathbf{Q}(x, 0)dx + \int_{0}^{T} \mathbf{F}(\mathbf{Q}(x_L, t))dt - \int_{0}^{T} \mathbf{F}(\mathbf{Q}(0, t))dt \ . \tag{225}$$

Evaluation of the first and second terms on the right hand side gives

$$\int_{x_L}^{0} \mathbf{Q}(x, 0)dx = -S_L T\mathbf{Q}_L \ ; \quad \int_{0}^{T} \mathbf{F}(\mathbf{Q}(x_L, t))dt = T\mathbf{F}(\mathbf{Q}_L) \ . \tag{226}$$

Inserting these into (225) and dividing through by T gives

$$\mathbf{F}_0 = \frac{1}{T}\int_{0}^{T} \mathbf{F}(\mathbf{Q}(0, t))dt = -S_L\mathbf{Q}_L + \mathbf{F}(\mathbf{Q}_L) - \frac{1}{T}\int_{x_L}^{0} \mathbf{Q}(x, T))dx \ . \tag{227}$$

To define $\mathbf{F}_0$ approximately it is sufficient to find an approximation to the integral on the right hand side of (227). This is accomplished by finding an approximate state $\mathbf{Q}(x, T)$ by adopting an approach analogous to the Lax-Wendroff method, or to the Godunov centred method; see [1]. Applying the integral form (225) of the conservation laws (204) in the control volume $[x_L, x_R] \times [0, T]$, see Fig. 39, we obtain

$$\int_{x_L}^{x_R} \mathbf{Q}(x, T)dx = \int_{x_L}^{x_R} \mathbf{Q}(x, 0)dx + \int_{0}^{T} \mathbf{F}(\mathbf{Q}(x_L, t))dt - \int_{0}^{T} \mathbf{F}(\mathbf{Q}(x_R, t))dt \ . \tag{228}$$

The first term on the right hand side gives

$$\int_{x_L}^{x_R} \mathbf{Q}(x, 0)dx = -S_L T\mathbf{Q}_L + S_R T\mathbf{Q}_R \ . \tag{229}$$

Substitution of this expression into (228) and evaluation of the integrals gives

$$\int_{x_L}^{x_R} \mathbf{Q}(x, T)dx = T[S_R\mathbf{Q}_R - S_L\mathbf{Q}_L + \mathbf{F}(\mathbf{Q}_L) - \mathbf{F}(\mathbf{Q}_R)] \ . \tag{230}$$

On division through by $x_R - x_L = T(S_R - S_L)$ we obtain the averaged state

$$\mathbf{Q}^{HLL} = \frac{1}{(x_R - x_L)} \int_{x_L}^{x_R} \mathbf{Q}(x, T)dx = \frac{S_R\mathbf{Q}_R - S_L\mathbf{Q}_L + \mathbf{F}(\mathbf{Q}_L) - \mathbf{F}(\mathbf{Q}_R)}{S_R - S_L} . \tag{231}$$

We now use the state $\mathbf{Q}^{HLL}$ to evaluate the integral on the right hand side of (227). The resulting intercell flux is

$$\mathbf{F}_0 = \frac{S_R\mathbf{F}(\mathbf{Q}_L) - S_L\mathbf{F}(\mathbf{Q}_R) + S_LS_R(\mathbf{Q}_R - \mathbf{Q}_L)}{S_R - S_L} . \tag{232}$$

The HLL Flux Finally the HLL flux for the approximate Godunov method is

$$\mathbf{F}^{HLL}_{i+\frac{1}{2}} = \begin{cases} \mathbf{F}_L & \text{if} \quad 0 \le S_L , \\ \dfrac{S_R\mathbf{F}(\mathbf{Q}_L) - S_L\mathbf{F}(\mathbf{Q}_R) + S_LS_R(\mathbf{Q}_R - \mathbf{Q}_L)}{S_R - S_L} & \text{if} \quad S_L \le 0 \le S_R , \\ \mathbf{F}_R & \text{if} \quad 0 \ge S_R . \end{cases} \tag{233}$$

To complete the HLL scheme it is necessary to find estimates for S_L and S_R. In [2], the following estimates are suggested

$$S_L = u_L - q_Lc_L , \quad S_R = u_R + q_Rc_R . \tag{234}$$

Here q_K $(K = L, R)$ are obtained according to the type of non-linear waves present

$$q_K = \begin{cases} \sqrt{\dfrac{1}{2}\dfrac{(\bar{h}_* + h_K)\bar{h}_*}{h_K^2}} & \text{if} \quad \bar{h}_* > h_K , \\ 1 & \text{if} \quad \bar{h}_* \le h_K . \end{cases} \tag{235}$$

The scheme is complete by defining $\bar{h}_* \approx h_*$, the depth in the Star Region. Here we suggest to use the simple but robust estimate from (222). Given wave speed estimates S_L and S_R, HLL is most easily implemented noting also that HLL is a **non-linear** Riemann solver and entropy satisfying. HLL is **complete** but only for systems of two equations. For larger systems HLL is **incomplete**.

HLL Rusanov and Lax-Friedrichs Schemes Well-known methods can be derived from HLL, as a special cases. For example, **The Rusanov flux** [8] can be derived

from HLL by assuming $S^+ = S_R$ and $S_L = -S^+$. Then we obtain

$$\mathbf{F}^{Rus}_{i+\frac{1}{2}} = \frac{1}{2}\left[\mathbf{F}(\mathbf{Q}_L) + \mathbf{F}(\mathbf{Q}_R)\right] - \frac{1}{2}S^+(\mathbf{Q}_R - \mathbf{Q}_L)\ . \tag{236}$$

The Rusanov scheme is the simplest upwind method, it has a 1-wave model and is non-linear. But obviously the Rusanov method is incomplete for any system of equations.

The well-known Lax-Friedrichs method can also be derived from HLL and more specifically from Rusanov by choosing $S^+ = \frac{\Delta x}{\Delta t}$, producing the Lax-Friedrichs flux

$$\mathbf{F}^{LF}_{i+\frac{1}{2}} = \frac{1}{2}\left[\mathbf{F}(\mathbf{Q}_L) + \mathbf{F}(\mathbf{Q}_R)\right] - \frac{1}{2}\frac{\Delta x}{\Delta t}(\mathbf{Q}_R - \mathbf{Q}_L)\ . \tag{237}$$

The wave model of the Lax-Friedrichs method has zero waves. It is the most diffusive (most inaccurate) stable method for hyperbolic equations. I would not recommend its use for practical computations.

3.5 The HLLC Riemann Solver

HLL ignores intermediate waves in systems of three or more equations, leading to excessive numerical dissipation for these waves. A possible improvement, called HLLC, was first proposed by Toro and collaborators in 1992 [9]; see also [10] and [11]. The HLLC approximate Riemann solver is a modification of HLL that accounts for intermediate waves in the solution of the Riemann problem. See Fig. 40.

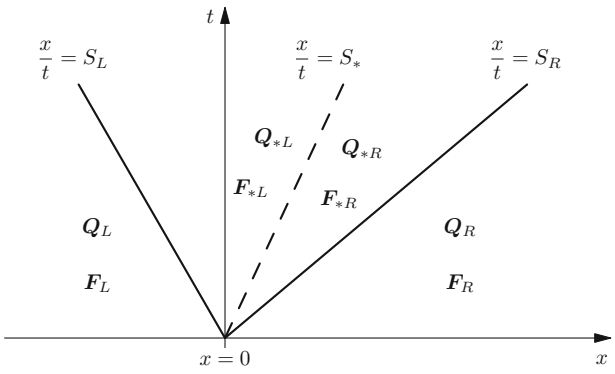

Fig. 40 Assumed wave pattern for the HLLC Riemann solver. The Star Region contains two sub-regions separated by the intermediate wave

Consider the wave pattern depicted in Fig. 40, where an intermediate wave of speed S_* is present. Application of the integral form of the conservation laws in $[x_L, 0] \times [0, T]$ and in $[0, x_R] \times [0, T]$ yield

$$\mathbf{F}_{*L} = \mathbf{F}_L + S_L(\mathbf{Q}_{*L} - \mathbf{Q}_L) \ , \quad \mathbf{F}_{*R} = \mathbf{F}_R + S_R(\mathbf{Q}_{*R} - \mathbf{Q}_R) \ . \tag{238}$$

Here there are two vector equations for four unknown vectors $\mathbf{Q}_{*L}$, $\mathbf{Q}_{*R}$, $\mathbf{F}_{*L}$ and $\mathbf{R}_{*R}$. To solve this overdetermined algebraic system we make the following additional assumptions

$$h_{*L} = h_{*R} = h_* \ , \quad u_{*L} = u_{*R} = u_* = S_* \ . \tag{239}$$

As a matter of fact the above assumptions are true for the exact Riemann solver, as seen in Sect. 2. From the first component of the first vector equation in (238) we write

$$h_* u_* = h_L u_L + S_L(h_* - h_L) \ . \tag{240}$$

From the first component of the second vector equation in (238) we write

$$h_* u_* = h_R u_R + S_R(h_* - h_R) \ . \tag{241}$$

From (240) and (241) we write

$$h_* = \frac{h_R(u_R - S_R)}{u_* - S_R} = \frac{h_L(u_L - S_L)}{u_* - S_L} \ . \tag{242}$$

From here we obtain

$$u_* = S_* = \frac{S_L h_R(u_R - S_R) - S_R h_L(u_L - S_L)}{h_R(u_R - S_R) - h_L(u_L - S_L)} \ . \tag{243}$$

If S_L and S_R are prescribed, then h_* is known from (242)–(243). Then the vectors $\mathbf{Q}_{*L}$ and $\mathbf{Q}_{*R}$ in (238) are given as

$$\mathbf{Q}_{*L} = h_* \begin{bmatrix} 1 \\ S_* \\ \psi_L \end{bmatrix} \ , \quad \mathbf{Q}_{*R} = h_* \begin{bmatrix} 1 \\ S_* \\ \psi_R \end{bmatrix} \ . \tag{244}$$

Now the vectors $\mathbf{F}_{*L}$ and $\mathbf{F}_{*R}$ in (238) are determined and finally the HLLC flux is given as

$$\mathbf{F}^{HLLC}_{i+\frac{1}{2}} = \begin{cases} \mathbf{F}_L & \text{if} \quad 0 \le S_L \ , \\ \mathbf{F}_{*L} = \mathbf{F}_L + S_L(\mathbf{Q}_{*L} - \mathbf{Q}_L) & \text{if} \quad S_L \le 0 \le S_* \ , \\ \mathbf{F}_{*R} = \mathbf{F}_R + S_R(\mathbf{Q}_{*R} - \mathbf{Q}_R) & \text{if} \quad S_* \le 0 \le S_R \ , \\ \mathbf{F}_R & \text{if} \quad 0 \ge S_R \ , \end{cases} \tag{245}$$

where the states $\mathbf{Q}_{*L}$, $\mathbf{Q}_{*R}$ are given by (244). The wave speed estimates for S_L and S_R are as for the HLL flux, see (234), and for S_* we use (243).

The use of HLLC instead of HLL for a system including the passive scalar ψ makes a dramatic difference to the resolution of the contact wave. This is particularly evident for long-time evolution problems.

3.6 The Dumbser-Osher-Toro Riemann Solver: DOT

Here we present a modification of the Osher-Solomon Riemann solver [12] that makes the approach much more practical and applicable to any hyperbolic system for which the complete eigenstructure is known, either analytically of numerically. The resulting scheme is non-linear and complete. The modification is due to Dumbser and Toro [13, 14].

3.6.1 Definitions and Notation

Consider a general $m \times m$ hyperbolic system

$$\partial_t \mathbf{Q} + \partial_x \mathbf{F}(\mathbf{Q}) = \mathbf{0} \,, \tag{246}$$

with conserved variables and flux vectors respectively denoted as

$$\mathbf{Q} = [q_1, q_2, \ldots, q_m]^T \,, \quad \mathbf{F} = [f_1, f_2, \ldots, f_m]^T \,. \tag{247}$$

The real eigenvalues are $\lambda_i(\mathbf{Q})$ and the corresponding right eigenvectors are $\mathbf{R}_i(\mathbf{Q})$, for $i = 1, 2, \ldots, m$. Here we consider Godunov-type finite volume schemes to solve (246)

$$\mathbf{Q}_i^{n+1} = \mathbf{Q}_i^n - \frac{\Delta t}{\Delta x}(\mathbf{F}_{i+\frac{1}{2}} - \mathbf{F}_{i-\frac{1}{2}}) \,, \tag{248}$$

where $\mathbf{F}_{i+\frac{1}{2}}$ is the numerical flux found by solving the Riemann problem for (246) with initial condition

$$\mathbf{Q}(x, 0) = \begin{cases} \mathbf{Q}_0 & \text{if } x < 0 \,, \\ \mathbf{Q}_1 & \text{if } x > 0 \,. \end{cases} \tag{249}$$

Recall that hyperbolicity of system (246) is equivalent to saying that the Jacobian matrix $\mathbf{A}(\mathbf{Q})$ of the flux $\mathbf{F}(\mathbf{Q})$ is diagonalizable, that is

$$\mathbf{A}(\mathbf{Q}) = \mathbf{R}(\mathbf{Q}) \Lambda(\mathbf{Q}) \mathbf{R}^{-1}(\mathbf{Q}) \,, \tag{250}$$

where $\mathbf{R}(\mathbf{Q})$ is the matrix formed by the right eigenvectors $\mathbf{R}_i(\mathbf{Q})$, $\mathbf{R}^{-1}(\mathbf{Q})$ is its inverse and $\Lambda(\mathbf{Q})$ is the diagonal matrix whose diagonal entries are the eigenvalues $\lambda_i(\mathbf{Q})$.

We introduce the definitions

$$\lambda_i^+(\mathbf{Q}) = \max(\lambda_i(\mathbf{Q}), 0) \ , \quad \lambda_i^-(\mathbf{Q}) = \min(\lambda_i(\mathbf{Q}), 0) \tag{251}$$

and consider the associated diagonal matrices $\Lambda^+(\mathbf{Q})$, $\Lambda^-(\mathbf{Q})$ and $|\Lambda^-(\mathbf{Q})|$, whose diagonal entries are $\lambda_i^+(\mathbf{Q})$, $\lambda_i^-(\mathbf{Q})$ and $|\lambda_i(\mathbf{Q})|$ respectively. Note that

$$|\lambda_i(\mathbf{Q})| = \lambda_i^+(\mathbf{Q}) - \lambda_i^-(\mathbf{Q}) \tag{252}$$

and hence

$$|\Lambda(\mathbf{Q})| = \Lambda^+(\mathbf{Q}) - \Lambda^-(\mathbf{Q}) \ . \tag{253}$$

Then we introduce

$$|\mathbf{A}(\mathbf{Q})| = \mathbf{R}(\mathbf{Q})|\Lambda(\mathbf{Q})|\mathbf{R}^{-1}(\mathbf{Q}) \ . \tag{254}$$

Osher and Solomon [12] defined the numerical flux as

$$\mathbf{F}_{i+\frac{1}{2}} = \frac{1}{2}(\mathbf{F}(\mathbf{Q}_0) + \mathbf{F}(\mathbf{Q}_1)) - \frac{1}{2}\int_{\mathbf{Q}_0}^{\mathbf{Q}_1} |\mathbf{A}(\mathbf{Q})| d\mathbf{Q} \ . \tag{255}$$

This requires the evaluation of an integral in phase space, which depends on the chosen integration path joining $\mathbf{Q}_0$ to $\mathbf{Q}_1$. Originally, Osher and Solomon proposed two ways of choosing integration paths *so as to make the actual integration tractable*, (a) the P-ordering and (b) the O-ordering. However, the analytical calculations to be performed are still too involved for general hyperbolic systems. Full details of the original Osher-Solomon Riemann solver are found in Chapter 12 of Toro [1].

3.6.2 The DOT Riemann Solver

Dumbser and Toro [13, 14] made two simple but effective suggestions: (i) choose any path, without considerations regarding computational tractability of the scheme; (ii) evaluate matrices by numerical integration in phase space. The simplest path to evaluate the integral in (255) is the *canonical path*

$$\psi(s; \mathbf{Q}_0, \mathbf{Q}_1) = \mathbf{Q}_0 + s(\mathbf{Q}_1 - \mathbf{Q}_0) \ , \quad s \in [0, 1] \ . \tag{256}$$

Obviously, other choices are available. Then, under a change of variables we obtain

$$\mathbf{F}_{i+\frac{1}{2}} = \frac{1}{2}(\mathbf{F}(\mathbf{Q}_0)+\mathbf{F}(\mathbf{Q}_1))-\frac{1}{2}\left(\int_0^1 |\mathbf{A}(\psi(s;\mathbf{Q}_0,\mathbf{Q}_1))|\,ds\right)(Q_1-Q_0)\ . \tag{257}$$

Finally, the integral in (257) is computed *numerically* along the path ψ using a Gauss type quadrature rule with G points s_j and associated weights ω_j in the unit interval $I = [0, 1]$. We obtain

$$\mathbf{F}_{i+\frac{1}{2}} = \frac{1}{2}(\mathbf{F}(\mathbf{Q}_0)+\mathbf{F}(\mathbf{Q}_1)) - \frac{1}{2}\left(\sum_{j=1}^{G}\omega_j\left|\mathbf{A}(\psi(s_j;\mathbf{Q}_0,\mathbf{Q}_1))\right|\right)(Q_1-Q_0)\,. \tag{258}$$

Note that $\left|\mathbf{A}(\psi(s_j;\mathbf{Q}_0,\mathbf{Q}_1))\right|$ must be decomposed as in (254) for each s_j.

Remarks on the DOT Scheme

1. The complete eigenstructure of the system is needed and is used at each integration point in (258).
2. The scheme is **non-linear and complete**, as it contains all characteristic fields of the exact problem.
3. The scheme is very general. The original version of Osher and Solomon was restricted to very simple hyperbolic systems.
4. The new DOT scheme also applies to non-conservative hyperbolic systems.

3.6.3 Sample Numerical Results, Accuracy and Efficiency

The purpose here is to show some numerical results for a wider range of equations than those studied in these lecture notes. We first show some selected numerical results for the Euler equations of gas dynamics; see [1] for background. Then we also address the crucial issues of accuracy and efficiency of Riemann solvers; this is done in terms of the blood flow equations [15].

Numerical Results for the Euler Equations Figure 41 shows computations from a linearised Riemann solver not studied here, namely the Roe Riemann solver [16]. Results shown are for the Euler equations [1]. The left frame shows results from the original Roe scheme without an *entropy fix*; an entropy violating shock (or rarefaction shock) is computed, which is not physically admissible. The right frame shows results from a modified Roe scheme through a so-called *entropy fix*; now the results look correct and also accurate, recalling that the corresponding Godunov method is only first order accurate.

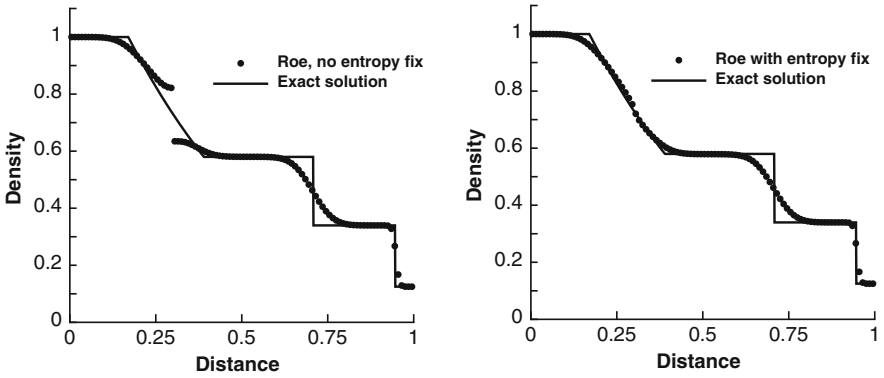

Fig. 41 Sonic flow test problem for the Euler equations taken from [1]. Comparison between numerical (symbol) and exact (line) solutions. Left: linearised Roe solver without entropy fix. Right: linearised Roe solver with entropy fix

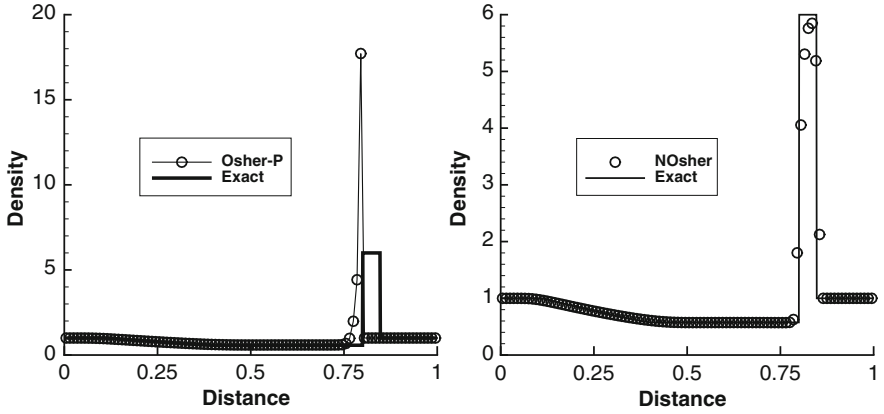

Fig. 42 Test problem for the Euler equations taken from [1]. Comparison between numerical (symbol) and exact (line) solutions. Left: Original Osher-Solomon scheme. Right: new DOT scheme

In Fig. 42 we show results for another test problem for the Euler equations taken from [1]. Comparison between numerical (symbol) and exact (line) solutions is shown. The left frame shows results from the original Osher-Solomon scheme [12], which as seen in the figure, are completely wrong. The right frame shows results from the new DOT scheme [13, 14]; these results are very accurate, especially for the narrow region between the contact discontinuity and the shock wave.

Figure 43 shows results for a special test problem for the Euler equations, also taken from [1]. The test problem consists of a single, isolated stationary contact discontinuity. The left frame shows numerical results from the HLL scheme [7] and the FORCE scheme [6]. Both numerical methods show large errors due to numerical diffusion of the intermediate wave in the Riemann problem for the Euler equations.

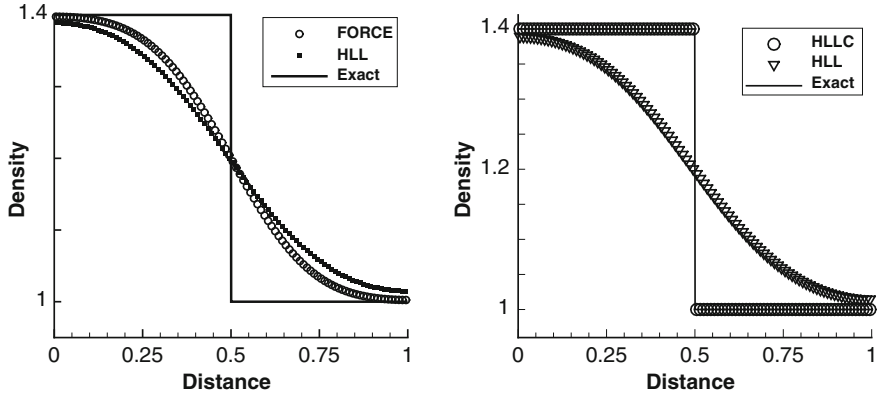

Fig. 43 Test problem for the Euler equations containing a single, isolated stationary contact discontinuity; taken from [1]. Left: FORCE and HLL versus the exact solution. Right: HLL and HLLC versus the exact solution

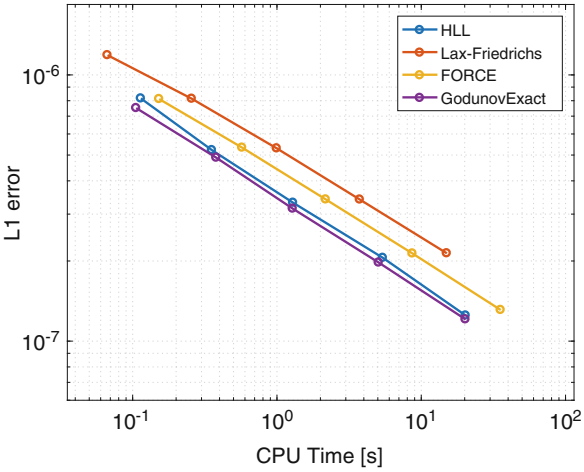

Fig. 44 Efficiency test for the blood flow equations. The test is a Riemann problem containing two rarefaction waves. Error against CPU time. Results are shown for the Godunov method used in conjunction with Exact Riemann solver, the HLL Riemann solver, FORCE and the Lax-Friedrichs flux (Courtesy of PhD student Christian Contarino, University of Trento, Italy)

The right frame shows results from HLL [7] and from HLLC [11], noting that the latter reproduces the exact solution.

Accuracy and Efficiency We have already mentioned the question of efficiency, which relates error (or accuracy) to computational cost. Figure 44 shows results from an efficiency test for the 1D blood flow equations [15], where error is measured against CPU time. Comparison is made for the Godunov method with four Riemann solvers: the exact Riemann solver, HLL, FORCE and Lax-Friedrichs.

What the results of Fig. 44 show is that for this test problem with smooth solution the Godunov method is the most efficient method. Compared to the Lax-Friedrichs method, it is about five times more efficient. To see this, imagine a horizontal line through the last point of the Lax-Friedrichs curve with the smallest error and look for its intersection with the exact Riemann solver curve; these two intersection points give two respective CPU times.

3.6.4 Concluding Remarks

The Godunov method for the augmented one-dimensional shallow water equations has been introduced. The Godunov scheme works with the exact and with approximate Riemann solvers. Examples of approximate Riemann solvers have also been presented, along with some selected numerical results for the Euler equations and for the blood flow equations, not studied here. The first-order Godunov schemes studied in this section can be extended to high order of accuracy following a variety of procedures available in the literature. In the next section we present the ADER approach to construct high-order numerical methods.

4 High Order Methods: The ADER Approach

In this section we present one approach, the ADER approach, to construct high-order accurate extensions of the first-order methods presented previously.

4.1 Overview

We are interested in time-dependent partial differential equations of the form

$$\left.\begin{array}{c} \partial_t \mathbf{Q}(\mathbf{x},t) + \mathbf{A}(\mathbf{Q}(\mathbf{x},t)) = \mathbf{S}(\mathbf{Q}(\mathbf{x},t)) + \mathbf{D}(\mathbf{Q}(\mathbf{x},t)) \ , \\ \\ \mathbf{x} \in \Omega \ , \quad t > 0 \ , \quad \text{ICs} \ , \quad \text{BCs} \ , \end{array}\right\} \tag{259}$$

along with appropriate initial and boundary conditions. Here $\mathbf{Q}(\mathbf{x},t)$ is the vector of unknowns; $\mathbf{A}(\mathbf{Q}(\mathbf{x},t))$ is an advection differential operator in 1D, 2D or 3D; $\mathbf{D}(\mathbf{Q}(\mathbf{x},t))$ is a dissipative operator in 1D, 2D or 3D and $\mathbf{S}(\mathbf{Q}(\mathbf{x},t))$ is a source term vector, a prescribed function of the unknowns.

The ADER approach was first presented by Toro and collaborators [17] for linear hyperbolic systems in 1D, 2D and 3D on structured meshes; schemes of upto 10th order of accuracy in space and time were constructed and implemented. The ADER schemes were further developed in [18] and [19] for non-linear systems;

in [20] ADER was formulated, in a unified manner, in both the finite volume and the discontinuous Galerkin finite element frameworks. For an introduction to ADER see Chapters 19 and 20 of [1] and the many references therein, up to 2009. Distinguishing features of the ADER approach include:

1. Accuracy is arbitrary in both **space and time**.
2. Schemes are non-linear schemes, in the sense of Godunov; computed shock waves and other discontinuities have none or controlled spurious oscillations.
3. Schemes are suitable for general geometries in multiple space dimensions, treated with both structured or unstructured meshes.
4. Schemes work in both the finite volume and the discontinuous Galerkin finite element frameworks.
5. Schemes are applicable to conservative and non-conservative hyperbolic systems.

Why is High Accuracy Important? Because of Efficiency Figure 45 shows computational results for an acoustic problem modelled by the linearised two dimensional Euler equations solved by ADER schemes taken from [21]. The

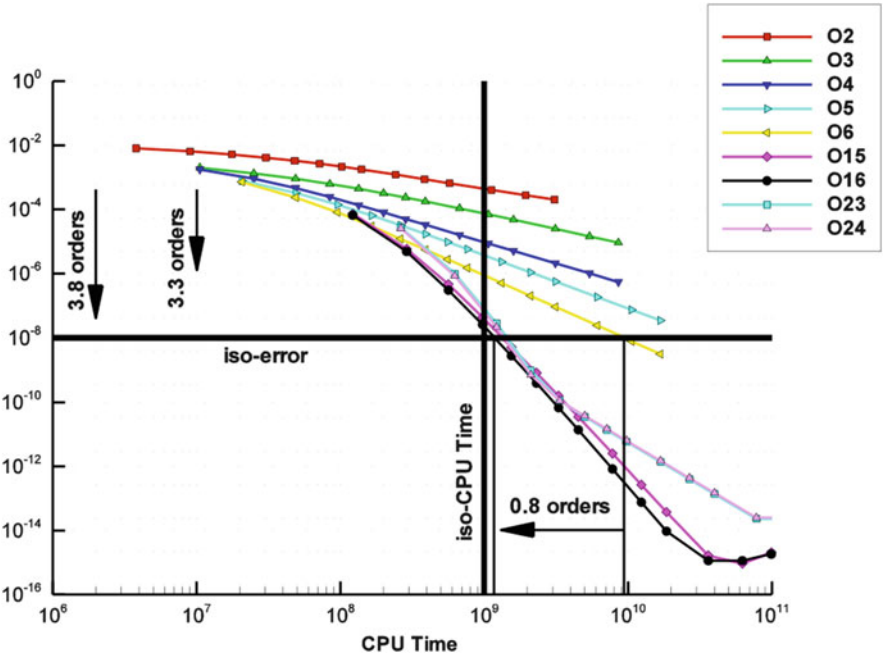

Fig. 45 Efficiency plot: error against CPU cost for nine high-order ADER schemes, from the 2nd order to the 24th order of accuracy. For a chosen fixed error there corresponds a horizontal line (e.g. black horizontal line); its intersection with the various curves gives corresponding times, which give the cost of the corresponding scheme to compute the solution with that error. Taken from [21]

original paper reports computations of orders of accuracy from 1 to 24 in space and time. Figure 45 displays some selected results from 2nd to 16th order.

4.2 ADER in the Finite Volume Framework

Consider the general system of hyperbolic equations with source terms (hyperbolic balance laws) in one space dimension

$$\partial_t \mathbf{Q}(x,t) + \mathbf{F}(\mathbf{Q}(x,t)) = \mathbf{S}(\mathbf{Q}(x,t)) \ . \tag{260}$$

Exact integration of (260) in the control volume $[x_{i-\frac{1}{2}}, x_{i+\frac{1}{2}}] \times [0, \Delta t]$ gives a finite volume like formula

$$\hat{\mathbf{Q}}_i^{n+1} = \hat{\mathbf{Q}}_i^n - \frac{\Delta t}{\Delta x}(\hat{\mathbf{F}}_{i+\frac{1}{2}} - \hat{\mathbf{F}}_{i-\frac{1}{2}}) + \Delta t \hat{\mathbf{S}}_i \ , \tag{261}$$

where

$$\left.\begin{aligned} \hat{\mathbf{Q}}_i^n &= \frac{1}{\Delta x}\int_{x_{i-\frac{1}{2}}}^{x_{i+\frac{1}{2}}} \mathbf{Q}(x,t^n)dx \ , \\ \hat{\mathbf{F}}_{i+\frac{1}{2}} &= \frac{1}{\Delta t}\int_{t^n}^{t^{n+1}} \mathbf{F}(\mathbf{Q}(x_{i+\frac{1}{2}},t))dt \ , \\ \hat{\mathbf{S}}_i &= \frac{1}{\Delta t \Delta x}\int_{t^n}^{t^{n+1}}\int_{x_{i-\frac{1}{2}}}^{x_{i+\frac{1}{2}}} \mathbf{S}(\mathbf{Q}(x,t))dxdt \ . \end{aligned}\right\} \tag{262}$$

Relation (261) with definitions (262) is exact and motivates an approximate formula, namely

$$\mathbf{Q}_i^{n+1} = \mathbf{Q}_i^n - \frac{\Delta t}{\Delta x}(\mathbf{F}_{i+\frac{1}{2}} - \mathbf{F}_{i-\frac{1}{2}}) + \Delta t \mathbf{S}_i \ . \tag{263}$$

See Sect. 1. Equation (263) defines a one-step, fully discrete finite volume numerical scheme with **numerical flux**

$$\mathbf{F}_{i+\frac{1}{2}} \approx \frac{1}{\Delta t}\int_0^{\Delta t} \mathbf{F}(\mathbf{Q}_{i+\frac{1}{2}}(\tau))d\tau \tag{264}$$

and **numerical source**

$$\mathbf{S}_i \approx \frac{1}{\Delta t \Delta x}\int_0^{\Delta t}\int_{x_{i-\frac{1}{2}}}^{x_{i+\frac{1}{2}}} \mathbf{S}(\mathbf{Q}_i(x,\tau))dxd\tau \ . \tag{265}$$

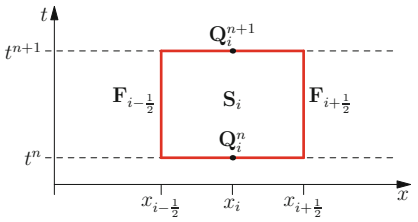

Fig. 46 Illustration of the finite volume scheme (263) to solve the system of hyperbolic equation (260) with source terms. The scheme requires numerical fluxes at interfaces and the numerical source within the control volume

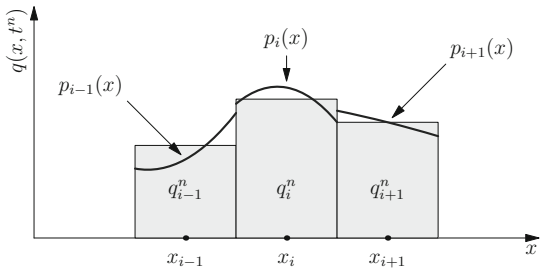

Fig. 47 Illustration of the reconstruction procedure for one variable $q(x, t)$ in one space dimension on a regular mesh. From the set of (constant) integral averages $\{q_i^n\}$ one obtains an interpolant $p_i(x)$ satisfying a conservation property and a non-linear property to circumvent Godunov's theorem, using for example criteria such as TVD, ENO and WENO. Note that at each interface one now has reconstructed data that defines a generalised Riemann problem

Figure 46 illustrates scheme (263) to solve (260). The finite volume ADER scheme (263) aims at computing approximations (264) and (265) as accurately as possible.

4.3 Ingredients of ADER

The ADER method to solve (260) is based on the finite volume formula (263) and requires the accurate evaluation of integrals (264) for the intercell numerical flux and (265) for the numerical source. In order to achieve this, the following steps are required.

1. **Reconstruction:** high-order *non-linear* spatial reconstruction, once per time step, using any of the methodologies available, such as TVD, ENO and WENO. Figure 47 illustrates the reconstruction process. For background on reconstruction techniques see for example [1, 4, 22, 23] and [24].

2. **Generalised Riemann problem (GRP) and numerical flux.** At each interface one must solve a Riemann problem with piece-wise smooth data, not piece-wise constant, as in the conventional case. This GRP may also include the source terms in case these are present in the equations.
3. **Numerical source.** This is an additional term in the case in which the equations include source term.

4.4 Generalized Riemann Problem

Starting from reconstructed data, at each interface one defines the following initial value problem, called the generalized Riemann problem, or GRP

$$\left.\begin{array}{l} \text{PDEs: } \partial_t \mathbf{Q} + \partial_x \mathbf{F}(\mathbf{Q}) = \mathbf{S}(\mathbf{Q}) \ , \quad x \in (-\infty, \infty) \ , \quad t > 0 \ , \\ \\ \text{ICs:} \quad \mathbf{Q}(x,0) = \begin{cases} \mathbf{Q}_L(x) & \text{if } \ x < 0 \ , \\ \\ \mathbf{Q}_R(x) & \text{if } \ x > 0 \ . \end{cases} \end{array}\right\} \tag{266}$$

In the GRP (266) the governing equations include source terms and the initial conditions are piece-wise smooth (e.g. polynomials of any degree). This Riemann problem also generalises the case in which the data is piece-wise linear, which is associated with the second-order GRP scheme of Ben-Artzi and Falcovitz [25].

Figure 48 illustrates the classical Riemann problem (left) and the generalised Riemann problem (right). Figure 49 shows an example of a generalised Riemann problem for the Euler equations of gas dynamics. There are so far several published methods for solving the generalised Riemann problem for hyperbolic systems. The first practical solver for non-linear hyperbolic systems with source terms is due to Toro and Titarev [18]. This solver is suitable for non-stiff source terms. Other solvers include [26–30]. An important development was that in [27] in which the proposed solver can deal with stiff source terms, reconciling in this way, stiffness and high-order of accuracy.

4.5 Numerical Examples

Here we show some sample numerical results, first for the 1D linear advection equation and then for the 2D Euler equations of gas dynamics with the ideal equation of state.

Figure 50 shows computed (symbols) and the exact solution (line) for linear advection equation using a mesh of $M = 50$ cells, a Courant number coefficient $C_{cfl} = 0.95$ at the output time $t_{out} = 1000\pi$. The top frame displays results from a

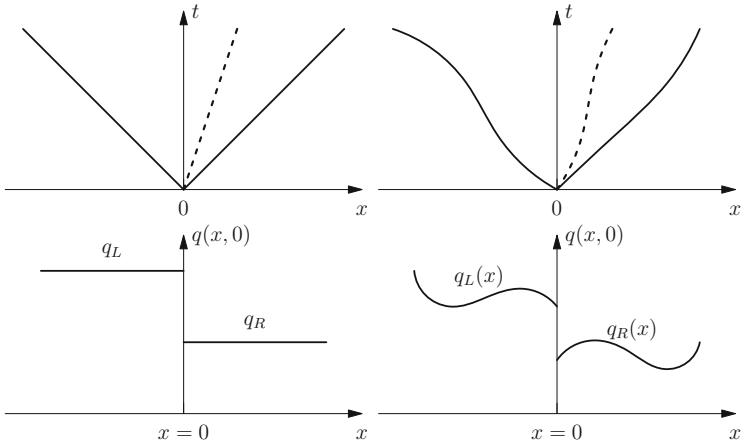

Fig. 48 Classical Riemann problem (left) and generalised Riemann problem (right). Bottom frames depict the initial conditions (for a single variable) and top frames depict the structure of the solution of the initial value problem in the $x - t$ plane

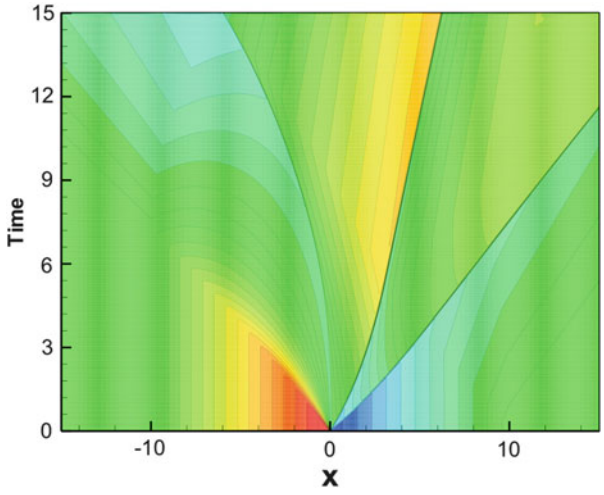

Fig. 49 Structure of the solution of a generalized Riemann problem for the Euler equations. Characteristics are curved in the $x - t$ plane (Courtesy of Dr VA Titarev)

second-order TVD method used in conjunction with the MINBEE limiter [1]. The bottom frame shows results from the 5th-order ADER scheme (5th order in space and time) with WENO (non-linear) reconstruction. The results speak by themselves. The second order TVD method is unable to resolve the wave packet and there is not even a hint of waves; the profile is virtually flat. The killer here is the long evolution time, $t_{out} = 1000\pi$. Long time evolution problems expose the limitations of low order methods. The fifth order method is just perfect.

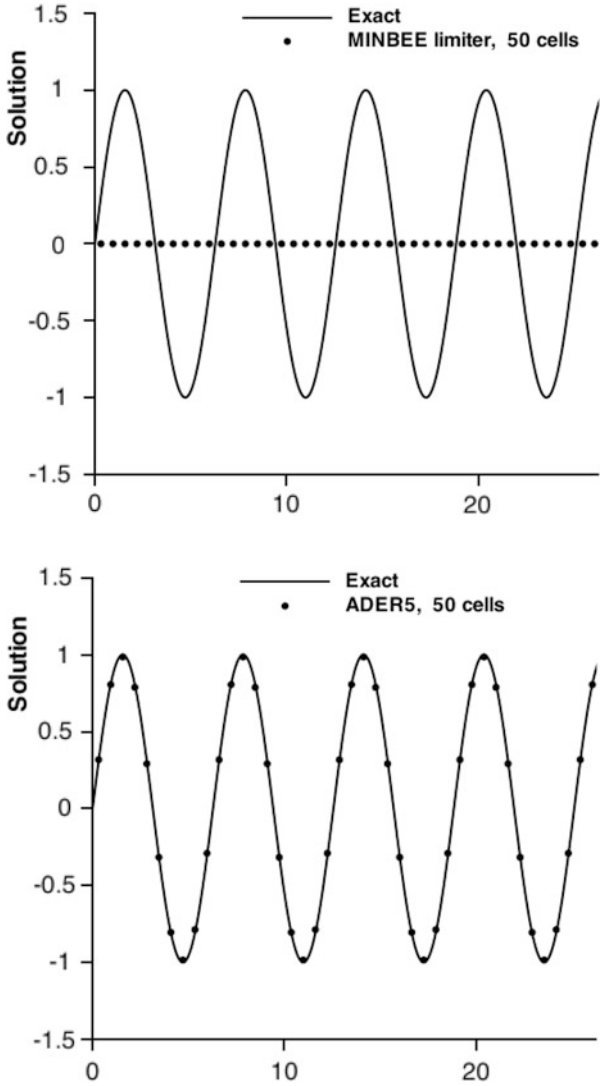

Fig. 50 Computed (symbols) and exact solution (line) of linear advection equation using a mesh of $M = 50$ cells, Courant number coefficient $C_{cfl} = 0.95$ and output time $t_{out} = 1000\pi$. Top frame displays results from second-order TVD method with the MINBEE limiter. Bottom frame shows results from the 5th-order ADER scheme with WENO reconstruction

Figure 51 shows computed results for the two-dimensional Euler equations of gas dynamics with the ideal gas equation of state. This test problem is well known in the gas dynamics community. The domain is a rectangular region with a solid fixed triangle in its interior (white object). The top and bottom boundaries are reflecting fixed walls, while the left and right boundaries are transmissive. The initial condition

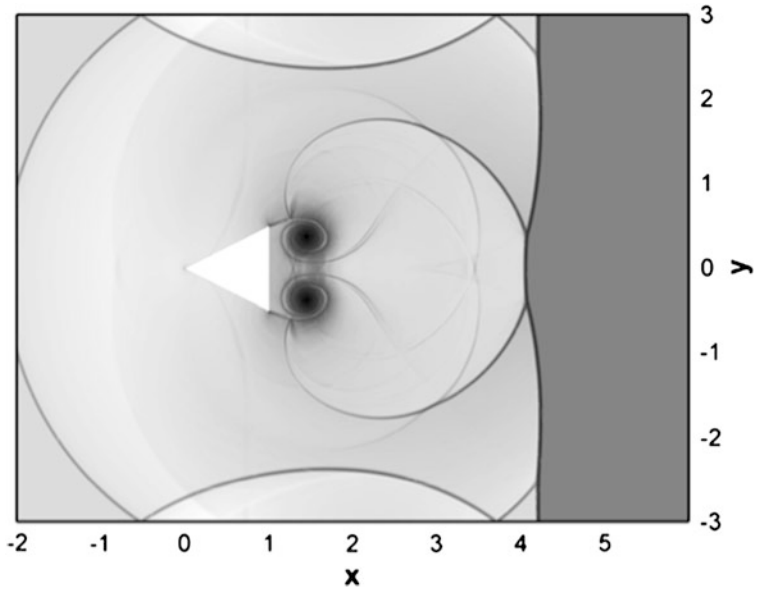

Fig. 51 Shock wave impinging on stationary triangular body. Numerical solution of the Euler equations of gas dynamics on a triangular mesh using a fourth order ADER method (Courtesy of Prof. M Dumbser, University of Trento, Italy)

is an isolated shock wave of Mach number 1.3 positioned between the left boundary and the triangle. The evolution of this initial condition gives rise to a complex pattern of waves propagating and interacting. There are experimental visualization results for this problem. The ADER solution represents those experiments well. In addition to the dominant shock waves everywhere there are also regions of smooth flow and many low amplitude waves; these are the flow features that are difficult to capture with low order methods, they are simply wiped out, just as seen for the linear advection example of Fig. 50.

4.6 Concluding Remarks

In this last section we have given a very brief introduction to one approach to construct high-order numerical methods for hyperbolic equations, namely the ADER approach. This is a fully discrete approach that requires a spatial reconstruction procedure and the solution of the generalised Riemann problem. There are indeed alternative methods to achieve high order of accuracy. Prominent examples are the ENO and WENO semidiscrete approaches pioneered by Shu and collaborators [22–24].

Accumulated experience over the last few years has shown that high-order methods are much more efficient than low order methods if small errors are sought, that is if accurate solutions are sought. By efficiency we mean that given an error deemed acceptable, then high order methods attain that error much more efficiently on a coarse mesh than low order methods on a fine mesh. This is illustrated in Fig. 45.

The issues of accurate solutions and efficiency are becoming increasingly important given the growing trend to use mathematical models (PDEs) to understand the physics they embody. Only very accurate solutions of the PDEs will achieve this and also reveal limitations of the mathematical models (the governing equations and their parameters). Very long time evolution simulations, as in wave propagation problems for long distances, require the use of high order methods, as illustrated in Fig. 50.

References

1. Toro, E.F.: Riemann Solvers and Numerical Methods for Fluid Dynamics. A Practical Introduction, 3rd edn. Springer, Berlin (2009). ISBN 978-3-540-25202-3. http://link.springer.com/book/10.1007%2Fb79761
2. Toro, E.F.: Shock-Capturing Methods for Free-Surface Shallow Flows. Wiley, Chichester (2001)
3. Godlewski, E., Raviart, P.A.: Numerical Approximation of Hyperbolic Systems of Conservation Laws. Springer, New York (1996)
4. LeVeque, R.J.: Finite Volume Methods for Hyperbolic Problems. Cambridge University Press, Cambridge (2002)
5. Godunov, S.K.: A Finite difference method for the computation of discontinuous solutions of the equations of fluid dynamics. Math. Sb. **47**, 357–393 (1959)
6. Toro, E.F., Billett, S.J.: Centred TVD schemes for hyperbolic conservation laws. IMA J. Numer. Anal. **20**, 47–79 (2000)
7. Harten, A., Lax, P.D., van Leer, B.: On spstream differencing and Godunov-type schemes for hyperbolic conservation laws. SIAM Rev. **25**(1), 35–36 (1983)
8. Rusanov, V.V.: Calculation of interaction of non-steady shock waves with obstacles. J. Comput. Math. Phys. USSR **1**, 267–279 (1961)
9. Toro, E.F., Spruce, M., Speares, W.: Restoration of the contact surface in the HLL Riemann solver. Technical Report, Department of Aerospace Science, College of Aeronautics, Cranfield Institute of Technology. CoA-9204 (1992)
10. Toro, E.F., Spruce, M., Speares, W.: Restoration of the contact surface in the HLL Riemann solver. Shock Waves **4**, 25–34 (1994)
11. Toro, E.F., Chakraborty, A.: Development of an approximate Riemann solver for the steady supersonic Euler equations. Aeronaut. J. **98**, 325–339 (1994)
12. Osher, S., Solomon, F.: Upwind difference schemes for hyperbolic conservation laws. Math. Comput. **38**(158), 339–374 (1982)
13. Dumbser, M., Toro, E.F.: A simple extension of the Osher Riemann solver to general non-conservative hyperbolic systems. J. Sci. Comput. **48**, 70–88 (2011)
14. Dumbser, M., Toro, E.F.: On universal Osher-type schemes for general nonlinear hyperbolic conservation laws. Commun. Comput. Phys. **10**, 635–671 (2011)
15. Toro, E.F.: Brain venous haemodynamics, neurological diseases and mathematical modelling. A review. Appl. Math. Comput. **272**, 542–579 (2016)

16. Roe, P.L.: Approximate Riemann solvers, parameter vectors and difference schemes. J. Comput. Phys. **43**, 357–372 (1981)
17. Toro, E.F., Millington, R.C., Nejad, L.A.M.: Towards very high-order Godunov schemes. In: Toro, E.F. (ed.) Godunov Methods: Theory and Applications. Edited Review. Conference in Honour of Godunov SK, vol. 1, pp. 897–902. Kluwer Academic/Plenum Publishers, New York (2001)
18. Toro, E.F., Titarev, V.A.: Solution of the generalised Riemann problem for advection-reaction equations. Proc. R. Soc. London, Ser. A **458**, 271–281 (2002)
19. Titarev, V.A., Toro, E.F.: ADER: arbitrary high order Godunov approach. J. Sci. Comput. **17**, 609–618 (2002)
20. Dumbser, M., Balsara, D., Toro, E.F., Munz, C.D.: A unified framework for the construction of one-step finite-volume and discontinuous Galerkin schemes on unstructured meshes. J. Comput. Phys. **227**, 8209–8253 (2008)
21. Dumbser, M., Schwartzkopff, T., Munz, C.D.: Arbitrary high order finite volume schemes for linear wave propagation. In: Computational Science and High Performance Computing II. Notes on Numerical Fluid Mechanics and Multidisciplinary Design Book Series (NNFM), vol. 91, pp. 129–144. Springer, Berlin (2006)
22. Shu, C.W., Osher, S.: Efficient implementation of essentially non-oscillatory shock-capturing schemes. J. Comput. Phys. **77**, 439–471 (1988)
23. Shu, C.W., Osher, S.: Efficient implementation of essentially non-oscillatory shock-capturing schemes II. J. Comput. Phys. **83**, 32–78 (1989)
24. Jiang, G.S., Shu, C.W.: Efficient implementation of weighted ENO schemes. J. Comput. Phys. **126**, 202–228 (1996)
25. Ben-Artzi, M., Falcovitz, J.: A second order Godunov-type scheme for compressible fluid dynamics. J. Comput. Phys. **55**, 1–32 (1984)
26. Castro, C.E., Toro, E.F.: Solvers for the high-order Riemann problem for hyperbolic balance laws. J. Comput. Phys. **227**, 2481–2513 (2008)
27. Dumbser, M., Enaux, C., Toro, E.F.: Finite volume schemes of very high order of accuracy for stiff hyperbolic balance laws. J. Comput. Phys. **227**, 3971–4001 (2008)
28. Toro, E.F., Montecinos, G.I.: Implicit, semi-analytical solution of the generalized Riemann problem for stiff hyperbolic balance laws. J. Comput. Phys. **303**, 146–172 (2015)
29. Götz, C.R., Iske, A.: Approximate solutions of generalized Riemann problems for nonlinear systems of hyperbolic conservation laws. Math. Comput. **85**, 35–62 (2016)
30. Götz, C.R., Dumbser, M.: A novel solver for the generalized Riemann problem based on a simplified LeFloch-Raviart expansion and a local space-time discontinuous Galerkin formulation. J. Sci. Comput. **69**(2), 805–840 (2016)

An Introduction to the Homogenization Modeling of Non-Newtonian and Electrokinetic Flows in Porous Media

Andro Mikelić

Abstract The flow of complex fluids through porous media is common to many engineering applications. The upscaling is a powerful tool for modeling non-homogeneous media and we consider homogenization of quasi-Newtonian and electrokinetic flows through porous media. For the quasi-Newtonian polymeric fluids, the incompressible Navier-Stokes equations with the invariants dependent viscosity is supposed to hold the pore scale level. The two-scale asymptotic expansions and the two-scale convergence of the monotone operators are applied to derive the reservoir level filtration law, given as a monotone relation between the filtration velocity and the pressure gradient. The second problem, we consider, is the quasi-static transport of an electrolyte through an electrically charged medium. The physical chemistry modeling is presented and used to get a dimensionless form of the problem. Next the equilibrium solutions are constructed through solving the Poisson-Boltzmann equation. For the solutions being close to the equilibrium, the two-scale convergence is applied to obtain the Onsager relations linking gradients of the pressure and of the chemical potentials to the filtration velocity and the ionic fluxes.

1 Introduction to the Homogenization

Using the equations of the continuum physics at pore scale for porous media is a promising approach to derive the overall equations, but meets many difficulties. The presence of the fluid and the solid parts in the soil obliges us to consider it as a multiphase medium. The phases are geometrically present in a heterogeneous way, with small pores and cavities.

A. Mikelić (✉)
Univ Lyon, Université Claude Bernard Lyon 1, CNRS UMR 5208, Institut Camille Jordan, Villeurbanne cedex, France
e-mail: Andro.Mikelic@univ-lyon1.fr

A. Farina et al. (eds.), *Non-Newtonian Fluid Mechanics and Complex Flows*,
Lecture Notes in Mathematics 2212, https://doi.org/10.1007/978-3-319-74796-5_4

Homogenization applied to heterogeneous media (porous media, composites, tissues, etc.) is a mathematical method that allows to "**upscale**" the fundamental equations from continuum physics, being valid at the microscopic level. Upscaling or homogenization signifies that the particular phases lose their independent presence in the model and will get "smeared". Rather than tracking behavior of every phase, we search to approximate the model with equations being valid everywhere. Phases get present in every point through new averaged unknowns like saturations and concentrations. This way it is not necessary to solve nonlinear PDEs of the fluid mechanics/elasticity/heat conduction in the complicated geometry of a heterogeneous medium. Note that, in addition, the pore geometry is usually unknown and available only through some statistical averages.

The **homogenization theory** of heterogeneous media studies the effects of the micro-structure (i.e. of the pore structure) upon solutions of PDEs of the continuum mechanics. Even in the simplest case of a viscous single phase flow through a porous medium, we are given a PDE with two natural **length scales**: a *macroscopic scale* (the scale of the piece of reservoir/soil) of size L_0 and a *microscopic scale* (the pore scale or the scale of perforations) of size $\ell << L_0$. This disparity in length scales is what provides us with our expansion parameter $\varepsilon = \ell/L_0$, measuring the scale of oscillations. For fixed, but small, characteristic pore length $\ell = \varepsilon L_0 > 0$ the solutions u^ε of the flow equations will in general be complicated, having different behaviors on the two length scales.

A closed-form solution is not achievable and a numerical solution would be nearly impossible to calculate. In the practical simulations of the flows through porous media, we use PDEs at the macroscale. Information about the pore structure is only kept through some averaged quantities as porosity and permeability.

Therefore, one of the fundamental questions in the modeling of flows through porous media is how to get the "**averaged**" or "**upscaled**" equations. Next we wish to calculate the **effective coefficients** describing the influence of the microstructure. Finally, it is of interest to know whether our derived model is correct, in the sense that it should approximate the original problem involving the micro-structure.

In the homogenization theory, the upscaling corresponds to the study of the limiting behavior $u^\varepsilon \to u$ as $\varepsilon \to 0$. The idea is that in this limit the micro-structure (generating the high-frequency oscillations) will "*average out*", and there will be a simple "averaged" or "*homogenized*" PDE, which will represent a filtration law.

As even the simple example of Darcy's law confirms, the homogenized PDE can differ much from the original one. In overcoming this fundamental difficulty it is useful to use **formal multiscale expansions** in ε, containing behavior on different length scales.

The idea is to suppose u^ε has the following expansion:

$$u^\varepsilon = \varepsilon^\beta \left\{ u_0(x, \frac{x}{\varepsilon}) + \varepsilon u_1(x, \frac{x}{\varepsilon}) + \varepsilon^2 u_2(x, \frac{x}{\varepsilon}) + \dots \right\} \tag{1}$$

Two-scale expansion (1) is plugged into the PDE and we search for a scale of equations determining the functions $u_i, i = 1, \ldots$. Nevertheless, before plugging expansion (1) into the PDE, we should somehow determine β.

In order to answer all those questions, we establish the following strategy, which we are going to apply in the sections which follow:

(A) A *description of the geometry of the heterogeneous medium* is given. It can be periodic, statistically homogeneous etc.
(B) A continuum physics model valid at the pore scale is written up. The model can come either from the well-established textbook modeling or from the molecular dynamics calculations allowing to go from the molecular structure to the continuum mechanics at micro/nano-metric scale.
(C) The *a priori estimates* for solutions of the PDE, uniform with respect to ε, are established. For the flow problems we usually need:

  (C1) A priori estimates for the velocity.
  (C2) A priori estimates for the pressure.

(D) Having obtained a priori estimates, *a formal multiscale expansion* is set up in the form (1). We shall see that for the linear and monotone problems it corresponds to passing to the homogenization limit in the sense of the *two-scale convergence*.
(E) The *upscaled problem* is studied. We prove uniqueness and regularity and undertake separation of the fast and slow scales. A numerical method for calculating the effective coefficients is proposed.

This short chapter will try to initiate the reader to the applications of the two-scale convergence technique in the homogenization of complex flow through porous media. We present three examples of complex flows through a porous medium: the first is homogenization of a quasi-Newtonian flow, the second is homogenization of a Bingham flow and the third is a derivation of the Onsager relations for the electrokinetic flows.

In connection with the homogenization in porous media, we recommend to the reader the book edited by U. Hornung [38]. It contains number of contributed chapters, and we mention the chapters on the two-scale convergence and on the derivation of Darcy's law by homogenization by G. Allaire, which we are going to quote frequently in this text. Also there is a chapter on the filtration of non-Newtonian fluids (see [54]).

As general references on homogenization we recommend the classic text by E. Sanchez-Palencia [71] and the recent engineering textbook by Mei and Vernescu [53]. More recent mathematical references are the books by Jikov, Kozlov and Oleinik [39], Cioranescu and Donato [28] and Pavliotis [66].

Classical references on two-scale convergence are papers by G. Allaire [5] and by G. Nguetseng [62].

2 Models for Quasi-Newtonian Fluids and a Derivation of the Filtration Laws by a Two-Scale Expansion

In this section we first present models of quasi-Newtonian fluids. Then we discuss their well-posedness and particularities of the geometry. After obtaining a priori estimates, we propose two-scale expansions. They allow achieving our goal of deriving formally equations describing filtration of a quasi-Newtonian fluid.

2.1 Continuum Physics Models for Quasi-Newtonian Fluids

We first recall the fluid mechanics equations at the pore level.

The incompressible quasi-Newtonian fluids are characterized by the viscosity depending on the principal invariants of the symmetric stretching tensor $D(\mathbf{v})$. In our notation, $\mathbf{v}$ is the velocity, p the pressure, $\nabla\mathbf{v}$ the gradient velocity tensor and $D(\mathbf{v}) = (\nabla\mathbf{v} + \nabla\mathbf{v}^t)/2$ will denote the rate-of-strain or the symmetric stretching) tensor. The principal invariants of $D(\mathbf{v})$ are

$$I_1(D) = \text{tr}\, D = \text{ div } \mathbf{v}, \quad I_2(D) = \frac{1}{2}\big((\text{ div } \mathbf{v})^2 - \text{tr}\, D^2\big) \quad \text{and} \quad I_3(D) = \det D.$$

σ is the stress tensor $\sigma = -pI + 2\eta_r D(\mathbf{v})$. The viscosity η_r is constant for a Newtonian fluid but dependent on the shear rate $\dot{\gamma} = \sqrt{|D(\mathbf{v})|^2/2} = \sqrt{I_2(D(\mathbf{v})}$, i.e. $\eta_r = \eta_r(\dot{\gamma})$, for viscous non-Newtonian fluids. The deviatoric stress tensor τ, i.e. the part of the total stress tensor that is zero at equilibrium, is then a nonlinear function of the symmetric stretching tensor $D(\mathbf{v})$,

$$\tau = \eta_r(\dot{\gamma})D(\mathbf{v}).$$

Two most widely used laws in engineering practice are the *power law* and the *Carreau-Yasuda law*. For more constitutive laws for the viscosity, we refer to [17] and [18].

The first most popular empiricism is the "power law" or Ostwald-de Waele model, where the expression for the shear rate dependent viscosity is

$$\eta_r(\xi) = \lambda_0|\xi|^{r-2} = \lambda_1|\ \dot{\gamma}\ |^{r-2} = \lambda_1|\ \dot{\gamma}\ |^{n-1}, \quad \xi \in \mathbb{R}^9, \tag{2}$$

where $n = r - 1$ is the power-law exponent and λ_1 is the consistency of the fluid. For $1 < r < 2$ the fluid is a shear thinning and for $r > 2$ a shear-thickening.

The simple power-law model (Eq. (2)) has a well-known singularity at zero shear rate, which must be carefully accounted for in kinematic analyses. The Carreau-Yasuda equation is an alternate generalized Newtonian model that enables the description of the plateaus in viscosity that are expected when the shear rate is very

small or very large. The empiricism for the viscosity η_r used in the Carreau-Yasuda law is

$$\eta_r(\xi) = (\eta_0 - \eta_\infty)\,(1 + \lambda|\xi|^2)^{r/2-1} + \eta_\infty, \qquad \xi \in \mathbb{R}^9, \tag{3}$$

with $\eta_0 \geq \eta_\infty > 0, \lambda > 0$, where η_0 is the zero-shear-rate viscosity, η_∞ is the infinite-shear-rate viscosity, λ is a time constant being the inverse of a characteristic shear rate at which shear thinning becomes important and $r - 1$ is a dimensionless constant describing the slope in the "power law region" of $\log \eta_r$ versus $\log \dot{\gamma}$.

The incompressible quasi-Newtonian Navier-Stokes system is given by

$$-\nabla \cdot \{\eta_r(\dot{\gamma})D(\mathbf{v})\} + \rho(\mathbf{v}\nabla)\mathbf{v} + \nabla p = \rho\mathbf{f} \qquad \text{in } \Omega_p, \tag{4}$$

$$\nabla \cdot \mathbf{v} = 0 \qquad \text{in } \Omega_p, \tag{5}$$

$$\mathbf{v} = 0 \qquad \text{on } \partial\Omega_p, \tag{6}$$

where Ω_p is the pore space of the porous medium.

The corresponding functional space for the velocity is

$$V_r(\Omega_p) = \{\mathbf{z} \in W_0^{1,r}(\Omega_p)^3 \,:\, \nabla \cdot \mathbf{z} = 0 \text{ in } \Omega_p\},$$

where $1 < r < +\infty$ and $W_0^{1,r}(\Omega_p) = \{z \in L^r(\Omega_p) \mid \nabla z \in L^r(\Omega_p)^3\}$. Ω_p is a bounded open set with a smooth boundary and $\mathbf{f}$ is a smooth function.

In two and three dimensions the classical theory from Lions, Cattabriga and Temam (see [25, 43] and [79]), and newly developed techniques from [24] give the existence of at least one weak solution $(\mathbf{v},\, p) \in V_r(\Omega_p) \times L_0^{r'}(\Omega_p)$ for (2),(4)–(6) (i.e. the power law) under assumption, $r > 2d/(d+2)$ (i.e. $r > 1$ in the two dimensional case and $r > 6/5$ in three dimension), with $r' = r/(r-1)$. For system (3)–(6) (i.e. for the case of Carreau-Yasuda law) we have existence of at least one weak solution $(\mathbf{v},\, p) \in V_2(\Omega_p) \times L_0^2(\Omega_p)$ for $1 < r \leq 2$ and $(\mathbf{v},\, p) \in V_r(\Omega_p) \times L_0^{r'}(\Omega_p)$ for $r > 2$.

In order to make modeling more precise, we define the dimensionless geometrical structure of the porous medium. We will divide Ω_p, which is a subset of $\Omega = (0, L)^3$, by the characteristic length L_0 and obtain Ω_ε.

2.2 *The Geometry of a Periodic Porous Medium and a Priori Estimates*

Now we consider a periodic porous medium $\Omega = (0, L/L_0)^3$ in $\mathbb{R}^3$ with a periodic arrangement of the pores. The formal description goes along the following lines: First we define the geometrical structure inside the unit cell $Y = (0, 1)^3$. Let Y_s (the solid part) be a closed subset of $\bar{Y}$ and $Y_F = Y \backslash Y_s$ (the fluid part). The liquid/solid interface is $S = \partial Y_s \setminus \partial Y$. See Fig. 1 for a typical unit cell.

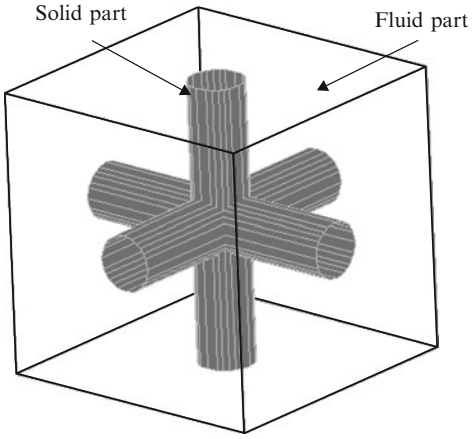

Fig. 1 Periodic cell with connected solid and liquid parts in three dimensions

We make the periodic repetition of Y_s all over $\mathbb{R}^3$ and set $Y_s^k = Y_s + k$, $k \in \mathbb{Z}^3$. Obviously the set $E_S = \bigcup_{k\in\mathbb{Z}^3} Y_s^k$ is a closed subset of $\mathbb{R}^3$ and $E_F = \mathbb{R}^3 \backslash E_S$ is an open set in $\mathbb{R}^3$. The following assumptions on Y_F and E_F have been made:

(i) Y_F is an open connected set of strictly positive measure, with a $C^{1,1}$ boundary and Y_s has strictly positive measure in $\bar{Y}$ as well.
(ii) E_F and the interior of E_S are open sets with the boundary of class $C^{1,1}$, which are locally located on one side of their boundary. Moreover E_F is connected and the solid part, E_S, is supposed connected in $\mathbb{R}^3$ as well (in two dimensions this hypothesis is not realistic).

Now we see that $\Omega = (0, L/L_0)^3$ is covered with a regular mesh of size ε, each cell being a cube $Y_i^\varepsilon = \varepsilon(Y + i)$, with $1 \le i \le N(\varepsilon) = |\Omega|\varepsilon^{-3}[1 + 0(1)]$. We define $Y_{s_i}^\varepsilon = \varepsilon(Y_s + i)$ and $Y_{f_i}^\varepsilon = \varepsilon(Y_F + i)$. For sufficiently small $\varepsilon > 0$ we consider $T_\varepsilon = \{k \in \mathbb{Z}^3 | Y_{s_k}^\varepsilon \subset \Omega\}$ and define

$$\Omega_s^\varepsilon = \bigcup_{k\in T_\varepsilon} Y_{s_k}^\varepsilon, \quad \Gamma^\varepsilon = \partial\Omega_s^\varepsilon, \quad \Omega_\varepsilon = \Omega \setminus \Omega_s^\varepsilon.$$

Obviously, $\partial\Omega_\varepsilon = \partial\Omega \cup \Gamma^\varepsilon$. The domains Ω_s^ε and Ω_ε represent, respectively, the solid and fluid parts of a porous medium Ω.

For simplicity, we will suppose that $L/(L_0\varepsilon)$ is an *integer*.

Remark 1 A two-dimensional porous medium could be seen as a section of a bundle of parallel fibers. Possible geometries are shown on Fig. 2.

The no-slip condition on the pore boundaries is at the origin of velocity oscillations. They are precisely described by the following, pore-size dependent, Poincaré's inequality in a porous medium

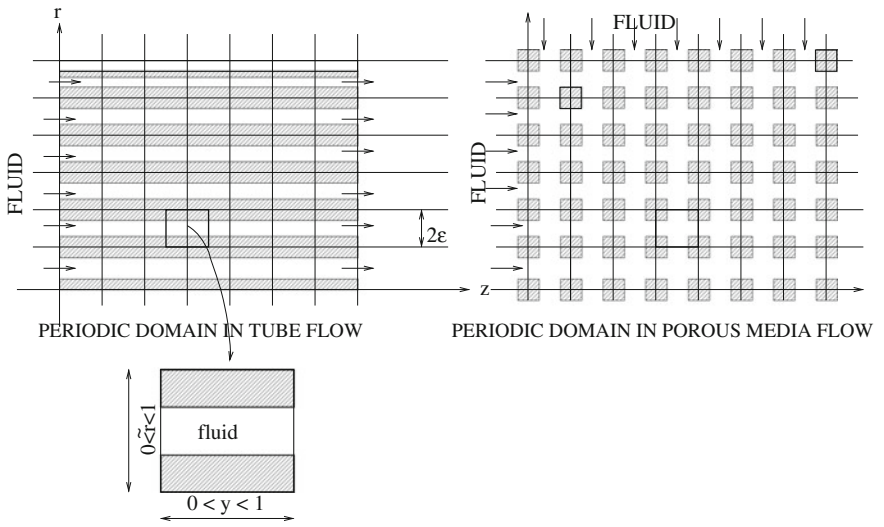

Fig. 2 Examples of two-dimensional porous media

Lemma 1 (See [71]) *For each* $\mathbf{w} \in W_0^{1,q}(\Omega_\varepsilon)^3$, *the inequality*

$$\|\mathbf{w}\|_{L^q(\Omega_\varepsilon)^3} \leq C\varepsilon \|D(\mathbf{w})\|_{L^q(\Omega_\varepsilon)^9}, \quad 1 < q < +\infty, \tag{7}$$

holds true.

The equivalence between the norms $\|D(\mathbf{w})\|_{L^q(\Omega_\varepsilon)^9}$ and $\|\nabla \mathbf{w}\|_{L^q(\Omega_\varepsilon)^9}$ is due to Korn's inequality in porous media

Proposition 1 (See [64] and References Therein) *For each* $\mathbf{w} \in W_0^{1,q}(\Omega_\varepsilon)^3$, $1 < q < +\infty$, *we have the inequality*

$$\|\nabla \mathbf{w}\|_{L^q(\Omega_\varepsilon)^9} \leq C \|D(\mathbf{w})\|_{L^q(\Omega_\varepsilon)^9}. \tag{8}$$

Next we test Eq. (4) with the solution and obtain

$$||\mathbf{v}||_{L^r} + \varepsilon ||D(\mathbf{v})||_{L^r} \leq C\varepsilon^{r/(r-1)} \tag{9}$$

in the case of the power law and

$$||\mathbf{v}||_{L^r} + \varepsilon ||D(\mathbf{v})||_{L^r} \leq C\varepsilon^{\beta}, \quad \beta = \min\{r/(r-1), 2\} \tag{10}$$

in the case of the Carreau-Yosuda law.

Hence the characteristic velocity U is of order $O(\varepsilon^\beta)$ and the Reynolds number $\mathrm{Re}=\rho L_0 U/\eta_0$ is small. Therefore, it is enough to consider the quasi-Newtonian Stokes equations.

Consequently, in the case of power law (2) we consider the dimensionless system

$$-\nabla \cdot \{|D(\mathbf{v}^\varepsilon)|^{r-2} D(\mathbf{v}^\varepsilon)\} + \nabla p^\varepsilon = \mathbf{f} \qquad \text{in } \Omega_\varepsilon, \tag{11}$$

$$\nabla \cdot \mathbf{v}^\varepsilon = 0 \qquad \text{in } \Omega_\varepsilon, \tag{12}$$

$$\mathbf{v}^\varepsilon = 0 \qquad \text{on } \partial\Omega_\varepsilon. \tag{13}$$

Problem (11)–(13) is equivalent to the minimization problem

$$\min_{\varphi \in V_r(\Omega_\varepsilon)} J(\varphi) = \min_{\varphi \in V_r(\Omega_\varepsilon)} \Big\{ \frac{1}{r} \int_{\Omega_\varepsilon} |D(\varphi)|^r \, dx - \int_{\Omega_\varepsilon} \mathbf{f} \cdot \varphi \, dx \Big\}. \tag{14}$$

For $1 < r < +\infty$, J is strictly convex, proper, continuous and coercive, which give the existence and the uniqueness of the minimizer $\mathbf{v}^\varepsilon \in V_r(\Omega_\varepsilon)$ (see [33]). The pressure field is recovered using the De Rham or Tartar's constructions (see [79]).

2.3 The Filtration Laws via Two-Scale Asymptotic Expansions: The Power-Law

The conclusion of the previous subsection is that we can take dimensionless problem (11)–(13) as the starting point for the asymptotic analysis.

$\mathbf{v}^\varepsilon$ satisfies a priori estimate (9). Obtaining the a priori estimate for the pressure field p^ε is more involved and we address the question in the next section. Motivated by the classical Darcy law, we expect that there would be a term $\mathbf{f} - \nabla_x p$ in the filtration law. Hence we expect to have the pressure p^ε uniformly bounded in $L^{r'}(\Omega_\varepsilon)$, $r' = r/(r-1)$.

After having obtained the a priori estimates, we can proceed with formal two-scale asymptotic expansions. We will use the two-scale asymptotic expansion (1) to perform the formal homogenization of the system (11)–(13). Introducing the fast variable $y = x/\varepsilon$, we assume that the solution of (11)–(13) can be developed in the following way

$$\begin{cases} \mathbf{v}^\varepsilon(x) = \varepsilon^{r/(r-1)} \{ \mathbf{v}^0(x,y) + \varepsilon \mathbf{v}^1(x,y) + \dots \}, \\ p^\varepsilon(x) = p^0(x,y) + \varepsilon p^1(x,y) + \dots . \end{cases}$$

The above two-scale expansion can be considered as a special case of the general expansions of this type from the monographs by Sanchez-Palencia [71] and Hornung [38]. In particular, a derivation of Darcy's law, for a Newtonian fluid, by formal two-scale expansions goes back to the seminal article by Ene and Sanchez-Palencia [34]. The differential operators transform as follows

$$\nabla \cdot = \frac{1}{\varepsilon} \nabla_y \cdot + \nabla_x \cdot; \quad D = \frac{1}{\varepsilon} D_y + D_x;$$

$$\nabla = \frac{1}{\varepsilon} \nabla_y + \nabla_x; \quad |D(\mathbf{v}^\varepsilon)|^{r-2} = \varepsilon^{(r-2)/(r-1)} |D_y(\mathbf{v}^0) + O(\varepsilon)|^{r-2}.$$

Insertion of the two-scale asymptotic expansion into the incompressibility condition (12) yields

$$\frac{1}{\varepsilon}\nabla_y \cdot \mathbf{v}^0 + \nabla_x \cdot \mathbf{v}^0 + \nabla_y \cdot \mathbf{v}^1 = O(\varepsilon).$$

Hence at order $O(1/\varepsilon)$ we have

$$\nabla_y \cdot \mathbf{v}^0 = 0 \quad \text{in} \quad Y_F; \quad \mathbf{v}^0 = 0 \quad \text{on} \quad S \tag{15}$$

and at order $O(1)$

$$\nabla_x \cdot \mathbf{v}^0 + \nabla_y \cdot \mathbf{v}^1 = 0 \quad \text{in} \quad Y_F; \quad \mathbf{v}^1 = 0 \quad \text{on} \quad S. \tag{16}$$

Integration of Eq. (16) over Y_F yields the macroscopic mass conservation equation

$$\nabla_x \cdot \Big(\int_{Y_F} \mathbf{v}^0(x, y)\, dy \Big) = 0 \quad \text{in} \quad \Omega. \tag{17}$$

Insertion of the two-scale expansion into the momentum equation (11) yields

$$-\Big\{\frac{1}{\varepsilon}\nabla_y \cdot + \nabla_x \cdot \Big\} \Big\{\varepsilon |D_y(\mathbf{v}^0) + O(\varepsilon)|^{r-2}(D_y(\mathbf{v}^0) + O(\varepsilon))\Big\} +$$
$$\frac{1}{\varepsilon}\nabla_y p^0 + \nabla_x p^0 + \nabla_y p^1 + O(\varepsilon) = \mathbf{f}. \tag{18}$$

At order $O(1/\varepsilon)$, Eq. (18) yields

$$\nabla_y p^0 = 0 \quad \Rightarrow p^0 = p^0(x). \tag{19}$$

At order $O(1)$ Eq. (18) yields

$$\nabla_y p^1 - \nabla_y \cdot \Big\{ |D_y(\mathbf{v}^0)|^{r-2} D_y(\mathbf{v}^0) \Big\} = \mathbf{f}(x) - \nabla_x p^0(x) \quad \text{in} \quad Y_F. \tag{20}$$

Now we are able to write the resulting homogenized two-scale system.

$$\nabla_y p^1 - \nabla_y \cdot \Big\{ |D_y(\mathbf{v}^0)|^{r-2} D_y(\mathbf{v}^0) \Big\} = \mathbf{f}(x) - \nabla_x p^0(x) \quad \text{in} \quad Y_F \times \Omega, \tag{21}$$

$$\nabla_y \cdot \mathbf{v}^0 = 0 \quad \text{in} \quad Y_F \times \Omega; \quad \mathbf{v}^0 = 0 \quad \text{on} \quad S \times \Omega, \tag{22}$$

$$\{\mathbf{v}^0, p^1\} \quad \text{are} \quad Y - \text{periodic}, \tag{23}$$

$$\nabla_x \cdot \Big(\int_{Y_F} \mathbf{v}^0(x, y)\, dy \Big) = 0 \quad \text{in} \quad \Omega, \tag{24}$$

$$\mathbf{n} \cdot \int_{Y_F} \mathbf{v}^0(x, y)\, dy = 0 \quad \text{on} \quad \partial\Omega. \tag{25}$$

System (21)–(25) is called the **two-pressures quasi-Newtonian Stokes problem**.

Let

$$V = \{\psi \in L^r(\Omega; W^{1,r}_{per}(Y_F)^3) \mid \psi \text{ satisfies conditions (22)–(25)}\}.$$

Then the variational form of system (21)–(25) is

Find $\mathbf{v}^0 \in V$ such that

$$\int_\Omega \int_{Y_F} |D_y(\mathbf{v}^0)|^{r-2} D_y(\mathbf{v}^0) : D_y(\psi)\, dydx = \int_\Omega \int_{Y_F} \mathbf{f} \cdot \psi\, dydx, \quad \forall \psi \in V. \tag{26}$$

After [16] and [33], the strict monotonicity, continuity and coercivity of the operator yields existence of a unique solution for problem (26).

Similar to the Newtonian case,

$$-\nabla_y \cdot \left\{|D_y(\mathbf{v}^0)|^{r-2} D_y(\mathbf{v}^0)\right\} - \mathbf{f} = 0 \quad \text{in} \quad V'$$

means that $-\nabla_y \cdot \left\{|D_y(\mathbf{v}^0)|^{r-2} D_y(\mathbf{v}^0)\right\} - \mathbf{f}$ is an element of the subspace

$$\tilde{V} = \{\nabla_x \varphi + \nabla_y \psi,\ \varphi \in W^{1,r/(r-1)}(\Omega) \text{ and } \psi \in L^{r/(r-1)}(\Omega, L^{r/(r-1)}_{per}(Y_F)/\mathbb{R})\}$$

of $L^{r/(r-1)}(\Omega, W^{-1,r/(r-1)}(Y_F)^3)$.

The uniqueness of the pressure field is linked to the following surjectivity property:

Lemma 2 (See [5]) *For any function $\theta \in L^q(\Omega)^3$, $1 < q < +\infty$, there exists $\sigma_\theta \in L^q(\Omega; W^{1,q}_{per}(Y_F)^3)$ such that*

$$\nabla_y \cdot \sigma_\theta = 0 \quad \text{in } Y_F; \quad \sigma_\theta = 0 \quad \text{on } S; \int_{Y_F} \sigma_\theta\, dy = \theta(x) \tag{27}$$

and $||\sigma||_{L^q(\Omega; W^{1,q}_{per}(Y_F)^3)} \leq C||\theta||_{L^q(\Omega)^3}$.

In the uniqueness proof, we get for the pressures differences $p = p^0_1 - p^0_2$ and $\pi = p^1_1 - p^1_2$, $\nabla_x p + \nabla_y \pi = 0$. Consequently,

$$-\nabla_x p \cdot \int_{Y_F} \xi(x, y)\, dy = 0 \quad \forall \xi \in W^{1,r}_{\text{per}}(Y_F)^3,$$

$$\nabla_y \cdot \xi = 0 \text{ in } Y_F \times \Omega,\ \xi = 0 \text{ on } S \times \Omega.$$

Now using Lemma 2 we get $\nabla_x p = 0$. It implies $p = 0$ in $L^{r/(r-1)}_0(\Omega) = \{z \in L^{r/(r-1)}(\Omega) | \int_\Omega z\, dx = 0\}$. Finally, $\nabla_y \pi = 0$ and $\pi = 0$.

Remark 2 After the discussion in [73] and [74], the filtration laws of the form

$$U_{filt} = M(\dot{\gamma}_{eff}, K, \varphi)\nabla p$$

are usually used in applications. U_{filt} is the filtration velocity and M is the effective mobility, defined as the ratio of the permeability to the effective viscosity and depending on the effective shear rate $\dot{\gamma}_{eff}$, permeability K and porosity φ. After our two-scale expansions, it makes sense to link the effective shear rate $\dot{\gamma}_{eff}$ to $\nabla_x p^0$.

The obtained two-scale filtration law (21)–(23) is not of Darcy law type and generally does not lead to the usual filtration law used in standard engineering treatment (e.g. as in [27, 80] and [67]):

$$\mathbf{v} = (\frac{K}{\mu_{eff}}[-\frac{\partial p}{\partial x}])^{1/(r-1)} \tag{28}$$

The above filtration law is obtained by modelling a porous medium as a collection of long capillary tubes through which the fully developed laminar flow occurs.

If we suppose the flow only in the x_1 direction then the variables x and y in two pressures quasi-Newtonian Stokes system (21)–(25) can be separated. Then solving (21)–(25) leads to a non-linear one dimensional power-like law, identical to the one used in the engineering literature. In our notation it reads

$$\int_{Y_F} \mathbf{v}(x, y)\, dy = |f - \frac{dp}{dx_1}|^{r'-2} \cdot (f - \frac{dp}{dx_1}) \int_{Y_F} \mathbf{u}(y)\, dy,$$

where $\mathbf{u}$ is the solution of two pressures quasi-Newtonian Stokes system (21)–(25) for the right hand side of (21) being $\mathbf{e}^1 = (1, 0, 0)$.

However, it should be noticed that this argument holds only in the one dimensional case. Our laws, except for a tubular porous medium, are nonlocal and they cannot be reduced to a multi-dimensional variant of (28), connecting the Darcy velocity $\mathbf{v}$ and some power of ∇p. Most laboratory experiments are performed for one-dimensional flows, which makes difficult observing any dimensional effect. From the engineering point of view, it is important to have not only a good laboratory prediction, but also the filtration laws for the oil fields.

In the case of tube flows, a detailed study of the filtration laws is in [21] and [55].

Remark 3 For more details on the formal two-scale expansions presented above we refer to [72] and [65].

Remark 4 The impossibility to separate slow scale x and the fast scale y in the homogenized momentum equation (21)–(23) has consequences to the numerical simulations. A numerical method of a good performance was introduced in [36]. A study of the analytic properties of the homogenized law was undertaken in [22].

2.4 The Filtration Laws via Two-Scale Asymptotic Expansions: Carreau Law

The analogous procedure applies to the case of the Carreau-Yasuda law.

We start with the a priori estimate pour Carreau law. As before, we use Poincaré's inequality in a porous medium (7). In the Carreau-Yosuda law $\eta_\infty \approx 0$ and we neglect it. Furthermore, we suppose $\lambda = \lambda_0/\varepsilon$ and $1 < r < 2$. Then, after testing Eq. (4) with the solution we obtain

$$||\mathbf{v}||_{L^r} + \varepsilon ||D(\mathbf{v})||_{L^r} \leq C\varepsilon^2, \tag{29}$$

in the case of Carreau's law.

Hence the characteristic velocity U is of order $O(\varepsilon^2)$ and the Reynolds number Re=$\rho L_0 U/\eta_0$ is small. Therefore, it is enough to consider the quasi-Newtonian Stokes equations.

Consequently, in the case of Carreau law (3), with $\eta_\infty = 0$, we consider the dimensionless system

$$-\nabla \cdot \{(1 + \frac{\lambda_0^2}{\varepsilon^2}|D(\mathbf{v}^\varepsilon)|^2)^{r/2-1} D(\mathbf{v}^\varepsilon)\} + \nabla p^\varepsilon = \mathbf{f} \qquad \text{in } \Omega_\varepsilon, \tag{30}$$

$$\nabla \cdot \mathbf{v}^\varepsilon = 0 \qquad \text{in } \Omega_\varepsilon, \tag{31}$$

$$\mathbf{v}^\varepsilon = 0 \qquad \text{on } \partial\Omega_\varepsilon. \tag{32}$$

Problem (30)–(32) is equivalent to the minimization problem

$$\min_{\varphi \in V_r(\Omega_\varepsilon)} J(\varphi) = \min_{\varphi \in V_r(\Omega_\varepsilon)} \{\frac{\varepsilon^2}{r\lambda_0^2} \int_{\Omega_\varepsilon} (1 + \frac{\lambda_0^2}{\varepsilon^2}|D(\mathbf{v}^\varepsilon)|^2)^{r/2}\, dx - \int_{\Omega_\varepsilon} \mathbf{f} \cdot \varphi\, dx\}. \tag{33}$$

For $1 < r < +\infty$, J is strictly convex, proper, continuous and coercive, which yields the existence and the uniqueness of the minimizer $\mathbf{v}^\varepsilon \in V_r(\Omega_\varepsilon)$. The pressure field is (again) recovered using the De Rham or Tartar's constructions.

$\mathbf{v}^\varepsilon$ satisfies a priori estimate (29) and we make a hypothesis that p^ε is uniformly bounded in $L^{r'}(\Omega_\varepsilon)$.

We will use the two-scale asymptotic expansion (1) to perform the formal homogenization of the system (30)–(32). Introducing the fast variable $y = x/\varepsilon$, we assume that the solution of (30)–(32) can be developed in the following way

$$\begin{cases} \mathbf{v}^\varepsilon(x) = \varepsilon^2\{\mathbf{v}^0(x,y) + \varepsilon \mathbf{v}^1(x,y) + \dots\}, \\ p^\varepsilon(x) = p^0(x,y) + \varepsilon p^1(x,y) + \dots. \end{cases}$$

As before, the differential operators transform as follows

$$\nabla\cdot = \frac{1}{\varepsilon}\nabla_y \cdot + \nabla_x\cdot; \quad D = \frac{1}{\varepsilon}D_y + D_x; \quad \nabla = \frac{1}{\varepsilon}\nabla_y + \nabla_x;$$

$$(1 + \frac{\lambda_0^2}{\varepsilon^2}|D(\mathbf{v}^\varepsilon)|^2)^{r/2-1} = |1 + \lambda_0^2|D_y(\mathbf{v}^0) + O(\varepsilon)|^2|^{r/2-1}.$$

In the case of Carreau's law, the formal asymptotic expansion for the *mass conservation equation* is identical to the case of the power law:

Insertion of the two-scale expansion into the incompressibility condition (31) yields

$$\frac{1}{\varepsilon}\nabla_y \cdot \mathbf{v}^0 + \nabla_x \cdot \mathbf{v}^0 + \nabla_y \cdot \mathbf{v}^1 = O(\varepsilon).$$

Hence at order $O(1/\varepsilon)$ we have

$$\nabla_y \cdot \mathbf{v}^0 = 0 \quad \text{in} \quad Y_F; \quad \mathbf{v}^0 = 0 \quad \text{on} \quad S \tag{34}$$

and at order $O(1)$

$$\nabla_x \cdot \mathbf{v}^0 + \nabla_y \cdot \mathbf{v}^1 = 0 \quad \text{in} \quad Y_F; \quad \mathbf{v}^1 = 0 \quad \text{on} \quad S. \tag{35}$$

Integration of Eq. (35) over Y_F yields the macroscopic mass conservation equation

$$\nabla_x \cdot \Big(\int_{Y_F} \mathbf{v}^0(x, y)\, dy \Big) = 0 \quad \text{in} \quad \Omega. \tag{36}$$

Insertion of the two-scale expansion into the *momentum equation* (30) is slightly different and yields

$$-\Big\{\frac{1}{\varepsilon}\nabla_y \cdot + \nabla_x \cdot \Big\} \Big\{\varepsilon|1 + \lambda_0^2|D_y(\mathbf{v}^0) + O(\varepsilon)|^2|^{r/2-1}(D_y(\mathbf{v}^0) + O(\varepsilon))\Big\}$$
$$+\frac{1}{\varepsilon}\nabla_y p^0 + \nabla_x p^0 + \nabla_y p^1 + O(\varepsilon) = \mathbf{f}. \tag{37}$$

At order $O(1/\varepsilon)$, Eq. (37) yields

$$\nabla_y p^0 = 0 \quad \Rightarrow p^0 = p^0(x). \tag{38}$$

At order $O(1)$ Eq. (37) yields

$$\nabla_y p^1 - \nabla_y \cdot \Big\{(1 + \lambda_0^2|D_y(\mathbf{v}^0)|^2)^{r/2-1} D_y(\mathbf{v}^0)\Big\} = \mathbf{f}(x) - \nabla_x p^0(x) \quad \text{in} \quad Y_F. \tag{39}$$

Now we are able to write the resulting homogenized two-scale system.

$$\nabla_y p^1 - \nabla_y \cdot \left\{(1+\lambda_0^2|D_y(\mathbf{v}^0)|^2)^{r/2-1} D_y(\mathbf{v}^0)\right\} = \mathbf{f}(x) - \nabla_x p^0(x) \quad \text{in} \quad Y_F \times \Omega, \tag{40}$$

$$\nabla_y \cdot \mathbf{v}^0 = 0 \quad \text{in} \quad Y_F \times \Omega; \quad \mathbf{v}^0 = 0 \quad \text{on} \quad S \times \Omega, \tag{41}$$

$$\{\mathbf{v}^0, p^1\} \quad \text{are} \quad Y - \text{periodic} \tag{42}$$

$$\nabla_x \cdot \Big(\int_{Y_F} \mathbf{v}^0(x,y)\, dy \Big) = 0 \quad \text{in} \quad \Omega, \tag{43}$$

$$\mathbf{n} \cdot \int_{Y_F} \mathbf{v}^0(x,y)\, dy = 0 \quad \text{on} \quad \partial\Omega. \tag{44}$$

System (40)–(44) is called the **two-pressures Carreau-Stokes problem**.

Let

$$V = \{\psi \in L^r(\Omega; W^{1,r}_{per}(Y_F)^3) \mid \psi \text{ satisfies conditions (41)–(44)}\}.$$

Then the variational form of system (40)–(44) is

Find $\mathbf{v}^0 \in V$ such that

$$\int_\Omega \int_{Y_F} (1+\lambda_0^2|D_y(\mathbf{v}^0)|^2)^{r/2-1} D_y(\mathbf{v}^0) : D_y(\psi)\, dydx = \int_\Omega \int_{Y_F} \mathbf{f} \cdot \psi\, dydx, \quad \forall \psi \in V. \tag{45}$$

After [16] and [33], the strict monotonicity, continuity and coercivity of the operator yields existence of a unique solution for problem (26).

Similar to the Newtonian case,

$$-\nabla_y \cdot \left\{(1+\lambda_0^2|D_y(\mathbf{v}^0)|^2)^{r/2-1} D_y(\mathbf{v}^0)\right\} - \mathbf{f} = 0 \quad \text{in} \quad V'$$

means that $-\nabla_y \cdot \left\{|D_y(\mathbf{v}^0)|^{r-2} D_y(\mathbf{v}^0)\right\} - \mathbf{f}$ is an element of the subspace

$$\tilde{V} = \{\nabla_x \varphi + \nabla_y \psi,\ \varphi \in W^{1,r/(r-1)} \text{ and } \psi \in L^{r/(r-1)}(\Omega, L^{r/(r-1)}_{per}(Y_F)/\mathbb{R})\}$$

of $L^{r/(r-1)}(\Omega, W^{-1,r/(r-1)}(Y_F)^3)$.

The uniqueness of the pressure field is proved similarly like to the power law case.

Remark 5 Finding the filtration laws of the form

$$U_{filt} = M(\dot{\gamma}_{eff}, K, \varphi)\nabla p$$

is even more complicated in this case. The consideration from [22] apply to the Carreau law case as well.

2.5 The Filtration Laws via Two-Scale Asymptotic Expansions: Bingham Fluid Case

In this subsection we discuss briefly the filtration laws for a Bingham fluid (a visco-plastic fluid) in a porous medium.

As in Sect. 2.3 let $\mathbf{v}$ be the velocity, p the pressure and $D(\mathbf{v}) = (\nabla\mathbf{v} + \nabla\mathbf{v}^t)/2$ the rate-of-strain tensor. In the case of the Bingham fluid, the stress tensor σ is given by

$$\sigma = -pI + (2\eta_0 + \frac{g}{\dot{\gamma}})D(\mathbf{v}), \tag{46}$$

where η_0 is the viscosity and $\dot{\gamma} = \sqrt{|D(\mathbf{v})|^2/2}$ is the shear rate. The deviatoric stress tensor τ, i.e. the part of the total stress tensor that is zero at equilibrium, is then a nonlinear function of the shear rate $D(\mathbf{v})$,

$$\tau = (2\eta_0 + \frac{g}{\dot{\gamma}})D(\mathbf{v}).$$

Constitutive law (46) is valid only if $\dot{\gamma} \neq 0$.

In [32], Duvaut and Lions have shown that this constitutive law is equivalent with the following one:

$$\begin{cases} |\tau|^2/2 \leq g \Rightarrow D(\mathbf{v}) = 0, \\ |\tau|^2/2 > g \Rightarrow D(\mathbf{v}) = (1 - g/\dot{\gamma})\tau/(2\eta_0). \end{cases} \tag{47}$$

This is a threshold law: as long as the shear stress is below g, the fluid behaves as a rigid solid. When the value of the shear stress exceeds g, the fluid flows and obeys a nonlinear constitutive law. Moreover, the fluid is incompressible.

We will deal with the variational formulation of the problem. Let

$$V(\Omega_p) = \{\psi | \psi \in H_0^1(\Omega_p)^3,\ \nabla \cdot \psi = 0 \ \text{ in } \Omega_p\}.$$

Then the variational problem reads as follows:

Find $\mathbf{v} \in V(\Omega)$ such that

$$2\eta_0 \int_{\Omega_p} D(\mathbf{v}) : D(\psi - \mathbf{v})\, dx + 2g \int_{\Omega_p} (\dot{\gamma}(\psi) - \dot{\gamma}(\mathbf{v}))\, dx \geq$$

$$\int_{\Omega_p} \mathbf{f} \cdot (\psi - \mathbf{v})\, dx, \forall \psi \in V(\Omega_p). \tag{48}$$

Problem (48) was studied in [32] and existence and uniqueness were proved. Furthermore, the corresponding differential interpretation result was established:

Proposition 2 *Let* $\mathbf{v}$ *be the solution for (48). Then there exist a matrix* $\mathscr{M}(x)$ *and a function* $p \in L^2_0(\Omega_p)$ *such that*

$$\mathscr{M}_{ij} \in L^\infty(\Omega_p);\ \mathscr{M}_{ij} = \mathscr{M}_{ji},\ \forall i,j;\ Tr(\mathscr{M}) = 0;$$
$$|\mathscr{M}| \leq 1 \text{ a.e. on } \Omega_p;\ \mathscr{M} : D(\mathbf{v}) = |D(\mathbf{v})| \text{ a.e. on } \Omega_p;$$
$$-\eta_0 \Delta \mathbf{v} - g\sqrt{2}\nabla \cdot \mathscr{M} = \mathbf{f} - \nabla p.$$

Following [44] we will study the following dimensionless Bingham flow model in a porous medium

Find $\mathbf{v}^\varepsilon \in V(\Omega_\varepsilon)$ such that

$$2\eta_0 \varepsilon^2 \int_{\Omega_\varepsilon} D(\mathbf{v}^\varepsilon) : D(\psi - \mathbf{v}^\varepsilon)\, dx + 2g\varepsilon \int_{\Omega_\varepsilon} (\dot{\gamma}\ (\psi) - \dot{\gamma}\ (\mathbf{v}^\varepsilon))\, dx \geq$$
$$\int_{\Omega_\varepsilon} \mathbf{f} \cdot (\psi - \mathbf{v}^\varepsilon)\, dx, \forall \psi \in V(\Omega_\varepsilon). \tag{49}$$

and study the behavior of the problem in the limit $\varepsilon \to 0$. The corresponding two-scale asymptotic expansion was developed in [44] and a detailed study of the homogenized problem undertaken. The computations are involved and the interested reader can consult article [44].

We will see that for variational inequality (49) direct use of the two-scale convergence is rigorous and shorter than using formal asymptotic expansions.

3 An Introduction to the Two-Scale Convergence with Special Attention to the Two-Scale Lower Semi-Continuity

We start with recalling basic facts from functional analysis. Let $Y = (0,1)^d$, $d = 1, 2, 3$, be the unit cube in $\mathbb{R}^d$ and Q a bounded open set in $\mathbb{R}^d$.

Definition 1 A sequence $\{u^\varepsilon\}$ in $L^q(Q)$, $1 \leq q < +\infty$ is said to converge *weakly* to $u \in L^q(Q)$ if

$$\lim_{\varepsilon \to 0} \int_Q u^\varepsilon(x) v(x)\, dx = \int_Q u(x) v(x)\, dx, \quad \forall v \in L^{q*}(Q);\ q^* = q/(q-1).$$

The notation is $u^\varepsilon \rightharpoonup u$. If $q = +\infty$, then $q^* = 1$ and we have the weak* convergence in $L^\infty(Q)$.

After [23], the weak topology on a Banach space E is the coarsest topology in which the linear forms are continuous.

Lemma 3 (A Property of the Mean Value—See e.g. [39]) *Let f be a $Y-$periodic function. Then*

$$f(\frac{x}{\varepsilon}) \rightharpoonup \frac{1}{|Y|}\int_Y f(y)\,dy \quad \text{weakly in} \quad L^q(Q), \quad \text{for } 1 \le q < +\infty,$$
$$\text{and weak}^* \text{ in } L^\infty(Q), \text{ as } \varepsilon \to 0. \tag{50}$$

Example 1 $\sin\frac{x}{\varepsilon} \rightharpoonup 0$ weakly in $L^q_{loc}(\mathbb{R}^d)$ for $1 \le q < +\infty$ and weak* in $L^\infty(Q)$, as $\varepsilon \to 0$.

Our difficulty is that in the homogenization problems we will have to calculate limits of the type

$$\lim_{\varepsilon\to 0}\int_Q A(\frac{x}{\varepsilon})\nabla u^\varepsilon \psi\, dx,$$

with weakly converging ∇u^ε and $A(\frac{x}{\varepsilon})$. Their product will not converge in general to the product of the weak limits.

Example 2 $\sin\frac{x}{\varepsilon} \rightharpoonup 0$ weakly, as $\varepsilon \to 0$, but $\sin^2\frac{x}{\varepsilon} \rightharpoonup 1/2$ weakly and not to 0.

Therefore the weak convergence is not well adapted to our needs and the strong convergence is out of reach for problems with oscillations.

There are several methods to pass to the limit in such products, like Tartar's energy method and the compensated compactness (see e.g. [39]).

Here we will present the two-scale convergence method, which involves a convergence which is weaker than the strong convergence but stronger than the weak convergence. We will see that it captures successfully the oscillations. It was introduced by Nguetseng in [62] and developed by Allaire in [5].

Definition 2 The bounded sequence $\{w^\varepsilon\} \subset L^q(Q)$, $1 < q < +\infty$, is said to <u>two-scale</u> converge to a limit $w \in L^q(Q \times Y)$ if and only if for any $\xi \in L^{q/(q-1)}(Q; C^\infty_{\text{per}}(Y))$ ("per" denotes Y-periodicity) one has

$$\lim_{\varepsilon\to 0}\int_Q w^\varepsilon(x)\xi(x, \frac{x}{\varepsilon})\,dx = \int_Q\int_Y w(x,y)\xi(x,y)\,dy\,dx\,.$$

We note that for ξ the values on the diagonal $y = x/\varepsilon$ have to make sense and for $\xi \in L^2(Q \times Y)$ it is not the case.

(*Admissible functions*) A function f belongs to $L^q(Q, C_{per}(Y))$, $1 < q < +\infty$, if and only if there exists a subset E of measure zero in Q such that

(a) For any $x \in Q\backslash E$, the function $y \to f(x, y)$ is continuous and $Y-$ periodic.
(b) For any $y \in Y$, the function $x \to f(x, y)$ is measurable.
(c) The function $x \to \sup_{y\in Y}|f(x, y)|$ has finite $L^q(Q)$ norm.

Furthermore, the function $x \to f(x, \frac{x}{\varepsilon})$ is measurable and

$$||f(x, \frac{x}{\varepsilon})||_{L^2(Q)} \leq ||f||_{L^2(Q;C_{per}(Y))}; \tag{51}$$

$$\lim_{\varepsilon \to 0} \int_Q |f(x, \frac{x}{\varepsilon})|^2 \, dx = \int_Q \int_Y |f(x,y)|^2 \, dxdy. \tag{52}$$

The spaces $L^q(Q, C_{per}(Y))$, $L^q_{loc}(Y, C(\overline{Q}))$ and $C(\overline{Q}, C_{per}(Y))$, $1 \leq q < +\infty$, are all separable Banach spaces, dense in $L^q(Q \times Y)$. We refer to [48] for more details about the notion of the two-scale convergence in L^q-setting and the admissibility conditions for the test functions.

Example 3 $\sin \frac{x}{\varepsilon} \rightharpoonup 0$ weakly but $\sin \frac{x}{\varepsilon} \to \sin y$ in two-scales, thus retaining the information on the shape of oscillations present in the sequence. Note that the two-scale convergence will not see the oscillations which are not in resonance with those of test functions: $u(x, x/\varepsilon^2) \to \int_Y u(x,y) \, dy$ in two-scales, as $\varepsilon \to 0$.

The Basic Compactness Theorem for the Two-Scale Convergence With the weak convergence/topology, we have less open sets than when using the strong topology but more compact sets. The situation is similar with the two-scale convergence. Boundedness of a sequence will be sufficient for relative two-scale compactness. The proof is based on

The Sequential Banach-Alaoglu Theorem (See [23]) Let X be a separable Banach space. Then every bounded sequence in X^* has a weak* convergent subsequence.

Theorem 1 *Let $\{u^\varepsilon\}$ be a bounded sequence in $L^q(Q)$, $1 < q < +\infty$. Then there exists a subsequence, denoted by the same subscripts, and $u^0 \in L^q(Q \times Y)$ such that $\{u^\varepsilon\}$ two-scales converges to u^0.*

Proof

Step 1. Let $\psi \in L^{q/(q-1)}(Q, C_{per}(Y))$. We define a sequence of functionals $\{\mu_\varepsilon\}$ on $L^{q/(q-1)}(Q, C_{per}(Y))$ by

$$< \mu_\varepsilon, \psi > = \int_Q u^\varepsilon(x) \psi(x, \frac{x}{\varepsilon}) \, dx.$$

It is easy to see that

$$| < \mu_\varepsilon, \psi > | \leq | \int_Q u^\varepsilon(x) \psi(x, \frac{x}{\varepsilon}) \, dx| \leq C||\psi(x, \frac{x}{\varepsilon})||_{L^{q/(q-1)}(Q)}$$
$$\leq C||\psi(x,y)||_{L^{q/(q-1)}(Q, C_{per}(Y))}.$$

Hence the sequence $\{\mu_\varepsilon\}$ is bounded in $(L^{q/(q-1)}(Q, C_{per}(Y)))^*$.

Step 2. $L^{q/(q-1)}(Q, C_{per}(Y))$ is separable and by the sequential Banach-Alaoglu theorem, there is a subsequence of $\{\mu_\varepsilon\}$ and a $\mu \in (L^{q/(q-1)}(Q, C_{per}(Y)))^*$ such that $\mu_\varepsilon \rightharpoonup \mu$ in the weak* topology in $(L^{q/(q-1)}(Q, C_{per}(Y)))^*$. Thus

$$< \mu_\varepsilon, \psi > \to < \mu, \psi >, \quad \forall \psi \in L^{q/(q-1)}(Q, C_{per}(Y)).$$

Step 3. Obviously

$$| < \mu, \psi > | \le C\Big(\int_Q |\psi(x, \frac{x}{\varepsilon})|^{q/(q-1)}\, dx\Big)^{1-1/q} \le C||\psi(x, y)||_{L^{q/(q-1)}(Q\times Y)}. \tag{53}$$

Since $L^{q/(q-1)}(Q, C_{per}(Y))$ is dense in $L^{q/(q-1)}(Q \times Y)$, we can extend μ to a bounded linear functional on $L^{q/(q-1)}(Q \times Y)$. The extension is denoted $\tilde{\mu}$.

$\tilde{\mu}$ satisfies estimate (53) and by the Riesz representation theorem $\tilde{\mu}$ can be identified with an element $u^0 \in L^q(Q \times Y)$. Then we have

$$\lim_{\varepsilon\to 0} \int_Q u^\varepsilon(x)\psi(x, \frac{x}{\varepsilon})\, dx = \lim_{\varepsilon\to 0} < \mu_\varepsilon, \psi > = < \mu, \psi >$$
$$= \int_Q \int_Y u^0(x, y)\sigma(x, y)\, dy\, dx\,,$$

for every $\psi \in L^{q/(q-1)}(Q, C_{per}(Y))$. This completes the proof.□

It is well-known that for PDEs the weak compactness in Sobolev spaces is of importance. It is the same with the two-scale compactness. We follow the approach of Allaire from [5]. Applying the basic compactness theorem for the two-scale convergence first to the functions and then to their derivatives, and then simply comparing the limits yields

Proposition 3 (See [5])

(a) Let w^ε and $\varepsilon\nabla w^\varepsilon$ be bounded sequences in $L^q(Q)$, $1 < q < +\infty$. Then there exists a function $w \in L^q(Q; W^{1,q}_{per}(Y))$ and a subsequence such that both w^ε and $\varepsilon\nabla w^\varepsilon$ two-scale converge to w and $\nabla_y w$, resp.

(b) Let w^ε and ∇w^ε be bounded sequences in $L^q(Q)$, $1 < q < +\infty$. Then there exists functions $w \in W^{1,q}(Q)$ and $w_1 \in L^q(Q; W^{1,q}_{per}(Y))$ and a subsequence such that both w^ε and ∇w^ε two-scale converge to w and $\nabla_x w + \nabla_y w_1$, resp.

(c) Let $\sigma \in L^q_{per}(Y)$, define $\sigma^\varepsilon(x) = \sigma(\frac{x}{\varepsilon})$, and let the sequence $\{w^\varepsilon\} \subset L^q(Q)$ two-scale converges to a limit $w \in L^q(Q \times Y)$. Then $\{\sigma^\varepsilon w^\varepsilon\}$ two-scale converges to a limit σw.

(d) Let $\mathbf{v}^\varepsilon$ be a divergence-free bounded sequence in $L^q(Q)^d$, $1 < q < +\infty$, which two-scale convergences to $\mathbf{v}^0 \in L^q(Q \times Y)^d$. then, the two-scale limit satisfies $div_y \mathbf{v}^0(x, y) = 0$ a.e. in $Q \times Y$ and $\int_Y div_x \mathbf{v}^0(x, y)\, dy = 0$.

Remark 6 Strong Convergence $\Rightarrow$ Two-scale Convergence $\Rightarrow$ Weak convergence
Weak Convergence $\not\Rightarrow$ Two-scale Convergence $\not\Rightarrow$ Strong convergence

After recalling these basic properties we give a sequential lower semicontinuity result for two-scale convergence in L^q, $1 < q < +\infty$.

Proposition 4 (See [5]) *Let $\Phi : \mathbb{R}^n \to \mathbb{R}^+$ be a continuous function satisfying $0 \leq \Phi(\lambda)$ for all $\lambda \in \mathbb{R}^n$, $\sigma \in C_0^\infty(Q; C_{per}^\infty(Y))^n$, and $\sigma^\varepsilon(x) = \sigma(x, \frac{x}{\varepsilon})$. Then*

$$\lim_{\varepsilon \to 0} \int_Q \Phi(\sigma^\varepsilon)\, dx = \int_Q \int_Y \Phi(\sigma)\, dy\, dx. \tag{54}$$

Furthermore, let Φ in addition be strictly convex and C^1 in $\mathbb{R}^{n^2}$, satisfying

$$c|\lambda|^q \leq \Phi(\lambda) \leq C(1 + |\lambda|^q), \quad \forall \lambda \in \mathbb{R}^d,\ 1 < q < +\infty.$$

Then, if $\mathbf{v}^\varepsilon$ is a bounded sequence from $L^q(\Omega)^n$ which two-scale converges towards $\mathbf{v}$, we have

$$\liminf_{\varepsilon \to 0} \int_Q \Phi(\mathbf{v}^\varepsilon)\, dx \geq \int_Q \int_Y \Phi(\mathbf{v})\, dy\, dx. \tag{55}$$

Remark 7 In fact the two scale semi-continuity result is not directly stated in [5], but it is contained in the proof of Theorem 3.3, pages 1500–1503. For $q = 2$ the result is stated in [6] as theorem 3.7 on page 243. For the confort of the reader we recall the argument from [5]:

Since Φ is convex and C^1, we have

$$\Phi(\mathbf{v}^\varepsilon) \geq \Phi(\boldsymbol{\psi}(x, \frac{x}{\varepsilon})) + \nabla_v \Phi(\boldsymbol{\psi}(x, \frac{x}{\varepsilon}))(\mathbf{v}^\varepsilon - \boldsymbol{\psi}(x, \frac{x}{\varepsilon})),$$

for every $\boldsymbol{\psi} \in C_0^\infty(\Omega; C_{per}^\infty(Y))^d$, implying

$$\liminf_{\varepsilon \to 0} \int_Q \Phi(\mathbf{v}^\varepsilon)\, dx \geq \liminf_{\varepsilon \to 0} \int_Q \Phi(\boldsymbol{\psi}(x, \frac{x}{\varepsilon})\, dx +$$

$$\liminf_{\varepsilon \to 0} \int_Q \nabla_v \Phi(\boldsymbol{\psi}(x, \frac{x}{\varepsilon}))(\mathbf{v}^\varepsilon - \boldsymbol{\psi}(x, \frac{x}{\varepsilon}))\, dx = \int_Q \int_Y \Phi(\boldsymbol{\psi}(x, y))\, dy\, dx +$$

$$\int_Q \int_Y \nabla_v \Phi(\boldsymbol{\psi}(x, y))(\mathbf{v}(x, y) - \boldsymbol{\psi}(x, y))\, dxdy. \tag{56}$$

Next, we take for $\boldsymbol{\psi}$ a sequence of smooth functions $\boldsymbol{\psi}_k \in C_0^\infty(\Omega; C_{per}^\infty(Y))^d$ which converges to $\mathbf{v}$ strongly in $L^q(Q \times Y)^d$. Due to the growth conditions on Φ and smoothness, inequality (56) holds also in the limit $\boldsymbol{\psi}_k \to \mathbf{v}$ in the two-scale sense and we obtain the inequality (55). Note that the coercivity is not required for the lower semi-continuity.

In several applications (Bingham flows, friction, ...) the functional

$$\psi \to \int_Q |\psi(x)|\, dx$$

arises. We have

Proposition 5 *Let* $\{\mathbf{v}^\varepsilon\}$ *be a bounded sequence from* $(L^q(\Omega))^n$, $1 < q < +\infty$, *which two-scale converges towards* $\mathbf{v}$, *we have*

$$\liminf_{\varepsilon\to 0} \int_Q |\mathbf{v}^\varepsilon(x)|\, dx \geq \int_Q \int_Y |\mathbf{v}(x,y)|\, dy\, dx. \tag{57}$$

Proof The functions $f_\delta = \sqrt{|x|^2+\delta^2} - \delta$ are C^1 with partial derivatives $\dfrac{\partial f_\delta}{\partial x_j} = x_j/\sqrt{|x|^2+\delta^2}$, $j = 1, \ldots, n$. We have

$$\int_Q ||\mathbf{v}^\varepsilon| - f_\delta(\mathbf{v}^\varepsilon)|\, dx \leq c\delta$$

and

$$\sqrt{|\mathbf{v}^\varepsilon|^2+\delta^2} - \delta \geq \sqrt{|\psi|^2(x,\frac{x}{\varepsilon})+\delta^2} - \delta + \sum_{j=1}^d \frac{\psi_j(x,\frac{x}{\varepsilon})}{\sqrt{|\psi|^2(x,\frac{x}{\varepsilon})+\delta^2}}(v_j^\varepsilon - \psi_j(x,\frac{x}{\varepsilon}))$$

for every smooth $\psi(x,y)$. Hence we have

$$\liminf_{\varepsilon\to 0} \int_Q (\sqrt{|\mathbf{v}^\varepsilon|^2+\delta^2} - \delta)\, dx \geq \int_Q \int_Y (\sqrt{|\psi|^2(x,y)+\delta^2} - \delta)\, dxdy +$$

$$\sum_{j=1}^d \int_Q \int_Y \frac{\psi_j(x,y)}{\sqrt{|\psi|^2(x,y)+\delta^2}}(v_j - \psi_j(x,y))\, dxdy$$

Now we take a sequence of smooth functions ψ, periodic in y, which strongly converges to $\mathbf{v}$. It yields

$$\liminf_{\varepsilon\to 0} \int_Q (\sqrt{|\mathbf{v}^\varepsilon|^2+\delta^2} - \delta)\, dx \geq \int_Q \int_Y (\sqrt{|\mathbf{v}|^2(x,y)+\delta^2} - \delta)\, dxdy \Rightarrow$$

$$\liminf_{\varepsilon\to 0} \int_Q |\mathbf{v}^\varepsilon(x)|\, dx \geq \liminf_{\varepsilon\to 0} \int_Q (\sqrt{|\mathbf{v}^\varepsilon|^2+\delta^2} - \delta)\, dx - C\delta \geq$$

$$\int_Q \int_Y (\sqrt{|\mathbf{v}|^2(x,y)+\delta^2} - \delta)\, dxdy - C\delta \geq \int_Q \int_Y |\mathbf{v}|\, dx - C\delta, \quad \forall \delta > 0$$

and the proposition is proved.□

Remark 8 It is important to note that two-scale convergence is a tool adapted to the particular problem one wants to solve. Consequently, other two-scale convergences can be introduced. An example are the problems with chemical reactions/biological processes on surfaces Γ^ε. Then the appropriate tool is the *two-scale convergence on the surfaces* developed in [7, 61] and [49]. Another example is the *two-scale convergence with drift*, designed to handle homogenization of reaction-diffusion equations with large Péclet and Damkohler's numbers. For details we refer to [10, 50] and [8].

4 The a Priori Estimates for the Pressure and the Two-Scale Limits in the Case of the Power Law Viscosity

In order to use the two-scale convergence, we first need a priori estimates. We suppose $d = 3$ and all result also hold for $d = 2$.

We recall the estimate (9), valid in the case of the power-law viscosity:

$$||\mathbf{v}^\varepsilon||_{L^r} + \varepsilon||D(\mathbf{v}^\varepsilon)||_{L^r} \leq C\varepsilon^{r/(r-1)}.$$

In order to investigate the behavior of solutions to (11)–(13), as $\varepsilon \to 0$, we need to extend $\mathbf{v}^\varepsilon$ and p^ε to the whole of Ω. We extend $\mathbf{v}^\varepsilon$ by zero in $\Omega\backslash\Omega_\varepsilon$. It is well known that extension by zero preserves L^q and $W_0^{1,q}$ norms for $1 < q < \infty$.

Extending the pressure is a much more difficult task. The extension is closely related to the construction of the restriction operator $R_q \in \mathscr{L}\big(W^{1,q}(Y)^d,\ W_S^{1,q}(Y_F)^n\big)$, $d = 2, 3$, where $W_S^{1,q}(Y_F) = \{\mathbf{z} \in W^{1,q}(Y_F) : z = 0$ on $S\}$.

A priori estimates for the pressure are derived using the a priori estimates for the velocity and the equation:

$$\nabla p^\varepsilon = \mathbf{f} + \nabla \cdot \{|D(\mathbf{v}^\varepsilon)|^{r-2}D(\mathbf{v}^\varepsilon)\} \Rightarrow$$

$$< \nabla p^\varepsilon, \psi >= \int_{\Omega_\varepsilon} (|D(\mathbf{v}^\varepsilon)|^{r-2}D(\mathbf{v}^\varepsilon) : D(\psi) + \mathbf{f} \cdot \psi)\, dx, \quad \forall \psi \in W_0^{1,r}(\Omega_\varepsilon)^3. \tag{58}$$

Hence the pressure p^ε satisfies the inequality

$$\|\nabla p^\varepsilon\|_{W^{-1,r'}(\Omega_\varepsilon)^3} \leq C\varepsilon. \tag{59}$$

The functional space $W^{-1,r'}(\Omega_\varepsilon)^3$ changes with ε and estimate (59) is difficult to use. Our strategy is to extend the pressure to the solid part of the porous medium.

Following the idea of Lipton, Avellaneda [45] and using the constructions by Tartar and Allaire (see [4, 6] and the Appendix of [71]) we define the extension of pressure p^ε by

$$\tilde{p}^\varepsilon = \begin{cases} p^\varepsilon, & \text{in} \quad \Omega_\varepsilon, \\ \dfrac{1}{|\varepsilon(Y_F + i)|} \displaystyle\int_{Y^\varepsilon_{F_i}} p^\varepsilon, & \text{in the } Y^\varepsilon_{S_i} \text{ for each } i, \end{cases} \tag{60}$$

where $Y^\varepsilon_{F_i}$ is the fluid part of the cell Y^ε_i. Note that solid part of the porous medium is an union of all $Y^\varepsilon_{S_i}$. We have

Proposition 6 (See [6]) *The pressure extension $\tilde{p}^\varepsilon \in L^{r'}_0(\Omega)$ of the function p^ε, defined by (60) satisfies the estimate*

$$\|\tilde{p}^\varepsilon\|_{L^{r'}(\Omega)} + \|\nabla\tilde{p}^\varepsilon\|_{W^{-1,r'}(\Omega)^3} \le C, \ n = 2, 3. \tag{61}$$

Furthermore for arbitrary sequence $\{w^\varepsilon\} \subset L^r_0(\Omega)^3$ which converges weakly to 0, we have

$$\int_\Omega \tilde{p}^\varepsilon w^\varepsilon \to 0 \quad \text{as } \varepsilon \to 0. \tag{62}$$

Proposition 7 *Let $\{\mathbf{v}^\varepsilon, p^\varepsilon\}$ be corresponding solutions of the power-law system (11)–(13). Then there exist subsequences of $\{\mathbf{v}^\varepsilon\}$ and $\{\tilde{p}^\varepsilon\}$ (again denoted by the same symbols) and functions $\mathbf{v}^*_0 \in L^r(\Omega \times Y)^3$, $p^* \in L^{r/(r-1)}_0(\Omega)$ and $\nabla_y \mathbf{v}^*_0 \in L^r(\Omega \times Y)^9$ such that*

$$\varepsilon^{-r/(r-1)}\mathbf{v}^\varepsilon \to \mathbf{v}^*_0 \quad \text{in the two-scale sense in } L^r, \tag{63}$$

$$\varepsilon^{-1/(r-1)}\nabla\mathbf{v}^\varepsilon \to \nabla_y \mathbf{v}^*_0 \in L^r(\Omega \times Y)^9 \text{ in the two-scale sense in } L^r, \tag{64}$$

$$\varepsilon^{-r/(r-1)}\mathbf{v}^\varepsilon \to \mathbf{v}^* = \int_{Y_F} \mathbf{v}^*_0 \, dy \text{ weakly in } L^r(\Omega)^3, \tag{65}$$

$$\tilde{p}^\varepsilon \to p^* \text{ in } L^{r/(r-1)}_0(\Omega), \tag{66}$$

as $\varepsilon \to 0$.

Proof Proof of Proposition 7 follows directly from (9) and (61), through the compactness results stated in Proposition 3. The pressure convergence (66) follows the formal two-scale expansion:

Let $\psi \in C^\infty_0\left(\Omega; C^\infty_{\text{per}}(Y_F)\right)^3$ such that $\psi(x, y) = 0$ on S for (a.e.) $x \in \Omega$ and set $\psi^\varepsilon(x) = \psi(x, \frac{x}{\varepsilon})$. We test Eq. (21) with $\varepsilon\psi^\varepsilon$. It yields

$$0 = \lim_{\varepsilon\to 0} \int_\Omega \tilde{p}^\varepsilon \nabla_y \cdot \psi^\varepsilon \, dx = \int_\Omega \int_Y p^* \nabla_y \cdot \psi(x, y) \, dx \, dy = < \nabla_y p^*, \psi >_{\Omega\times Y} .$$

Hence p^* is independent of y. The information is enough for passing to the limit in the terms containing the pressure, but after [71], (62) implies also the strong convergence of $\tilde{p}^\varepsilon$. $\square$.

Using the incompressibility and the weak convergence (65), we find out that the average $\mathbf{v}^*$ satisfies the equations

$$\nabla_x \cdot \mathbf{v}^* = 0 \text{ in } \Omega, \quad \mathbf{v}^* \cdot \mathbf{n} = 0 \text{ on } \partial\Omega. \tag{67}$$

Lemma 4 $\mathbf{v}_0^* \in L^r\big(\Omega; W_S^{1,r}(Y_F)^3\big)$ *and* $\nabla_y \cdot \mathbf{v}_0^* = 0$ *in* Y_F.

Proof Let ψ be a smooth function. Then

$$0 = -\int_{\Omega_\varepsilon} \varepsilon^{-r/(r-1)} \mathbf{v}^\varepsilon \cdot \varepsilon \nabla \psi(x, \frac{x}{\varepsilon})\, dx \to -\int_\Omega \int_{Y_F} \mathbf{v}_0^* \cdot \nabla_y \psi \, dy dx = 0.$$

$\Rightarrow \nabla_y \cdot \mathbf{v}_0^* = 0$ in Y_F.$\square$

Proposition 8 *The functions* $\mathbf{v}_0^*$ *and* p^* *defined, respectively, by (63) and (66) satisfy the two-pressures quasi-Newtonian Stokes problem (21)–(25).*

Proof It remains only to justify the momentum equation (21):

$$\nabla \cdot \left\{ |D_y(\mathbf{v}_0^*)|^{r-2} D_y(\mathbf{v}_0^*) \right\} + \nabla_y \pi(x, y) = \mathbf{f} - \nabla_x p^*(x) \text{ in } Y_F \times \Omega.$$

We use equation

$$\int_{\Omega_\varepsilon} |D(\mathbf{v}^\varepsilon)|^{r-2} D(\mathbf{v}^\varepsilon) : D(\psi)\, dx + < \nabla p^\varepsilon - \mathbf{f}, \psi >= 0, \ \forall \psi \in W_0^{1,r}(\Omega_\varepsilon). \tag{68}$$

Using Minty's lemma[1] we write it in as a minimization problem with a given pressure:

$$\int_\Omega \frac{1}{r} |\varepsilon D(\psi)|^r \, dx - \int_\Omega \frac{1}{r} |\varepsilon D(\varepsilon^{-r/(r-1)} \mathbf{v}^\varepsilon)|^r \, dx \geq$$
$$-\langle f - \nabla \tilde{p}^\varepsilon, \ \psi - \varepsilon^{-r/(r-1)} \mathbf{v}^\varepsilon \rangle_\Omega, \quad \forall \psi \in W_0^{1,r}(\Omega_\varepsilon)^3. \tag{69}$$

[1] *Minty's lemma* (see [33]) Let F be a convex lower semi-continuous and proper functional on a reflexive Banach space B. Then for $u \in B$ the following three conditions are equivalent to each other:

(a) u solves the problem $\inf_{v \in B} F(v)$.
(b) $< F'(u), v - u >\geq 0, \quad \forall\, v \in B.$
(c) $< F'(v), v - u >\geq 0, \quad \forall\, v \in B.$

Next we choose $\psi \in C_0^\infty\big(\Omega; C^\infty_{\rm per}(Y_F)\big)^3$ such that $\psi(x,y) = 0$ on S for (a.e.) $x \in \Omega$, $\nabla_y \cdot \psi = 0$ in Y_F and set $\psi^\varepsilon(x) = \psi(x, \frac{x}{\varepsilon})$.

We insert $\psi = \psi^\varepsilon$ as a test function in (69). It yields

$$-\langle \nabla \tilde{p}^\varepsilon, \psi^\varepsilon \rangle_\Omega = \int_\Omega \tilde{p}^\varepsilon \nabla_x \cdot \psi^\varepsilon \to \int_\Omega \int_Y p^* \nabla_x \cdot \psi(x,y)\, dx\, dy, \quad \text{as } \varepsilon \to 0.$$

The above limit and Proposition 4 imply

$$\int_\Omega \int_Y \frac{1}{r} |D_y(\psi)|^r \, dx\, dy - \int_\Omega \int_Y \frac{1}{r} |D_y(\mathbf{v}_0^*)|^r \, dx\, dy \geq$$
$$\langle \mathbf{f} - \nabla p^*(x), \int_Y (\psi - \mathbf{v}_0^*)\, dy \rangle_\Omega. \tag{70}$$

Using again Minty's lemma and de Rham's formula yield

$$-\nabla_y \cdot \{|D_y(\mathbf{v}_0^*)|^{r-2} D_y(\mathbf{v}_0^*)\} + \nabla_y \pi(x,y) = \mathbf{f} - \nabla p^*(x) \ \text{ in } \ Y_F$$
$$\nabla_y \cdot \mathbf{v}_0^* = 0 \ \text{ in } \ Y_F, \quad \mathbf{v}_0^* = 0 \ \text{ on } \ S,$$

and (21) is justified.□

Therefore we justified rigorously the two-pressures quasi-Newtonian Stokes problem. The uniqueness theorem from Sect. 2.1 implies that the whole sequence converges towards $\{\mathbf{v}_0^*, p^*\} = \{\mathbf{v}^0, p^0\}$.

4.1 A Priori Estimates and the Two-Scale Convergence for the Case of the Law of Carreau

We recall the Carreau-Stokes system, corresponding to Carreau law (3):

$$-\nabla \cdot \{(1 + \frac{\lambda_0^2}{\varepsilon^2} |D(\mathbf{v}^\varepsilon)|^2)^{r/2-1} D(\mathbf{v}^\varepsilon)\} + \nabla p^\varepsilon = \mathbf{f} \ \text{ in } \Omega_\varepsilon, \tag{71}$$
$$\nabla \cdot \mathbf{v}^\varepsilon = 0 \qquad \text{in } \Omega_\varepsilon, \tag{72}$$
$$\mathbf{v}^\varepsilon = 0 \qquad \text{on } \partial\Omega_\varepsilon. \tag{73}$$

We also recall the a priori estimate (10) for the velocity:

$$||\mathbf{v}^\varepsilon||_{L^r} + \varepsilon ||D(\mathbf{v}^\varepsilon)||_{L^r} \leq C\varepsilon^2.$$

In order to investigate the behavior of solutions to (71)–(73), as $\varepsilon \to 0$, we need to extend v^ε and p^ε to the whole of Ω. We extend v^ε by zero in $\Omega \backslash \Omega_\varepsilon$. It is well known that extension by zero preserves L^q and $W_0^{1,q}$ norms for $1 < q < \infty$.

Extending the pressure is a much more difficult task. A priori estimates for the pressure are derived using the a priori estimates for the velocity and the momentum equation (30):

$$\nabla p^\varepsilon = \mathbf{f} + \nabla \cdot \{(1 + \frac{\lambda_0^2}{\varepsilon^2}|D(\mathbf{v}^\varepsilon)|^2)^{r/2-1} D(\mathbf{v}^\varepsilon)\} \Rightarrow$$

$$< \nabla p^\varepsilon, \psi >= \int_{\Omega_\varepsilon} ((1 + \frac{\lambda_0^2}{\varepsilon^2}|D(\mathbf{v}^\varepsilon)|^2)^{r/2-1} D(\mathbf{v}^\varepsilon) : D(\psi) + \mathbf{f} \cdot \psi)\, dx,$$

$$\forall \psi \in W_0^{1,r}(\Omega_\varepsilon)^3. \tag{74}$$

Hence the pressure p^ε satisfies the inequality

$$\|\nabla p^\varepsilon\|_{W^{-1,r'}(\Omega_\varepsilon)^3} \leq C\varepsilon, \quad r' = r/(r-1). \tag{75}$$

Extension of the pressure to the solid part of the porous medium is done again using formula (60) and estimate (61) is valid again..

Furthermore for arbitrary sequence $\{w^\varepsilon\} \subset L_0^r(\Omega)^3$ which converges weakly to 0, we have

$$\int_\Omega \tilde{p}^\varepsilon w^\varepsilon \to 0 \quad \text{as } \varepsilon \to 0. \tag{76}$$

Proposition 9 *Let $\{\mathbf{v}^\varepsilon, p^\varepsilon\}$ be the corresponding solutions of the Carreau-Stokes system (71)–(73). Then there exist subsequences of $\{\mathbf{v}^\varepsilon\}$ and $\{\tilde{p}^\varepsilon\}$ (again denoted by the same symbols) and functions $\mathbf{v}_0^* \in L^r(\Omega \times Y)^3$, $p^* \in L_0^{r'}(\Omega)$ and $\nabla_y \mathbf{v}_0^* \in L^r(\Omega \times Y)^9$ such that*

$$\varepsilon^{-2}\mathbf{v}^\varepsilon \to \mathbf{v}_0^C \quad \textit{in the two-scale sense in } L^r, \tag{77}$$

$$\varepsilon^{-1}\nabla \mathbf{v}^\varepsilon \to \nabla_y \mathbf{v}_0^C \in L^r(\Omega \times Y)^9 \quad \textit{in the two-scale sense in } L^r, \tag{78}$$

$$\varepsilon^{-2}\mathbf{v}^\varepsilon \to \mathbf{v}^C = \int_{Y_F} \mathbf{v}_0^C\, dy \quad \textit{weakly in } L^r(\Omega)^3, \tag{79}$$

$$\tilde{p}^\varepsilon \to p^C \quad \textit{in } L_0^{r'}(\Omega), \tag{80}$$

as $\varepsilon \to 0$.

Derivation of the macro and micro level mass conservation laws in the case of Carreau law is exactly the same as in the case of the power law. Only the momentum equations differs slightly.

Proposition 10 *The functions* $\mathbf{v}_0^C$ *and* p^C *defined, respectively, by (77) and (80) satisfy the two-pressures Carreau-Stokes problem (40)–(44).*

Proof It remains only to justify the momentum equation (40):

$$\nabla_y p^1 - \nabla_y \cdot \left\{(1+\lambda_0^2|D_y(\mathbf{v}_0^C)|^2)^{r/2-1} D_y(\mathbf{v}_0^C)\right\} = \mathbf{f}(x) - \nabla_x p^C(x)$$
$$\text{in } Y_F \times \Omega.$$

We use the variational equation

$$\int_{\Omega_\varepsilon} (1+\frac{\lambda_0^2}{\varepsilon^2}|D(\mathbf{v}^\varepsilon)|^2)^{r/2-1} D(\mathbf{v}^\varepsilon) : D(\psi)\, dx + < \nabla p^\varepsilon - \mathbf{f}, \psi >= 0,$$
$$\forall \psi \in W_0^{1,r}(\Omega_\varepsilon)^3, \tag{81}$$

and write it in as a minimization problem for a given pressure:

$$\int_\Omega \frac{1}{r\lambda_0^2}(1+\lambda_0^2|\varepsilon D(\psi)|^2)^{r/2}\, dx - \int_\Omega \frac{1}{r\lambda_0^2}(1+\lambda_0^2|\varepsilon^{-1} D(\mathbf{v}^\varepsilon)|^2)^{r/2}\, dx \geq$$
$$-\langle f - \nabla \tilde{p}^\varepsilon,\ \psi - \varepsilon^{-2}\mathbf{v}^\varepsilon\rangle_\Omega, \quad \forall \psi \in W_0^{1,r}(\Omega_\varepsilon)^3. \tag{82}$$

Now we choose $\psi \in C_0^\infty\left(\Omega; C_{\text{per}}^\infty(Y_F)\right)^3$, such that $\psi(x,y) = 0$ on S for (a.e.) $x \in \Omega$, $\nabla_y \cdot \psi = 0$ in Y_F, and define $\psi^\varepsilon(x) = \psi(x, \frac{x}{\varepsilon})$.

We insert $\psi = \psi^\varepsilon$ in (82). Then

$$-\langle \nabla \tilde{p}^\varepsilon, \psi^\varepsilon\rangle_\Omega = \int_\Omega \tilde{p}^\varepsilon \nabla_x \cdot \psi^\varepsilon \to \int_\Omega \int_Y p^C \nabla_x \cdot \psi(x,y)\, dx\, dy \text{ as } \varepsilon \to 0.$$

The above limit and Proposition 4 imply

$$\int_\Omega \int_Y \frac{1}{r}|D_y(\psi)|^r\, dx\, dy - \int_\Omega \int_Y \frac{1}{r}|D_y(\mathbf{v}_0^C)|^r\, dx\, dy \geq$$
$$\langle \mathbf{f} - \nabla p^C(x), \int_Y (\psi - \mathbf{v}_0^C)\, dy\rangle_\Omega. \tag{83}$$

After recalling Minty's lemma, using de Rham's formula yields

$$-\nabla_y \cdot \{(1+\lambda_0^2|D_y(\mathbf{v}_0^C)|^2)^{r/2-1} D_y(\mathbf{v}_0^C)\} + \nabla_y \pi(x,y) = \mathbf{f} - \nabla p^C(x) \text{ in } Y_F$$
$$\nabla_y \cdot \mathbf{v}_0^C = 0 \text{ in } Y_F, \quad \mathbf{v}_0^C = 0 \text{ on } S,$$

and (40) is justified.□

Therefore we justified rigorously the two-pressures Carreau-Newtonian Stokes problem. The uniqueness theorem from Sect. 2.1 implies that the whole sequence converges towards $\{\mathbf{v}_0^C, p^C\} = \{\mathbf{v}^0, p^0\}$.

Remark 9 We note that other scalings are discussed in [20]. In other cases, depending on the scaling of λ, the limit could be either the classical Darcy law or the power law.

4.2 A Priori Estimates and the Two-Scale Convergence for the Case of the Bingham Flow

In the case of the Bingham flow through a porous medium we study variational problem (49). The proofs follow reference [19].

Find $\mathbf{u}_\varepsilon \in V(\Omega_\varepsilon)$ such that

$$2\eta_0\varepsilon^2 \int_{\Omega_\varepsilon} D(\mathbf{u}_\varepsilon) : D(\psi - \mathbf{u}_\varepsilon)\, dx + 2g\varepsilon \int_{\Omega_\varepsilon} (\dot{\gamma}\ (\psi) - \dot{\gamma}\ (\mathbf{u}_\varepsilon))\, dx \geq$$

$$\int_{\Omega_\varepsilon} \mathbf{f} \cdot (\psi - \mathbf{u}_\varepsilon)\, dx, \quad \forall \psi \in V(\Omega_\varepsilon). \tag{84}$$

and study the behavior of the solution $\mathbf{u}_\varepsilon$ to problem (84) in the limit $\varepsilon \to 0$.

We start with estimates for the velocity $\mathbf{u}_\varepsilon$, then we obtain a priori estimates for the pressure and extend the pressure to the solid part of the porous medium.

Proposition 11 *Let $(\mathbf{u}_\varepsilon, p_\varepsilon)$ be a solution for (49). Then we have*

$$\|\mathbf{u}_\varepsilon\|_{L^2(\Omega_\varepsilon)^3} \leq C, \tag{85}$$

$$\varepsilon \|\nabla \mathbf{u}_\varepsilon\|_{L^2(\Omega_\varepsilon)^9} \leq C, \tag{86}$$

$$\|\nabla p_\varepsilon\|_{H^{-1}(\Omega_\varepsilon)^3} \leq C\varepsilon. \tag{87}$$

Proof Proof of the estimates (85) and (86) is obtained by taking the solution $\mathbf{u}_\varepsilon$ as a test function in (49). Next, from (49)) we get the inequality

$$| < \nabla p_\varepsilon, v >_{\Omega_\varepsilon} | \leq |(f, v)_{\Omega_\varepsilon}| + |2\eta_0\varepsilon^2 \int_{\Omega_\varepsilon} D(\mathbf{u}_\varepsilon) : D(\psi)\, dx| + g\sqrt{2}\varepsilon \int_{\Omega_\varepsilon} |D(v)|\, dx \tag{88}$$

and (87) follows.□

We extend velocity $\mathbf{u}_\varepsilon$ by zero to the $\Omega \setminus \Omega_\varepsilon$ and denote the extension by the same symbol. Obviously estimates (85) and (86) remain valid and the extension is

divergence free too. The extension of the pressure p_ε is constructed as before and we summarize its properties in the following lemma:

Proposition 12 *The pressure extension $\tilde{p}^\varepsilon \in L^2_0(\Omega)$ of the function p_ε, defined by (60) satisfies the estimate*

$$\|\tilde{p}_\varepsilon\|_{L^2(\Omega)} + \|\nabla \tilde{p}_\varepsilon\|_{H^{-1}(\Omega)^3} \leq C. \tag{89}$$

Furthermore for arbitrary sequence $\{w^\varepsilon\} \subset L^2_0(\Omega)^3$, which converges weakly to 0, we have

$$\int_\Omega \tilde{p}_\varepsilon w^\varepsilon \to 0 \quad \text{as } \varepsilon \to 0. \tag{90}$$

Proposition 13 *Let $\{\mathbf{u}_\varepsilon, p_\varepsilon\}$ be the corresponding solutions of the Bingham system (49). Then there exist subsequences of $\{\mathbf{u}_\varepsilon\}$ and $\{\tilde{p}_\varepsilon\}$ (again denoted by the same symbols) and functions $\mathbf{u}_0^B \in L^2(\Omega \times Y)^3$, $p^B \in L^2_0(\Omega)$ and $\nabla_y \mathbf{u}_0^B \in L^2(\Omega \times Y)^9$ such that*

$$\mathbf{u}_\varepsilon \to \mathbf{u}_0^B \quad \text{in the two-scale sense in } L^2, \tag{91}$$

$$\varepsilon \nabla \mathbf{u}_\varepsilon \to \nabla_y \mathbf{u}_0^B \in L^r(\Omega \times Y)^9 \quad \text{in the two-scale sense in } L^2, \tag{92}$$

$$\mathbf{u}_\varepsilon \to \mathbf{u}^B = \int_{Y_F} \mathbf{u}_0^B \, dy \quad \text{weakly in } L^2(\Omega)^3, \tag{93}$$

$$\tilde{p}_\varepsilon \to p^B \quad \text{in } L^2_0(\Omega), \tag{94}$$

as $\varepsilon \to 0$.

Derivation of the macro and micro level mass conservation laws in the case of the Bingham flow is exactly the same as before. Only passing to the limit in the momentum equation is different.

Proposition 14 *Let*

$$V(Y_F) = \{\psi \mid \psi \in H^1_{per}(Y_F)^3, \ \psi = 0 \text{ on } S, \ \nabla_y \cdot \psi = 0 \text{ in } Y_F\},$$

$$\mathscr{W} = \{\phi \mid \phi \in L^2(\Omega; V(Y_F)), \ \nabla_x \cdot \int_{Y_F} \phi \, dy = 0 \quad \text{in } \Omega$$

$$\text{and } \mathbf{n} \cdot \int_{Y_F} \phi \, dv = 0 \text{ on } \partial\Omega\}.$$

The functions $\mathbf{u}_0^B \in \mathscr{W}$ *and* p^B *defined, respectively, by (91) and (94) satisfy the following two-pressures Bingham variational inequality*

$$2\eta_0 \int_{Y_F} D_y(\mathbf{u}_0^B) : D(\psi - \mathbf{u}_0^B)\, dy + 2g \int_{Y_F} (\dot{\gamma}_y(\psi) - \dot{\gamma}_y(\mathbf{u}_0^B))\, dx \geq$$

$$\int_{Y_F} (\mathbf{f} - \nabla_x p^B) \cdot (\psi - \mathbf{u}_0^B)\, dx, \quad \forall \psi \in V(Y_F). \tag{95}$$

Proof We choose $\psi \in C_0^\infty\big(\Omega; C^\infty_{\mathrm{per}}(Y_F)\big)^3$ such that $\psi(x,y) = 0$ on S for (a.e.) $x \in \Omega$, $\nabla_y \cdot \psi = 0$ in Y_F and define $\psi^\varepsilon(x) = \psi(x, \frac{x}{\varepsilon})$.

Then we write (49) in the form

$$2\eta_0 \varepsilon^2 \int_{\Omega_\varepsilon} D(\mathbf{u}_\varepsilon) : D(\psi^\varepsilon)\, dx + \int_{\Omega_\varepsilon} (g\sqrt{2}\varepsilon |D(\psi^\varepsilon)| - p_\varepsilon \nabla_x \cdot \psi^\varepsilon - \mathbf{f} \cdot \psi^\varepsilon)\, dx \geq$$

$$\int_{\Omega_\varepsilon} (2\eta_0 \varepsilon^2 |D(\mathbf{u}_\varepsilon)|^2 + g\sqrt{2}\varepsilon |D(\mathbf{u}_\varepsilon)| - \mathbf{f} \cdot \mathbf{u}_\varepsilon)\, dx, \tag{96}$$

Next as $\varepsilon \to 0$ we get

$$\int_\Omega \tilde{p}^\varepsilon \nabla_x \cdot \psi^\varepsilon \to \int_\Omega \int_Y p^B(x) \nabla_x \cdot \psi(x,y)\, dx\, dy, \tag{97}$$

$$\int_{\Omega_\varepsilon} g\varepsilon |D(\psi^\varepsilon)|\, dx \to \int_\Omega \int_{Y_F} g |D_y(\psi)|\, dy. \tag{98}$$

Next

$$2\eta_0 \varepsilon^2 \int_{\Omega_\varepsilon} D(\mathbf{u}_\varepsilon) : D(\psi^\varepsilon)\, dx \to \int_\Omega \int_{Y_F} 2\eta_0 D_y(\mathbf{u}_0^B) : D_y(\psi)\, dy dx, \tag{99}$$

$$\int_{\Omega_\varepsilon} (2\eta_0 \varepsilon^2 |D(\mathbf{u}_\varepsilon)|^2 + g\sqrt{2}\varepsilon |D(\mathbf{u}_\varepsilon)|)\, dx \geq$$

$$\int_\Omega \int_{Y_F} (2\eta_0 |D_y(\mathbf{u}_0^B)|^2 + g\sqrt{2} |D_y(\mathbf{u}_0^B)|)\, dy dx \ \text{ as } \ \varepsilon \to 0. \tag{100}$$

Hence we passed to the limit in all terms and the Proposition is proved.□

Therefore we justified rigorously the two-pressures Bingham-Stokes problem (95), (41)–(44). The uniqueness theorem from [44] implies that the whole sequence converges towards $\{\mathbf{u}_0^B, p^B\}$.

4.3 Concluding Remarks on Filtration Laws for Non-Newtonian Fluids

(a) Solving cell problems in the case of the quasi-Newtonian and Bingham flows poses numerical difficulties. See [36] for an efficient numerical method and [22] for an analytic study of the filtration laws, corresponding to the power and Carreau law viscosities.
(b) For the (formal) homogenization of a linear Oldroyd fluid in a bundle of capillary tubes at low Reynolds and Deborah numbers see [42] . Very little is known concerning filtration laws for non-Newtonian fluids, which are more complicated than the quasi-Newtonian ones discussed in this chapter.
(c) Homogenization in Orlicz spaces of the quasi-Newtonian flow equations with more general viscosity laws, was undertaken in [40]. Some viscosity laws, as e.g. Ellis' law

$$\eta_r(\dot{\gamma}) = \frac{\eta_0}{1 + (\dot{\gamma}\ \eta_r(\dot{\gamma}))^{\alpha-1}/\tau_{1/2}^{\alpha-1}} \tag{101}$$

enter into the implicit constitutive laws considered in [24].
(d) An interesting open question is to get a corrector result of the type $\varepsilon^{-r/(r-1)}\mathbf{v}^\varepsilon - \mathbf{v}^0(x, x/\varepsilon) \to 0$ in $L^r(\Omega)^3$, as $\varepsilon \to 0$. For the Newtonian case we refer to [6].

5 Homogenization of the Linearized Ionic Transport Equations in Rigid Periodic Porous Media

The quasi-static transport of an electrolyte through an electrically charged porous medium is an important and well-known multiscale problem in geosciences and porous materials modeling. An N-component electrolyte is a dilute solution of N species of charged particles, or ions, in a fluid which saturates a charged porous medium. The porous medium can be either rigid or deformable.

The overall behavior of such a system is controlled by several phenomena. First there is an effective filtration. It is caused by the hydrodynamic flow in the pore space, heavily influenced by the charge distributions of the system. Second, there is a migration of ions because of an electric field. Third, the diffusive transport of the ions takes place. Finally, we have to take into account electrokinetic phenomena due to the **electric double layer** (EDL) which is formed as a result of the interaction of the electrolyte solution neutralizing the charge of the solid phase at the pore solid-liquid interface.

The EDL can be split into several parts, depending on the strength of the electrostatic coupling. There is a condensed layer of heavily adsorbed ions depending on the molecular nature of the interface. It is generally known as the **Stern layer** and its characteristic width (the Gouy length) is typically less than one nanometer. Adjacent

to the Stern layer the **electrostatic diffuse layer** or **Debye's layer** is formed, where the ion density varies. The EDL is the union of Stern and diffuse layers. The thickness of the diffuse layer is predicted by the Debye length λ_D which depends on the electrolyte concentration. For low to moderate electrolyte concentrations λ_D is in the nanometric range. Outside Debye's layer, in the remaining bulk fluid, the solvent can be considered as electrically neutral.

A detailed, mathematically oriented, presentation of the fundamental concepts of electroosmotic flow in nanochannels can be found in the book [41] by Karniadakis et al., pages 447–470, from which we borrow the notations and definitions.

In the case of porous media with large pores, the electro-osmotic effects are modeled by introducing an effective slip velocity (the Smoluchowski slip) at the solid-liquid interfaces. Such models are not valid for numerous systems, such as clays because the characteristic pore size is also of the order of the EDL size (a few hundreds of nanometers or even less). Therefore the Debye's layer fills largely the pores and its effect cannot anymore be modeled by an effective slip boundary condition at the liquid-solid interface.

In this section, we consider continuum physics equations as the right model for the description of porous media at the pore scale where the EDL phenomena and the pore geometry interact and will search to upscale them. It would allow to derive and validate the macroscopic models used for engineering simulations (see the works of Adler and collaborators [2, 3, 15, 29, 37, 51, 70]). The typical length scale for which the continuum mechanics equations are valid is confirmed to be both experimentally (see e.g. [26]) and theoretically [31, 52] close to 1 nm. Therefore, at the microscopic level we couple the incompressible Stokes equations for the fluid with the electrokinetic model made of a global electrostatic equation and one convection-diffusion equation for each type of ions of an N-component electrolyte in a dilute Newtonian solvent.

We start with the following mass conservation laws

$$\operatorname{div}\left(\mathbf{j}_i + \mathbf{v}n_i\right) = 0 \quad \text{in} \quad \Omega_p, \quad i = 1, \ldots, N, \tag{102}$$

where Ω_p is the pore space of the porous medium, i denotes the solute species, $\mathbf{v}$ is the hydrodynamic velocity and n_i is the ith species concentration. For each species i, $\mathbf{v}n_i$ is its convective flux and $\mathbf{j}_i$ its migration-diffusion flux.

The solute velocity satisfies the incompressible Stokes equations with a forcing term consisting of an exterior hydrodynamical force $\mathbf{f}$ and of the electric force

$$\eta \Delta \mathbf{v} = \mathbf{f} + \nabla p + e \sum_{j=1}^{N} z_j n_j \nabla \Psi \qquad \text{in} \quad \Omega_p, \tag{103}$$

$$\operatorname{div} \mathbf{v} = 0 \qquad \text{in} \quad \Omega_p \quad \text{and} \quad \mathbf{v} = 0 \qquad \text{on} \quad \partial\Omega_p \setminus \partial\Omega, \tag{104}$$

where $\eta > 0$ is the shear viscosity, $\mathbf{f}$ is the external body force, p is the pressure, e is the elementary charge, z_i is the charge number of the species i and Ψ is the electrostatic potential.

We assume that all valencies z_j are different integers. If not, we lump together different ions with the same valency. We rank them by increasing order and we assume that they are both anions and cations, namely positive and negative valencies,

$$z_1 < z_2 < \ldots < z_N, \quad z_1 < 0 < z_N, \tag{105}$$

and we denote by j^+ and j^- the sets of positive and negative valencies.

The migration-diffusion flux $\mathbf{j}_i$ is given by the following semi-linear relationship

$$\mathbf{j}_i = -\sum_{j=1}^{N} L_{ij}(n_1, \ldots, n_N)\big(\nabla \mu_j + z_j e \nabla \Psi\big), \quad i = 1, \ldots, N, \tag{106}$$

where $L_{ij}(n_1, \ldots, n_N)$ is the Onsager coefficient between i and j and μ_j is the chemical potential of the species j given by

$$\mu_j = \mu_j^0 + k_B T \ln n_j + k_B T \ln \gamma_j(n_1, \ldots, n_N), \quad j = 1, \ldots, N, \tag{107}$$

with γ_j being the **activity coefficient** of the species j, k_B is the Boltzmann constant, μ_j^0 is the standard chemical potential expressed at infinite dilution and T is the absolute temperature. The Onsager tensor $\big[L_{ij}\big]$ consists of the linear Onsager coefficients describing interactions between the species i and j. It is symmetric and positive definite. Furthermore, on the fluid/solid interfaces the no-flux condition is imposed

$$\mathbf{j}_i \cdot \nu = 0 \quad \text{on} \quad \partial\Omega_p \setminus \partial\Omega, \quad i = 1, \ldots, N. \tag{108}$$

The electrostatic potential is calculated from Poisson equation with the electric charge density as the bulk source term

$$\mathscr{E} \Delta \Psi = -e \sum_{j=1}^{N} z_j n_j \qquad \text{in} \quad \Omega_p, \tag{109}$$

where $\mathscr{E}$ is the dielectric constant of the solvent. The surface charge Σ is assumed to be given at the pores boundaries and the boundary condition reads

$$\mathscr{E} \nabla \Psi \cdot \nu = -\Sigma \qquad \text{on} \quad \partial\Omega_p \setminus \partial\Omega, \tag{110}$$

where ν is the unit exterior normal to Ω_p.

The various parameters appearing in (102)–(110) are defined in Table 1.

Table 1 Data description

	Quantity	Characteristic value
e	Electron charge	1.6e−19 C (Coulomb)
D_i^0	Diffusivity of the ith species	$D_i^0 \in (1.333, 2.032)$e−09 m^2/s
k_B	Boltzmann constant	1.38e−23 J/K
n_c	Characteristic concentration	$(6.02\,10^{24}, 6.02\,10^{26})$ particles/m^3
T	Temperature	293°K (Kelvin)
$\mathscr{E}$	Dielectric constant	6.93e−10 C/(mV)
η	Dynamic viscosity	1e−3 kg/(m s)
ℓ	Pore size	5e−9 m
λ_D	Debye's length	$\sqrt{\mathscr{E}k_BT/(e^2n_c)} \in (0.042, 0.42)$ nm
z_j	j-th electrolyte valence	Given integer
Σ	Surface charge density	0.129 C/m^2 (clays)
$\mathbf{f}$	Given applied force	N/m^3
σ_j	j-th hard sphere diameter	2e−10 m
Ψ_c	Characteristic electrokinetic potential	0.02527 V (Volt)
L_B	Bjerrum length	7.3e−10 m

The activity coefficients γ_i and the Onsager coefficients L_{ij} depend on the electrolyte. The large majority of theoretical works are concerned with a simple (so-called **ideal**) descriptions of charged porous media. It is based on the Poisson-Nernst-Planck formalism for which the local activity coefficients of ions are neglected and the transport properties are modeled solely from the mobility at infinite dilution. In the **ideal** description we have

$$\gamma_i = 1 \quad \text{and} \quad L_{ij} = \delta_{ij} n_i D_i^0/(k_B T),$$

where $D_i^0 > 0$ is the diffusion coefficient of species i at infinite dilution.

In this section we will suppose that we have an infinite dilution, i.e. an ideal description.

Remark 10 At finite concentration, the non-ideal effects modify the ion transport and they are to be taken into account if a good quantitative description of the system is required. Different models can be used and a widely accepted model is the **Mean Spherical Approximation (MSA)** in its simplified form from [30]. It is valid if the diameters of the ions are not too different. The activity coefficients read

$$\ln \gamma_j = -\frac{L_B \Gamma z_j^2}{1 + \Gamma \sigma_j} + \ln \gamma^{HS}, \quad j = 1, \ldots, N, \tag{111}$$

where σ_j is the j-th ion diameter, L_B is the Bjerrum length, γ^{HS} is the hard sphere term defined by (113), and Γ is the **MSA screening parameter** defined by

$$\Gamma^2 = \pi L_B \sum_{k=1}^{N} \frac{n_k z_k^2}{(1 + \Gamma \sigma_k)^2}. \tag{112}$$

For dilute solutions, i.e., when all n_j are small, we have

$$2\Gamma \approx \kappa = \frac{1}{\lambda_D} \quad \text{with} \quad \lambda_D = \sqrt{\frac{\mathscr{E} k_B T}{e^2 \sum_{k=1}^{N} n_k z_k^2}},$$

where λ_D is the Debye length. Thus, $1/2\Gamma$ generalizes λ_D at finite concentration and it represents the size of the ionic spheres when the ion diameters σ_i are different from zero. In (111) γ^{HS} is the hard sphere term given by

$$\ln \gamma^{HS} = p(\xi) \equiv \xi \frac{8 - 9\xi + 3\xi^2}{(1-\xi)^3}, \quad \text{with} \quad \xi = \frac{\pi}{6} \sum_{k=1}^{N} n_k \sigma_k^3, \tag{113}$$

where ξ is the solute packing fraction.

The Onsager coefficients L_{ij} are given by

$$L_{ij}(n_1, \ldots, n_N) = n_i \left(\frac{D_i^0}{k_B T} \delta_{ij} + \Theta_{ij} \right) \left(1 + \mathscr{R}_{ij} \right), \ i, j = 1, \ldots, N, \tag{114}$$

where $\Theta_{ij} = \Theta_{ij}^c + \Theta_{ij}^{HS}$ stands for the hydrodynamic interactions in the MSA formalism. It is divided into two terms: the Coulomb part is

$$\Theta_{ij}^c = -\frac{1}{3\eta} \frac{z_i z_j L_B n_j}{(1 + \Gamma\sigma_i)(1 + \Gamma\sigma_j) \left(\Gamma + \sum_{k=1}^{N} n_k \frac{\pi L_B z_k^2 \sigma_k}{(1 + \Gamma\sigma_k)^2} \right)}, \tag{115}$$

and the hard sphere part is

$$\Theta_{ij}^{HS} = -\frac{\left(\sigma_i + \sigma_j\right)^2}{12\eta} n_j \frac{1 - \tilde{Y}_3/5 + (\tilde{Y}_3)^2/10}{1 + 2\tilde{Y}_3}, \tag{116}$$

with

$$\tilde{Y}_3 = \frac{\pi}{6} \sum_{i=1}^{N} n_i \frac{3Y_1 Y_2 + Y_3 Y_0}{4Y_0^2} \quad \text{and} \quad Y_k = \frac{\pi}{6} \sum_{i=1}^{N} n_i \sigma_i^k. \tag{117}$$

In (114) $\mathscr{R}_{ij}$ is the electrostatic relaxation term given by

$$\mathscr{R}_{ij} = \frac{\kappa_q^2 e^2 z_i z_j}{3\mathscr{E} k_B T (\sigma_i + \sigma_j)(1 + \Gamma\sigma_i)(1 + \Gamma\sigma_j)} \frac{1 - e^{-2\kappa_q(\sigma_i + \sigma_j)}}{\kappa_q^2 + 2\Gamma\kappa_q + 2\Gamma^2 - 2\pi L_B \sum_{k=1}^{N} n_k \frac{z_k^2 e^{-\kappa_q \sigma_k}}{(1 + \Gamma\sigma_k)^2}} \tag{118}$$

where $\kappa_q > 0$ is defined by

$$\kappa_q^2 = \frac{e^2}{\mathscr{E} k_B T} \frac{\sum_{i=1}^N n_i z_i^2 D_i^0}{\sum_{i=1}^N D_i^0}. \tag{119}$$

Note that when the concentrations n_j are small, all entries L_{ij} are first order perturbations of the ideal values $\delta_{ij} n_i D_i^0/(k_B T)$ and thus the Onsager tensor is positive at first order.

Remark 11 Homogenization of the non-ideal MSA model was undertaken in [14].

At the outer boundary of the porous medium we set

$$\Psi + \Psi^{ext}(x)\ ,\ n_i\ ,\ \mathbf{v} \text{ and } p \text{ are } \Omega - \text{periodic}. \tag{120}$$

The applied exterior potential $\Psi^{ext}(x)$ can typically be linear, equal to $\mathbf{E} \cdot \mathbf{x}$, where $\mathbf{E}$ is an imposed electrical field. Note that the applied exterior force $\mathbf{f}$ in the Stokes equations (103) can also be interpreted as some imposed pressure drop or gravity force. Due to the complexity of the geometry and of the equations, it is necessary for engineering applications to upscale the system (102)–(110), (120) and to replace the flow equations with a Darcy type law, including electro-osmotic effects.

A representative class of porous media are those having a periodic microstructure. We suppose the same periodic microstructure as in Sect. 2.2. For such media, and in the ideal case, formal two-scale asymptotic analysis of system (102)–(110), (120) has been performed in many previous papers. Many of these works rely on a preliminary linearization of the problem, introduced by O'Brien et al. [63]. Let us mention in particular the work of Looker and Carnie in [47], where the formal two-scale expansions were undertaken and the resulting Onsager relations written explicitly. We will present the rigorous justification of the homogenization result, following article [9]. The numerical experiments are provided in [13]. Other relevant references include [68, 69, 76, 77] and [78] .

Remark 12 in this review we will consider only **rigid** porous media. In many important applications porous media are *deformable*. Derivations of the homogenized models for deformable charge porous media were undertaken by Moyne and Murad in [56–60]. For a mathematically rigourous analysis we refer to [12].

The goal of the section is to present the results from [9] and [13], providing the homogenized system for a semi-linearized version of (102)–(110), (120) in a rigid periodic porous medium. The semi-linearization means that we study the solutions being a perturbation of a so-called equilibrium solution which satisfies the full nonlinear system (102)–(110), (120) with vanishing fluxes.

The homogenized system is an elliptic system of $(N+1)$ equations

$$-\operatorname{div}_x \mathscr{M} \nabla(p^0, \{\mu_j\}_{1 \le j \le N}) = \mathscr{S} \quad \text{in } \Omega, \tag{121}$$

where p^0 is the pressure, μ_j the chemical potential of the j-th species, $\mathscr{M}$ the Onsager homogenized tensor and $\mathscr{S}$ a source term. Our goal is to derive rigorously Eq. (121).

Before studying its homogenization, we need a **dimensionless** form of the Eqs. (102)–(110), (120). We follow the same approach as in [9] and [13]. The known data are listed in Table 1 and concern the characteristic pore size ℓ, the characteristic domain size L, the surface charge density Σ (having the characteristic value Σ_c), the characteristic concentrations n_c, the static electrical potential Ψ^{ext} and the applied fluid force $\mathbf{f}$. As usual, we introduce a small parameter ε which is the ratio between the pore size and the medium size, $\varepsilon = \ell/L << 1$.

Table 1 permits calculating Debye's length $\lambda_D = \sqrt{\mathscr{E} k_B T/(e^2 n_c)}$. Following [41], we introduce the characteristic potential $\zeta = k_B T/e$ and the parameter β related to the Debye-Hückel parameter $\kappa = 1/\lambda_D$, is given by $\beta = \left(\dfrac{\ell}{\lambda_D}\right)^2$. Next we rescale the space variable by setting $x' = x/L$ (we shall drop the primes for simplicity in the sequel). The pore space becomes $\Omega_\varepsilon = \Omega_p/L$ which is a periodically perforated domain with period ε. Still following [41], we define other characteristic quantities

$$\Gamma_c = \sqrt{\pi L_B n_c}, \quad p_c = n_c k_B T, \quad u_c = \varepsilon^2 \frac{k_B T n_c L}{\eta},$$

where p_c is a pressure equilibrating the electrokinetic forces in (103) and u_c is the velocity corresponding to a Poiseuille flow in a tube of diameter ℓ, length L and pressure drop p_c. We also introduce adimensionalized forcing terms

$$\Psi^{ext,*} = \frac{e\Psi^{ext}}{k_B T}, \quad \mathbf{f}^* = \frac{\mathbf{f} L}{p_c}, \quad \Sigma^* = \frac{\Sigma}{\Sigma_c}, \quad N_\sigma = \frac{e\Sigma_c \ell}{\mathscr{E} k_B T},$$

and adimensionalized unknowns

$$p^\varepsilon = \frac{p}{p_c}, \ \mathbf{v}^\varepsilon = \frac{\mathbf{v}}{u_c}, \ \Psi^\varepsilon = \frac{e\Psi}{k_B T}, \ n_j^\varepsilon = \frac{n_j}{n_c}, \ \mathbf{j}_j^\varepsilon = \frac{\mathbf{j}_j L}{n_c D_j^0}.$$

The dimensionless equations for hydrodynamical and electrostatic part are thus

$$\varepsilon^2 \Delta \mathbf{v}^\varepsilon - \nabla p^\varepsilon = \mathbf{f}^* + \sum_{j=1}^N z_j n_j^\varepsilon(x) \nabla \Psi^\varepsilon \quad \text{in} \quad \Omega_\varepsilon, \tag{122}$$

$$\mathbf{v}^\varepsilon = 0 \quad \text{on} \quad \partial\Omega_\varepsilon \setminus \partial\Omega, \quad \operatorname{div} \mathbf{v}^\varepsilon = 0 \quad \text{in} \quad \Omega_\varepsilon, \tag{123}$$

$$-\varepsilon^2 \Delta \Psi^\varepsilon = \beta \sum_{j=1}^N z_j n_j^\varepsilon(x) \quad \text{in} \quad \Omega_\varepsilon, \tag{124}$$

$$\varepsilon \nabla \Psi^{\varepsilon} \cdot \nu = -N_{\sigma} \Sigma^{*} \text{ on } \partial \Omega_{\varepsilon} \setminus \partial \Omega, \tag{125}$$

$$(\Psi^{\varepsilon} + \Psi^{ext,*}), \quad n_i^{\varepsilon}, \quad \mathbf{v}^{\varepsilon} \text{ and } p^{\varepsilon} \quad \text{are } \Omega - \text{periodic in } x, \tag{126}$$

$$\text{div} \left(\mathbf{j}_i^{\varepsilon} + \mathbf{Pe}_i \, n_i^{\varepsilon} \mathbf{v}^{\varepsilon} \right) = 0 \quad \text{in} \quad \Omega_{\varepsilon}, \ i = 1, \ldots, N, \tag{127}$$

$$\mathbf{j}_i^{\varepsilon} \cdot \nu = 0 \text{ on } \partial \Omega_{\varepsilon} \setminus \partial \Omega, \ i = 1, \ldots, N, \tag{128}$$

$$\mathbf{j}_i^{\varepsilon} = -n_i^{\varepsilon} \nabla M_i^{\varepsilon} \quad \text{and} \quad M_i^{\varepsilon} = \ln \left(n_i^{\varepsilon} e^{z_i \Psi^{\varepsilon}} \right), \ i = 1, \ldots, N, \tag{129}$$

where the Péclet number for the i-th species is $\text{Pe}_i = \dfrac{u_c L}{D_i^0} = O(1)$.

Remark 13 Existence results for a coupled Navier–Stokes–Nernst–Planck–Poisson system are in [75].

Remark 14 After writing the dimensionless form, we are able to precise in which sense the non-ideal MSA model from Remark 10 is close to the ideal case. The small parameter is the characteristic value $\xi_c = \dfrac{\pi}{6} n_c \sigma_c^3$ of the solute packing fraction, where σ_c is the characteristic ion diameter. In [14] it was established that, under the hypothesis that

$$bi = \frac{L_B}{\sigma_c} \text{ (Bjerrum's parameter)} \quad \text{and} \quad S = \frac{k_B T}{\eta D_c^0 \sigma_c}$$

are $O(1)$, then the ideal case model is the vanishing solute packing fraction ξ_c limit of our non-ideal MSA model. Note that small ξ_c means a low concentration, weighted by the ion size. Namely, we have

$$\left(\frac{D_i^0}{k_B T} \delta_{ij} + \Theta_{ij} \right) \left(1 + \mathscr{R}_{ij} \right) = \delta_{ij} + O(\sqrt{\xi_c}), \quad \text{and} \quad \ln \gamma_j^{\varepsilon} = O(\sqrt{\xi_c}). \tag{130}$$

5.1 Equilibrium Solution

The goal of this subsection is to find a so-called **equilibrium solution** of system (122)–(129) when the exterior forces are vanishing $\mathbf{f} = 0$ and $\Psi^{ext} = 0$. However, the surface charge density Σ^* is not assumed to vanish or to be small. This equilibrium solution will be a reference solution around which we shall linearize system (122)–(129) in the next subsection.

Then we perform the homogenization of the (partially) linearized system. We denote by $n_i^{0,\varepsilon}$, $\Psi^{0,\varepsilon}$, $\mathbf{v}^{0,\varepsilon}$, $M_i^{0,\varepsilon}$, $p^{0,\varepsilon}$ the equilibrium quantities.

In the case $\mathbf{f} = 0$ and $\Psi^{ext} = 0$, one can find an equilibrium solution by choosing a zero fluid velocity and taking all diffusion fluxes equal to zero. More precisely, we require

$$\mathbf{v}^{0,\varepsilon} = 0 \quad \text{and} \quad \nabla M_j^{0,\varepsilon} = 0, \tag{131}$$

which obviously implies that $\mathbf{j}_i^{0,\varepsilon} = 0$ and Eqs. (127)–(128) are satisfied. From $\nabla M_j^{0,\varepsilon} = 0$ and relations (129) we deduce that there exists constant $n_j^0(\infty) > 0$ such that

$$n_j^{0,\varepsilon}(x) = n_j^0(\infty) \exp\{-z_j \Psi^{0,\varepsilon}(x)\}. \tag{132}$$

The Stokes equation (122) shall give the corresponding value of the pressure satisfying

$$\nabla p^{0,\varepsilon}(x) = -\sum_{j=1}^{N} z_j n_j^{0,\varepsilon}(x) \nabla \Psi^{0,\varepsilon}(x) \Rightarrow p^{0,\varepsilon}(x) = \sum_{j=1}^{N} n_j^0(\infty)(x) e^{-z_j \Psi^{0,\varepsilon}(x)}.$$

The value $n_j^0(\infty)$ is the reservoir concentration (also called the infinite dilute concentration) which will be later assumed to satisfy the bulk electroneutrality condition for zero potential.

Then electrostatic equation (124) reduces to the Poisson-Boltzmann equation which is a nonlinear partial differential equation for the unknown $\Psi^{0,\varepsilon}$

$$\begin{cases} -\varepsilon^2 \Delta \Psi^{0,\varepsilon} = \beta \displaystyle\sum_{j=1}^{N} z_j n_j^0(\infty) \exp\left\{-z_j \Psi^{0,\varepsilon}\right\} \ \text{ in } \ \Omega_\varepsilon, \\ \varepsilon \nabla \Psi^{0,\varepsilon} \cdot \nu = -N_\sigma \Sigma^*(\dfrac{x}{\varepsilon}) \ \text{ on } \ \partial\Omega_\varepsilon \setminus \partial\Omega, \ \Psi^{0,\varepsilon} \ \text{ is } \Omega - \text{periodic}. \end{cases} \tag{133}$$

We note that problem (133) is equivalent to the following minimization problem:

$$\inf_{\varphi \in V_\varepsilon} J_\varepsilon(\varphi), \tag{134}$$

with $V_\varepsilon = \{\varphi \in H^1(\Omega_\varepsilon), \ \varphi \text{ is } \Omega - \text{periodic}\}$ and

$$J_\varepsilon(\varphi) = \frac{\varepsilon^2}{2} \int_{\Omega_\varepsilon} |\nabla \varphi|^2 \, dx + \beta \sum_{j=1}^{N} \int_{\Omega_\varepsilon} n_j^0(\infty) e^{-z_j \phi} \, dx + \varepsilon N_\sigma \int_{\Gamma^\varepsilon} \Sigma^*(\frac{x}{\varepsilon}) \varphi \, dS.$$

The functional J_ε is strictly convex, which gives the uniqueness of the minimizer. Nevertheless, for arbitrary non-negative β, $n_j^0(\infty)$ and N_σ, J_ε may be **not coercive** on V_ε if all z_j's have the same sign (take φ to be constant, of the same sign as the z_j's

and tending to infinity). Therefore, we must put a condition on the z_j's so that the minimization problem (134) admits a solution. Following the literature, we impose the **bulk electroneutrality condition**

$$\sum_{j=1}^{N} z_j n_j^0(\infty) = 0, \tag{135}$$

which guarantees that for $\Sigma^* = 0$, the unique solution is $\Psi^{0,\varepsilon} = 0$. Under (135) it is easy to see that J_ε is coercive on V_ε.

We recall that we suppose a periodic porous medium as introduced in Sect. 2.2. By the uniqueness, $\Psi^{0,\varepsilon}(x) = \Psi^0(x/\varepsilon)$, where $\Psi^0(y)$ is a solution to the problem

$$\inf_{\varphi \in V} J(\varphi), \tag{136}$$

with $V = \{\varphi \in H^1(Y_F),\ \varphi \text{ is } 1-\text{periodic}\}$ and

$$J(\varphi) = \frac{1}{2}\int_{Y_F} |\nabla_y \varphi(y)|^2\, dy + \beta \sum_{j=1}^{N} \int_{Y_F} n_j^c \exp\{-z_j\varphi\}\, dy + N_\sigma \int_S \Sigma^*(y)\varphi\, dS.$$

Note that J is strictly convex, which gives the uniqueness of the minimizer. Under condition (135) it is easy to see that J is coercive on V.

Next difficulty is with the continuity of the functional J. In fact it is not defined on V, but on its proper subspace $V_1 = \{\varphi \in H^1(Y_F),\ \exp\{\max_j |z_j||\varphi|\} \in L^1(Y_F)\}$. This situation complicates the solvability of problem (136). The corresponding existence result was established in [46], using a penalization, with a cut-off of the nonlinear terms and applying the theory of pseudo-monotone operators. It reads as follows:

Lemma 5 ([46]) *Assume that the bulk electroneutrality condition (135) holds true and $\Sigma^* \in L^2(S)$. Then problem (136) has a unique solution $\Psi^0 \in V$ such that*

$$\sum_{j=1}^{N} z_j e^{-z_j\Psi^0} \in L^1(Y_F) \quad \text{and} \quad \Psi^0 \sum_{j=1}^{N} z_j e^{-z_j\Psi^0} \in L^1(Y_F).$$

We need that $n_j^0 = n_j^c \exp\{-z_j\Psi^0\}$ satisfies the lower bound $n_j^0(y) \geq C > 0$ in Y_F. It is a consequence of the L^∞-estimate for Ψ^0 from [11], proved by using elementary comparison arguments (a similar result is also proved in [35]).

It is based on the comparison with the solution to the following auxiliary Neumann problem

$$\begin{cases} -\Delta U = \dfrac{1}{|Y_F|}\displaystyle\int_S \Sigma^*\, dS \ \text{ in } \ Y_F, \\ \nabla U \cdot \boldsymbol{\nu} = -\Sigma^* \ \text{ on } \ S, \\ U \ \text{ is } 1-\text{periodic}, \quad \int_{Y_F} U(y)\, dy = 0. \end{cases} \tag{137}$$

Problem (137) admits a unique solution $U \in H^1_{per}(Y_F) \cap C(\overline{Y}_F)$. If Σ^* and S are C^∞, then U is C^∞ as well. U achieves its minimum and maximum in $\overline{Y_F}$.

The L^∞-bound for Ψ^0 reads as follows

Proposition 15 (See [11]) *The solution Ψ^0 of problem (136) satisfies the following bounds*

$$U(y) - U_m - \frac{1}{z_1} \log \max \left(1, \frac{\overline{\sigma}}{\beta z_1 n_1^0(\infty)} - \sum_{j \in j^+} \frac{z_j n_j^0(\infty)}{z_1 n_1^0(\infty)} \right) \geq \Psi^0(y) \geq$$

$$U(y) - U_M - \frac{1}{z_N} \log \max \left(1, \frac{\overline{\sigma}}{\beta z_N n_N^0(\infty)} - \sum_{j \in j^-} \frac{z_j n_j^0(\infty)}{z_N n_N^0(\infty)} \right), \tag{138}$$

where the symbols j^+ and j^- denote the sets of positive and negative valences, respectively, and

$$\overline{\sigma} = \frac{1}{|Y_F|} \int_S \Sigma^* \, dS, \quad U_m = \min_{y \in \overline{Y_F}} U(y) \text{ and } \quad U_M = \max_{y \in \overline{Y_F}} U(y).$$

By classical regularity theory for elliptic partial differential equations, we easily deduce that for $S \in C^\infty$ and $\sigma \in C^\infty_{per}(S)$, $\Psi^0 \in C^\infty(\bar{Y}_F)$.

Remark 15 In [11] the asymptotic analysis of (136), when β goes to zero, was undertaken. This case corresponds to very small pores, $\ell << \lambda_D$. The asymptotic regime depends on the sign of the averaged charge $\int_S \Sigma^* \, dS$. If it is negative (which means that the surface is positively charged), then only the anion with the most negative valence (z_1) is important and that the potential behaves as

$$\Psi^0 \approx \frac{\log \beta}{z_1} + \varphi_0,$$

where φ_0 is the solution of the reduced system, involving only the species 1,

$$\begin{cases} \Delta \varphi_0 = -z_1 n_1^0(\infty) e^{-z_1 \varphi_0} & \text{in the bulk } Y_F, \\ \nabla \varphi_0 \cdot \boldsymbol{\nu} = -\Sigma^*(y) & \text{on the surface } S. \end{cases}$$

As a consequence, the cation concentrations go to zero while the ion concentrations blow up as $n_j = O(\beta^{-z_j/z_1})$ and $n_1 >> n_j$ for $j \neq 1$.

Remark 16 The opposite situation, when β goes to infinity, was also addressed in [11]. This scaling corresponds to very large pores, $\ell >> \lambda_D$. The Debye's layer, describing the behavior of the solution close to the surface, was constructed in a general geometric setting and a rigorous error estimate was given. If we choose the characteristic concentration $n_c = \sum_{k=1}^N z_k^2 n_k^0(\infty)$, then $\sum_{k=1}^N z_k^2 n_k^0(\infty) = 1$ and locally, close to the surface, the potential behaves as

$$\Psi(y) \approx \frac{-\Sigma^*}{\sqrt{\beta}} \exp\left\{ -d(y)\sqrt{\beta} \right\},$$

where $d(y)$ is the distance between the point y and the surface. Away from the surface, the concentrations n_j are constant and satisfy the so-called bulk electroneutrality condition.

The boundary condition for the electrostatic interaction between the two phases is very often simplified by replacing surface charge Σ^*, which corresponds to the chemistry of the system, by a surface potential. Its boundary value at the no slip plane is known as the zeta potential ζ. In [11] the asymptotic behavior for large β was established. It is again a boundary layer but with a totally different profile. More precisely we established

$$\Psi(y) \approx \Psi_{0,\zeta}\left(\sqrt{\beta}d(y)\right)$$

where $d(y)$ is the distance between the point y and the surface and $\Psi_{0,\zeta}$ is the solution of the nonlinear ordinary differential equation

$$\begin{cases} \Psi_{0,\zeta}|_{\xi=0} = \zeta, \quad \mathscr{C}(x) = \sum_{j=1}^{N} n_j^0(\infty)e^{-z_j x} \\ \dfrac{d}{d\xi}\Psi_{0,\zeta} = -2\,\mathrm{sign}(\zeta)\sqrt{\mathscr{C}(\Psi_{0,\zeta}) - \mathscr{C}(0)}. \end{cases} \tag{139}$$

which, starting from the boundary value ζ on the surface, is exponentially decaying at infinity. In many situations, the explicit solutions for $\Psi_{0,\zeta}$ are known. For example, in the case $-z_1 = 1 = z_2$ and $n_1^0(\infty) = n_2^0(\infty) = 1/2$, we have the following Gouy-Chapman solution

$$\Psi_{0,\zeta}(q', \xi) = 2\ln\frac{1 + \tanh(\zeta/2)e^{-\xi}}{1 - \tanh(\zeta/2)e^{-\xi}}.$$

Hence in the case of given potential at the boundary the normal component of the electrical field will behave as $\sqrt{\beta}$, which is unrealistic. In fact, it is rather the surface charge density Σ, proportional to the normal derivative of Ψ, than ζ, which is the relevant parameter for the physical modeling.

5.2 *Linearization and the a Priori Estimates for the Perturbation*

We now proceed to the linearization of electrokinetic equations (122)–(129) around the equilibrium solution computed in Sect. 5.1. We therefore assume that the external forces, namely the static electric potential $\Psi^{ext}(x)$ and the hydrodynamic force $\mathbf{f}(x)$, are small. Note that the surface charge density Σ^* on the pore walls Γ^ε need not to be small since it is part of the equilibrium problem. Such a linearization

process is classical in the ideal case (see the seminal paper [63] by O'Brien et al.). For small exterior forces, we write the perturbed electrokinetic unknowns as

$$n_i^\varepsilon(x) = n_i^{0,\varepsilon}(x) + \delta n_i^\varepsilon(x), \quad \Psi^\varepsilon(x) = \Psi^{0,\varepsilon}(x) + \delta\Psi^\varepsilon(x),$$
$$\mathbf{v}^\varepsilon(x) = \mathbf{v}s^{0,\varepsilon}(x) + \delta\mathbf{v}^\varepsilon(x), \quad p^\varepsilon(x) = p^{0,\varepsilon}(x) + \delta p^\varepsilon(x),$$

where $n_i^{0,\varepsilon}$, $\Psi^{0,\varepsilon}$, $\mathbf{v}^{0,\varepsilon}$, $p^{0,\varepsilon}$ are the equilibrium quantities, corresponding to $\mathbf{f} = 0$ and $\Psi^{ext} = 0$. The δ prefix indicates a perturbation. Since the equilibrium velocity vanishes $\mathbf{v}^{0,\varepsilon} = 0$, we identify in the sequel $\mathbf{v}^\varepsilon = \delta\mathbf{v}^\varepsilon$.

Motivated by the form of the Boltzmann equilibrium distribution and the calculation of $n_i^{0,\varepsilon}$, we follow the lead of [63] and introduce a so-called ionic potential Φ_i^ε which is defined in terms of n_i^ε by

$$n_i^\varepsilon(x) = n_i^0(\infty)\exp\{-z_i(\Psi^\varepsilon(x) + \Phi_i^\varepsilon(x) + \Psi^{ext,*}(x))\}, \tag{140}$$

After linearization (140) yields

$$\delta n_i^\varepsilon(x) = -z_i n_i^{0,\varepsilon}(x)(\delta\Psi^\varepsilon(x) + \Phi_i^\varepsilon(x) + \Psi^{ext,*}(x)). \tag{141}$$

Introducing (141) into (122)–(127) and linearizing yields the following equations for $\delta\Psi^\varepsilon$, $\delta\mathbf{v}^\varepsilon$, δp^ε and Φ_i^ε

$$-\varepsilon^2\Delta(\delta\Psi^\varepsilon) + \beta\left(\sum_{j=1}^N z_j^2 n_j^{0,\varepsilon}(x)\right)\delta\Psi^\varepsilon =$$
$$-\beta\left(\sum_{j=1}^N z_j^2 n_j^{0,\varepsilon}(x)(\Phi_j^\varepsilon + \Psi^{ext,*})\right) \text{ in } \Omega_\varepsilon, \tag{142}$$
$$\varepsilon\nabla\delta\Psi^\varepsilon\cdot\nu = 0 \text{ on } \partial\Omega_\varepsilon\setminus\partial\Omega, \tag{143}$$
$$\delta\Psi^\varepsilon(x) + \Psi^{ext,*}(x) \text{ is } \Omega-\text{periodic}, \tag{144}$$
$$\varepsilon^2\Delta\delta\mathbf{v}^\varepsilon - \nabla\left(\delta p^\varepsilon + \sum_{j=1}^N z_j n_j^{0,\varepsilon}(\delta\Psi^\varepsilon + \Phi_j^\varepsilon + \Psi^{ext,*})\right) =$$
$$\mathbf{f}^* - \sum_{j=1}^N z_j n_j^{0,\varepsilon}(x)(\nabla\Phi_j^\varepsilon + \mathbf{E}^*) \text{ in } \Omega_\varepsilon, \tag{145}$$
$$\text{div}\,\delta\mathbf{v}^\varepsilon = 0 \quad \text{in} \quad \Omega_\varepsilon, \quad \delta\mathbf{v}^\varepsilon = 0 \quad \text{on} \quad \partial\Omega_\varepsilon\setminus\partial\Omega, \tag{146}$$
$$\delta\mathbf{v}^\varepsilon \quad \text{and} \quad \delta p^\varepsilon \text{ are } \Omega-\text{periodic}. \tag{147}$$

Note that the perturbed velocity is actually equal to the overall velocity and that it is convenient to introduce a global pressure P^ε

$$\delta \mathbf{v}^\varepsilon = \mathbf{v}^\varepsilon,\ P^\varepsilon = \delta p^\varepsilon + \sum_{j=1}^{N} z_j n_j^{0,\varepsilon} \left(\delta \Psi^\varepsilon + \Phi_j^\varepsilon + \Psi^{ext,*} \right). \tag{148}$$

A straightforward calculation yields for Φ_j^ε

$$\mathbf{div} \left(n_j^{0,\varepsilon}(x) \left(\nabla \Phi_j^\varepsilon + \mathbf{E}^* + \frac{\mathbf{Pe}_j}{z_j} \mathbf{v}^\varepsilon \right) \right) = 0 \quad \text{in} \quad \Omega_\varepsilon, \tag{149}$$

$$(\nabla \Phi_j^\varepsilon + \mathbf{E}^*) \cdot \nu = 0 \ \text{ on } \quad \partial \Omega_\varepsilon \setminus \partial \Omega, \tag{150}$$

$$\Phi_j^\varepsilon \ \text{ is } \ \Omega - \text{periodic.} \tag{151}$$

$\delta \Psi^\varepsilon$ does not enter Eqs. (145)–(147), (149)–(151) and thus is **decoupled** from the main unknowns $\mathbf{v}^\varepsilon$, P^ε and Φ_i^ε. The system (132), (133), (145)–(148), (149)–(151) is the same microscopic linearized system for the ionic transport as in the work of Looker and Carnie [47].

Next, we establish the variational formulation of system (145)–(147), (149)–(151) for the unknowns $\{\mathbf{v}^\varepsilon, P^\varepsilon, \{\Phi_j^\varepsilon\}_{j=1,\dots,N}\}$ and prove that it admits a unique solution. The functional spaces related to the velocity field are

$$W^\varepsilon = \{\mathbf{g} \in H^1(\Omega_\varepsilon)^3,\ \mathbf{g} = 0 \text{ on } \partial \Omega_\varepsilon \setminus \partial \Omega,\ \Omega - \text{periodic in } x\}$$

and

$$H^\varepsilon = \{\mathbf{g} \in W^\varepsilon,\ \text{div } \mathbf{g} = 0 \ \text{ in } \ \Omega_\varepsilon\}.$$

The variational formulation of (145)–(151) is:

Find $\mathbf{v}^\varepsilon \in H^\varepsilon$ and $\{\Phi_j^\varepsilon\}_{j=1,\dots,N} \in H^1(\Omega_\varepsilon)^N$, Φ_j^ε being Ω-periodic, such that, for any test functions $\mathbf{g} \in H^\varepsilon$ and $\mathbf{b} \in H^1(\Omega_\varepsilon)^N$, $\mathbf{b}$ being Ω-periodic,

$$a\left((\mathbf{v}^\varepsilon, \{\Phi_j^\varepsilon\}), (\mathbf{g}, \mathbf{b}) \right) = \langle \mathscr{L}, (\mathbf{g}, \mathbf{b}) \rangle,$$

where the bilinear form a and the linear form $\mathscr{L}$ are defined by

$$a\left((\mathbf{v}^\varepsilon, \{\Phi_j^\varepsilon\}), (\mathbf{g}, \mathbf{b}) \right) := \varepsilon^2 \int_{\Omega_\varepsilon} \nabla \mathbf{v}^\varepsilon : \nabla \mathbf{g}\, dx + \sum_{i=1}^{N} \frac{z_i^2}{\mathrm{Pe}_i} \int_{\Omega_\varepsilon} n_i^{0,\varepsilon} \nabla \Phi_i^\varepsilon \cdot \nabla b_i\, dx$$

$$+ \sum_{j=1}^{N} z_j \int_{\Omega_\varepsilon} n_j^{0,\varepsilon} \left(\mathbf{v}^\varepsilon \cdot \nabla b_j - \mathbf{g} \cdot \nabla \Phi_j^\varepsilon \right) dx, \tag{152}$$

$$\langle \mathscr{L}, (\mathbf{g}, \mathbf{b}) \rangle := \sum_{i=1}^{N} z_i \int_{\Omega_\varepsilon} n_i^{0,\varepsilon} \mathbf{E}^* \cdot \left(\mathbf{g} - \frac{z_i}{\mathrm{Pe}_i} \nabla \phi_i \right) dx - \int_{\Omega_\varepsilon} \mathbf{f}^* \cdot \mathbf{v}\, dx, \tag{153}$$

where, for simplicity, we denote by $\mathbf{E}^*$ the electric field corresponding to the potential $\Psi^{ext,*}$, i.e., $\mathbf{E}^*(x) = \nabla\Psi^{ext,*}(x)$.

Lemma 6 (See [9]) *Let $\mathbf{E}^*$ and $\mathbf{f}^*$ be given elements of $L^2(\Omega)^3$. The variational formulation (152)–(153) admits a unique solution $(\mathbf{v}^\varepsilon, \{\Phi_j^\varepsilon\}) \in H^\varepsilon \times H^1(\Omega_\varepsilon)^3$, such that Φ_j^ε are 1-periodic and $\int_{\Omega_\varepsilon} \Phi_j^\varepsilon(x)\,dx = 0$. Furthermore, there exists a positive constant C, independent of ε, such that*

$$\|\mathbf{v}^\varepsilon\|_{L^2(\Omega_\varepsilon)^3} + \varepsilon\|\nabla\mathbf{v}^\varepsilon\|_{L^2(\Omega_\varepsilon)^9} + \max_{1\le j\le N}\|\Phi_j^\varepsilon\|_{H^1(\Omega_\varepsilon)} \le$$

$$C\left(\|\mathbf{E}^*\|_{L^2(\Omega)^3} + \|\mathbf{f}^*\|_{L^2(\Omega)^3}\right). \tag{154}$$

Note that the a priori estimates (154) follow by testing the problem (152)–(153) by the solution, using the L^∞-estimate for Ψ^0 and using the well-known scaled Poincaré inequality in Ω_ε (7).

In order to use the two-scale convergence from Sect. 3, we need that our unknowns are $(\mathbf{v}^\varepsilon, P^\varepsilon, \{\Phi_j^\varepsilon\})$ are defined on Ω. As in Sect. 4, $\mathbf{v}^\varepsilon$ is extended by zero to $\Omega \setminus \Omega_\varepsilon$. The pressure field is reconstructed using de Rham's theorem and extended by formula (60) from Sect. 4 to $\tilde{P}^\varepsilon$, being uniformly bounded, with respect to ε, in $L^2_0(\Omega)$. For $\{\Phi_j^\varepsilon\}$ we use an extension operator from the perforated domain Ω^ε into Ω. As was proved in [1], under the assumptions on the geometry from Sect. 2.2, there exists such an extension operator T^ε from $H^1(\Omega_\varepsilon)$ in $H^1(\Omega)$ satisfying $T^\varepsilon\,\phi|_{\Omega^\varepsilon} = \phi$ and the inequalities

$$\|T^\varepsilon\phi\|_{L^2(\Omega)} \le C\|\phi\|_{L^2(\Omega_\varepsilon)},\ \|\nabla(T^\varepsilon\phi)\|_{L^2(\Omega)} \le C\|\nabla\phi\|_{L^2(\Omega_\varepsilon)}$$

with a constant C independent of ε, for any $\phi \in H^1(\Omega_\varepsilon)$. We keep for the extended function $T^\varepsilon\ \Phi_j^\varepsilon$ the same notation Φ_j^ε.

Hence the extensions satisfy estimates (154).

5.3 Homogenization via the Two-Scale Convergence

The formal two-scale asymptotic expansion method from Sects. 1 and 2 can be applied to system (145)–(147), (149)–(151), as in [47] and [9]. Introducing the fast variable $y = x/\varepsilon$, it assumes that the solution of (145)–(147), (149)–(151) is given by

$$\begin{cases} \mathbf{v}^\varepsilon(x) = \mathbf{v}^0(x, x/\varepsilon) + \varepsilon\mathbf{v}^1(x, x/\varepsilon) + \ldots, \\ \tilde{P}^\varepsilon(x) = p^0(x) + \varepsilon p^1(x, x/\varepsilon) + \ldots, \\ \Phi_j^\varepsilon(x) = \Phi_j^0(x) + \varepsilon\Phi_j^1(x, x/\varepsilon) + \ldots. \end{cases} \tag{155}$$

We then plug this ansatz in the Eqs. (145)–(147), (149)–(151). In the way analogous to the calculations in Sect. 2, we identify the various powers of ε and obtain a cascade of equations from which we retain only the leading ones that constitute the two-scale homogenized problem. For details we refer to [47]. We will present a rigorous passing to the limit using the two-scale convergence from Sect. 3.

Lemma 6 and the two-scale compactness Proposition 4 from Sect. 3 imply

Theorem 2 (See [9]) *Under the assumptions of Lemma 6, there exist*

$$(\mathbf{v}^0, p^0) \in L^2(\Omega; H^1_{per}(Y)^3) \times L^2_0(\Omega) \quad \text{and}$$

$$\{\Phi^0_j, \Phi^1_j\}_{j=1,\dots,N} \in \Big(H^1(\Omega) \times L^2(\Omega; H^1_{per}(Y))\Big)^N$$

such that for a subsequence, denoted by the same indices, the solution of (145)–(147), (149)–(151) converges in the following sense

$$\mathbf{v}^\varepsilon \to \mathbf{v}^0(x,y) \quad \textit{in the two-scale sense}$$

$$\varepsilon \nabla \mathbf{v}^\varepsilon \to \nabla_y \mathbf{v}^0(x,y) \quad \textit{in the two-scale sense}$$

$$\tilde{P}^\varepsilon \to p^0(x) \quad \textit{strongly in } L^2(\Omega)$$

$$\Phi^\varepsilon_j \to \Phi^0_j(x) \quad \textit{weakly in } H^1(\Omega) \textit{ and strongly in } L^2(\Omega)$$

$$\nabla \Phi^\varepsilon_j \to \nabla_x \Phi^0_j(x) + \nabla_y \Phi^1_j(x,y) \quad \textit{in the two-scale sense}$$

$$n^{0,\varepsilon}_j \to n^0_j(x,y) \quad \textit{and} \quad \Psi^{0,\varepsilon} \to \Psi^0(y)$$

$$\textit{in the two-scale sense in } L^q, \quad 1 < q < +\infty, \ j = 1, \dots, N.$$

Next we rewrite the variational problem (152)–(153) in the equivalent form, where the velocity test function are not divergence-free and the pressure term is explicitly present:

$$\varepsilon^2 \int_{\Omega_\varepsilon} \nabla \mathbf{v}^\varepsilon : \nabla \xi \, dx - \int_{\Omega_\varepsilon} p^\varepsilon \operatorname{div} \xi \, dx + \sum_{j=1}^N \int_{\Omega_\varepsilon} z_j n^{0,\varepsilon}_j \big(- \xi \cdot \nabla \Phi^\varepsilon_j + \mathbf{v}^\varepsilon \cdot \nabla b_j \big) \, dx +$$

$$\sum_{j=1}^N \frac{z_j^2}{\mathrm{Pe}_j} \int_{\Omega_\varepsilon} n^{0,\varepsilon}_j \nabla \Phi^\varepsilon_j \cdot \nabla b_j \, dx = - \sum_{j=1}^N \frac{z_j^2}{\mathrm{Pe}_j} \int_{\Omega_\varepsilon} n^{0,\varepsilon}_j \mathbf{E}^* \cdot \nabla b_j \, dx$$

$$+ \sum_{j=1}^N \int_{\Omega_\varepsilon} z_j n^{0,\varepsilon}_j \mathbf{E}^* \cdot \xi \, dx - \int_{\Omega_\varepsilon} \mathbf{f}^* \cdot \xi \, dx, \tag{156}$$

for any test functions $\xi \in W^{\varepsilon}$ and $\mathbf{g} \in H^1(\Omega_\varepsilon)^N$, b_j being 1-periodic, $1 \leq j \leq N$. We keep the divergence constraint $\operatorname{div} \mathbf{v}^{\varepsilon} = 0$ in Ω_ε. Next we define the two-scale test functions:

$$\xi^{\varepsilon}(x) = \xi(x, \frac{x}{\varepsilon}), \quad \xi \in C^{\infty}_{per}(\Omega; H^1_{per}(Y)^3),$$

$$\xi = 0 \text{ on } \Omega \times S, \quad \operatorname{div}_y \xi(x, y) = 0 \text{ on } \Omega \times Y, \tag{157}$$

$$b_j^{\varepsilon}(x) = \varphi_j(x) + \varepsilon \gamma_j(x, \frac{x}{\varepsilon}), \ \varphi_j \in C^{\infty}_{per}(\Omega), \quad \gamma_j \in C^{\infty}_{per}(\Omega; H^1_{per}(Y_F)). \tag{158}$$

We take as test function in Eq. (156) $(\xi^{\varepsilon}, \mathbf{b}^{\varepsilon})$. Now we can pass to the limit in (156), along the same lines as in Sect. 4. For the solution we use the convergences from Theorem 2. After passing to the two-scale limit in (156) we get that the limit $(\mathbf{v}^0, p^0, \{\Phi_j^0, \Phi_j^1\})$ satisfy the following two-scale variational formulation:

Theorem 3 *Let*

$$(\mathbf{v}^0, p^0) \in L^2(\Omega; H^1_{per}(Y)^3) \times L^2_0(\Omega) \quad \textit{and}$$

$$\{\Phi_j^0, \Phi_j^1\}_{j=1,\ldots,N} \in \left(H^1(\Omega) \times L^2(\Omega; H^1_{per}(Y))\right)^N$$

be a limit from Theorem 2 . Then it satisfies the two-scale two-pressures homogenized problem

$$-\Delta_y \mathbf{v}^0(x, y) + \nabla_y p^1(x, y) = -\nabla_x p^0(x) - \mathbf{f}^*(x)$$

$$+ \sum_{j=1}^{N} z_j n_j^0(y) \left(\nabla_x \Phi_j^0(x) + \nabla_y \Phi_j^1(x, y) + \mathbf{E}^*(x)\right) \ \textit{in } \Omega \times Y_F, \tag{159}$$

$$div_{\,y} \mathbf{v}^0(x, y) = 0 \ \textit{in } \Omega \times Y_F, \quad \mathbf{v}^0(x, y) = 0 \ \textit{on } \Omega \times S, \tag{160}$$

$$div_x \left(\int_{Y_F} \mathbf{v}^0(x, y)\, dy \right) = 0 \ \textit{in } \Omega, \tag{161}$$

$$-div_y \left(n_i^0(y) \left(\nabla_y \Phi_i^1(x, y) + \nabla_x \Phi_i^0(x) + \mathbf{E}^*(x) + \frac{Pe_i}{z_i} \mathbf{v}^0(x, y) \right) \right) = 0$$

$$\textit{in} \quad \Omega \times Y_F, \quad i = 1, \ldots, N, \tag{162}$$

$$\left(\nabla_y \Phi_i^1 + \nabla_x \Phi_i^0 + \mathbf{E}^* \right) \cdot \nu(y) = 0 \ \textit{on } \Omega \times S, \quad i = 1, \ldots, N, \tag{163}$$

$$-div_x \int_{Y_F} n_i^0(y) \left(\nabla_y \Phi_i^1(x, y) + \nabla_x \Phi_i^0(x) + \mathbf{E}^*(x) + \right.$$

$$\left. \frac{Pe_i}{z_i} \mathbf{v}^0(x, y) \right) dy = 0 \quad \textit{in } \Omega, \quad i = 1, \ldots, N, \tag{164}$$

$$\Phi_i^0 \ , \ \int_{Y_F} \mathbf{v}^0 \, dy \ \textit{ and } \ p^0 \ \textit{being } \Omega\textit{-periodic in } x, \tag{165}$$

with periodic boundary conditions on the unit cell Y_F for all functions depending on y and $S = \partial Y_S \setminus \partial Y$.

Remark 17 The limit problem features two incompressibility constraints (160) and (161) which are exactly dual to the two pressures $p^0(x)$ and $p^1(x, y)$ which are their corresponding Lagrange multipliers. Remark that Eqs. (159), (160) and (162) are just the leading order terms in the ansatz of the original equations. On the other hand, Eqs. (161) and (164) are averages on the unit cell Y_F of the next order terms in the ansatz. For example, (161) is deduced from

$$\mathrm{div}_y \mathbf{v}^1(x, y) + \mathrm{div}_x \mathbf{v}^0(x, y) = 0 \ \text{ in } \ \Omega \times Y_F$$

by averaging on Y_F, recalling that $\mathbf{v}^1(x, y) = 0$ on $\Omega \times S$.

The detailed proof of convergence and the derivation of the homogenized system corresponds to Theorem 1 in [9]. The limiting procedure gives us the variational form of problem (159)–(165) and it deserves to be recalled here in other to prove the well-posedness of the two-scale homogenized problem.

Following [6], we introduce the functional space for the velocities

$$V = \{\mathbf{v}^0(x, y) \in L^2_{per}\left(\Omega; H^1_{per}(Y_F)^3\right) \ \text{ satisfying } \ (160)\text{–}(161)\},$$

which is known to be orthogonal in $L^2_{per}\left(\Omega; H^1_{per}(Y_F)^3\right)$ to the space of gradients of the form $\nabla_x q(x) + \nabla_y q_1(x, y)$ with $q(x) \in H^1_{per}(\Omega)/\mathbb{R}$ and $q_1(x, y) \in L^2_{per}\left(\Omega; L^2_{per}(Y_F)/\mathbb{R}\right)$. We define the functional space

$$X = V \times H^1_{per}(\Omega)/\mathbb{R} \times L^2_{per}(\Omega; H^1_{per}(Y_F)^d/\mathbb{R})$$

and the variational formulation of (159)–(165) is to find $(\mathbf{v}^0, \{\Phi^0_j, \Phi^1_j\}) \in X$ such that, for any test functions $(\mathbf{v}, \{\phi^0_j, \phi^1_j\}) \in X$,

$$a\left((\mathbf{v}^0, \{\Phi^0_j, \Phi^1_j\}), (\mathbf{v}, \{\phi^0_j, \phi^1_j\})\right) = \langle \mathscr{L}, (\mathbf{v}, \{\phi^0_j, \phi^1_j\})\rangle, \tag{166}$$

where the bilinear form a and the linear form $\mathscr{L}$ are defined by

$$\begin{aligned} a\left((\mathbf{v}^0, \{\Phi^0_j, \Phi^1_j\}), (\mathbf{v}, \{\phi^0_j, \phi^1_j\})\right) &:= \int_\Omega \int_{Y_F} \nabla_y \mathbf{v}^0 : \nabla \mathbf{v} \, dx\, dy \\ + \sum_{i=1}^N \frac{z_i^2}{\mathrm{Pe}_i} \int_\Omega \int_{Y_F} n_i^0 (\nabla_x \Phi_i^0 + \nabla_y \Phi_i^1) \cdot (\nabla_x \phi_i^0 + \nabla_y \phi_i^1) \, dx\, dy & \\ + \sum_{j=1}^N z_j \int_\Omega \int_{Y_F} n_j^0 \left(\mathbf{v}^0 \cdot (\nabla_x \phi_j^0 + \nabla_y \phi_j^1) - \mathbf{v} \cdot (\nabla_x \Phi_j^0 + \nabla_y \Phi_j^1)\right) dx\, dy & \end{aligned} \tag{167}$$

and

$$< \mathscr{L}, (\mathbf{v}, \{\phi_j\}) >:= \sum_{j=1}^{N} z_j \int_\Omega \int_{Y_F} n_j^0 \mathbf{E}^* \cdot \mathbf{v}\, dx\, dy - \int_\Omega \int_{Y_F} \mathbf{f}^* \cdot \mathbf{v}\, dx\, dy$$

$$- \sum_{i=1}^{N} \frac{z_i^2}{\mathrm{Pe}_i} \int_\Omega \int_{Y_F} n_i^0 \mathbf{E}^* \cdot (\nabla_x \phi_i^0 + \nabla_y \phi_i^1)\, dx\, dy,$$

We apply the Lax-Milgram lemma to prove the existence and uniqueness of the solution in X of (166). The only point which requires to be checked is the coercivity of the bilinear form. We take $\mathbf{v} = \mathbf{v}^0$, $\phi_j^0 = \Phi_j^0$ and $\phi_j^1 = \Phi_j^1$ as the test functions in (166).

Using the incompressibility constraints (161) and the anti-symmetry of the third integral in (167), we obtain the quadratic form

$$a\left((\mathbf{v}^0, \{\Phi_j^0, \Phi_j^1\}), (\mathbf{v}^0, \{\Phi_j^0, \Phi_j^1\})\right) = \int_{\Omega \times Y_F} |\nabla_y \mathbf{v}^0(x, y)|^2\, dxdy +$$

$$\sum_{j=1}^{N} \frac{z_j^2}{\mathrm{Pe}_j} \int_{\Omega \times Y_F} n_j^0(y) |\nabla_x \Phi_j^0(x) + \nabla_y \Phi_j^1(x, y)|^2\, dxdy. \tag{168}$$

Recalling from Lemma 5 that $n_j^0(y) \geq C > 0$ in Y_F, it is easy to check that each term in the sum on the second line of (168) is bounded from below by

$$C\left(\int_\Omega |\nabla_x \Phi_j^0(x)|^2\, dx + \int_{\Omega \times Y_F} |\nabla_y \Phi_j^1(x, y)|^2\, dxdy\right),$$

which proves that our bilinear form is V-elliptic.

Hence we have proved

Theorem 4 *Problem (159)–(165) has a unique solution*

$$(\mathbf{v}^0, p^0) \in L^2(\Omega; H^1_{per}(Y)^3) \times L^2_0(\Omega) \quad \textit{and}$$

$$\{\Phi_j^0, \Phi_j^1\}_{j=1,\ldots,N} \in \left(H^1(\Omega) \times L^2(\Omega; H^1_{per}(Y))\right)^N.$$

and whole sequence $(\mathbf{v}^\varepsilon, \tilde{P}^\varepsilon, \{\Phi_j^\varepsilon\})$ *converges towards it.*

5.4 The Separation of the Fast and the Slow Scales and the Onsager Relations

From the point of view of applications, it is important to extract from (159)–(165) the macroscopic homogenized problem. Obviously, it requires to separate the fast

and slow scale. It was undertaken by Looker and Carnie in [47] and further improved in [9] and [13].

The main idea is to recognize in the two-scale homogenized problem (159)–(165) that there are two different macroscopic fluxes, namely $(\nabla_x p^0(x) + \mathbf{f}^*(x))$ and $\{\nabla_x \Phi_j^0(x) + \mathbf{E}^*(x)\}_{1\le j\le N}$. Therefore we introduce two families of cell problems, indexed by $k \in \{1, 2, 3\}$ for each component of these fluxes. We denote by $\{\mathbf{e}^k\}_{1\le k\le 3}$ the canonical basis of $\mathbb{R}^3$.

The first cell problem, corresponding to the macroscopic pressure gradient, is

$$-\Delta_y \mathbf{v}^{0,k}(y) + \nabla_y \pi^{0,k}(y) = \mathbf{e}^k + \sum_{j=1}^{N} z_j n_j^0(y) \nabla_y \theta_j^{0,k}(y) \ \text{ in } Y_F, \tag{169}$$

$$\operatorname{div}_y \mathbf{v}^{0,k}(y) = 0 \quad \text{in } Y_F, \quad \mathbf{v}^{0,k}(y) = 0 \ \text{ on } S, \tag{170}$$

$$-\operatorname{div}_y \Big(n_i^0(y) (\nabla_y \theta_i^{0,k}(y) + \frac{\mathrm{Pe}_i}{z_i} \mathbf{v}^{0,k}(y)) \Big) = 0 \ \text{ in } Y_F, \tag{171}$$

$$\nabla_y \theta_i^{0,k}(y) \cdot \nu = 0 \ \text{ on } S. \tag{172}$$

The second cell problem, corresponding to the macroscopic diffusive flux, is for each species $l \in \{1, \dots, N\}$

$$-\Delta_y \mathbf{v}^{l,k}(y) + \nabla_y \pi^{l,k}(y) = \sum_{j=1}^{N} z_j n_j^0(y) (\delta_{lj} \mathbf{e}^k + \nabla_y \theta_j^{l,k}(y)) \ \text{ in } Y_F, \tag{173}$$

$$\operatorname{div}_y \mathbf{v}^{l,k}(y) = 0 \quad \text{in } Y_F, \quad \mathbf{v}^{l,k}(y) = 0 \quad \text{on } S, \tag{174}$$

$$-\operatorname{div}_y \Big(n_i^0(y) (\delta_{ij} \mathbf{e}^k + \nabla_y \theta_j^{i,k}(y)) + \frac{\mathrm{Pe}_i}{z_i} \mathbf{v}^{i,k}(y)) \Big) = 0 \ \text{ in } Y_F, \tag{175}$$

$$\big(\delta_{ij} \mathbf{e}^k + \nabla_y \theta_j^{i,k}(y) \big) \cdot \nu = 0 \ \text{ on } S, \tag{176}$$

where δ_{ij} is the Kronecker symbol. As usual the cell problems are complemented with periodic boundary conditions.

Then, we can decompose the solution of (159)–(165) as

$$\mathbf{v}^0(x, y) = \sum_{k=1}^{3} \left(-\mathbf{v}^{0,k}(y) \left(\frac{\partial p^0}{\partial x_k} + f_k^* \right)(x) + \sum_{i=1}^{N} \mathbf{v}^{i,k}(y) \left(E_k^* + \frac{\partial \Phi_i^0}{\partial x_k} \right)(x) \right), \tag{177}$$

$$p^1(x, y) = \sum_{k=1}^{3} \left(-\pi^{0,k}(y) \left(\frac{\partial p^0}{\partial x_k} + f_k^* \right)(x) + \sum_{i=1}^{N} \pi^{i,k}(y) \left(E_k^* + \frac{\partial \Phi_i^0}{\partial x_k} \right)(x) \right), \tag{178}$$

$$\Phi_j^1(x, y) = \sum_{k=1}^{3} \left(-\theta_j^{0,k}(y) \left(\frac{\partial p^0}{\partial x_k} + f_k^* \right)(x) + \sum_{i=1}^{N} \theta_j^{i,k}(y) \left(E_k^* + \frac{\partial \Phi_i^0}{\partial x_k} \right)(x) \right). \tag{179}$$

We average (177)–(179) in order to get a purely macroscopic homogenized problem. We define the homogenized quantities: first, the electrochemical potential

$$\mu_j(x) = -z_j(\Phi_j^0(x) + \Psi^{ext,*}(x)), \tag{180}$$

then, the ionic flux of the jth species

$$\mathbf{j}_j(x) = \frac{1}{|Y_F|}\int_{Y_F} n_j^0(y)\Big(\frac{z_j}{\mathrm{Pe}_j}\big(\nabla_y\Phi_l^1(x,y) + \nabla_x\Phi_l^0(x) + \mathbf{E}^*(x)\big) + \mathbf{v}^0\Big)dy, \tag{181}$$

and finally the filtration velocity

$$\mathbf{v}(x) = \frac{1}{|Y_F|}\int_{Y_F} \mathbf{v}^0(x,y)\,dy. \tag{182}$$

From (177)–(179) we deduce the homogenized or upscaled equations for the above effective fields.

Proposition 16 *Introducing the flux* $\mathscr{J}(x) = (\mathbf{v}, \{\mathbf{j}_j\}_{1\le j\le N})$ *and the gradient* $\mathscr{F}(x) = (\nabla_x p^0, \{\nabla_x \mu_j\}_{1\le j\le N})$, *the macroscopic equations are*

$$div_x\,\mathscr{J} = 0 \quad in\ \ \Omega, \tag{183}$$

$$\mathscr{J} = -\mathscr{M}\mathscr{F} - \mathscr{M}(\mathbf{f}^*, \{0\}), \tag{184}$$

with a homogenized tensor $\mathscr{M}$ *defined by*

$$\mathscr{M} = \begin{pmatrix} \mathbb{K} & \frac{\mathbb{J}_1}{z_1} & \cdots & \frac{\mathbb{J}_N}{z_N} \\ \mathbb{L}_1 & \frac{\mathbb{D}_{11}}{z_1} & \cdots & \frac{\mathbb{D}_{1N}}{z_N} \\ \vdots & \vdots & \ddots & \vdots \\ \mathbb{L}_N & \frac{\mathbb{D}_{N1}}{z_1} & \cdots & \frac{\mathbb{D}_{NN}}{z_N} \end{pmatrix}, \tag{185}$$

and complemented with periodic boundary conditions for p^0 *and* $\{\Phi_j^0\}_{1\le j\le N}$. *The matrices* $\mathbb{J}_i$, $\mathbb{K}$, $\mathbb{D}_{ji}$ *and* $\mathbb{L}_j$ *are defined by their entries*

$$\{\mathbb{J}_i\}_{lk} = \frac{1}{|Y_F|}\int_{Y_F} \mathbf{v}^{i,k}(y)\cdot\mathbf{e}^l\,dy,$$

$$\{\mathbb{K}\}_{lk} = \frac{1}{|Y_F|}\int_{Y_F} \mathbf{v}^{0,k}(y)\cdot\mathbf{e}^l\,dy,$$

$$\{\mathbb{D}_{ji}\}_{lk} = \frac{1}{|Y_F|}\int_{Y_F} n_j^0(y)\Big(\mathbf{v}^{i,k}(y) + \frac{z_j}{Pe_j}\Big(\delta_{ij}\mathbf{e}^k + \nabla_y\theta_j^{i,k}(y)\Big)\Big)\cdot\mathbf{e}^l\,dy,$$

$$\{\mathbb{L}_j\}_{lk} = \frac{1}{|Y_F|}\int_{Y_F} n_j^0(y)\Big(\mathbf{v}^{0,k}(y) + \frac{z_j}{Pe_j}\nabla_y\theta_j^{0,k}(y)\Big)\cdot\mathbf{e}^l\,dy.$$

Furthermore, $\mathscr{M}$ is symmetric positive definite, which implies that the homogenized equations (183)–(184) have a unique solution.

Remark 18 The symmetry of $\mathscr{M}$ is equivalent to the famous Onsager reciprocal relations. The symmetry of the tensor $\mathscr{M}$ was proved in [47] and its positive definiteness in [9].

Proof The conservation law (183) is just a rewriting of (161) and (164). The constitutive equation (184) is an immediate consequence of the definitions (181) and (182) of the homogenized fluxes, taking into account the decomposition (177)–(179).

We now prove that $\mathscr{M}$ is positive definite. For any vectors $\lambda^0, \{\lambda^i\}_{1\le i\le N} \in \mathbb{R}^3$ let us introduce the following linear combinations of the cell solutions

$$\mathbf{v}^\lambda = \sum_{k=1}^{3}\left(\lambda_k^0 \mathbf{v}^{0,k} + \sum_{i=1}^{N}\lambda_k^i \mathbf{v}^{i,k}\right), \quad \theta_j^\lambda = \sum_{k=1}^{3}\left(\lambda_k^0 \theta_j^{0,k} + \sum_{i=1}^{N}\lambda_k^i \theta_j^{i,k}\right), \tag{186}$$

which satisfy

$$-\Delta_y \mathbf{v}^\lambda(y) + \nabla_y \pi^\lambda(y) = \lambda^0 + \sum_{j=1}^{N} z_j n_j^0(y)\left(\lambda^j + \nabla_y \theta_j^\lambda(y)\right) \quad \text{in } Y_F \tag{187}$$

$$\operatorname{div}_y \mathbf{v}^\lambda(y) = 0 \quad \text{in } Y_F, \quad \mathbf{v}^\lambda(y) = 0 \quad \text{on } S, \tag{188}$$

$$-\operatorname{div}_y\left(n_i^0(y)\left(z_i(\lambda^i + \nabla_y \theta_i^\lambda(y)) + \mathrm{Pe}_i \mathbf{v}^\lambda(y)\right)\right) = 0 \ \text{ in } Y_F \tag{189}$$

$$(\lambda^i + \nabla_y \theta_i^\lambda(y)) \cdot \nu = 0 \ \text{ on } S. \tag{190}$$

Multiplying the Stokes equation (187) by $\mathbf{v}^\lambda$, the convection-diffusion equation (189) by θ_j^λ and summing up, we obtain

$$\begin{aligned}
&\int_{Y_F}\left(|\nabla_y \mathbf{v}^\lambda(y)|^2 + \sum_{i=1}^{N}\frac{z_i^2}{\mathrm{Pe}_i} n_i^0(y)(\nabla_y \theta_i^\lambda(y) + \lambda^i)\cdot(\nabla_y \theta_i^\lambda(y) + \lambda^i)\right) dy \\
&= \int_{Y_F} \lambda^0 \cdot \mathbf{v}^\lambda \, dy + \sum_{i=1}^{N}\int_{Y_F} z_i n_i^0 \lambda^i \cdot \mathbf{v}^\lambda \, dy + \sum_{i=1}^{N}\int_{Y_F}\frac{z_i^2}{\mathrm{Pe}_i} n_i^0(\nabla_y \theta_i^\lambda + \lambda^i)\cdot\lambda^i \, dy \\
&= \mathbb{K}\lambda^0 \cdot \lambda^0 + \sum_{i=1}^{N}\mathbb{J}_i \lambda^i \cdot \lambda^0 + \sum_{i,j=1}^{N} z_i \lambda^i \cdot \mathbb{D}_{ij}\lambda^j + \sum_{i=1}^{N} z_i \lambda^i \cdot \mathbb{L}_i \lambda^0 \\
&= \mathscr{M}(\lambda^0, \{z_i\lambda^i\})^T \cdot (\lambda^0, \{z_i\lambda^i\})^T.
\end{aligned}$$

The left hand side of the above equality is positive. This proves the positive definite character of $\mathscr{M}$.

It remains to prove the symmetry of $\mathscr{M}$. For another set of vectors $\tilde{\lambda}^0, \{\tilde{\lambda}^i\}_{1\le i\le N} \in \mathbb{R}^3$, we define $\mathbf{v}^{\tilde{\lambda}}$ and $\theta_j^{\tilde{\lambda}}$ by (186). Multiplying the Stokes equation for $\mathbf{v}^{\lambda}$ by $\mathbf{v}^{\tilde{\lambda}}$ and the convection-diffusion equation for $\theta_j^{\tilde{\lambda}}$ by θ_j^{λ} (note the skew-symmetry of this computation), then adding the two variational formulations yields

$$\int_{Y_F} \nabla_y \mathbf{v}^{\lambda} \cdot \nabla_y \mathbf{v}^{\tilde{\lambda}}\, dy + \sum_{i=1}^{N} \int_{Y_F} \frac{z_i^2}{\mathrm{Pe}_i} n_i^0 \nabla_y \theta_i^{\tilde{\lambda}} \cdot \nabla_y \theta_i^{\lambda}\, dy =$$

$$\int_{Y_F} \lambda^0 \cdot \mathbf{v}^{\tilde{\lambda}}\, dy + \sum_{j=1}^{N} \int_{Y_F} z_j n_j^0 \lambda^j \cdot \mathbf{v}^{\tilde{\lambda}}\, dy - \sum_{i=1}^{N} \int_{Y_F} \frac{z_i^2}{\mathrm{Pe}_i} n_i^0 \tilde{\lambda}^i \cdot \nabla_y \theta_i^{\lambda}\, dy. \tag{191}$$

Therefore, the left hand side of (191) is symmetric in $\lambda, \tilde{\lambda}$. Exchanging the last term in (191), we deduce by symmetry

$$\int_{Y_F} \lambda^0 \cdot \mathbf{v}^{\tilde{\lambda}}\, dy + \sum_{j=1}^{N} \int_{Y_F} z_j n_j^0 \lambda^j \cdot \mathbf{v}^{\tilde{\lambda}}\, dy + \sum_{i=1}^{N} \int_{Y_F} \frac{z_i^2}{\mathrm{Pe}_i} n_i^0 \lambda^i \cdot \nabla_y \theta_i^{\tilde{\lambda}}\, dy$$

$$= \int_{Y_F} \tilde{\lambda}^0 \cdot \mathbf{v}^{\lambda}\, dy + \sum_{j=1}^{N} \int_{Y_F} z_j n_j^0 \tilde{\lambda}^j \cdot \mathbf{v}^{\lambda}\, dy + \sum_{i=1}^{N} \int_{Y_F} \frac{z_i^2}{\mathrm{Pe}_i} n_i^0 \tilde{\lambda}^i \cdot \nabla_y \theta_i^{\lambda}\, dy,$$

which is equivalent to the desired symmetry

$$\mathscr{M}(\tilde{\lambda}^0, \{z_i \tilde{\lambda}^i\})^T \cdot (\lambda^0, \{z_i \lambda^i\})^T = \mathscr{M}(\lambda^0, \{z_i \lambda^i\})^T \cdot (\tilde{\lambda}^0, \{z_i \tilde{\lambda}^i\})^T.$$

The norm-closeness of the solution to the homogenized problem, to the solution of the original problem is given by the following result.

Theorem 5 ([9]) *Let $(p^0, \{\Phi_j^0\}_{1\le j\le N})$ be defined by (183)–(184). Let $\mathbf{v}^0$ be given by (177) and $\{\Phi_j^1\}_{1\le j\le N}$ by (179). Then in the limit $\varepsilon \to 0$ we have*

$$\int_{\Omega_\varepsilon} \left(\left| \mathbf{v}^{\varepsilon}(x) - \mathbf{v}^0(x, \frac{x}{\varepsilon}) \right|^2 + |\tilde{P}^{\varepsilon}(x) - p^0(x)|^2 \right) dx \to 0 \tag{192}$$

and

$$\int_{\Omega_\varepsilon} \left| \nabla \left(\Phi_j^{\varepsilon}(x) - \Phi_j^0(x) - \varepsilon \Phi_j^1(x, \frac{x}{\varepsilon}) \right) \right|^2 dx \to 0. \tag{193}$$

Acknowledgements This research was partially supported by the MOCOMIPOC project (Modélisation multiéchelles des écoulements complexes en présence de gaz dans les milieux chargés) from the NEEDS program (Projet fédérateur Milieux Poreux MIPOR), part of CNRS, France and by the LABEX MILYON (ANR-10-LABX-0070) of Université de Lyon, within the program "Investissements d'Avenir" (ANR-11-IDEX-0007) operated by the French National Research Agency (ANR).

References

1. Acerbi, E., Chiadò Piat, V., Dal Maso, G., Percivale, D.: An extension theorem from connected sets, and homogenization in general periodic domains. Nonlinear Anal., TMA **18**, 481–496 (1992)
2. Adler, P.M.: Macroscopic electroosmotic coupling coefficient in random porous media. Math. Geol. **33**(1), 63–93 (2001)
3. Adler, P.M., Mityushev, V.: Effective medium approximation and exact formulae for electrokinetic phenomena in porous media. J. Phys. A: Math. Gen. **36**, 391–404 (2003)
4. Allaire, G. : Homogenization of the stokes flow in a connected porous medium. Asymptot. Anal. **2**, 203–222 (1989)
5. Allaire, G.: Homogenization and two-scale convergence. SIAM J. Math. Anal. **23**, 1482–1518 (1992)
6. Allaire, G.: One-phase newtonian flow. In: Hornung, U. (ed.) Homogenization and Porous Media, pp. 45–68. Springer, New-York (1997)
7. Allaire, G., A. Damlamian, A., Hornung, U.: Two-scale convergence on periodic surfaces and applications. In: Bourgeat, A., Carasso, C., Luckhaus, S., Mikelić, A. (eds.) Mathematical Modelling of Flow through Porous Media, pp. 15–25. World Scientific, Singapore (1995)
8. Allaire, G., Mikelić, A., Piatnitski, A.: Homogenization approach to the dispersion theory for reactive transport through porous media. SIAM J. Math. Anal. **42**, 125–144 (2010)
9. Allaire, G., Mikelić, A., Piatnitski, A.: Homogenization of the linearized ionic transport equations in rigid periodic porous media. J. Math. Phys. **51**, 123103 (2010). Erratum in the same journal, 52, 063701 (2011).
10. Allaire, G., Brizzi, R., Mikelić, A., Piatnitski, A.: Two-scale expansion with drift approach to the Taylor dispersion for reactive transport through porous media. Chem. Eng. Sci. **65**, 2292–2300 (2010)
11. Allaire, G., Dufrêche, J.-F., Mikelić, A., Piatnitski, A.: Asymptotic analysis of the Poisson-Boltzmann equation describing electrokinetics in porous media. Nonlinearity **26**, 881–910 (2013)
12. Allaire, G., Bernard, O., Dufrêche, J.-F., Mikelić, A.: Ion transport through deformable porous media: derivation of the macroscopic equations using upscaling. Comp. Appl. Math. **36**, 1431–1462 (2017)
13. Allaire, G., Brizzi, R., Dufrêche, J.-F., Mikelić, A. Piatnitski, A. : Ion transport in porous media: derivation of the macroscopic equations using upscaling and properties of the effective coefficients. Comp. Geosci. **17**, 479–495 (2013)
14. Allaire, G., Brizzi, R. , Dufrêche, J.-F., Mikelić, A., Piatnitski, A.: Role of non-ideality for the ion transport in porous media: derivation of the macroscopic equations using upscaling. Phys. D. **282** , 39–60 (2014)
15. Auriault, J.L. , Strzelecki, T.: On the electro-osmotic flow in a saturated porous medium. Int. J. Engng Sci. **19**, 915–928 (1981)
16. Baranger, J. , Najib, K.: Analyse numérique des écoulements quasi-newtoniens dont la viscosité obéit à la loi puissance ou la loi de Carreau. Numer. Math. **58**, 35–49 (1990)
17. Bird, R.B., Stewart, W.E.N., Lightfoot, E.N.: Transport Phenomena. Wiley, New York (1960)
18. Bird, R.B., Armstrong R.C., Hassager, O.: Dynamics of Polymeric Liquids, Vol.1, Fluid Mechanics. Wiley, New York, (1987)
19. Bourgeat, A., Mikelić, A.: Note on the homogenization of Bingham flow through porous medium. J. Math. Pures Appl. **72**, 405–414 (1993)
20. Bourgeat, A., Mikelić, A.: Homogenization of the non-newtonian flow through porous medium. Nonlinear Anal. Theory Methods Appl. **26**, 1221–1253 (1996)
21. Bourgeat, A., Mikelić, A., Tapiero, R.: Dérivation des équations moyennées décrivant un écoulement non newtonien dans un domaine de faible épaisseur. C. R. Acad. Sci. Paris, Sér. I **316**, 965–970 (1993)

22. Bourgeat, A., Gipouloux, O., Marusic-Paloka, E.: Filtration law for polymer flow through porous media. Multiscale Model. Simul. **1**, 432–457 (2003)
23. Brezis, H.: Functional analysis, Sobolev spaces and partial differential equations. Springer Science and Business Media, New York (2010)
24. Bulíček, M. , Gwiazda, P. , Málek, J., Świerczewska-Gwiazda, A.: On steady flows of incompressible fluids with implicit power-law-like rheology. Adv. Calc. Var. **2**, 109–136 (2009)
25. Cattabriga, L.: Su un problema al contorno relativo al sistema di equazioni di Stokes. Rendiconti Seminario Matematico della Università di Padova, **31**, 308–340 (1961)
26. Chan, D.Y., Horn, R.G.: The drainage of thin liquid films between solid surfaces. J. Chem. Phys. **83**, 5311–5325 (1985)
27. Christopher, R.H., Middleman, S.: Power-law flow through porous media. Ind. Eng. Cheni. Fund. **4**, 422 (1965)
28. Cioranescu, D., Donato, P.: An Introduction to Homogenization. Oxford University Press, Oxford (2000)
29. Coelho, D., Shapiro, M., Thovert, J.-F. , Adler, P.M. : Electro-osmotic phenomena in porous media. J. Colloid Interface Sci. **181**, 169–90 (1996)
30. Dufrêche, J.-F. , Bernard, O. , Durand-Vidal, S. , Turq, P.: Analytical theories of transport in concentrated electrolyte solutions from the MSA. J. Phys. Chem. B **109**, 9873 (2005)
31. Dufrêche, J.-F., Marry, V. , Malikova, N. , Turq, P., : Molecular hydrodynamics for electro-osmosis in clays: from Kubo to Smoluchowski. J. Mol. Liq. **118**, 145 (2005)
32. Duvaut G., Lions J.L.: Inequalities in Mechanics and Physics. Springer, Heidelberg (1976)
33. Ekeland, I., Temam, R. : Analyse Convexe et Problèmes Variationnels. Gauthier-Villars, Paris (1973)
34. Ene, H.I. , Sanchez-Palencia, E.: Equations et phénomènes de surface pour l'écoulement dans un modèle de milieu poreux. J. Mécan. **14**, 73–108 (1975)
35. Ern, A. , Joubaud, R. , Lelièvre, T.: Mathematical study of non-ideal electrostatic correlations in equilibrium electrolytes. Nonlinearity **25**, 1635–1652 (2012)
36. Gipouloux, O., Zine, A.M.: Computation of the filtration laws through porous media for a non-Newtonian fluid obeying the power law. Comput. Geosci. **1**, 127–153 (1997)
37. Gupta, A.K. , Coelho, D. , Adler, P.M.: Electroosmosis in porous solids for high zeta potentials. J. Colloid Interface Sci. **303**, 593–603 (2006)
38. Hornung, U. (ed.) : Homogenization and Porous Media. Interdisciplinary Applied Mathematics Series, vol. 6. Springer, New York (1997)
39. Jikov, V.V., Kozlov, S., Oleinik, O.: Homogenization of Differential Operators and Integral Functionals. Springer, New York, (1994)
40. Kaloušek, M. : Homogenization of incompressible generalized Stokes flows through a porous medium. Nonlinear Anal. Theory Methods Appl. **136**, 1–39 (2016)
41. Karniadakis, G., Beskok, A., Aluru, N.: Microflows and Nanoflows. Fundamentals and Simulation. Interdisciplinary Applied Mathematics, Vol. 29. Springer, New York (2005)
42. Khuzhayorov, B., Auriault, J.-L., Royer, P. : Derivation of macroscopic filtration law for transient linear viscoelastic fluid flow in porous media. Int. J. Eng. Sci. **38**, 487–504 (2000)
43. Lions, J.L. : Quelques méthodes de résolution des problèmes aux limites non linéaires. Dunod Gauthier-Villars, Paris (1969)
44. Lions, J.L., Sanchez-Palencia, E.: Écoulement d'un fluide viscoplastique de Bingham dans un milieu poreux. J. Math. pures et appl. **60**, 341–360 (1981)
45. Lipton, R., Avellaneda, M. : A darcy law for slow viscous flow past a stationary array of bubbles. Proc. Royal Soc. Edinburgh **114A**, 71–79 (1990)
46. Looker, J.R. : Semilinear elliptic Neumann problems and rapid growth in the nonlinearity. Bull. Aust. Math. Soc., **74**, 161–175 (2006)
47. Looker, J.R., Carnie, S.L.: Homogenization of the ionic transport equations in periodic porous media. Transp. Porous Media **65**, 107–131 (2006)
48. Lukkassen, D., Nguetseng, G., Wall, P.: Two-scale convergence. Int. J. Pure Appl. Math. Sci. **2**, 35–86 (2002)

49. Marciniak-Czochra, A., Ptashnyk, M.: Derivation of a macroscopic receptor-based model using homogenization techniques. SIAM J. Math. Anal. **40**, 215–237 (2008)
50. Marušić-Paloka, E., Piatnitski, A.: Homogenization of a nonlinear convection-diffusion equation with rapidly oscillating coefficients and strong convection. J. Lond. Math. Soc. **72**, 391–409 (2005)
51. Marino, S., Shapiro, M., Adler, P.M. : Coupled transports in heterogeneous media. J. Colloid Interface Sci. **243**, 391–419 (2001)
52. Marry, V., Dufrêche, J.-F., Jardat, M., Turq, P.: Equilibrium and electrokinetic phenomena in charged porous media from microscopic and mesoscopic models: electro-osmosis in montmorillonite. Mol. Phys. **101**, 3111 (2005)
53. Mei, C.C. , Vernescu, B.: Homogenization Methods for Multiscale Mechanics. World Scientific Publishing Company, Singapore (2010)
54. Mikelić, A.: Non-newtonian flow. In: Hornung, U. (ed.) Homogenization and Porous Media, pp. 69–95. Springer, New-York (1997)
55. Mikelić, A., Tapiero, R. : Mathematical derivation of the power law describing polymer flow through a thin slab. Math. Modell. Numer. Anal. **29**, 3–22 (1995)
56. Moyne, C., Murad, M. : Electro-chemo-mechanical couplings in swelling clays derived from a micro/macro-homogenization procedure. Int. J. Solids Struct. **39**, 6159–6190 (2002)
57. Moyne, C., Murad, M.: Macroscopic behavior of swelling porous media derived from micromechanical analysis. Transp. Porous Media **50**, 127–151 (2003)
58. Moyne, C., Murad, M. : A Two-scale model for coupled electro-chemomechanical phenomena and Onsager's reciprocity relations in expansive clays: I homogenization analysis, Transp. Porous Media **62**, 333–380 (2006)
59. Moyne, C., Murad, M. : A two-scale model for coupled electro-chemo-mechanical phenomena and Onsager's reciprocity relations in expansive clays: II. Computational validation. Transp. Porous Media **63(1)**, 13–56 (2006)
60. Moyne, C., Murad, M. : A dual-porosity model for ionic solute transport in expansive clays. Comput. Geosci. **12**, 47–82 (2008)
61. Neuss-Radu, M. : Some extensions of two-scale convergence. C. R. Acad. Sci. Paris Sér. I Math. **322**(9), 899–904 (1996)
62. Nguetseng, G.: A general convergence result for a functional related to the theory of homogenization. SIAM J. Math. Anal. **20**, 608–623 (1989)
63. O'Brien, R.W., White, L.R.: Electrophoretic mobility of a spherical colloidal particle. J. Chem. Soc. Faraday Trans. 2 **74**(2) , 1607–1626 (1978)
64. Oleinik, O.A.E., Shamaev, A.S., Yosifian, G.A.: Mathematical Problems in Elasticity and Homogenization, vol. 2. Elsevier, Amsterdam (2009)
65. Orgéas, L., Idris, Z., Geindreau, C., Bloch, J.-F., Auriault, J.-L.: Modelling the flow of power-law fluids through anisotropic porous media at low-pore Reynolds number. Chem. Eng. Sci. **61**, 4490–4502 (2006)
66. Pavliotis, G.A., Stuart, A.: Multiscale Methods: Averaging and Homogenization. Springer, New York (2008)
67. Pearson, J., Tardy, P.: Models for flow of non-newtonian and complex fluids through porous media. J. Non-Newtonian Fluid Mech. **102**, 447–473 (2002)
68. Ray, N., Muntean, A., Knabner, P.: Rigorous homogenization of a Stokes-Nernst-Planck-Poisson system. J. Math. Anal. Appl. **390**(1), 374–393 (2012)
69. Ray, N. , Eck, Ch., Muntean, A., Knabner, P.: Variable Choices of Scaling in the Homogenization of a Nernst-Planck-Poisson Problem. Preprint no. 344, Institut für Angewandte Mathematik, Universitaet Erlangen-Nürnberg (2011)
70. Rosanne, M., Paszkuta, M., Adler, P.M.: Electrokinetic phenomena in saturated compact clays. J. Colloid Interface Sci. **297**, 353–364 (2006)
71. Sanchez-Palencia, E.: Non-Homogeneous Media and Vibration Theory. Lecture Notes in Physics, vol. 127. Springer, Heidelberg (1980)
72. Shah, C.B. , Yortsos, Y.C.: Aspects of flow of power-law fluids in porous media. AIChE J. **41**, 1099–1112 (1995)

73. Shahsavari, S., McKinley, G.H.: Mobility of power-law and Carreau fluids through fibrous media. Physical Review E **92**, 063012 (2015)
74. Shahsavari, S., McKinley, G.H.: Mobility and pore-scale fluid dynamics of rate-dependent yield-stress fluids flowing through fibrous porous media. J. Non-Newtonian Fluid Mech. **235**, 76–82 (2016)
75. Schmuck, M.: Analysis of the Navier–Stokes–Nernst–Planck–Poisson system. Math. Models Methods Appl. Sci. **19**, 993–1014 (2009)
76. Schmuck, M.: Modeling and deriving porous media Stokes-Poisson-Nernst-Planck equations by a multiple-scale approach. Commun. Math. Sci. **9**(3), 685–710 (2011)
77. Schmuck, M.: First error bounds for the porous media approximation of the Poisson-Nernst-Planck equations. ZAMM (J. Appl. Math. Mech./Zeitschrift für Angewandte Mathematik und Mechanik). **92**, 304–319 (2012)
78. Schmuck, M.: New porous medium Poisson-Nernst-Planck equations for strongly oscillating electric potentials. J. Math. Phys. **54**, 021504 (2013)
79. Temam, R.: Navier–Stokes Equations. Elsevier, Amsterdam (1984)
80. Wu, Y.S., Pruess, K. , Witherspoon, P.A. : Displacement of a newtonian fluid by a non-newtonian fluid in a porous medium. Trans. Porous Media. **6**, 115 (1991)

Viscoplastic Fluids: Mathematical Modeling and Applications

Angiolo Farina and Lorenzo Fusi

Abstract Bingham fluids constitute a very important class of non-Newtonian fluids. The modeling of Bingham materials is of crucial importance in industrial applications, since a large variety of materials (e.g. foams, pastes, slurries, oils, ceramics, etc.) exhibit the fundamental character of viscoplasticity, that is the capability of flowing only if the stress is above some critical value. The flow of these materials is difficult to predict, because of the presence of unknown interfaces separating the yielded and the unyielded regions which are difficult to track. This is particularly evident when the flow occurs in complex geometries and when major simplifications, such as lubrication approximation, can be applied. Indeed, in some cases the Bingham model may even lead to a paradox, known as the "lubrication paradox". In this chapter we focus on some practical situations of Bingham flow which are the subject of a current mathematical research (lubrication flows, asymptotic expansions, etc.). Such issues and developments arise, for example, in the petroleum industry and in many natural contexts.

1 Introduction

Bingham fluids, or yield stress fluids, are encountered in a wide range of applications: toothpastes, cements, mortars, foams, muds, mayonnaise, etc. The fundamental character of these fluids is that they are able to deform indefinitely only if they are submitted to a stress above some critical value. Actually, toothpaste

A chapter to appear in "*New trends in non-newtonian fluid mechanics and complex flow*", Lecture Notes Centro Internazionale Matematico Estivo (C.I.M.E.) Series, Lecture Notes in Mathematics, Springer, 2017. The corresponding lectures were given at the CIME-CISM Course "New trends in non-newtonian fluid mechanics and complex flows" held in Levico Terme, Italia, August 28–September 2, 2016

A. Farina (✉) · L. Fusi
Dipartimento di Matematica e Informatica "Ulisse Dini", Firenze, Italy
e-mail: angiolo.farina@unifi.it; lorenzo.fusi@unifi.it

A. Farina et al. (eds.), *Non-Newtonian Fluid Mechanics and Complex Flows*,
Lecture Notes in Mathematics 2212, https://doi.org/10.1007/978-3-319-74796-5_5

visually exhibits the fundamental character of such a fluid model: it flows when the applied stress exceeds a certain value, otherwise it does not flow, behaving as a solid body (actually below the critical stress toothpaste deforms in finite way). Despite the apparent simplicity in the constitutive modeling (especially within the implicit framework theory developed by Rajagopal and co-workers [22–25]), the flow characteristics of these materials are difficult to be predicted, since they involve unknown boundaries separating the liquid and the solid regions. Readers are referred to the books by Huilgol [14] and by Ionescu, Sofonea [15] where several issues concerning the Bingham model (constitutive equations, mathematical techniques, numerical methods and so on) are deeply analyzed.

A well known example of materials which are often modeled as Bingham Fluids are waxy crude oils (i.e. oils with an high paraffin content). These fluids are known to cause handling and pipelining difficulties. The flow properties depend strongly on the yield stress which, in turn, depends on the shear history [31]. This leads to a definable minimum operating point below which flow in a waxy crude oil pipeline would cease.

Familiar examples of non-Newtonian fluids described by the Bingham model include also mud (see [18] and the references therein cited), lubricated pipelining [13], and materials used in ceramic casting [16].

2 Constitutive Model

The simplest shear-stress experiment that characterizes the Bingham fluid is represented in Fig. 1. On the top surface of a layer of material a uniform shear force F is applied. If A is the area of the surface, the applied shear is F/A. If the applied shear load (i.e. force per unit surface) does not exceed a certain threshold, τ_o, the material does not move (the bottom of the layer is fixed on the "floor"). When the applied shear load exceeds the τ_o, the material flows as a linear viscous fluid.

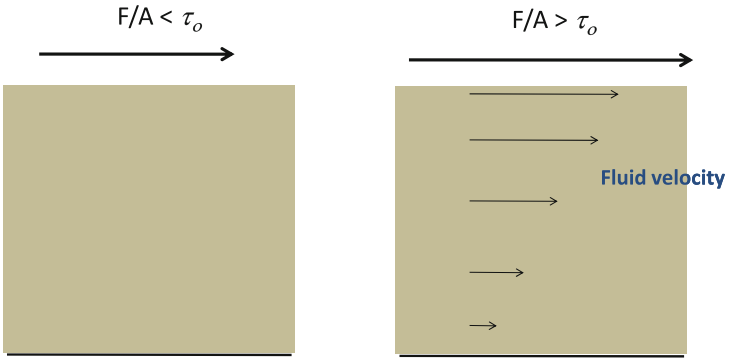

Fig. 1 A schematic representation of the 1D shear stress experiment. F is the shear force and A which is uniformly applied on a surface A so that the shear stress is F/A. The threshold is τ_o

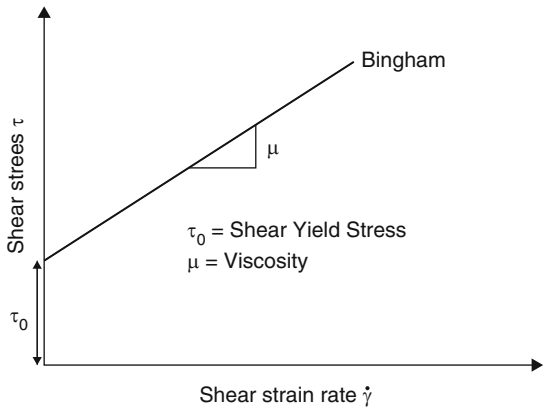

Fig. 2 The shear stress—shear rate curve for the Bingham model

Actually such a peculiar rheological behavior is well highlighted by the experimental tests performed in cylindrical viscometers. We just mention the recent review by Coussot [5] and the numerous experimental papers therein cited. Hence, considering a simple one-dimensional shear flow, if τ denote the modulus of the shear stress and $\dot{\gamma}$ the modulus of the strain rate, the constitutive Bingham model writes as

$$\tau = \tau_o + \mu\dot{\gamma}, \quad \text{if} \quad \tau > \tau_o, \quad \text{(flow)}, \tag{1}$$

and

$$\dot{\gamma} = 0, \quad \text{if} \quad \tau \leq \tau_o, \quad \text{(no flow)}. \tag{2}$$

Indeed (2) means, from the physical point of view, rigid behavior [11]. The threshold τ_o is usually defined shear yield stress, or simply yield stress, and μ is referred to as viscosity. In Fig. 2 we have reported the shear stress-shear rate curve for a Bingham fluid. The model (1), (2) was introduced for the first time by E.C. Bingham [1, 2]. We note that in the Bingham model is much more natural to express the modulus of the shear rate $\dot{\gamma}$ in terms of the modulus of the shear stress τ. Indeed (1), (2) can be rewritten (see also Fig. 3)

$$\dot{\gamma} = \frac{(\tau - \tau_o)_+}{\mu}, \tag{3}$$

where $(\quad)_+$ denotes the positive part, namely

$$(\tau - \tau_o)_+ = \begin{cases} \tau - \tau_o, & \text{if} \quad \tau \geq \tau_o, \\ 0, & \text{if} \quad \tau < \tau_o. \end{cases}$$

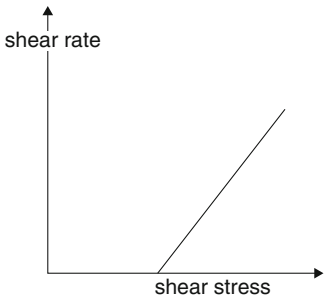

Fig. 3 Shear stress—shear rate according to (3)

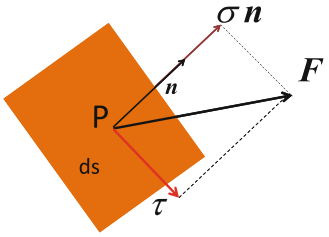

Fig. 4 Decomposition of the force $\boldsymbol{F}$

In the example of Fig. 1 it is easy to identify the shear stress and formulate the yield criterion. But how can we formulate the yield criterion in the general 3D case? What is in this case the shear stress? Let us consider a point P and a small facet of area ds surrounding. The normal to the facet is $\boldsymbol{n}$. If we denote by $\boldsymbol{F}$ the force acting on ds we have

$$\boldsymbol{F} = \mathbf{T}(P)\,\boldsymbol{n},$$

where $\mathbf{T}(P)$ is the Cauchy stress. The force vector $\boldsymbol{F}$ can be splitted into its component along $\boldsymbol{n}$ and in a tangential vector $\boldsymbol{\tau}$ (said tangential or shear force)

$$\boldsymbol{F} = \boldsymbol{\tau} + \sigma \boldsymbol{n},$$

where $\sigma = \boldsymbol{F}\cdot\boldsymbol{n} = \mathbf{T}(P)\,\boldsymbol{n}\cdot\boldsymbol{n}$ (see Fig. 4). Obviously $|\boldsymbol{F}|^2 = \sigma^2 + \tau^2$, where $\tau = |\boldsymbol{\tau}|$. We then consider a reference frame in which $\mathbf{T}(P)$ is diagonal, namely

$$\mathbf{T}(P) = \begin{pmatrix} T_1 & 0 & 0 \\ 0 & T_2 & 0 \\ 0 & 0 & T_3 \end{pmatrix},$$

and assume $T_1 > T_2 > T_3$. Hence

$$|\boldsymbol{F}|^2 = \sigma^2 + \tau^2 = \left| \begin{pmatrix} T_1 & 0 & 0 \\ 0 & T_2 & 0 \\ 0 & 0 & T_3 \end{pmatrix} \begin{pmatrix} n_1 \\ n_2 \\ n_3 \end{pmatrix} \right|^2$$

$$= T_1^2 n_1^2 + T_2^2 n_2^2 + T_3^2 n_3^2,$$

and

$$\begin{aligned}\sigma &= \boldsymbol{F}\cdot\boldsymbol{n} = \mathbf{T}(P)\,\boldsymbol{n}\cdot\boldsymbol{n}\\ &= \begin{pmatrix} T_1 & 0 & 0\\ 0 & T_2 & 0\\ 0 & 0 & T_3\end{pmatrix}\begin{pmatrix} n_1\\ n_2\\ n_3\end{pmatrix}\cdot\begin{pmatrix} n_1\\ n_2\\ n_3\end{pmatrix} = T_1n_1^2 + T_2n_2^2 + T_3n_3^2\,.\end{aligned}$$

We thus get the system

$$\begin{cases} |\boldsymbol{n}|^2 = 1,\\ |\boldsymbol{F}|^2 = \sigma^2+\tau^2,\\ \boldsymbol{F}\cdot\boldsymbol{n} = \sigma,\end{cases}\quad\Longrightarrow\quad\begin{cases} n_1^2+n_2^2+n_3^2 = 1,\\ T_1^2n_1^2+T_2^2n_2^2+T_3^2n_3^2 = \sigma^2+\tau^2,\\ T_1n_1^2+T_2n_2^2+T_3n_3^2 = \sigma,\end{cases}$$

which, once solved with respect to n_1^2, n_2^2, n_3^2, gives

$$\begin{cases} n_1^2 = \dfrac{\left(\sigma-\dfrac{T_2+T_3}{2}\right)^2+\tau^2-\left(\dfrac{T_2-T_3}{2}\right)^2}{(T_2-T_1)(T_3-T_1)} \ge 0,\\ n_2^2 = -\dfrac{\left(\sigma-\dfrac{T_1+T_3}{2}\right)^2+\tau^2-\left(\dfrac{T_3-T_1}{2}\right)^2}{(T_2-T_3)(T_1-T_2)} \ge 0,\\ n_3^2 = \dfrac{\left(\sigma-\dfrac{T_2+T_1}{2}\right)^2+\tau^2-\left(\dfrac{T_2-T_1}{2}\right)^2}{(T_1-T_3)(T_2-T_3)} \ge 0.\end{cases}$$

Thus, in the (σ,τ) plane a domain is defined

$$\begin{aligned}\left(\sigma-\frac{T_2+T_3}{2}\right)^2+\tau^2 &\ge \left(\frac{T_2-T_3}{2}\right)^2,\\ \left(\sigma-\frac{T_1+T_3}{2}\right)^2+\tau^2 &\le \left(\frac{T_3-T_1}{2}\right)^2,\\ \left(\sigma-\frac{T_2+T_1}{2}\right)^2+\tau^2 &\ge \left(\frac{T_2-T_1}{2}\right)^2,\end{aligned}$$

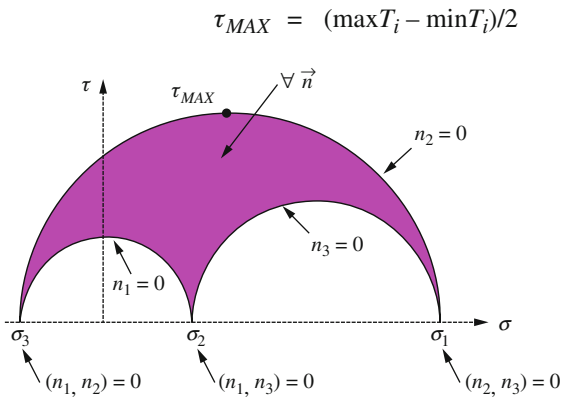

Fig. 5 Three points on the horizontal axis correspond to the three main stresses. The figure shows that the maximum shear is equal to the radius of the largest circle

which corresponds to the area bordered by three circles, the so-called three Mohr circles (see Fig. 5). Thus, since the maximum shear stress is τ_{MAX}, a possible yield criterion is

$$\begin{cases} \tau_{MAX} \leq \dfrac{\tau_o}{2}, & \text{no flow,} \\ \\ \tau_{MAX} > \dfrac{\tau_o}{2}, & \text{flow,} \end{cases} \tag{4}$$

where

$$\tau_{MAX} = \frac{1}{2} \max \left\{ |T_1 - T_2|\,,\ |T_2 - T_3|\,,\ |T_3 - T_1| \right\}. \tag{5}$$

Such a criterion is known as Tresca criterion [3]. The representation in the principal stress space of the surface (5), known as Tresca Surface, or

$$\left[(T_1 - T_2)^2 - \tau_o^2 \right] \left[(T_1 - T_3)^2 - \tau_o^2 \right] \left[(T_3 - T_2)^2 - \tau_o^2 \right] = 0,$$

is a cylindrical unbounded surface with hexagonal section and axis (1,1,1). So, according to the Tresca criterion, at every point of the material we have to compute the eigenvalues of the stress tensor. If all the eigenvalues are within the Tresca surface then the material is in a rigid state. if at least one of the eigenvalues is outside the surface then the material is in a fluid state.

The Tresca criterion, unfortunately, is not very practical to use. For this reason it is preferred to use the Von Mises criterion [30], based on the second invariant of the stress tensor. The maximum shear stress criterion (4) is replaced by

$$\begin{cases} \tau_{VM} \leq \dfrac{\tau_o}{2}, & \text{no flow,} \\ \\ \tau_{VM} > \dfrac{\tau_o}{2}, & \text{flow,} \end{cases}$$

where

$$\tau_{VM} = \sqrt{\frac{1}{2}\left[(T_1 - T_2)^2 + (T_2 - T_3)^2 + (T_3 - T_1)^2\right]}.$$

Thus, splitting the Cauchy stress as $\mathbf{T} = -P\mathbf{I} + \mathbf{S}$, where $P = 1/3\text{tr}\mathbf{T}$ and $\mathbf{S}$ is the extra-stress, we immediately realize that σ_{VM} coincides with the second invariant of the extra-stress, namely

$$\sigma_{VM} = II_{\mathbf{S}} = \sqrt{\frac{1}{2}\text{tr}\,\mathbf{S}^2}.$$

Therefore the generalization of the Bingham model (1), (2) to the 3D case is the following

$$\mathbf{S} = \left(2\mu + \frac{\tau_o}{II_{\mathbf{D}}}\right)\mathbf{D}, \quad \text{if} \quad II_{\mathbf{S}} > \tau_o, \quad \text{(flow)}, \tag{6}$$

and

$$\mathbf{D} = 0, \quad \text{if} \quad |\tau| \leq \tau_o, \quad \text{(no flow)}, \tag{7}$$

where

$$\mathbf{D} = \frac{1}{2}\left(\nabla \boldsymbol{v} + \nabla \boldsymbol{v}^{\text{T}}\right) \qquad II_{\mathbf{D}} = \sqrt{\frac{1}{2}\,\text{tr}\,\mathbf{D}},$$

and where $\boldsymbol{v}$ is the fluid velocity field. We remark that the Bingham constitutive equation can be written in the implicit form (see [22–24, 26])

$$\mathbf{D} = \left(\frac{II_{\mathbf{D}}}{2\mu II_{\mathbf{D}} + \tau_o}\right)\mathbf{S}. \tag{8}$$

The above constitutive equation allows to express $\mathbf{S}$ as a function of $\mathbf{D}$ only when $II_{\mathbf{S}} > \tau_o$, while $\mathbf{D} = 0$, entails only $II_{\mathbf{S}} \leq \tau_o$, the stress being constitutively undetermined.

3 Flow in a Channel

We consider the flow of an incompressible Bingham fluid in a symmetric channel of length L and width $2H$. We consider a laminar flow so that the velocity field is

$$\boldsymbol{v} = v(y, t)\boldsymbol{e}_x,$$

where, as shown in Fig. 6, x, y are the longitudinal and transversal coordinates respectively. Due to symmetry we consider just the upper part of the channel. The the inlet pressure ΔP is prescribed and we rescale the outlet pressure to 0. Hence

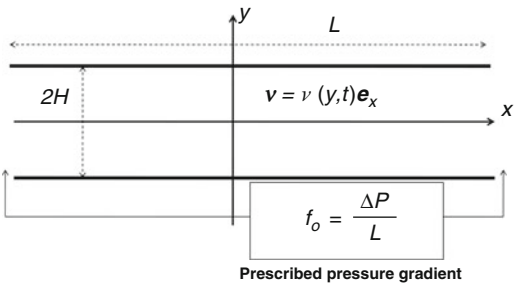

Fig. 6 Sketch of the channel

the pressure gradient driving the flow is given by

$$f_o = \frac{\Delta P}{L}\,.$$

In principle $f_o = f_o\,(t)$ since ΔP may depend on time. In such a simple setting

$$\mathbf{D} = \begin{pmatrix} 0 & v_y & 0 \\ v_y & 0 & 0 \\ 0 & 0 & 0 \end{pmatrix}, \qquad \mathbf{T} = \begin{pmatrix} -P & S_{12} & 0 \\ S_{12} & -P & 0 \\ 0 & 0 & -P \end{pmatrix},$$

so that $II_{\mathbf{S}} = |S_{12}|$ and $II_{\mathbf{D}} = \left|v_y\right|$. Hence, (6), (7) give

$$II_{\mathbf{S}} > \tau_o, \quad \Longrightarrow \quad S_{12} = -\tau_o + \mu v_y,$$

$$II_{\mathbf{S}} \leq \tau_o, \quad \Longrightarrow \quad v_y = 0.$$

Next, we assume that the viscous region, namely $II_{\mathbf{S}} > \tau_o$, and the rigid region, $II_{\mathbf{S}} \leq \tau_o$, are separated by a sharp interface $y = s(t)$ a priori unknown, i.e. a free boundary. In the fluid region, i.e. $s\,(t) < y < H$, the motion equation reduces to

$$\rho v_t = \mu v_{yy} + f_o,$$

coupled with the no-slip condition on $y = H$,

$$v\,(H, t) = 0,$$

and with the threshold condition on the free boundary $s\,(t)$

$$S_{12}|_{y=s} = \tau_o, \quad \Longrightarrow \quad v_y\,\big|_{y=s} = 0.$$

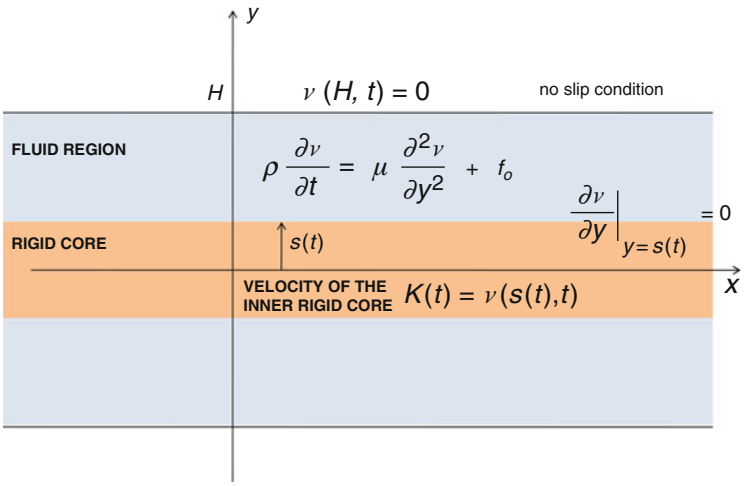

Fig. 7 The position $s(t)$ of the "fluid – rigid" is unknown. Indeed we deal with a free boundary problem

In particular, we assume no-slip also at the interface $s\,(t)$, so that the velocity of the rigid core is

$$\kappa\,(t) = v\,(s\,(t)\,,t)\,.$$

Figure 7 represents a sketch of the problem we have to solve. We need an evolution for the interface $s\,(t)$. According to the approach developed in [12], which is based on the pioneering works by Safronchik [29] and Rubinstein [28], the unyielded region is treated as an evolving non material volume, whose motion is determined by using the integral (or global) momentum balance. The dynamics of the unyielded domain

$$\Omega\,(t) = \{0 < x < L,\ \ -s\,(t) < y < s\,(t)\}\,,$$

is thus given by (see, e.g., [3])

$$\frac{d}{dt}\int_{\Omega(t)} \rho \boldsymbol{v} dV = \int_{\partial\Omega(t)} \mathbf{T}\boldsymbol{n}\, dS - \int_{\partial\Omega(t)} \rho \boldsymbol{v}\,[(\boldsymbol{v}-\boldsymbol{w})\cdot\boldsymbol{n}]\, dS, \tag{9}$$

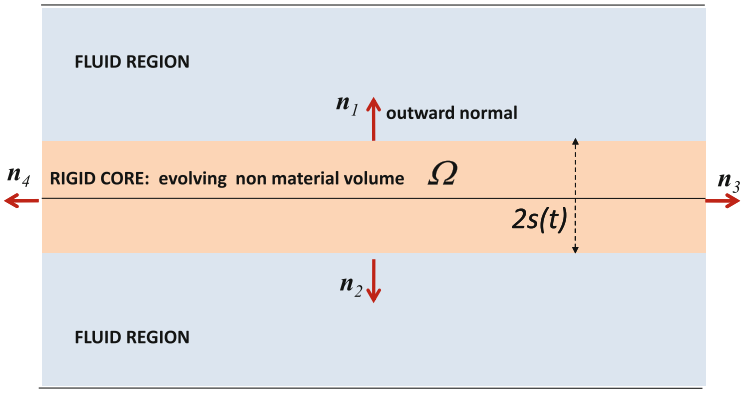

Fig. 8 The evolving non-material domain Ω

where $\boldsymbol{w}$ is the velocity of the boundary[1] $\partial\Omega$ and $\boldsymbol{n}$ its outward normal. Taking Fig. 8 into account relation (9) reduces to[2]

$$v_t\left(s\left(t\right),t\right)=\frac{1}{\rho}\left(f_o-\frac{\tau_o}{s\left(t\right)}\right).$$

We thus end up with this free boundary problem

$$\begin{cases}\rho v_t=\mu v_{yy}-f_o, & s\left(t\right)<y<H,\ t>0\\ v\left(H,t\right)=0, & t>0,\\ v_y\left(s\left(t\right),t\right)=0, & t>0,\\ \rho v_t\left(s\left(t\right),t\right)=f_o-\dfrac{\tau_o}{s\left(t\right)}, & t>0,\\ v\left(y,0\right)=v_o\left(y\right) & 0<y<s_o,\\ s\left(0\right)=s_o.\end{cases}\tag{10}$$

The domain of the problem is represented in Fig. 9. The problem (10) is a free boundary problem but not of Stefan type, because in the evolution equation for the free boundary $\dot{s}$ does not appear. However if we consider as new dependent variable

[1] In the 1D case, considering just the upper part of Ω, $\boldsymbol{w}=\dot{s}\left(t\right)\boldsymbol{e}_y$.

[2] We remark that $\dot{\kappa}\left(t\right)\neq v_t\left(s\left(t\right),t\right)$.

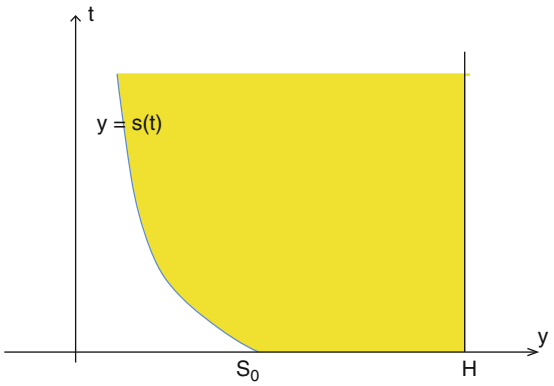

Fig. 9 Sketch of the domain of problem (10)

$z(y.t) = v_t(y,t)$, problem (10) rewrites as

$$\begin{cases} \rho z_t = \mu z_{yy}, & s(t) < y < H,\ t > 0 \\ z(H,t) = 0, & t > 0, \\ \rho z(s(t),t) = f_o - \dfrac{\tau_o}{s(t)}, & t > 0, \\ z_y(s(t),t) = \dfrac{\tau_o}{s(t)}\dot{s}, & t > 0, \\ v(y,0) = v_o(y) & 0 < y < s_o, \\ s(0) = s_o. \end{cases} \tag{11}$$

In [4] global well posedness of problem (11) has been proved.

4 Bingham Model with Deformable Core

The Bingham model predicts that the material behaves as a rigid body if the shear stress is less than the threshold τ_o. It is however evident that the schematization of the rigid body is not plausible from a physical point of view (think, for example, to the mayonnaise). Oldroyd [20] and Yoshimura et al. [32] have proposed to treat the "solid phase" as deformable. In [7] Fusi et al. have studied an extension of the 1D problem (10) to the case of an elastic core. The model has been developed within the context of the theory of natural configurations [24, 25]. In [10] Fusi et al. have extended the problem studied in [7] to a 2D channel flow where the channel amplitude is not uniform.

Actually, other models have been proposed for Bingham-like fluids whose unyielded core is deformable. In [8, 9], for instance, the material in the non-fluid region has been modeled as a visco-elastic fluid.

4.1 Channel Flow of a Bingham-Like Fluid with Linear Elastic Core

Here we consider a channel flow of a Bingham-like fluid driven by a known pressure gradient, assuming that the continuum behaves as a linear viscous fluid if the stress is above the yield stress and as a linear elastic solid when the stress is below such a threshold. In particular we assume that the domain may be split in two sub-domains, see Fig. 10. The inner core, in which the material behaves as a linear elastic material, and the outer part (i.e. the one close to the channel walls) where a linear viscous behavior occurs. The two regions are separated by the unknown sharp interfaces $y = \pm\sigma(x, t)$. Moreover the channel width varies along x, so that the channel walls are given by the function $y = H(x)$. The channel is finite and we denote its length by L. As in Sect. 3, we limit our analysis to the upper part of the channel because of symmetry. The motion equations are obtained by imposing the mass and momentum balance. The evolution equation of the interface $y = \sigma(x, t)$, as well as the boundary conditions, are derived imposing Rankine-Hugoniot conditions and Von Mises yield criterion. The general mathematical problem is therefore a two-dimensional free boundary problem. We develop the model assuming that the characteristic height of the upper part H is far less than L, i.e. the aspect ratio

$$\varepsilon = \frac{H}{L} \ll 1$$

is very small.

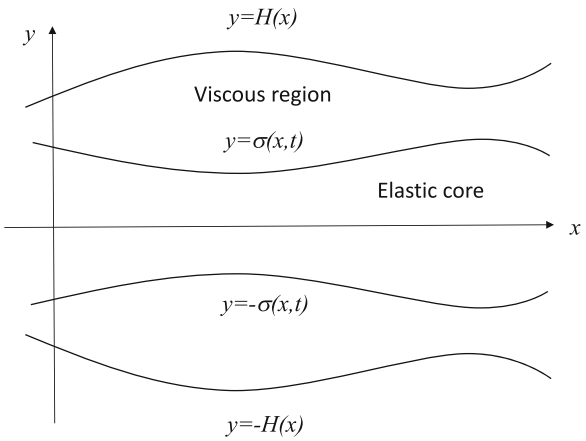

Fig. 10 A schematic representation of the channel flow with deformable core

4.2 Kinematics and Constitutive Equation

Consider a two dimensional setting and assume that the motion is given by

$$\boldsymbol{x} = \boldsymbol{\chi}\ (\boldsymbol{X}, t), \tag{12}$$

where $\boldsymbol{\chi}$ is a differentiable and invertible mapping from $\mathbf{R}^2 \rightarrow \mathbf{R}^2$. The vectors $\boldsymbol{x}$, $\boldsymbol{X}$ are the Eulerian and Lagrangian coordinates, respectively. The deformation tensor is[3]

$$\mathbf{F} = \text{grad}\boldsymbol{\chi}\ (\boldsymbol{X}, t)$$

and mechanical incompressibility entails $\det \mathbf{F} = 1$.The Eulerian velocity and acceleration are defined as

$$\boldsymbol{v}\ (\boldsymbol{x}, t) = \left.\frac{\partial \boldsymbol{\chi}}{\partial t}\right|_{\boldsymbol{X}=\boldsymbol{\chi}^{-1}(\boldsymbol{x},t)}$$

$$\boldsymbol{a}\ (\boldsymbol{x}, t) = \left.\frac{\partial^2 \boldsymbol{\chi}}{\partial t^2}\right|_{\boldsymbol{X}=\boldsymbol{\chi}^{-1}(\boldsymbol{x},t)}$$

respectively. The strain rate tensor is

$$\mathbf{D} = \begin{pmatrix} \dfrac{\partial v_1}{\partial x} & \dfrac{1}{2}\left(\dfrac{\partial v_1}{\partial y} + \dfrac{\partial v_2}{\partial x}\right) \\ \dfrac{1}{2}\left(\dfrac{\partial v_1}{\partial y} + \dfrac{\partial v_2}{\partial x}\right) & \dfrac{\partial v_2}{\partial y} \end{pmatrix},$$

and mechanical incompressibility gives

$$\text{tr}\,\mathbf{D} = \frac{\partial v_1}{\partial x} + \frac{\partial v_2}{\partial y} = 0. \tag{13}$$

Splitting, as usual, the Cauchy stress as $\mathbf{T} = -P\mathbf{I} + \mathbf{S}$, with $P = 1/3\text{tr}\mathbf{T}$, we extend we extend the constitutive relation (6), (7) to the case in which the region $II_{\mathbf{S}} < \tau_o$ behaves as a linear elastic material[4] (see [7, 10]).

$$\left[\mathbf{S} - \left(2\mu + \frac{\tau_o}{II_{\mathbf{D}}}\right)\mathbf{D}\right] \Theta\ (II_{\mathbf{S}} - \tau_o) + (\mathbf{S} - 2\eta\mathbf{E})\ \Theta\ (\tau_o - II_{\mathbf{S}}) = 0, \tag{14}$$

[3]Here grad denotes the gradient operator w.r.t. Lagrangian coordinates, while ∇ the gradient w.r.t. Eulerian coordinates.

[4]We are considering a linear elastic model even if $\|\mathbf{F}\|$ may be, in general, not very "small" , as we shall see in Sect. 4.3.3.

where

$$\mathbf{E} = \frac{1}{2}\left[\nabla \boldsymbol{f} + (\nabla \boldsymbol{f})^{\mathrm{T}}\right]$$

is the linearized strain tensor, $\boldsymbol{f} = \boldsymbol{\chi} - \boldsymbol{X}$ is the displacement , η is the elastic modulus and Θ is the Heaviside function

$$\Theta(z) = \begin{cases} 0, \text{ if } z < 0, \\ \\ 1, \text{ if } z \geqslant 0. \end{cases}$$

From (14) it is clear that, whenever $II_{\mathbf{S}} \leq \tau_o$, the continuum behaves as a linear elastic solid whereas the viscous behavior occurs when $II_{\mathbf{S}} \geq \tau_o$.

4.3 Flow in a Channel

We rescale the longitudinal variable as

$$\tilde{x} = \frac{x}{L} \qquad \tilde{h}(x) = \frac{H(x)}{H} \qquad \tilde{\sigma} = \frac{\sigma}{H} \qquad H = \max_{x \in [0,L]} H(x)$$

and we introduce the Reynolds and Bingham number

$$\mathsf{Re} = \frac{\rho U H}{\mu}, \quad \mathsf{Bn} = \frac{\tau_o H}{\mu U}, \tag{15}$$

where U is the characteristic velocity and ρ is the material density. The we set

$$\tilde{y} = \frac{1}{\varepsilon}\frac{y}{L} \qquad \tilde{t} = \frac{t}{t_c} \qquad t_c = \frac{L}{U}.$$

Concerning velocity and pressure, we introduce

$$\tilde{v}_1 = \frac{v_1}{U}, \quad \tilde{v}_2 = \frac{v_2}{\varepsilon U}, \quad \tilde{P} = \frac{P}{P_c} \quad P_c = \frac{\mu U L}{H^2}$$

where P_c comes from the classical Poiseuille formula. Rescaling $\mathbf{S}$ as

$$\mathbf{S} = \frac{\mu U}{H}\begin{pmatrix} \tilde{S}_{11} & \tilde{S}_{12} \\ \\ \tilde{S}_{12} & \tilde{S}_{22} \end{pmatrix},$$

the motion equations become[5]

$$\frac{\mathrm{Re}}{\varepsilon}\left(\frac{\partial v_1}{\partial t}+\frac{\partial v_1}{\partial x}v_1+\frac{\partial v_1}{\partial y}v_2\right)=-\frac{1}{\varepsilon^2}\frac{\partial P}{\partial x}+\frac{1}{\varepsilon}\frac{\partial}{\partial x}\left(S_{11}\right)+\frac{1}{\varepsilon^2}\frac{\partial}{\partial y}\left(S_{12}\right), \tag{16}$$

$$\frac{\mathrm{Re}}{\varepsilon}\left(\frac{\partial v_2}{\partial t}+\frac{\partial v_2}{\partial x}v_1+\frac{\partial v_2}{\partial y}v_2\right)=-\frac{1}{\varepsilon^4}\frac{\partial P}{\partial y}+\frac{1}{\varepsilon^2}\left[\frac{\partial}{\partial x}\left(S_{12}\right)+\frac{1}{\varepsilon}\frac{\partial}{\partial y}\left(S_{22}\right)\right], \tag{17}$$

and mass conservation is

$$\frac{\partial v_1}{\partial x}+\frac{\partial v_2}{\partial y}=0. \tag{18}$$

The displacement is rescaled as

$$\tilde{f}_1=\frac{f_1}{L}\qquad \tilde{f}_2=\frac{1}{\varepsilon}\frac{f_2}{L},$$

so that[6]

$$\mathbf{E}=\begin{pmatrix}\dfrac{\partial f_1}{\partial x} & \dfrac{1}{2}\left(\dfrac{1}{\varepsilon}\dfrac{\partial f_1}{\partial y}+\varepsilon\dfrac{\partial f_2}{\partial x}\right)\\ \dfrac{1}{2}\left(\dfrac{1}{\varepsilon}\dfrac{\partial f_1}{\partial y}+\varepsilon\dfrac{\partial f_2}{\partial x}\right) & \dfrac{\partial f_2}{\partial y}\end{pmatrix}.$$

The sharp interface $y=\sigma(x,t)$ separates the elastic domain from the viscous domain, as shown in Fig. 2. We remark that the interface σ is unknown and it is not material. The dimensionless normal velocity of the interface is

$$w=\frac{\varepsilon}{\sqrt{1+\varepsilon^2\left(\dfrac{\partial\sigma}{\partial x}\right)^2}}\frac{\partial\sigma}{\partial t}.$$

The dimensionless strain rate tensor is

$$\mathbf{D}=\begin{pmatrix}\varepsilon\dfrac{\partial v_1}{\partial x} & \dfrac{1}{2}\left(\dfrac{\partial v_1}{\partial y}+\varepsilon^2\dfrac{\partial v_2}{\partial x}\right)\\ \dfrac{1}{2}\left(\dfrac{\partial v_1}{\partial y}+\varepsilon^2\dfrac{\partial v_2}{\partial x}\right) & \varepsilon\dfrac{\partial v_2}{\partial y}\end{pmatrix},$$

[5]We omit "˜" to keep notation simple.

[6]Again, we have omitted " ".

while the dimensionless invariant $II_{\mathbf{D}}$ is

$$II_{\mathbf{D}} = \frac{1}{2}\sqrt{\left(\frac{\partial v_1}{\partial y} + \varepsilon^2 \frac{\partial v_2}{\partial x}\right)^2 + 2\varepsilon^2 \left[\left(\frac{\partial v_1}{\partial x}\right)^2 + \left(\frac{\partial v_2}{\partial y}\right)^2\right]}. \tag{19}$$

The yield criterion becomes

$$II_{\mathbf{S}} \lesseqgtr \mathsf{Bn}. \tag{20}$$

4.3.1 Boundary Conditions

Let $[\![\cdot]\!]$ denotes the "jump" across the surface $y = \sigma$. Assuming no-slip on σ we get

$$[\![v_1]\!] = [\![v_2]\!] = 0. \tag{21}$$

The continuity of the stress gives

$$-[\![P]\!]\left(1 + \varepsilon^2 \left(\frac{\partial \sigma}{\partial x}\right)^2\right) + \left[\!\!\left[\varepsilon^3 S_{11} \left(\frac{\partial \sigma}{\partial x}\right)^2 - 2\varepsilon^2 S_{12} \frac{\partial \sigma}{\partial x} + \varepsilon S_{22} \right]\!\!\right] = 0, \tag{22}$$

and

$$[\![S_{12}]\!] + \varepsilon \frac{\partial \sigma}{\partial x}\left[\!\!\left[S_{22} - S_{11} - \varepsilon S_{12} \frac{\partial \sigma}{\partial x} \right]\!\!\right] = 0. \tag{23}$$

Remark 1 If we neglect $\mathscr{O}(\varepsilon)$ terms, then $[\![P]\!] = [\![S_{12}]\!] = 0$, provided that S_{ij} are bounded.

On the channel wall $y = h$ the no-slip condition yields $\boldsymbol{v}(x, h, t) \equiv 0$, while the boundary conditions for the pressure are

$$P(0, y, t) = P_{in}(t), \quad \text{and} \quad P(1, y, t) = P_{in}(t) - \Delta P(t), \quad \text{with} \ \Delta P \geq 0.$$

Finally, we impose the symmetry conditions:

$$\frac{\partial f_1(x, 0, t)}{\partial y} = 0, \qquad f_2(x, 0, t) = 0, \qquad \frac{\partial f_2(x, 0, t)}{\partial y} = 0, \qquad \frac{\partial f_2(x, 0, t)}{\partial t} = 0. \tag{24}$$

4.3.2 The Elastic Domain and the Viscous Domain

Let us first consider the elastic domain $y \in [0, \sigma]$. According to (14)

$$\mathbf{S} = \frac{\mathsf{Re}}{\lambda^2} \begin{pmatrix} 2\dfrac{\partial f_1}{\partial x} & \dfrac{1}{\varepsilon}\dfrac{\partial f_1}{\partial y} + \varepsilon \dfrac{\partial f_2}{\partial x} \\ \dfrac{1}{\varepsilon}\dfrac{\partial f_1}{\partial y} + \varepsilon \dfrac{\partial f_2}{\partial x} & 2\dfrac{\partial f_2}{\partial y} \end{pmatrix},$$

with

$$\lambda^2 = \left(\frac{U}{c}\right)^2 \qquad c^2 = \frac{\eta}{\rho}. \tag{25}$$

The momentum balance yields

$$\begin{aligned} &\mathsf{Re}\left(\frac{\partial^2 f_1}{\partial t^2} + \frac{\partial^2 f_1}{\partial x \partial t}\frac{\partial f_1}{\partial t} + \frac{\partial^2 f_1}{\partial y \partial t}\frac{\partial f_2}{\partial t}\right) \\ &\quad = -\frac{1}{\varepsilon}\frac{\partial P}{\partial x} + \frac{\mathsf{Re}}{\lambda^2}\left(2\frac{\partial^2 f_1}{\partial x^2} + \frac{1}{\varepsilon^2}\frac{\partial^2 f_1}{\partial y^2} + \frac{1}{\varepsilon}\frac{\partial^2 f_2}{\partial y \partial x}\right), \end{aligned} \tag{26}$$

$$\begin{aligned} &\mathsf{Re}\left(\frac{\partial^2 f_2}{\partial t^2} + \frac{\partial^2 f_2}{\partial x \partial t}\frac{\partial f_1}{\partial t} + \frac{\partial^2 f_2}{\partial y \partial t}\frac{\partial f_2}{\partial t}\right) \\ &\quad = -\frac{1}{\varepsilon^3}\frac{\partial P}{\partial y} + \frac{\mathsf{Re}}{\lambda^2}\left(\frac{1}{\varepsilon^2}\frac{\partial^2 f_1}{\partial x \partial y} + \frac{\partial^2 f_2}{\partial x^2} + \frac{2}{\varepsilon^2}\frac{\partial^2 f_2}{\partial y^2}\right). \end{aligned} \tag{27}$$

In the viscous domain $y \in [\sigma, 1]$

$$\mathbf{S} = \left(1 + \frac{\mathsf{Bn}}{2II_{\mathbf{D}}}\right) \begin{pmatrix} 2\varepsilon\dfrac{\partial v_1}{\partial x} & \dfrac{\partial v_1}{\partial y} + \varepsilon^2 \dfrac{\partial v_2}{\partial x} \\ \dfrac{\partial v_1}{\partial y} + \varepsilon^2 \dfrac{\partial v_2}{\partial x} & 2\varepsilon\dfrac{\partial v_2}{\partial y} \end{pmatrix},$$

The momentum equations are

$$\begin{aligned} &\frac{\mathsf{Re}}{\varepsilon}\left(\frac{\partial v_1}{\partial t} + \frac{\partial v_1}{\partial x}v_1 + \frac{\partial v_1}{\partial y}v_2\right) \\ &\quad = -\frac{1}{\varepsilon^2}\frac{\partial P}{\partial x} + 2\frac{\partial}{\partial x}\left[\left(1 + \frac{\mathsf{Bn}}{2II_{\mathbf{D}}}\right)\frac{\partial v_1}{\partial x}\right] \end{aligned}$$

$$+\frac{1}{\varepsilon^2}\frac{\partial}{\partial y}\left[\left(1+\frac{\mathsf{Bn}}{2II_{\mathbf{D}}}\right)\left(\frac{\partial v_1}{\partial y}\ \ \varepsilon^2\frac{\partial v_2}{\partial x}\right)\right], \tag{28}$$

$$\frac{\mathsf{Re}}{\varepsilon}\left(\frac{\partial v_2}{\partial t}+\frac{\partial v_2}{\partial x}v_1+\frac{\partial v_2}{\partial y}v_2\right)=-\frac{1}{\varepsilon^4}\frac{\partial P}{\partial y}$$
$$+\frac{1}{\varepsilon^2}\left\{\frac{\partial}{\partial x}\left[\left(1+\frac{\mathsf{Bn}}{2II_{\mathbf{D}}}\right)\left(\frac{\partial v_1}{\partial y}\ +\ \varepsilon^2\frac{\partial v_2}{\partial x}\right)\right]+2\frac{\partial}{\partial y}\left[\left(1+\frac{\mathsf{Bn}}{2II_{\mathbf{D}}}\right)\frac{\partial v_2}{\partial y}\right]\right\}. \tag{29}$$

The model is consistent if $II_{\mathbf{S}} < \mathsf{Bn}$ for $y \in [0, \sigma]$, i.e.

$$\sqrt{\left(\frac{\partial f_1}{\partial y}+\varepsilon^2\frac{\partial f_2}{\partial x}\right)^2+2\varepsilon^2\left[\left(\frac{\partial f_1}{\partial x}\right)^2+\left(\frac{\partial f_2}{\partial y}\right)^2\right]}\leq\frac{\mathsf{Bn}\lambda^2\varepsilon}{\mathsf{Re}}. \tag{30}$$

and if $II_{\mathbf{S}} \geq \mathsf{Bn}$ for $y \in [\sigma, 1]$, i.e. $II_{\mathbf{D}} \geq 0$. Finally we notice that

$$\varepsilon[\![\ S_{12}\ ]\!]=\varepsilon\left[\left(1+\frac{\mathsf{Bn}}{2II_{\mathbf{D}}}\right)\left(\frac{\partial v_1}{\partial y}+\varepsilon^2\frac{\partial v_2}{\partial x}\right)\right]_{y=\sigma^+}$$
$$-\frac{\mathsf{Re}}{\lambda^2}\left[\frac{\partial f_1}{\partial y}+\varepsilon^2\frac{\partial f_2}{\partial x}\right]_{y=\sigma^-}. \tag{31}$$

4.3.3 Asymptotic Expansion

The assumption $\varepsilon \ll 1$, allows to seek the unknown fields (i.e. v_1, v_2, P, etc.) in the following form

$$\phi=\sum_{j=0}^{\infty}\phi^{(j)}\varepsilon^j$$

Substituting into the governing equations we get a hierarchy of problems that must be matched together. The matching procedure requires the specification of Re, Bi, and λ^2. We consider: $\mathsf{Re} \leq \mathscr{O}(1)$, i.e. laminar flow and $\mathsf{Bn} = \mathscr{O}(1)$. We introduce the dimensionless parameter

$$\Gamma=\frac{\eta H}{\mu U}=\frac{\mathsf{Re}}{\lambda^2}, \tag{32}$$

and consider two different cases which correspond to different behaviors of the inner core:

(1) $\Gamma = \mathcal{O}(1)$.
(2) $\Gamma = \mathcal{O}(\varepsilon)$.

When $\Gamma = \mathcal{O}(1)$, namely $\mathsf{Re} = \mathcal{O}\left(\lambda^2\right)$, we have an almost rigid inner core, while the case $\Gamma = \mathcal{O}(\varepsilon)$, i.e. $\mathsf{Re} = \mathcal{O}\left(\varepsilon\lambda^2\right)$, corresponds to a " soft" inner core where deformations are non-negligible. Let us show that the first case leads to the classical Bingham model. Indeed, considering $\mathsf{Re} = \mathcal{O}\left(\lambda^2\right)$

$$\mathcal{O}(1) = \Gamma = \varepsilon\frac{t_c\eta}{\mu}, \quad \Rightarrow \quad \frac{t_c\eta}{\mu} = \mathcal{O}\left(\varepsilon^{-1}\right). \tag{33}$$

Evaluating the order of magnitude of the elastic stress S_{el} and of the viscous stress S_{vis} we have

$$S_{vis} = \mu\frac{U}{H} \qquad S_{el} = \delta\eta\frac{L}{H},$$

where δ is the dimensionless order of magnitude of the longitudinal displacement. The continuity of the shear stress at the interface yields

$$\frac{S_{el}}{S_{vis}} = \mathcal{O}(1) \qquad \Rightarrow \qquad \delta\frac{t_c\eta}{\mu} = \mathcal{O}(1). \tag{34}$$

Hence we find $\delta = \mathcal{O}(\varepsilon)$, meaning an almost uniform longitudinal displacement as in the classical Bingham model. In the second case

$$\mathsf{Re} = \mathcal{O}(\varepsilon\lambda^2) \qquad \Rightarrow \qquad \frac{t_c\eta}{\mu} = \mathcal{O}(1)$$

which entails $\delta = \mathcal{O}(1)$. As a consequence the longitudinal displacement is not uniform.

4.3.4 First Case: $\Gamma = \mathcal{O}(1)$

We start considering the elastic domain, and we focus on the zero order terms. From (27) we obtain $P^{(0)} = P^{(0)}(x,t)$. Next, since $[\![\, P \,]\!] = 0$ on the interface, we have that in the whole elastic region $P^{(0)} = P^{(0)}\left(x, \sigma^+, t\right)$. From (26) we have

$$\begin{cases} \dfrac{\partial^2 f_1{}^{(0)}}{\partial y^2} = 0, \\ \dfrac{\partial f_1{}^{(0)}}{\partial y}\Big|_{y=0} = 0, \end{cases} \quad \Longrightarrow \; f_1{}^{(0)} = f_1{}^{(0)}(x,t).$$

Mass conservation in the elastic domain becomes

$$\frac{\partial^2 f_1^{(0)}}{\partial x \partial t} + \frac{\partial^2 f_2^{(0)}}{\partial y \partial t} = 0. \tag{35}$$

Recalling (24) it is easy to show that

$$\frac{\partial}{\partial x}\left(\frac{\partial f_1^{(0)}}{\partial t}\right) = 0. \tag{36}$$

Therefore setting

$$\kappa = \frac{\partial f_1^{(0)}}{\partial t},$$

we have $\kappa = \kappa(t)$. From (21) we find

$$\kappa = v_1^{(0)}\left(x, \sigma^+, t\right). \tag{37}$$

From (35)

$$\frac{\partial f_2^{(0)}}{\partial t} \text{ depends only on } t.$$

and the transversal velocity vanishes everywhere in the elastic region, so that

$$v_2^{(0)}\left(x, \sigma^+, t\right) = 0. \tag{38}$$

Let us now consider relation (31) at the zero order approximation. We get

$$\frac{\mathsf{Re}}{\lambda^2}\left.\frac{\partial f_1^{(1)}}{\partial y}\right|_{y=\sigma^-} = \left[\left(1 + \frac{\mathsf{Bn}}{2II_{\mathbf{D}}^{(0)}}\right)\frac{\partial v_1^{(0)}}{\partial y}\right]_{y=\sigma^+}. \tag{39}$$

The latter forces to analyze the first order term in (26), (27), namely

$$\begin{cases} \dfrac{\partial^2 f_1^{(1)}}{\partial y^2} = \dfrac{\lambda^2}{\mathsf{Re}}\dfrac{\partial P^{(0)}}{\partial x}, \\ \left.\dfrac{\partial f_1^{(1)}}{\partial y}\right|_{y=0} = 0, \end{cases} \quad \Longrightarrow \quad f_1^{(1)} = \frac{\lambda^2}{2\,\mathsf{Re}}\frac{\partial P^{(0)}}{\partial x}y^2 + B(x,t).$$

Hence (39) becomes

$$\frac{\partial P^{(0)}}{\partial x}\sigma = \left[\left(1 + \frac{\mathsf{Bn}}{2II_{\mathbf{D}}^{(0)}}\right)\frac{\partial v_1^{(0)}}{\partial y}\right]_{y=\sigma^+}. \tag{40}$$

It is easy to show that

$$II_{\mathbf{S}} = \left|\frac{\partial P^{(0)}}{\partial x}\right| y + \mathscr{O}(\varepsilon)$$

in the elastic region so that condition (30) is fulfilled when

$$\left|\frac{\partial P^{(0)}}{\partial x}\right| \sigma \leq \mathsf{Bn}. \tag{41}$$

We now focus on the viscous part $\sigma < y < 1$. Here (29) entails $P^{(0)} = P^{(0)}(x, t)$, so that the pressure is uniform on any channel section. Next, we observe that

$$II_{\mathbf{S}} = \left|\frac{\partial v_1^{(0)}}{\partial y} + \mathsf{Bi}\ \mathrm{sign}\left(\frac{\partial v_1^{(0)}}{\partial y}\right)\right| + \mathscr{O}(\varepsilon)$$

and (39) can be rewritten as

$$\underbrace{\left|\frac{\partial P^{(0)}}{\partial x}\right|\sigma}_{II_{\mathbf{S}} \leq \mathsf{Bn}} = \underbrace{\left|\left.\frac{\partial v_1^{(0)}}{\partial y}\right|_{y=\sigma^+} + \mathsf{Bi}\ \mathrm{sign}\left(\left.\frac{\partial v_1^{(0)}}{\partial y}\right|_{y=\sigma^+}\right)\right|}_{II_{\mathbf{S}} \geq \mathsf{Bn}}.$$

We conclude that

$$\left.\frac{\partial v_1^{(0)}}{\partial y}\right|_{y=\sigma^+} = 0 \qquad \frac{\partial P^{(0)}}{\partial x}\sigma = \mathsf{Bi}\ \mathrm{sign}\left(\left.\frac{\partial v_1^{(0)}}{\partial y}\right|_{y=\sigma^+}\right). \tag{42}$$

Focussing now on (28) we find

$$-\frac{\partial P^{(0)}}{\partial x} + \frac{\partial}{\partial y}\left[\frac{\partial v_1^{(0)}}{\partial y} + \mathsf{Bi}\ \mathrm{sign}\left(\frac{\partial v_1^{(0)}}{\partial y}\right)\right] = 0,$$

so that

$$\begin{cases} -\dfrac{\partial P^{(0)}}{\partial x} + \dfrac{\partial^2 v_1^{(0)}}{\partial y^2} = 0, \\ v_1^{(0)}(x, h, t) = 0, \\ \left.\dfrac{\partial v_1^{(0)}}{\partial y}\right|_{y=\sigma^+} = 0, \end{cases} \tag{43}$$

Solving (43) we get

$$v_1^{(0)}(x, y, t) = -\frac{1}{2}\frac{\partial P^{(0)}}{\partial x}\left(h^2 - y^2\right) + \mathsf{Bi}\ \mathrm{sign}\left(\left.\frac{\partial v_1^{(0)}}{\partial y}\right|_{y=\sigma^+}\right)(h - y). \tag{44}$$

In particular, (37) yields

$$\kappa = -\frac{1}{2}\frac{\partial P^{(0)}}{\partial x}(h - \sigma)^2, \quad \text{with} \quad \omega = \omega(t). \tag{45}$$

Remark 2 We remark that

$$\kappa = -\frac{\mathsf{Bn}}{2\sigma}\mathrm{sign}\left(\left.\frac{\partial v_1^{(0)}}{\partial y}\right|_{y=\sigma^+}\right)(h - \sigma)^2. \tag{46}$$

Therefore the derivative w.r.t. x of the r.h.s. of (46) must vanish and

$$\frac{\partial h}{\partial x} = \frac{h + \sigma}{2\sigma}\frac{\partial \sigma}{\partial x}. \tag{47}$$

From (18)

$$\int_\sigma^h \frac{\partial v_1^{(0)}}{\partial x} dy = 0, \tag{48}$$

since $v_2^{(0)}(x, h, t) = v_2^{(0)}\left(x, \sigma^+, t\right) = 0$. Hence, exploiting (44)

$$\frac{\partial v_1^{(0)}}{\partial x} = -\frac{1}{2}\frac{\partial^2 P^{(0)}}{\partial x^2}\left(h^2 - y^2\right) - \frac{\partial P^{(0)}}{\partial x}\frac{\partial h}{\partial x}h + \frac{\partial P^{(0)}}{\partial x}\sigma\frac{\partial h}{\partial x}.$$

Thus (48) yields

$$(h-\sigma)^2\left[\frac{1}{6}\frac{\partial^2 P^{(0)}}{\partial x^2}(\sigma+2h)+\frac{\partial P^{(0)}}{\partial x}\frac{\partial h}{\partial x}\right]=0. \tag{49}$$

In case h is uniform we get

$$\frac{\partial^2 P^{(0)}}{\partial x^2}=0 \quad \Rightarrow \quad P^{(0)}(x,t)=P_{in}(t)-x\Delta P(t),$$

and

$$\sigma(t)=\frac{\mathsf{Bn}}{\Delta P(t)},$$

from which we derive the classical Bingham flow condition we find in [4]

$$\frac{\mathsf{Bn}}{\Delta P(t)}<h,$$

ensuring the flow within the channel.

Remark 3 In case h does depend on x (49) does not give rise to any solution consistent with (47) (a well known paradox of the Bingham model). Indeed, form $(42)_2$

$$\frac{\partial^2 P^{(0)}}{\partial x^2}=-\frac{1}{\sigma}\frac{\partial \sigma}{\partial x}\frac{\partial P^{(0)}}{\partial x},$$

that inserted into (49) yields

$$\frac{\partial P^{(0)}}{\partial x}(h-\sigma)^2\left[\frac{\partial h}{\partial x}-\frac{\partial \sigma}{\partial x}\frac{\sigma+2h}{6\sigma}\right]=0.$$

The above implies

$$\frac{\partial \sigma}{\partial x}\frac{\sigma+2h}{6\sigma}=\frac{\partial h}{\partial x} \tag{50}$$

Inserting (50) into (47) we get $h=-2\sigma$, that is a contradiction (lubrication paradox, see [6, 17, 21, 27]).

4.3.5 Second Case $\Gamma = \mathscr{O}(\varepsilon)$

Set $\varepsilon\hat{\Gamma} = \Gamma$ with $\hat{\Gamma} = \mathscr{O}(1)$. From (31)

$$\left[\left(1+\frac{\mathsf{Bn}}{2II_{\mathbf{D}}}\right)\left(\frac{\partial v_1}{\partial y}+\varepsilon^2\frac{\partial v_2}{\partial x}\right)\right]_{y=\sigma^+} = \hat{\Gamma}\left[\frac{\partial f_1}{\partial y}+\varepsilon^2\frac{\partial f_2}{\partial x}\right]_{y=\sigma^-}, \tag{51}$$

Once again $P^{(0)} = P^{(0)}(x,t)$ in the whole domain. In the elastic part

$$\begin{cases} \dfrac{\partial^2 f_1^{(0)}}{\partial y^2} = \dfrac{1}{\hat{\Gamma}}\dfrac{\partial P^{(0)}}{\partial x}, \\ \left.\dfrac{\partial f_1^{(0)}}{\partial y}\right|_{y=0} = 0, \end{cases} \quad \Rightarrow \quad f_1^{(0)} = \frac{1}{2\,\hat{\Gamma}}\frac{\partial P^{(0)}}{\partial x}y^2 + a(x,t), \tag{52}$$

so that (51) implies

$$\frac{\partial P^{(0)}}{\partial x}\sigma = \left[\left(1+\frac{\mathsf{Bn}}{2II_{\mathbf{D}}^{(0)}}\right)\frac{\partial v_1^{(0)}}{\partial y}\right]_{y=\sigma^+}.$$

The term $a(x,t)$ is unknown at this stage while $v_1^{(0)}$ is

$$v_1^{(0)} = \frac{1}{2\,\hat{\Gamma}}\frac{\partial^2 P^{(0)}}{\partial t \partial x}y^2 + \kappa(x,t),$$

where now

$$\kappa(x,t) = \frac{\partial a(x,t)}{\partial t}, \tag{53}$$

can be interpreted as the uniform part of the longitudinal velocity. Checking condition (30) we find again (41).

Remark 4 At the leading order the longitudinal displacement is a superposition of a uniform displacement $a(x,t)$ and a non uniform displacement modulated by the pressure gradient. The latter becomes negligible for large values of $\hat{\Gamma}$ and the first case is recovered for $\hat{\Gamma} \gg 1$.

In the fluid region

$$\frac{\partial P^{(0)}}{\partial x}\sigma = -\mathsf{Bn}.$$

Moreover

$$v_1^{(0)}(x,y,t) = -\frac{1}{2}\frac{\partial P^{(0)}}{\partial x}\left(h^2 - y^2\right) + \frac{\partial P^{(0)}}{\partial x}\sigma\,(h-y)\,.$$

The jump condition (21) yields

$$\frac{1}{2\,\hat{\Gamma}}\frac{\partial^2 P^{(0)}}{\partial t \partial x}\sigma^2 + \omega\,(x,t) = -\frac{1}{2}\frac{\partial P^{(0)}}{\partial x}\,(h-\sigma)^2\,,$$

with ω given by (53). From mass balance and boundary conditions

$$0 = \int_0^h \frac{\partial v_1^{(0)}}{\partial x}dy = \int_0^\sigma \frac{\partial}{\partial x}\left(\frac{\partial f_1^{(0)}}{\partial t}\right)dy + \int_\sigma^h \frac{\partial v_1^{(0)}}{\partial x}dy,$$

which, after some of algebra, gives

$$(h-\sigma)^2\left[\frac{1}{6}\frac{\partial^2 P^{(0)}}{\partial x^2}\,(2h+\sigma) + \frac{\partial P^{(0)}}{\partial x}\frac{\partial h}{\partial x}\right] - \frac{\sigma^3}{6\,\hat{\Gamma}}\frac{\partial^3 P^{(0)}}{\partial x^2 \partial t} - \sigma\frac{\partial \omega}{\partial x} = 0.$$

Therefore the mathematical problem at the zero order approximation is the following

$$\begin{cases} \dfrac{\partial P^{(0)}}{\partial x}\sigma = -\mathsf{Bn}, \\ \dfrac{1}{2\,\hat{\Gamma}}\dfrac{\partial^2 P^{(0)}}{\partial t \partial x}\sigma^2 + \kappa\,(x,t) = -\dfrac{1}{2}\dfrac{\partial P^{(0)}}{\partial x}\,(h-\sigma)^2\,, \\ -(h-\sigma)^2\left[\dfrac{1}{6}\dfrac{\partial^2 P^{(0)}}{\partial x^2}\,(2h+\sigma) + \dfrac{\partial P^{(0)}}{\partial x}\dfrac{\partial h}{\partial x}\right] \\ \qquad + \dfrac{\sigma^3}{6\,\hat{\Gamma}}\dfrac{\partial}{\partial t}\left(\dfrac{\partial^2 P^{(0)}}{\partial x^2}\right) + \sigma\dfrac{\partial \kappa}{\partial x} = 0. \end{cases} \tag{54}$$

Example 1 Consider the stationary problem when $h \equiv 1$

$$\begin{cases} \dfrac{\partial P^{(0)}}{\partial x}\sigma = -\mathsf{Bn}, \;\Rightarrow\; \dfrac{\partial \sigma}{\partial x}\dfrac{\partial P^{(0)}}{\partial x} = -\dfrac{\partial^2 P^{(0)}}{\partial x^2}\sigma, \\ \kappa\,(x,t) = -\dfrac{1}{2}\dfrac{\partial P^{(0)}}{\partial x}\,(1-\sigma)^2\,, \;\Rightarrow\; \dfrac{\partial \kappa}{\partial x} = -\dfrac{1}{2}\dfrac{\partial^2 P^{(0)}}{\partial x^2}\left(1-\sigma^2\right), \\ -\dfrac{(1-\sigma)^2}{6}\dfrac{\partial^2 P^{(0)}}{\partial x^2}\,(2+\sigma) + \sigma\dfrac{\partial \kappa}{\partial x} = 0. \end{cases} \tag{55}$$

We get

$$\frac{1}{3}\frac{\partial^2 P^{(0)}}{\partial x^2}\left(1-\sigma^3\right)=0,$$

yielding $\sigma = 1$ (which we do not consider) and $P^{(0)} = P_{in} - \Delta P x$, with ΔP known. Therefore

$$\sigma = = \frac{\mathsf{Bn}}{\Delta P}, \tag{56}$$

$$\kappa = \frac{\Delta P}{2}\left(1-\frac{\mathsf{Bn}}{\Delta P}\right)^2. \tag{57}$$

Requiring $\sigma < 1$ we get the usual Bingham flow condition.

4.3.6 Stationary Version of (54)

We show that the stationary version of system (54), namely

$$\begin{cases} \dfrac{\partial P^{(0)}}{\partial x}\sigma = -\mathsf{Bn}, \\ \omega(x,t) = -\dfrac{1}{2}\dfrac{\partial P^{(0)}}{\partial x}(h-\sigma)^2, \\ -(h-\sigma)^2\left[\dfrac{1}{6}\dfrac{\partial^2 P^{(0)}}{\partial x^2}(2h+\sigma)+\dfrac{\partial P^{(0)}}{\partial x}\dfrac{\partial h}{\partial x}\right]+\sigma\dfrac{\partial \omega}{\partial x}=0, \end{cases} \tag{58}$$

admits a unique solution when h is a smooth bounded function of x with $h \in [h_m, h_M]$. From $(58)_1$

$$\frac{\partial^2 P^{(0)}}{\partial x^2} = \frac{\mathsf{Bn}}{\sigma^2}\frac{\partial \sigma}{\partial x}, \tag{59}$$

and from $(58)_2$

$$\kappa(x,t) = \frac{\mathsf{Bn}}{2\,\sigma}(h-\sigma)^2, \quad \text{and} \quad \frac{\partial \kappa}{\partial x} = \frac{\mathsf{Bn}\ (h-\sigma)}{2\sigma^2}\left[2\sigma\frac{\partial h}{\partial x}-\frac{\partial \sigma}{\partial x}(h+\sigma)\right].$$

Hence, system (58) can be rewritten as

$$\begin{cases} \dfrac{\partial P^{(0)}}{\partial x}\sigma = -\mathsf{Bn}, \\ \\ -(h-\sigma)^2\left[\dfrac{1}{6}\dfrac{\partial^2 P^{(0)}}{\partial x^2}(2h+\sigma) + \dfrac{\partial P^{(0)}}{\partial x}\dfrac{\partial h}{\partial x}\right] + \\ \dfrac{\mathsf{Bn}\ (h-\sigma)}{2\sigma}\left[2\sigma\dfrac{\partial h}{\partial x} - \dfrac{\partial \sigma}{\partial x}(h+\sigma)\right] = 0. \end{cases} \tag{60}$$

In [10] it has been proved that there exists a unique pair of sufficiently regular functions $\left(\sigma(x), P^{(0)}(x)\right)$ such that:

(a) $0 < \sigma(x) < h(x)$, for all $x \in [0, 1]$.
(b) $P^{(0)}(0) = P_{in}$, and $P^{(0)}(1) = P_{in} - \Delta P$.
(c) $\sigma(x)$ and $P^{(0)}(x)$ fulfill the equations of (60).

Remark 5 Assuming that (60) is solvable according to the above definition, we find immediately a new "flow condition". Indeed, integrating $(60)_1$ between 0 and 1, we obtain

$$\frac{\Delta P}{\mathsf{Bn}} = \int_0^1 \frac{dx}{\sigma(x)}.$$

Since

$$\int_0^1 \frac{dx}{\sigma(x)} > \int_0^1 \frac{dx}{h(x)}, \tag{61}$$

if (60) admits a solution, the following inequality holds true

$$\frac{\Delta P}{\mathsf{Bn}} > \int_0^1 \frac{dx}{h(x)}. \tag{62}$$

Going back to dimension variables we get

$$\frac{\Delta P}{\tau_o} > \int_0^L \frac{dx}{H(x)},$$

which generalizes the classical Bingham flow condition.

4.4 Numerical Simulations

We present some numerical simulations to investigate the stationary behavior of $\sigma(x)$ when $\Gamma = \mathcal{O}(1)$. Suppose following function

$$h(x) = \frac{1}{2} - \frac{1}{10}\arctan\left[200\left(x - \frac{1}{2}\right)\right],$$

The channel profile and the free boundary separating the elastic and the viscous phase are shown in Figs. 11, 12, 13, 14 for different values of $\Delta P/\mathsf{Bn}$ satisfying condition (62). We see that

$$\int_0^1 \frac{dx'}{h(x')} = 2.2,$$

and consequently we perform numerical simulation with $\Delta P/\mathsf{Bn} > 2.2$.
The amplitude of the inner core decreases as $\Delta P/\mathsf{Bn}$ increases. When $\Delta P/\mathsf{Bn} \gg 1$ (Fig. 14), the inner core approximately disappears and the system becomes almost purely viscous. In the same way, we observe that when $\Delta P/\mathsf{Bn}$ is close to 2.2 then $\sigma \to h$ (Fig. 11) and the viscous part tends to disappear. Also in this case we speak of a limit, since condition (62) must be fulfilled.

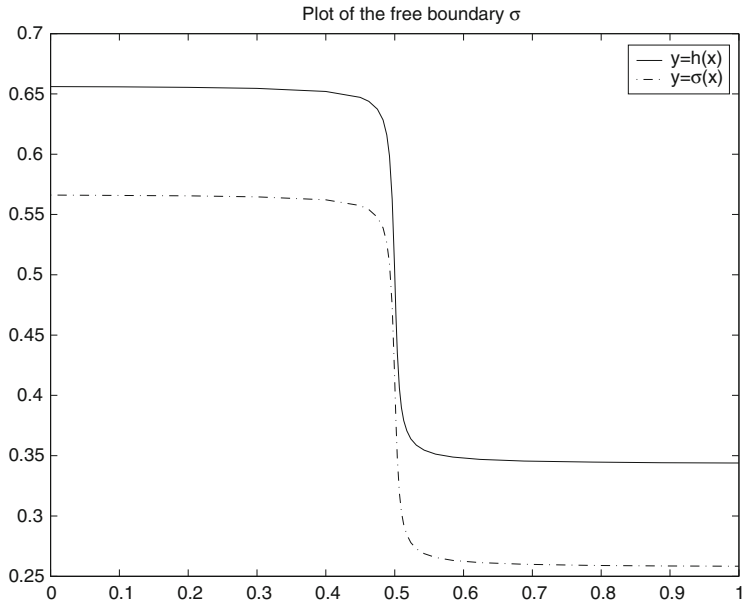

Fig. 11 Plot of the free boundary (dashed line) $y = \sigma(x)$ with $\Delta P/\mathsf{Bn} = 2.5$ and with condition (62) fulfilled

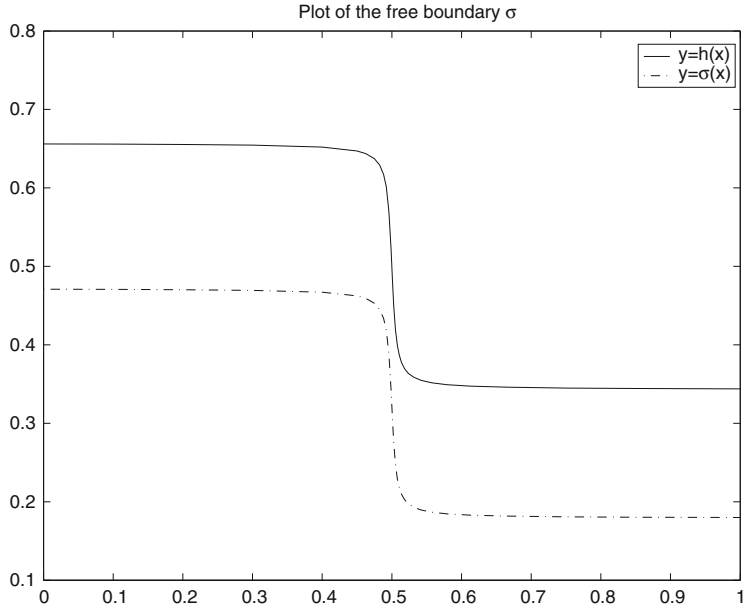

Fig. 12 Plot of the free boundary (dashed line) $y = \sigma(x)$ with $\Delta P/\mathsf{Bn} = 3.5$ and with condition (62) fulfilled

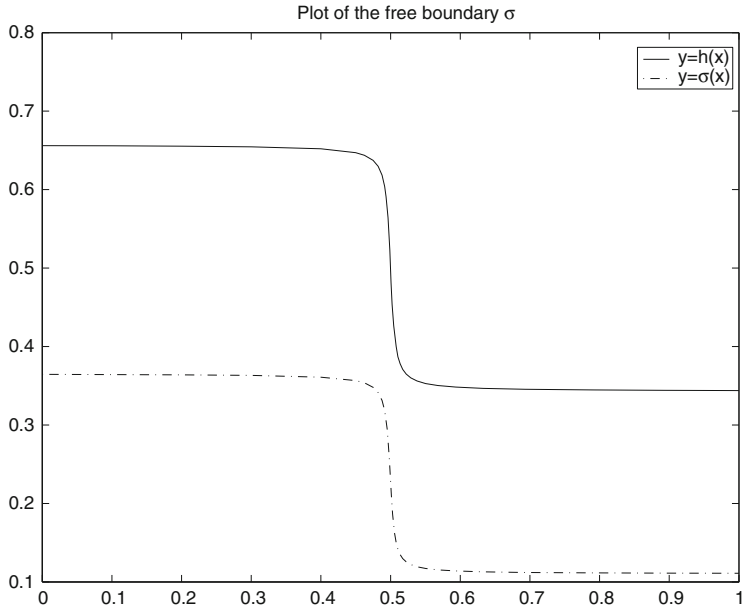

Fig. 13 Plot of the free boundary (dashed line) $y = \sigma(x)$ with $\Delta P/\mathsf{Bn} = 5.5$ and with condition (62) fulfilled

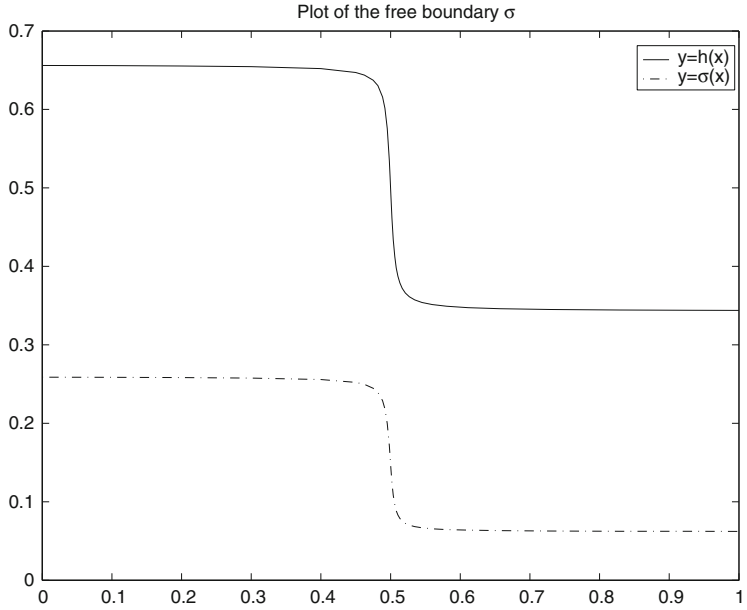

Fig. 14 Plot of the free boundary (dashed line) $y = \sigma(x)$ with $\Delta P/\mathsf{Bn} = 9.5$ and with condition (62) fulfilled

5 Two Dimensional Channel Flow: A New Approach

To model the flow of a Bingham fluid one considers the balance of linear momentum written in the differential form

$$\rho \frac{D\mathbf{v}}{Dt} = -\nabla P + \nabla \cdot \mathbf{S}, \tag{63}$$

where ρ is density, $\mathbf{v}$ is velocity, P is pressure and $\mathbf{S}$ is the deviatoric part of the stress. Equation (63) is typically used in the whole domain, assuming that the velocity and the stress are continuous across the fluid/rigid interface. Within the liquid domain the fluid is assumed to behave as a viscous incompressible fluid, whereas in the rigid part the stress is indetermined. Indeed in the unyielded part we only know that the strain rate vanishes, i.e. $\mathbf{D} = 0$. Assuming that Eq. (63) holds in every part of the domain may lead to paradoxes, as the one that occurs in lubrication regimes, [6, 17].

To avoid this occurrence we propose a novel approach which essentially consists in using a integral formulation for the balance of linear momentum within the unyielded part. We apply this approach to study the flow in a bidimensional channel

of varying amplitude, with the driving force being an applied pressure gradient (Poiseuille flow). We assume that the aspect ratio of the channel is small, so that the lubrication approximation is suitable. In this case, Eq. (63) can be simplified introducing the ratio $\varepsilon \ll 1$ between the length and the maximum amplitude and rescaling the problem in a nondimensional form. The solution can be sought as power series of ε, where the leading order is the one we are interested in. With this procedure one tacitly assumes that the nondimensional variables and their derivatives are $\mathcal{O}(1)$ in the liquid and solid domain. In particular the stress components S_{ij} are assumed to be everywhere $\mathcal{O}(1)$, but this latter hypothesis can be checked "a posteriori" only in the liquid part, since in the rigid domain the stress is not determined.

This point is the central importance for our procedure. Indeed, the assumption $S_{ij} = \mathcal{O}(1)$ and the use of (63) to derive the motion in the rigid part, leads to the well known "lubrication paradox" , which consists in a plug velocity that depends on the longitudinal coordinate. Note that the paradox disappears when one considers a deformable core, as shown in the previous sections. If one does not use Eq. (63) in the unyielded part and write the balance of linear momentum using an integral global approach similar to the one presented in [29] and in [28], the paradox is no longer present. Therefore, the unyielded part is treated as an evolving non material volume Ω_t and its dynamics is modelled writing the balance of linear momentum as

$$\int_{\Omega_t} \frac{\partial}{\partial t} (\rho \mathbf{v})\, dV + \int_{\partial \Omega_t} \rho \mathbf{v}\, (\mathbf{v} \cdot \mathbf{n})\, dS = \int_{\partial \Omega_t} (\mathbf{T}\mathbf{n}) dS, \tag{64}$$

where $\mathbf{T} = -P\mathbf{I} + \mathbf{S}$, is the Cauchy stress tensor and $\mathbf{w}$ the velocity of the boundary $\partial \Omega_t$. The advantage of this approach lies in the fact that the knowledge of the stress inside the rigid part is no longer needed and no guess has to be made on the order of magnitude of the stress components. Only the stress acting on the boundary of Ω_t is required.

Therefore we need to know: (1) the forces acting on the yield surface σ (see Fig. 15); (2) the forces acting on the inlet and outlet of the channel. On σ the viscous stress is given once the problem in the viscous domain is solved. On the channel inlet and outlet the applied pressure, assumed to be a given datum of the problem, is required.

When dealing with the leading order approximation in the channel flow, Eq. (64) becomes an integro-differential equation for the pressure P, whose solution allows to determine explicit expressions for the velocity field $\mathbf{v}$ and the yield surface σ. We prove that the longitudinal velocity is spatially uniform, while the transversal velocity vanishes (no paradox). We also show that these results can be also extended to the case of fluids with constant density and pressure dependent viscosity.

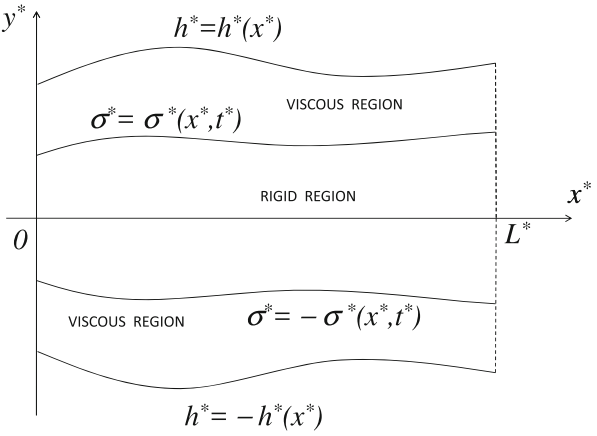

Fig. 15 Sketch of the domain of the problem

5.1 The Physical Model

Let us consider the flow of an incompressible Bingham fluid in a channel of length L and amplitude $2h\,(x)$. Because of symmetry, we may limit our analysis to the upper part of the layer $[0, h(x)]$. The velocity field is given by

$$\mathbf{v} = v_1(x, y, t)\mathbf{i} + v_2(x, y, t)\mathbf{j},$$

The Cauchy stress is $\mathbf{T} = -P\mathbf{I}+\mathbf{S}$, where the deviatoric part is the one of a Bingham fluid

$$\mathbf{S} = \left(2\mu + \frac{\tau_o}{II_{\mathbf{D}}}\right)\mathbf{D}. \tag{65}$$

In the above μ is the viscosity, τ_o is the yield stress. If $\mathbf{D} \neq 0$ we get

$$II_{\mathbf{S}} = 2\mu II_{\mathbf{D}} + \tau_o$$

which holds with $II_{\mathbf{S}} \geq \tau_o$. Therefore, whenever $\mathbf{D} = 0$, we have $II_{\mathbf{S}} \leq \tau_o$ and the stress is not determined. We assume that the viscous and the rigid regions are separated by a sharp interface $y = \pm\sigma\,(x, t)$. Assuming incompressibility we write

$$\text{tr}\,\mathbf{D} = \frac{\partial v_1}{\partial x} + \frac{\partial v_2}{\partial y} = 0. \tag{66}$$

5.2 The Viscous Domain

We write the governing equations in the viscous region neglecting body forces. These are the incompressibility condition (66) and

$$\rho\left(\frac{\partial v_1}{\partial t}+v_1\frac{\partial v_1}{\partial x}+v_2\frac{\partial v_1}{\partial y}\right)=-\frac{\partial P}{\partial x}+\frac{\partial S_{11}}{\partial x}+\frac{\partial S_{12}}{\partial y}, \tag{67}$$

$$\rho\left(\frac{\partial v_2}{\partial t}+v_1\frac{\partial v_2}{\partial x}+v_2\frac{\partial v_2^*}{\partial y}\right)=-\frac{\partial P}{\partial y}+\frac{\partial S_{12}}{\partial x}+\frac{\partial S_{22}}{\partial y}, \tag{68}$$

5.3 The Rigid Domain

The rigid domain Ω_t at some time $t>0$ is given by

$$\Omega_t=\{(x,y):\quad x\in[0,L],\quad y\in[-\sigma,\sigma]\}.$$

The integral momentum balance for the whole domain Ω_t in the absence of body forces is given by (64). Focussing on the upper part of the domain ($y>0$) we find that (64) can be rewritten as

$$2\frac{\partial}{\partial t}(\rho\mathbf{v})\int_0^L\sigma(x,t)dx+2\rho\mathbf{v}\int_0^L\frac{\partial\sigma}{\partial t}(x,t)dx=\int_{\partial\Omega_t}\mathbf{Tn}\,dS.$$

The external forces acting on the boundary $\partial\Omega_t$ are expressed by the surface integral on the r.h.s. Assuming that P_{in}, P_{out} are the (uniform) pressures acting on the inlet and outlet of the channel, we find

$$\begin{aligned}\int_{\partial\Omega_t}(\mathbf{Tn})dS=2\int_0^L\begin{bmatrix}(-\sigma_xT_{11}+T_{12})_\sigma\\ \\ 0\end{bmatrix}dx\\ +2\int_0^{\sigma_{out}}\begin{pmatrix}-P_{out}\\ \\ 0\end{pmatrix}dy+2\int_0^{\sigma_{in}}\begin{pmatrix}P_{in}\\ \\ 0\end{pmatrix}dy,\end{aligned}$$

where $\sigma_{in}=\sigma(0,t)$, $\sigma_{out}=\sigma(L,t)$. Recalling that in the rigid plug velocity is

$$\begin{cases}v_1=k_1(t),\\ \\ v_2=k_2(t)=0\quad(\text{by symmetry}),\end{cases} \tag{69}$$

the dynamics of the whole rigid region is expressed only by the first component of (64), that is

$$\int_0^L \frac{\partial}{\partial t}\left(\rho k_1 \sigma\right) dx = \int_0^L \left[-\sigma_x T_{11} + T_{12}\right]_\sigma \, dx + P_{in}\sigma_{in} - P_{out}\sigma_{out}, \tag{70}$$

Hence the prescribed pressure difference driving the flow is

$$\Delta P = P_{in} - P_{out}. \tag{71}$$

The boundary condition on the channel wall is

$$\mathbf{v}(x, h, t) = 0 \tag{72}$$

i.e. the no-slip condition. On σ we impose

$$\left[\!\left[\mathbf{v}\cdot\mathbf{t}\right]\!\right]_{y=\sigma} = 0, \qquad \left[\!\left[\mathbf{v}\cdot\mathbf{n}\right]\!\right]_{y=\sigma} = 0, \tag{73}$$

$$\left[\!\left[\mathbf{T}\mathbf{n}\cdot\mathbf{t}\right]\!\right]_{y=\sigma} = 0, \qquad \left[\!\left[\mathbf{T}\mathbf{n}\cdot\mathbf{n}\right]\!\right]_{y=\sigma} = 0, \tag{74}$$

which express the continuity of the velocity and of the stress across the yield surface $y = \sigma$ ($\mathbf{t}$ and $\mathbf{n}$ are the tangent and normal unit vector to σ).

Remark 6 In Sect. 5.10 we will extend our model the case in which the viscosity depends on pressure, namely $\mu = \mu\mu\,(P)$.

5.4 Scaling

Set

$$H = \sup_{x\in[0,L]} h(x),$$

and introduce

$$\varepsilon = \frac{H}{L} \ll 1,$$

which is crucial for applying the classical thin film approach. We rescale the problem using the following non dimensional variables

$$\tilde{x} = \frac{x}{L}, \qquad \tilde{y} = \frac{y}{\varepsilon L}, \qquad \tilde{\sigma} = \frac{\sigma}{\varepsilon L}, \qquad \tilde{h} = \frac{h}{\varepsilon L}, \qquad \tilde{t} = \frac{t}{(L/U)},$$

$$\tilde{v}_1 = \frac{v_1}{U}, \quad v_2 = \frac{v_2}{\varepsilon U}, \quad \tilde{P} = \frac{P - P_{out}}{P_c}, \quad \Delta\tilde{P} = \frac{\Delta P}{P_c}, \tag{75}$$

$$\tilde{\mathbf{S}} = \frac{\mathbf{S}}{(\mu U/H)}, \quad \tilde{\mathbf{D}} = \frac{\mathbf{D}}{(U/H)}, \quad \tilde{II}_D = \frac{II_D}{(U/H)}, \quad \tilde{II}_S = \frac{II_S}{(\mu U/H)},$$

where we select the reference pressure using the Poiseuille formula

$$P_c = \frac{\mu L U}{H^2} \tag{76}$$

After some algebra (and neglecting the tildas) we find

$$\mathbf{S} = \left(2 + \frac{\mathsf{Bn}}{II_D}\right)\mathbf{D},$$

where

$$\mathsf{Bn} = \frac{\tau_o H}{\mu U}$$

is the Bingham number. Moreover

$$II_D = \sqrt{\varepsilon^2\left(\frac{\partial v_1}{\partial x}\right)^2 + \frac{1}{4}\left(\frac{\partial v_1}{\partial y} + \varepsilon^2\frac{\partial v_2}{\partial x}\right)^2}.$$

Equations (66)–(68) become

$$\frac{\partial v_1}{\partial x} + \frac{\partial v_2}{\partial y} = 0, \tag{77}$$

$$\varepsilon\mathsf{Re}\left(\frac{\partial v_1}{\partial t} + v_1\frac{\partial v_1}{\partial x} + v_2\frac{\partial v_1}{\partial y}\right) = -\frac{\partial P}{\partial x} + \varepsilon\frac{\partial S_{11}}{\partial x} + \frac{\partial S_{12}}{\partial y}, \tag{78}$$

$$\varepsilon^3\mathsf{Re}\left(\frac{\partial v_2}{\partial t} + v_1\frac{\partial v_2}{\partial x} + v_2\frac{\partial v_2}{\partial y}\right) = -\frac{\partial P}{\partial y} + \varepsilon^2\frac{\partial S_{12}}{\partial x} + \varepsilon\frac{\partial S_{22}}{\partial y}, \tag{79}$$

where

$$\mathsf{Re} = \left(\frac{\rho U H}{\mu}\right)$$

is the Reynolds number. The inner core equation (70) becomes

$$\varepsilon\mathsf{Re}\int_0^1 \frac{\partial}{\partial t}(k_1\sigma)dx = \int_0^1 \left[P\sigma_x - \varepsilon\sigma_x S_{11} + S_{12}\right]_{\sigma^+} dx + \Delta P\sigma_{in}. \tag{80}$$

The boundary conditions (72)–(74) become

$$\mathbf{v}(x, h, t) = 0, \tag{81}$$

$$[\![v_1]\!]_{y=\sigma} = [\![v_2]\!]_{y=\sigma} = 0, \tag{82}$$

$$\begin{cases} [\![P]\!]\left[1 + \varepsilon^2\left(\dfrac{\partial\sigma}{\partial x}\right)^2\right]_{y=\sigma} + \left[\varepsilon^3 S_{11}\left(\dfrac{\partial\sigma}{\partial x}\right)^2 - 2\varepsilon^2 S_{12}\left(\dfrac{\partial\sigma}{\partial x}\right) + \varepsilon S_{22}\right]_{y=\sigma} = 0, \\ [\![S_{12}]\!]_{y=\sigma} + \varepsilon\left(\dfrac{\partial\sigma}{\partial x}\right)\left[S_{22} - S_{11} - \varepsilon S_{12}\dfrac{\partial\sigma}{\partial x}\right]_{y=\sigma} = 0. \end{cases} \tag{83}$$

In the rigid domain the non dimensional velocity field is

$$\begin{cases} v_1 = k_1(t), \\ v_2 = 0, \end{cases} \tag{84}$$

with $k_1 = k_1/U$.

5.5 The Leading Order Approximation

We look for a solution in which the main variables of the problem can be expressed as power series of ε

$$\mathbf{v} = \sum_{j=0}^{\infty} \mathbf{v}^{(j)}\varepsilon^j \qquad P = \sum_{j=0}^{\infty} P^{(j)}\varepsilon^j \qquad \sigma = \sum_{j=0}^{\infty} \sigma^{(j)}\varepsilon^j$$

We further assume that $h(x)$ is such that

$$\frac{\partial h}{\partial x} = O(1)$$

and we limit our analysis to the leading order, assuming that $\mathsf{Bi} = \mathscr{O}(1)$ and $\mathsf{Re} \leqslant \mathscr{O}(1)$. We begin by observing that

$$S_{12}^{(0)} = \left[1 + \frac{\mathsf{Bn}}{|v_{1y}^{(0)}|}\right] v_{1y}^{(0)},$$

and, since we are looking for a solution with $v_{1y}^{(0)} < 0$ in the upper part of the channel, we write

$$S_{12}^{(0)} = v_{1y}^{(0)} - \mathsf{Bn}.$$

The problem reduces to

$$\begin{cases} \dfrac{\partial v_1^{(0)}}{\partial x} + \dfrac{\partial v_2^{(0)}}{\partial y} = 0, \\ -\dfrac{\partial P^{(0)}}{\partial x} + \dfrac{\partial}{\partial y}\left(\dfrac{\partial v_1^{(0)}}{\partial y}\right) = 0, \\ -\dfrac{\partial P^{(0)}}{\partial y} = 0, \end{cases} \tag{85}$$

with boundary conditions

$$\begin{cases} \left.\dfrac{\partial v_1^{(0)}}{\partial y}\right|_{y=\sigma^{(0)}} = 0, \\ v_1^{(0)}(x,h,t) = 0. \end{cases} \tag{86}$$

Integrating we find

$$v_1^{(0)} = -P_x^{(0)} \frac{(h-y)(y-2\sigma^{(0)}+h)}{6}. \tag{87}$$

Exploiting the continuity equation we get

$$v_2^{(0)} = -\frac{\partial}{\partial x}\left[P_x^{(0)} \frac{(y-h)^2(y-3\sigma^{(0)}+2h)}{6}\right]. \tag{88}$$

Evaluating the velocity components on the yield surface we get

$$\left.v_1^{(0)}\right|_{y=\sigma^{(0)}} = k_1^{(0)}(t) = -P_x^{(0)} \frac{(h-\sigma^{(0)})^2}{2}, \tag{89}$$

$$\left.v_2^{(0)}\right|_{y=\sigma^{(0)}} = \frac{\partial}{\partial x}\left[-P_x^{(0)} \frac{(h-\sigma^{(0)})^3}{3}\right] - \sigma_x^{(0)} P_x^{(0)} \frac{(h-\sigma^{(0)})^2}{2} = 0,$$

which entails

$$\underbrace{\left(-P_x^{(0)}\frac{(h-\sigma^{(0)})^2}{2}\right)}_{k_1^{(0)}}\cdot\frac{\partial}{\partial x}\left[\frac{2}{3}(h-\sigma^{(0)})\right]=-\sigma_x^{(0)}\underbrace{\left(-P_x^{(0)}\frac{(h-\sigma^{(0)})^2}{2}\right)}_{k_1^{(0)}}.$$

Supposing $k_1^{(0)}\neq 0$, we find

$$\sigma^{(0)}(x,t)=-2h(x)-C, \tag{90}$$

where C is unknown. Let us now consider the rigid core equation (80) at the zero order

$$\int_0^1 P^{(0)}\sigma_x^{(0)}dx-\mathsf{Bn}+\Delta P\sigma_{in}^{(0)}=0,$$

which, after an integration by parts, reduces to

$$-\int_0^1 P_x^{(0)}\sigma^{(0)}dx=\mathsf{Bn}. \tag{91}$$

Substituting (90) into (91), we obtain

$$C=\frac{2\int_0^1 P_x^{(0)}hdx-\mathsf{Bn}}{\Delta P}.$$

We thus have

$$\sigma^{(0)}=-2h(x)+\frac{\mathsf{Bi}-2\int_0^1 P_x^{(0)}h\,dx}{\Delta P}, \tag{92}$$

or equivalently

$$\sigma^{(0)}=2(h_{in}-h(x))+\frac{\mathsf{Bi}}{\Delta P}+\frac{2}{\Delta P}\int_0^1 P^{(0)}h_x dx, \tag{93}$$

where $h_{in}=h(0)$. Defining the viscous region width as

$$\ell^{(0)}=h(x)-\sigma^{(0)}(x,t), \tag{94}$$

formula (92) entails

$$\ell^{(0)} = 3h\,(x) + \frac{2\int_0^1 P_x^{(0)} h\,dx - \mathsf{Bn}}{\Delta P}. \tag{95}$$

Hence

$$k_1^{(0)} = -P_x^{(0)} \frac{\ell^{(0)2}}{2}. \tag{96}$$

Now, differentiating (96) with respect to x, we obtain

$$P_{xx}^{(0)} + 6\frac{h_x}{\ell^{(0)}} P_x^{(0)} = 0,$$

that is the integro-differential equation

$$P_{xx}^{(0)} + \frac{6h_x}{\left[3h + \dfrac{2\int_0^1 P_x^{(0)} h\,dx - \mathsf{Bn}}{\Delta P\,(t)}\right]} P_x^{(0)} = 0. \tag{97}$$

The boundary conditions are $P^{(0)}\big|_{x=0} = \Delta P$, and $P^{(0)}\big|_{x=1} = 0$. The solution $P^{(0)}$ of (97) is then used to evaluate the $v_1^{(0)}$ via (87), $v_2^{(0)}$ via (88) and the yield surface $\sigma^{(0)}$ via (93).

Remark 7 From (92) we observe that $\sigma_x^{(0)} = -2h_x$, meaning that the amplitude of the rigid core becomes larger as the channel narrows, whereas it shrinks as the channel becomes wider. This is in accordance with what found in [21].

5.6 Flow Condition

Let us investigate the conditions on ΔP that prevent the system from coming to a halt. Let $h\,(x) \equiv h_{in}$. From (93) we get:

- $\Delta P > \dfrac{\mathsf{Bn}}{h_{in}}, \Longrightarrow \sigma^{(0)} < h_{in}$ (the fluid is flowing)
- $\Delta P < \dfrac{\mathsf{Bn}}{h_{in}}, \Longrightarrow \sigma^{(0)} > h_{in}$ (no flow)

When $h(x)$ is not uniform we have to ensure that $\sigma^{(0)} < h(x)$, in order to prevent the flow from stopping. Recalling (95) we must impose

$$\ell^{(0)} \geq 3h_{min} - 2h_{in} - \frac{\mathsf{Bn}}{\Delta P} - \frac{2}{\Delta P}\int_0^1 P^{(0)} h_x dx, \tag{98}$$

where $h_{\min} = \min_{x\in[0,1]} h$. To estimate the integral in the r.h.s. we remark that $P^{(0)}$ fulfils Eq. (97), that is an equation of elliptic type. Maximum principle entails $0 \leq P^{(0)} \leq \Delta P$. So, writing

$$\int_0^1 P^{(0)} h_x dx = \underbrace{\int_{\{h_x\leq 0\}} P^{(0)} h_x dx}_{\leq 0} + \underbrace{\int_{\{h_x\geq 0\}} P^{(0)} h_x dx}_{\geq 0},$$

we have

$$\Delta P \min\left\{\underline{h}_x; 0\right\} \leq \Delta P \max\left\{\overline{h}_x; 0\right\},$$

where

$$\underline{h}_x = \min_{x\in[0,1]} h_x(x), \quad \text{and} \quad \overline{h}_x = \min_{x\in[0,1]} h_x(x).$$

In conclusion

$$2\min\left\{\underline{h}_x; 0\right\} \leq \frac{2}{\Delta P}\int_0^1 P^{(0)} h_x dx \leq 2\max\left\{\overline{h}_x; 0\right\}. \tag{99}$$

Therefore, recalling (98), we have

$$\begin{aligned}\ell^{(0)} &\geq 3h_{\min} - 2h_{in} - \frac{\mathsf{Bn}}{\Delta P} - \frac{2}{\Delta P}\int_0^1 P^{(0)} h_x dx \\ &\geq 3h_{\min} - 2\max\left\{\overline{h}_x; 0\right\} - 2h_{in} - \frac{\mathsf{Bn}}{\Delta P},\end{aligned} \tag{100}$$

If we assume

$$\left(3h_{\min} - 2\max\left\{\overline{h}_x; 0\right\} - 2h_{in}\right) > 0$$

and require that

$$3h_{\min} - 2\max\left\{\overline{h}_x; 0\right\} - 2h_{in} - \frac{\mathsf{Bi}}{\Delta P} > 0,$$

which implies

$$\Delta P > \frac{\mathsf{Bn}}{3h_{\min} - 2\max\left\{\overline{h}_x; 0\right\} - 2h_{in}}, \tag{101}$$

we are sure that the flow never comes to a stop.

Example 2 If we consider a linear wall profile

$$h = h_{in} + \underbrace{(h_{out} - h_{in})}_{\Delta h} x,$$

where $h_{out} > 0$, there are two possibilities:

- $\Delta h > 0, \Rightarrow h_{\min} = h_{in}$, and $\max\left\{\overline{h}_x; 0\right\} = \Delta h$. Condition (101) yields

$$\frac{\mathsf{Bn}}{\Delta P} < \underbrace{h_{in} - 2\Delta h}_{2h_{out} - 3h_{in}}, \quad \Leftrightarrow \quad \Delta P > \frac{\mathsf{Bn}}{2h_{out} - 3h_{in}},$$

  where, of course, we assume $2h_{out} - 3h_{in} > 0$
- $\Delta h < 0, \Rightarrow h_{\min} = h_{out}$, and $\max\left\{\overline{h}_x; 0\right\} = 0$. Inequality (101) entails

$$\frac{\mathsf{Bn}}{\Delta P} < \underbrace{2\Delta h + h_{out}}_{3h_{out} - 2h_{in}}, \quad \Leftrightarrow \quad \Delta P > \frac{\mathsf{Bn}}{3h_{out} - 2h_{in}},$$

  where now we require $3h_{out} - 2h_{in} > 0$.

5.7 Inner Core Appearance or Disappearance

A non uniform channel profile may cause the appearance/disappearance of the rigid plug. These phenomena (highlighted also in [6] and [21]) are not possible when the channel profile is uniform, namely when $h(x) \equiv h_{in}$. Recalling (93), we set

$$\sigma^{(0)} = \max\left\{0;\ 2(h_{in} - h) + \frac{\mathsf{Bn}}{\Delta P} + \frac{2}{\Delta P}\int_0^1 P^{(0)} h_x dx\right\},$$

in order to avoid physical inconsistencies. Hence, $\sigma^{(0)}$ vanishes when

$$h \geq h_{in} + \frac{\mathsf{Bn}}{2\Delta P} + \frac{1}{\Delta P}\int_0^1 P^{(0)} h_x dx. \tag{102}$$

The r.h.s. of (102) is a critical value, that we denote as h_{crt}, such that, whenever $h \geq h_{crt}$ the core disappears.

Example 3 Let us consider the channel profile

$$h(x) = \frac{\arctan\left[5\left(\frac{1}{2} - x\right)\right]}{4\arctan\left(\frac{5}{2}\right)} + \frac{3}{4}. \tag{103}$$

depicted with the dashed line in Fig. 20. We now estimate h_{crt} exploiting (102), when $\Delta P = 10$, and $\mathsf{Bi} = 5$,

$$\begin{aligned} h(x) &\geq 1 + \frac{\mathsf{Bn}}{2\Delta P} - \frac{1}{\Delta P}\int_0^1 P^{(0)}\,|h_x|\,dx \\ &\geq 1 + \frac{\mathsf{Bn}}{2\Delta P} - \|h_x\|_{L^2} \geq 1 + \frac{\mathsf{Bn}}{2\Delta P} - 0.58 \approx 0.67. \end{aligned}$$

The core-free region is thus obtained solving $h \geq h_{crt}$, which we approximate with $h \geq 0.67$, whose solution is the interval $1 \leq x \leq 0.58$. Looking at Fig. 20 the actual core-free region is $1 \leq x \leq 0.55$, which substantially agrees with the above estimate.

5.8 Solution for an Almost Flat Channel

When $h(x) \equiv h_{in}$ (i.e. uniform channel) equation (93) gives

$$\sigma^{(0)} = \frac{\mathsf{Bn}}{\Delta P}. \tag{104}$$

Equation (97) yields

$$P^{(0)} = (1 - x)\,\Delta P.$$

The velocity field becomes[7]

$$\begin{cases} v_1^{(0)} = -\Delta P\left[\dfrac{(y - \sigma^{(0)})^2}{2} - \dfrac{(1 - \sigma^{(0)})^2}{2}\right], \\ \\ v_2^{(0)} = 0, \end{cases} \tag{105}$$

[7] We set, for the sake of simplicity, $h_{in} = 1$.

and we also find

$$k_1^{(0)} = \frac{\Delta P}{2}(1-\sigma^{(0)})^2.$$

Let us now consider a non-uniform channel profile $h(x)$, assuming that amplitude width variation is small. We thus set

$$h(x) = \langle h \rangle + \phi(x), \tag{106}$$

where $\langle h \rangle$ denotes the spatial average along the channel, i.e.

$$\langle h \rangle = \int_0^1 h(x)\, dx$$

and assume that $\max|\phi(x)|$ is small, that is we consider an almost flat channel. We look for $P^{(0)}$ in the form

$$P^{(0)} = (1-x)\,\Delta P + \Pi, \tag{107}$$

where $\Pi|_{x=0} = \Pi|_{x=1} = 0$, and where we expect that both $\max|\Pi|$, $\max|\Pi_x|$ are small. Inserting (107) into (92) we obtain

$$\sigma^{(0)} = \frac{\mathsf{Bn}}{\Delta P} - 2\phi(x) - \frac{2}{\Delta P}\int_0^1 \Pi_x \phi\, dx \approx \frac{\mathsf{Bn}}{\Delta P} - 2\phi(x). \tag{108}$$

Concerning $\ell^{(0)}$ we have

$$\ell^{(0)}(x,t) \approx \langle h \rangle - \frac{\mathsf{Bn}}{\Delta P(t)} + 3\phi(x). \tag{109}$$

Exploiting then (97) we compute the pressure field solving

$$\Pi_{xx} + \frac{6\phi_x}{\ell^{(0)}}(-\Delta P + \Pi_x) = 0.$$

Neglecting $\phi_x \Pi_x$ we end up with the following problem

$$\begin{cases} \Pi_{xx} - 2\Delta P\left[\dfrac{\phi_x}{\phi + \mathscr{A}}\right] = 0, \quad \text{where} \quad \mathscr{A} = \dfrac{< h >}{3} - \dfrac{\mathsf{Bn}}{3\Delta P}, \\ \\ \Pi|_{x=0} = \Pi|_{x=1} = 0, \end{cases}$$

so that

$$\Pi_x = (const) + 2\Delta P \ln\left[1 + \frac{\phi\,(x)}{\mathscr{A}}\right] \approx (const) + 2\Delta P \frac{\phi\,(x)}{\mathscr{A}}.$$

In conclusion

$$\Pi = \frac{2\Delta P\,(t)}{\mathscr{A}} \int_0^x \phi(x^{'}) dx^{'},$$

which yields

$$P^{(0)} = \Delta P\,(1-x) + \frac{6\Delta P^2}{\langle h\rangle\,\Delta P - \mathsf{Bn}} \int_0^x \phi\left(x'\right) dx'. \tag{110}$$

Example 4 Let us consider $h\,(x) = 1 + mx$, with m small. We write

$$h\,(x) = \underbrace{1 + \frac{m}{2}}_{\langle h\rangle} + \underbrace{m\left(x - \frac{1}{2}\right)}_{\phi(x)}.$$

In this case

$$\sigma^{(0)} = \frac{\mathsf{Bn}}{\Delta P} - 2m\left(x - \frac{1}{2}\right),$$

and

$$P^{(0)} = \Delta P\,(1-x) + \frac{3m\Delta P^2}{\langle h\rangle\,\Delta P - \mathsf{Bn}} x\,(x-1)\,.$$

We see that $\sigma_x^{(0)} = -2m$, i.e. the core amplitude widens for $m < 0$ and shrinks for $m > 0$.

Example 5 Let us consider a wavy channel

$$h(x) = 1 - \theta \cos\left[2\pi\delta\left(x - \frac{1}{2}\right)\right], \tag{111}$$

where $\delta > 0$, and $\theta \ll 1$. We write

$$h\,(x) = \underbrace{\left[1 - \frac{\theta}{\pi\,\delta}\sin\left(\pi\,\delta\right)\right]}_{\langle h\rangle} + \underbrace{\theta\left[\frac{\sin\left(\pi\,\delta\right)}{\pi\,\delta} - \cos\left(2\pi\,\delta\left(x - \frac{1}{2}\right)\right)\right]}_{\phi(x)},$$

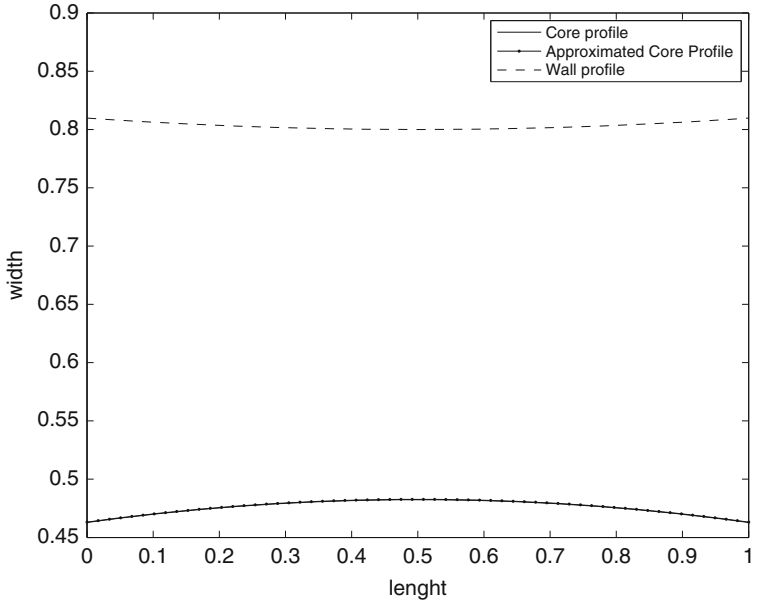

Fig. 16 The channel profile $h(x)$ is (111) and of $\sigma^{(0)}$ given by (92), (112), with $\mathsf{Bn} = 5$, $\Delta P = 10.5$, $\delta = 0.2$, $\theta = 0.1$

with $\max|\phi| = \mathscr{O}(\theta) \ll 1$. Exploiting (108) we obtain

$$\sigma^{(0)} \approx \frac{\mathsf{Bn}}{\Delta P} - 2\theta\left[\frac{\sin(\pi\delta)}{\pi\delta} - \cos\left(2\pi\delta\left(x - \frac{1}{2}\right)\right)\right], \tag{112}$$

The behavior for $\theta = 0.1$, and $\delta = 1/5$ is shown in Figs. 16 and 17. In particular in Fig. 17 a close-up showing the difference between the approximated solution (112) and the computed one (see next section) is displayed.

5.9 Numerical Simulations

Setting $F = P_x^{(0)}$, the elliptic problem (97) can be transformed in the following integral equation

$$F = -\Delta P \frac{\exp\left\{-\int_0^x \frac{6h_{x'}}{\ell_F}dx'\right\}}{\int_0^1 \exp\left\{-\int_0^x \frac{6h_{x'}}{\ell_F}dx'\right\}dx}, \tag{113}$$

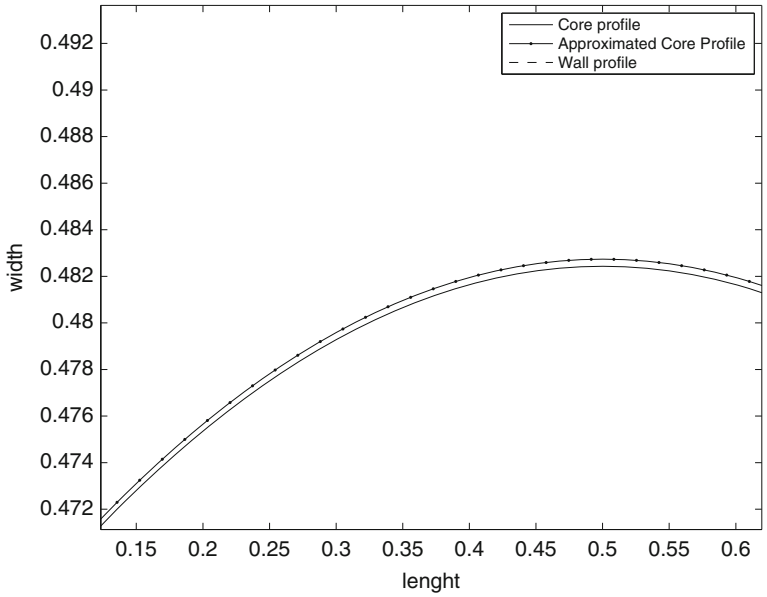

Fig. 17 Close up for the difference between $\sigma^{(0)}$ given by (112) and $\sigma^{(0)}$ given by (92)

where, recalling (95),

$$\ell_F = \min\left\{ h(x)\,,\ 3h(x) + \frac{2\int_0^1 Fh\,dx - \mathsf{Bn}}{\Delta P} \right\}.$$

Now, if the conditions ensuring that $\ell^{(0)}$ is strictly positive (Sect. 5.6) are fulfilled, we can solve (113) through the following iterative procedure:

Step $j = 0$. Set $F_0 = -\Delta P$, and $\ell_{F,\,0} = \min\left\{ h(x)\,,\ 3h(x) - \dfrac{\mathsf{Bn}}{\Delta P} - 2\int_0^1 h\,dx \right\}$.

Step $j = 1$. $F_1 = -\Delta P \dfrac{\exp\left\{ -\displaystyle\int_0^x \frac{6h_{x'}}{\ell_{F,\,0}} dx' \right\}}{\displaystyle\int_0^1 \exp\left\{ -\int_0^x \frac{6h_{x'}}{\ell_{F,\,0}} dx' \right\} dx}$.

.....

Step $j > 1$. $F_j = -\Delta P \dfrac{\exp\left\{ -\displaystyle\int_0^x \frac{6h_{x'}}{\ell_{F,\,j-1}} dx' \right\}}{\displaystyle\int_0^1 \exp\left\{ -\int_0^x \frac{6h_{x'}}{\ell_{F,\,j-1}} dx' \right\} dx}$, with

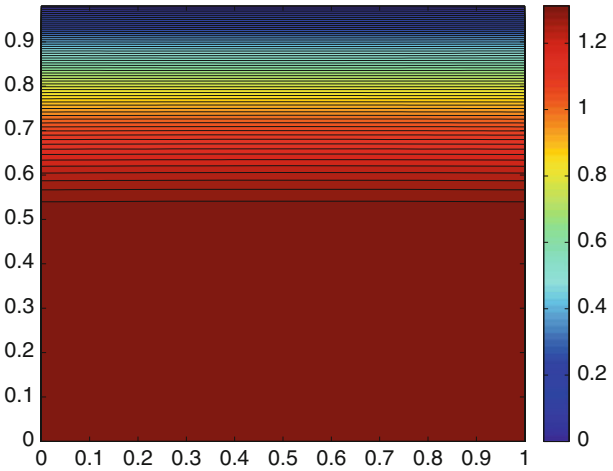

Fig. 18 Plot of x-component of the velocity, h given by (111), $\delta = 0.1$, $\theta = 0.02$, and $\mathsf{Bn} = 5$, $\Delta P = 10.5$

$$\ell_{F,\,j-1} = \min \left\{ h\,(x)\,,\ 3h\,(x) + \frac{2\displaystyle\int_0^1 F_{j-1}\,h\,dx - \mathsf{Bi}}{\Delta P} \right\}.$$

Iterating the procedure until the desired tolerance is reached, we determine the solution $F = P_x^{(0)}$. Integration then provides the pressure field $P^{(0)}$. We can show that, under suitable hypotheses, the solution of (113) exists and is unique.

In Figs. 16, 17 we have plotted $h(x)$ and $\sigma^{(0)}(x)$ for the wavy channel profile given by (111). In Figs. 18, 19 we have reported the contour plots of $v_1^{(0)}$, and $v_2^{(0)}$, when $h(x)$ is given by (111), with $\delta = 0.1$, $\theta = 0.02$, and $\mathsf{Bn} = 5$.
The solid colored regions of Figs. 18 and 19 denote the core, with vanishing transversal velocity and uniform longitudinal velocity. Notice also the symmetry of the transversal velocity shown in Fig. 19. In Figs. 20, 21, 22 we have considered the profile (103). The yield surface $\sigma^{(0)}$ and the velocities $v_1^{(0)}$, $v_2^{(0)}$ are reported respectively.

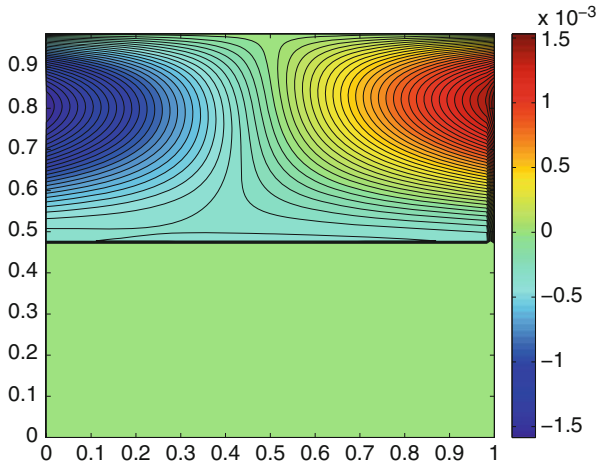

Fig. 19 Plot of y-component of the velocity, h given by (111), $\delta = 0.1$, $\theta = 0.02$, and $\mathsf{Bn} = 5$, $\Delta P = 10.5$

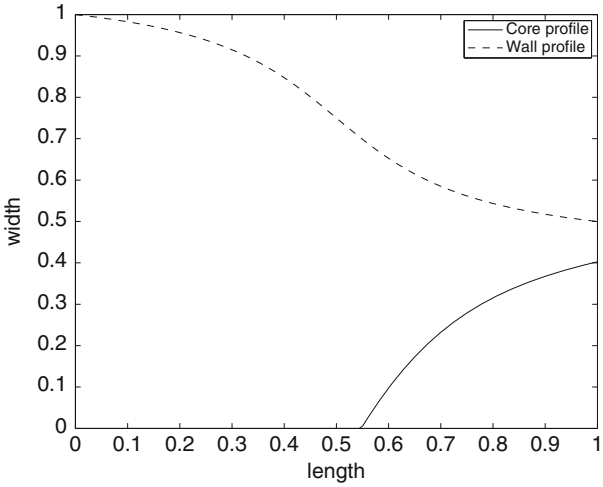

Fig. 20 Plot of $\sigma^{(0)}$ and h, when h is given by (103). $\mathsf{Bn} = 5$, $\Delta P = 10.5$

5.10 Model with Pressure Dependent Viscosity

In this section we extend our model to the case of a pressure-dependent viscosity. Going back to dimensional variables equation (65) rewrites in this way

$$\mathbf{D} = \frac{II_{\mathbf{D}}}{2\mu\,(P)\,II_{\mathbf{D}} + \tau_o}\mathbf{S}.$$

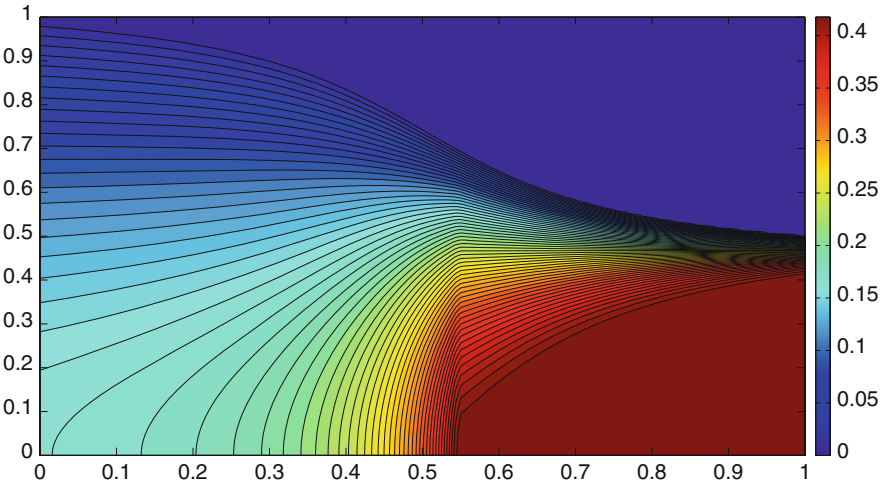

Fig. 21 Plot of x-component of the velocity, h given by (103). $\mathsf{Bn} = 5$, $\Delta P = 10.5$

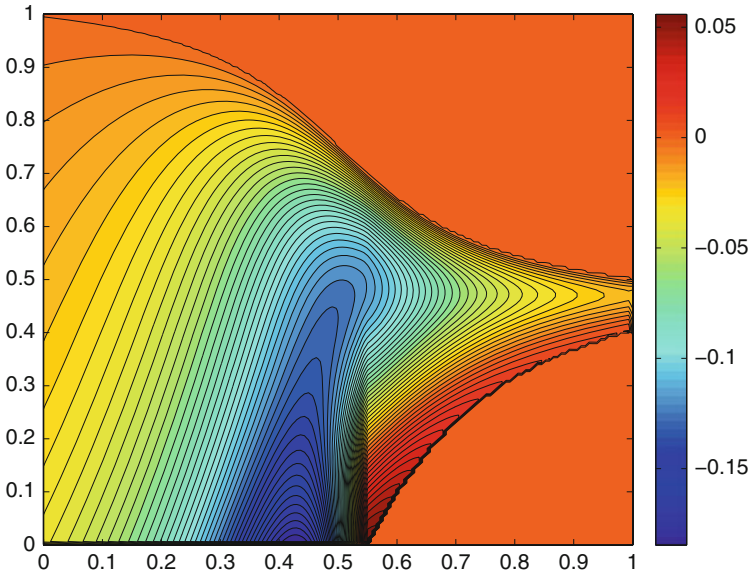

Fig. 22 Plot of y-component of the velocity, h given by (103). $\mathsf{Bn} = 5$, $\Delta P = 10.5$

The viscosity is expanded considering

$$\mu(P) = \mu\Big(P^{(0)} + \varepsilon P^{(1)} + \varepsilon^2 P^{(2)} + \ldots\ldots\Big),$$

so that, around $\varepsilon = 0$, we get $\mu = \mu^{(0)} + \varepsilon\mu^{(1)} + \varepsilon^2\mu^{(2)} + \ldots$, where

$$\mu^{(0)} = \mu(P^{(0)}), \qquad \mu^{(1)} = \frac{d\mu}{dP}(P^{(0)})\, P^{(1)}. \tag{114}$$

Following the same procedure described in Sect. 5.5, the non-dimensional leading order problem becomes

$$\begin{cases} \dfrac{\partial v_1^{(0)}}{\partial x} + \dfrac{\partial v_2^{(0)}}{\partial y} = 0, \\ -\dfrac{\partial P^{(0)}}{\partial x} + \dfrac{\partial}{\partial y}\left(\mu^{(0)}\left(P^{(0)}\right)\dfrac{\partial v_1^{(0)}}{\partial y}\right) = 0, \\ -\dfrac{\partial P^{(0)}}{\partial y} = 0, \end{cases}$$

whose boundary conditions are still given by (86). We get

$$\begin{cases} v_1^{(0)} = \dfrac{P_x^{(0)}}{\mu^{(0)}\left(P^{(0)}\right)}\dfrac{(y-h^{(0)})(y-2\sigma^{(0)}+h^{(0)})}{6}, \\ v_2^{(0)} = \dfrac{\partial}{\partial x}\left[\dfrac{P_x^{(0)}}{\mu^{(0)}\left(P^{(0)}\right)}\dfrac{(y-h^{(0)})^2(y-3\sigma^{(0)}+2h^{(0)})}{6}\right], \end{cases}$$

and

$$k_1^{(0)} = -\frac{P_x^{(0)}}{\mu(P^{(0)})}\frac{(h^{(0)}-\sigma^{(0)})^2}{2}.$$

The interface $\sigma^{(0)}$ is still given by (92), while Eq. (97) modifies in this way

$$\left(\frac{P_x^{(0)}}{\mu(P^{(0)})}\right)_x + 6\frac{h_x}{\ell^{(0)}}\frac{P_x^{(0)}}{\mu(P^{(0)})} = 0, \tag{115}$$

where $\ell^{(0)}$ is given by (95).

Example 6 In case $\mu(P) = e^{\gamma P}$, and $h \equiv 1$, we get

$$\begin{cases} v_1^{(0)} = \dfrac{[e^{-\gamma P_{in}} - e^{-\gamma P_{out}}]}{\gamma} \left[\dfrac{(y - \sigma^{(0)})^2}{2} - \dfrac{(1 - \sigma^{(0)})^2}{2} \right], \\ v_2^{(0)} = 0, \\ \sigma^{(0)} = \dfrac{\mathsf{Bn}}{\Delta P}, \\ P = P_{in} - \dfrac{1}{\gamma} \ln \left[1 + \left(e^{\gamma \Delta P} - 1 \right) x \right]. \end{cases} \tag{116}$$

We now consider $h^{(0)} = 1 + mf(x)$, with m small perturbation. We look for a solution of (115) of the form

$$P^{(0)} = P_{in} - \frac{1}{\gamma} \ln \left[1 + \left(e^{\gamma \Delta P} - 1 \right) x \right] + m\Pi, \tag{117}$$

with $\Pi = 0$ on $x = 0, 1$. After inserting (117) into (115) and neglecting the m^2, we find

$$\Pi = -\frac{6}{\gamma} \frac{\left(e^{\gamma \Delta P} - 1 \right)}{1 + \left(e^{\gamma \Delta P} - 1 \right) x} \left[x \int_0^1 f(\xi) d\xi - \int_0^x f(\xi) d\xi \right],$$

and

$$\sigma^{(0)} = \frac{\mathsf{Bn}}{\Delta P} - m \left[2f(x) - \frac{2}{\gamma \Delta P} \int_0^1 \frac{f(\xi) \left(e^{\gamma \Delta P} - 1 \right)}{1 + \left(e^{\gamma \Delta P} - 1 \right) \xi} d\xi \right].$$

6 Planar Squeeze

We consider the flow of an incompressible Bingham fluid placed between parallel plates of length in a channel of length L. The gap between the plates occupied by the fluid has amplitude $2h(t)$, as depicted in Fig. 23 (see also [19]). Because of symmetry, we confine our analysis to the upper part of the layer, namely $[0, h(t)]$. The velocity field is $\mathbf{v} = u(x, y, t)\mathbf{i} + v(x, y, t)\mathbf{j}$, where x, y are the longitudinal and transversal coordinate respectively.

We assume that the region where $II_{\mathbf{S}} \geq \tau_o$ (yielded) and the region where $II_{\mathbf{S}} \leq \tau_o$ (unyielded) are separated by a sharp interface $y = \pm Y(x, t)$ representing the yield surface. We also define the inner plug

$$\Omega_p = \{(x, y) : \quad x \in [0, L], \quad y \in [-Y, Y]\}.$$

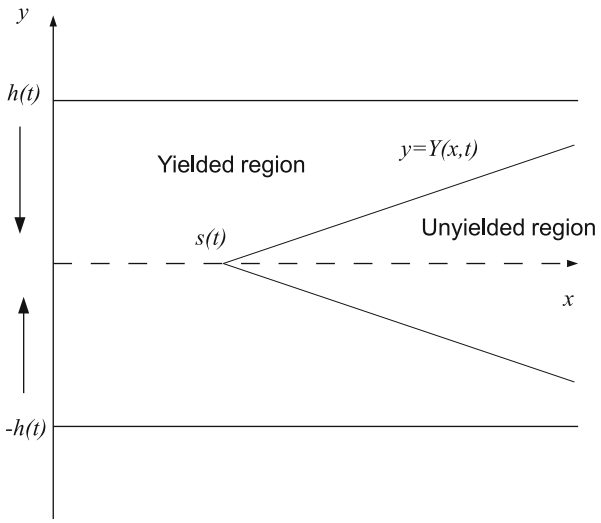

Fig. 23 A schematic representation of the squeezing channel

We may have $Y(x, t) = 0$ for some $x \in (0, L)$ and for some t, so that Ω_p becomes a segment of zero measure. The rigid plug Ω_p moves uniformly with velocity

$$\begin{cases} u = u_p(t), \\ \\ v = 0, \quad \text{(by symmetry)}. \end{cases} \tag{118}$$

Neglecting inertia and body forces, the governing equations in the viscous phase are

$$\text{tr}\mathbf{D} = 0,$$

and

$$-\frac{\partial P}{\partial x} + \frac{\partial S_{11}}{\partial x} + \frac{\partial S_{12}}{\partial y} = 0, \tag{119}$$

$$-\frac{\partial P}{\partial y} + \frac{\partial S_{12}}{\partial x} + \frac{\partial S_{22}}{\partial y} = 0, \tag{120}$$

The integral momentum balance for the domain Ω_p is given by

$$\int_{\Omega_p} \frac{\partial}{\partial t} (\rho \mathbf{v})\, dV + \int_{\partial\Omega_p} \rho \mathbf{v}\, (\mathbf{v} \cdot \mathbf{n})\, dS = \int_{\partial\Omega_p} (\mathbf{Tn}) dS, \tag{121}$$

where ρ is the material density. Neglecting the inertial terms, we get following equation[8]

$$\int_0^L [-Y_x T_{11} + T_{12}]_{Y^+} \, dx + P_{Y_0} Y_0 - P_{Y_1} Y_1 = 0. \tag{122}$$

where P_{Y_o}, P_{Y_1} represent the normal stresses on $x = 0$ and $x = L$. As usual we impose

$$\boldsymbol{v}|_{y=h} \cdot \mathbf{t} = 0, \qquad \left(\mathbf{v}|_{y=h} - \mathbf{w}\right) \cdot \mathbf{n} = 0, \tag{123}$$

where $\mathbf{w} \cdot \mathbf{n}$ is the wall normal velocity and $\mathbf{t}$ is the wall tangent vector. On Y we write

$$[\![\mathbf{v}]\!]_{y=Y} = 0, \tag{124}$$

$$[\![\mathbf{Tn} \cdot \mathbf{t}]\!]_{y=Y} = 0, \qquad [\![\mathbf{Tn} \cdot \mathbf{n}]\!]_{y=Y} = 0, \tag{125}$$

while at $x = 0$

$$\begin{cases} u = 0, \\ \\ S_{12} = 0, \end{cases} \tag{126}$$

6.1 Squeezing Between Parallel Plates

We assume $h = h\,(t)$ and we set

$$H = \max_{t \geq 0} h(t).$$

We define the aspect ratio $\varepsilon = H/L$, assuming $\varepsilon \ll 1$. Then we rescale the problem using the following non dimensional variables

$$\tilde{x} = \frac{x}{L}, \qquad \tilde{y} = \frac{y}{\varepsilon L}, \qquad \tilde{Y} = \frac{Y}{\varepsilon L}, \qquad \tilde{h} = \frac{h}{H}, \qquad \tilde{t} = \frac{t}{T},$$

where T is the characteristic time scale, i.e. the "squeezing time". We define the characteristic transversal velocity as $V = H/T$, and the longitudinal velocity as $U = V/\varepsilon$, so that $u = u/U$, $v = v/V = v^*/(\varepsilon U)$. Pressure is again rescaled

[8]The expression $[-Y_x T_{11} + T_{12}]_{Y^+}$ represents the force exerted by the viscous region on the lateral side of the inner rigid core.

exploiting the Poiseuille formula $P_c = (\mu LU)/H^2$ and we set $P = P/P_c$, $P_{out} = P_{out}/P_c$, where P_{out} is the (given) pressure field applied at the channel outlet. We suppose that P_{out} is constant in time and space. Next we introduce

$$\mathbf{S} = \frac{\mathbf{S}}{(\mu U/H)}, \qquad \mathbf{D} = \frac{\mathbf{D}}{(U/H)}, \qquad \mathit{II}_{\mathbf{D}} = \frac{\mathit{II}_{\mathbf{D}}}{(U/H)}, \qquad \mathit{II}_{\mathbf{S}} = \frac{\mathit{II}_{\mathbf{S}}}{(\mu U/H)},$$

so that

$$\mathbf{S} = \left(2 + \frac{\mathsf{Bn}}{\mathit{II}_D}\right)\mathbf{D},$$

where

$$\mathsf{Bn} = \frac{\tau_o H}{\mu U}$$

is again the Bingham number. The mechanical incompressibility constraint and momentum balance become (neglect the tildas)

$$\frac{\partial u}{\partial x} + \frac{\partial v}{\partial y} = 0, \tag{127}$$

$$-\frac{\partial P}{\partial x} + \varepsilon \frac{\partial S_{11}}{\partial x} + \frac{\partial S_{12}}{\partial y} = 0, \tag{128}$$

$$-\frac{\partial P}{\partial y} + \varepsilon^2 \frac{\partial S_{12}}{\partial x} + \varepsilon \frac{\partial S_{22}}{\partial y} = 0. \tag{129}$$

Equation (122) can be rewritten as

$$\int_0^1 [PY_x - \varepsilon Y_x S_{11} + S_{12}]_{Y^+}\, dx + P_{Y_0} Y_0 - P_{out} Y_1 = 0, \tag{130}$$

where $P_{out} = P_{Y_1}$. Boundary conditions (123) become

$$u|_h = 0, \qquad v|_h = \dot{h}, \tag{131}$$

since the squeezing velocity is

$$\dot{h} = \frac{\partial h}{\partial t} < 0$$

Jump conditions on Y become

$$[\![u]\!]_{y=Y} = [\![v]\!]_{y=Y} = 0, \tag{132}$$

$$\begin{cases} [\![P]\!]\left[1+\varepsilon^2\left(\dfrac{\partial Y}{\partial x}\right)^2\right]_{y=Y} + \left[\varepsilon^3 S_{11}\left(\dfrac{\partial Y}{\partial x}\right)^2 - 2\varepsilon^2 S_{12}\left(\dfrac{\partial Y}{\partial x}\right) + \varepsilon S_{22}\right]_{y=Y} = 0, \\ [\![S_{12}]\!]_{y=Y} + \varepsilon\left(\dfrac{\partial Y}{\partial x}\right)\left[S_{22} - S_{11} - \varepsilon S_{12}\dfrac{\partial Y}{\partial x}\right]_{y=Y} = 0, \end{cases} \tag{133}$$

while conditions (126) become

$$\begin{cases} u = 0, \\ S_{12} = 0. \end{cases} \tag{134}$$

6.2 Problem at the Leading Order

As for the channel, we look for a solution expressed as power series of ε, assuming $\mathsf{Bi} = \mathscr{O}(1)$. We get

$$S_{12}^{(0)} = u_y^{(0)} - \mathsf{Bn}$$

since we are looking for a solution with $u_y^{(0)} < 0$ in the upper part of the channel. Equations (127)–(129) reduces to

$$\begin{cases} \dfrac{\partial u^{(0)}}{\partial x} + \dfrac{\partial v^{(0)}}{\partial y} = 0, \\ -\dfrac{\partial P^{(0)}}{\partial x} + \dfrac{\partial}{\partial y}\left(\dfrac{\partial u^{(0)}}{\partial y}\right) = 0, \\ -\dfrac{\partial P^{(0)}}{\partial y} = 0, \end{cases} \tag{135}$$

with boundary conditions

$$\begin{cases} \left.\dfrac{\partial u^{(0)}}{\partial y}\right|_{y=Y} = 0 \\ u^{(0)}(x, h, t) = 0 \end{cases} \tag{136}$$

For the sake of simplicity we suppress the superscript (0). Since $P = P(x, t)$ we get

$$u = -P_x \frac{(h-y)(y-2Y+h)}{2}. \tag{137}$$

Moreover exploiting mass conservation

$$\dot{h} - v(y,t) = \int_y^h \frac{\partial}{\partial x}\left[P_x \frac{(h-y')(y'-2Y+h)}{2}\right] dy'.$$

Evaluating u, v on Y and recalling conditions (132), we obtain

$$u_p(t) = -P_x \frac{(Y-h)^2}{2}, \tag{138}$$

$$v|_{y=Y} = \dot{h} + \frac{\partial}{\partial x}\left[P_x \frac{(Y-h)^3}{3}\right] - \frac{Y_x}{2} P_x (Y-h)^2 = 0. \tag{139}$$

The plug equation (130) becomes

$$-\int_0^1 P_x Y dx = \mathsf{Bn}. \tag{140}$$

Recalling (134) we have $u_y = 0$ in $x = 0$ implying $P_x|_{x=0} = 0$. The solid region must be detached from $x = 0$, since otherwise $u_p \equiv 0$, i.e. no rigid domain motion. Accordingly there must be some $s(t) \in [0, 1]$, not a priori known, such that $Y(x, t) \equiv 0$, for $0 \le x \le s(t)$. Hence the spatial domain $[0, 1]$ can be split in two sub-domains (see Fig. 23):

- $0 \le x \le s(t)$, where $Y \equiv 0$;
- $s(t) < x \le 1$, where Y does not vanish.

Assuming that the longitudinal velocity is continuous across $s(t)$, we have

$$u_p(t) = -\frac{P_x(s,t)}{2}(\underbrace{Y(s,t)}_{0} - h)^2 = -\frac{P_x(s,t)}{2} h^2, \tag{141}$$

where $P_x(s, t)$ is unknown at this stage. From (139) we get

$$-\dot{h} + \frac{2}{3}\frac{\partial}{\partial x}\Big[\underbrace{-\frac{P_x}{2}(Y-h)^2}_{u_p(t)}(Y-h)\Big] - Y_x \underbrace{\Big[-\frac{P_x}{2}(Y-h)^2\Big]}_{u_p(t)} = 0,$$

that is

$$\dot{h} + \frac{1}{3} u_p(t) Y_x = 0, \tag{142}$$

In order to avoid physical inconsistencies, we set

$$Y(x,t) = \max\left\{0, -\frac{3\dot{h}s(t)}{u_p(t)}\left(\frac{x}{s(t)} - 1\right)\right\}. \tag{143}$$

The local instantaneous discharge is given by

$$Q(x,t) = \int_0^Y u_p dy + \int_Y^h u dy = u_p Y - \frac{P_x(x,t)}{3}(h-Y)^3. \tag{144}$$

Mass conservation then requires $Q(x,t) = -\dot{h}x$, so that $Q(s,t) = -\dot{h}s$ so that

$$u_p(t) = -\frac{3}{2}\frac{\dot{h}}{h}s, \tag{145}$$

which is positive since $\dot{h} < 0$. As a consequence

$$Y(x,t) = \max\left\{0,\ 2h(t)\left(\frac{x}{s(t)} - 1\right)\right\}. \tag{146}$$

Therefore the fluid squeezes out of the channel only if $Y(1,t) < h(t)$, namely when $s(t) > 2/3$. In $x \in [0,s]$ we have $Y = 0$ and the pressure fulfills Eq. (139) with the boundary condition $P_x(0,t) = 0$

$$\begin{cases} P_{xx} = \dfrac{3}{h^3}\dot{h}, \quad 0 < x < s, \quad t \geq 0 \\ \\ P_x(0,t) = 0 \ t \geq 0. \end{cases}$$

Therefore

$$P(x,t) = \frac{3\dot{h}}{2h^3}x^2 + A(t),$$

with $A(t)$ still unknown at this stage. Recalling that Y is linear in x we integrate (138) between x and 1 getting

$$P(x,t) = P_{out} + \frac{3}{2}\dot{h}\left(\frac{s}{h}\right)^3\left[\frac{1}{2-3s} - \frac{1}{2x-3s}\right], \qquad s(t) < x \leq 1. \tag{147}$$

Then imposing the continuity of P across $x = s$ we get

$$P(x,t) = \frac{3\dot{h}}{2h^3}\left(x^2 - s^2\right) + P_{out} - 3\dot{h}\frac{s^2}{h^3}\left(\frac{s-1}{2-3s}\right), \qquad 0 \leq x \leq s(t). \tag{148}$$

Finally rewriting (140) as

$$\int_s^1 P_x Y dx = -\mathsf{Bn},$$

we get

$$f(s) = s^2 \left[\frac{2\,(1-s)}{3s-2} + \ln\left(\frac{3s-2}{s}\right)\right] = -\frac{2}{3}\frac{\mathsf{Bn}h^2}{\dot{h}}. \tag{149}$$

Hence, solving (149) we find $s\,(t)$ and we are able to determine the pressure field in the whole channel and the rigid domain as well. We observe that $s(t)$ is not a material point so that, in principle, $s(t)$ can also be still (i.e. $\dot{s}(t) = 0$), while the rigid plug is moving with velocity $u_p(t)$. Figure 24 shows the behavior of the function $f(s)$ in the l.h.s. of (149) with $s \in (2/3, 1)$. We easily realize that $f(s)$ is monotonically decreasing for $2/3 < s \leq 1$ and that its range is $[0, +\infty)$. So, given any $-(2\mathsf{Bn}h^2)/(3\dot{h}) > 0$, there exists one and only one s fulfilling (149). The force acting on the unit surface of upper plate is

$$P\,(t) = \int_0^1 P\,(x,\,t)\,dx = P_{out} + \frac{\dot{h}s^3}{2h^3}\frac{5-3s}{2-3s} - \frac{3\dot{h}s^3}{4h^3}\ln\left(\frac{3s-2}{s}\right).$$

Exploiting (149) we get

$$P\,(t) - P_{out} = \frac{\mathsf{Bn}}{2}\frac{s}{h} - \dot{h}\left(\frac{s}{h}\right)^3 \frac{1}{(3s-2)}. \tag{150}$$

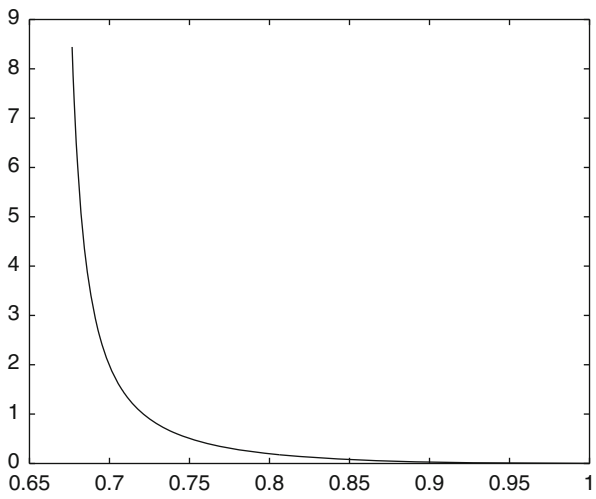

Fig. 24 Behavior of $f\,(s)$ for $2/3 < s \leq 1$

Remark 8 When $\mathsf{Bn} \to 0$, the solution of (149) is simply $s = 1$, i.e. the solid region does not exists at all (as physically expected for a Newtonian fluid). Furthermore formula (150) reduces to

$$P(t) - P_{out} = -\frac{\dot{h}}{h^3},$$

corresponding to the Newtonian fluid planar squeezing, [17]. These results confirms the physical consistency of our model.

6.3 Numerical Simulation

We perform here some numerical simulations to investigate the behavior of our asymptotic solution at the leading order. To illustrate the dependence of the solution on the Bingham number we consider the cases: $\mathsf{Bn} = 1$ and $\mathsf{Bn} = 25$. We plot the yield surface Y, the pressure field P and the axial velocity u, assuming that the plates have constant velocity so that

$$h(t) = 1 - t, \qquad \dot{h}(t) = -1. \tag{151}$$

We consider $t \in [0, 0.6]$, which guarantees that the plates do not come in touch in the select time interval. We set $h_f = h(0.6)$, representing the half gap width at time $t_f = 0.6$ and $s_f = s(0.6)$ representing the onset of the rigid plug at time $t = 0.6$. The yield surface Y and pressure field P are plotted for different times t belonging to the selected time interval and for $x \in [0, 1]$. The axial velocity u is plotted at time $t = 0.6$ (i.e. when $h = h_f$) for a finite number of $x \in [s_f, 1]$ and for y ranging in $[0, h_f]$.

In Figs. 25, 26 we have plotted the yield surface $Y(x, t)$ and the upper plate $y = h(t)$ at different times in the time interval $[0, t_f]$. We have plotted the upper plate only for $x \in [s(t), 1]$ so that the evolution of the onset of the plug $x = s(t)$ is visible. We notice that the slope of the unyielded plug becomes smaller as $s(t)$ increases, as expected. In Figs. 27, 28 we have plotted the pressure field at different times in the time interval $[0, t_f]$ in the whole domain $x \in [0, 1]$. Also for this case the position $x = s(t)$ has been put in evidence. We notice that the pressure within the gap increases as Bn increases.

In Figs. 29, 30 we have plot the axial velocity profile at time $t = 0.6$ for some fixed $x \in [s_f, 1]$. In particular velocity is plotted for $x = 0.69$, $x = 0.73$, $x = 0.77$, $x = 0.81$, $x = 0.85$. As one can easily observe the velocity of the plug is the same for each (x, y) belonging to the plug.

Finally in Figs. 31, 32 we have plotted the squeeze force given in (150) for different values of the Bingham number, Bn. We have plotted (150) for the linear

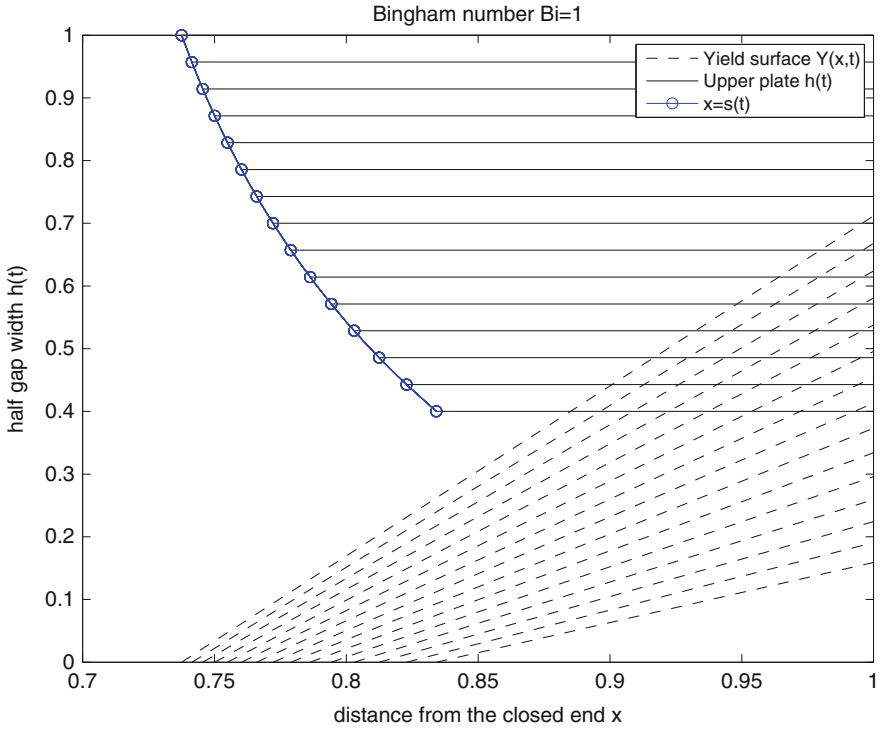

Fig. 25 Y for $\mathsf{Bn} = 1$ and h given by (151)

squeezing (151) and for the exponential squeezing

$$h(t) = \exp(-t), \qquad \dot{h}(t) = -\exp(-t). \tag{152}$$

We observe that the linear squeezing requires a grater squeezing force than the exponential squeezing. This is physically consistent, since in the linear case the plates move faster than in the exponential case.

6.4 Squeezing Between Surfaces

In this section we generalize the problem to the case in which the parallel plates are surfaces $y = \pm h(x, t)$ that are approaching the channel centerline, as shown in Fig. 33. In this case

$$H = \max_{\substack{x\in[0,L]\\ t>0}} h(x, t),$$

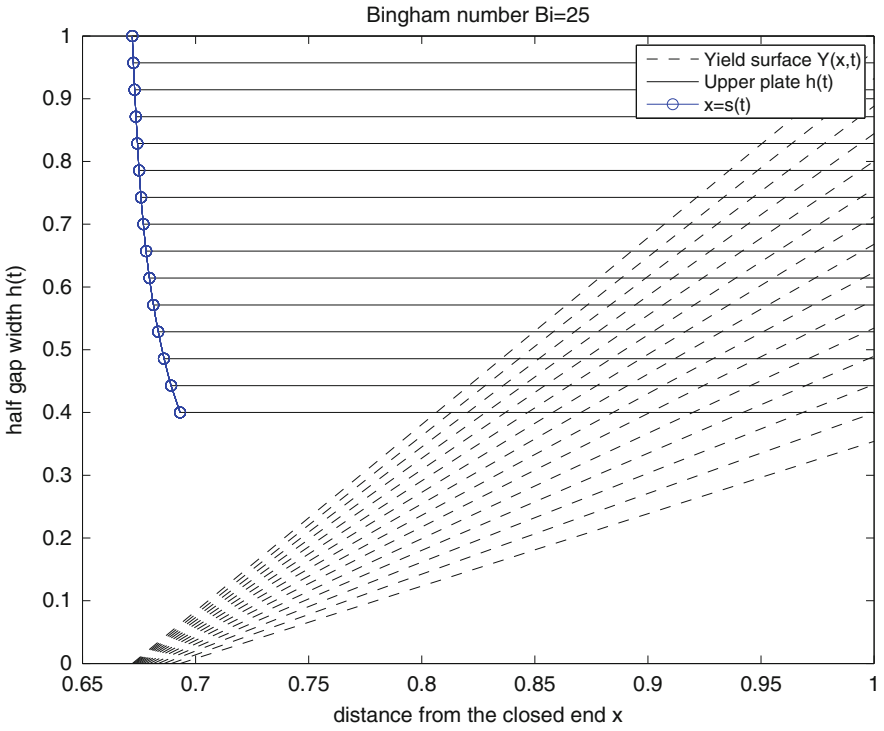

Fig. 26 Y for $\mathsf{Bn} = 25$ and h given by (151)

and we again assume $H/L = \varepsilon \ll 1$. The theory develops exactly as in Sect. 6.1, so that (140) still holds. We split $[0, 1]$ into $[0, s]$ and $[s, 1]$, so that continuity of u across $s\,(t)$ yields

$$u_p(t) = -\frac{P_x\,(s,t)}{2} h(s,t)^2.$$

Recalling (139) we find

$$h_t + \frac{1}{3} u_p(t) Y_x + \frac{2}{3} u_p(t) h_x = 0,$$

which generalizes (142). We thus get the following Cauchy problem

$$\begin{cases} Y_x = \dfrac{3}{u_p}\left[-h_t - \dfrac{2}{3} u_p h_x\right], \\ \\ Y(s,t) = 0, \end{cases}$$

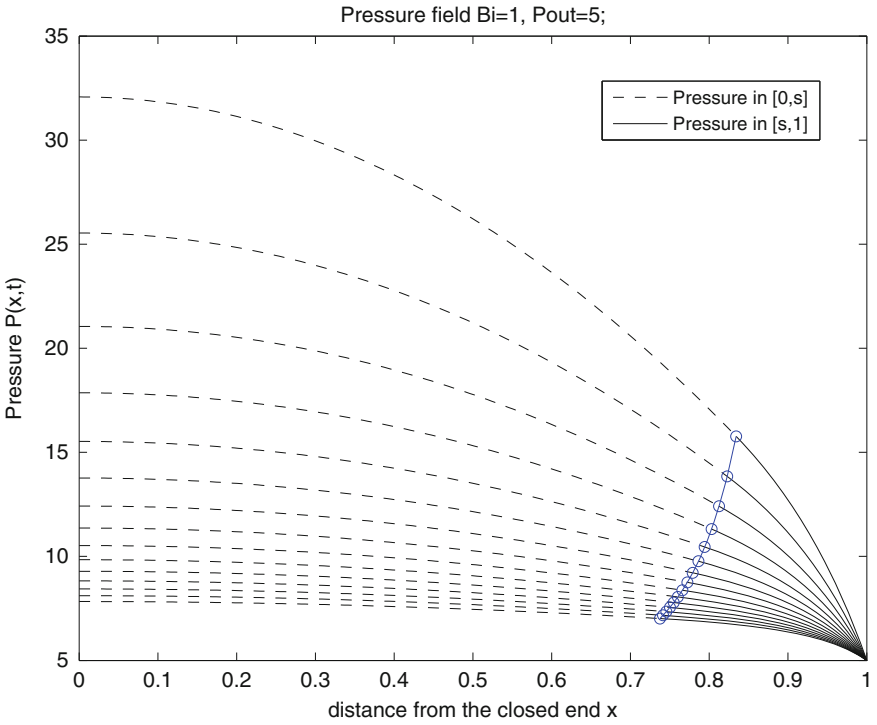

Fig. 27 P for $\mathsf{Bn} = 1$ and h given by (151)

whose solution is

$$Y(x,t) = \frac{3}{u_p}\left[-\int_s^x h_t d\xi - \frac{2}{3}u_p(h(x,t) - h(s,t))\right], \tag{153}$$

where s is still unknown. Following (143) we set

$$Y(x,t) = \max\left\{0, \ -\frac{3}{u_p}\int_s^x h_t d\xi - 2(h(x,t) - h(s,t))\right\}. \tag{154}$$

The local discharge is

$$Q(x,t) = \underbrace{\int_0^Y u_p dy}_{u_p Y} + \underbrace{\int_Y^h \left[-P_x \frac{(h-y)(y-2Y+h)}{2}\right] dy}_{-\frac{P_x(x,t)}{3}(h-Y)^3},$$

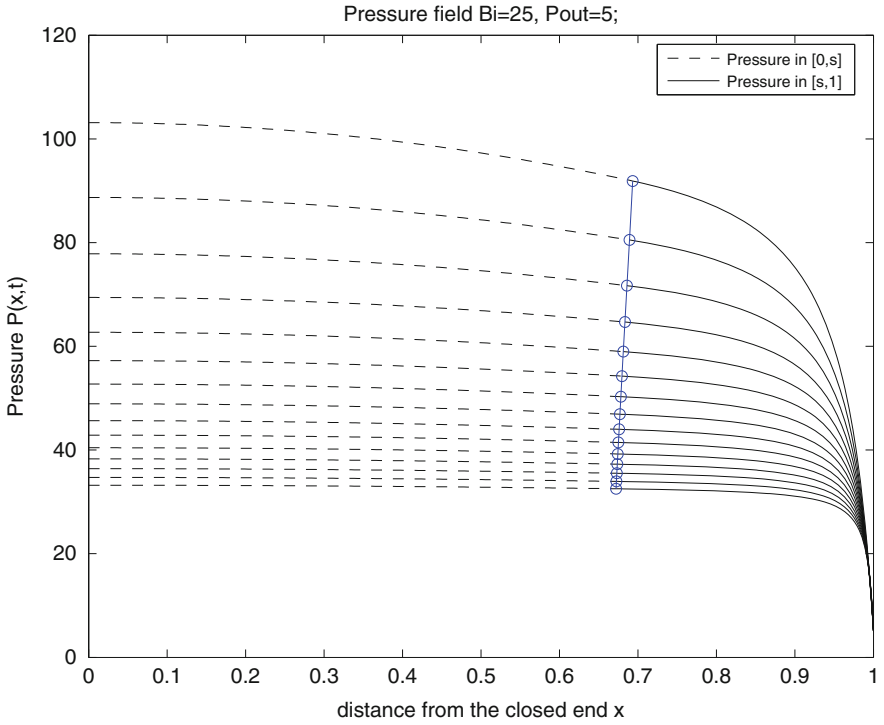

Fig. 28 P for $\mathsf{Bn} = 25$ and h given by (151)

while mass conservation $h_t + Q_x = 0$ implies

$$Q(x,t) = -\int_0^x h_t d\xi,$$

since $Q(0,t) = 0$. We find

$$Q(s,t) = -\int_0^s h_t d\xi = \underbrace{-\frac{P_x(s,t)h^2(s,t)}{2}}_{u_p} \frac{2h(s,t)}{3},$$

implying

$$u_p(t) = -\frac{3}{2}\frac{1}{h(s,t)}\int_0^s h_t d\xi, \tag{155}$$

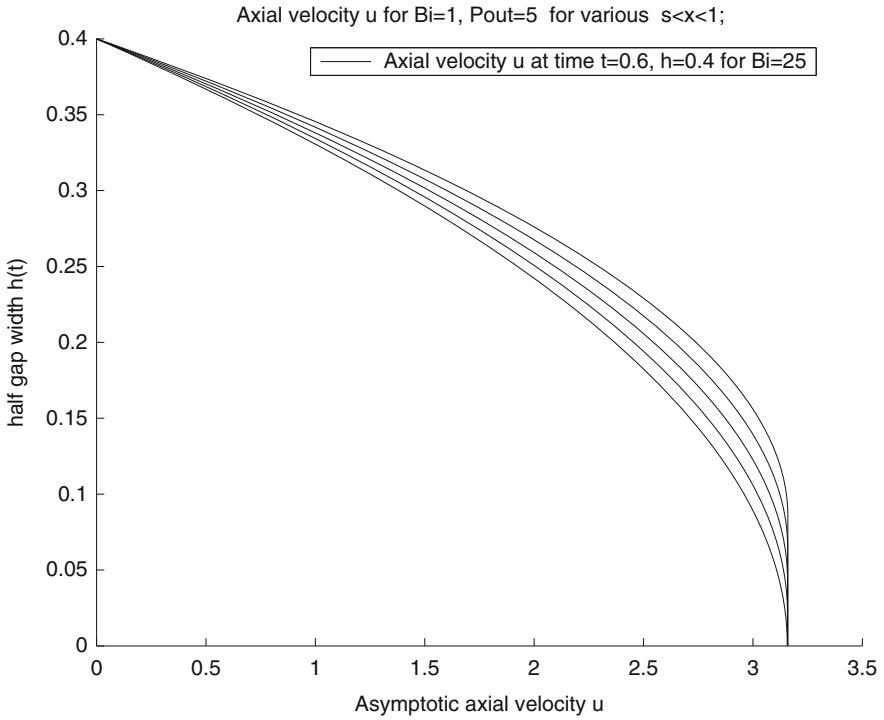

Fig. 29 u for $\mathsf{Bn} = 1$ and h given by (151)

which is the generalization of (145). In conclusion, substituting (155) into (154), we find

$$Y(x,t) = \max\left\{0, \ -2h(x,t) + 2h(s,t)\frac{\int_0^x h_t d\xi}{\int_0^s h_t d\xi}\right\}. \tag{156}$$

In $x \in [0, s]$ the pressure fulfils

$$\begin{cases} -h_t + \dfrac{\partial}{\partial x}\left[P_x \dfrac{h^3}{3}\right] = 0, & 0 < x < s(t), \\ & t \geq 0, \\ P_x(0,t) = 0, & t \geq 0, \end{cases} \tag{157}$$

so that

$$P(x,t) = \int_0^x \left[\frac{3}{h(\tilde{x},t)^3}\int_0^{\tilde{x}} h_t d\xi\right] d\tilde{x} + A(t), \tag{158}$$

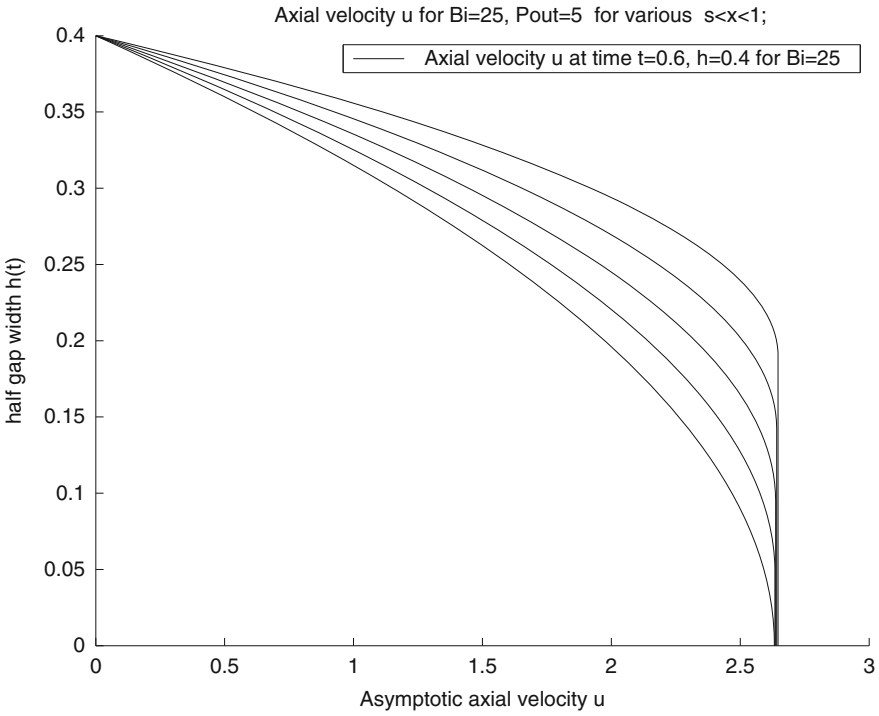

Fig. 30 u for $\mathsf{Bn} = 25$ and h given by (151)

with $A(t)$ to be determined. In $x \in [s, 1]$ we have

$$P_x(x,t) = -\frac{2u_p(t)}{(h-Y)^2},$$

so that

$$P_x = \frac{3}{h(s,t)\left[h(x,t) - Y(x,t)\right]^2} \int_0^s h_t d\xi, \tag{159}$$

with Y given by (156). We observe that (157) and (159) yield $P_x|_{s^-} = P_x|_{s^+}$. Let us now integrate (159) between x and 1 with the boundary condition $P(1,t) = P_{out}$. We find

$$P_{out} - P(x,t) = \frac{3}{h(s,t)} \int_0^s h_t d\xi \left[\int_x^1 \frac{d\tilde{x}}{\left(h(\tilde{x},t) - Y(\tilde{x},t)\right)^2} \right] \tag{160}$$

Imposing $P|_{s^-} = P|_{s^+}$, from (158), (160) we find $A(t)$, so that the pressure can be written in terms of s throughout the whole domain. Substituting (156) and (159)

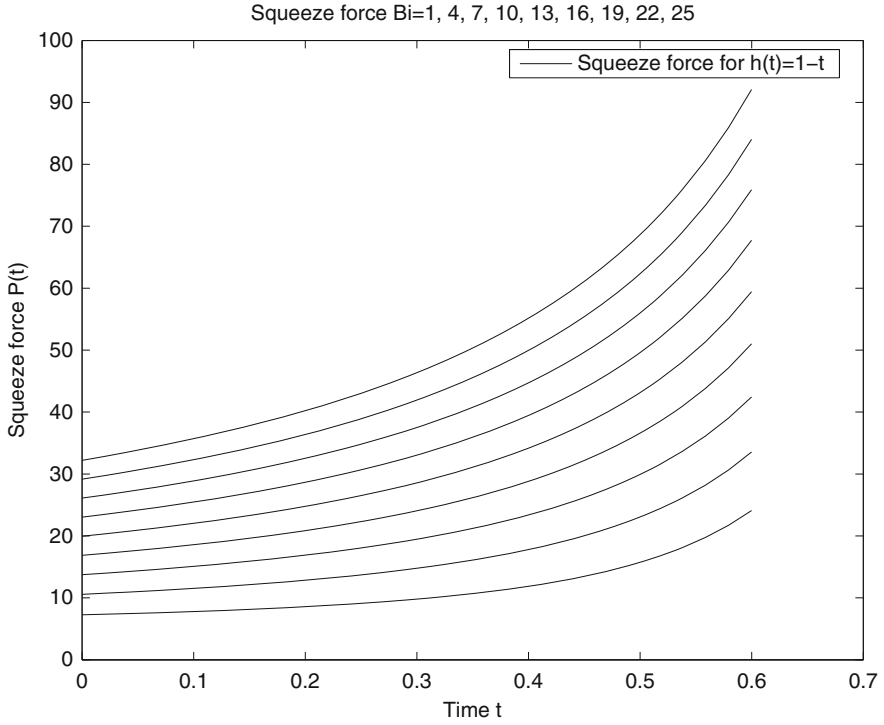

Fig. 31 Squeeze force for linear $h(t)$, (151)

into (140) we get

$$\int_s^1 \frac{\left[-2h(\tilde{x},t)+2h(s,t)\dfrac{\int_0^{\tilde{x}} h_t d\xi}{\int_0^s h_t d\xi}\right]_+}{\left[h(\tilde{x},t)-\left[-2h(\tilde{x},t)+2h(s,t)\dfrac{\int_0^{\tilde{x}} h_t d\xi}{\int_0^s h_t d\xi}\right]_+\right]^2} d\tilde{x} = -\frac{\mathrm{Bn}}{\left[\dfrac{3}{h(s,t)}\int_0^s h_t d\xi\right]}, \tag{161}$$

which provides an integral equation for the unknown $s(t)$. Equation (161) can be solved once we know the explicit form of the function $h(x,t)$.

When $h(x,t) = f(x)g(t)$, with $f \cdot g > 0$, then (161) can be rewritten as

$$\left(\int_0^s f d\xi\right)^2 \int_s^1 \frac{\left[-f(\tilde{x})\left(\int_0^s f d\xi\right)+f(s)\left(\int_0^{\tilde{x}} f d\xi\right)\right]_+ d\tilde{x}}{\left[\dfrac{f(\tilde{x})}{2}\left(\int_0^s f d\xi\right)-\left[-f(\tilde{x})\left(\int_0^s f d\xi\right)+f(s)\left(\int_0^{\tilde{x}} f d\xi\right)\right]_+\right]^2}$$
$$= -\frac{2\mathrm{Bn} f(s) g(t)^2}{3\dot{g}(t)}. \tag{162}$$

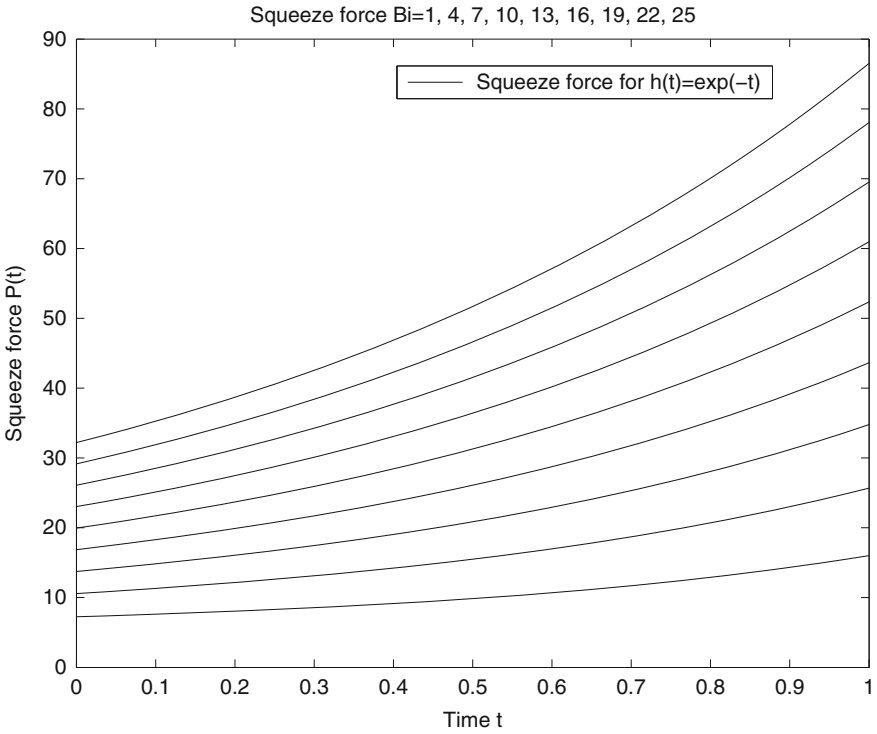

Fig. 32 Squeeze force for exponential $h(t)$, (152)

Example 7 Let us consider

$$h(x,t) = f(x)g(t), \quad \text{with} \quad f(x) = e^{-\beta x}, \quad g(t) = e^{-\alpha t},$$

where α, and β both positive. Exploiting (162) we find

$$\frac{4(1-e^{-\beta s})^2}{\beta}\int_s^1 \frac{(e^{-\beta s}-e^{-\beta x})}{\left[e^{-\beta x}(3-e^{-\beta s})-2e^{-\beta s}\right]^2}dx = \left(\frac{2\mathsf{Bn}}{3\alpha}\right)e^{-\beta s}e^{-\alpha t}. \tag{163}$$

or equivalently

$$\underbrace{\frac{(1-e^{-\beta s})^2}{\beta^2 e^{-2\beta s}}\left[\ln\frac{|2+e^{-\beta}-3e^{\beta(s-1)}|}{|e^{-\beta}-e^{\beta(s-1)}|}+\frac{2(e^{\beta(s-1)}-1)}{2+e^{-\beta}-3e^{\beta(s-1)}}\right]}_{\mathscr{G}(s)} = \left(\frac{2\mathsf{Bn}}{3\alpha}\right)e^{-\alpha t}, \tag{164}$$

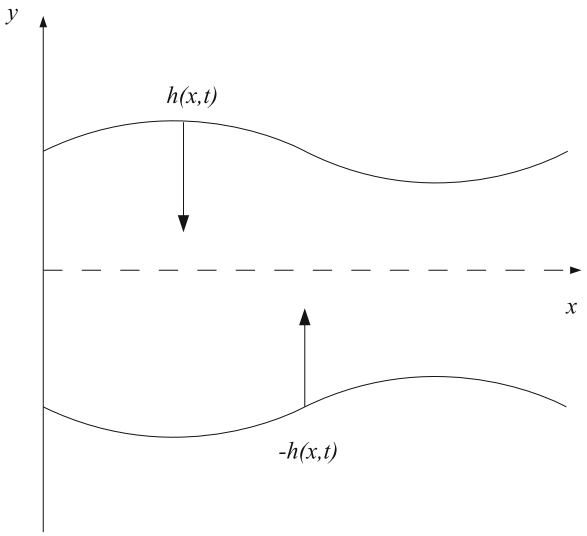

Fig. 33 A schematic representation of the squeezing channel

which is an implicit equation for $s(t)$. Notice that taking the limit $\beta \to 0$ of the l.h.s. of (164) we recover the l.h.s. of (149), as expected. We immediately realize that (164) admits a unique solution $s(t) \in (\hat{s}(\beta), 1]$, with

$$\hat{s}(\beta) = 1 + \frac{1}{\beta} \ln \left[\frac{e^{-\beta} + 2}{3} \right],$$

for each value of $(2\mathsf{Bn}/3\alpha)\, e^{-\alpha t}$. In particular it is easy to show that

$$\frac{2}{3} < \hat{s}(\beta) < 1, \qquad \forall \beta > 0,$$

so that $s \in (2/3, 1)$ for all $t > 0$. Recalling (156) we get

$$Y(x,t) = 2e^{-\alpha t} \left[\frac{e^{-\beta s} - e^{-\beta x}}{(1 - e^{-\beta s})} \right]. \tag{165}$$

Clearly $Y > 0$ for every $x > s$, and $Y = 0$ at $x = s$. Actually we can show that Y and h never meets. Indeed, suppose that $Y(x,t) < h(x,t)$, then

$$2 \left[\frac{e^{-\beta s} - e^{-\beta x}}{(1 - e^{-\beta s})} \right] < e^{-\beta x},$$

or analogously

$$2e^{\beta x} < 3e^{\beta s} - 1. \tag{166}$$

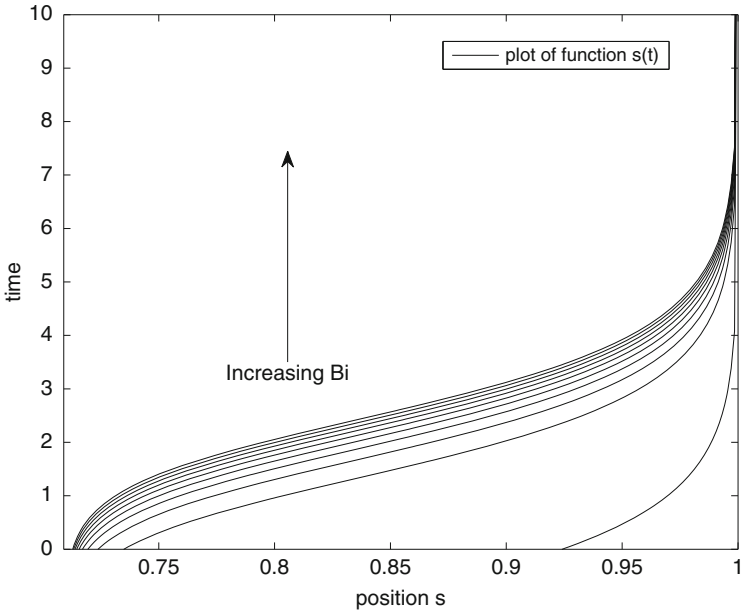

Fig. 34 The advance of the front $x = s(t)$ for Bn ranging between 0.1 and 100

Hence $Y < h$ if and only if (166) holds true for each $x \geq s$. Now recall that $s \geq \hat{s}(\beta) > 2/3$, for every finite time $t > 0$ and $\beta > 0$. Therefore

$$2e^{\beta x} \leq \max_{x\in[s,1]} \{2e^{\beta x}\} = 2e^{\beta} = 3e^{\beta\hat{s}} - 1 < 3e^{\beta s} - 1,$$

which proves that (166) holds true. As a consequence we get

$$0 \leq Y(x,t) < h(x,t), \quad \forall\ x \geq s, \quad t > 0.$$

We observe that $Y \to h$, which in turn tends to 0, only in the limit $t \to \infty$. In Fig. 34 we have plot the advancing front $x = s(t)$ for different values of Bn ranging from $\mathrm{Bn} = 0.1$ to $\mathrm{Bn} = 100$. The parameters used are $\alpha = 2$ and $\beta = 0.4$.

References

1. Bingham, E.C.: An investigation of the laws of plastic flow. U.S. Bur. Stand. Bull. **13**, 309–353 (1916)
2. Bingham, E.C.: Fluidity and Plasticity. McGraw Hill, New York (1922)
3. Coirier, J.: Mécanique des Milieux Continus. Dunod, Paris (1997)
4. Comparini, E.: A one-dimensional Bingham flow. J. Math. Anal. Appl. **169**, 127–139 (1992)

5. Coussot, P.: Yield stress fluid flows: a review of experimental data. J. Non-Newtonian Fluid Mech. **211**, 31–49 (2014)
6. Frigaard, I.A., Ryanb, D.P.: Flow of a visco-plastic fluid in a channel of slowly varying width. J. Non-Newtonian Fluid Mech. **123**, 67–83 (2004)
7. Fusi, L., Farina, A.: An extension of the Bingham model to the case of an elastic core. Adv. Math. Sci. Appl. **13**, 113–163 (2003)
8. Fusi, L., Farina, A.: A mathematical model for Bingham-like fluids with visco-elastic core. ZAMP **55**, 826–847 (2004)
9. Fusi, L., Farina, A.: Modelling of Bingham-like fluids with deformable core. Comput. Math. Appl. **53**, 583–594 (2007)
10. Fusi, L., Farina, A., Rosso, F.: Flow of a Bingham-like fluid in a finite channel of varying width: a two-scale approach. J. Non-Newtonian Fluid Mech. **177–178**, 76–88 (2012)
11. Fusi, L., Farina, A., Rosso F.: Retrieving the Bingham model from a bi-viscous model: some explanatory remarks. Appl. Math. Lett. **27**, 11–14 (2014)
12. Fusi, L., Farina, A., Rosso, F., Roscani, S.: Pressure driven lubrication flow of a Bingham fluid in a channel: a novel approach. J. Non-Newtonian Fluid Mech. **221** 66–75 (2015)
13. Hormozi, S., Dunbrack, G., Frigaard, I.A.: Visco-plastic sculpting. Phys. Fluids **26** (2014). http://dx.doi.org/10.1063/1.4894076
14. Huilgol, R.R.: Fluid Mechanics of Viscoplasticity. Springer, Berlin (2015)
15. Ionescu, I.R., Sofonea, M.: Functional and Numerical Methods in Viscoplasticity. Oxford University Press, Oxford (1993)
16. Joshi, S.C., Lam, Y.C., Boey, F.Y.C., Tok, A.I.Y.: Power law fluids and Bingham plastics flow models for ceramic tape casting. J. Materials Process. Technol. **120**, 215–225 (2002)
17. Lipscomb, G.G., Denn, M.M.: Flow of Bingham fluids in complex geometries. J. Non-Newtonian Fluid Mech. **14**, 337–346 (1984)
18. Liu, K., Mei, C.C.: Roll waves on a layer of a muddy fluid flowing down a gentle slope - a Bingham model. Phys. Fluids **6**, 2577–2590 (1994)
19. Muravleva, L.: Squeeze plane flow of viscoplastic Bingham material. J. Non-Newtonian Fluid Mech. **220**, 148–161 (2015)
20. Oldroyd, S.G.: A rational formulation of the equation of plastic flow for Bingham solid. Proc. Camb. Philos. Soc. **45**, 100–105 (1947)
21. Putz, A., Frigaard, I.A., Martinez, D.M.: On the lubrication paradox and the use of regularisation methods for lubrication flows. J. Non-Newtonian Fluid Mech. **163**, 62–77 (2009)
22. Rajagopal, K.R.: On implicit constitutive theories. Appl. Math. **48**, 279–319 (2003)
23. Rajagopal, K.R.: On implicit constitutive theories for fluids. J. Fluid Mech. **550**, 243–249 (2006)
24. Rajagopal, K.R., Srinivasa, A.R.: A thermodynamic frame work for rate type fluid models. J. Non-Newtonian Fluid Mech. **88**, 207–227 (2000)
25. Rajagopal, K.R., Srinivasa, A.R.: On the thermomechanics of materials that have multiple natural configurations Part I: viscoelasticity and classical plasticity. ZAMP **55**, 861–893 (2004)
26. Rajagopal, K.R., Srinivasa, A.R.: On the thermodynamics of fluids defined by implicit constitutive relations. ZAMP **59**, 715–729 (2008)
27. Roussel, N., Lanos, C.: Plastic fluid flow parameters identification using a simple squeezing test. Appl. Rheol. **13**, 132–141 (2003)
28. Rubinstein, L.I.: The Stefan Problem. Translations of Mathematical Monographs, vol. 27. American Mathematical Society, Providence, RI (1971)
29. Safronchik, A.I.: Nonstationary flow of a visco-plastic material between parallel walls. J. Appl. Math. Mech. **23**, 1314–1327 (1959)
30. Von Mises R., Mechanik der festen Körper im plastisch deformablen Zustand, Göttin. Nachr. Math. Phys. **1**, 582–592 (1913)
31. Wardhaugh, L.T., Boger, D.V.: Flow characteristics of waxy crude oils: application to pipeline design. AIChE J. **6**, 871–885 (1991)
32. Yoshimura, A.S., Prud'homme, R.K.: Response of an elastic Bingham fluid to oscillatory shear. Rheol. Acta **26**, 428–436 (1987)

Correction to: Non-Newtonian Fluid Mechanics and Complex Flows

Angiolo Farina, Lorenzo Fusi, Andro Mikelić, Giuseppe Saccomandi, Adélia Sequeira, and Eleuterio F. Toro

Correction to:
A. Farina et al. (eds.), *Non-Newtonian Fluid Mechanics and Complex Flows*, Lecture Notes in Mathematics 2212, https://doi.org/10.1007/978-3-319-74796-5

This book was inadvertly published where second author Lorenzo Fusi was missed to be added on the copyright page.

This has now been appended in the copyright page to reflect as

Lorenzo Fusi
Dipartimento di Matematica e
Informatica “Ulisse Dini”
Università degli Studi di Firenze
Firenze, Italy

The updated online version of the book can be found at
https://doi.org/10.1007/978-3-319-74796-5

A. Farina et al. (eds.), *Non-Newtonian Fluid Mechanics and Complex Flows*,
Lecture Notes in Mathematics 2212, https://doi.org/10.1007/978-3-319-74796-5_6

LECTURE NOTES IN MATHEMATICS Springer

Editors in Chief: J.-M. Morel, B. Teissier;

Editorial Policy

1. Lecture Notes aim to report new developments in all areas of mathematics and their applications – quickly, informally and at a high level. Mathematical texts analysing new developments in modelling and numerical simulation are welcome.

   Manuscripts should be reasonably self-contained and rounded off. Thus they may, and often will, present not only results of the author but also related work by other people. They may be based on specialised lecture courses. Furthermore, the manuscripts should provide sufficient motivation, examples and applications. This clearly distinguishes Lecture Notes from journal articles or technical reports which normally are very concise. Articles intended for a journal but too long to be accepted by most journals, usually do not have this "lecture notes" character. For similar reasons it is unusual for doctoral theses to be accepted for the Lecture Notes series, though habilitation theses may be appropriate.

2. Besides monographs, multi-author manuscripts resulting from SUMMER SCHOOLS or similar INTENSIVE COURSES are welcome, provided their objective was held to present an active mathematical topic to an audience at the beginning or intermediate graduate level (a list of participants should be provided).

   The resulting manuscript should not be just a collection of course notes, but should require advance planning and coordination among the main lecturers. The subject matter should dictate the structure of the book. This structure should be motivated and explained in a scientific introduction, and the notation, references, index and formulation of results should be, if possible, unified by the editors. Each contribution should have an abstract and an introduction referring to the other contributions. In other words, more preparatory work must go into a multi-authored volume than simply assembling a disparate collection of papers, communicated at the event.

3. Manuscripts should be submitted either online at www.editorialmanager.com/lnm to Springer's mathematics editorial in Heidelberg, or electronically to one of the series editors. Authors should be aware that incomplete or insufficiently close-to-final manuscripts almost always result in longer refereeing times and nevertheless unclear referees' recommendations, making further refereeing of a final draft necessary. The strict minimum amount of material that will be considered should include a detailed outline describing the planned contents of each chapter, a bibliography and several sample chapters. Parallel submission of a manuscript to another publisher while under consideration for LNM is not acceptable and can lead to rejection.

4. In general, **monographs** will be sent out to at least 2 external referees for evaluation.

   A final decision to publish can be made only on the basis of the complete manuscript, however a refereeing process leading to a preliminary decision can be based on a pre-final or incomplete manuscript.

   Volume Editors of **multi-author works** are expected to arrange for the refereeing, to the usual scientific standards, of the individual contributions. If the resulting reports can be

forwarded to the LNM Editorial Board, this is very helpful. If no reports are forwarded or if other questions remain unclear in respect of homogeneity etc, the series editors may wish to consult external referees for an overall evaluation of the volume.

5. Manuscripts should in general be submitted in English. Final manuscripts should contain at least 100 pages of mathematical text and should always include
   - a table of contents;
   - an informative introduction, with adequate motivation and perhaps some historical remarks: it should be accessible to a reader not intimately familiar with the topic treated;
   - a subject index: as a rule this is genuinely helpful for the reader.
   - For evaluation purposes, manuscripts should be submitted as pdf files.

6. Careful preparation of the manuscripts will help keep production time short besides ensuring satisfactory appearance of the finished book in print and online. After acceptance of the manuscript authors will be asked to prepare the final LaTeX source files (see LaTeX templates online: https://www.springer.com/gb/authors-editors/book-authors-editors/manuscriptpreparation/5636) plus the corresponding pdf- or zipped ps-file. The LaTeX source files are essential for producing the full-text online version of the book, see http://link.springer.com/bookseries/304 for the existing online volumes of LNM). The technical production of a Lecture Notes volume takes approximately 12 weeks. Additional instructions, if necessary, are available on request from lnm@springer.com.

7. Authors receive a total of 30 free copies of their volume and free access to their book on SpringerLink, but no royalties. They are entitled to a discount of 33.3 % on the price of Springer books purchased for their personal use, if ordering directly from Springer.

8. Commitment to publish is made by a *Publishing Agreement*; contributing authors of multiauthor books are requested to sign a *Consent to Publish form*. Springer-Verlag registers the copyright for each volume. Authors are free to reuse material contained in their LNM volumes in later publications: a brief written (or e-mail) request for formal permission is sufficient.

Addresses:
Professor Jean-Michel Morel, CMLA, École Normale Supérieure de Cachan, France
E-mail: moreljeanmichel@gmail.com

Professor Bernard Teissier, Equipe Géométrie et Dynamique,
Institut de Mathématiques de Jussieu – Paris Rive Gauche, Paris, France
E-mail: bernard.teissier@imj-prg.fr

Springer: Ute McCrory, Mathematics, Heidelberg, Germany,
E-mail: lnm@springer.com